

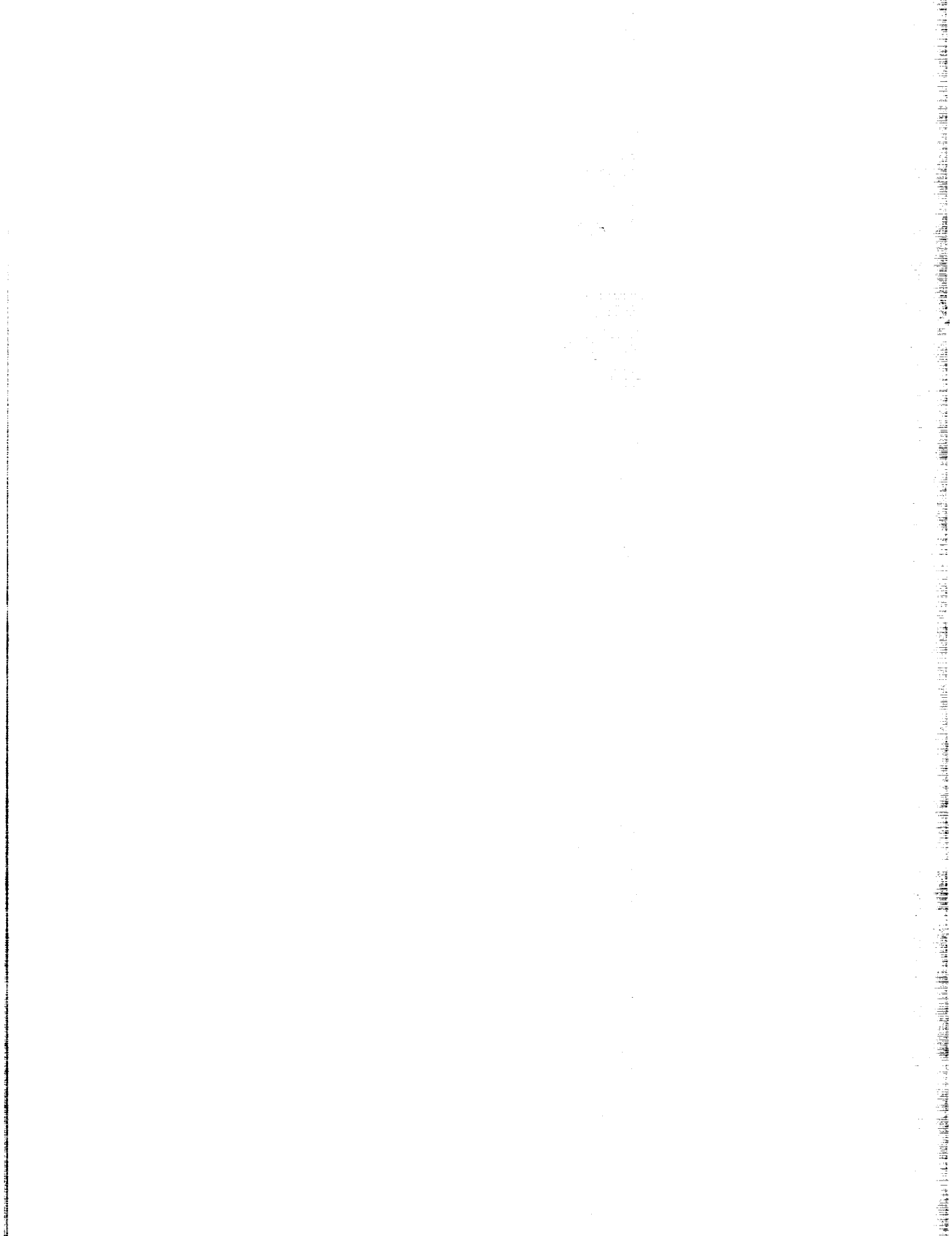
NASA Conference Publication 3157

Current Technology for Thermal Protection Systems

(NASA-CP-71-147) CURRENT TECHNOLOGY
FOR THERMAL PROTECTION SYSTEMS
(NASA) 381 p

93-12447
--THRU--
N93-12460
Unclas

H1/18 0123630



NASA Conference Publication 3157

Current Technology for Thermal Protection Systems

Compiled by
Stephen J. Scotti
NASA Langley Research Center
Hampton, Virginia

Proceedings of a workshop sponsored by the
National Aeronautics and Space Administration,
Washington, D.C., and held at
Langley Research Center
Hampton, Virginia
February 11–12, 1992

NASA

National Aeronautics and
Space Administration

Office of Management

Scientific and Technical
Information Program

1992

PREFACE

Interest in thermal protection systems (TPS) for high-speed vehicles is increasing because of the stringent requirements of proposed new projects such as the Space Exploration Initiative, the National Aero-Space Plane, and the High-Speed Civil Transport, as well as the needs for improved capabilities in existing thermal protection systems for the Space Shuttle and for turbojet engines. As new aerospace systems become more complicated and the operational requirements more severe, workers within one discipline will need greater understanding of the fundamental problems of other disciplines. A TPS design, though nominally satisfying only thermal requirements, impacts many other disciplines. For example, a thermal protection system designer needs to know the structural temperature limits and the operational requirements (i.e., inspectability, damage tolerance, and repairability) of the TPS. A computational fluid mechanics technologist needs to know the surface temperature conditions and possibly the surface catalycity when he calculates thermal loads. A materials scientist developing high-temperature coatings needs to know the oxidizing environment of the flow. A structural designer needs to know the structural support requirements of the TPS. The list goes on, and the interactions become even more complex, especially when hot structures or actively cooled structures are considered.

The present collection of papers on TPS resulted from a workshop held at NASA Langley Research Center in February 1992. The Langley Thermophysics Committee sponsored the "Current Technology for Thermal Protection Systems" workshop in response to the need for improved understanding of TPS technology by all the disciplines involved in high-speed research. To achieve the technical level desired for the workshop, only a limited number of presenters from both NASA and industry were invited to participate in the workshop. Most of the 13 papers in the present collection are presented at a level such that someone with a technical background can understand the fundamental problems and the approaches taken in the development of TPS for high-speed vehicles. The papers can be divided into four categories: (1) NASA's historical and operational experience with TPS from the X-15 and Mercury programs to the Space Shuttle; (2) development of external ceramic and metallic thermal protection systems (i.e., those designed to be the aerodynamic surfaces of a vehicle); (3) refractory materials and coatings; and (4) actively cooled, and two-phase thermal control systems.

In reviewing this collection of papers, an observation regarding thermal protection systems for high-speed vehicles can be made. Even the best thermal protection system is never adequate. As soon as one requirement, such as a reuse-temperature goal, is met, additional requirements, such as improved durability or reduced weight, are forced upon the TPS designer to improve overall vehicle performance, or to allow for new applications. Despite the years of research that have been devoted to thermal protection systems, additional progress will be required for future thermal protection systems.

The Langley Thermophysics Committee (1991-1992)

Obie H. Bradley, Jr., Chairman
Johnny W. Allred
Dr. Ronald K. Clark
Dr. John J. Korte
Dennis H. Petley
Stephen J. Scotti
Robert E. Wright, Jr.
E. Vincent Zoby

Certain materials and processes are identified in this publication in order to adequately specify procedures. In no case does such identification imply recommendation or endorsement by the government, nor does it imply that the materials or processes are the only or best ones available for the purpose.

CONTENTS

Preface	iii
The Langley Thermophysics Committee (1991-1992)	iv
Reusable Thermal Protection System Development—a Prospective Howard Goldstein	1
Thermal Protection Systems—Manned Spacecraft Flight Experience Donald M. Curry	19
Advanced Ceramic Matrix Composites For TPS Daniel J. Rasky	43
Thermal Protection Using Very High Temperature Ceramics George R. Adamczyk	63
Superplastic Forming of Ceramic Insulation T. G. Nieh, J. P. Wittenauer, and J. Wadsworth	77
Ceramic TBS/Porous Metal Compliant Layer Robert P. Tolokan and G. P. Jarrabet	89
Predicted and Tested Performance of Durable TPS John L. Shideler	97
Recent Advances in Carbon-Carbon Substrate Technology at NASA Langley Research Center Philip O. Ransone, Y. Robert Yamaki, and Howard G. Maahs	131
Current Research in Oxidation-Resistant Carbon-Carbon Composites at NASA Langley Craig W. Ohlhorst, W. L. Vaughan, and D. M. Barrett	149
Thermal Control/Oxidation Resistant Coatings for Titanium-Based Alloys Ronald K. Clark, Terryl A. Wallace, George R. Cunningham, and Karl E. Wiedemann	169
Active Cooling from the Sixties to NASP H. Neale Kelly and Max L. Blosser	189
Advanced Two-Phase Heat Transfer Systems Theodore D. Swanson	251
Thermostructural Applications of Heat Pipes for Cooling Leading Edges of High-Speed Aerospace Vehicles Charles J. Camarda and David E. Glass	291
Attendees	319

REUSABLE THERMAL PROTECTION SYSTEM DEVELOPMENT - A PROSPECTIVE

Howard Goldstein

NASA Ames Research Center
Moffett Field, California

ABSTRACT

This paper describes the state of the art in passive reusable thermal protection system materials. Development of the Space Shuttle Orbiter, which was the first reusable space vehicle, is discussed. The thermal protection materials and design concepts and some of the shuttle development and manufacturing problems are described. Evolution of a family of rigid and flexible ceramic external insulation materials from the initial shuttle concept in the early 1970s to the present time is described. The important properties and their evolution are documented. Application of these materials to vehicles currently being developed and plans for research to meet the space programs future needs are summarized.

INTRODUCTION

Three types of passive thermal protection systems have been developed over the not very long history of supersonic/hypersonic flight. These include heat sinks which store the incoming heat, ablative thermal protection systems which dissipate the heat by decomposing and reradiating it to the environment, and insulative systems which reradiate nearly all the heat to the environment. In the early days of hypersonic flight the first two thermal protection schemes were used most of the time because they were self regulating, could be designed with a large margin of safety to compensate for the unknowns in the entry heating environment and were capable of surviving the high heat fluxes experienced by ballistic reentry vehicles. Most used ablative thermal protection including Apollo, Gemini, Viking and virtually all ballistic missiles. A few, such as PAET, used heat sink. In the sixties research on reusable manned high L/D reentry vehicles was initiated. Many potential reusable thermal protection systems were studied. It was found that for manned reentry vehicles which experienced mild heating environments, a passive insulation system was the most weight efficient and generally the safest. Active thermal protection concepts, which are used in propulsion systems and have been studied extensively for manned reentry vehicles, are discussed by others in this workshop.

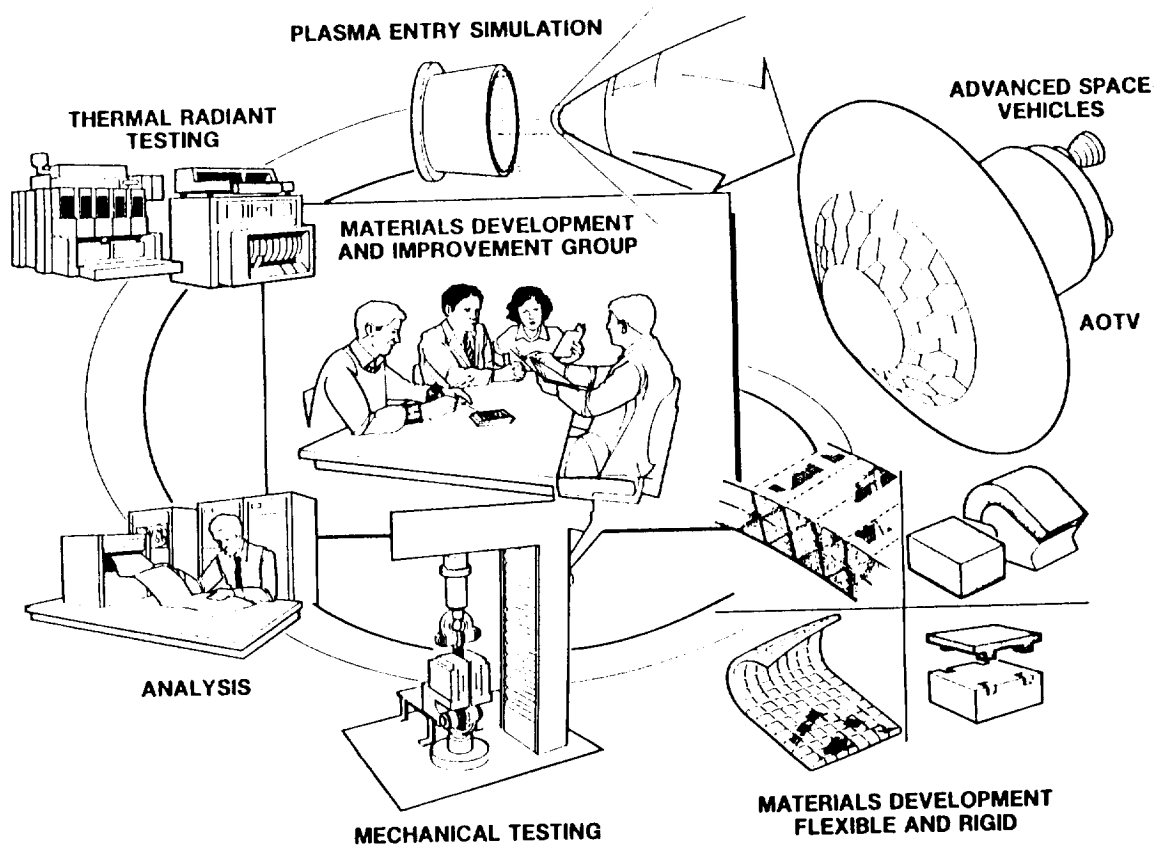
Passive insulation systems can be divided into two groups: the load carrying hot structure type of TPS, such as carbon/carbon, which requires an insulator under it to protect the cold structure, and the surface insulation type which is nonload carrying but transmits the aerodynamic loads to the structure through a strain isolator and is itself the thermal protection system. Both metallic and ceramic insulations have been studied. In this paper I will discuss the ceramic Reusable Surface Insulation (RSI), which is the type primarily being used today. RSI absorbs the incoming radiative or convective heat at its surface

Original figures unavailable at time of publication.

and then reradiates most of it to the environment while conducting the smallest amount possible (usually less than 3%) to the structure. The RSI heat shielding concept was originally developed by Lockheed Missiles and Space Company in the early 1960s and was adopted by NASA for the Space Shuttle Orbiter in the early 1970s. The original heat shield material adopted for the Space Shuttle in 1973 was LI-900. Families of rigid and flexible external insulations have subsequently been developed over the last twenty years. This paper will discuss the evolution, characteristics, and state of the art of RSI with particular emphasis on the materials and systems developed by NASA-Ames Research Center.

THERMAL PROTECTION SYSTEM DEVELOPMENT PROCESS

This chart illustrates the closed loop development process at Ames where thermal protection materials are processed from raw materials inhouse, and tested mechanically, chemically, thermally and then can be evaluated under reentry conditions in our arc jet facilities. Materials supplied by industry and other government laboratories can be and are integrated into this process at any point in their development. The products of this development procedure are often materials including manufacturing specifications that can be adopted by industry and the test data required for certification.



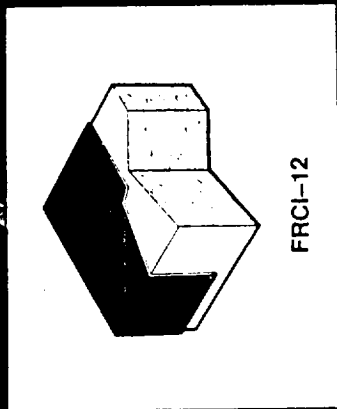
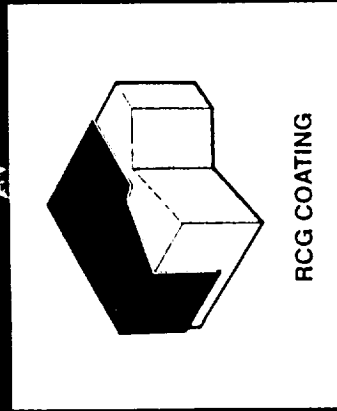
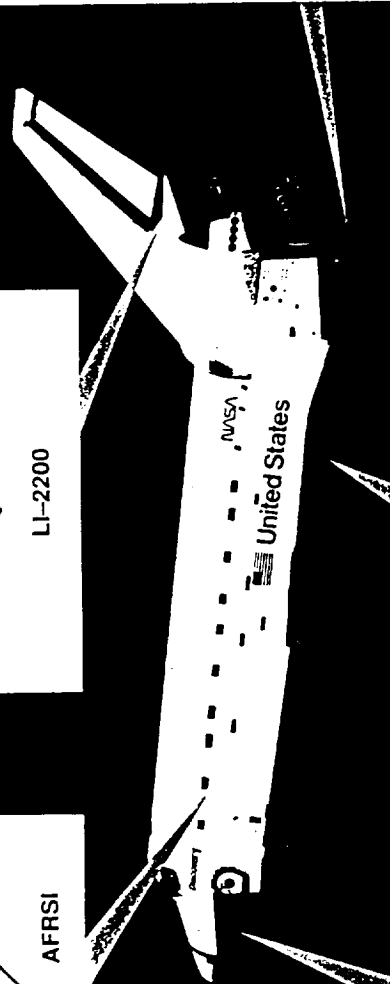
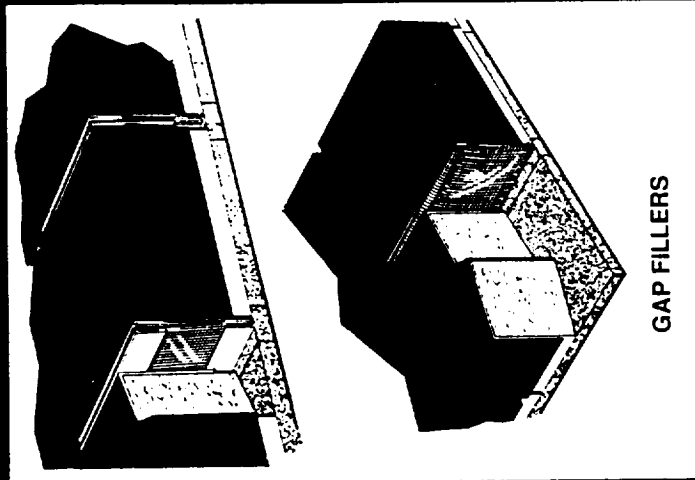
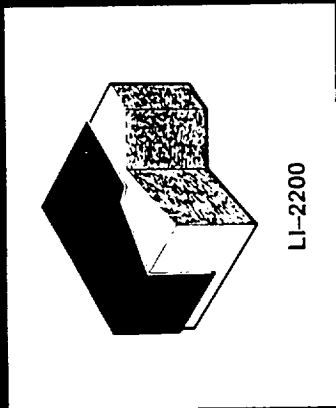
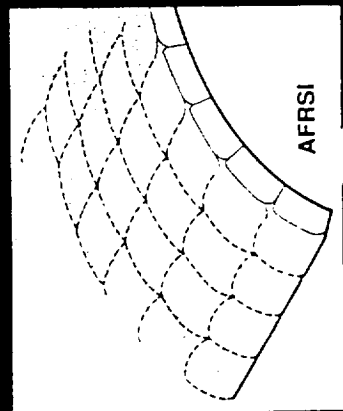
EXAMPLES OF SHUTTLE RSI DEVELOPMENT CHALLENGES

Among the most challenging aspects of Space Shuttle Orbiter design and manufacturing were the development of the new reusable surface insulations. Not only did the materials start as laboratory curiosities but even the raw materials had to be upgraded and in some cases new processes developed to meet the shuttle requirements. The purity of the silica fibers manufactured by Johns Manville were improved substantially to meet the requirement that RSI tiles had to be reusable for 100 flights. A new manufacturing process developed for the modified Vycor glass used in the tile coating is now used by Corning Glass Works. Several new tile and coating materials were developed including The Reaction Cured Glass Coating, LI2200, Fibrous Refractory Composite Insulation etc. and are now manufactured by LMSC, Rockwell and others.

Among the other difficult problems in development of the thermal protection system were designing and manufacturing it so that the TPS was durable and properly strain isolated from the structure. Meeting the smoothness and tile gap requirements were great challenges. The system finally developed is deceptively simple in appearance, but reflects an extraordinary accomplishment by the NASA/industrial team.

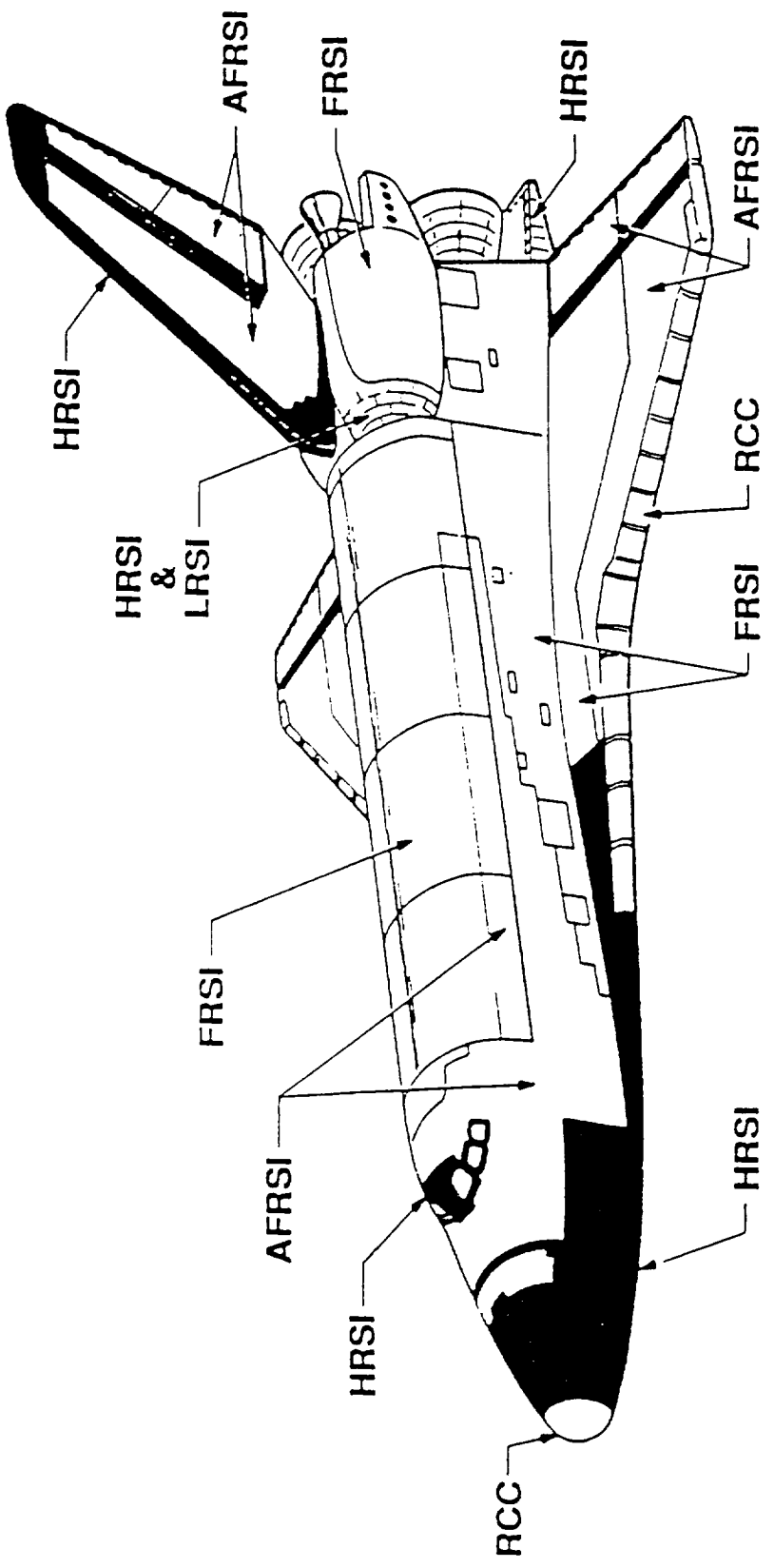
- MANUFACTURING
 - RAW MATERIALS: FIBERS, COATING COMPONENTS
 - PROCESSES: SLURRY BLENDING, PRODUCTION UNIT MOLDING, SINTERING, TILE MACHINING, GLAZING
- DESIGN
 - TILE PLANFORM SIZE
 - STRAIN ISOLATION
 - GAP HEATING
- INSTALLATION
 - BONDING, BOND VERIFICATION
 - TOLERANCES
 - QUALITY CONTROL
- OPERATION
 - DURABILITY
 - WATERPROOFING

AMES DEVELOPED THERMAL PROTECTION MATERIALS



SHUTTLE ORBITERS TPS LOCATIONS

TOTAL RSI CERAMIC TILES - 24,300
REINFORCED CARBON/CARBON (RCC) (44 PANELS/NOSE CAP)
FELT REUSABLE SURFACE INSULATION (FRSI) (3,581 FT²)
ADVANCED FLEXIBLE REUSABLE SURFACE INSULATION (AFRSI) (4,100 FT²)



LESSONS LEARNED

There is a tendency to be overly optimistic in the beginning of a development program. Even when a new system being developed is intentionally simple such as the RSI, unexpected problems will occur. The design requirements must be carefully defined and adequate testing done early so that problems are caught before the commitment to manufacturing becomes too costly to modify. Details such as the adequacy of the tile bonding specifications and quality control cannot be ignored. End to end system testing must be done early.

- **MURPHY'S LAW ALWAYS APPLIES TO NEW MATERIALS**
- **BE SURE DESIGN REQUIREMENTS ARE NECESSARY AND REALISTIC**
- **TEST PROGRAMS MUST BE ADEQUATE AND EARLY**
- **CANNOT IGNORE DETAILS**

NEW THERMAL PROTECTION TECHNOLOGY DIRECTED TOWARDS:

- **SAVING WEIGHT**
- **LOWERING COST**
- **INCREASED TEMPERATURE CAPABILITY**
- **INCREASED DURABILITY**
- **IMPROVED RELIABILITY**

THERMAL PROTECTION MATERIALS AND STRUCTURES TECHNICAL DEVELOPMENT PRIORITIES

- **VERY-HIGH TEMPERATURE, REUSABLE MATERIAL (4000F+)**
 - zirconium and hafnium based ceramics (diborides and zirconia development)
- **HIGH TEMPERATURE, HIGH STRENGTH TO WEIGHT MATERIALS**
 - ceramic matrix composites (sic/sic, c/sic, etc)
- **LIGHT WEIGHT REUSABLE SURFACE INSULATIONS**
 - flexible (TABI, CFBI) and rigid (TUFI, FRCI, AETB, ASMI)
- **HIGH EMITTANCE, LOW CATALYTIC EFFICIENCY COATINGS**
 - coating development/evaluations
- **NEW LEADING EDGE, NOSE TIP AND THERMAL PROTECTION CONCEPTS**
 - small radius non ablating leading edges and nose caps
 - spinning leading edge
 - Pegasus wing glove

NASA Ames-Thermal Protection Materials Branch

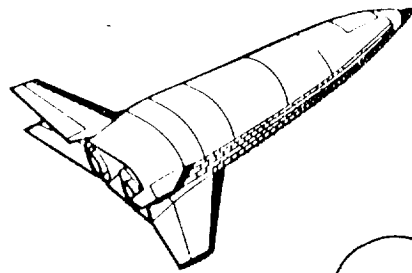
PRIORITY RATIONALE

- **VERY-HIGH TEMPERATURE MATERIALS (4000F+) REPRESENT A POTENTIAL BREAK THROUGH IN THE DEVELOPMENT OF ADVANCED HEAT SHIELDS (2 TO 5 TIMES HEAT FLUX CAPABILITY OF CC OR SIC)**
- **SIC/SIC AND C/SIC CERAMICS(HIGH TEMPERATURE/HIGH STRENGTH TO WEIGHT MATERIALS) HAVE POTENTIAL FOR GREATER CAPABILITY AND DURABILITY THAN CC**
- ADVANCED LIGHT WEIGHT REUSABLE EXTERNAL INSULATIONS, THE "WORK HORSE" OF THERMAL PROTECTION MATERIALS, ARE IN CONTINUING DEMAND BY INDUSTRY, NASA AND DOD**
- IMPROVED HIGH EMITTANCE, LOW CATALYTIC EFFICIENCY COATINGS WILL HAVE A LARGE IMPACT ON THE PERFORMANCE OF THERMAL PROTECTION SYSTEMS**
- ALL THESE MATERIAL RESEARCH AREAS ARE CRITICAL TO THE DEVELOPMENT OF HYPERSONIC CRUISE AND SPACE EXPLORATION VEHICLES**
- APPLICATION OF THESE MATERIALS TO REALISTIC STRUCTURES AND VEHICLES (LEADING EDGES, NOSETIP AND THERMAL PROTECTION CONCEPTS) IS CRITICAL TO THEIR DEVELOPMENT AND EVENTUAL USE**

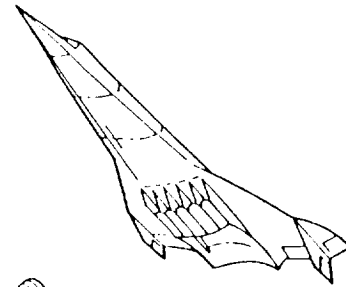
FUTURE MISSIONS

- **SPACE SHUTTLE UPGRADE**
- **NEXT GENERATION SPACE TRANSPORTATION SYSTEM**
 - NATIONAL AEROSPACE PLANE
 - SHUTTLE EVOLUTION-II/C
 - NATIONAL LAUNCH SYSTEM (ADVANCED LAUNCH SYSTEM)
 - ASSURED CREW RETURN VEHICLE FOR SPACE STATION (PERSONAL LAUNCH SYSTEM)
- **SPACE EXPLORATION**
 - MARS SAMPLE RETURN
 - LUNAR RETURN AEROBRAKES
 - MANNED MARS AEROBRAKE AND RETURN.
 - PLANETARY PROBES: NEPTUNE, TITAN, VENUS, URANUS
- **FLIGHT EXPERIMENTS**
 - AEROASSIST FLIGHT EXPERIMENT, ??
 - SWERVE-PEGASUS

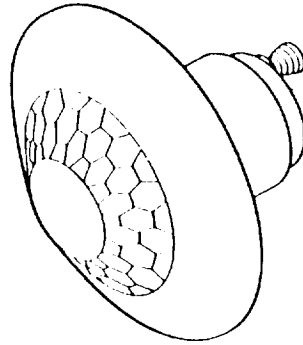
ADVANCED SPACE VEHICLES



TRANSATMOSPHERIC VEHICLE

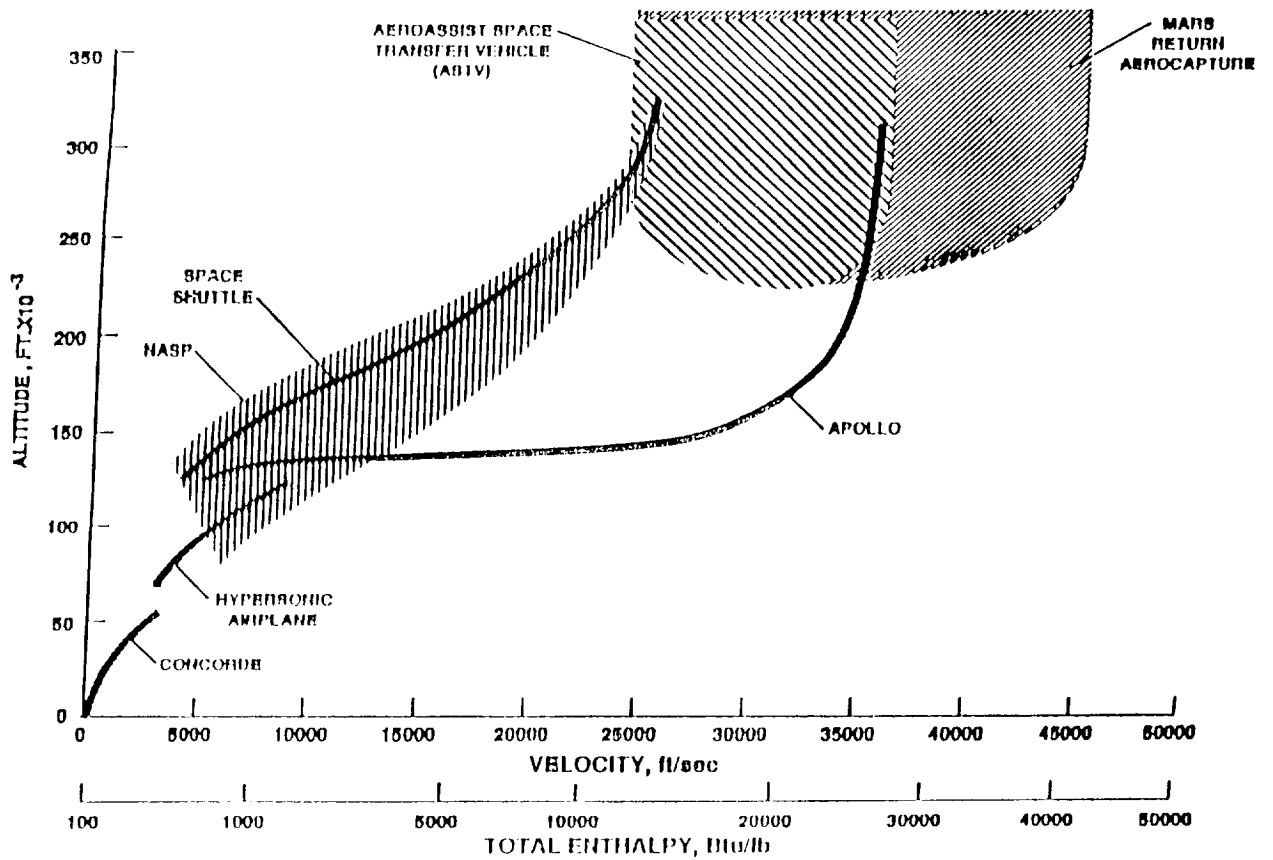


AEROSPACE PLANE



AEROBRAKING ORBITAL TRANSFER VEHICLE

COMPARISON OF VEHICLE REGIMES IN EARTH'S ATMOSPHERE



SEI/PATHFINDER

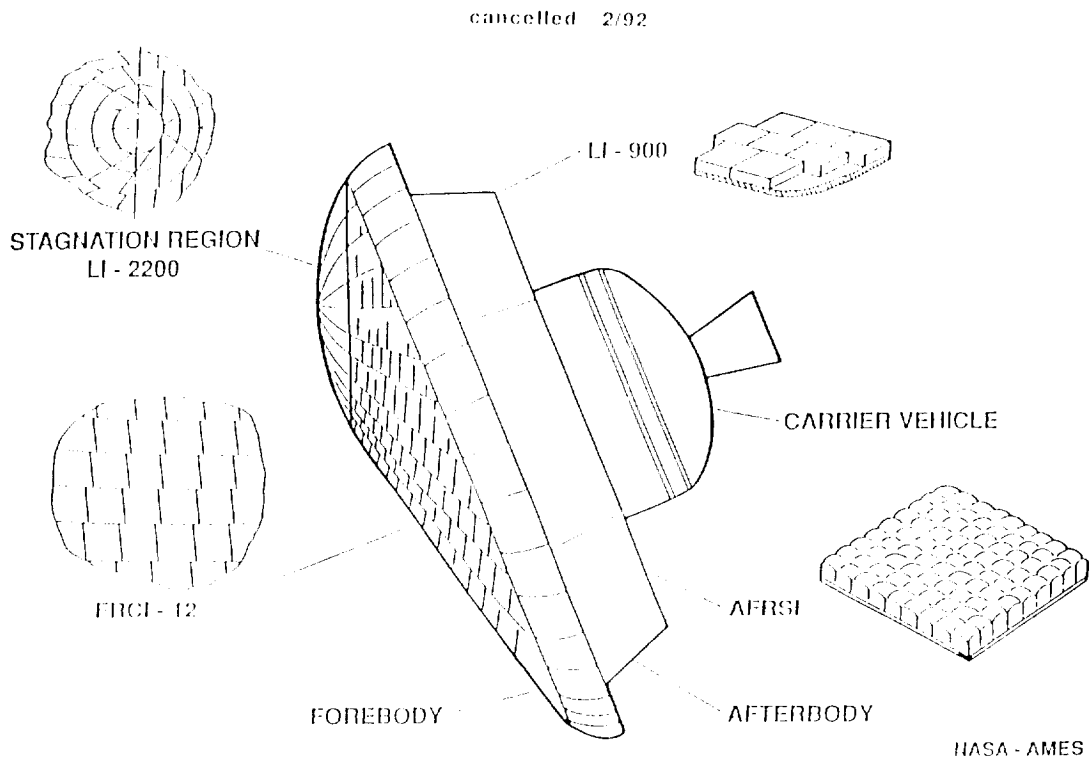
COMPARISON OF ASTV AND SHUTTLE TPS REQUIREMENTS

	SHUTTLE	LUNAR RETURN ASTV	MARS RETURN ASTV
• PEAK CONVECTIVE HEATING BTU/FI ² -SEC	60	3-60	50-1500
• PEAK VELOCITY, MI/SEC	4	7+	11+
• PEAK RADIANT HEATING, BTU/FI ² -SEC	< 2	3 - 30	25-800
• PEAK DYNAMIC PRESSURE, PSF	200	< 30	< 30
• TURBULENT HEATING	YES	NO	YES
• ENTRY HEATING TIME, SEC	1200	< 400	< 400
• EXPOSURE TO ADVERSE ENVIRONMENTS			
- HANDLING	YES	NO*	NO*
- RAIN/WEATHER	YES	NO	NO*
- AEROACOUSTICS (dB)	160+	< 90	< 90
- DEBRIS IMPACT			
- LAUNCH	YES	NO	NO
- ON ORBIT/IN FLIGHT	LESS	MORE	MORE

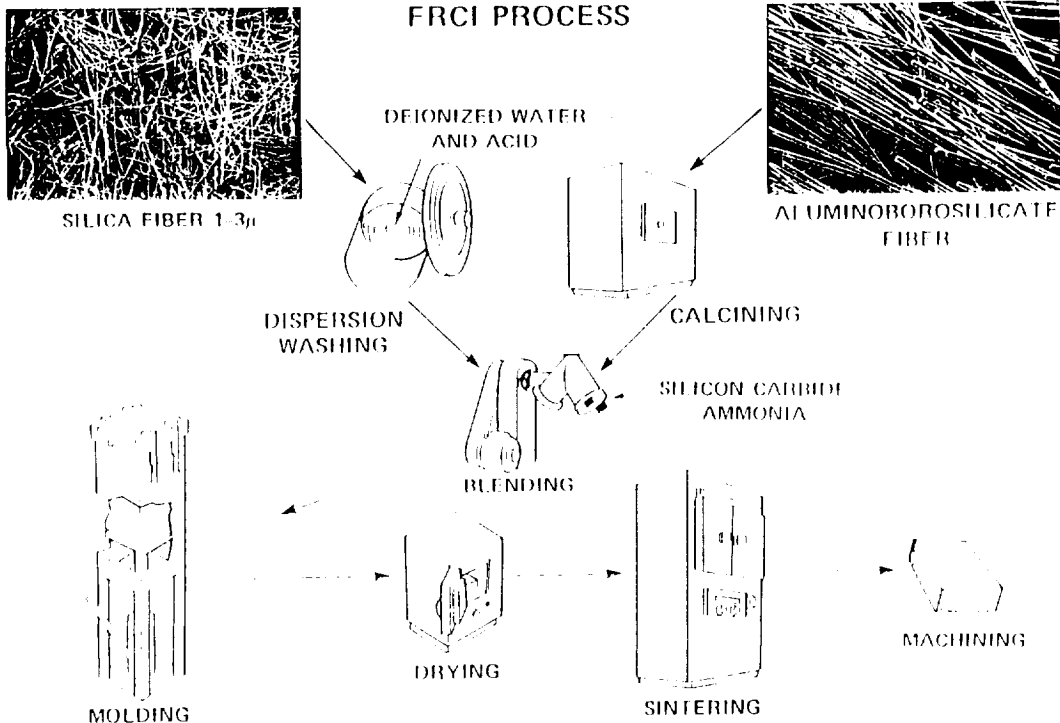
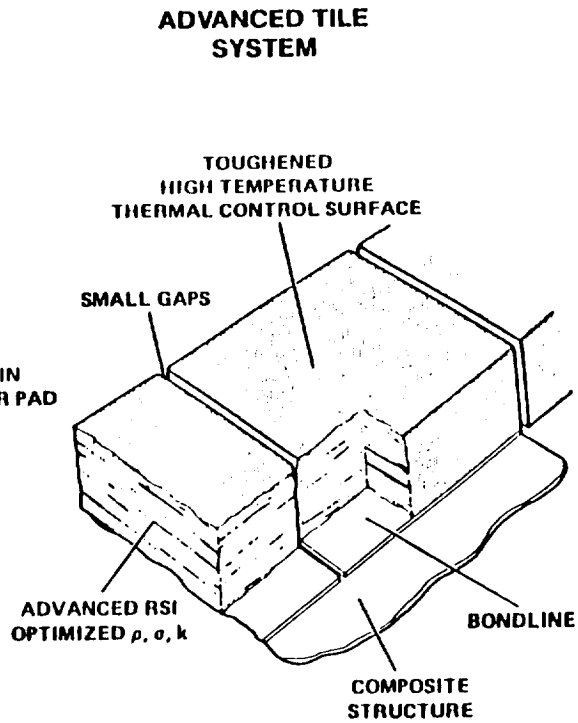
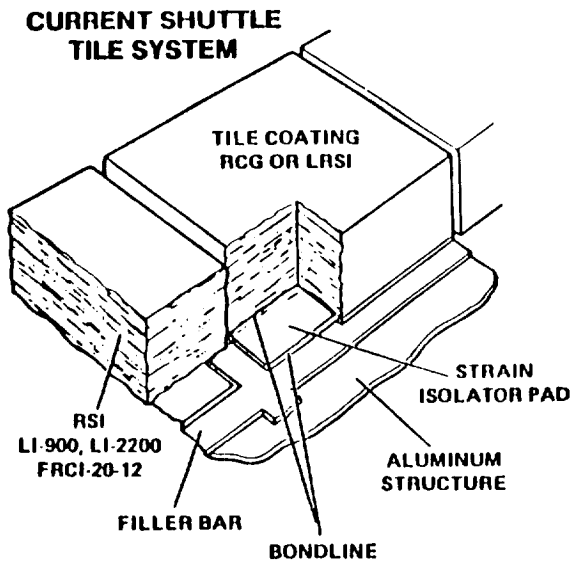
*ONCE DEPLOYED

THERMAL PROTECTION SYSTEM DESIGN FOR AEROASSIST FLIGHT EXPERIMENT (AFE)

The Aeroassist Flight Experiment (AFE) was funded and developed in the late 1980s. Flight was to occur about 1996. This figure illustrates the thermal protection system design. The aerobrake was designed and built by JSC. Shuttle state of the art RSI tiles and blankets used were manufactured by Lockheed Missiles and Space Company and Johns Manville. Lessons learned on the shuttle were taken into account, resulting in a thermally efficient, very cost effective design and trouble free manufacturing process. Advanced RSI tiles and Flexible insulations shown in the following charts were to be flown as experiments. Unfortunately, AFE was cancelled in early 1992.

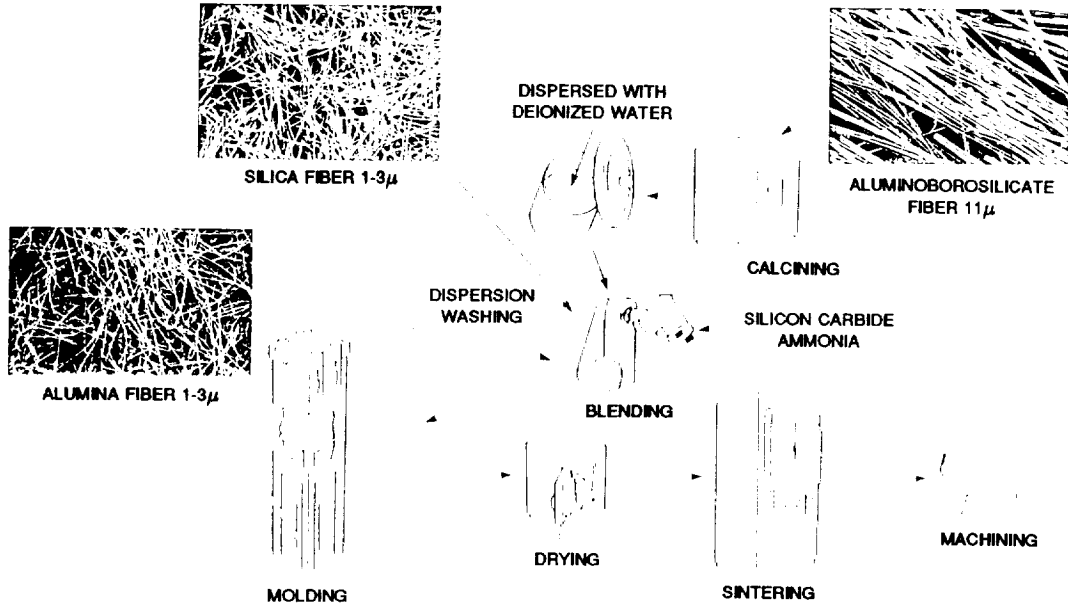


ADVANCED RSI THERMAL PROTECTION SYSTEMS



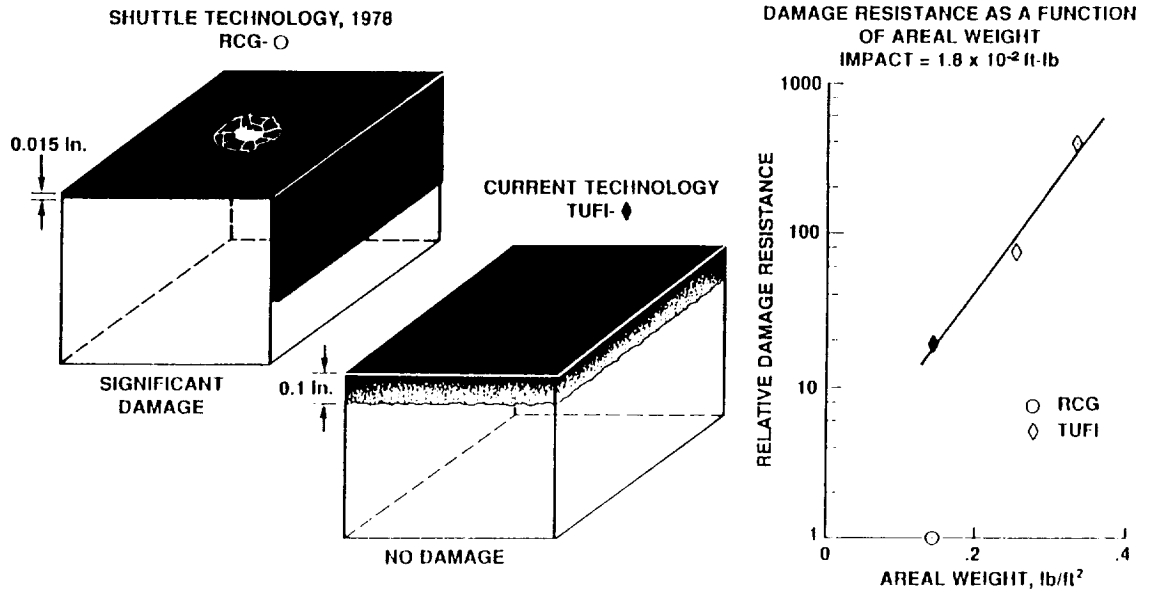
Original figure unavailable

AETB PROCESS



Original figure unavailable

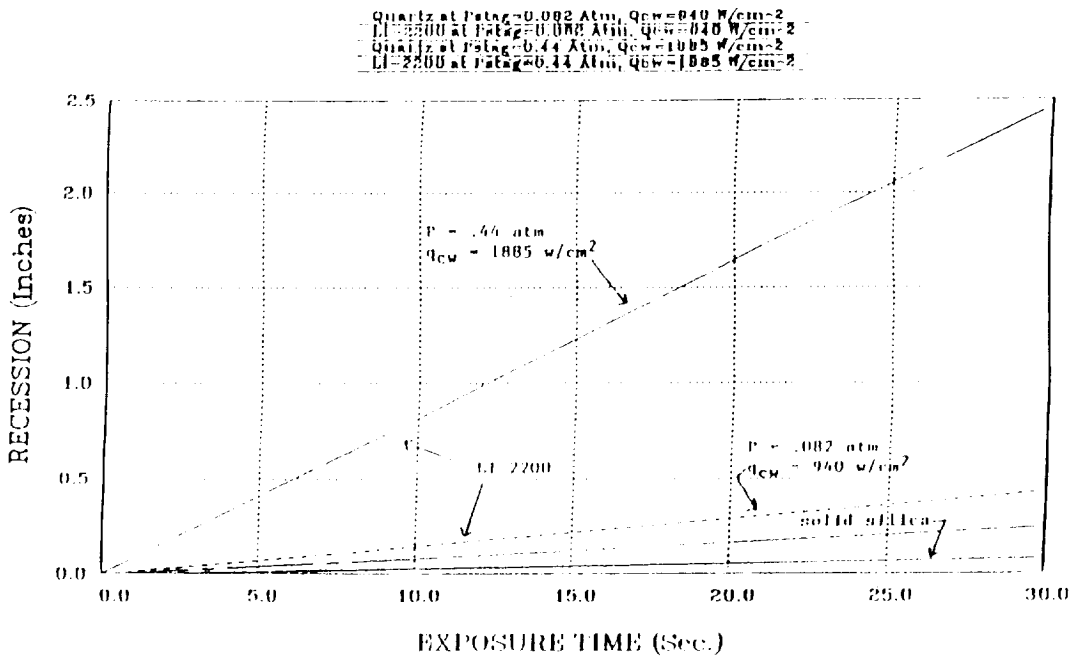
IMPACT RESISTANCE OF RSI COATING SYSTEMS



RIGID RSI PROPERTY COMPARISON

PROPERTIES	RIGID RSI MATERIALS					
	LI-900	LI-2200	FRCI-12	AETB-12	FRCI-12-20*	
DENSITY, LBM/FT ³	9	22	12	12	20	
TENSILE STRENGTH	IP (PSI)	68	181	256	157	630
	III (PSI)	24	73	81	120	330
	MODULUS					
IP (KSI)	25	80	50	32	110	
III (KSI)	7	27	10	16	46	
TEMPERATURE CAPABILITY (ISOTHERMAL SHRINK)						
	2700°F - 4HR (%)	91		77	42	67
	2500°F - 4HR (%)	53	37	44	12	38
THERMAL CONDUCTIVITY PRESSURE = 10 ⁻³ ATM, T = 1000°F BTU-IN/FT ² -HR°F	0.021	0.030	0.027	0.024		
YEAR DEVELOPED	1973	1977	1980	1985	1991	

**RECESSION DATA FOR ABLATION OF LI-2200 (RSI)
COMPARED TO SOLID QUARTZ (AMES 60 MW Arc-Jet)**



Original figure unavailable

**MANNED MARS/EARTH RETURN
THERMAL PROTECTION ABLATOR MATERIALS COMPARISON***
(RAKED CONE GEOMETRY) $R_N = 1$ METER

$V_E = 14$ km/sec, $L/D = 0.5$, $\beta = 300$ kg/m²

	CARBON ¹ PHENOLIC	AVCOAT ²	RSI (LI-2200) ³	AVCOAT (APOLLO) [†]
ABLATOR THICKNESS (IN)	1.1	1.75	2.75	0.5 - 2.5
INSULATION ** THICKNESS (IN)	2.0	1.0	1.0	(---) ^{††}
AVERAGE MASS LOADING (lbm/ft ²)	9.66	5.71	5.79	1.5 - 7.0
TPS MASS	3478	2056	2084	1635
TPS WT. %	23.2%	13.7%	13.8%	13.2%

* FOREBODY HEATSHIELD ONLY; BASED ON NON-OPTIMIZED DESIGN, I.E. UNIFORM THICKNESS; DOES NOT INCLUDE TPS SUPPORT STRUCTURE

** LI-900 RSI INSULATION

† APOLLO ENTRY VELOCITY, $V_E = 11$ km/sec, $R_N = 10$ ft, $\beta = 350$ kg/m²

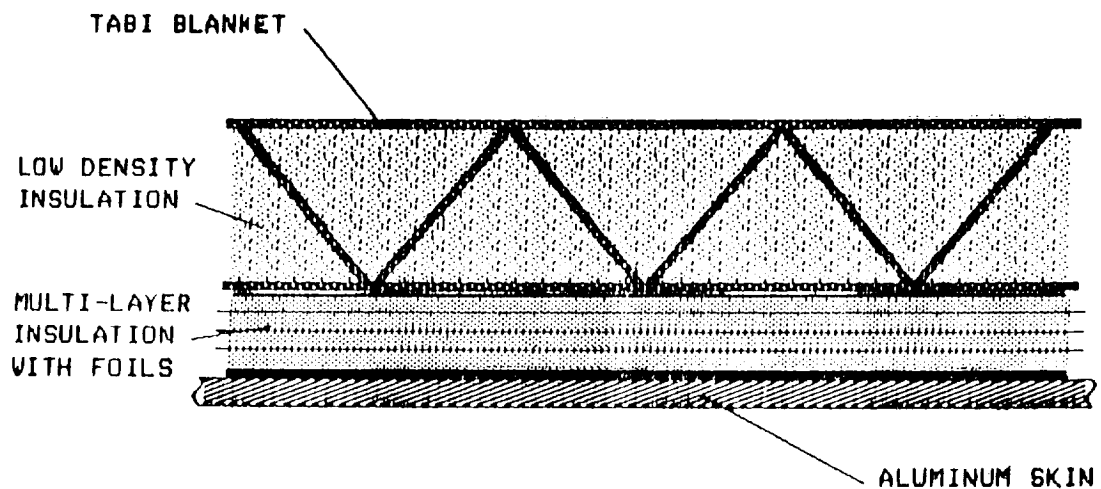
†† APOLLO INSULATION IS Q-FELT/STAINLESS STEEL HONEYCOMB (Q-FELT INCLUDED IN TPS MASS)

¹ INITIAL DENSITY, $\rho_o = 89$ lb/ft³

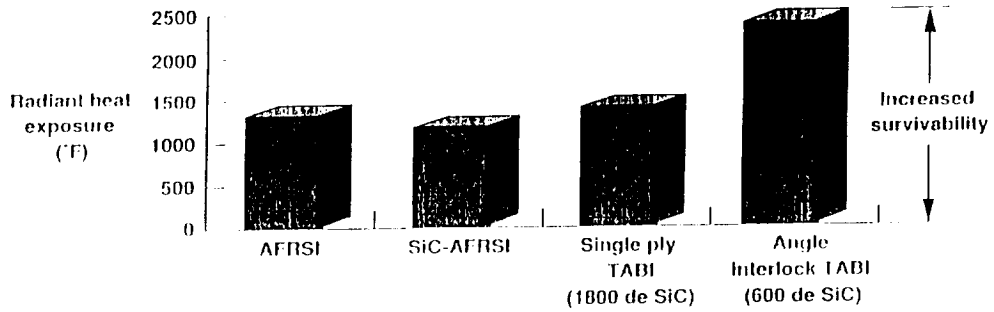
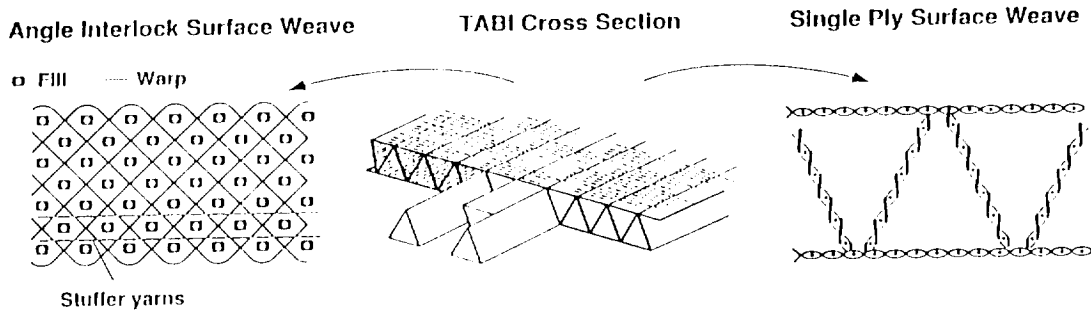
² INITIAL DENSITY $\rho_o = 34$ lbm/ft³

³ INITIAL DENSITY, $\rho_o = 22$ lbm/ft³

FLEXIBLE TPS CONSTRUCTION

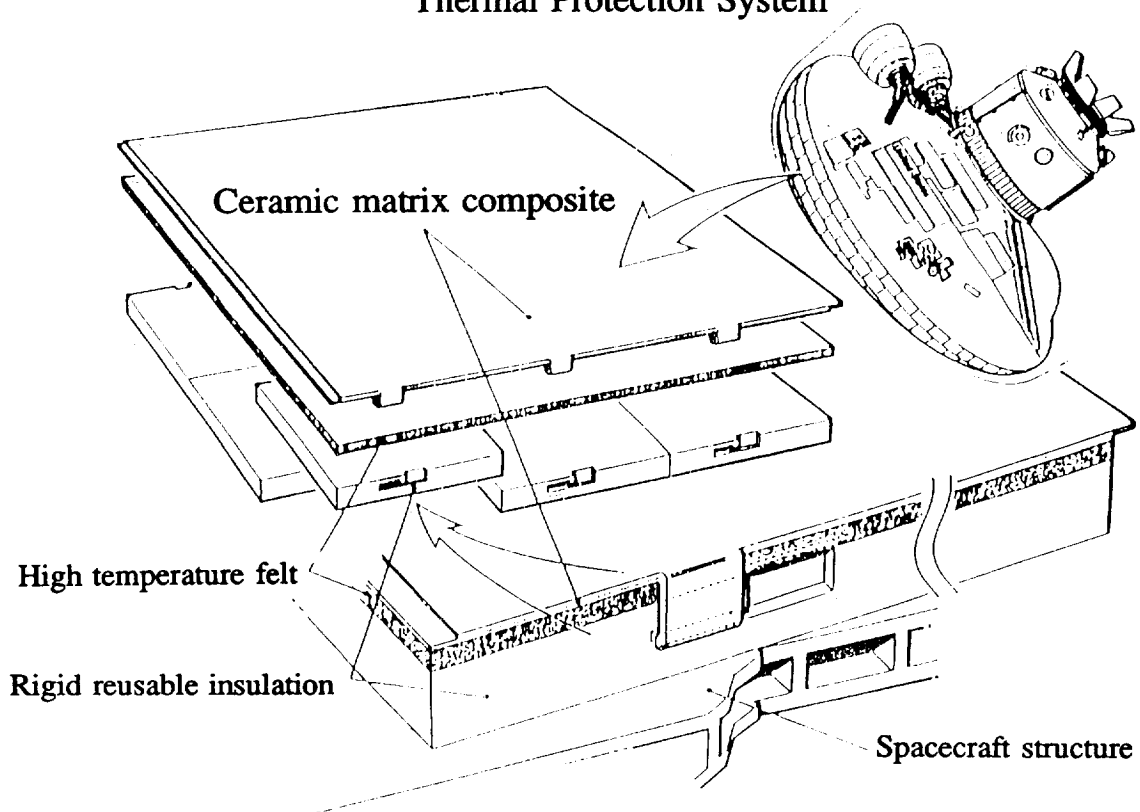


SURFACE TOUGHENING OF TABI TO AEROACOUSTIC ENVIRONMENTS



Aeroacoustic survival of flexible TPS after 600 sec at 170 dB
(after exposure to radiant heat cycle)

TOP HAT Thermal Protection System



CURRENT HEAT SHIELD MATERIALS THERMAL LIMITS

MATERIAL	MAXIMUM USE TEMPERATURE, °F		EMITTANCE (@ °F)	MAXIMUM HEAT FLUX CAPABILITY* BTU/FT ² -SEC	EQUIVALENT USE TEMPERATURE, °F***
	MULTIPLE FLIGHT	SINGLE FLIGHT			
FLEXIBLE ORGANIC					
FRSI	700	800	.9(800)	1.4	885
PBI	900+	1100	.9(1100)	2.7	1125
AFRSI, TABI, CFBI					
SILICA	1200	2000	.43(2000)	4.4	1480
NEXTEL	> 2000	> 2000	.40(2000)	> 7.5	1820
NICALON	2000	> 2400	.58(2000)	> 30	
RIGID CERAMIC INSULATION					
LI-900	2500	2700	.9(2500)	60	2980
LI-2200	2600	2800 (2900 FOR AFE)		(80)	
FRCI-12	2600	2800	.9(2500)	70	3115
AETB-12/TUFI	2500	2700**		60	
AETB-12/RCG	2600+**	2800+**		70	
ASMI	2600+**	2900**		80	
AETB-8/RCG	2600**	2800+**		70	
METAL					
TITANIUM	1000		.8	1.7	1000
RENE 41	1600			6.9	1600
INCONEL 617	2000			14	2000
RCC/ACC					
	3000		.8	55 (F.C.) 100 N.C.	3000 3560

THERMAL PROTECTION TECHNOLOGY FOR HYPERSONIC VEHICLES

STATUS OF DEVELOPMENT

- RIGID LOW DENSITY CERAMIC
 - SHUTTLE TPS FLIGHT PROVEN
 - LI-900, LI-2200, FRCI-20-12
 - IMPROVED MATERIALS DEVELOPED
 - FRCI, AETB, HIP
 - TOUGHENED COATING
 - OPTIMIZED MATERIALS TO BE DEFINED
- RIGID HIGH DENSITY CERAMIC
 - SHUTTLE CARBON/CARBON TPS FLIGHT PROVEN
 - CERAMIC MATRIX COMPOSITES IN DEVELOPMENT
 - DIBORIDE COMPOSITES RESEARCH INITIATED
- FLEXIBLE
 - SHUTTLE TPS FLIGHT PROVEN FRSI, AFRSI
 - IMPROVED MATERIALS UNDER DEVELOPMENT TABI, CFBI, MLI CERAMIC COMPOSITS
- ABLATORS
 - APOLLO, MERCURY, GEMINI LOW DENSITY TPS FLIGHT PROVEN
 - AVCOAT 5026, SLA 561, etc.
 - BALLISTIC MISSILE, GALILEO HIGH HEAT FLUX TPS FLIGHT PROVEN
 - CARBON/PHENOLIC, CARBON/CARBON
 - NON CATALYTIC REFLECTIVE INSULATIVE ABLATORS DEVELOPMENT STARTING

THERMAL PROTECTION SYSTEMS
MANNED SPACECRAFT FLIGHT EXPERIENCE

Donald M. Curry
NASA/Johnson Space Center
Houston, Texas

INTRODUCTION

Since the first U. S. manned entry, Mercury (May 5, 1961), seventy-five manned entries (figs. 1, 2) have been made resulting in significant progress in the understanding and development of Thermal Protection Systems (TPS) for manned rated spacecraft. Figures 3 and 4 compare the TPS materials and systems installed on these spacecraft. The first three vehicles (Mercury, Gemini, Apollo) used ablative (single-use systems) while the Space Shuttle Orbiter TPS is a multimission system. A TPS figure of merit, unit weight lb/ft², illustrates the advances in TPS material performance from Mercury (10.2 lb/ft²) to the Space Shuttle (1.7 lb/ft²).

Vehicle	No. of Entries
Orbital Return	
Mercury (1961-63)	6
Gemini (1965-66)	10
Apollo (1968-75)	5
Shuttle (Thru Feb., 1992)	44
Lunar Return	
Apollo (1969-72)	10

Figure 1. U.S. manned spacecraft.

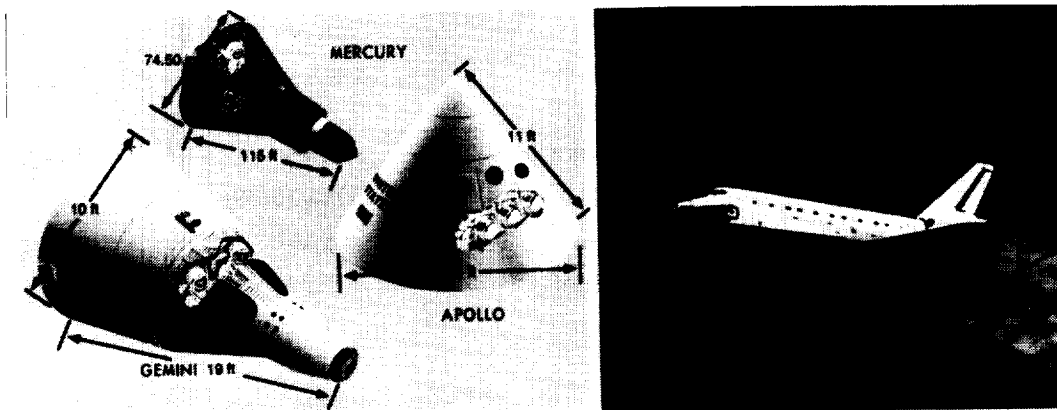
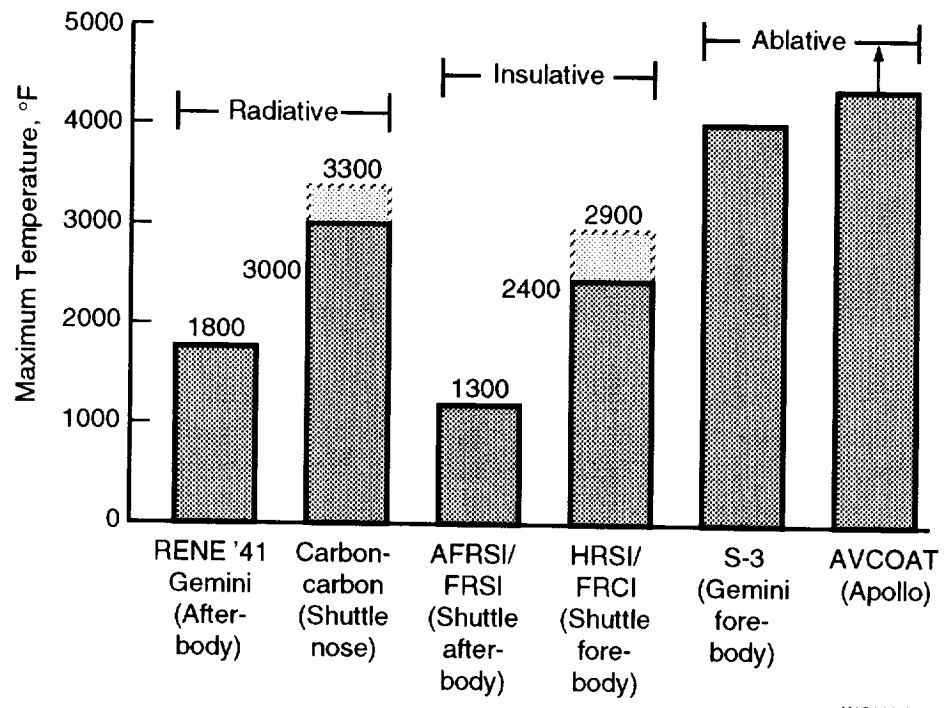
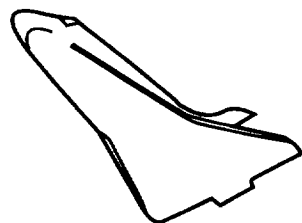


Figure 2. Manned spacecraft entry vehicles.



X101441M

Figure 3. Manned spacecraft thermal protection materials.

	Mercury	Gemini	Apollo	Shuttle
				
Area	32 ft ²	45 ft ²	365 ft ²	11 895 ft ²
Weight	315 lb	348 lb	1465 lb	18 904 lb
Wt/ft ²	10.2	7.5	3.9	1.7
Material	Ablator (Fiberglass-phenolic)	Ablator (Corning DC 235)	Ablator (AVCO 5026-39)	Rigidized silica fibers
Density	114 lb/ft ³	54 lb/ft ³	32 lb/ft ³	9-22 lb/ft ³
Usage	1 flight	1 flight	1 flight	100 flights

X101442M

Figure 4. Manned spacecraft entry TPS.

ABLATIVE THERMAL PROTECTION SYSTEMS

In the design of a passive TPS for atmospheric entries, ablative materials have provided a number of inherent advantages in both thermal performance and structural-mechanical properties. Ablative materials were successfully used for both Earth-orbital (Mercury, Gemini) and lunar return (Apollo) velocities. The Apollo TPS material (AVCO 5026-39 HCG) was characterized using both ground tests (plasma jet and radiant) and unmanned flight tests (earth-orbital/lunar return). Design of this TPS was accomplished using two trajectories; maximum heat rate (~ 700 BTU/ft²-sec) for surface temperature/recession and heat load ($\sim 44,000$ BTU/ft²) for structural temperature. The conservatively designed TPS thickness, measured surface recession and char thickness, for a typical Apollo-lunar return is illustrated in figure 5.

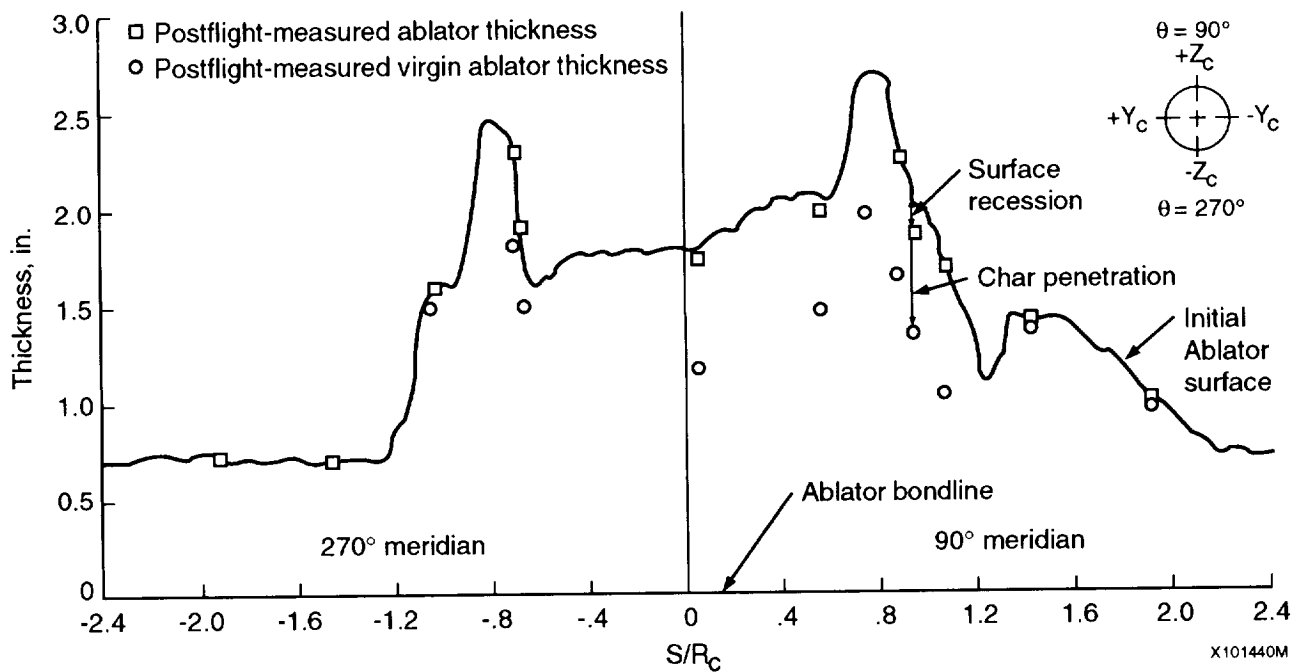
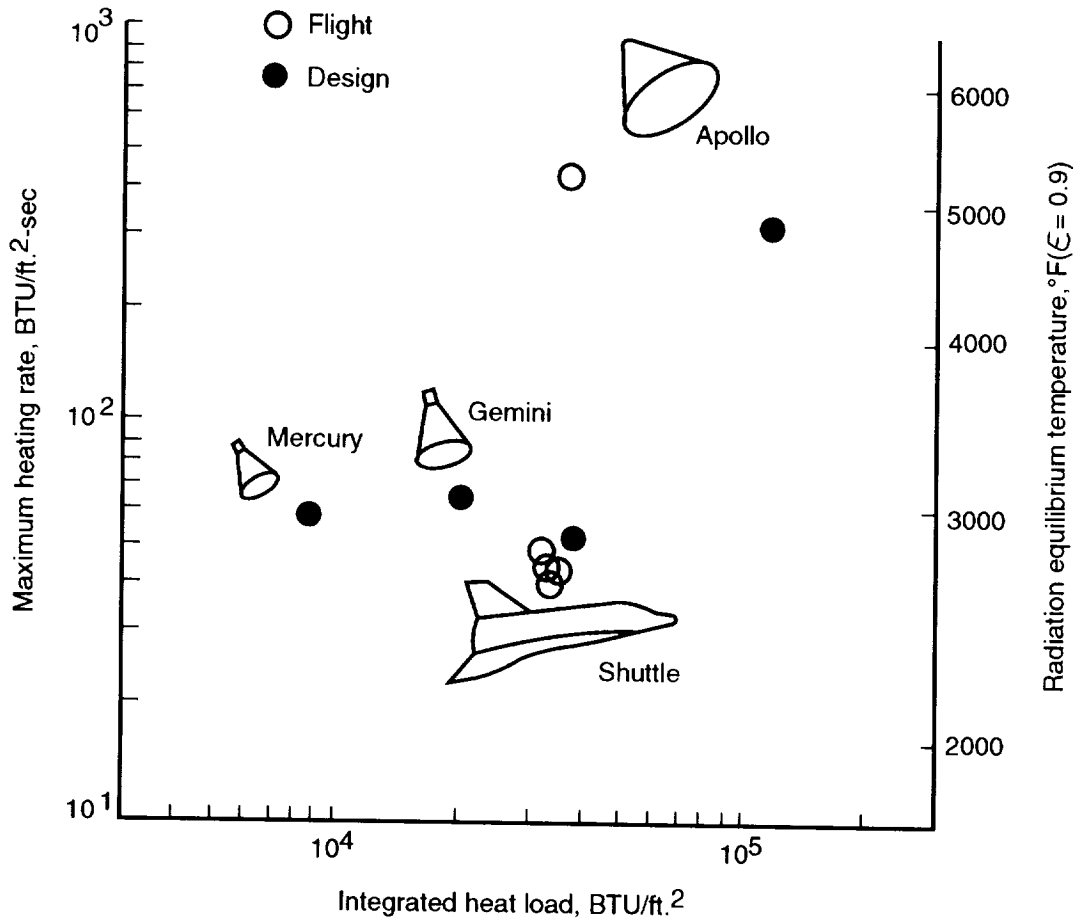


Figure 5. Comparisons of measured ablator thermal performance.

REUSABLE THERMAL PROTECTION SYSTEMS

Prior to the Space Shuttle program, all manned space vehicles used ablator materials having a one-mission capability. In contrast, the Space Shuttle Orbiter TPS had to be reusable to minimize costs and minimum weight to meet vehicle requirements. The Orbiter TPS design, in contrast to previous spacecraft, was verified with flight data from the first five manned flights of the Orbiter Columbia. A comparison of the design and flight environments for the Space Shuttle Orbiter is shown in figure 6. The Orbiter flight parameters, in particular the 40° angle of attack, allowed relatively lower reference total heat load and heating rate than was predicted for the design trajectory.



X000909M

Figure 6. TPS design and flight test environments.

ORBITER TPS MATERIALS

The Orbiter TPS (fig. 7) consists basically of two material systems, reusable surface insulation (RSI) and reinforced carbon-carbon (RCC). The RSI-TPS is further characterized by three rigid ceramic insulation materials:

- high temperature reusable surface insulation (HRSI) consisting of black-coated LI-900/ LI2200 coated tiles,
- low temperature reusable surface insulation (LRSI) consisting of white-coated LI-900 tiles,
- fibrous refractory composite insulation (FRCI-12) with black coating

And two flexible insulation materials:

- flexible reusable surface insulation (FRSI)
- advanced flexible reusable surface insulation (AFRSI).

The rigidized ceramic material is used over the major portion of the Orbiter for temperatures ranging from 1300 to 2300°F. The upper surface areas, where temperatures are generally less than 1300°F, the flexible insulation materials are used. The RCC is used for those areas (i.e., nose cap, wing leading edge) where temperatures exceed 2300°F. Material distribution (peak temperature) and thickness determination (heat load) were selected to minimize weight while retaining a multi-mission capability. AFRSI and FRCI were not part of the original TPS design, AFRSI was first flown on STS-6 (OV-099) and FRCI on the fourth flight of OV-099 (41B).

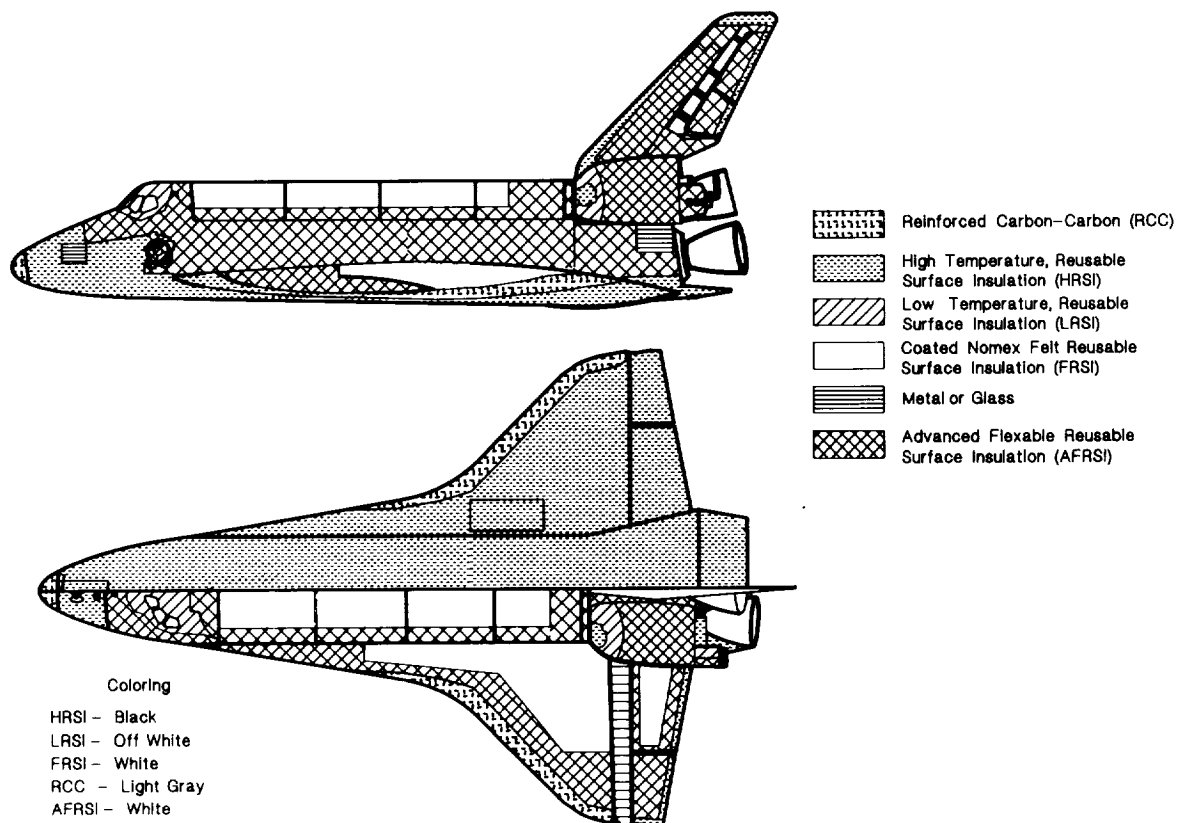
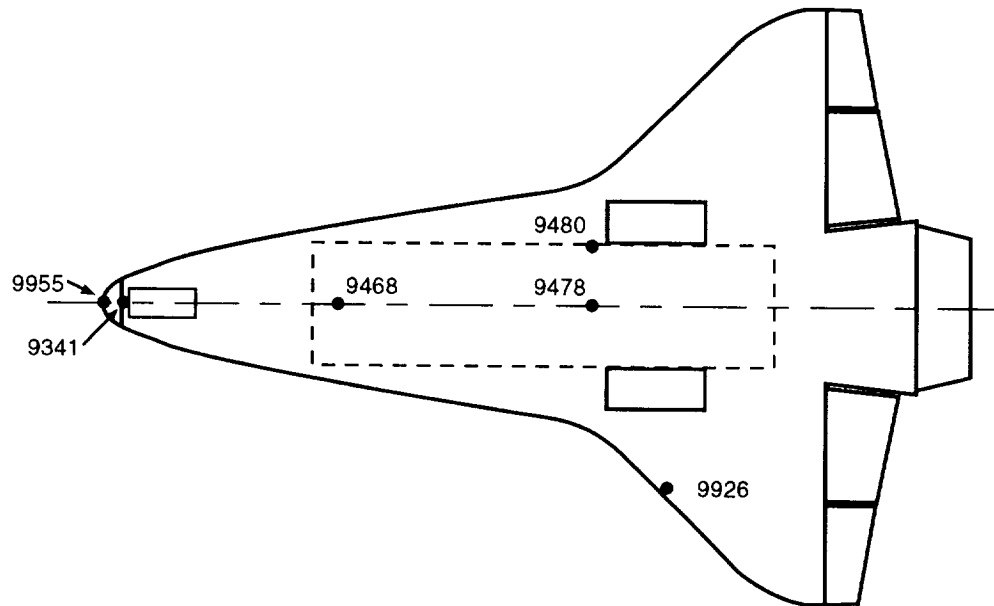


Figure 7. Thermal protection system, Orbiter 103 and subsequent orbiters.

ORBITER TPS PEAK SURFACE TEMPERATURE

A limited number of surface temperature measurements have been made for the various Orbiter flights. Figure 8 presents some typical results. These surface temperature measurements are used in the identification of any anomalies during the entry (i.e., gap/step heating, transition effects). These temperatures are also used to indicate changes in the surface condition of the RSI tiles (i.e., surface catalysis, emissivity).



Flight	Vehicle	VO7T- 9468	VO7T- 9478	VO7T- 9480	VO9T- 9341	VO9T- 9955	VO9T- 9926
STS-1	OV-102	-	-	-	-	-	-
STS-2	OV-102	1530	1560	1500	2080	-	2470 **
STS-3	OV-102	2035 *	1470	1460	-	-	2460 **
STS-4	OV-102	-	-	-	-	-	-
STS-5	OV-102	1750 *	1600 *	1400	2160	2605 **	2501 **
STS-26	OV-103	1505	-	1465	-	-	-
STS-27	OV-104	-	1600	1600	-	-	-
STS-29	OV-103	-	-	-	-	-	-
STS-30	OV-104	-	1435	1400	-	-	-
STS-28	OV-102	1350	1750	1790	-	-	-
STS-34	OV-104	-	1440	1470	-	-	-
STS-33	OV-103	1560	-	1490	-	-	-
STS-32	OV-102	1390	1380	1400	-	-	-
STS-36	OV-104	-	1450	1340	-	-	-
STS-31	OV-103	1590	-	1480	-	-	-
STS-41	OV-103	-	-	1500	-	-	-
STS-38	OV-104	-	1410	1300	-	-	-
STS-35	OV-102	-	-	-	-	-	-
STS-37	OV-104	-	1400	1310	-	-	-
STS-39	OV-103	1420	-	1460	-	-	-
STS-40	OV-102	1430	1520	1500	-	-	-
STS-43	OV-104	-	1390	-	-	-	-
STS-48	OV-103	1620	-	1700	-	-	-
STS-44	OV-104	-	-	-	-	-	-

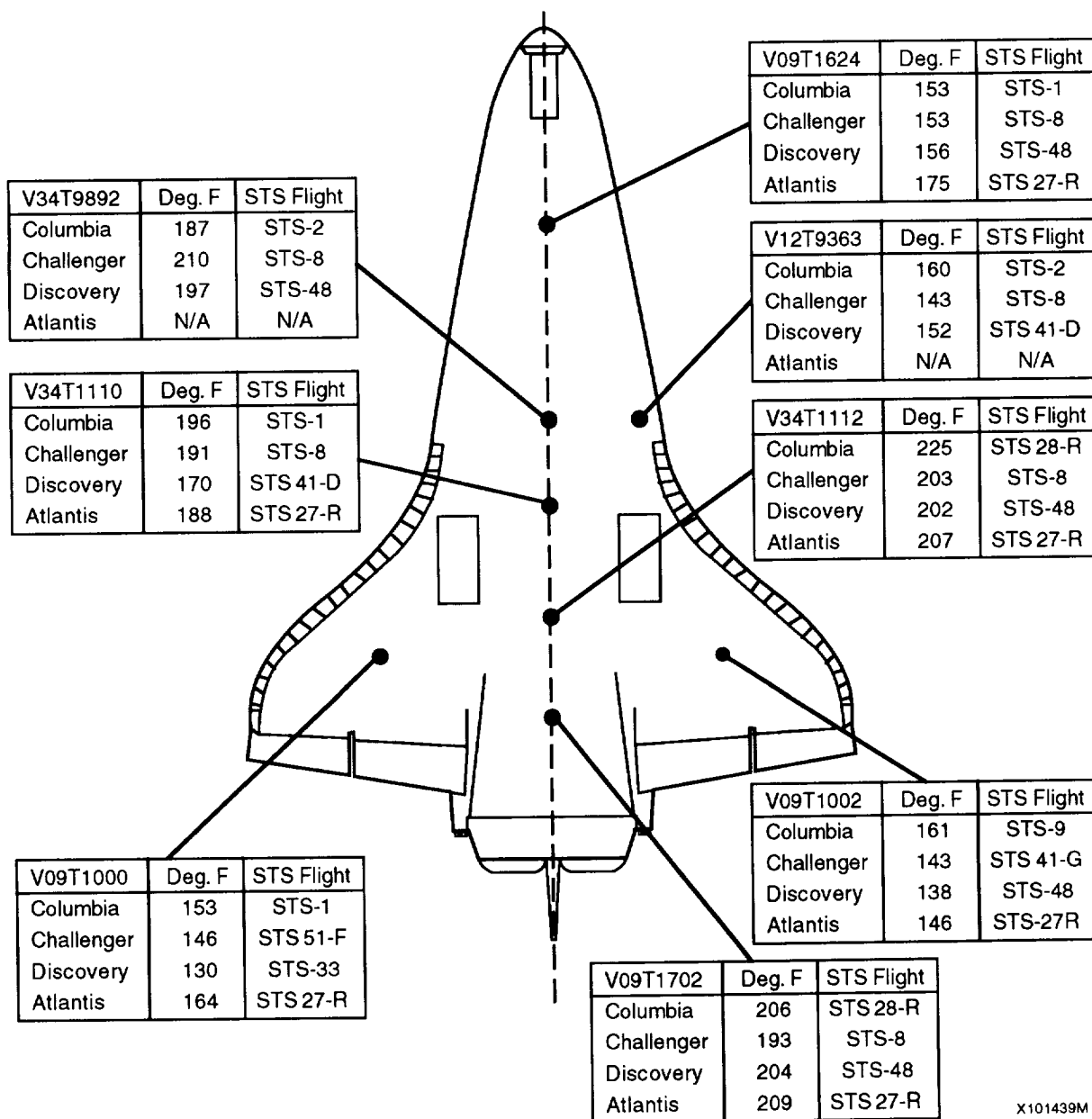
* Catalytic coated tile
 ** RCC Inner Surface

X101438M

Figure 8. Orbiter peak surface temperatures.

ORBITER PEAK STRUCTURAL TEMPERATURE

The RSI performs the required thermal protection function during entry by two primary means of heat dissipation. A large percentage (~95 percent) of the heat energy is reradiated to the atmosphere and the remaining heat energy is effectively retarded by the low diffusivity of the basic insulation material. The basic thermal performance of the RSI can be evaluated by three important parameters: the induced surface temperature profile, the transient response of the RSI interior, and the structural temperature response. Figure 9 shows a typical distribution of STS flight measure peak structural temperatures. Since the Orbiter flight envelope and the design trajectory are relatively equal (heat rate/heat load); these low structural temperatures (350° design) provide a positive thermal margin. As with surface temperature, these structural temperatures can be used to indicate any potential degradation in RSI material with reuse.



X101439M

Figure 9. Orbiter maximum structure temperatures.

ORBITER TPS FLIGHT EXPERIENCE AERODYNAMIC FLOW DAMAGE

The RSI system thermal/structural integrity for the most part has been excellent for all STS flights. The major areas of TPS requiring repair/refurbishment, replacement and/or design change have involved impact damage, gap filler degradation, gas heating in joint regions, seal performance, and penetrations and prevention of hot gas radiation leaks. An example of aerodynamic flow damage occurred on STS-6. The leading edge area of the orbital maneuvering system (OMS) pod was covered with AFRSI material. As can be seen in figure 10a, the AFRSI sustained severe damage from loss of the outer fabric to complete removal of thermal insulation. Postflight and laboratory investigations indicated no evidence of thermal degradation, therefore, the damage was attributed primarily to mechanical loading of the AFRSI blankets due to aerodynamic flow forces. This area was subsequently redesigned using rigid ceramic tiles (fig. 10b).

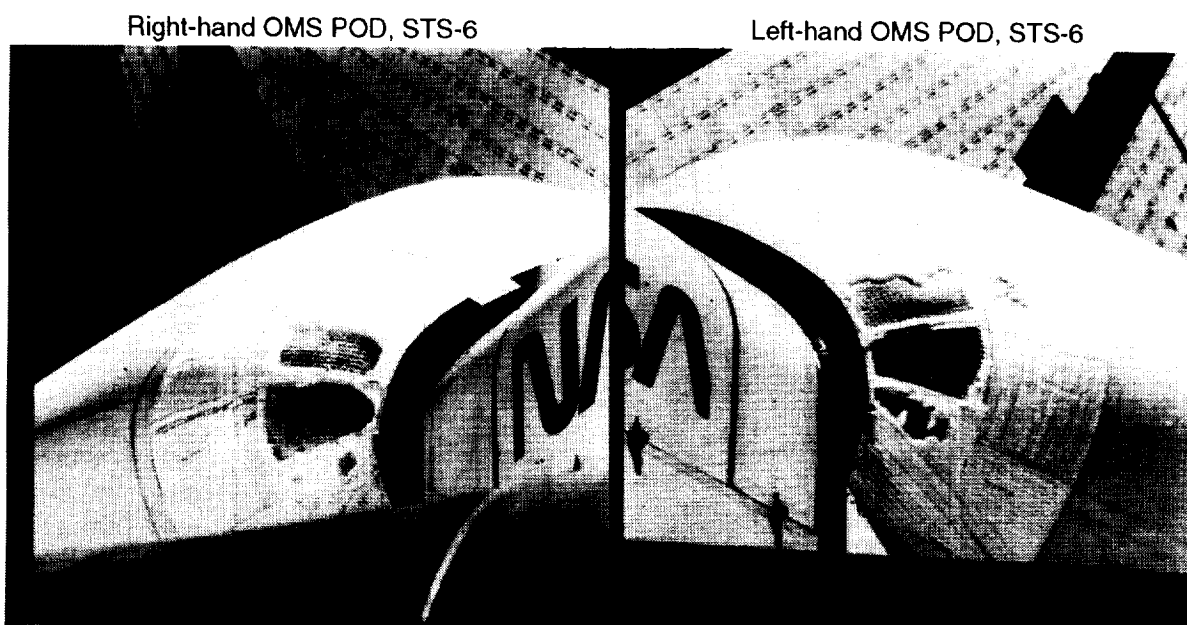


Figure 10a. OMS POD-AFRSI damage.

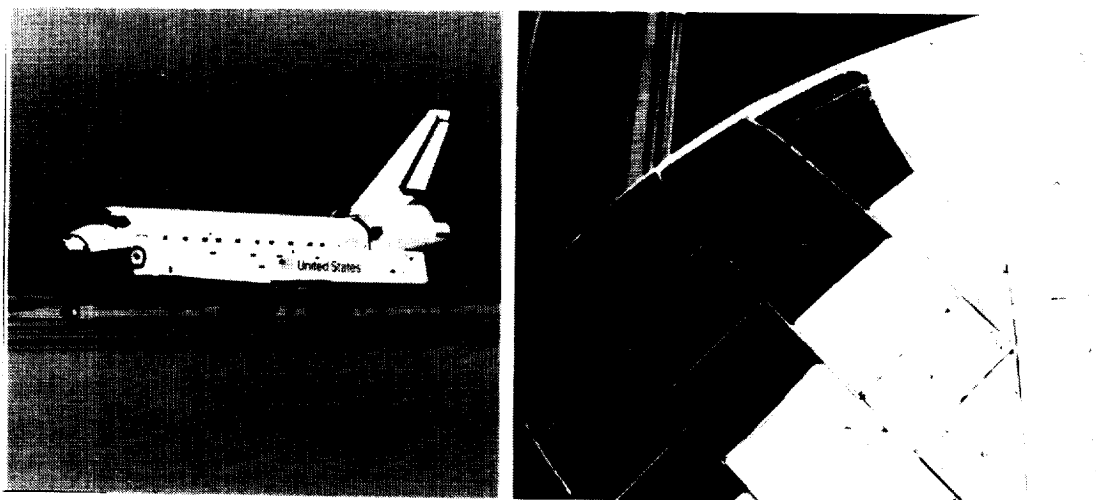


Figure 10b. OMS-POD tile redesign.

ORBITER TPS FLIGHT EXPERIENCE RSI TILE IMPACT DAMAGE

While the Orbiter is in the launch configuration, the TPS is not protected from the natural environment (i.e., rain, hail, etc.) Likewise, during the launch phase, on-orbit and landing phases, as well as the ferry flight configuration; the Orbiter TPS is exposed to damage from ice, foreign objects, debris, etc. An example of debris impact damage on the lower surface of the wing is shown in figure 11. The reaction curved glass (RCG) coating has been lost as a result of the impact exposing the basic silica material. Depending on the size and depth of the damage, a series of repairs have been developed to return the tile to full service.

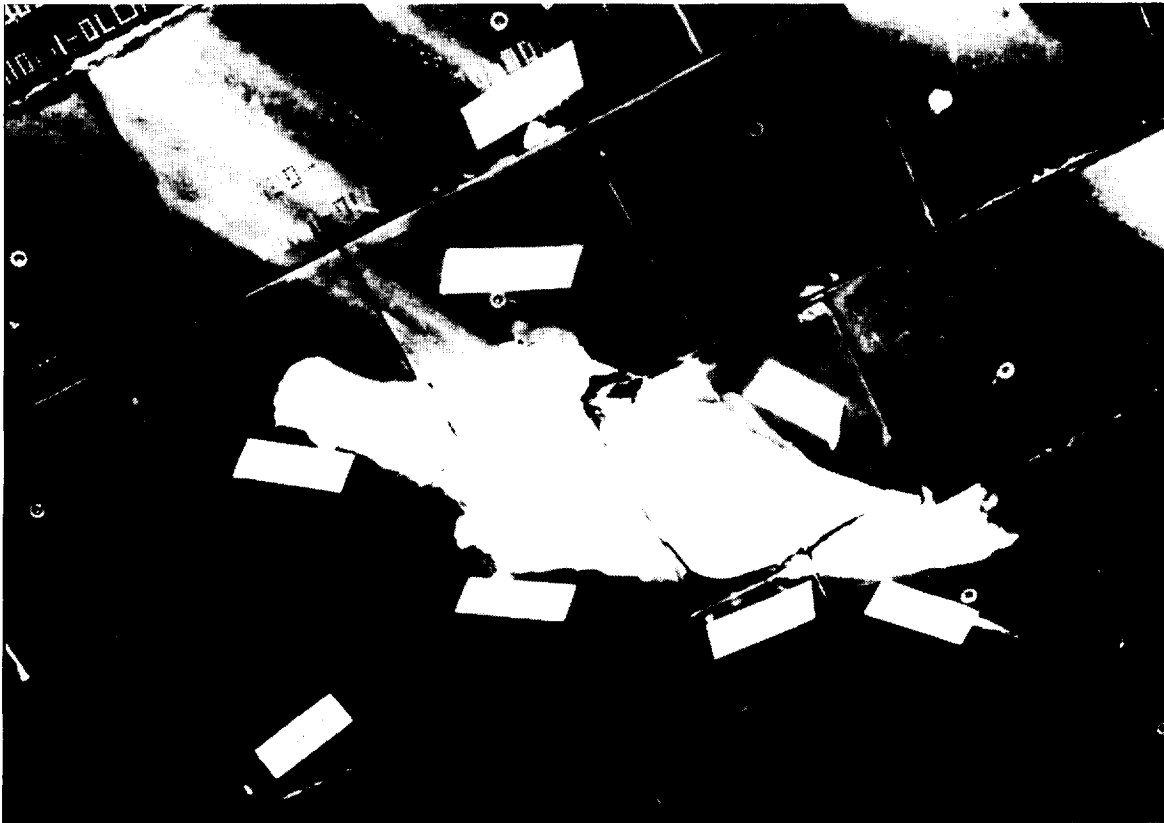


Figure 11. Wing debris impact gouge.

ORIGINAL PAGE
BLACK AND WHITE PHOTOGRAPH

ORBITER TPS FLIGHT EXPERIENCE
RSI TILE IMPACT DAMAGE

For the most part, tile damage due to rain, hail or debris impact has not resulted in tile loss. STS-27 (OV-104) was an example of complete tile removal due to a combination of impact and reentry thermal exposure (fig. 12). The loss of tile occurred prior to entry (probably during launch) as evidenced by thermal degradation of strain isolation pad (SIP) and filler bar; however, no structural burn-thru occurred. The structure was refurbished and new tiles installed.

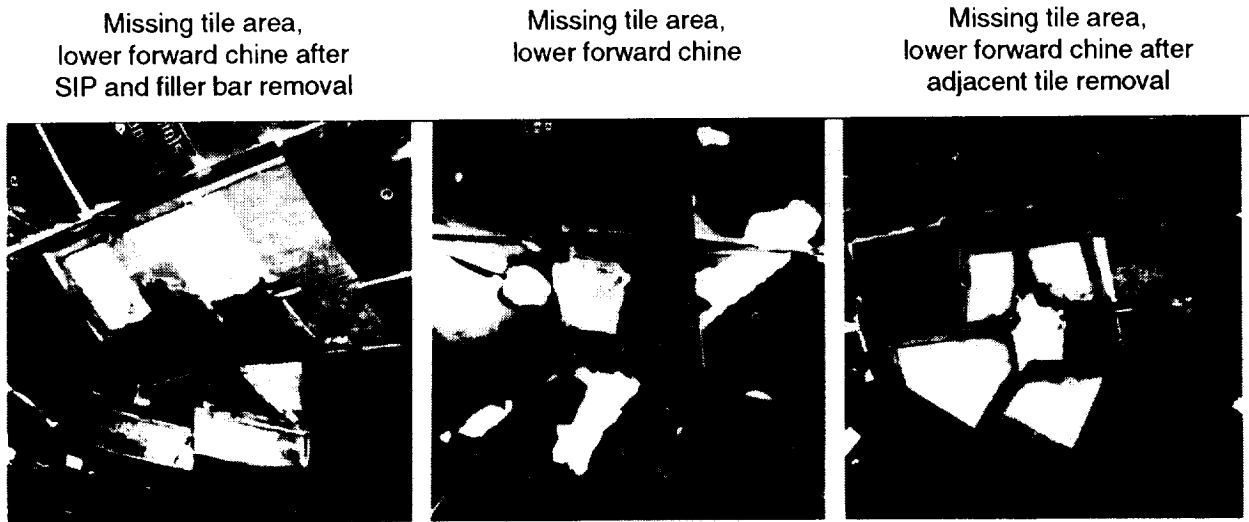


Figure 12. Lower forward chine missing tile.

ORIGINAL PAGE
BLACK AND WHITE PHOTOGRAPH

ORBITER TPS FLIGHT EXPERIENCE GAP FILLER DAMAGE

Fabric/ceramic gap fillers and flow stoppers are used extensively between tiles, TPS penetrations, RCC/RSI interfaces, and moveable interfaces. Gap fillers fabricated from quartz and Nextel become brittle and breach with continued reuse and cycling at temperatures in excess of 2000°F. Significant handling damage occurs once the gap filler is brittle. Gap filler shrinkage between tiles results in higher tile temperature (due to gap/step heating) and subsequent localized tile shrinkage/melting. An example of gap filler breaching and tile slumping is shown in figure 13. The use of a ceramic (colloidal silica) coating (designated C-9) significantly enhances the performance of the gap filler surface. C-9 coated gap fillers (Nextel and quartz) have successfully survived arc testing to 2500°F and are now installed in the Orbiter fleet. C-9 coating also has been applied to rigidize the AFRSI blankets and provide additional resistance to handling and impact damage.

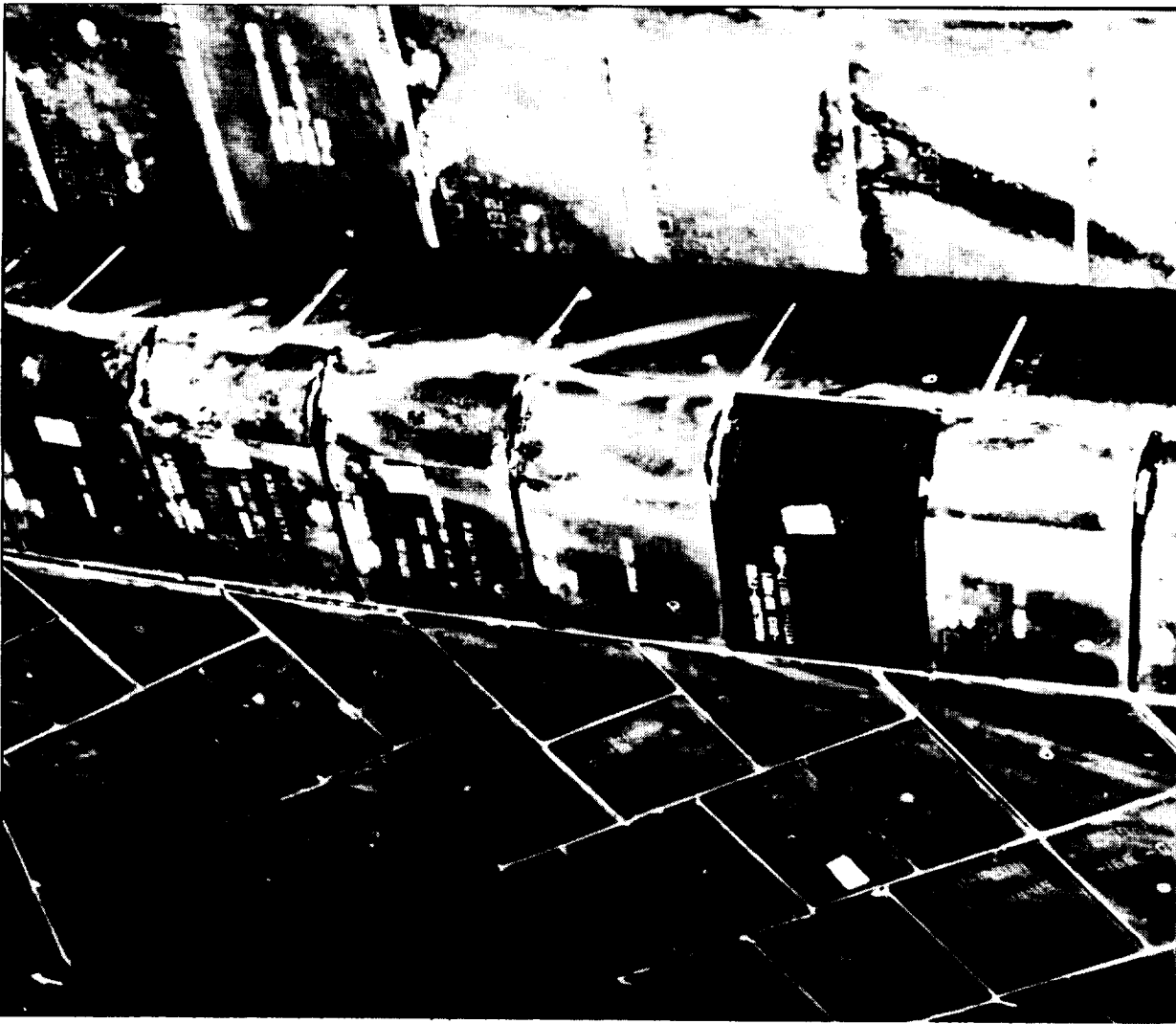
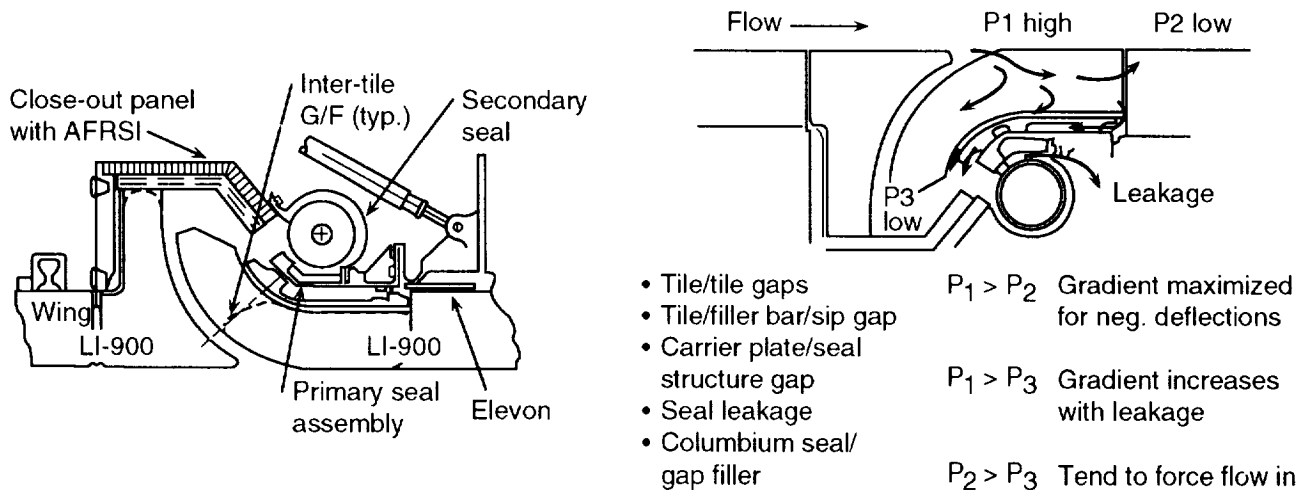


Figure 13. Elevon-elevon gap heating/tile slumping.

ORBITER TPS FLIGHT EXPERIENCE ELEVON LEADING EDGE

All three Orbiter vehicles have experienced TPS damage, over temperature of the elevon leading edge carrier plates, and primary seal holder. This damage has consisted of gas filler breaches, tile slumping, tile failure, and structure melting. The basic nature of the elevon leading edge/cove geometry (fig. 14a) creates pressure and heating gradients within the tile installation. This increased heating and pressure results in degradation of the gap fillers along the entire span. Potential leak sources (seal, gap filler, carrier plate, Columbia seal) also increase degradation of the gap filler.

Once the gas filler degrades, slumping on adjacent and downstream tiles occurs resulting in hot gas flow into the elevon seal/cove area. The worst damage was experienced on STS-51D (OV-103), where significant melting occurred on the aluminum carrier panel (Fig. 14b). This damage was worse than had been experienced on previous Orbiter flights and is generally attributed to more negative elevon deflection and higher surface roughness. Elimination of leak paths and reduction of the wing elevon roughness has been implemented to minimize elevon leading edge damage.



X101437M

Figure 14a. Elevon leading edge design components and flow paths.

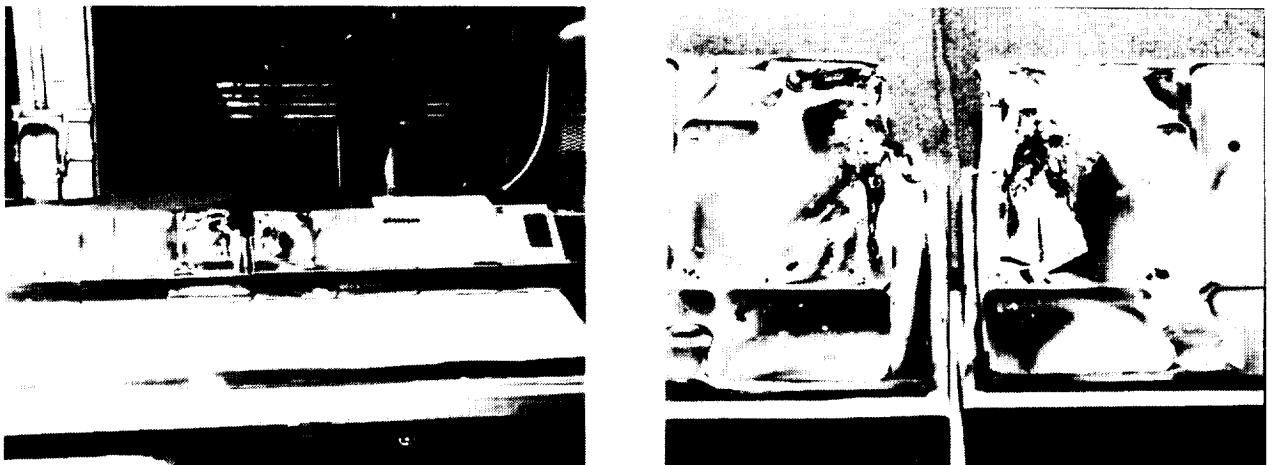


Figure 14b. Elevon cove carrier panel damage.

ORBITER TPS FLIGHT EXPERIENCE
NOSE GAP LOWER SURFACE INTERFACE TILE DAMAGE

Damage to the nose cap lower windward surface interface tiles (slumping of tiles along tile outer edge) forward of the nose gear door has occurred on several STS flights. The most significant damage occurred on STS-5 when hot gas penetration into the gap between two interface tiles caused slumping/melting of the tiles; thermal damage to the gap fillers, filler bars, and flow stoppers; and local melting of the aluminum carrier plate (fig. 15).

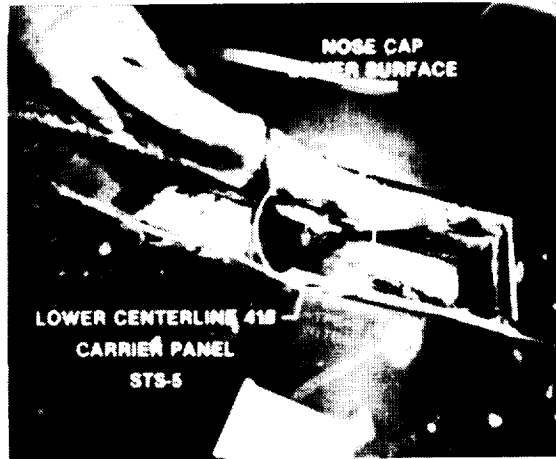


Figure 15. Nose cap lower surface interface tile damage - STS-5.

ORBITER TPS FLIGHT EXPERIENCE RCC CHIN PANEL

The RSI tiles installed between the nose gap and the nose landing gear doors have been vulnerable to external tank debris impact damage and have experienced tile slumping as a result of overheating. Additionally, the tiles have presented installation difficulties as well as problems with meeting step (differences in height between adjacent tiles) and gap (space between adjacent tiles) specifications. As a solution to these anomalies, the RCC chin panel assembly was designed and installed as a direct replacement for the RSI tiles located in this area (fig. 16). The Orbiter forward fuselage structures were strengthened and stiffened by the addition of new attach fittings. For the chin panel installation, these structural modifications significantly reduced the installation difficulties associated with RSI tiles.

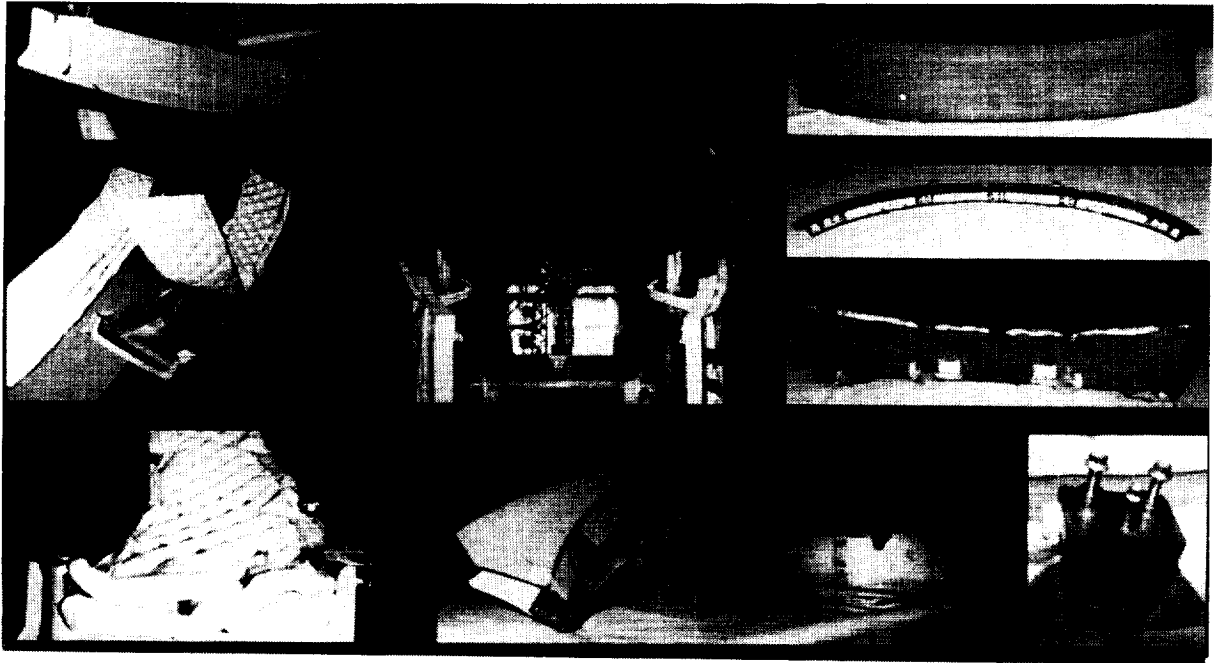


Figure 16. Orbiter RCC chin panel.

ORIGINAL PAGE
BLACK AND WHITE PHOTOGRAPH

ORBITER TPS FLIGHT EXPERIENCE RCC CHIN PANEL THERMOELASTIC DESIGN

Flight performance of the chin panel has been outstanding; however, thermoelastic analyses of the flange areas have revealed higher values of thermally induced stress than originally estimated. The flange area of the chin panel was designed to minimize thermal stress (fig. 17). The low thermoelastic margins of safety (down to zero) are evaluated on flight-to-flight basis to assure chin panel acceptability.

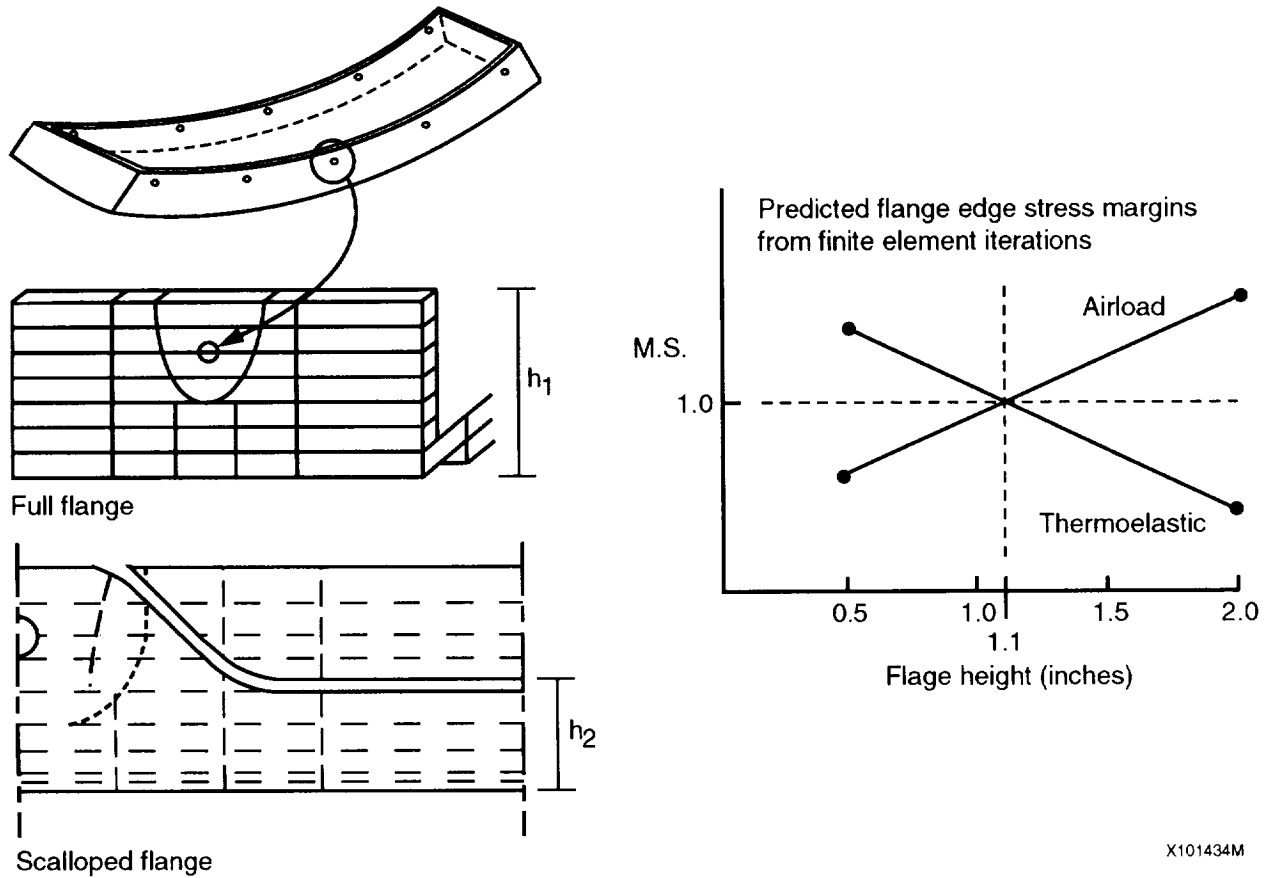


Figure 17. Chin panel flange height determination.

ORBITER TPS FLIGHT EXPERIENCE RCC TEMPERATURE LIMITS

The reusable, oxidation protected RCC has been successfully flown on forty-three Space Shuttle Orbiter flights. The multimission life of the RCC components has been established through extensive thermal (plasma arc and radiant) and structural component tests. The RCC was originally developed to have nominal multimission capability (i.e., no surface recession) with a maximum temperature of 2800°F. However, Orbiter abort conditions can result in RCC temperatures significantly higher (>3000°F) than the multimission design value. Accordingly, an over-temperature test (3000-3400°F) program was conducted to develop surface recession correlations and establish single mission limit temperature for the RCC material. A comparison with available passive/active oxidation data in the literature for Si-O-C/Si-O-N systems, indicates that oxidation protected RCC remains passive for temperatures of 3250-3300°F (fig. 18).

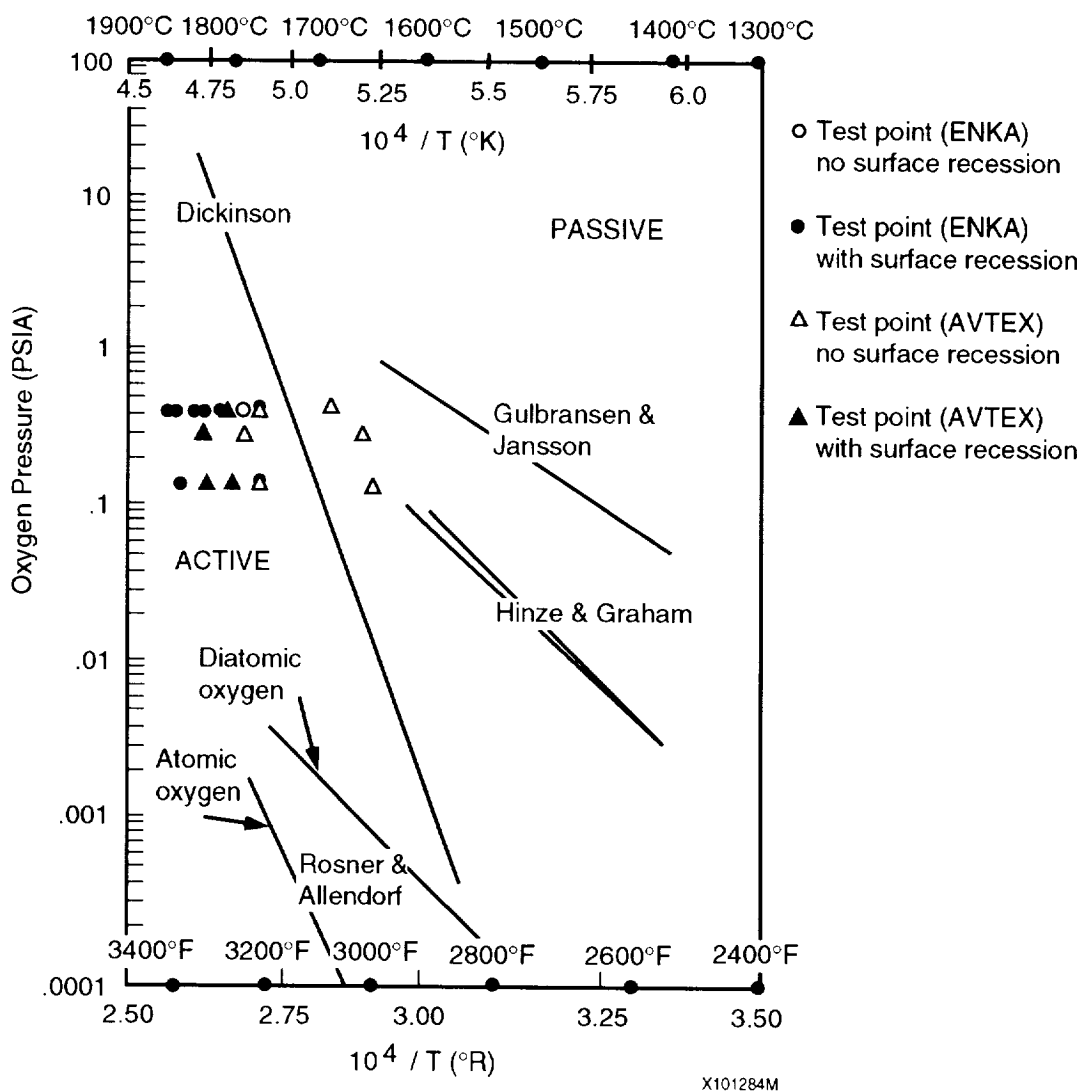


Figure 18. Active-pressure transition oxygen pressures comparisons with test conditions.

ORBITER TPS FLIGHT EXPERIENCE RCC OPERATIONAL LIMITS

The RCC over-temperature test data has been used to increase the Orbiter ranging capability to ensure safety of flight for both nominal and off-nominal (abort) entries. A typical nominal and abort trajectory are shown on an active/passive oxidation plot (fig. 19). A nominal Earth entry is always passive but an abort condition does result in active oxidation during the entry. The time spent in the active oxidation regime is critical in assessing a potential system failure.

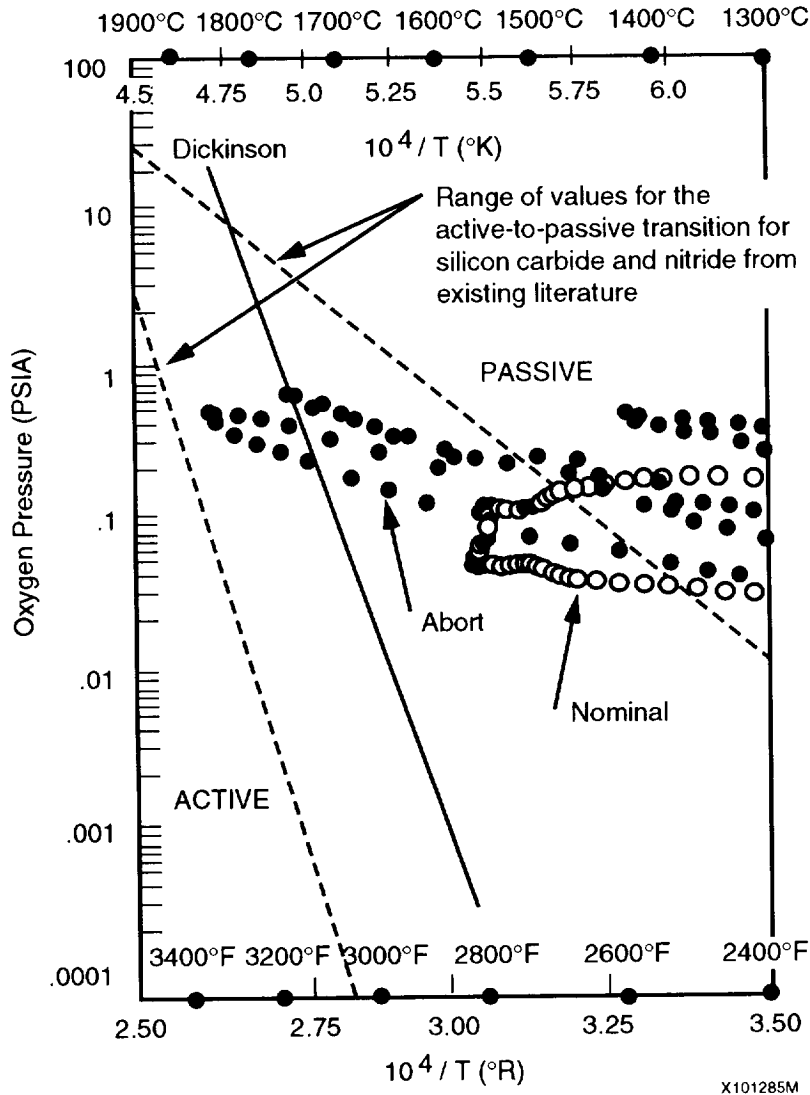


Figure 19. Active-passive transition oxygen pressures comparisons with flight conditions.

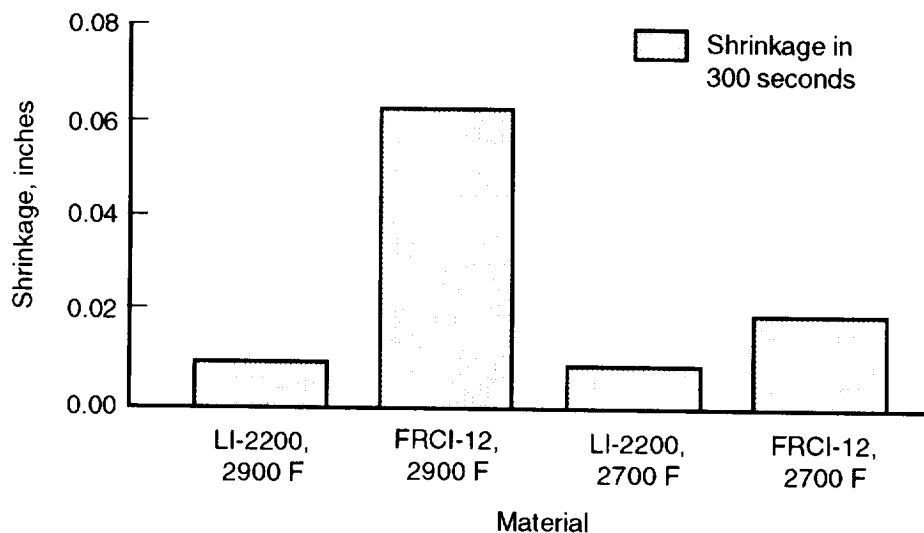
AEROBRAKE TPS MATERIALS

The design goal for a non-ablating, flight-certified material for the Aeroassist Flight Experiment (AFE) aerobrake TPS was accomplished by selecting an RSI material compatible with the thermal environment for a single mission use. Three rigid, reusable surface insulation materials, which were flight certified for the Space Shuttle Orbiter TPS, were considered:

LI-900/LI-2200 materials, which are basically 95% pure silica with densities of 9 lb/ft³ and 22 lb/ft³, respectively, and

FRCI-12, a fibrous refractory composite insulation with a density of 12 lb/ft³.

The aerobrake heating/temperature distribution required stability at higher temperature in the stagnation region than in the other areas (2900°F). Therefore, the LI-2200 material was selected based on its shrinkage characteristics and the requirement to maintain dimensional control (fig. 20). FRCI-12 was used as the TPS material in the remaining areas.



X101433M

Figure 20. Over temperature RSI shrinkage evaluation.

AEROBRAKE TILE INSTALLATION

The aerobrake tiles are installed using the process developed for the Space Shuttle Orbiter (fig. 21). To isolate the tiles from stress induced by structure deflection or temperature-induced structural expansion, the tiles are bonded to a SIP, which is then bonded to the aerobrake skin. The SIP is a 0.16-inch Nomex nylon felt material. The bonding is performed using Room Temperature Vulcanizing adhesive #560 (RTV-560). The gaps between the tiles are filled with the Ceramic Ames Gap Filler (CAGF) to prevent plasma flow from heating the inner-tile gap. These gap fillers are composed of several layers of Nextel (alumina silicate) cloth (AB312) impregnated with a ceramic coating. Several layers are bonded to the bottom sidewall of one neighboring tile with a ceramic adhesive. Gap filler installation and the use of a full footprint SIP are modifications to the Orbiter tile installation.

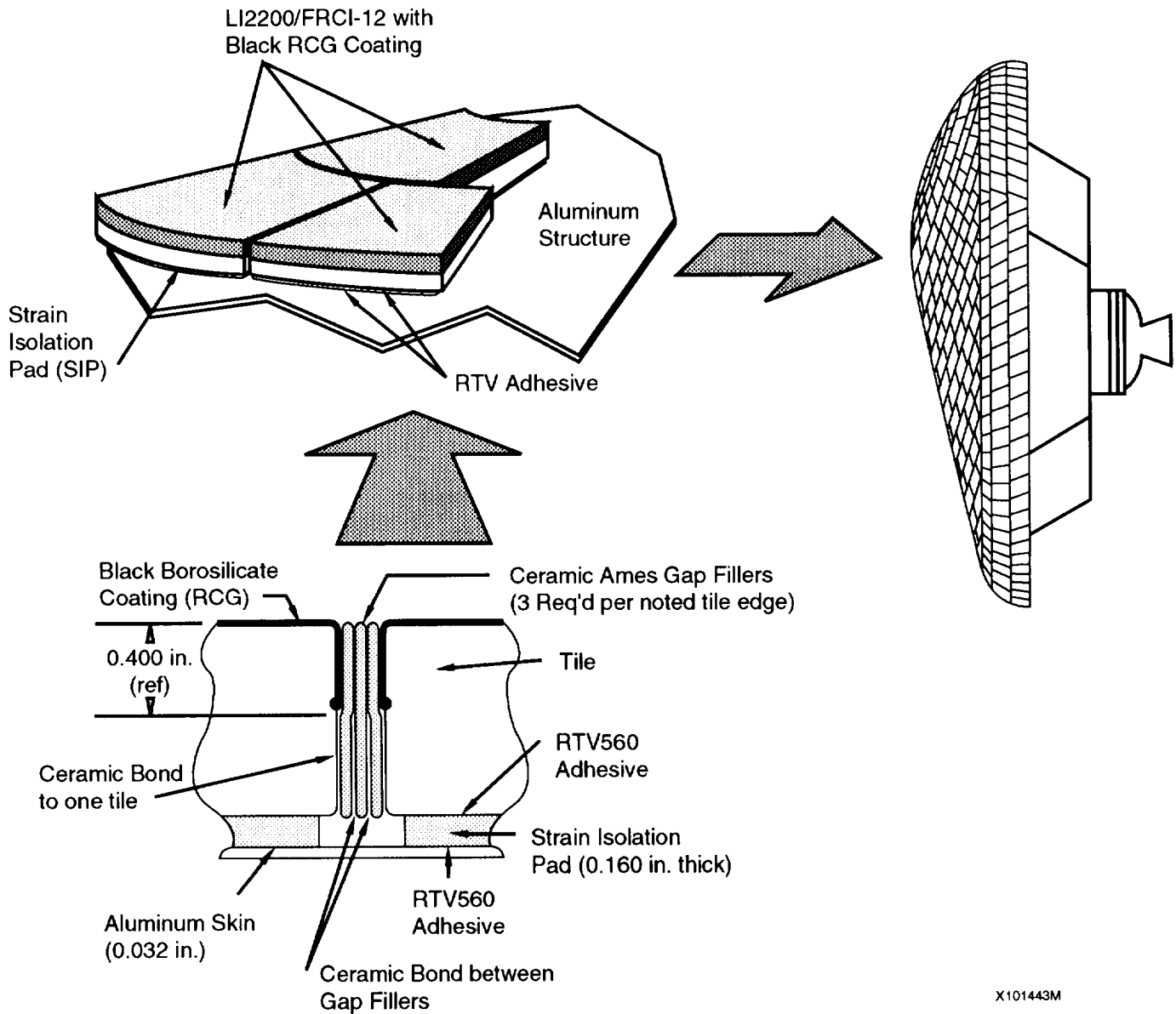


Figure 21. Aerobrake TPS installation.

AEROBRAKE TILE CONFIGURATION/MANUFACTURING

The LI-2200 tiles on the ellipsoid were made larger than baseline Space Shuttle Orbiter tiles (6-inch by 6-inch), due to the more rigid structure of the ellipsoid and the higher strength of the LI2200 material. In the cone and skirt area, the FRCI-12 tiles were sized smaller, as much larger skin deflections are expected in those area (fig. 22).

Numerically controlled machining processes were used to manufacture AFE tiles, as was done for the Orbiter. The Calma CAD system was utilized to automate the design process and facilitate efficient transfer of data to the N-C machining process. This resulted in cost and time savings by reducing the N-C programming efforts and the number of close-out tiles needed, and by eliminating the need to sand the inner moldline of each individual tile during installation.

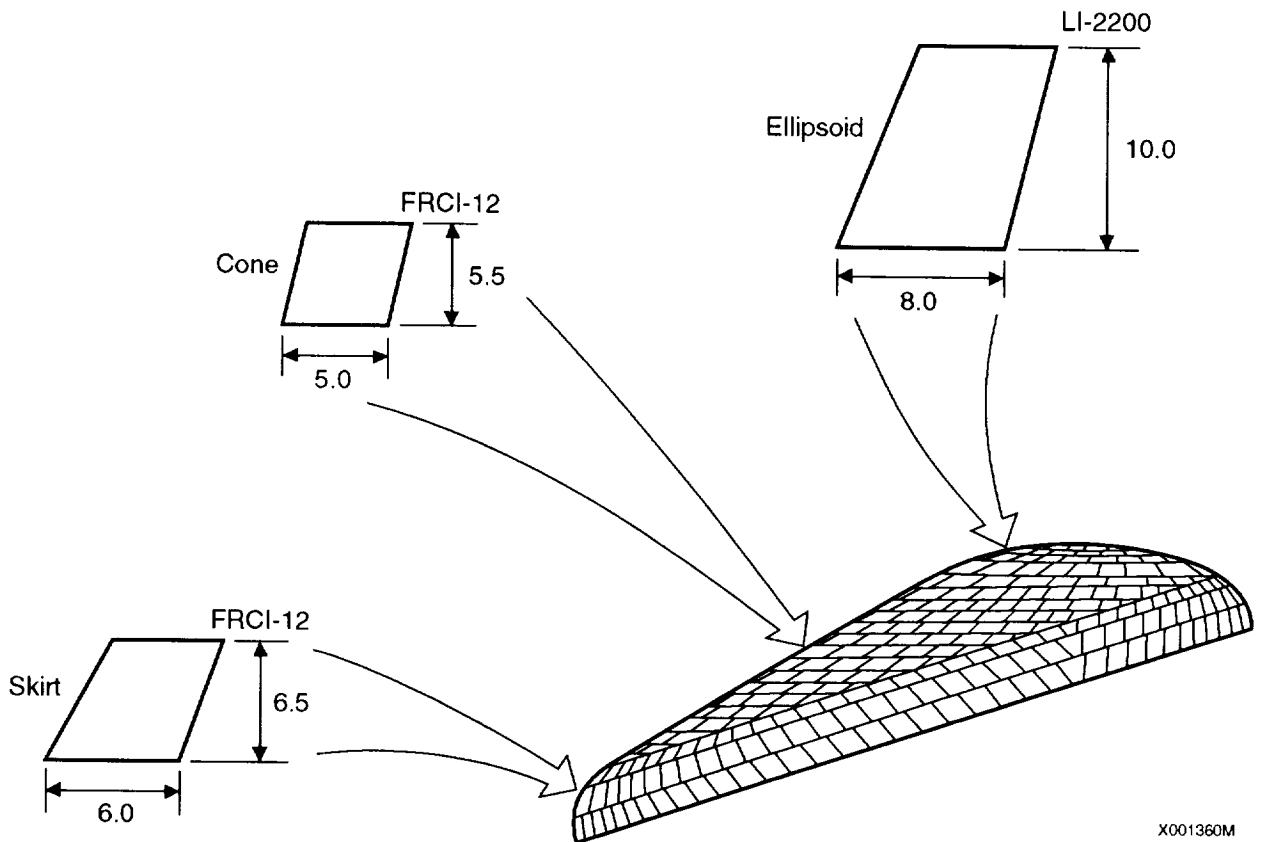


Figure 22. Typical tile sizes and materials.

TPS DESIGN FOR AEROBRAKING AT EARTH AND MARS

Thermal protection systems are being designed for advanced vehicle configuration and future missions using state-of-the-art materials for a wide range of entry conditions. The performance of an ablation material (5026-H/CG) applied to a 40-foot aerobrake (AFE configuration) that performs two aerocaptures (Mars and Earth) without refurbishment was analyzed.

The ablation analysis was performed in two steps: surface recession and mass loss were first predicted for Mars entry, then these values were used as initial conditions for the Earth aerocapture.

The results of this analysis suggest that optimal ablator thickness can be determined such that more than one successful entry can be made without refurbishment. Critical sizing of the ablator was established from the thermal response for the Earth return. Material degradation (density ratio) can be used to assess thermal/structural performance (fig. 23).

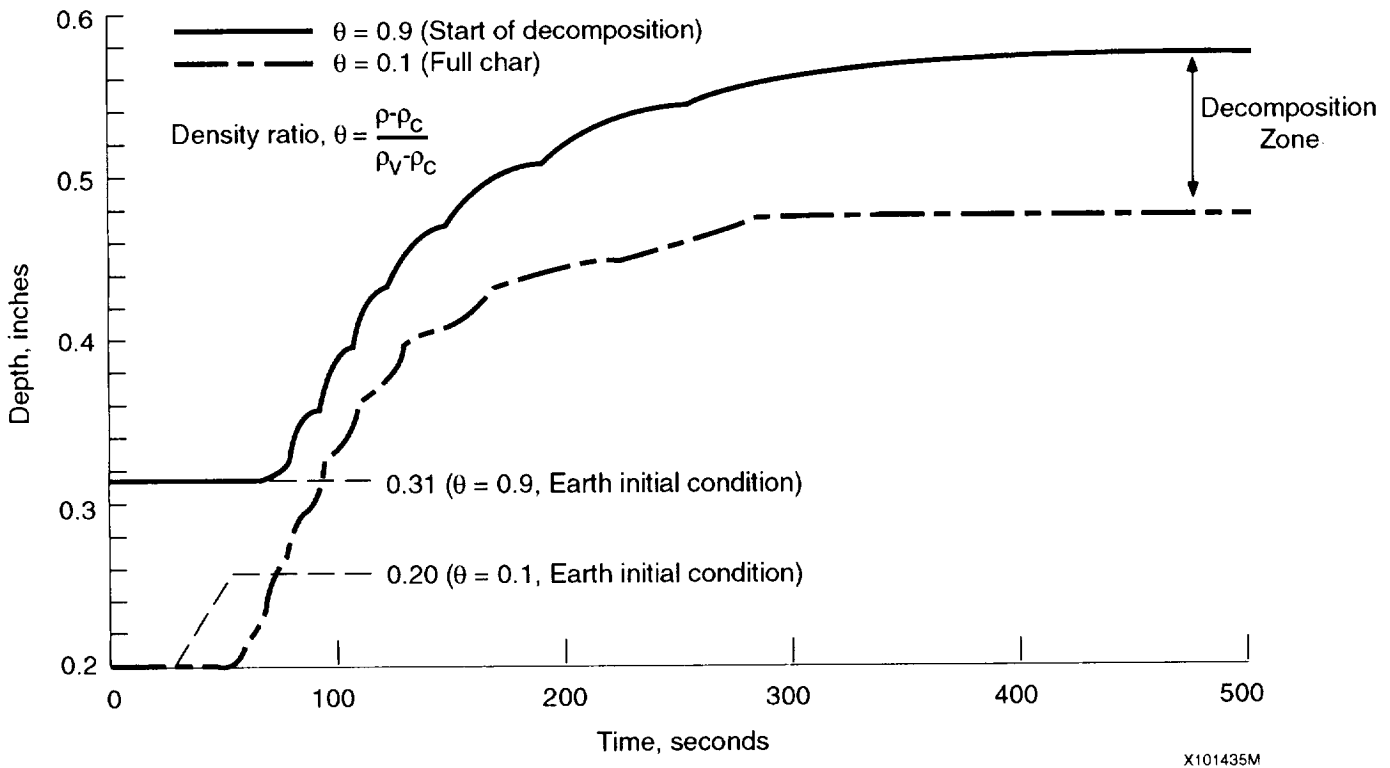


Figure 23. Earth aerocapture for the 40 ft. AFE- 0.9 and 0.1 density ratio depths at the stagnation point.

TPS DESIGN FOR AEROBRAKING WEIGHT PENALTY

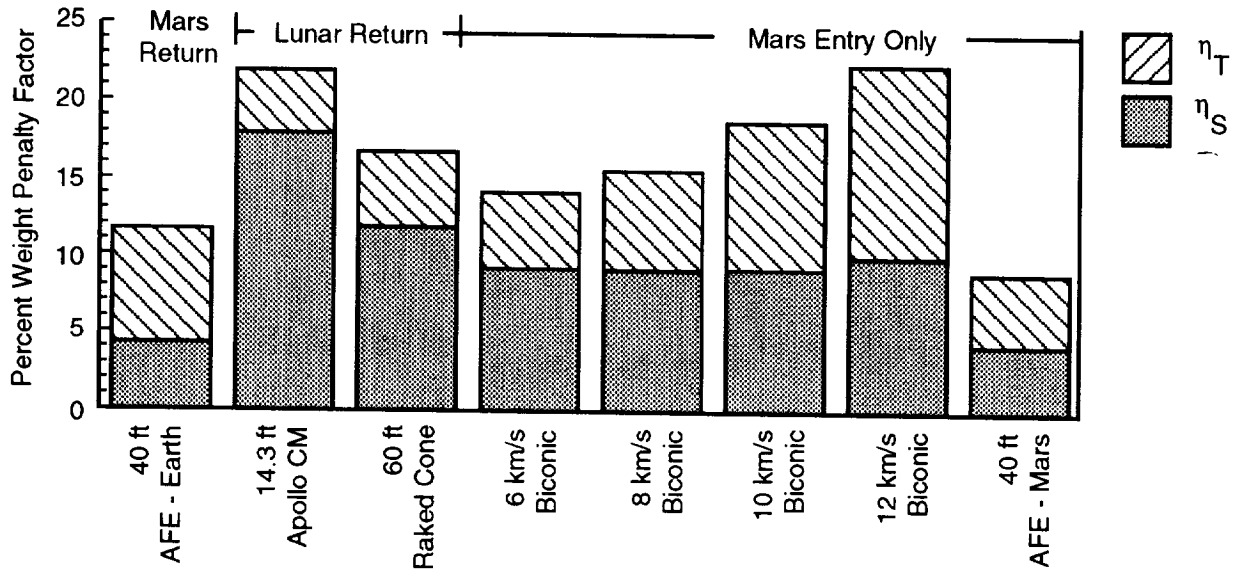
TPS assessments for future vehicle and missions can be made using TPS weight penalty factors. A TPS penalty factor can be defined as:

$$\eta_t = \frac{\text{TPS Weight}}{\text{Total Vehicle Weight}}$$

$$\eta_s = \frac{\text{Structural Weight}}{\text{Total Vehicle Weight}}$$

$$\eta_{ts} = \eta_t + \eta_s$$

Figure 24 a, b shows the relationship between η_s and η_t for several vehicle configurations used for an aerocapture at Earth and Mars. These results indicate that an η_{ts} of 15-20 percent is possible utilizing aerobraking, which results in a predicted 50-80 percent increase in payload over an all-propulsive design.



X101445M

Figure 24a. Weight penalty factors for TPS/structure weights.

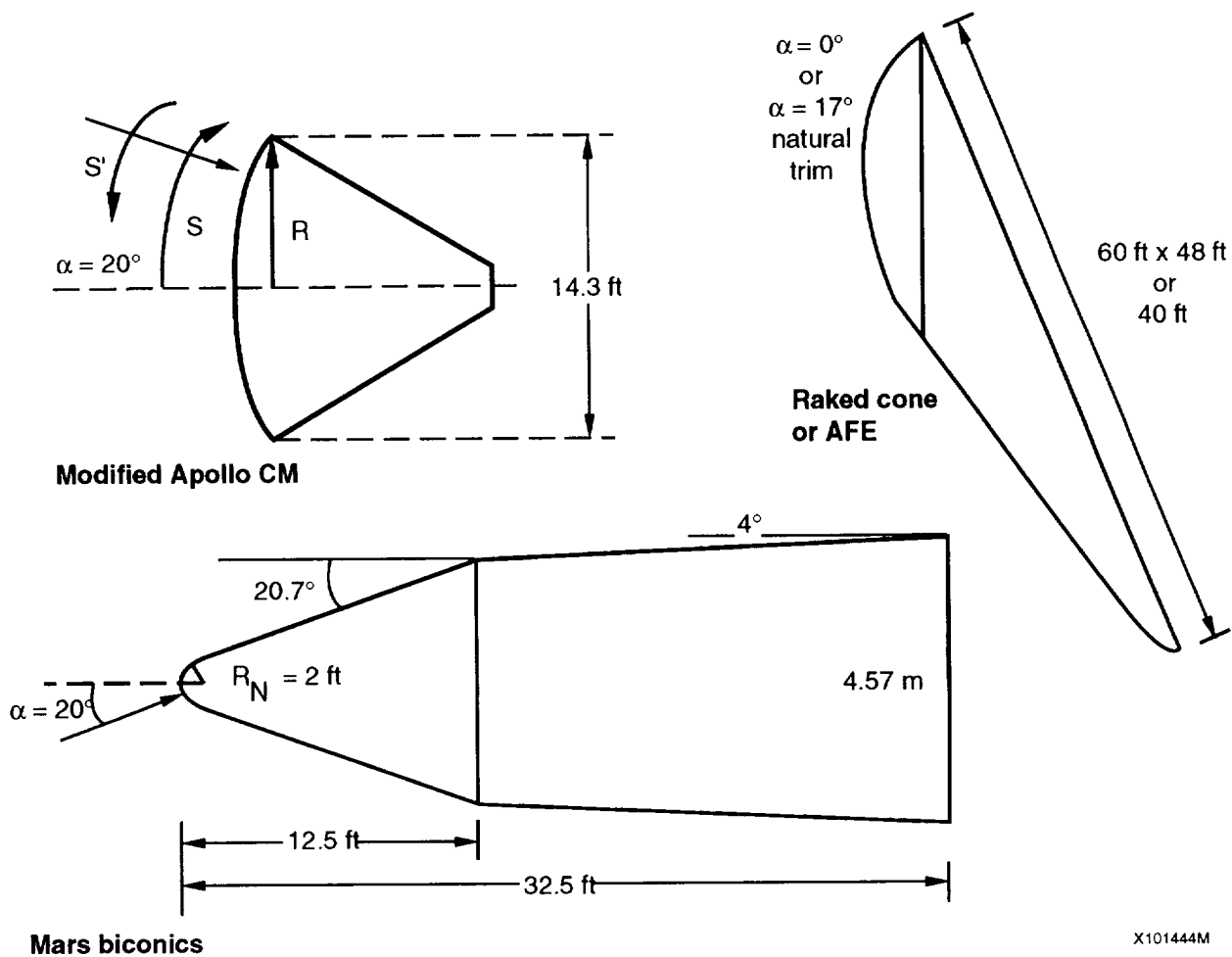


Figure 24b. Earth/Mars aerocapture vehicles.

SUMMARY

- Significant advances have been made in the design, fabrication, and certification of TPS on manned entry vehicles (Mercury through Shuttle Orbiter)
- Shuttle experience has identified some key design and operational issues
- State-of-the-art ceramic insulation materials developed in the 1970s for the Space Shuttle Orbiter have been used in the initial designs of aerobrakes
- This TPS material experience has identified the need to develop a technology base from which a new class of higher temperature materials will emerge for advanced space transportation vehicles.

ADVANCED CERAMIC MATRIX COMPOSITES FOR TPS

**Daniel J. Rasky
NASA Ames Research Center
Moffett Field, CA**

Abstract

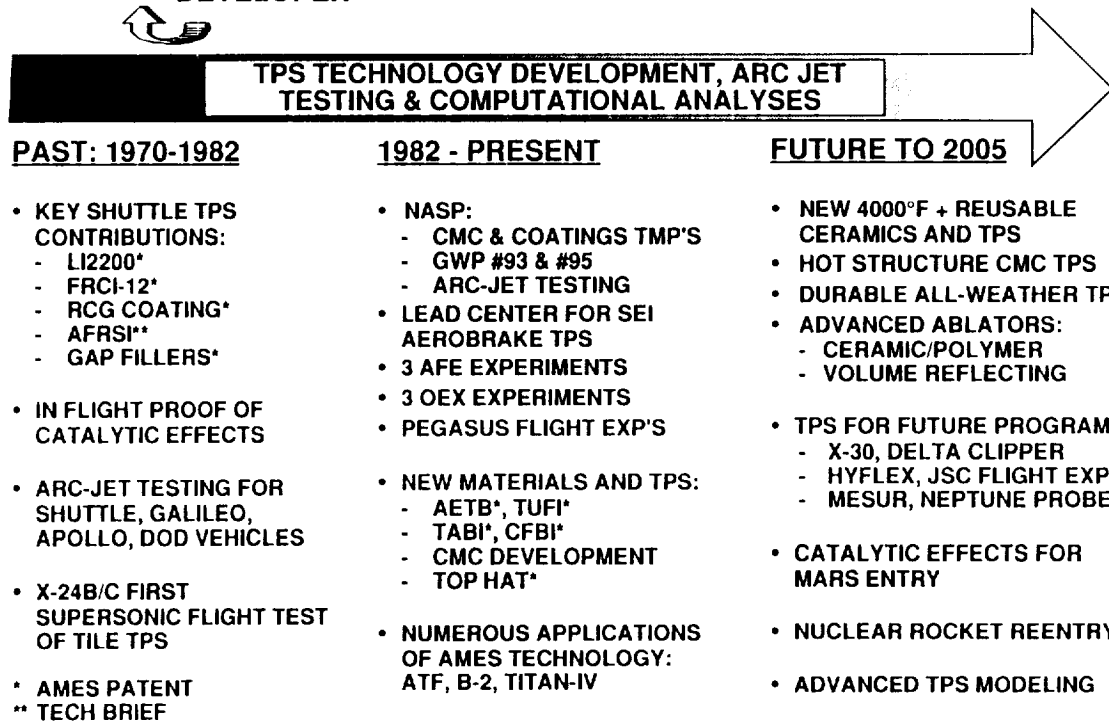
Recent advances in ceramic matrix composite (CMC) technology provide considerable opportunity for application to future aircraft thermal protection systems (TPS), providing materials with higher temperature capability, lower weight, and higher strength and stiffness than traditional materials. The Thermal Protection Material Branch at NASA Ames Research Center has been making significant progress in the development, characterization, and entry simulation (arc-jet) testing of new CMC's. This presentation gives a general overview of the Ames Thermal Protection Materials Branch research activities, followed by more detailed descriptions of recent advances in very-high temperature Zr and Hf based ceramics, high temperature, high strength SiC matrix composites, and some activities in polymer precursors and ceramic coating processing. The presentation closes with a brief comparison of maximum heat flux capabilities of advanced TPS materials.

Long Range Goal of the Ames Thermal Protection Materials Branch

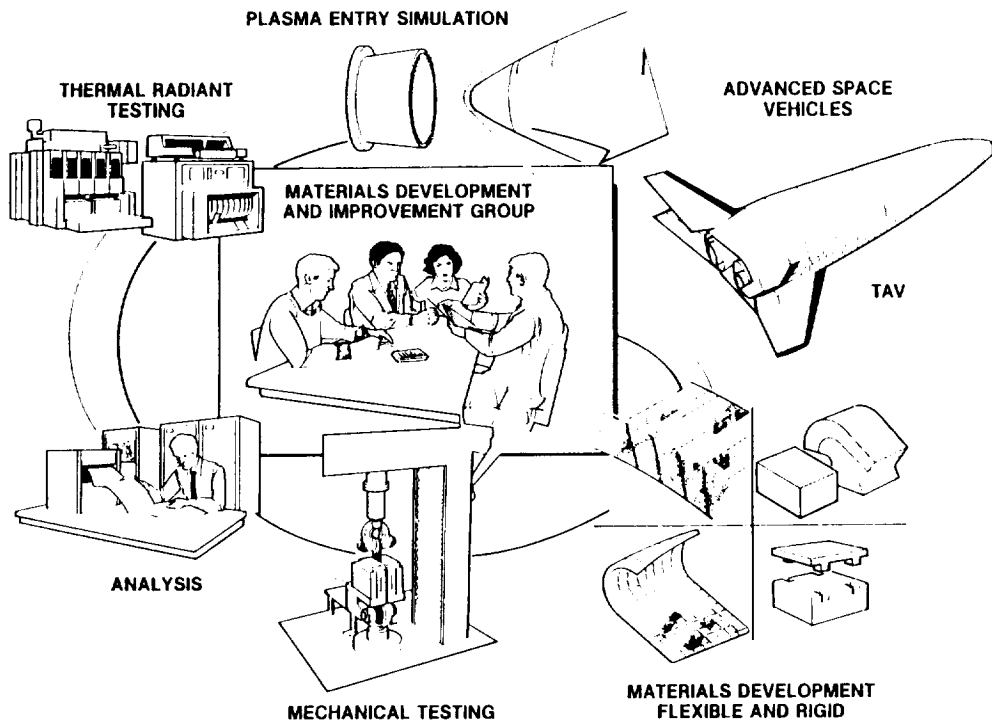
To Provide Thermal Protection
Materials, Systems, and Analysis
Methods for Heat Shields of Entry,
Aerobraking and Hypersonic Cruise
Vehicles and Planetary Probes

THERMAL PROTECTION MATERIALS

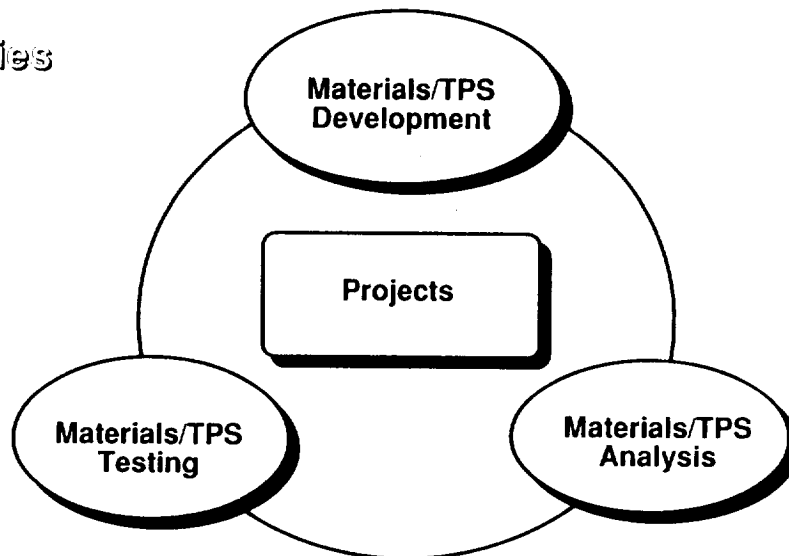

 AMES VEHICLE DEVELOPER → GROUND/FLIGHT EXPERIMENTS → FLIGHT TPS



THERMAL PROTECTION SYSTEM DEVELOPMENT PROCESS



Activities



- ➡ **A Synergistic, Multi-disciplinary Approach**
- ➡ **Continual Research/Technology Development Supports Projects**

Projects

NASA Programs

- SEI: Recent Langley "Aerobrake Assembly with Minimum Accommodation" study performed by Lockheed baselined Ames developed "TOP HAT" CMC/rigid tile TPS.
- Shuttle: Working with KSC, JSC, NASA HQ and Rockwell to fly Ames developed TUF1 TPS on the Orbiters in high erosion areas.
- MESUR: Performed initial TPS sizing and trades. Identified a light weight silicon rubber TPS (SLA-561) which allows a 50% increase in scientific payload.
- Pegasus: Teaming with Dryden and LaRC for boundary layer cross flow transition experiment (scheduled to fly in FY92). Constructing Pegasus Wing-Glove and PI for and TPS performance evaluation experiment. Wing fillet heating experiment flown on first two Pegasus launches.
- HYFLEX: Working with a multi-agency team to define vehicle. Diboride leading edges and nosetip being evaluated.
- Wave-Rider: Discussions with McDonnell Douglas regarding leading edge design.

NASP

- Responsibility for government work packages #93 and #95 for arc-jet testing and internal TPS insulation design.
- Both have been highly praised by NPO/JPO and Industry Leads (i.e. General Dynamics, Rockwell, Pratt Whitney).

DoD

- Delta Clipper: Cooperative research program being developed with McDonnell Douglas and SDIO. Cooperative efforts proposed in three areas:
 - 1) TPS design and consultation
 - 2) Arc-jet testing
 - 3) Computational studies

Material/TPS Testing Areas

- **Arc-Jet Testing**
 - Aerodynamic Heating Facility (20 MW)
 - Interactive Heating Facility (60 MW)
 - Panel Test Facility (20 MW)
- **Material Characterization**
 - SEM, XRF, Optical Microscopes
 - XRD, Large Sample TGA
 - Dilatometer, Instron
 - Infrared & Ultraviolet Spectrometers
 - ICP Mass Spectrometer (inorganic)
- **Special Testing**
 - Laser Time-of-Flight Mass Spectrometer (SALI)
 - Side Arm Reactor

Material/TPS Analysis Areas

- **Computational Surface Thermochemistry**
 - Surface heating and catalysis effects (NSCAND, BLIMPK, LAURA, VSL, GASP)
 - Ablation, erosion, and shape change computations (ASC, CMA, ACE)
- **Computational Solid Mechanics**
 - Multi-dimensional conduction/radiation analyses (SINDA, TRASYS)
 - Multi-dimensional thermal-stress analyses (COSMOS)
- **Computational Materials**
 - CVD/CVI Processing (GENMIX, NACHOS)
 - Reflective TPS analyses
 - Composite material properties (MATX)

Material/TPS Development Areas

Advanced Material Families

- **Ceramic Matrix Composites**
 - Very-High Temperature Ceramics (HfB₂ +SiC)
 - High Temperature, High Strength Ceramics (C/SiC)
 - Polymer Precursors (Si/C/B fibers, tape casting)
 - Ceramic coatings processing
- **Light Weight Ceramic Insulations**
 - Rigid Tiles (AETB, SMI, UltraLight)
 - TABI and CFBI Flexible Blankets
 - Aerogel Studies
- **Light Weight Ablators**
 - Rigid Ceramic Insulation with a Polymer Filler
- **Surface Coatings**
 - Low Catalytic Efficiency, High Emissivity
 - Reflective

Diboride Materials

- **Manlabs Inc. (Cambridge MA) tested and compiled a data base on a large number of refractory materials in the 60's and early 70's**
- **The diborides of zirconium and hafnium (ZrB₂ and HfB₂) were found to be the most oxidation resistant, high temperature materials in the study, e.g.**

Arc testing of ZrB₂ + 20 v/o SiC

surface temp. 2510 C, stagn. press. 1.0 atm,
stagn. enthalpy 11.6 kJ/gm

recession: 0.66 mm/2 hrs
equivalent graphite recession: 30 cm !
equivalent SiC recession: 45 cm !

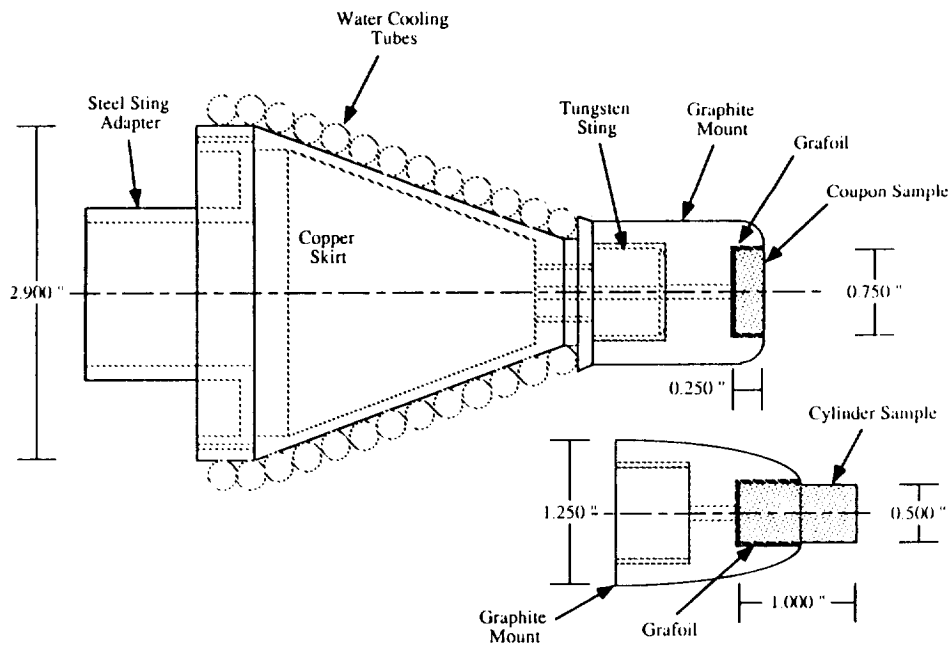
"These results illustrate the reuse capability of the boride composites... This capability is unrivaled by any other material system." - Quote from Dr. Larry Kaufman, Principal Investigator in the Manlabs Studies

Research Highlights for FY91

Very-High Temperature Ceramics

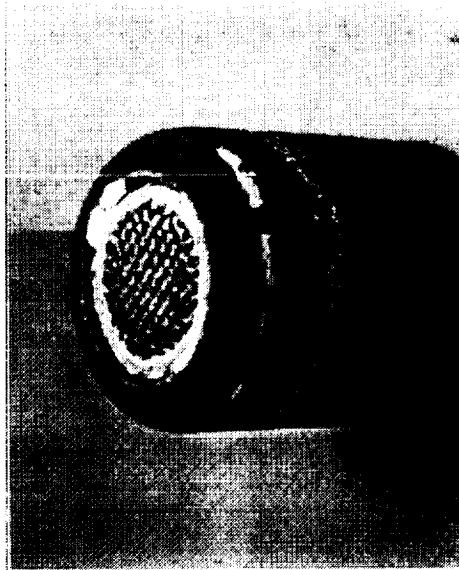
- Phase I arc-jet testing completed
- 19 reinforced Zr and Hf based ceramics tested (from Manlabs, Cerac, Lanxide, SAIC)
- Arc-jet data in good agreement with earlier Manlabs results
- Over 2 times RCC maximum heat flux capability demonstrated
- 2200°C+ (4000°F+) capability demonstrated
- Successfully applied ZrB₂ coatings to RCC using RF sputtering
- Phase II testing of disk samples, nosetip and leading edge components currently in progress

Sample Model Holder



Post-Test Photographs of RCC and ZrB₂ + 20 v/o SiC Samples

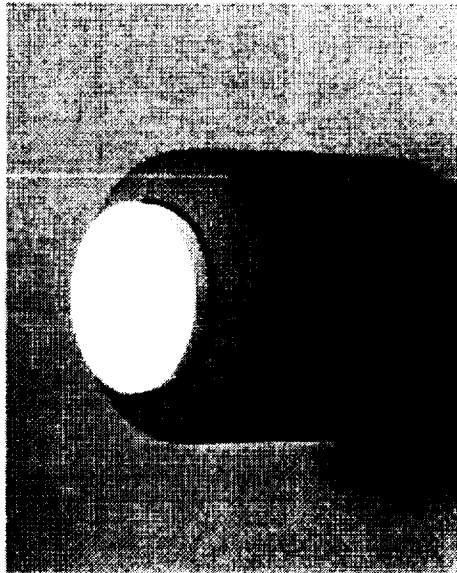
Test Conditions: test time = 3 min, cold wall heat flux = 295 W/cm²,
stag. press. = 0.046 atm, stag. enth. = 25 kJ/gm



**LTV-t1n2a
RCC**

**Recession: 2.0 mm
Weight loss: 1.31 gm
Peak temp.: 2040 C**

**SiC coating lost after
approximately 100 sec.**



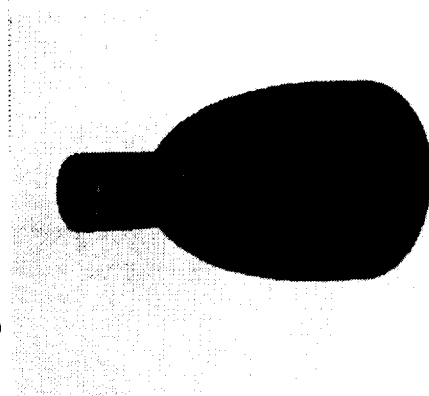
**Cerac-t2n4a
ZrB₂ + 20v/o SiC**

**Recession: -0.03 mm
Weight loss: 0.01 gm
Peak temp.: 1820 C**

**Adherent, thin, glassy coating
formed on sample**

Post-Test Photographs of Two HfB₂ + 20 v/o SiC Samples

Test time = 5 min
Cold wall heat flux = 560 W/cm²
Stag. press. = 0.075 atm
Stag. enth. = 27 kJ/gm

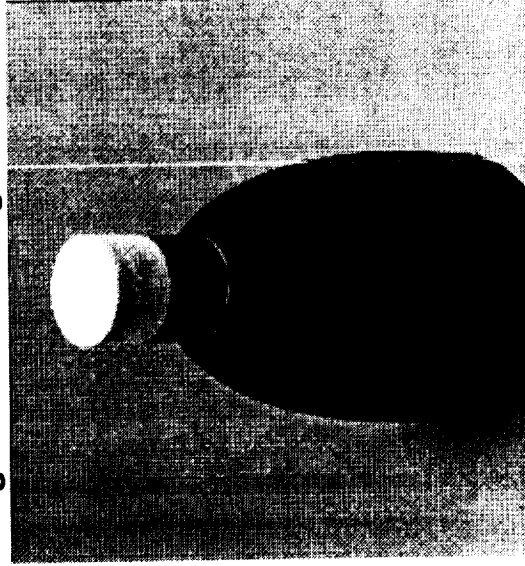


Man-441
(A-7-1)
HfB₂ + 20v/o SiC

Recession: -0.05 mm
Weight loss: 0.00 gm
Peak temp.: 1740 C

Clear glassy coating
formed on sample

Test time = 3 min
Cold wall heat flux = 730 W/cm²
Stag. press. = 0.105 atm
Stag. enth. = 27 kJ/gm

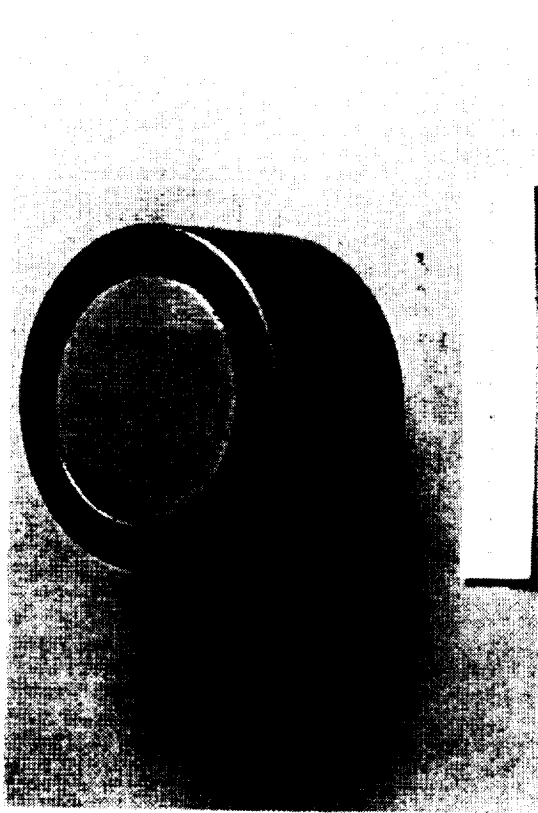


Recession: -0.03 mm
Weight loss: 0.08 gm
Peak temp.: 2460 C

Adherent, thin oxide coating
formed on sample

Diboride Components

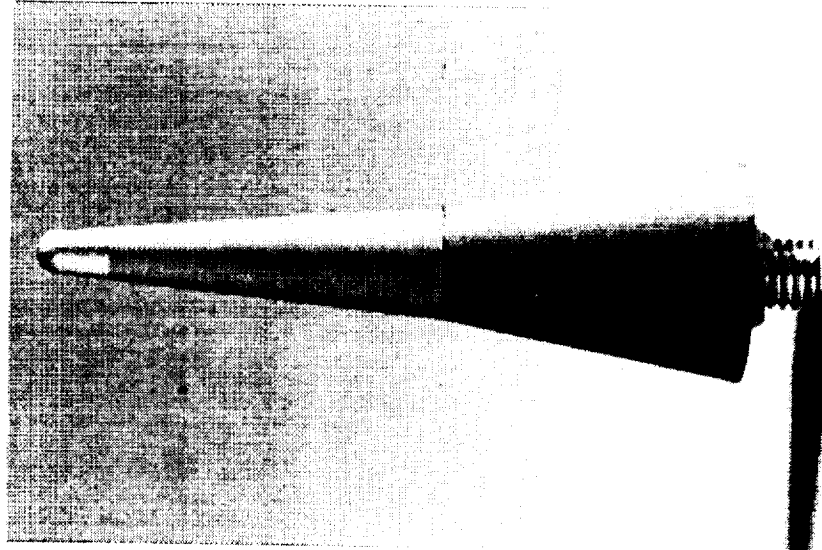
ZrB₂ + 20v/o SiC &
HfB₂ + 20v/o SiC Materials



Disk Sample (3" diam. x 0.25")



Leading Edge (4.0" x 0.5" diam.)



Hypersonic Vehicle Nosetip
(0.141" nose radius)

Table 1: Sample Components
Advanced Refractory Composites (Testing Program Phase II)
10/28/91

Sample Component	Matrix/ Reinforcement	Geometry/Dimension	Quantity
ManLabs-C1	ZrB ₂ /SiC _p	Coupons/2.8" Dia. x 0.25"	3
ManLabs-C2	ZrB ₂ /SiC _{pl}	Coupons/2.8" Dia. x 0.25"	3
ManLabs-C3	ZrB ₂ /SiC _{pl} +C _{fch}	Coupons/2.8" Dia. x 0.25"	3
ManLabs-I.E	ZrB ₂ /SiC _{pl}	Leading Edge/0.75" Dia. x 2.75"	2
ManLabs-H1	HfB ₂ /SiC _{pl}	Hemisphere/0.700" Radius	1
ManLabs-H2	HfB ₂ /SiC _{pl}	Hemisphere/0.500" Radius	1
ManLabs-H3	HfB ₂ /SiC _{pl}	Hemisphere/0.125" Radius	1
ManLabs-NT	HfB ₂ /SiC _{pl}	Nose Tip/0.141" Radius on	3
ManLabs-S	ZrB ₂ /SiC _p	5.25 Deg. Cone Half Angle Skirt	1
Cerac-S	ZrB ₂ /SiC _p	5.25 Deg. Cone Half Angle Skirt	2
Cerac-C	ZrB ₂ /SiC _p	Coupons/2.8" Dia. x 0.25"	3
ACR-C1	ZrB ₂ /SiC _p +C _{fc}	Coupons/2.8" Dia. x 0.25"	2
ACR-C2	ZrB ₂ /SiC _p +SiC _{fc}	Coupons/2.8" Dia. x 0.25"	2
ARC-C1	ZrB ₂ Coated RCC	Coupons/2.8" Dia. x 0.25"	1
ARC-C2	ZrB ₂ Coated RCC	Coupons/2.8" Dia. x 0.25"	1
GA-C1	RS-HfB ₂ Coated C/C	Coupons/2" Dia. x 0.25"	2
GA-C2	HfO ₂ Coated RS-HfB ₂ Coated C/C	Coupons/2" Dia. x 0.25"	2
SAIC-C1	ZrB ₂ /SiC+C _{fc}	Coupons/2.8" Dia. x 0.25"	1
SAIC-C2	ZrB ₂ /SiC+C _{fc}	Coupons/2.8" Dia. x 0.25"	1
Total			35

Subscript definitions: p = particulate, pl = platelet, fc = continuous fiber, fch = chopped fiber

Material/TPS Development Areas

Advanced Material Families

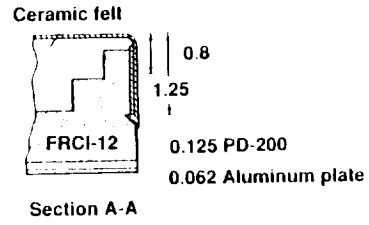
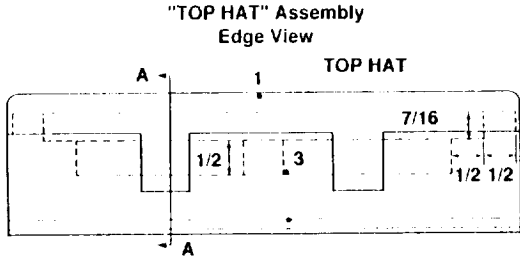
- **Ceramic Matrix Composites**
 - Very-High Temperature Ceramics (HfB₂ + SiC)
 - High Temperature, High Strength Ceramics (C/SiC)
 - Polymer Precursors (Si/C/B fibers, tape casting)
 - Ceramic coatings processing
- **Light Weight Ceramic Insulations**
 - Rigid Tiles (AETB, SMI, UltraLight)
 - TABI and CFBI Flexible Blankets
 - Aerogel Studies
- **Light Weight Ablators**
 - Polymer Filler + Rigid Ceramic Insulation
- **Surface Coatings**
 - Low Catalytic Efficiency, High Emissivity
 - Reflective

Research Highlights for FY91

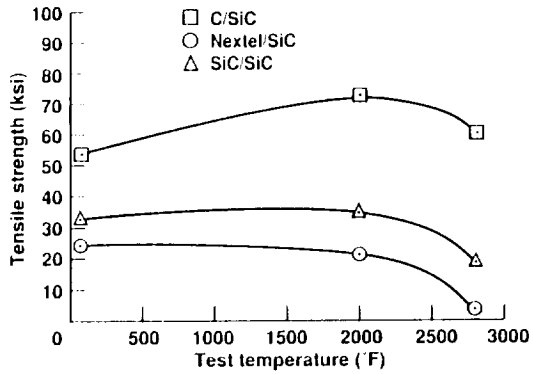
Ceramic Matrix Composites

- DuPont and SEP fabricated Nicalon, Nextel, and carbon fiber reinforced SiC matrix composites evaluated for aerothermal and mechanical performance
- Pre and post-test mechanical property characterization showed that carbon fiber reinforced materials have little degradation after arc-jet exposure to 2700°F for ten cycles of ten minutes each
- DuPont material found to be equivalent or better (particularly in quasi-isotropic configuration) than SEP material.
- Mass loss and mechanical property retention results in very good agreement with radiative heating testing data recently reported by General Dynamics
- New Ames developed "TOP HAT" CMC/rigid tile TPS, using Ames CVD/CVI fabricated C/SiC CMC, shown to survive multiple arc-jet exposures to 3100°F

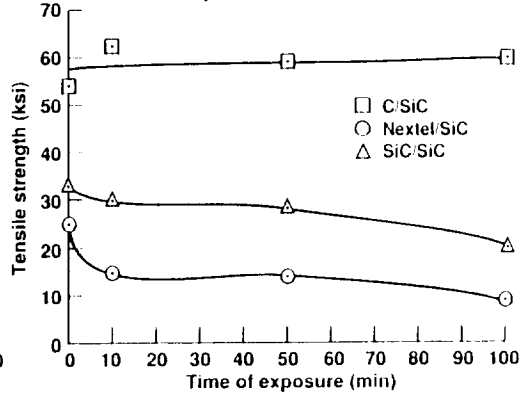
CERAMIC MATRIX COMPOSITES PROGRAM



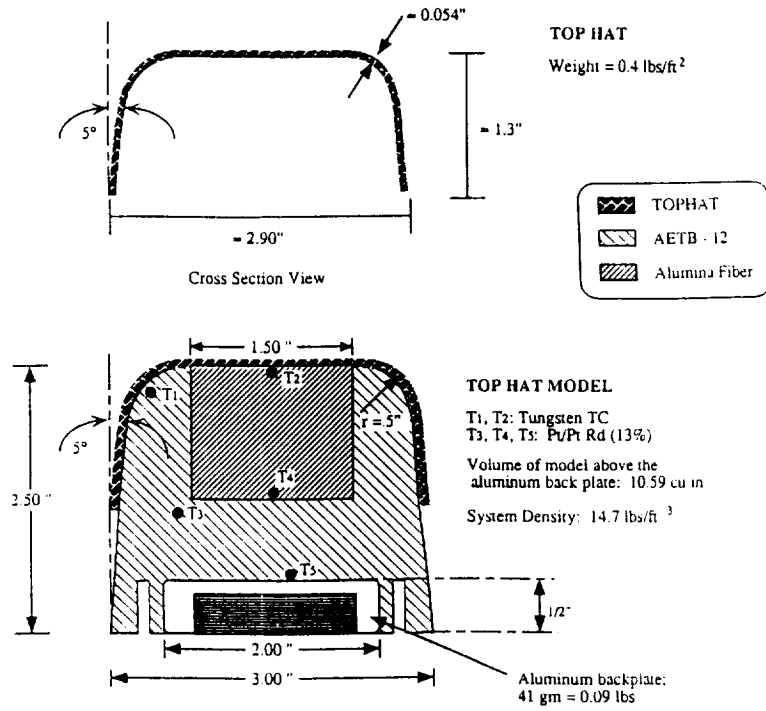
Average Tensile Strength vs. Temperature
Pre-aeroconvective Exposure (U)



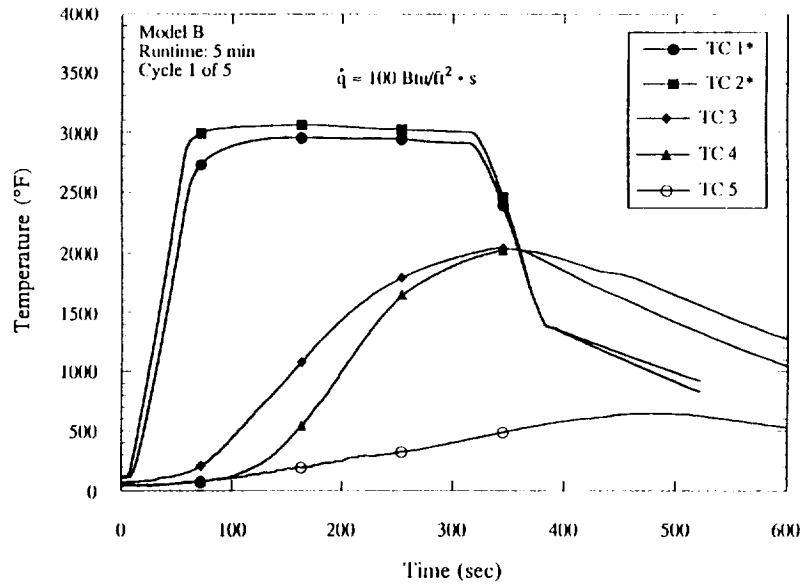
Average Tensile Strength (70 °F, Ar) of Carbon/SiC,
Nextel/SiC, and SiC/SiC vs. Time of Aeroconvective
Exposure (2700 °F)



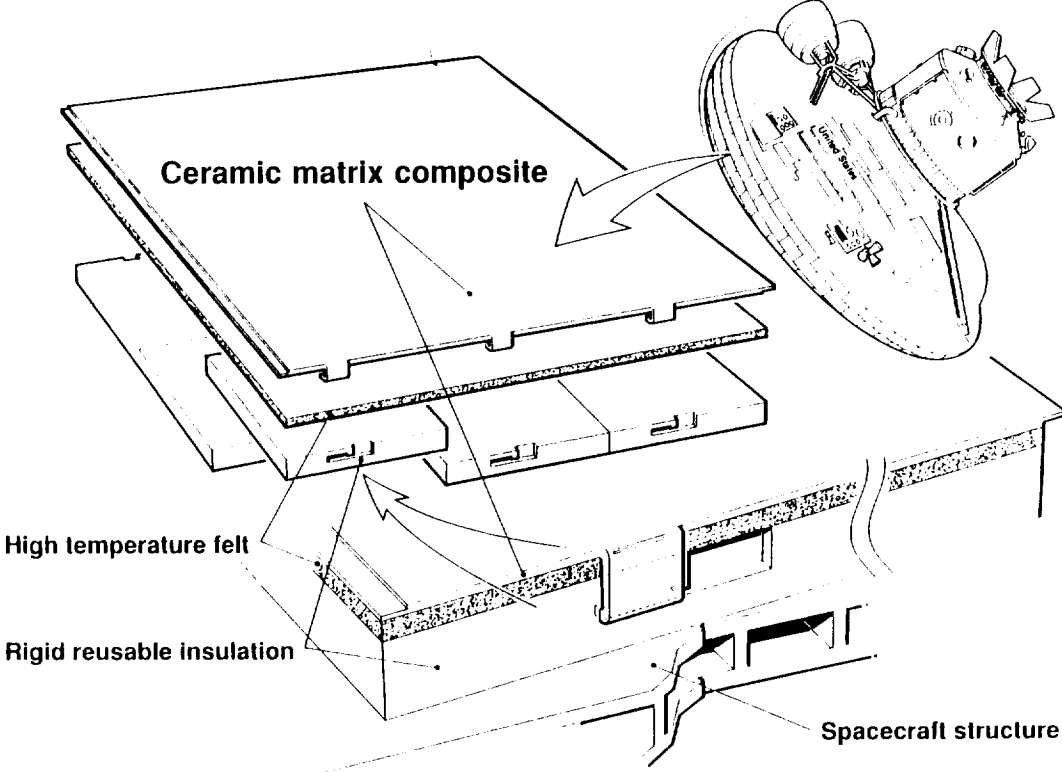
TOPHAT Thermal Protection System Arc-Jet Model Design



Thermal Response Of TOPHAT Model In An Aeroconvective Environment



TOP HAT Thermal Protection System



Material/TPS Development Areas

Advanced Material Families

- **Ceramic Matrix Composites**
 - Very-High Temperature Ceramics (HfB₂ +SiC)
 - High Temperature, High Strength Ceramics (C/SiC)
 - Polymer Precursors (Si/C/B fibers, tape casting)
 - Ceramic coatings processing
- **Light Weight Ceramic Insulations**
 - Rigid Tiles (AETB, SMI, UltraLight)
 - TABI and CFBI Flexible Blankets
 - Aerogel Studies
- **Light Weight Ablators**
 - Polymer Filler + Rigid Ceramic Insulation
- **Surface Coatings**
 - Low Catalytic Efficiency, High Emissivity
 - Reflective

Research Highlights for FY91

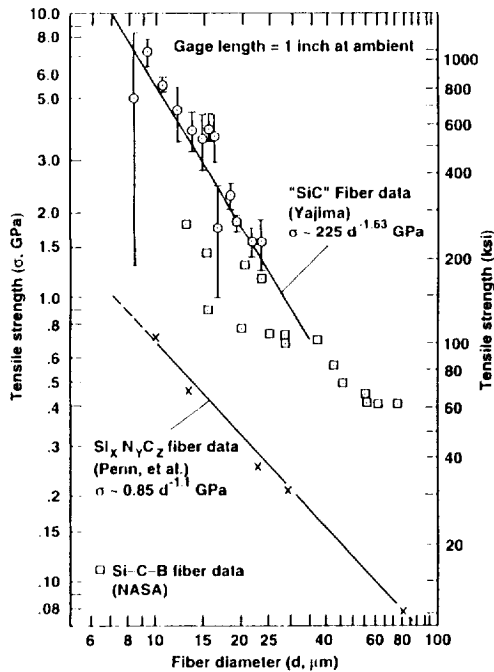
Polymer Precursors

- Low oxygen content Si/C/B polymers synthesized
- UV air and non-oxygen cure procedure demonstrated
- Ceramic fibers show tensile strength retention to 1300°C
- Successfully synthesized Zircon/ZrB₂/SiC 20 mil tapes using a combination of tape casting and sol-gel processing

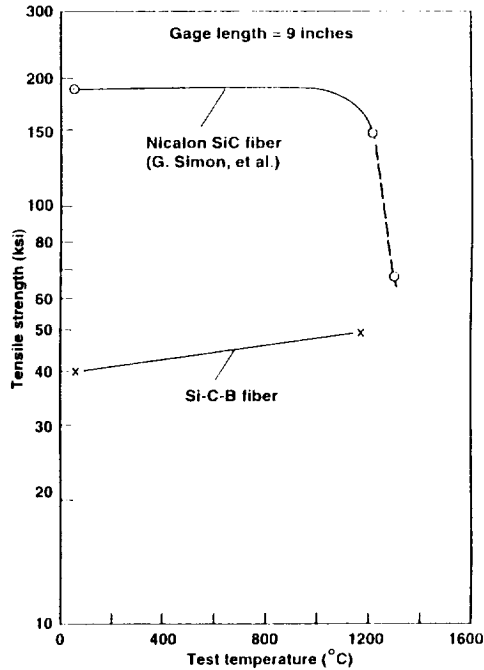
Ceramic Coating Processing

- Successfully applied thin (20 micron) coatings for ZrB₂ to a SiC substrate using RF sputtering
- Planning initial trials for plasma spraying ZrB₂ and ZrB₂/SiC using a constricted arc-jet

TENSILE STRENGTH OF SiC, Si-C-N and Si-C-B FIBERS AS A FUNCTION OF FIBER DIAMETER



TEMPERATURE EFFECTS ON FIBER TENSILE STRENGTH IN AIR



Ref. K.J. Wynne and R.W. Rice, Ann. Rev. Mater. Sci., 14, 297 - 334 (1984).

Maximum Cold Wall Heat Flux Computations

- For one-dimensional, radiative equilibrium, the maximum cold wall heat flux, Q_{cw} , can be computed from the maximum material use temperature, T_{max} , by:

$$Q_{cw} = \epsilon \sigma T_{max}^4 / (1 - H_w/H_r)$$

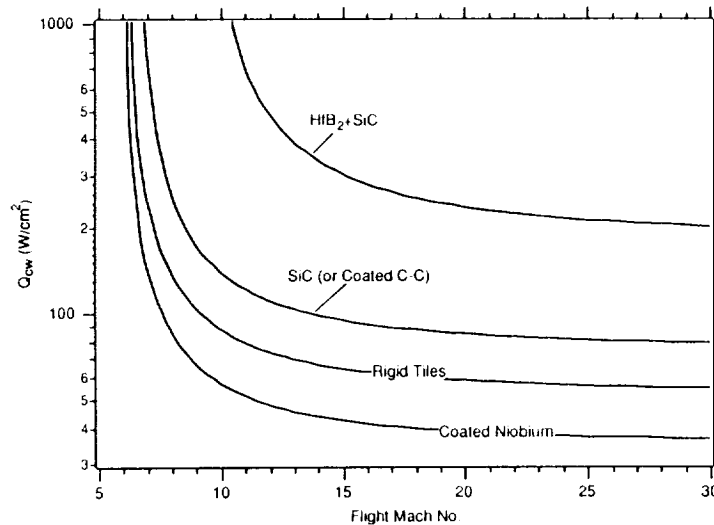
where ϵ is the emissivity and H_w is the wall gas enthalpy at T_{max} , and H_r is the local recovery enthalpy

- Surface catalytic effects all roll into the value of H_w
- With values for the material maximum use temperature and emissivity, Q_{cw} can be easily computed

Material	Maximum Use Temp. (C)	Emissivity
HfB ₂ +SiC	2480	0.62
SiC (or Coated C-C)	1760	0.76
Rigid Tiles	1540	0.85
Coated Niobium	1530	0.65

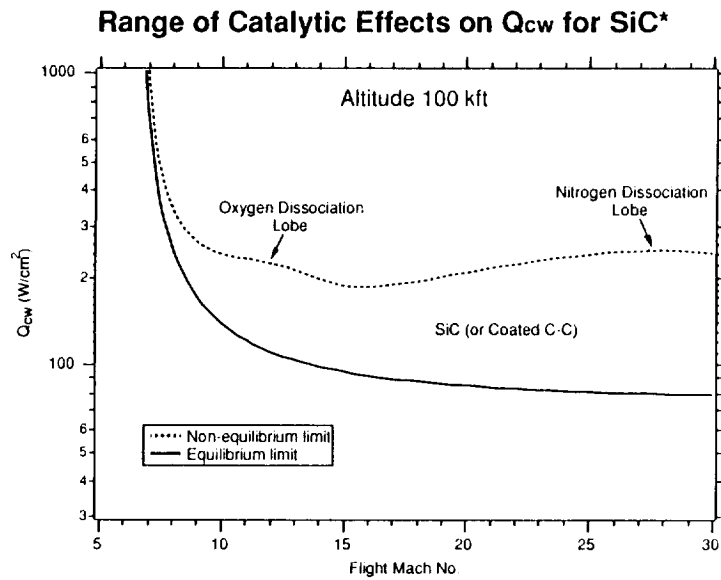
Maximum Cold Wall Heat Flux Computations

Q_{cw} for a Fully Catalytic Surface*



* H_w evaluated assuming chemical equilibrium

Maximum Cold Wall Heat Flux Computations



* H_w evaluated varying from equilibrium to maximum non-equilibrium value

THERMAL PROTECTION USING VERY HIGH TEMPERATURE CERAMICS

George R. Adamczyk
Supermaterials Research and Development Corp.
Cleveland, Ohio

INTRODUCTION

Thermal barrier coatings sprayed by Plasma gun and monolithic structures sprayed from high temperature ceramics and refractory metals are possible utilizing a proprietary plasma gun system capable of melting virtually any material in existence. Materials can be sprayed mixed with other materials, in gradated proportions or in pure form. With this technology, critical parts such as insert coated jet engine turbine blades, fuel nozzles, combustor cans, rocket nozzles, and "stealth" outer skins with embedded electronic sensors can be created or coated.

These unique ceramics, applied usually to commercially available metal structures, offer high temperature resistance, heat transfer, and abrasion/corrosion resistance characteristics without the typical drawbacks of industrial ceramics. Many are flexible, structurally non-brittle and uncommonly impact-resistant.

After ten plus years of development, advanced plasma gun sprayed ceramics technology offers practical, economical solutions to the forward-looking challenges in ultra-supersonic high altitude aircraft skins, ultra-high temperature engines, and rocket and space shuttle protective applications.

PLASMA GUN SPRAY TECHNOLOGY

PROCESS

Figures 1 and 2 show schematically the proprietary plasma gun system presently used at Supermaterials. The plasma gun design is a trade secret of Supermaterials. Therefore, the specifics of the design will not be discussed in detail. The design is based on a modified DC plasma gun. The thermal spray process uses an accelerating hydrogen plasma stream heated to temperatures greater than 35,000° F (19,500° C) and at speeds initially in excess of 12,000 ft/sec (3700 m/sec). The system consumes up to 100 KW of power to generate these requirements. Simultaneously, argon, nitrogen or helium is mixed in the plasma stream at the gun end along with a pumped stream of particles (ceramic and/or metal powders). These particles become molten or semi-molten as they accelerate toward the sprayed surface. As they hit the surface, they splat and rapid solidification occurs. Over 27 million watts per cm² is pumped around the gas stream. During the spraying process, the sprayed surface reaches a maximum of 300° F (150° C). Materials such as cardboard, plastic, ceramic, glass and metal can be coated because of such low surface temperatures.

The large particles sprayed from the plasma gun system become nearly teardrop in shape then splatter onto the surface, cooling instantaneously and forming lenticular platelets upon smaller nearly spherical particle layers. These layers, not the usual in conventional spray coatings, provide unique characteristics. By adjustment of over 50 control parameters, new materials can be created.

Principally with the oxides that we spray, it appears that our system knocks off the loosely attached oxygen atoms (ref. 1). Aluminum oxide, for instance, becomes more stabilized so that this ceramic no longer absorbs or gives up oxygen when subjected to oxygen enriched gases, or a hotter environment. Gases, metals and metal oxides, when subject to certain settings of our system, appear to decouple the magnetic spins of the material's atoms. Materials which

are normally magnetic, become non-magnetic. Some are magnetic, but don't conduct electricity.

PROPERTIES

In the previous section, it was stated that over 50 parameters can be changed to create new materials. Adjustments of these parameters alter one or more of the following material characteristics:

- | | | |
|--------------------------|--------------------------|-------------------|
| ◦Abrasion Resistance | ◦Corrosion Resistance | ◦Catalytic Action |
| ◦Thermal Insulation | ◦Electrically Conductive | ◦Lubricity |
| ◦Electrically Insulative | ◦EMI/RFI Shielding | ◦Hardness |
| ◦Non-Sparking | ◦Toughness/Shock | ◦Refractory |
| ◦Non-Wet | ◦Flexible | ◦Thermal Shock |

You can heat up a metal plate coated with our plasma sprayed ceramic to near its melting point and drop it into water with no spalling, cracking, or delaminating. Stress adjusting microscopic checking may occur, but the integrity of the bond is still intact. Hitting the plate with a hammer shows no noticeable chipping or cracking.

CAPABILITIES

New material alloys can be created by mixing almost any material. Spraying high temperature materials such as hafnia is possible as long as it is available in powder form. The thickness can vary. The ceramic thickness can range from .001-.160 of an inch or a combined metal/ceramic coating in excess of an inch. The materials can be gradated. A coating can

gradually transition from one material (ceramic or metal) to another. This gradient can occur from inside to outside or along a length (figure 3). By using a removable mandrel/core, a free standing monolithic structure can be sprayed-up to stand alone. External processing (i.e., diffusion coating, sintering) can be used to enhance and seal the top surface of the coating and change the strength and durability. Virtually any metal/ceramic known can be sprayed with the system. Figure 4 shows a range of materials and their melting points that are known to withstand high temperatures. Many of the materials listed already have been sprayed at Supermaterials.

Through the use of multiple axes slides and manipulators, almost any shape can be sprayed as long as it can be set in the line of sight of the spray. Some limitations exist in the spraying of inside diameters of tubes that are below 2.6 inches. Small diameter tubes are best fabricated in their entirety by spraying them up upon mandrels.

These coatings also can be adjusted to be "fluffier" (lower overall density) or can be packed tightly into a dense compact material.

APPLICATIONS

Aerospace can benefit from plasma spray technology. Critical components such as jet engine turbine blades, fuel and rocket nozzles, combustor cans and other protective skins with imbedded sensors can be sprayed. Composite structures using ceramic sprayed carbon-carbon bodies have been tested and in use for several years. Their long term durability in high temperature and pressure environments have stretched the capability of these structures. The increasing performance requirements of aerospace has created a new set of problems. Rocket motor nozzles are being pushed toward operating temperatures of 6000° F (3315° C), high pressures and severe oxidizing fuels.

Throat erosion in a rocket nozzle affects the speed, accuracy and fuel economy (hence range) of the rocket. Materials such as Rhenium (ref. 2) and carbides such as of tantalum (TaC) and Hafnium (HfC) are being coated over carbon-carbon substrates. Historically, results over carbon-carbon structures show promise, however currently do not meet the higher performance requirements. Another disadvantage is the high cost. It has been shown that plasma sprayed monolithic rocket nozzles are a possible economical solution to the rigorous imposed standards.

ROCKET NOZZLE PROGRAM

Our plasma sprayed up monolithic ceramic nozzles were compared to 21 other nozzles made of such materials as reinforced ceramic, carbon-carbon, refractory metal, graphite and ceramic nozzles (ref. 3). The nozzles were to be ultimately used for a solid staged combustion propulsion system. The solid staged combustion system combines both the oxidizer-rich and fuel-rich gases burning at 3000° F (1649° C) in a mixing chamber so they can reburn at temperatures over 5000° F (2760° C) in a mixing chamber (figure 5).

The nozzles were fabricated in sizes and shapes to produce Mach numbers from 0.1 to 1.0. When placed in a standard test motor, the nozzles were subject to a 25 second test to be followed by a 30 second test.

Table 1 and figure 6 show the results from the prefire and postfire measurements. It can be observed that our sintered plasma spray monolithic nozzles (tests 13 and 14) had no perceptible change in throat measurements. The structure exhibited no ablation. Later unauthorized tests at higher temperatures were done with similar results. Unsuccessful attempts were made to cut the nozzle in half for examination. The material was just too hard to be cut. One other nozzle we sprayed, which was not sintered, did not survive. This demonstrates the need for additional processing and working of the material after it has been sprayed.

Originally in the program we were asked to coat a carbon-carbon structure. However, we refused because we felt that the carbon-carbon portion would not survive. Our structure is slightly denser than carbon-carbon; however, it withstood the environment. Capability to operate at higher temperatures and pressures compensate for the increased weight.

CONCLUSION

The purpose of the paper is to expose the reader to a technology that may solve some of the toughest materials problems facing thermal protection for use in aerospace. Supermaterials has created a system capable of producing unique material properties. Over 10 years and many man-hours have been invested in the development of this technology. Applications range from the food industry to the rigors of outer space. The flexibility of the system allows for customization not found in many other processes and at a reasonable cost. The ranges of materials and alloys that can be created are endless. Many cases with unique characteristics have been identified and we can expect even more with further development .

References

1. Sahley, L. W.: *Discussion of Superconductive Materials Research & Product Development*. Internal Supermaterials Manufacturing Company Report.
2. Harding, John T., Sherman, Andrew J. and Tuffias, Robert H.: *Refractory Metals For Hot Gas Valves*. Presented at the 1989 JANNAF Propulsion Meeting at Cleveland, OH, 24 May 1989.
3. Oberth, M. H. and Marchol, P. J.: *Evaluation Of Oxidizer Rich Propellant Gas Handling Materials For Solid Staged Combustion*. Report under Air Force Rocket Propulsion Laboratory Contract FO4611-83-C-0039.

Table 1. Results of Rocket Nozzle Test

TEST	MATERIAL	PLANNED DURATION _SEC_	ACTUAL PROPELLANT DURATION _SEC_	WEIGHT _gm_	PREBURN IN			POSTBURN IN			CHANGE		
					D ₁	D ₂	D ₃	D ₁	D ₂	D ₃	D ₁	D ₂	D ₃
1	Molybdenum	10	12	562.8	0.470	0.197	0.255	N/C	0.200	N/C	0	0.003	0
2	Molybdenum	40	55	1951.3	0.450	0.191	0.255	0.530	0.530	0.475	0.080	0.243	0.240
3	4D Carbon-Carbon	25	60	1335.0	0.482	0.196	0.255	0.567	0.258	0.293	0.085	0.062	0.038
4	R-512 Niobium	25	63	1401.1	0.500	0.194	0.263	0.923	0.953	0.990	0.423	0.759	0.727
5	Aremcolox 502-1400	20	24	1113.0	0.479	0.197	0.225	0.480	0.202	0.270	0.001	0.005	0.015
6	NCM	25	27	1384.0	0.490	0.190	0.259	0.495	0.223	0.266	0.005	0.033	0.007
7	K-Karb	25	30	1388.6	0.464	0.191	0.244	-0.500	-0.225	-0.270	-0.010	-0.035	-0.011
8	SIC/SIC	25	23	1386.0	0.460	0.171	0.161	0.473	0.357	0.274	0.014	0.166	0.030
9	P.C. Washers	25	26	1379.8	0.478	0.195	0.253	N/C	0.700	0.244	N/C	0.529	0.083
10	Graphitol	25	43	1385.0	0.487	0.199	0.251	0.485	0.217	0.256	0.009	0.022	0.003
11	Calcium-Infiltrated Tungsten	25	48	1388.0	0.488	0.195	0.265	0.527	0.240	0.265	0.040	0.041	0.014
*12	"Unfired" Zirconia Diffusion Coated	25	55	1409.0	0.470	0.209	0.290	0.520	0.245	0.268	0.032	0.050	N/C
*13	Molybdenum Diffusion Coated	25	21	1400.0	0.489	0.192	0.254	-0.248	0.484	0.227	0.014	0.018	0.009
*14	"Fired" Zirconia Diffusion Coated	40	38	2061.0	0.503	0.183	0.263	-0.487	-0.228	0.299	N/C	-0.017	-0.019
15	Molybdenum AB Plane PG	25	68	1760.8	0.490	0.191	0.274	0.489	0.192	0.254	N/C	N/C	N/C
16	Gadolinium Fluoride (Low Temp Ox)	25	13	1801.5	0.484	0.195	0.264	0.503	0.183	0.265	N/C	N/C	N/C
17	Gadolinium Fluoride	25	52	1387.0	0.495	0.198	0.270	0.584	0.311	0.359	0.074	0.120	0.085
18	SIC-Reinforced LaB ⁶	25	68	1508.2	0.490	0.200	0.269	-0.584	0.218	0.266	0.094	0.118	0.118
19	SIC-Reinforced Alumina	25	38	1567.8	0.502	0.195	0.270	0.485	0.218	0.266	0.001	0.023	0.002
20	Zirconia/Zirconium	25	25	690.0 ^a	0.320 ^b	0.128 ^b	0.173 ^a	0.510	0.248	0.280	0.015	0.052	0.010
21	SIC-Reinforced	25	40	1568 ^c	0.483	0.230 ^d	0.260	-0.531	0.280	0.280	-0.038	0.052	0.010
22	Ca Infiltrated Carbon-Carbon	25	105	1818	0.472	0.202	0.257	0.504	0.261	0.280	0.014	0.081	0.011
23	Halnia/SiC/Graphitol	25	120+	1542.8 ^e	0.478	0.173	0.248	0.580	0.230	0.323	0.078	0.035	0.053
24	Halnia/Hafnium	25	10+ 60+	1719.2	0.492	0.195	0.260	0.307	0.108	0.179	(0.013) ^f	(0.020) ^g	0.006
								0.612-	0.483	0.379-	0.159-	0.253	0.119-
								0.612-	0.510-	0.538-	0.140-	0.308	0.281-
								0.822	0.522	0.740	0.350	0.483	0.483
								0.615	0.390	0.457	0.137	0.217	0.209
								0.478	0.274 ^h	-	-0.014	0.079 ⁱ	-

^a Throat originally sized for low temperature oxidizer.

^b Diameters shrank due to swelling of material.

^c Throat was larger than desired, therefore grain was modified for increased surface area.

^d Throat was smaller than desired, therefore grain was modified for decreased surface area.

^e Throat area actually was gone. This is the minimum reading of what is left.

^f Latter third of nozzle missing.

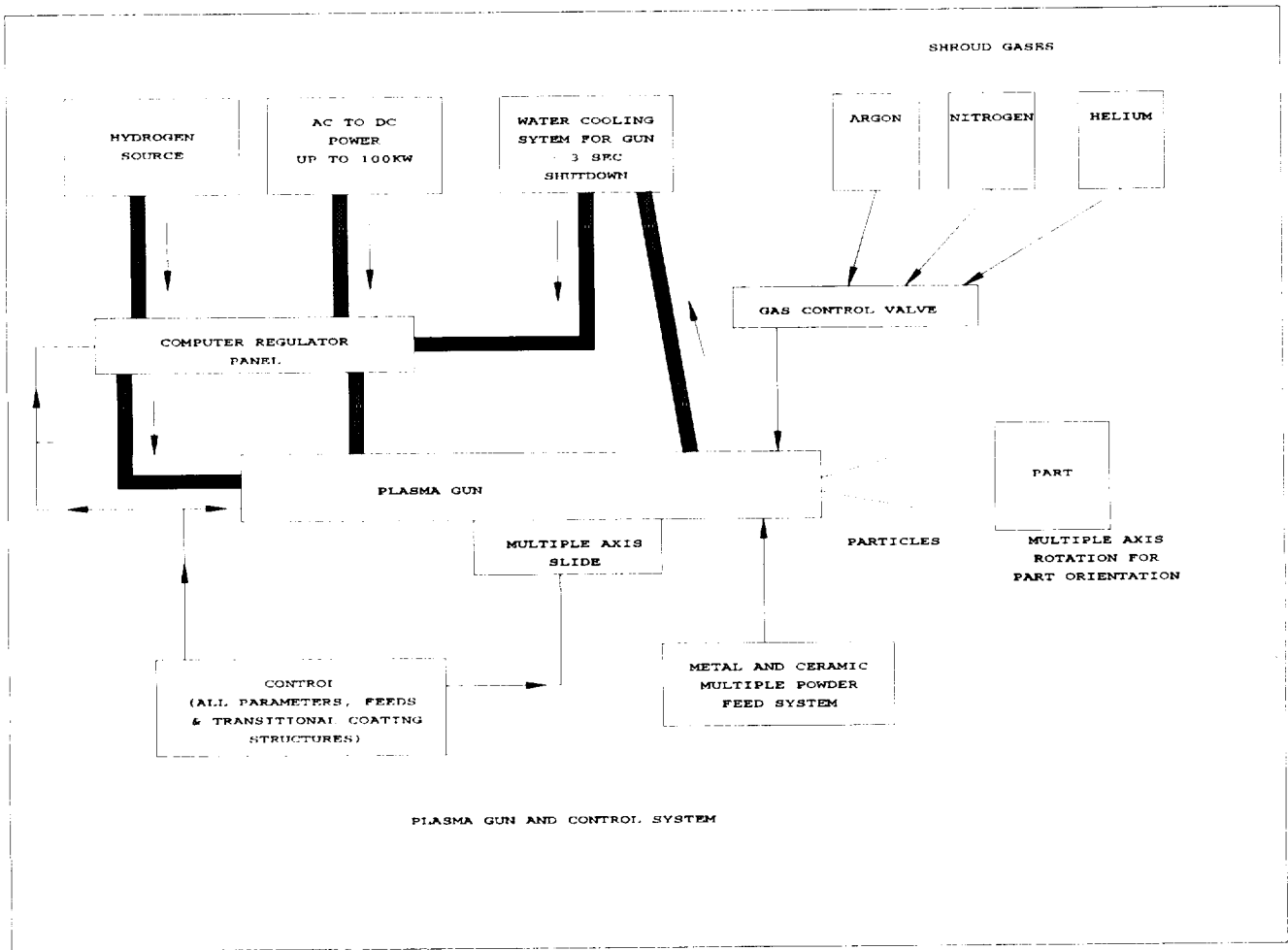


Figure 1. Plasma Gun System Schematic

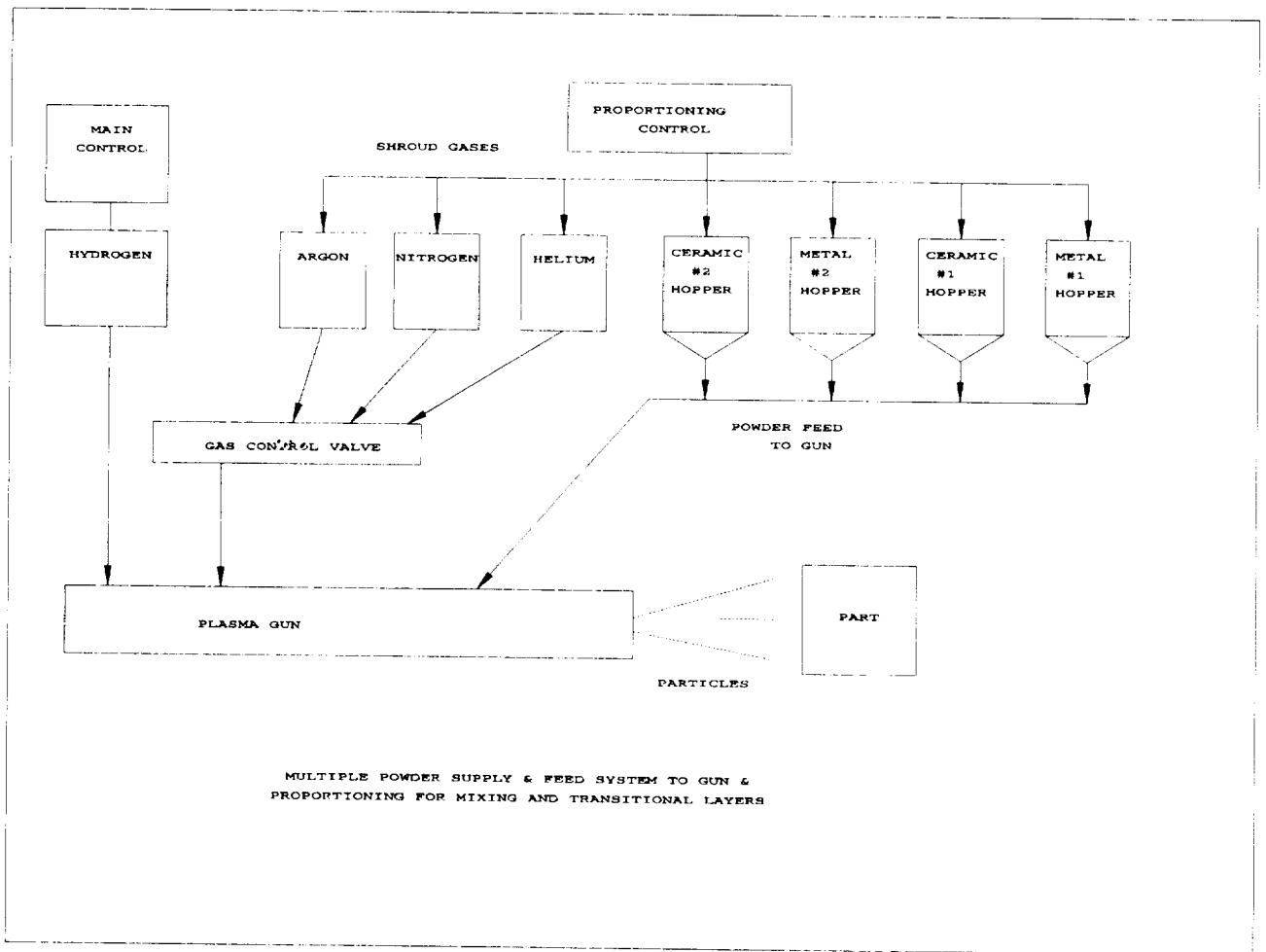


Figure 2

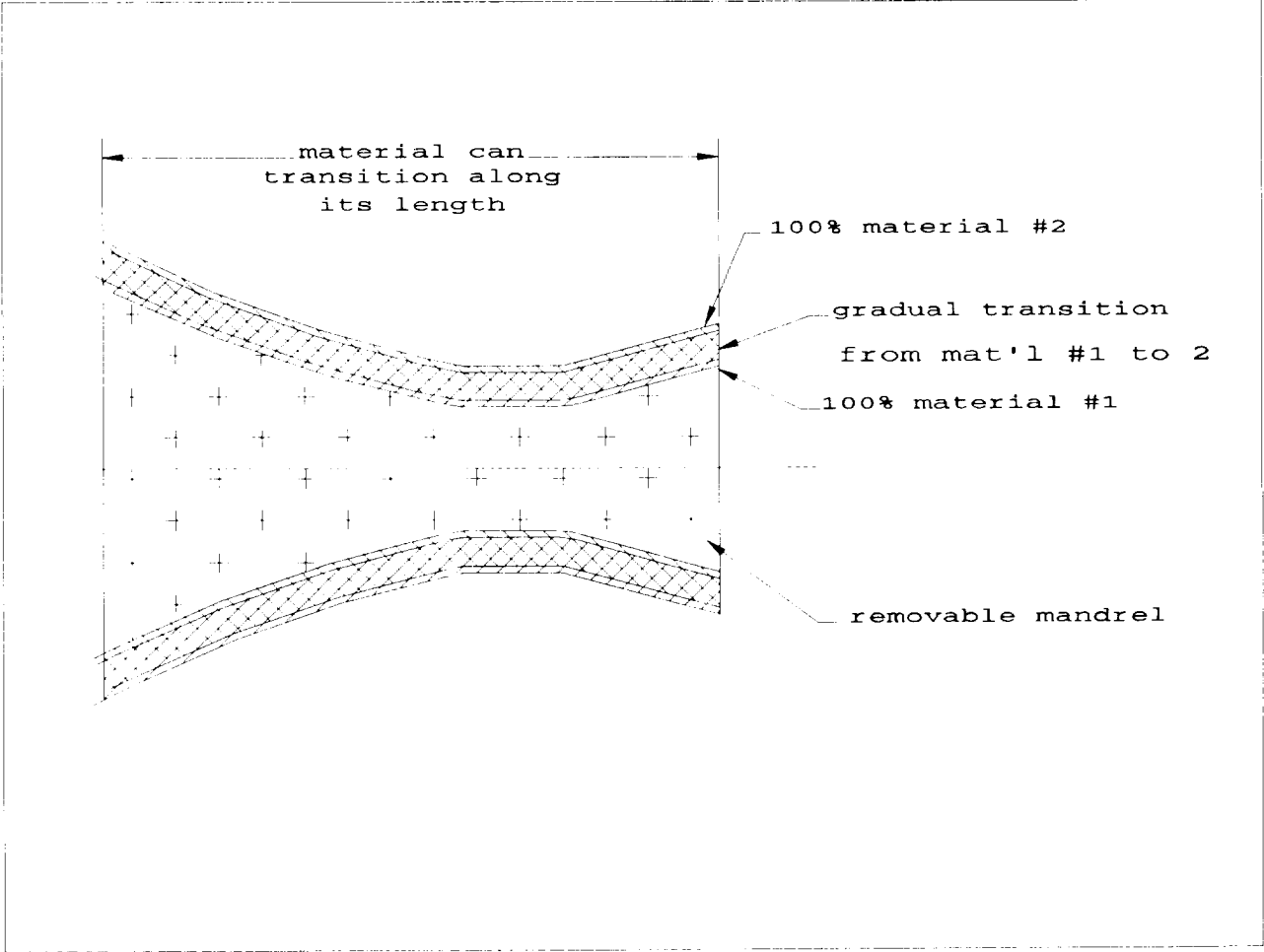


Figure 3. Plasma Sprayed Monolithic Structure

REFRACTORY MELTING POINTS

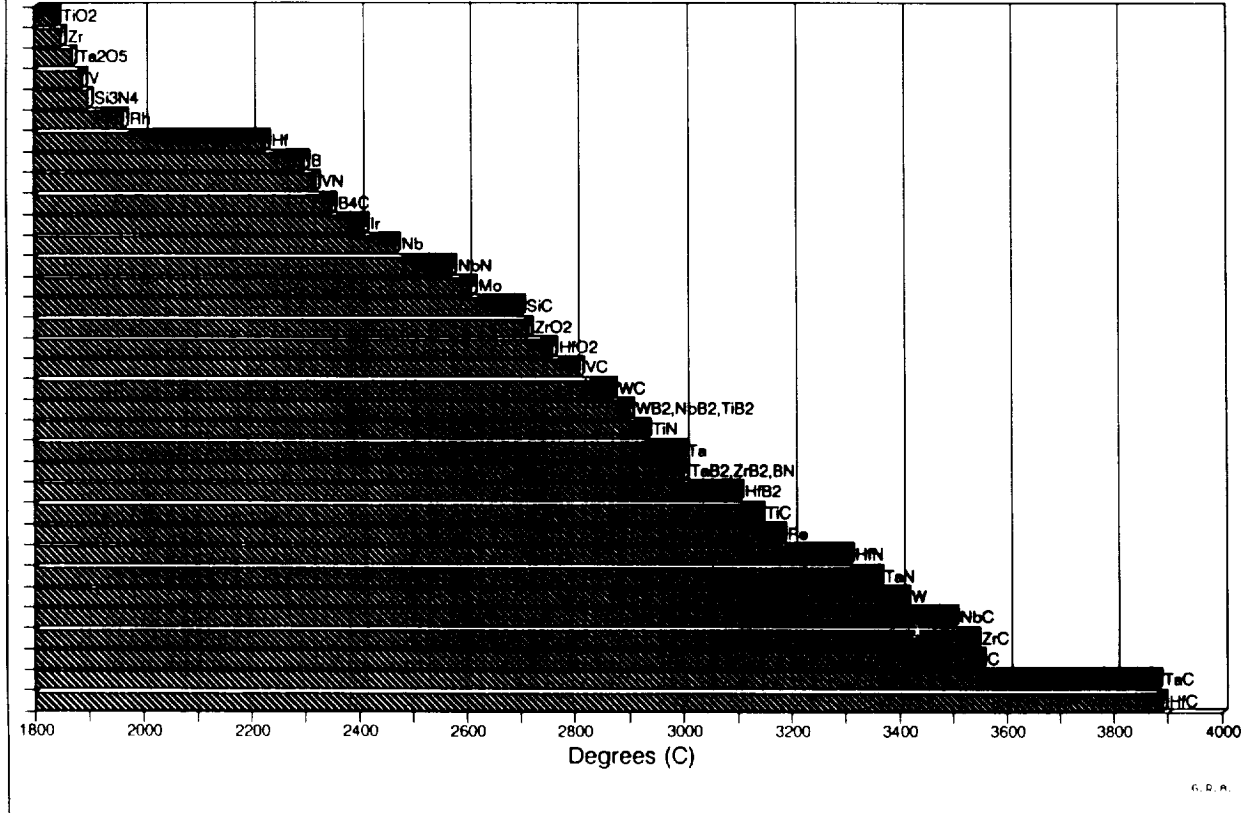


Figure 4

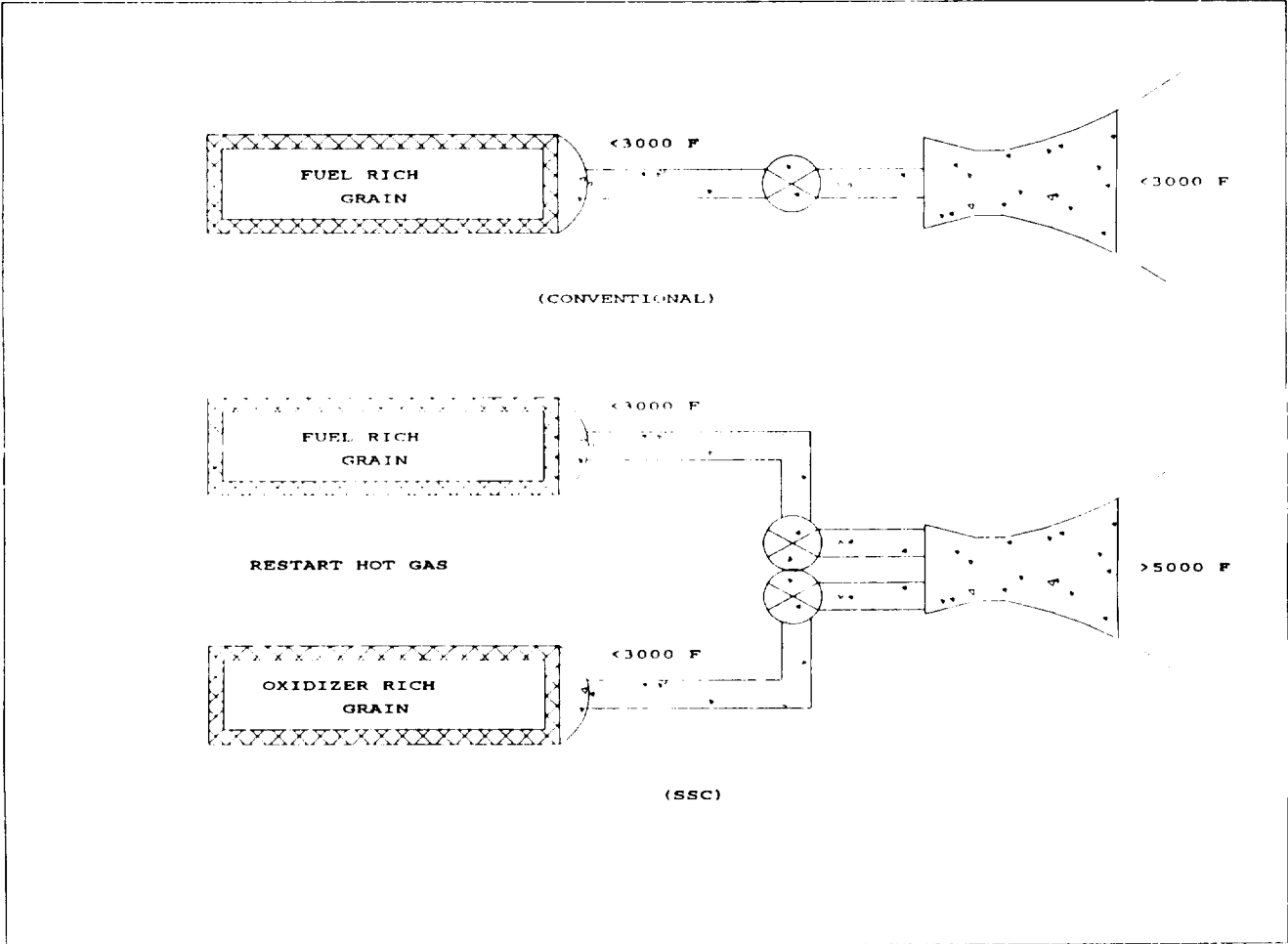


Figure 5

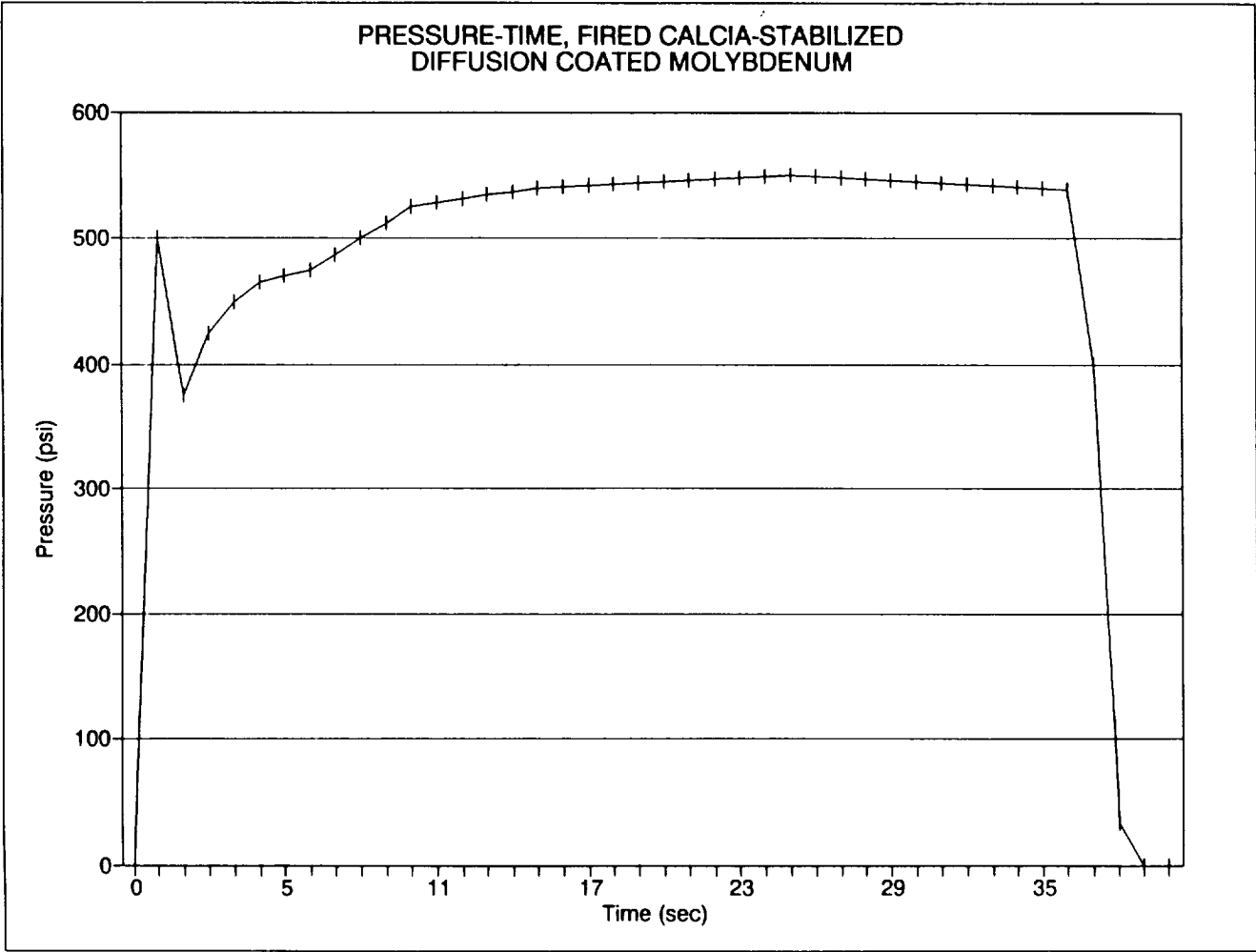


Figure 6

SUPERPLASTIC FORMING OF CERAMIC INSULATION

T.G. Nieh, J.P. Wittenauer, and J. Wadsworth

*Lockheed Missiles & Space Company, Inc. O/9310, B/204
3251 Hanover Street, Palo Alto, CA 94304*

INTRODUCTION

The forming of ceramics is generally difficult because the melting points of ceramics are relatively high and, consequently, the temperatures required to thermally activate plastic deformation in ceramics are also high. In addition, the propensity for grain boundary separation in ceramics is well known. In the 1950s, extensive efforts were made in the western world to hot fabricate ceramics using conventional metallurgical processes such as extrusion, rolling, and forging [1-5]. (It is of interest to note that there was also some evidence indicating that a comprehensive Soviet activity was underway to improve ductility and fabricability in complex ceramics and ceramic composites [6,7].) The goal was to produce near-net-shape parts in order to avoid the expensive machining of ceramics. A number of structural oxides, including CaO, MgO, SiO₂, ZrO₂, BeO, ThO₂, and Al₂O₃, were studied [2]. As a result of this work, an improved understanding of ceramic deformation was developed but certain problems, and in particular the requirement for relatively high forming temperatures, still existed. For example, the temperature required for hot forging Al₂O₃ was found to be about 1900°C which is extremely high from a practical standpoint. Subsequently, the concept of thermomechanical processing of ceramics was more or less abandoned.

Recently, two major technical advances have changed this picture. First, ceramic powder processing technology has been greatly advanced and the quality of ceramic powders is greatly improved. High-purity ceramics of submicron grain size and more consistent microstructures are routinely prepared. Secondly, fine-grained superplasticity in metallic alloys has been extensively studied and has already found commercial applications [8]. Because of these two advances, together with the observation that fine-grained ceramics generally possess the microstructural prerequisites for superplasticity in metals, the concept of hot forming, and in particular, superplastic forming of ceramics has become an area of intense study.

Since about 1986, many fine-grained polycrystalline ceramics have been demonstrated to be superplastic. These include yttria-stabilized tetragonal zirconia polycrystal (Y-TZP) [9,10], Y-doped Al₂O₃ [11], β-spodumene glass ceramics [12], ZnS [13], and Al₂O₃-reinforced Y-TZP (Al₂O₃/YTZ) [14,15] and SiC-reinforced Si₃N₄ (SiC/Si₃N₄) [16] composites. Among these materials, a 3 mol% yttria-stabilized tetragonal zirconia polycrystal (3Y-TZP) was the first true polycrystalline ceramic demonstrated to be

superplastic. The material is brittle at low temperatures, but becomes ductile at $T > 1000^{\circ}\text{C}$. Its tensile ductility depends critically on temperature rather than on strain rate at low temperatures. Tensile elongations of only 5 and 60% were measured at 1000 and 1200°C , respectively, but elongations of greater than 100% were routinely obtained at temperatures above 1350°C . A maximum value of elongation-to-failure of 800% has been recorded in a sample tested at 1550°C and a strain rate of $8.3 \times 10^{-5} \text{ s}^{-1}$. A direct comparison of this superplastically deformed sample with an untested sample is given in Fig.1. It is evident that macroscopic necking does not occur until near the final fracture of the test sample. Superplastic flow in 3Y-TZP has been characterized as a diffusion-controlled process and the strain rate, $\dot{\epsilon}$, can be expressed as [17]

$$\dot{\epsilon} = A \cdot \frac{1}{d^3} \cdot \left[\frac{\sigma}{E} \right] \cdot \exp \left[- \frac{510,000}{RT} \right] \quad (1)$$

where σ is the flow stress, E is the elastic modulus, d is the grain size, A is a material constant, R is the gas constant, and T is the absolute temperature.

In the area of superplastic forming, so far, several parts have been successfully formed from fine-grained 3Y-TZP. For example, Kellett *et al.* [18] demonstrated that submicron-sized ($\sim 0.23 \mu\text{m}$) 3Y-TZP powders can be extruded superplastically, with an 8 to 1 reduction in area ratio (or a true strain of -2.2), at 1500°C to near full density; this is illustrated in Fig.1. Panda *et al.* [19] and Yamana *et al.* [20] have applied a sinter-forging technique to form bulk ZrO_2 stabilized by various amounts of Y_2O_3 from fine powders to full density at 1400°C . Recently, Wakai *et al.* [21] successfully bent a 3Y-TZP sheet sample to a large strain at 1450°C in air using SiC tools. Wu and Chen [22], on the other hand, demonstrated that a 2Y-TZP containing 0.3 mol% CuO can be biaxially stretched into hemispheric dome shapes at 1150°C , using a tungsten punch. This low temperature forming was a direct result of the decreasing melting point of the grain boundary glassy phase caused by the CuO addition. It is worth noting that Kellett and Lange [23] have successfully hot forged a 20 vol% $\text{ZrO}_2/\text{Al}_2\text{O}_3$ to 60% reduction in thickness at 1500°C .

The diffusion bonding technique has also been demonstrated successfully in Y-TZP and its composites. For example, Nagano *et al.* [24] and Wakai *et al.* [25] successfully performed diffusion bonding between $\text{Al}_2\text{O}_3/\text{YTZ}$ composites and 3Y-TZP at the superplastic temperatures, i.e., $1450\text{-}1550^{\circ}\text{C}$, for the parent materials. The bond strength was found to depend on the bonding temperature and the compositions of the parent materials (similar and dissimilar). A maximum bond strength of greater than 1300 MPa was recorded in a 20% $\text{Al}_2\text{O}_3/\text{YTZ}$ composite diffusion bonded at 1470°C [24].

The purpose of this paper is not to discuss general superplasticity in ceramics *per se*, but to present the first results of studies involving the free, biaxial, gas-pressure deformation of the superplastic 3Y-TZP and 20% $\text{Al}_2\text{O}_3/\text{YTZ}$ composite. Additionally, the purpose is to address the technological implications of this

superplastic forming technology and its potential applications to the forming and shaping of various ceramics, particularly ceramics used for thermal insulation, such as zirconia and its composites.

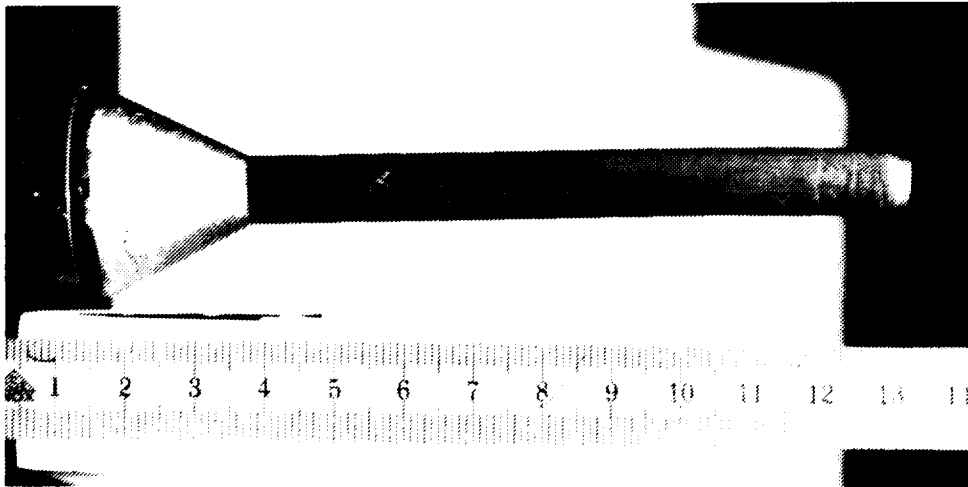


Fig.1 Fine-grained Y-TZP extruded at 1500°C with a reduction in area ratio of 8. (from Ref. 18)

EXPERIMENTAL PROCEDURE

The materials used in this study were a fine-grained 3Y-TZP and its composite containing 20 wt%Al₂O₃ (Al₂O₃/YTZ); both were obtained as 50 mm diameter discs, 1.5 mm in thickness, from Nikkato Corp., Japan. The microstructure exhibited an equiaxed grain morphology. The grain size of 3Y-TZP was about 0.3 μm, while it was about 0.5 μm (both zirconia and alumina grains) in the composite. Data regarding the microstructure, superplastic flow properties, grain growth behavior, and cavitation characteristics of these two materials (under uniaxial tension conditions) have previously been reported [10,26,27]. Building upon information from these previous studies, a gas-pressure forming apparatus was constructed with the capability to operate at temperatures of as high as 1700°C at gas forming pressures of as high as 2.5 MPa. A two-part die was designed and incorporated to impart a clamping force to the periphery of the ceramic sheet permitting an unconstrained diaphragm diameter of 38 mm. Deformation of the diaphragm was accomplished through the controlled application of Ar as a forming gas. An ambient pressure of 3 x 10⁴ Pa of Ar was maintained during all forming experiments. In order to accomplish the on-line sensing of the progress of the diaphragm deformation, a high-temperature contact LVDT was specially constructed and integrated into the forming apparatus.

RESULTS AND DISCUSSION

Generally, gas-pressure biaxial forming uses one of two experimental techniques to achieve the desired deformation- constant applied pressure or constant applied stress. The former technique of utilizing constant

applied gas pressure has been used for the study of other superplastic alloys [28,29]. With this method, both the flow stress and strain rate in the deforming shell change continuously during the experiment. Thus, it is difficult to interpret data from these tests in terms of basic materials properties. From a practical point of view, however, the constant applied gas-pressure technique is probably more applicable to a manufacturing environment than is the constant applied flow stress test. In contrast to this technique, an alternative method of constant applied flow stress in the deforming shell has also been used for forming Ti-based alloys [30]. The principal advantage of this technique is that it allows for the direct comparison of biaxial deformation behavior with data obtained from uniaxial tension testing. (Most studies of superplastic deformation involve the application of a constant strain rate or constant flow stress in uniaxial tension or compression.)

In the present study, experiments were conducted under conditions designed to approach that of a constant applied flow stress in the deforming shell. The deformation process was accomplished through a consideration of the pressure-curvature relationship for a spherical shell (as shown in Fig.2):

$$\sigma = \frac{P r}{2 t} \quad (2)$$

where σ is the flow stress, P is the applied gas pressure, r is the instantaneous radius of curvature, and t is the instantaneous shell thickness. It is noted that during the course of an experiment, P is varied as a function of r (and therefore t) in order to achieve a predetermined value of σ in the shell. The thickness t was assumed to vary uniformly over the deforming shell and to decrease steadily in a manner which was calculated assuming a constant volume. (Although expedient for the design of this initial series of experiments, the uniform thickness assumption is not rigorously correct.) The height of a deforming hemispherical cap may be related to its radius through a consideration of the cap geometry, as schematically shown in Fig.2. A hemispherical cap of apex height h and having a base radius of r_o may be considered as a section of a sphere of radius r and included angle 2α . The included half-angle α may be determined by measuring the height h of the cap:

$$\tan\left(\frac{\alpha}{2}\right) = \frac{h}{r_o} \quad (3)$$

The radius of curvature r may then be determined as

$$r = \frac{r_o}{\sin\alpha} \quad (4)$$

By preselecting a shell stress for a particular experiment, the values of Ar gas pressures required to compensate for the changing dome height and shell thickness during deformation could be adjusted accordingly.

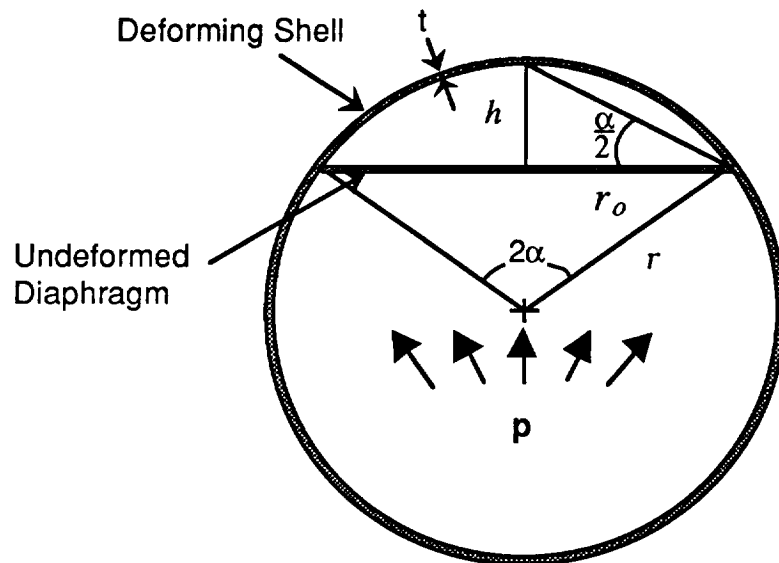


Fig.2 A hemispherical cap of height h and basal radius r_0 may be considered to be a section of a sphere of radius r and included angle 2α .

The result of one series of experiments to demonstrate the formability of the $\text{Al}_2\text{O}_3/\text{YTZ}$ sheet is shown in Fig.3. Interrupted tests illustrating the progressive deformation of the $\text{Al}_2\text{O}_3/\text{YTZ}$ at various strain levels are shown at an applied shell stress of 13.8 MPa for tests conducted at 1475°C . (Similar results were also obtained for the 3Y-TZP sheet.) A forming temperature of 1475°C was selected as a compromise between higher temperatures which would result in excessive grain growth rates, and lower temperatures which would result in unacceptably low strain rates. All shells in Fig.3 were noted to deform to symmetrical spherical sections with no evidence of inhomogeneous flow or fracture resulting from the imposed clamping pressure.

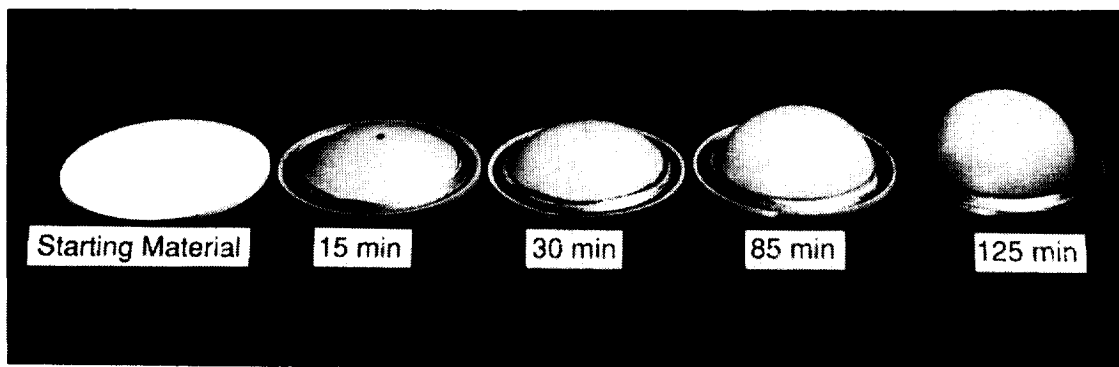


Fig.3 Progressive deformation of 20% $\text{Al}_2\text{O}_3/\text{YTZ}$ at 1475°C and 13.8 MPa flow stress.

Experiments were also conducted with $\text{Al}_2\text{O}_3/\text{YTZ}$ at 1475°C for different applied shell stresses. The apex height as a function of forming time for three applied stresses is shown in Fig.4. Since these experiments were carried out under constant-stress conditions, the curves in Fig.4 are similar to those observed during the creep of most metal alloys. (Strictly speaking, the constant-stress condition is only an approximation. This is a result of the fact that Eq.{1} is based on the assumption of uniform thickness which, in actuality, is not rigorously correct.) In terms of formability, all the above applied stresses produce good-quality hemispherical domes; applied stresses only affect the forming rates.

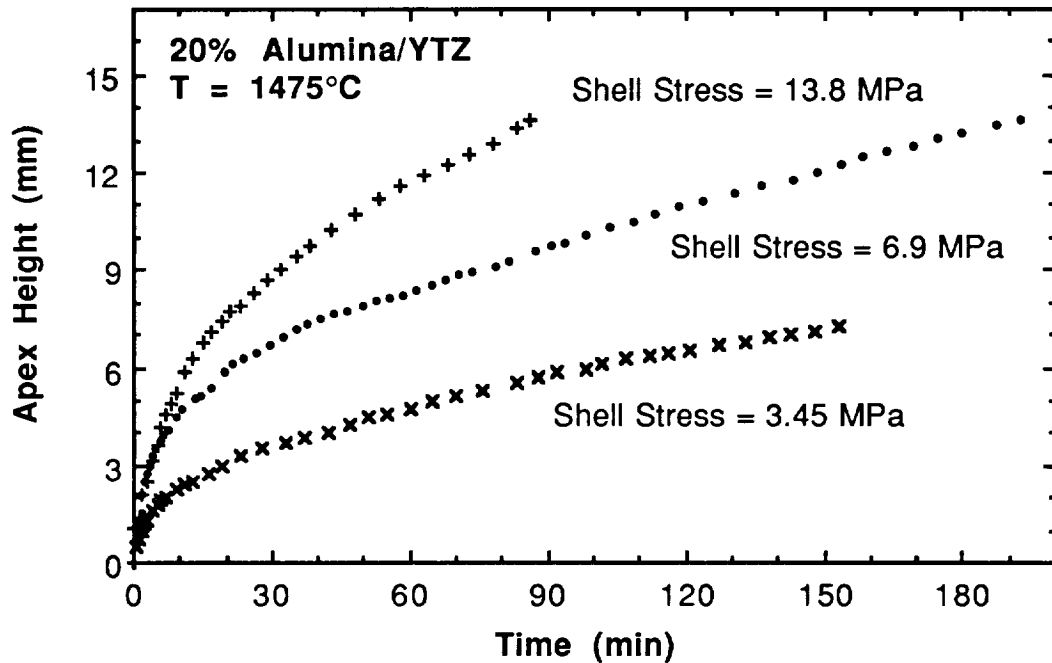


Fig.4 Apex height as a function of forming time for 20% $\text{Al}_2\text{O}_3/\text{YTZ}$ at 1475°C and at various shell stresses.

To demonstrate further the versatility of the above gas-pressure forming technique, we also conducted experiments to form superplastic ceramics into shapes other than a simple hemisphere. One of the examples is given in Fig.5, which illustrates schematically the design of a forming die and the conceptual forming operation. Experiments were subsequently carried out with 3Y-TZP samples at temperatures between 1500 , 1550 , and 1575°C and at an applied gas pressure of 0.28 MPa (about 6.9 MPa nominal shell stress) to verify the above forming process. Shown in Fig.6 are three 3Y-TZP samples illustrating the progressive deformation of the 3Y-TZP gas-pressure formed at various strain levels. These samples fully demonstrate the excellent superplastic formability of 3Y-TZP sheet.

(It is worth noting that both deformed 3Y-TZP and $\text{Al}_2\text{O}_3/\text{YTZ}$ samples appear dark. This is a result of the fact that the experiments were carried out in a vacuum-inert gas atmosphere and it is known that 3Y-TZP

darkens in vacuum, i.e., an oxygen-depleted environment. The expected white color can be easily recovered by annealing at 1200°C in air for 0.5 h.)

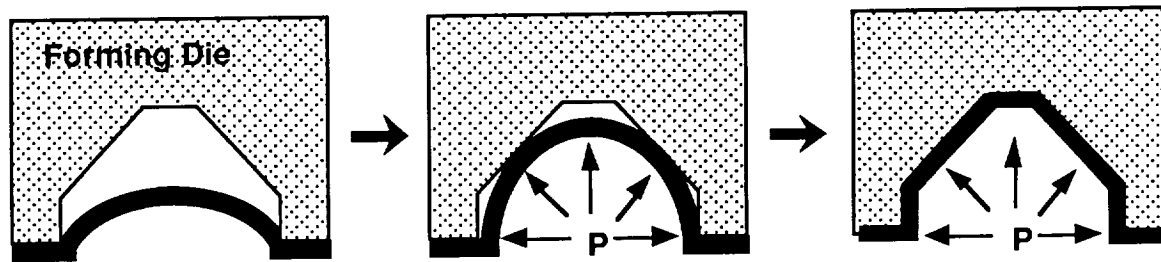


Fig.5 Schematic illustration of the gas-pressure forming process for superplastic ceramic sheet.



Fig.6 3Y-TZP samples progressively deformed, according to the diagrams shown in Fig.5, to various strain levels.

It is noted that the thickness of a gas-pressure formed sample is generally not uniform. This is because the center of a deforming diaphragm is in a stress state of equibiaxial tension (plane stress), while at the clamped periphery of the diaphragm there is a state of plane strain. When a diaphragm is deformed through the action of an applied gas pressure, the stress state varies between the apex and the periphery. As a result of this stress gradient, deformation occurs under a corresponding strain rate gradient. The degree of thickness variation is therefore closely related to the strain rate sensitivity of the deforming material. The development of an analytical model to describe the thickness distribution in gas-pressure formed samples is underway. Technologically, however, the problem of thickness nonuniformity has been encountered by the metal industries, and was overcome by a number of techniques, including a reverse forming operation [31].

PERSPECTIVE

Future hypersonic flight vehicles impose many distinct design restrictions in terms of vehicle size, weight, takeoff and landing characteristics, safety, and logistics. These requirements for hypersonic flight

created a unique challenge in the selection of fuels and thermal management. For example, the maximum speed for an aircraft, with a combined ramjet-turbojet propulsion, with the given range and weight requirements is most likely to be about Mach 5 [32]. The temperature of the ramjet combustor and engine nozzle wall for such a flight vehicle are expected to be near 4200°F; this is schematically shown in Fig.7.

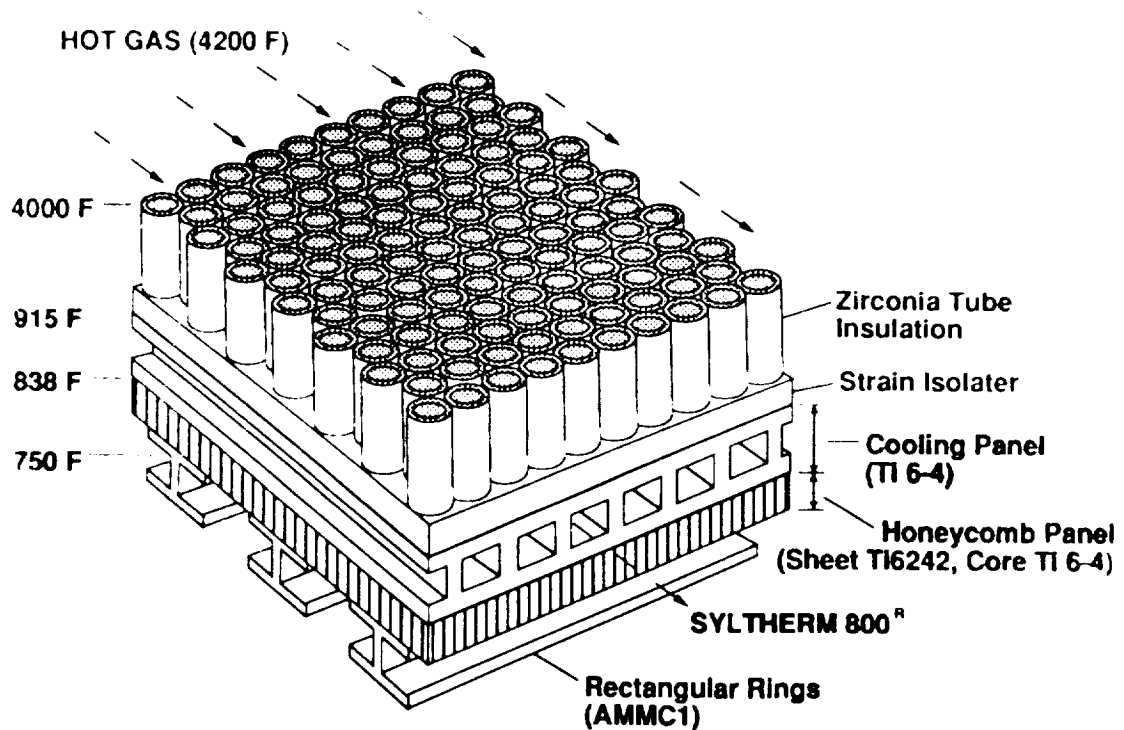


Fig.7 Ramjet combustor and engine nozzle wall construction for a Mach-5 hypersonic aircraft with with a combined ramjet-turbojet propulsion. (from Ref. 32)

Zirconia is probably the only insulation material that is capable of withstanding such a high temperature. There is no other known insulation material which is designed to withstand exposure to gases at temperatures above 4000°F. The insulation in Fig.7 is proposed to consist of 1/8 inch O.D. zirconia tubes filled with a foam of the same material. This insulation design is a state-of-the-art concept.

Technically, zirconia tubes may be produced by conventional powder metallurgy and/or slip casting techniques which are primarily batch processes. This poses two major problems - product reliability and cost. From both the cost and product reliability points of view, the process of superplastic extrusion of Y-TZP tubes using existing metallurgical facilities would be extremely attractive. In particular, this process has already been proven with fine zirconia powders [18]. Using the superplastic extrusion technique, zirconia tubes with given diameters can be produced in large quantities. The extruded tubes can be subsequently sliced into proper lengths for applications. In addition, since tube extrusion is a bulk process, product reliability will be greatly improved and will certainly reduce the production cost significantly.

CONCLUSION

Superplasticity has been demonstrated in many fine-grained structural ceramics and ceramic composites, including yttria-stabilized tetragonal zirconia polycrystal (YTZP), alumina, and Al₂O₃-reinforced zirconia (Al₂O₃/YTZ) duplex composites and SiC-reinforced Si₃N₄. These superplastic ceramics obviously offer the potential benefit of forming net shape or near net shape parts. This could be particularly useful for forming complicated shapes that are difficult to achieve using conventional forming techniques, or require elaborate, subsequent machining. In the present study, we successfully demonstrated the following:

- 1) Superplastic 3Y-TZP and 20%Al₂O₃/YTZ composite have for the first time been successfully deformed into hemispherical caps via a biaxial gas-pressure forming technique.
- 2) No experimental difficulty was encountered in applying the required gas pressures and temperatures to achieve the results presented in this report. Thus, it is certain that higher rates of deformation than those presented in this study will be possible by using the current test apparatus at higher temperatures and pressures.
- 3) An analytical model incorporating material parameters, such as variations during forming in the strain rate sensitivity exponent and grain growth-induced strain hardening, is needed to model accurately and therefore precisely control the biaxial gas-pressure forming of superplastic ceramics.

Based on the results of this study, we propose to fabricate zirconia insulation tubes by superplastic extrusion of zirconia polycrystal. This would not only reduce the cost, but also improve the reliability of the tube products.

ACKNOWLEDGMENT

This work was supported by both the Lockheed Independent Research Program and the Army Research Office under contract DAAL03-89-C-0028, monitored by Dr. Andrew Crowson.

REFERENCES

1. Fulrath, R.M.: *Ceram. Bull.*, 43, 1964, 880-886.
2. Rice, R.W.: in '*High Temperature Oxides, Refractory Materials*, 5-111', (ed. A.M. Alper), New York, Academic Press, 1970, pp. 235-280.
3. Rice, R.W.: in *Ultrafine-Grain Ceramics*, (ed. J.J. Burke et al.), Syracuse University Press, New York, 1970, pp. 203-25.
4. Morgan, P.E.D.: in *Ultrafine-Grain Ceramics*, (ed. J.J. Burke et al.), Syracuse University Press, New York, 1970, pp. 251-271.

5. Bradt, R.C.: in *Advances in Deformation Processing*, (ed. J.J. Burke and V. Weiss), Plenum Press, New York, 1978, pp. 405-423.
6. Frankhouser, W.L. : *A working Paper, Soviet Developments in Regard to Superplasticity in Ceramic Materials*, Report SPC 849, System Planning Corporation, Arlington, Virginia, September, 1982.
7. *Conference on High-Melting Compounds, Dedicated to Academician G.V. Samsonov*; *Investiya Akademii Nauk SSR, Neorganicheskie Materialy*, 15 (4), 1979, 549.
8. Henshall, C. A., Wadsworth, J., Reynolds, M. J., Barnes, A. J.: *Materials and Design* VIII (6), 1987, pp. 324-330
9. Wakai, F.; Sakaguchi, S.; and Matsuno, Y.: *Adv. Ceram. Mater.*, 1, 1986, pp. 259-263.
10. Nieh, T.G. and Wadsworth, J.: *Acta Metall. Mater.*, 38, 1990, pp. 1121-1133.
11. Gruffel, P; Carry, P.; and Mocellin, A.: in *Science of Ceramics - Vol. 14*, (ed. D. Taylor), The Institute of Ceramics, Selton, UK, 1988, pp. 587-592.
12. Wang, J.-G. and Raj, R.: *J. Amer. Ceram. Soc.*, 67, 1984, pp. 399-409.
13. Xue, L.A. and Raj, R.: *J. Amer. Ceram. Soc.*, 72, 1989, pp. 1792-1796.
14. Wakai, F. and Kato, H.: *Adv. Ceram. Mater.*, 3, 1988, pp. 71-76.
15. Nieh, T.G.; McNally, C.M.; and Wadsworth, J.: *Scripta Metall.*, 23, 1989, pp. 457-460.
16. Wakai, F.; Kodama, Y.; Sakaguchi, S.; Murayama, N.; Izaki, K.; and Niihara, K.: *Nature*, 344, 1990, pp. 421-423.
17. T.G. Nieh and J. Wadsworth, in *Superplasticity in Metals, Ceramics, and Intermetallics*, MRS Proceeding No. 196,(edited by M.J. Mayo, M. Kobayashi, and J. Wadsworth), Materials Research Society, Pittsburgh, Pennsylvania (1990), pp. 331-336.
18. Kellett, B.; Carry, P.; and Mocellin, A.: in *Superplasticity and Superplastic Forming*, (eds. C.H. Hamilton and N.E. Paton), The Minerals, Metals, and Materials Society, Warrendale, Pennsylvania, 1988, pp. 625-630.
19. Panda, P.C.; Wang, J.W.; and Raj, R.: *J. Amer. Ceram. Soc.*, 71, 1988, pp. C-507-C-508.
20. Yamana, Y.; Yamamoto, Y.; Nakamura, S.; Kitagawa, K.; Yoshimura, T.; Mano, T.; and Shintani, Y.: *J. Ceram. Soc. Japan*, 97, 1989, pp. 758-761.
21. Wakai, F.: *Brit. Ceram. Trans. J.*, 88, 1989, pp. 205-208.
22. Wu, X. and Chen, I.W.: *J. Am. Ceram. Soc.*, 73, 1990, pp. 746-749.
23. Kellett, B.J. and Lange, F.F.: *J. Mater. Res.*, 3(3), 1988, pp. 545-551.
24. Nagano, T.; Kato, H.; and Wakai, F.: *J. Amer. Ceram. Soc.*, 73, 1990, pp. 3776-80.
25. Wakai, F.; Sakaguchi, S.; Kanayama, K.; Kato, H.; and Onishi, H.: in *Ceramic Materials and Components for Engine*, (ed. W. Bunk and H. Hauser), Deutsche Keramische Gesellschaft, Lubeck-Travemunde, FRG, 1986, pp. 315-322.

26. Nieh, T.G. and Wadsworth, J.: *J. Amer. Ceram. Soc.*, 72, 1989, pp. 1469-1472.
27. Schissler, D.J.; Chokshi, A.H.; Nieh, T.G.; and Wadsworth, J.: *Acta Metall. Mater.*, 39(12), 1991, pp. 3227-3236.
28. Guo, Z.X.; Pilling, J.; and Ridley, N.: in *Superplasticity and Superplastic Forming*, (eds. C.H. Hamilton and N.E. Paton), The Minerals, Metals, and Materials Society, Warrendale, Pennsylvania, 1988, pp. 303-308.
29. Jovane, F.: *Int. J. mech. Sci.*, 10, 1968, pp. 403-427.
30. Ghosh, A.K. and Hamilton, C.H.: *Metall. Trans.*, 13A, 1982, pp. 733-743.
31. Hales, S.J.; Bales, T.T.; James, W.F.; and Shinn, J.M.: in *Superplasticity in Aerospace II* (eds. McNelly, T.R. and Heikkinen, H.C.), The Minerals, Metals, and Materials Society, Warrendale, Pennsylvania, 1990, pp. 167-185.
32. Petley, D.H. and Jones, S.C.: AIAA 90-3284-CP, October 3-5, 1990.

CERAMIC TBS/POROUS METAL
COMPLIANT LAYER

R. P. Tolokan, G. P. Jarrabet
Technetics Corporation
1600 Industrial Drive
DeLand, FL 32724

INTRODUCTION

- o Technetics Corporation manufactures metal fiber materials and components used in aerospace applications.
- o Our technology base is fiber metal porous sheet material made from sinter bonded metal fibers.
- o Fiber metals have % densities (metal content by volume) from 10 to 65%.

FIBER METAL MATERIALS

- o Fiber metals have distinct controllable properties including porosity, pore size, tensile strength and mechanical properties, permeability, thermal conductivity, electrical resistance and weight.
- o Properties are controlled through choice of product alloy, % density, thickness, fiber diameter and sintering parameters.
- o Fiber metals are tailored to a defined set of properties.

COMPLIANT LAYER TBCs

- o One application for fiber metals materials is as a compliant interlayer for ceramic thermal barrier coating systems.
- o The fiber metal compliant layer, which we call pad, is brazed to the metal substrate.
- o The ceramic coating, typically 8% yttria stabilized zirconia, is plasma flame sprayed (PFS) onto the pad after depositing a NiCrAlY bond coat to roughen the pad surface.

- o The ceramic coating has also been applied by direct bonding monolithic ceramics to the pad and by sintering Sol-Gel powder to the pad.
- o The pad interlayer partly decouples the ceramic coating from the metal backing.
- o The ceramic-pad approach allows .060-.100" thick PFS coatings that survive cyclic thermal shock in gas turbine engines. Coating thickness "limits" have not been fully explored.

PAD PROPERTIES

- o Sinter bonded fiber structure.
- o Supplied densities: 10% - 65% of solid alloy.
- o Alloys supplied: Hoskins 875 (FeCrAlY), 347ss.
- o Fiber diameters: .0056" and .004"
- o Typical thickness: .020-.250"
- o Oxidation life of Hoskins 875 Pad (7% wt. gain): 10,000 hrs. @ 1800°F.
- o Shapes available: flat sheet, or 3D shapes by custom order.
- o Pad properties in plane at 35% density:
 - o UTS - RT/1500°F
4800/1000 PSI
 - o MOE - RT/1500°F
1.4/.26 MILLION PSI
 - o Thermal conductivity RT/1500°F 8.5/21
(BTU-IN/HR-FT²-°F)
 - o Pad is low modulus, a good insulator, porous and with oxidation capability to 1800°F. The thermal conductivity of the pad is similar to that of the zirconia ceramic coating.

CERAMIC/PAD TBC DESIGN

- o Considerations we believe to be important in using pad as a ceramic coating interlayer are:
 - the low modulus compliance of the pad.

--the insulating capability of the pad which retards heat relaxation of the backing during PFS and thermal cycling.

--the formation of a low residual stress ceramic coating on the compliant pad.

- o In designing a ceramic-pad TBC coating, the following constraints must be considered:
 - 1) The expansion match of ceramic and pad with the backing
 - 2) The geometry of the hardware
 - 3) The desired thermal benefit influenced by thermal conductivities, thickness, composition and porosity of the coating
 - 4) Operating environment
 - 5) Pad properties
 - 6) PFS parameters

THERMAL SHOCK RIG

- o Design concepts are evaluated on 1 x 3" coupons on a thermal shock rig.
- o The rig is designed to simulate the rapid temperature excursions seen in gas turbine engines.
- o About 1.5 million thermal shock cycles have been accumulated on our rig to provide a database on coating system performance.
- o The rig consists of a station with one 3100°F propane/oxygen/air torch and two cold air jets.
- o Two samples are run at each station, one in the torch flame and one at a cold air jet. The sample face cycles between torch and cold air jet in 5-7 seconds.
- o The sample backside is continuously cooled by two air jets. The sample TBC face cycles between 2500°F and 200°F. A 90 second cycle is used to insure steady state conditions at each position.
- o Samples are cycled 5000 times or to failure if that occurs first. Failures typically occur at less than 100, 2500 OR 4000 cycles.

- o The current rig configuration has 18 stations which can cycle 36 samples at one time.

FABRICATION

- o Pad is brazed to the metal substrate using superalloy braze alloys such as AMS 4777 using expansion fixturing.
- o Backing and pad processing is designed to weld, machine and anneal hardware before coating application to remove residual stress.
- o PFS coatings are applied using robotic gun positioning to insure reproducibility of the multi-layer coating.

APPLICATIONS

- o The primary application of this system has been in the hot sections of gas turbine engines.
- o Compliant layer ceramic TBCs are currently used in rub tolerant turbine seal systems for gas turbine engines. These .060" ceramic, .060" thick pad systems provide rub tolerance and erosion resistance coupled with substantial system insulating capability to contain and utilize heat in the turbine section. To date, a limited number of production engines use ceramic-pad TBC systems.
- o Ceramic-pad TBCs have also been developed for thermal protection of high temperature combustors. A "composite matrix" approach was developed (Ref. 1). In this approach, a tiled ceramic was employed on a continuous compliant pad interlayer/sheet metal backing. Low flow cooling of the pad was accomplished by through pad air flow. The concept has successfully tested to 2500°F gas temperatures, with further testing to 3000°F planned.
- o The compliant matrix combustor was fabricated as three ceramic-pad TBC sections: outer liner and inner liner (cylindrical), outer transition (complex half bagel shape). The pad-backing was produced as flat sheet stock. The outer and inner liners were roll formed and welded to produce the pad-backing cylinders. The transition was hydroformed. The zirconia ceramic tiles were formed in place during plasma spraying. Tile slots were formed via shadowing by the spray masking grid.
- o Ceramic coated porous core vanes have also been investigated (Ref. 2). This approach utilized the

cooling distribution characteristics of the porous compliant core as a ceramic TBC support.

- o A number of non-compliant layer TBCs have been investigated. These coatings utilize the bond coat, stress distribution and substrate cooling methods learned in developing ceramic-pad systems. Ceramic TBCs have been directly applied to substrates including stainless steels, superalloys, cast iron, aluminum, titanium, silicon carbide, silicon nitride, and carbon matrix composites.

SUMMARY

- o Ceramic-compliant layer TBCs offer a means of applying a relatively thick TBC system with good heat insulating qualities.
- o The ceramic-pad TBC is produced by brazing pad to a metal backing and applying the TBC by plasma spraying.
- o Ceramic/pad TBCs have proven to be durable in gas turbine engines surviving rapid thermal excursion, vibrations, mechanical loading, high temperatures, gas erosion and rotating blade/ceramic interaction.
- o Enhanced thermal protection of the substrate is possible using low air flow rates through the compliant pad.

REFERENCES

1. "Composite Matrix Cooling Scheme for Small Gas Turbine Combustors", M. Paskin, W. Acosta et al, AIAA 90-2158, July 1990.
2. "Small Gas Turbine Combustor Study - Compliant Metal/Ceramic Liner Performance Evaluation", W. Acosta, C. Mongren, AIAA 86-1452, June 1986.
3. "Gas Turbine Ceramic-Coated Vane Concept with Convection-Cooled Porous Metal Core", A. Kascak, C. Liebert et al, NASA TP 1942, AVRADCOM TR 81-C7, December 1981.
4. "Strain Isolated Ceramic Coatings for Gas Turbine Engines", R. Tolokan, G. Jarrabet, J. Brady, ASME 85-GT-96, March 1985.
5. "Metal Fiber Based Clearance Control Seals for Gas Turbine Engines", R. Tolokan, G. Jarrabet, H. Howe, ISROMAC-4, April 1992



Figure 1

Zirconia - Compliant Layer - Backing Cross Section

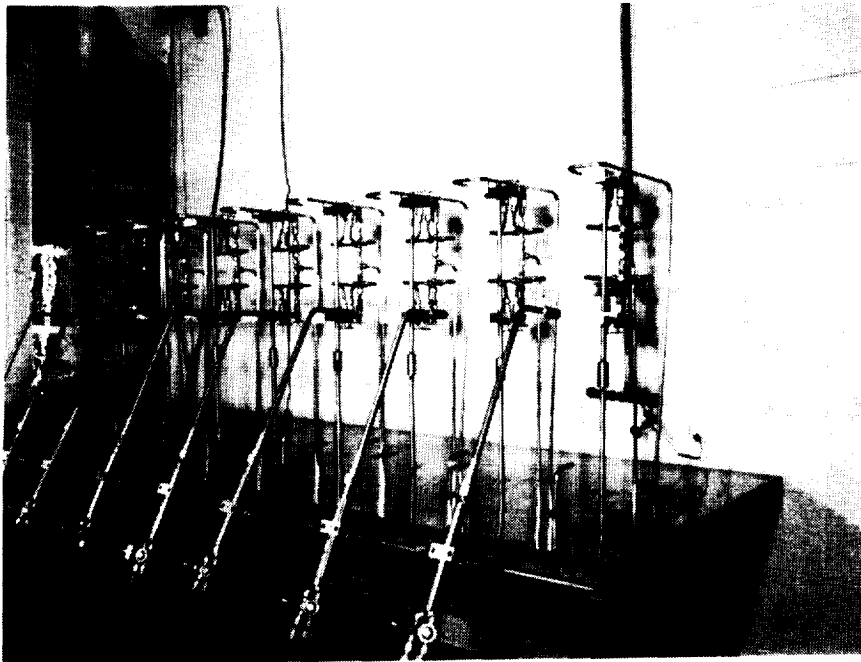


Figure 2

Eight Torch Thermal Shock Rig

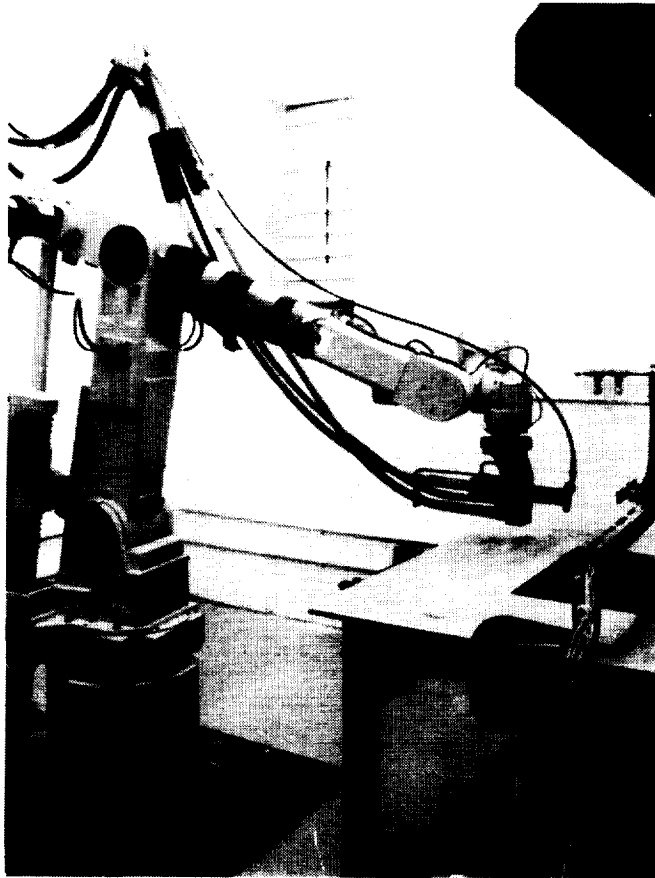


Figure 3
CNC Robotic Plasma
Spray Gun Positioning

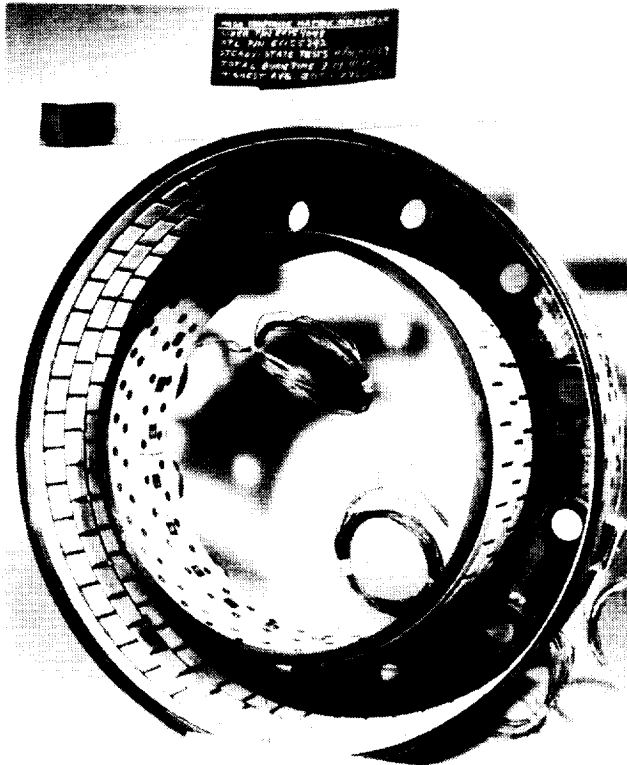


Figure 4
Army-NASA Tiled
Compliant Matrix Combustor

PREDICTED AND TESTED PERFORMANCE OF DURABLE TPS

John L. Shideler
NASA Langley Research Center
Hampton, VA

INTRODUCTION

The development of thermal protection systems (TPS) for aerospace vehicles involves combining material selection, concept design, and verification tests to evaluate the effectiveness of the system. The present paper reviews verification tests of two metallic and one carbon-carbon thermal protection system. The test conditions are, in general, representative of Space Shuttle design flight conditions which may be more or less severe than conditions required for future space transportation systems. The results of this study are intended to help establish a preliminary data base from which the designers of future entry vehicles can evaluate the applicability of future concepts to their vehicles.

SPACE SHUTTLE

The reusable surface insulation (RSI) selected for use on the Space Shuttle (fig. 1) was only one of many thermal protection concepts that were considered during the early shuttle design stages. One type of thermal protection that was considered was a radiative metallic system (ref. 1).



Figure 1

TYPICAL METALLIC THERMAL PROTECTION SYSTEM

The radiative stand-off thermal protection system shown in figure 2 (ref. 1) is typical of many of the metallic TPS concepts that were developed during the Space Shuttle design process. They consisted of a beaded or corrugated heat shield attached to flexible supports which were, in turn, attached to the vehicle structure. The heat shield protected fibrous insulation, which was usually encapsulated in a flexible package intended to be water-proof. Overlapping expansion joints accommodated thermal growth in the flow direction, and the beads or corrugations accommodated thermal growth in the direction transverse to the flow. Assembly of the heat shields and the stand-off supports to the vehicle structure required many fasteners. Therefore, the metallic concepts were perceived to be associated with high part count and to be heavy compared to the RSI. Consequently, at the time of Space Shuttle TPS concept selection, at least two of the factors that led to the rejection of the metallic systems were fabrication complexity and weight.

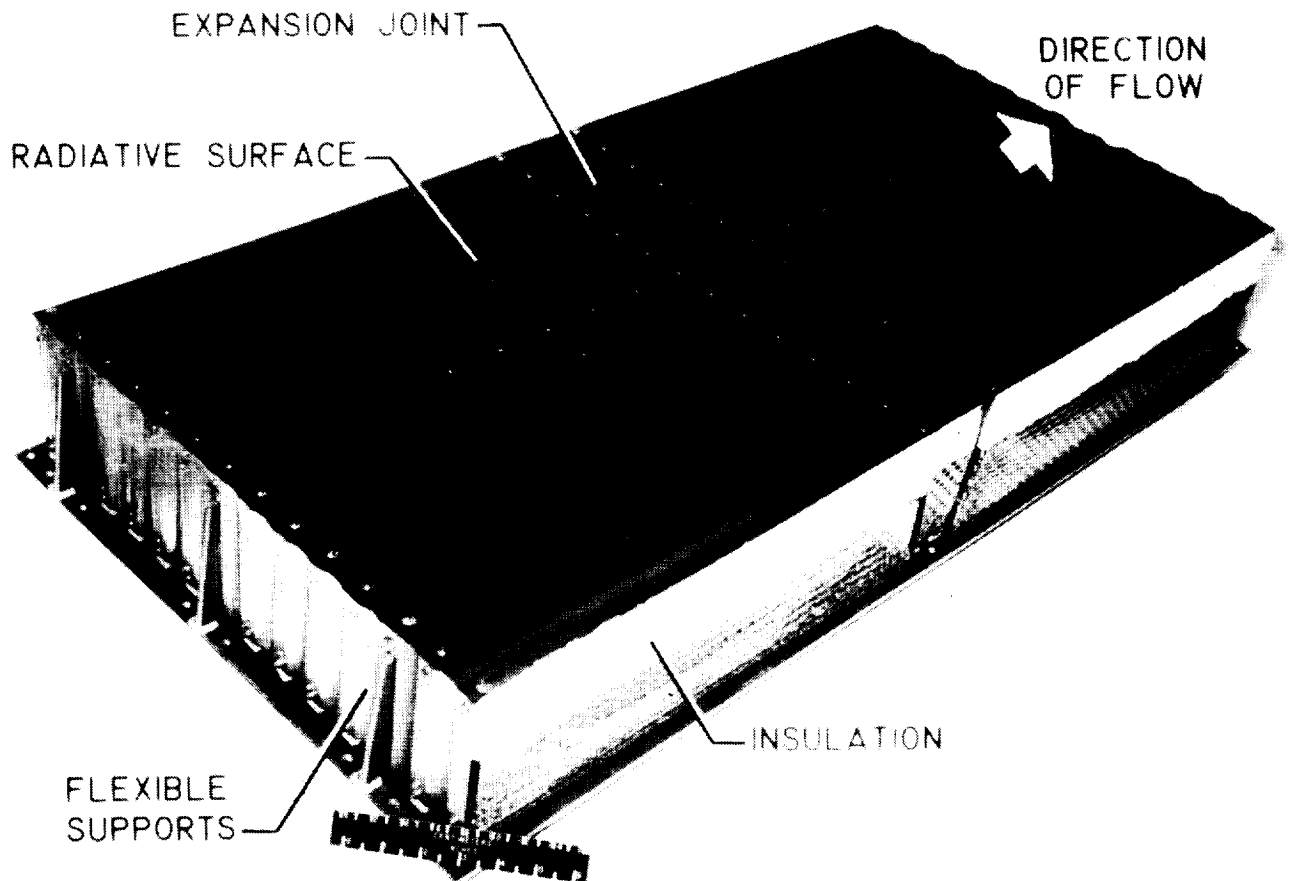


Figure 2

DURABLE TPS CONCEPTS

Although the RSI is an excellent insulator, it is very fragile. Titanium multiwall (M/W), superalloy honeycomb (SA/HC), and advanced carbon-carbon (ACC) multipost thermal protection system (TPS) concepts are being developed to provide more durable thermal protection for surfaces of future space transportation systems that operate at temperatures up to about 2300 °F. The two metallic prepackaged concepts shown in figure 3 are discrete panels that have a 1.0-in.-wide, 0.190-in.-thick strip of RTV-coated Nomex felt beneath the perimeter of each panel to prevent hot-gas flow beneath the panels. The ACC concept is a standoff design. The three concepts are described in detail in figures 4 and 5.

The goals of the TPS development program are to provide a durable surface of mechanically attached panels with overlapping edges that cover the gaps between the panels to reduce gap heating. As shown by the symbols in figure 3, these three concepts are mass competitive with the RSI TPS, the mass of which is indicated by the cross-hatched area.

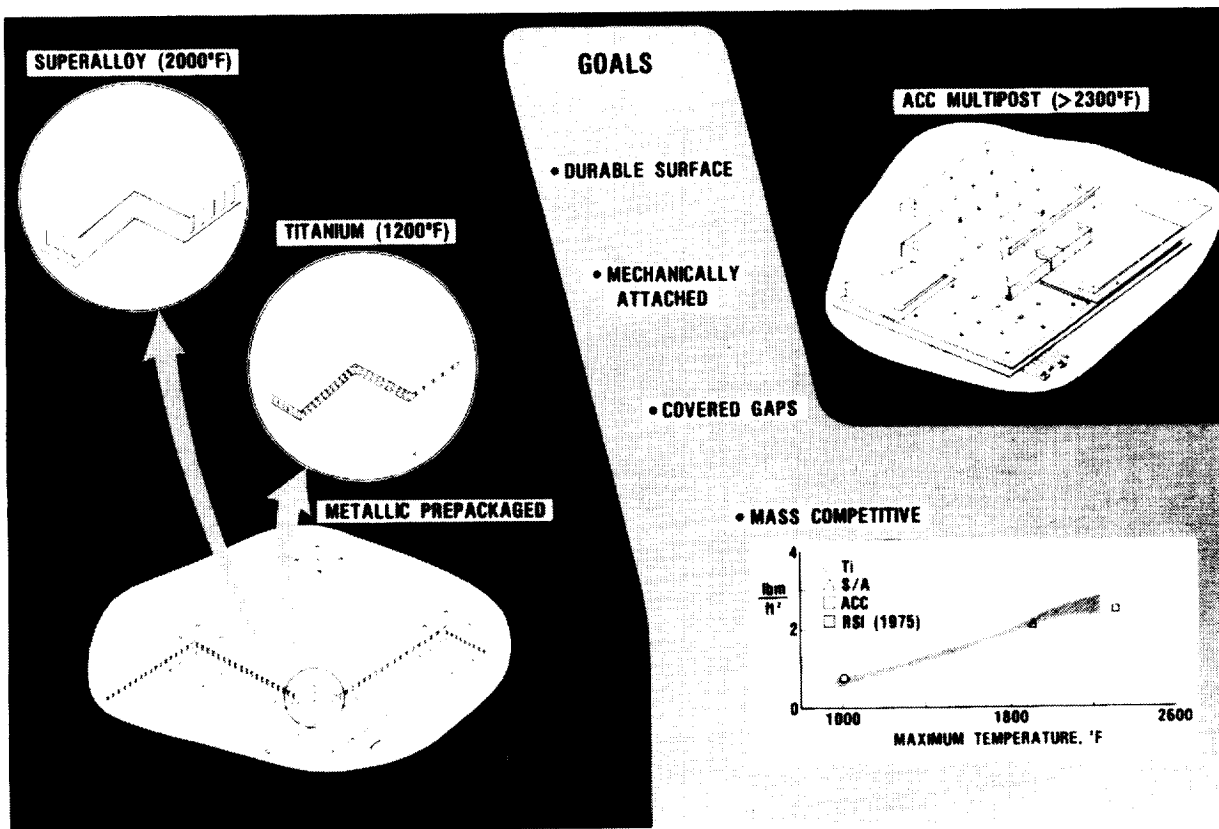


Figure 3

METALLIC TPS CONCEPTS

The titanium multiwall concept (See figure 4) consists of layers of dimpled 0.003-in.-thick titanium foil liquid-interface-diffusion (LID) bonded together at the dimples with a flat 0.0015-in.-thick foil sheet sandwiched between each dimpled sheet. The superalloy honeycomb concept consists of an Inconel 617 honeycomb outer surface panel with 0.005-in.-thick face sheets, layered fibrous insulation, and a titanium honeycomb inner surface panel with 0.006-in.-thick face sheets. The edges of the two metallic concepts are covered with 0.003-in.-thick beaded closures to form discrete panels nominally 12 in. square. The panels are vented by a 0.31-in.-diameter hole in the bottom that is covered with a 400-mesh screen. The titanium multiwall and superalloy honeycomb panels are described in detail in references 2 and 3, respectively.

The two types of attachments shown in figure 4 can be applied to either of the TPS concepts. The bayonet-clip attachment, shown with the titanium multiwall concept, consists of two clips and a metal tab (bayonet) LID bonded to the lower surface of the panel. One clip is mechanically attached to the vehicle surface and one clip is LID bonded to the lower surface of an adjacent panel. Thus, a single bayonet attaches a corner from each of two adjacent panels. The through-panel fastener, shown with the superalloy honeycomb concept, consists of a thin-walled Inconel 617 cylinder through the panel that allows access to a bolt which fastens the panel corner to the vehicle structure. The cylinder, which contains fibrous insulation, is covered with an Inconel 617 threaded plug. These fasteners are described in detail in reference 3.

The mass of the titanium multiwall panel designed for a location on the Space Shuttle with a maximum temperature of 1000° F is 0.806 lbm/ft² including bayonet attachments and uncoated Nomex felt, and the mass of the superalloy honeycomb panel designed for a location with a maximum surface temperature of 1900° F is 2.201 lbm/ft² including through-panel attachments and felt.

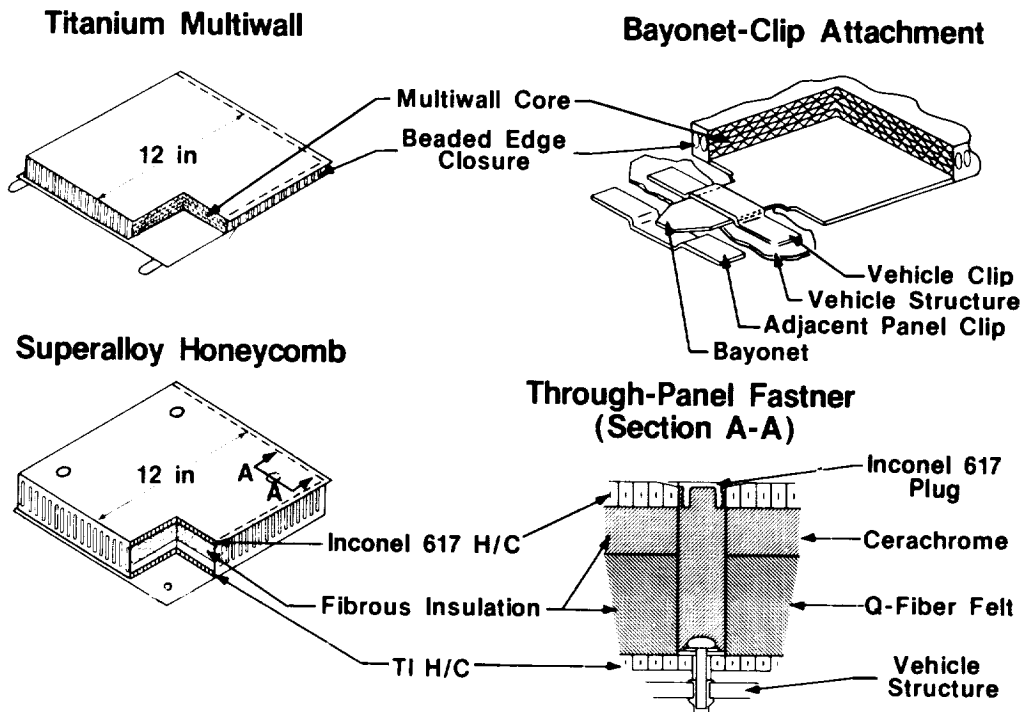


Figure 4

ADVANCED CARBON-CARBON MULTIPOST STANDOFF TPS CONCEPT

The advanced carbon-carbon multipost concept shown in figure 5 consists of a rib-stiffened ACC sheet attached to the vehicle primary structure by posts with fibrous insulation packaged in a ceramic cloth between the ACC panel and the vehicle structure. The surface of the single ACC panel is nominally 36 in. square. The ACC multipost concept is described in detail in reference 4, and fabrication of the ACC test model shown in later figures is described in reference 5.

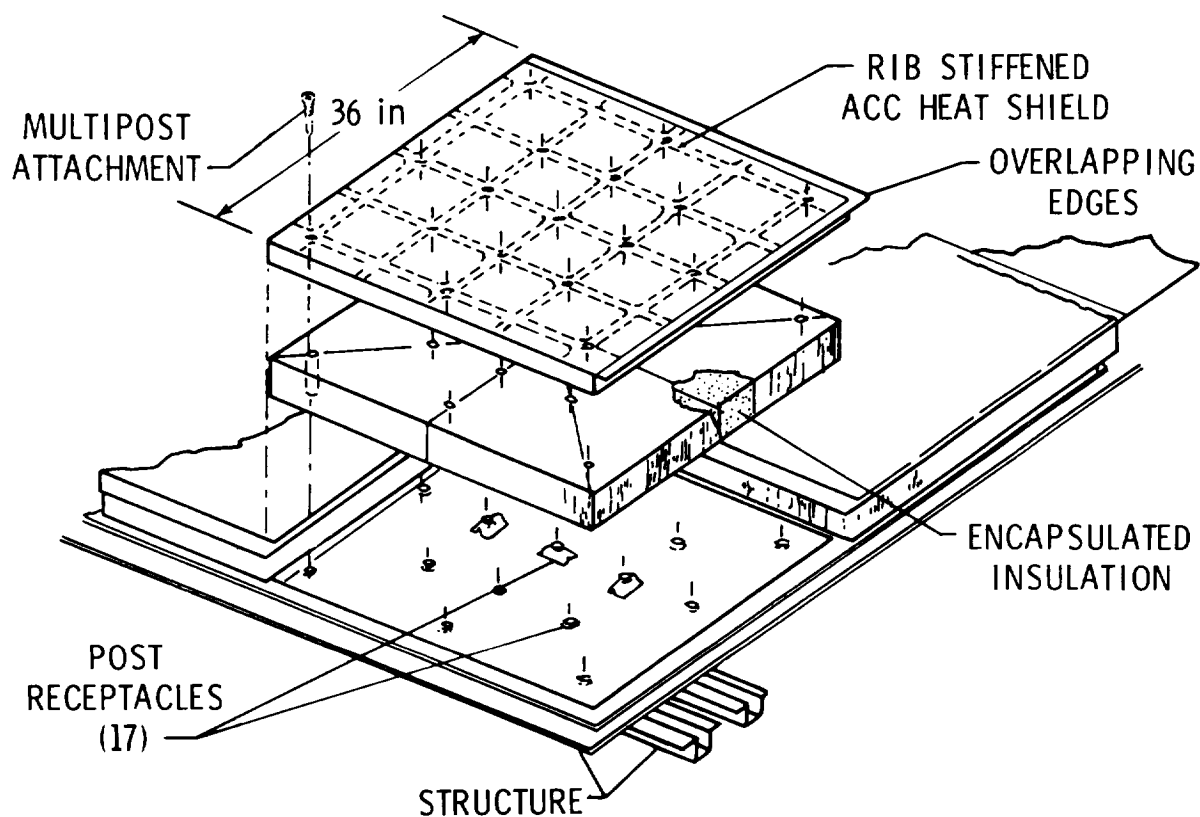


Figure 5

VERIFICATION TEST FACILITIES

NASA test facilities at Johnson Space Center (JSC), Kennedy Space Center (KSC), and Langley Research Center (LaRC) were used for verification tests of the three TPS concepts. The metallic concepts were exposed to thermal/vacuum, vibration, acoustic, environmental exposure, lightning strike, and wind tunnel tests. The ACC multipost concept was exposed to thermal/vacuum and arc tunnel tests. The test loads are, in general, representative of Space Shuttle design loads, which may be more or less severe than loads required for future space transportation systems.

TPS test models were exposed to combined temperature and pressure histories in thermal/vacuum test facilities at JSC, KSC, and LaRC to obtain thermal response characteristics of the concepts. In the facility at JSC, shown in figure 6, the heater system is mounted in a boiler-plate Apollo command module test chamber that is evacuated by a mechanical vacuum pump. The heater consists of electrically heated graphite elements enclosed in a fixture box purged with nitrogen.

Dynamic response of the metallic concepts was evaluated by shaker-table vibration tests, by acoustic exposure in a sound chamber at JSC, and by acoustic exposure in a progressive wave facility at LaRC. The acoustic exposure levels were representative of those experienced during Space Shuttle liftoff. The test panels were attached to the side wall of the test section of the LaRC facility shown in the figure. (The ACC test model was also exposed to thermal/vacuum tests in the facility. Graphite heaters are added to the test-section side wall opposite the test panel to provide radiant heating.)

Environmental tests to assess water retention and the effects of atmospheric contamination on metallic TPS were conducted near the KSC Space Shuttle launch site 39B shown in the figure. Lightning strike tests were conducted at LaRC to determine how much damage lightning impact caused on the metallic panels. The facility operates by charging a bank of capacitors and rapidly discharging the capacitors to a grounded test model. Arrays of metallic TPS panels were tested in the LaRC 8-foot High Temperature Tunnel (8HTT), and an array of four corner segments of an ACC panel was tested in the LaRC 20 MW Aerothermal Arc Tunnel to evaluate the performance of the concepts in an aerothermal environment.

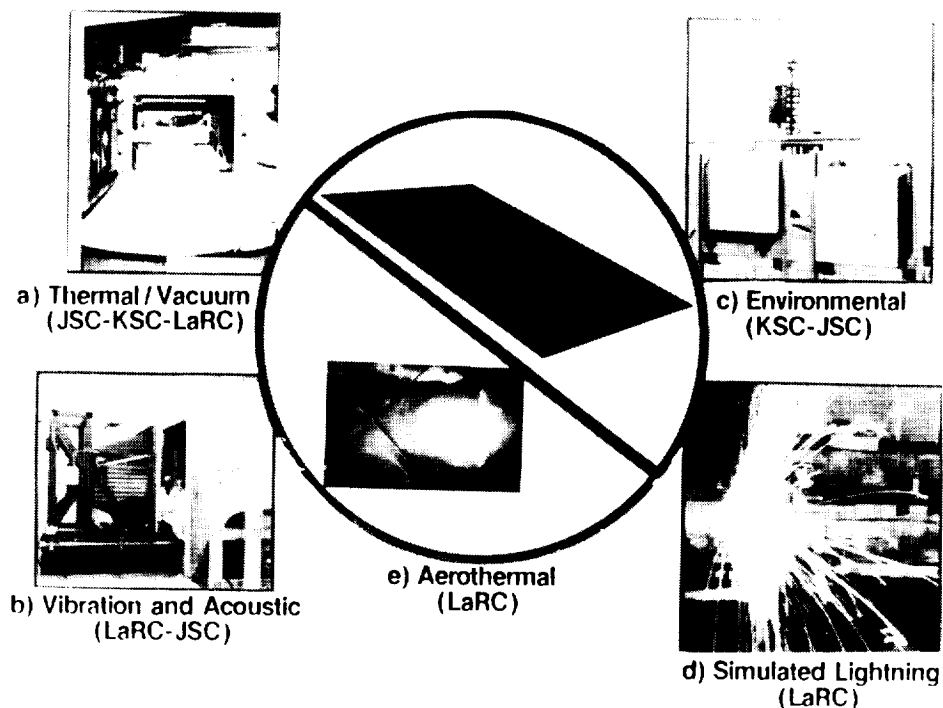


Figure 6

THERMAL/VACUUM TESTS

Typical results from the thermal vacuum tests of the titanium multiwall, superalloy honeycomb, and ACC panels are presented in figure 7. The panels were exposed to pressure histories in addition to temperature histories because the thermal conductivity of the fibrous insulation is a function of pressure. The surface temperature histories (lines 1) were imposed during the test and were used as input to a one-dimensional thermal analysis (ref. 6). Temperatures were calculated at thermocouple locations in the TPS (lines 2) and at aluminum plates (lines 3) that were sized to represent the thermal mass of a typical Space Shuttle structure where the TPS panels might be applied. The surface temperature histories for the titanium and superalloy panels are temperatures predicted at respective points on the Space Shuttle based on design trajectory 14414.1C. The measured back-surface temperatures on the metallic TPS models indicate acceptable thermal performance in that they did not exceed 350°F, the maximum allowable temperature for the aluminum structure. The ACC model was subjected to a surface temperature history similar to that expected for the arc tunnel tests. (The arc tunnel cannot provide the low heating rates that occur early in the shuttle entry trajectory.) The calculated temperatures were in reasonable agreement with the measured temperatures.

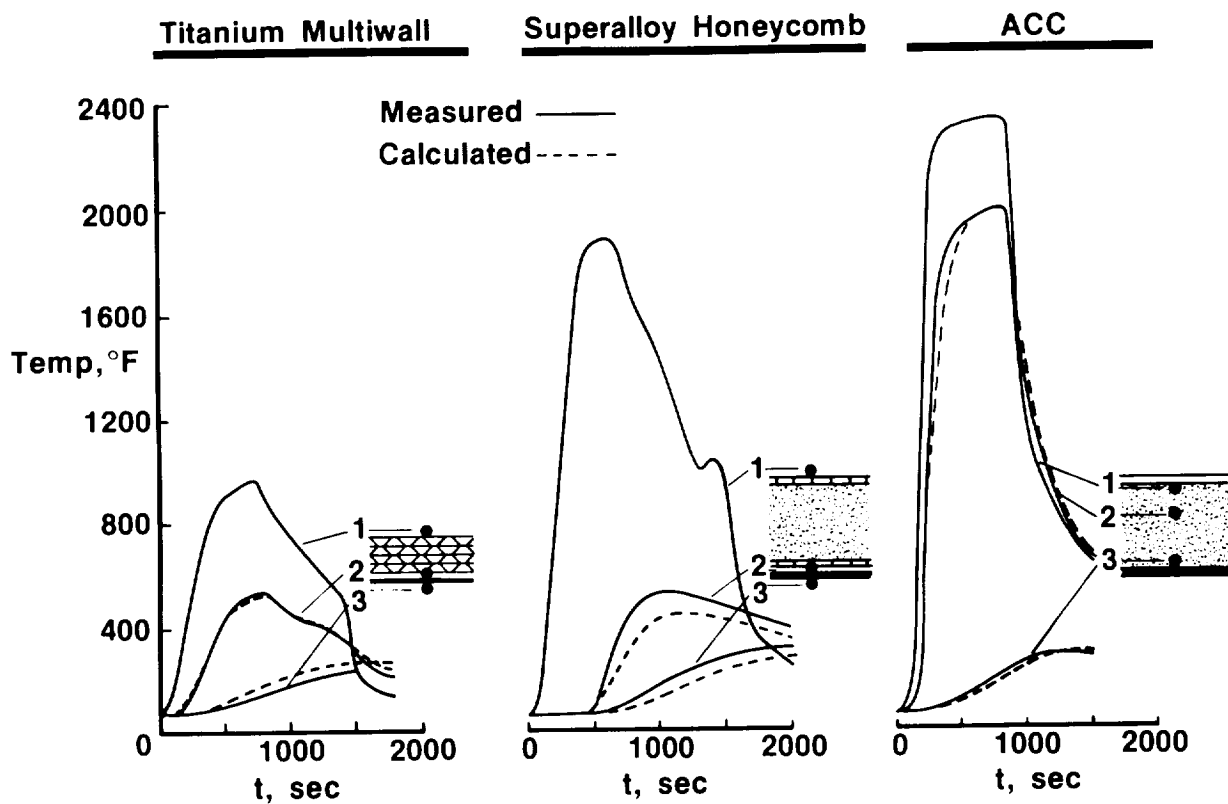


Figure 7

SUPERALLOY HONEYCOMB 2-PANEL ARRAY

The photograph to the left of figure 8 shows the superalloy honeycomb two-panel array before testing. The photograph on the right, taken at a different angle, shows the array after exposure to 25 thermal/vacuum cycles with a maximum surface temperature of 1900° F for each cycle. The array was exposed to one over-temperature test to 2000° F (cycle 26). No damage occurred to the panel; however, the central 4.5 in. of the overhanging lip covering the gap between panels buckled slightly. The amplitude of the buckle pattern was about 0.050 in. from crest to valley, and the wave length was about 1.5 in. from crest to crest. Such surface roughness is not expected to have an effect on the thermal performance of the TPS system because it would be within the boundary layer over most of the vehicle surface. The array was exposed to 161 dB for 15 minutes between cycles 16 and 17 (acoustic exposure is discussed later). No change in thermal performance occurred during these tests. Results from similar tests for the titanium multiwall two-panel array at temperatures up to 1200° F did not identify any deficiencies in the multiwall design.

Thermal Vacuum Tests

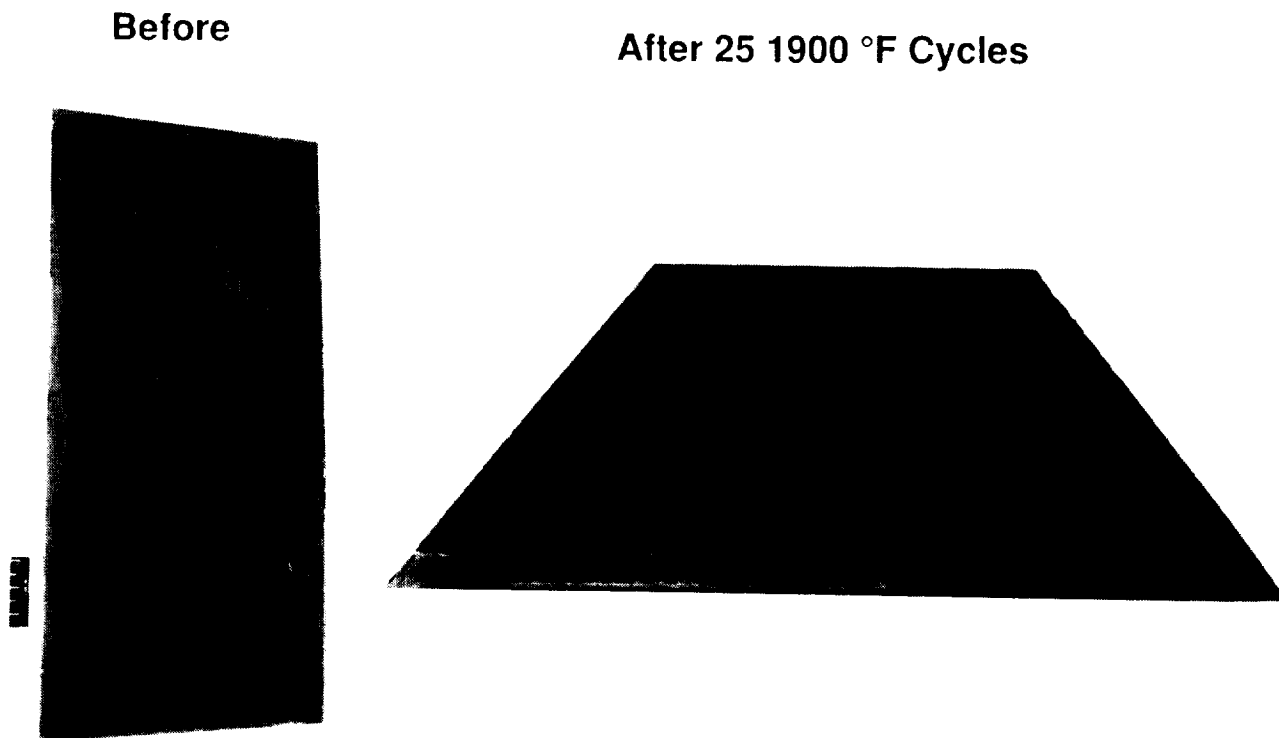


Figure 8

ORIGINAL PAGE
BLACK AND WHITE PHOTOGRAPH

SHAKER-TABLE TESTS ON M/W AND SA/HC PANELS WITH THROUGH-PANEL FASTENERS

Titanium multiwall and superalloy honeycomb panels, each with through-panel attachments, were vibrated on an LaRC shaker table at three different *g* levels. The results of the tests are summarized in figure 9. The panels were exposed to 10 and 20 *g* levels of random vibration on each of three axes for 600 s/*g*-level. They were then exposed to 30 *g*'s on each of three axes for 485 s. This exposure approximates 25 missions. The titanium multiwall panel was not damaged; however, the attachment screws on the superalloy panel became worn from repeated installation and removal. This wear caused the four fasteners to loosen during the last 30 *g* test and resulted in elongation of the fastener holes, the failure of two fasteners, and the bending of the other two. These results indicate that new screws should be used on reinstallation.

<u>Concept</u>	<u>Exposure level (3-axes)</u>	<u>Time</u>	<u>Comments</u>
Ti M/W	10 g's	600 sec/axes	Approximates 25 missions-- no damage
	20	600	
	30	485	
SA/HC	10 g's	600 sec/axes	Approximates 25 missions-- attachment screws worn from repeated disassembly
	20	600	
	30	485	

Figure 9

ACOUSTIC TESTS ON M/W AND SA/IC PANELS

Both the titanium multiwall and the superalloy honeycomb concepts were exposed to the acoustic environments shown in figure 10. Two facilities were used, a sound chamber at JSC operating at an overall sound pressure level (OASPL) of 161 dB and a progressive wave facility at LaRC operating at 159 dB. The spectrums are representative of the sound environment for the Space Shuttle at locations where the TPS concepts might be applied. Two-panel arrays tested at JSC had bayonet-clip attachments and were exposed to sound for 15 minutes, which is representative of about 25 missions with a scatter factor of 4. Single panels tested at LaRC had through-panel fasteners and were tested for 60 minutes, which corresponds to about 100 missions with a scatter factor of 4.

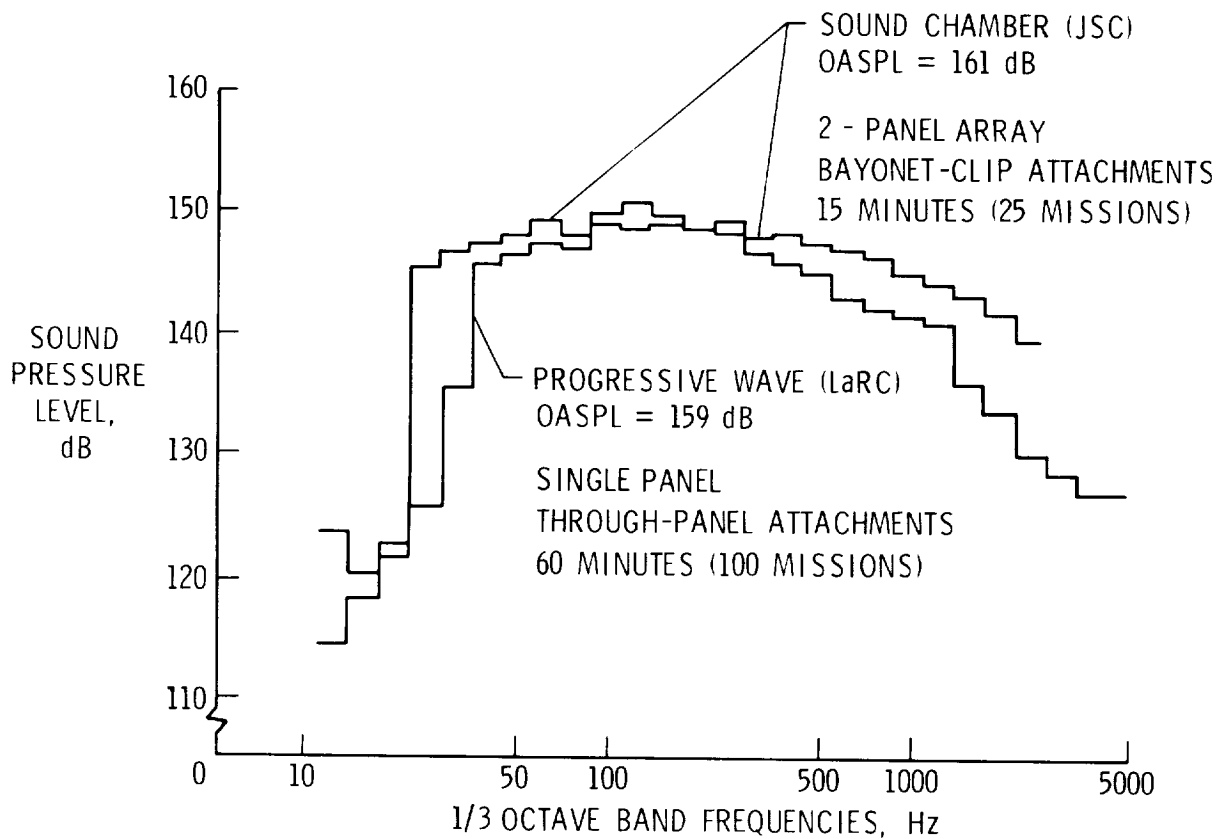


Figure 10

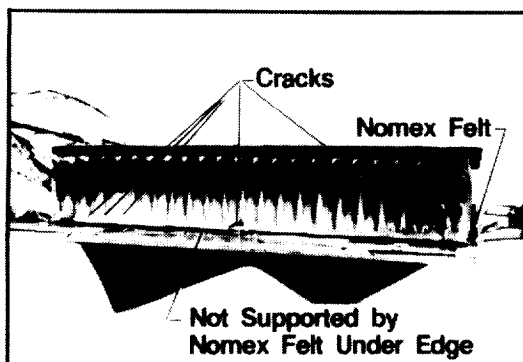
DAMAGE FROM ACOUSTIC TESTS OF SUPERALLOY HONEYCOMB PANELS

No damage occurred to the titanium multiwall panels in the tests in either of the facilities described in figure 10. However, the superalloy honeycomb panels sustained some damage in each facility. An edge view of one of the two superalloy honeycomb panels tested in the JSC sound chamber is shown in Figure 11. Prior to the test, the overhanging lip along the right half of the panel edge shown was bent down (in a pattern which fits a human hand), and some buckling along the bottom edge of the side closure occurred. Additionally, as identified in the figure, this edge was not properly supported by Nomex felt. All other edges were supported by a 1-in.-wide strip of Nomex felt as specified in the concept design. During the tests, numerous cracks occurred on the bottom edge of the unsupported side closure. Since the other seven side closures on the two panels suffered no damage during the tests, the cracks probably occurred due to the lack of felt support and handling damage.

One side closure of the superalloy honeycomb panel tested in the LaRC progressive wave facility was buckled in shipment. The panel was judged to be acceptable for vibration tests since the buckling was limited to only one edge. Upon completion of the vibration tests with no visible damage, the panel was exposed to acoustic load for 60 minutes. After the first 15 minutes, small cracks at the bottom of the buckled side closure were noticed. These cracks were monitored during the remaining acoustic exposure, but negligible growth occurred. A typical crack is shown in figure 11. Because the only damage was on the side buckled in shipment, the cracks that developed were probably due to the shipping damage.

Since the titanium multiwall panels showed no damage from the acoustic tests, and since the only cracks that developed on the superalloy honeycomb panels both at JSC and LaRC occurred in areas that had suffered handling damage prior to the tests, it appears that both concepts will survive sonic environments as high as 161 dB. However, demonstrated proof of survival would require additional acoustic tests.

a) Tested in JSC Sound Chamber



b) Tested LaRC Progressive Wave Facility

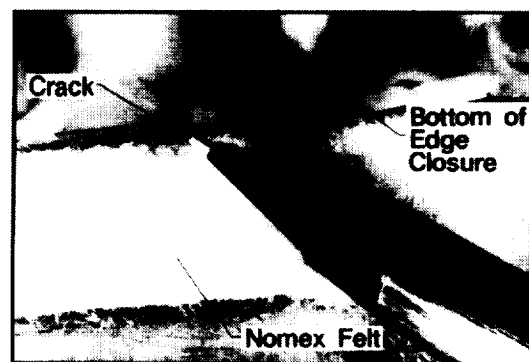
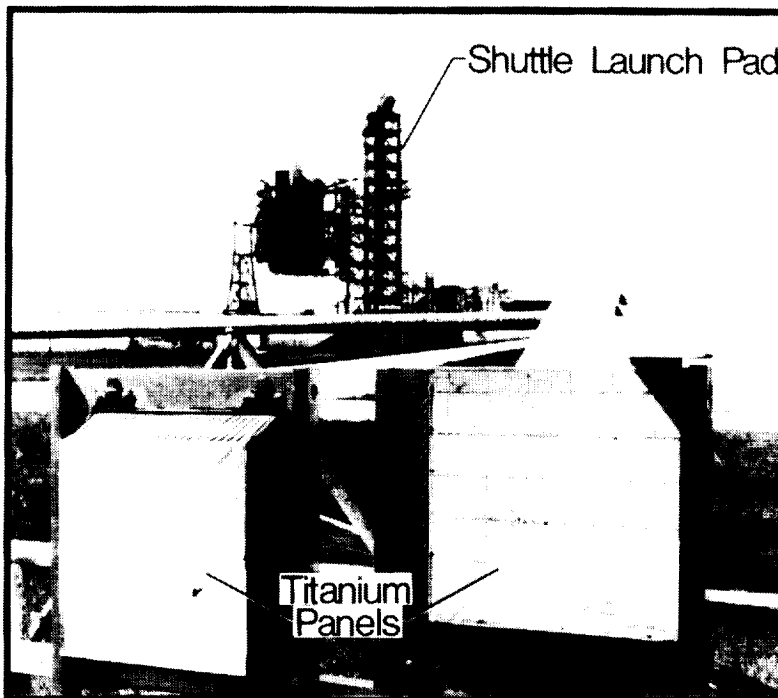


Figure 11

ENVIRONMENTAL EXPOSURE OF METALLIC PANELS AT KSC

Since thunderstorms occur frequently during the summer months at KSC and are characterized by heavy rainfall and occasional hail, environmental tests were designed to determine the water absorption/retention characteristics of multiwall TPS panels under actual rainfall conditions. Two first-generation titanium multiwall panels were exposed to the weather environment at Shuttle Launch Complex 39B at KSC shown in figure 12. Test results showed that water absorption is not a problem. During a three-month exposure period at the launch pad, no water was detected within the titanium multiwall panels. The water detection methods included measuring panel weight gain and using neutron radiography to detect small amounts of water.

Because KSC is near the Atlantic Ocean, salt and other contaminants can accumulate on the TPS surface over a period of time. Tests are planned to couple launch pad exposure with mission simulations to evaluate long-term environmental effects on metallic TPS. Current plans are to test titanium multiwall and superalloy honeycomb panels by subjecting them to repeated exposure to contaminants and thermal/vacuum cycles. During the test program, x-ray and other non-destructive techniques will be used to detect any physical changes with the metallic TPS.



- **2-Week Exposure Cycles to Accumulate Contaminates**
- **Radiant Thermal/Vacuum Cycles to Simulate Mission Environment**
- **Repeat Exposure and Mission Cycles to Evaluate Long-Term Multi-Mission Effects**

Figure 12

ORIGINAL PAGE
BLACK AND WHITE PHOTOGRAPH

SIMULATED LIGHTNING STRIKES ON METALLIC TPS

A titanium multiwall panel and a superalloy honeycomb panel were exposed to simulated lightning strikes. Damage from these tests is shown in figure 13. The strike on the titanium multiwall resulted in a conical hole through all the layers of the panel with a hole of approximately 1/8 inch in diameter in the lower surface. However, the damage to the superalloy honeycomb panel was limited to the Inconel surface. A spot on the surface of the panel about the size of a dime was indented as though it were hit with a ballpeen hammer. In addition, the face sheet was burned away locally, exposing two of the honeycomb cells. The intensity of these strikes (100 kA) meets the Space Shuttle criteria for lightning strikes on acreage surfaces (ref. 7).

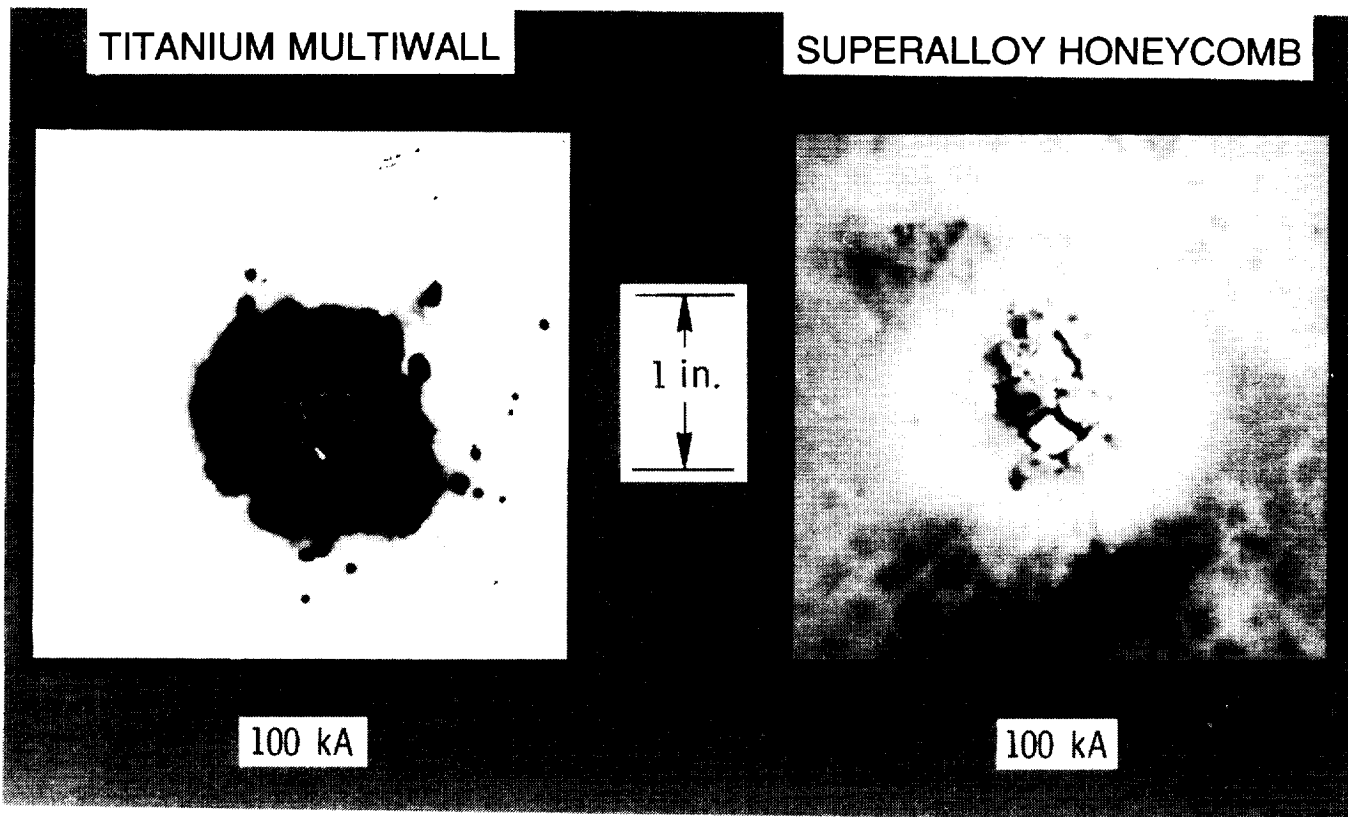


Figure 13

ORIGINAL PAGE
BLACK AND WHITE PHOTOGRAPH

METALLIC TPS ARRAYS FOR 8-FT HTT TESTS

A titanium multiwall array of panels and a superalloy honeycomb array of panels were fabricated for radiant and aerothermal tests in the 8' High Temperature Tunnel (HTT) at LaRC. These arrays, shown in figure 14, consisted of 20 panels and were configured to fit a standard panel holder used in the 8' HTT. The panel holder has an opening, 60 in. by 42.5 in., and can accept test-specimen thicknesses up to about 12 inches. Since the standard metallic TPS panel is 12 in. square and the panel holder is 42.5 in. wide, panels approximately 6 in. wide were used to complete the array.

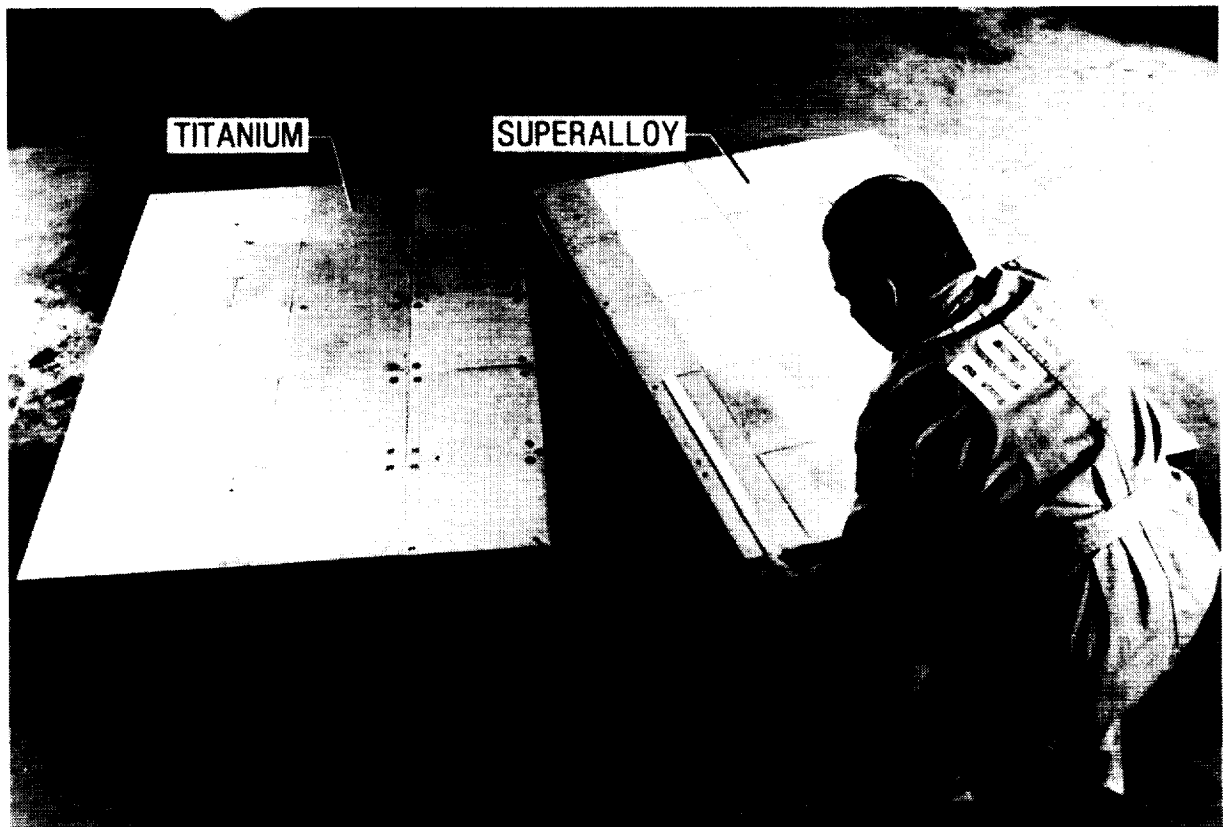


Figure 14

ORIGINAL PAGE
BLACK AND WHITE PHOTOGRAPH

TITANIUM MULTIWALL 20-PANEL ARRAY IN LARC 8' HIGH TEMPERATURE TUNNEL

The titanium multiwall TPS 20-panel array mounted in the panel holder and installed in the 8' High Temperature Tunnel is shown in figure 15. The view is looking downstream in the tunnel. Fences attached to each side of the panel holder provide relatively uniform two-dimensional flow on the surface of the panel holder. The array of panels was installed so that the gaps between panels were parallel to the flow direction. This installation configuration is considered a "worst case" orientation of the panels with respect to the flow.

The insert in figure 15 shows a schematic view of the major components of the 8' High Temperature Tunnel, which is a "blow-down" tunnel. The model is held in a pod beneath the test section and covered by radiant heaters which not only preheat the model but also protect the model from tunnel start-up and shut-down loads. After the model is preheated and the tunnel is started, the radiant heaters are turned off and retracted by hydraulic actuators. The model is then rapidly inserted into the 8-foot-diameter test stream by a hydraulically-operated 15-ton elevator which raises the model to the test position in approximately 1 second. For shutdown, the procedure is reversed. The total aerothermal test duration is up to two minutes depending on test conditions.

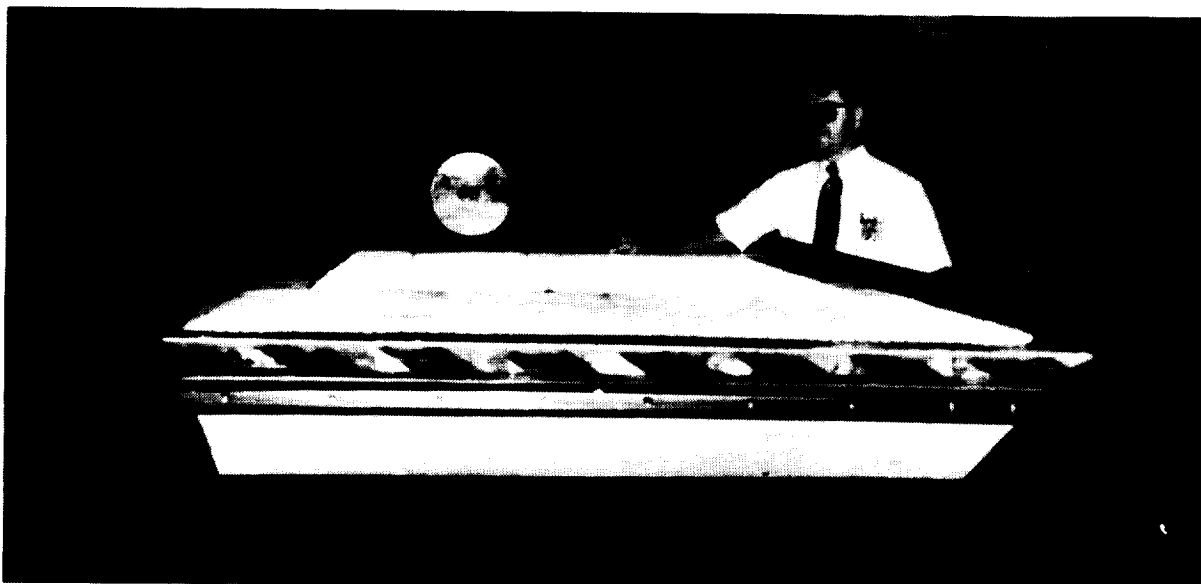
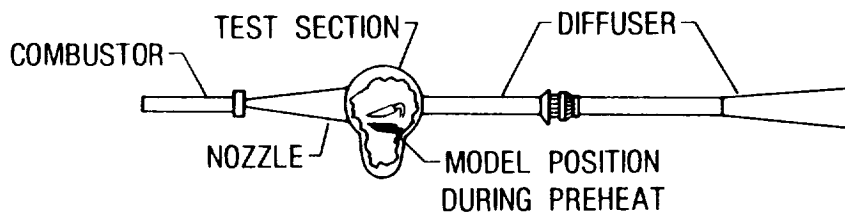


Figure 15

EFFECT OF AEROTHERMAL EXPOSURE ON GAP TEMPERATURE

One of the objectives of the aerothermal tests in the 8' High Temperature Tunnel was to determine if temperatures in the gaps between panels would be increased by exposure to the flow. Such an increase would indicate that the panel edge overlay covering the gap is not adequate by itself to prevent gap heating when the flow is parallel to the gap. Tests of an array of first-generation titanium multiwall panels indicated that flow did not occur in the gaps when the panels were oriented 30 degrees to the flow (ref. 8).

Surface temperatures and temperatures at the bottom of the gap are shown in figure 16 for both the titanium multiwall array and the superalloy honeycomb array. The dashed curves represent temperatures measured during a 200 second portion of an aerothermal test when the array was inserted into the tunnel stream. The solid curves represent temperatures recorded at the same locations and time intervals during a static radiant heating test.

For the time interval shown, the surface and gap temperatures of the titanium multiwall model were at equilibrium. When the model was inserted into the flow, negligible temperature change occurred at the bottom of the gap, thus indicating no additional gap heating occurred.

Although the surface of the superalloy honeycomb panel reached equilibrium, the temperature at the bottom of the gap was still approaching equilibrium when the radiant heaters were turned off and the model was inserted into the flow. Immediately after the superalloy model was inserted into the flow, the temperature at the bottom of the gap increased quickly. This high, quick temperature rise indicates that hot gases flowed into the gaps between the panels. Thus, when the edges of the superalloy panels are parallel to the flow, the overlapping edges did not provide an adequate seal. Superalloy honeycomb panels may be more susceptible to gap heating because the gap is much larger than the gap between titanium multiwall panels. Consequently, when thermal expansion closes the top of the gap, the bottom of the gap remains partly open because it is much cooler.

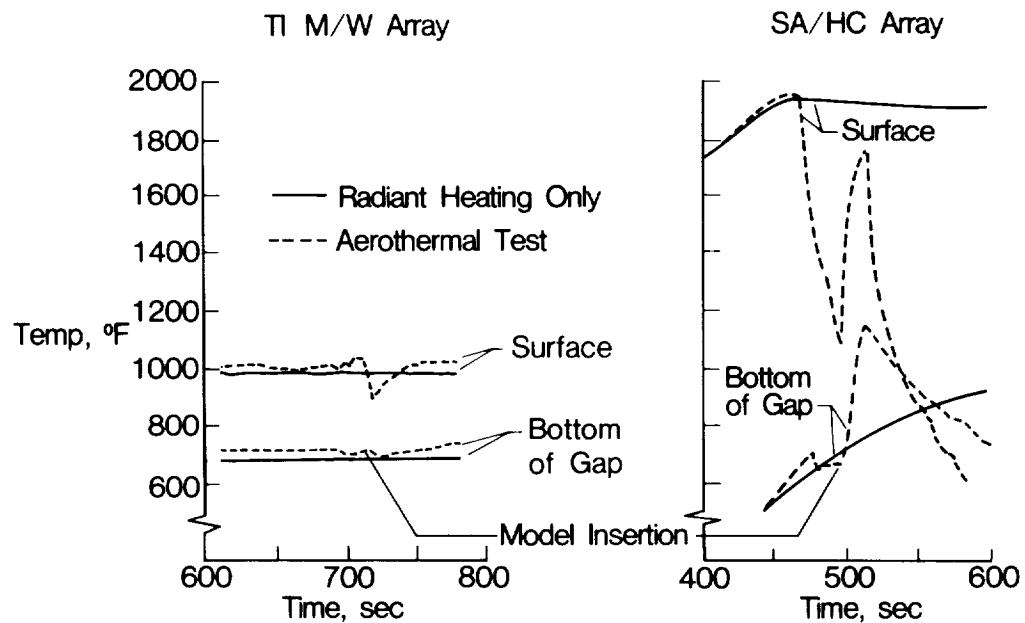


Figure 16

TEMPERATURE HISTORIES AT 4 GAP LOCATIONS

Even though the previous figure indicates that aerothermal heating in the gap between panels occurred at one location, the cause of such heating is not clear. The temperature histories at four gap locations for four different tests are shown in figure 17. In each of the four tests, the temperatures measured at the bottom of the gap at three different locations in the array (solid lines) increased rapidly when the model was inserted into the test stream. These temperatures were measured by thermocouples attached to the external surface of the side closure. However, the temperatures measured at a fourth location where the thermocouple was attached to the internal surface of the side closure (dashed lines) did not increase when the model was inserted into the stream. These results are consistent for all 4 tests and suggest that the presence of the thermocouple and thermocouple wire in the gaps between panels may have caused the heating in the gaps at those locations. Consequently, a definitive conclusion about the severity of aerothermal heating in gaps that are parallel to the flow is not possible at this time.

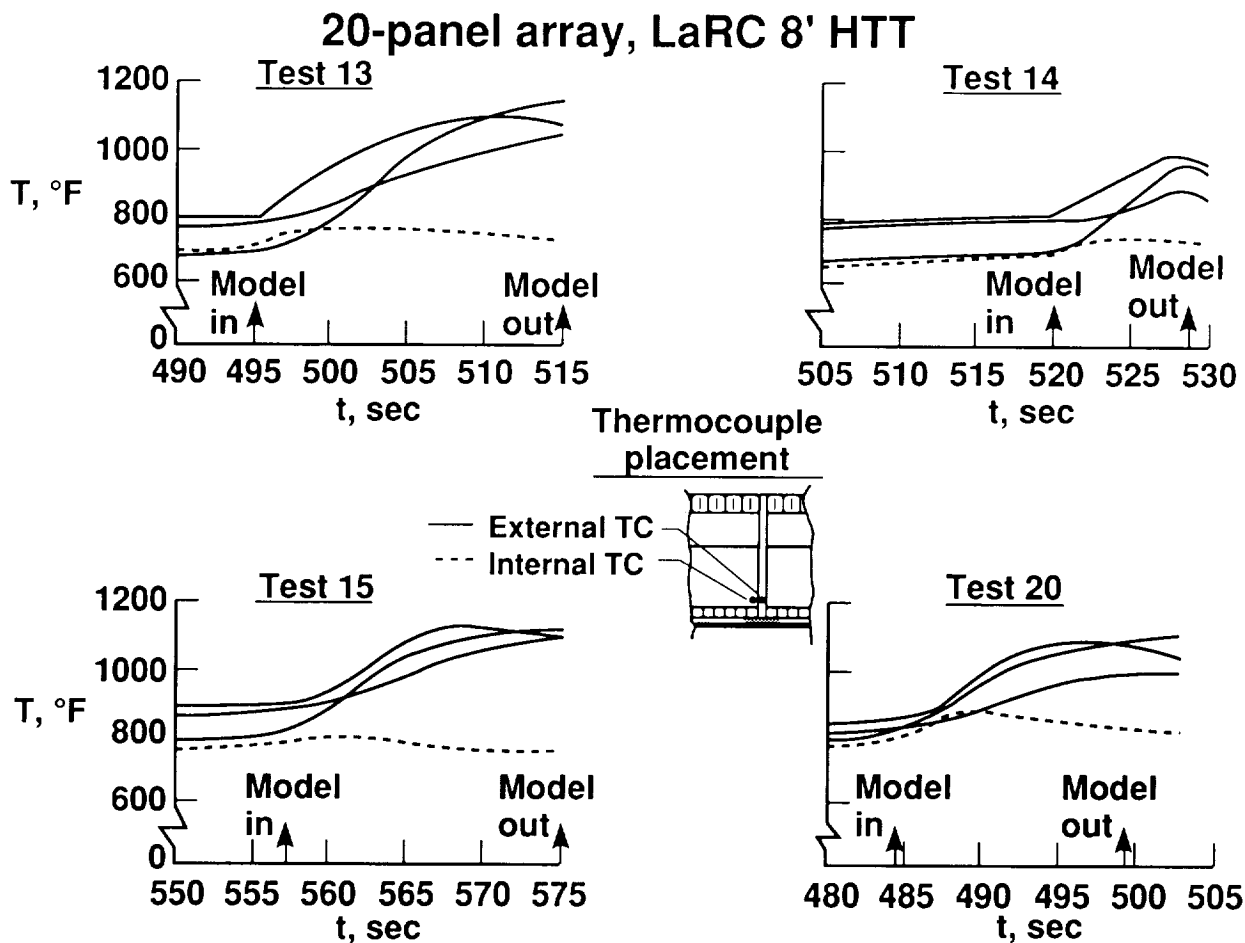


Figure 17

INTENTIONAL SURFACE DAMAGE TO SA/HIC 20-PANEL ARRAY

The original test plan for the 20-panel arrays included aerothermal tests with the lightning-damaged panels included in the arrays. The lightning-damaged titanium multiwall panel was unchanged by the aerothermal test. Furthermore, a negligible increase in temperature (less than 10° F) occurred on the backside of the panel at the area of damage. Thus, lightning damage of the titanium multiwall concept does not appear to be a design concern.

The lightning-damaged superalloy honeycomb panel could not be installed into the array in a timely manner; therefore, panels already in the array were intentionally damaged to simulate the lightning damage. The types of damage inflicted on the panels are shown in figure 18. An opening was created in the outer surface of several panels by grinding, punching or burning with a torch. Additionally, one attachment plug was intentionally left out. The honeycomb core was left near the surface only at the torch burn-through. The two rows of panels in the foreground of figure 18, which were coated with a ceramic non-catalytic coating (ref. 9), were the panels that received the damage to the outer face sheet. (The dark panels in the background were coated with a high-temperature, high-emittance paint.) The array was then again exposed to aerothermal heating in the 8' High Temperature Tunnel.

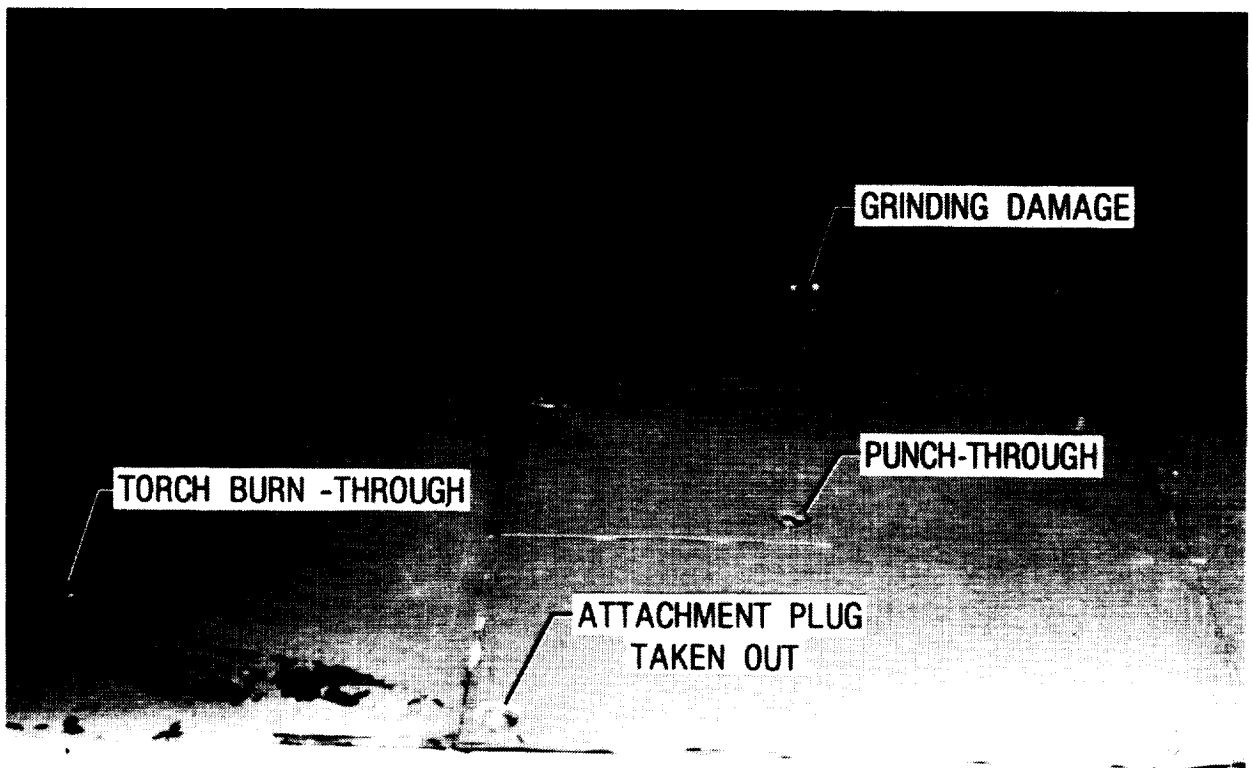


Figure 18

SA/HC 20-PANEL ARRAY IN 8' HIGH TEMPERATURE TUNNEL

The superalloy honeycomb 20-panel array with the intentionally damaged panels is shown in figure 19. The figure was made from a frame of movie film taken during the last aerothermal test of the array (run 20). The only light used to expose the film was that radiating from the model, which was at a temperature of about 1850° F. The thermal deflections of the heated model resulted in panel "pillowing", which caused slightly higher temperatures to occur on the upstream side than on the downstream side of the individual panels (ref. 10). The greater brightness (and higher temperature) of the right-hand side of the array (looking downstream) was caused by the lower emittance of the panels with the non-catalytic coating.

Several hot spots can be seen where the face sheet buckled and delaminated from the honeycomb core. The damage occurred early in the test program when fiberglass curtains, used to protect surrounding structure from radiation from the quartz heaters, melted and fell on the panels. The buckles and delaminations did not propagate during the balance of the test program. A hot spot was caused by the torch burn-through discussed in figure 18. This hot spot may have occurred because the exposed honeycomb core was near the flow stream. The other two damaged locations and the open attachment hole did not appear to cause any significant overheating. Bent gap covers also appeared as hot spots since they protrude into the airflow. The gap covers in the rear of the model were in contact with the rigid Glassrock material that surrounded the array and were deformed when the panels bowed thermally. The single gap cover hot spot that occurred at the intersection of four panels was probably caused by thermal bowing interference between panels with different attachments. This location was the only intersection where a bayonet-clip-attached panel overhung a panel with through-panel attachments.

Post-test inspection of the array was not possible because, at the end of this test, part of the panel holder broke and caused the tunnel to "unstart". The strong shock wave (10 psi pressure rise in about 0.2 seconds) passing through the test section completely destroyed the array of panels, which were designed for 2 psi.

RUN 20

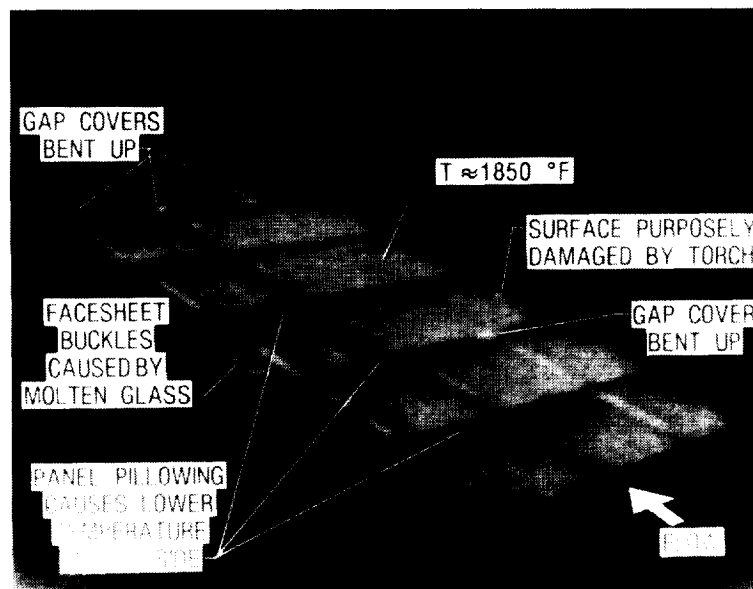


Figure 19

NON-CATALYTIC COATING ARC-TUNNEL TEST RESULTS

For the same entry conditions, a metallic surface of an entry vehicle will be subjected to a higher heating rate than a nonmetallic surface. This difference occurs because oxides of high-temperature structural metals are generally catalytic to the recombination of dissociated air molecules, and the energy of dissociation released during recombination adds to the heat load (ref. 11). A non-catalytic coating will reduce the heat load to the surface and greatly increase the thermal efficiency of metallic TPS.

A commercially available, water-base, silica-alumina ceramic coating was evaluated by exposing coated and uncoated Inconel 617 specimens in the LaRC 1 MW Aerothermal Arc Tunnel using air as a test medium. Prior to the arc tunnel tests, the emittances of the specimens were measured, and coated specimens were subjected to 80 thermal shock cycles in a 2000° F furnace to evaluate the adhesion of the coating to the metal (ref. 9). The measured emittance of the coated and uncoated (but oxidized) specimens were 0.65 and 0.8, respectively. The coating remained attached during the thermal shock cycles, and the emittance did not change.

The results of the arc tunnel tests are shown in figure 20. Arc tunnel test conditions were established that resulted in a temperature of 1753° F on the uncoated specimen. The coated specimen was tested at the same condition, but reached only 1353° F. Modification of the coating composition to increase surface emittance without harming the non-catalytic and adherence characteristics would further reduce the temperature. Radiation equilibrium heating rates were calculated using the maximum measured surface temperatures and the measured emittances. The heating rate on the coated specimen was only 37 percent of the heating rate on the uncoated specimen.

This coating was applied to several superalloy honeycomb TPS test panels exposed to wind tunnel, thermal/vacuum, lightning strike, vibration, and acoustic tests. Results from these tests further indicate that the non-catalytic coating adheres well. Thus, an adhering, non-catalytic coating is feasible and should be used for metallic TPS; however, emittance greater than 0.65 is desirable.

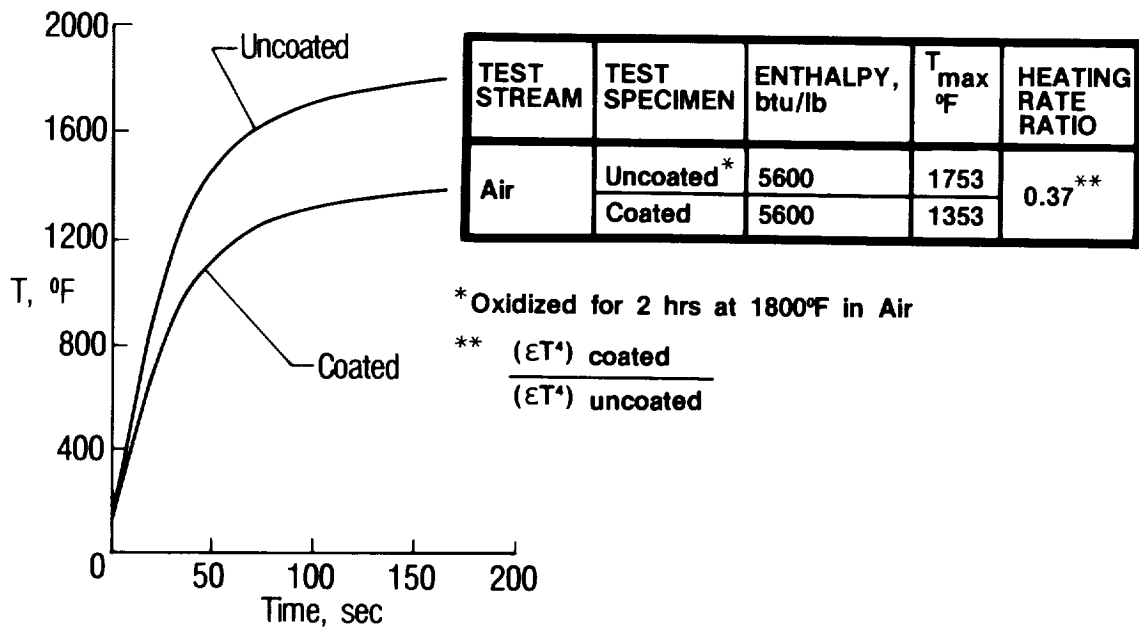


Figure 20

EFFECT OF CURVATURE ON THERMAL STRESS OF UNCONSTRAINED PANEL

One of the main differences between the design of flat and curved TPS is the effect of curvature on thermal stress. The thermal stresses in an unconstrained TPS structure are zero if the temperature distributions through the structure are linear when they are measured in a rectangular Cartesian coordinate system (ref. 12). The flat panel shown in figure 21 has a linear temperature distribution through the depth, and since this distribution results in a linear (constant in this instance) temperature distribution in the plane $z=constant$, no thermal stress occurs. However, the same linear temperature distribution through the depth of the curved panel shown in the figure results in a nonlinear temperature distribution in the plane $z=constant$. Consequently, thermal stresses occur in the curved panel even if the temperature distribution through the depth is assumed to be linear.

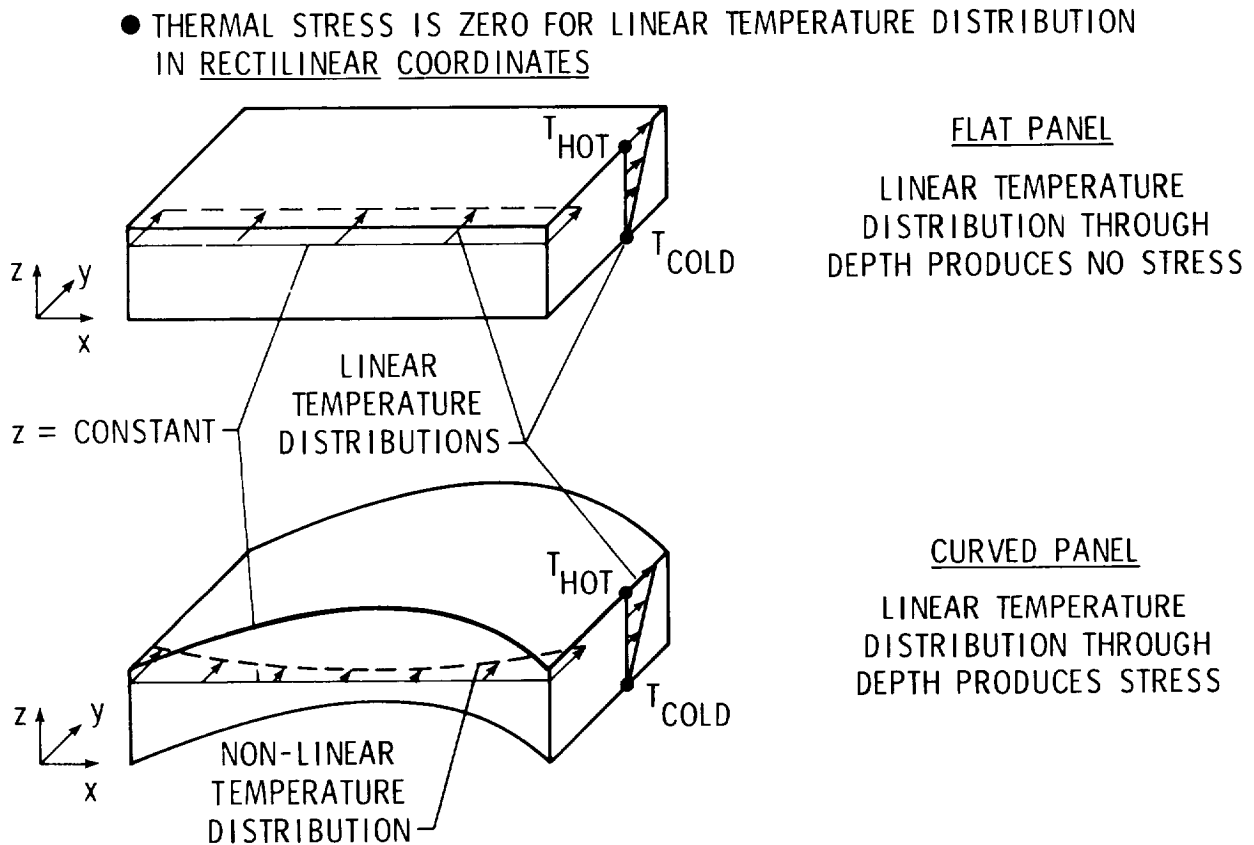


Figure 21

SPAR FINITE ELEMENT MODEL OF SA/H/C TPS

The SPAR finite element structural analysis computer program (ref. 13) was used to study thermal stress in a curved TPS panel. The thickness of the panel was 2.35 inches, and the radius of curvature was 12 inches. The nominal size of the panel analyzed was 12 inches long and 9.42 inches wide (measured in the direction of curvature). By using planes of symmetry, only 1/4 of a panel needed to be modeled. As shown in figure 22, the outer superalloy honeycomb sandwich (0.280 inches thick) and inner titanium honeycomb sandwich (0.170 inches thick) were modeled using membrane elements for the face sheets and solid elements for the cores. The Inconel 617 side closures were modeled using rod elements and shear elements. The model had 745 elements and 520 nodes. The model was unconstrained from deformations except for rigid body displacements and rotations.

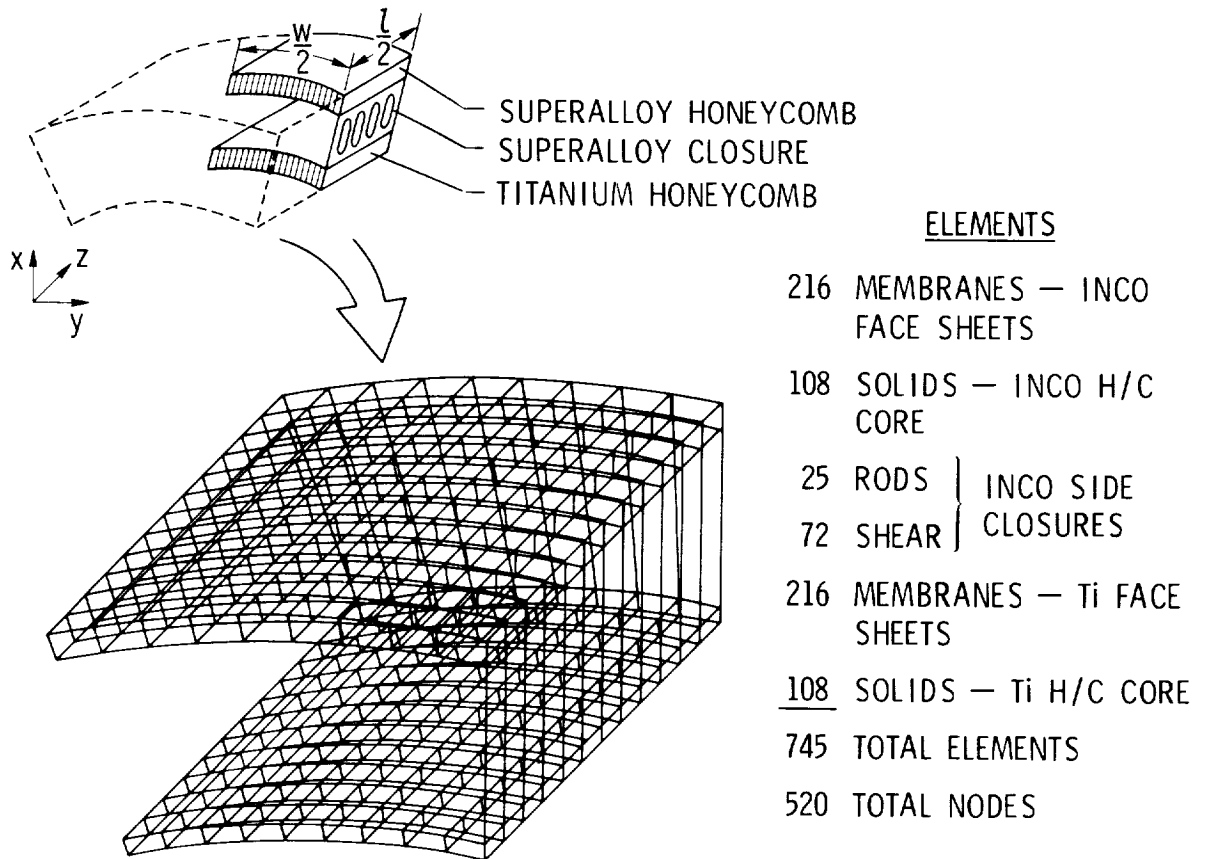


Figure 22

TEMPERATURES FOR FINITE ELEMENT ANALYSIS

The surface temperature history associated with Space Shuttle trajectory 14414.1C at body point 1300 (ref. 3) was used as a typical design condition to calculate temperatures for the finite element thermal stress analysis. The panel cross section in figure 23 shows the Inconel 617 honeycomb, the titanium honeycomb, two types of fibrous insulation contained within the panel, and the aluminum plate which is sized to represent the thermal mass of Shuttle structure at body point 1300. The symbols on the sketch to the right of the cross section identify 5 of the 18 locations used in a one-dimensional thermal analysis modified to account for the side closures. Two of the symbols represent temperatures of the Inconel face sheets; two of the symbols represent temperatures of the titanium face sheets; and one symbol represents the temperature of the aluminum plate. The analysis of reference 3 used the MITAS finite difference computer program.

The maximum temperature difference through the thickness of the panel occurs at about 500 seconds when the surface temperature reaches 1900° F. The inner superalloy face sheet is at 1875° F, and the titanium face sheets are both at about 200° F. These face sheet temperatures were applied at the appropriate nodes of the finite element model. The temperature distribution was assumed to be uniform for each face sheet.

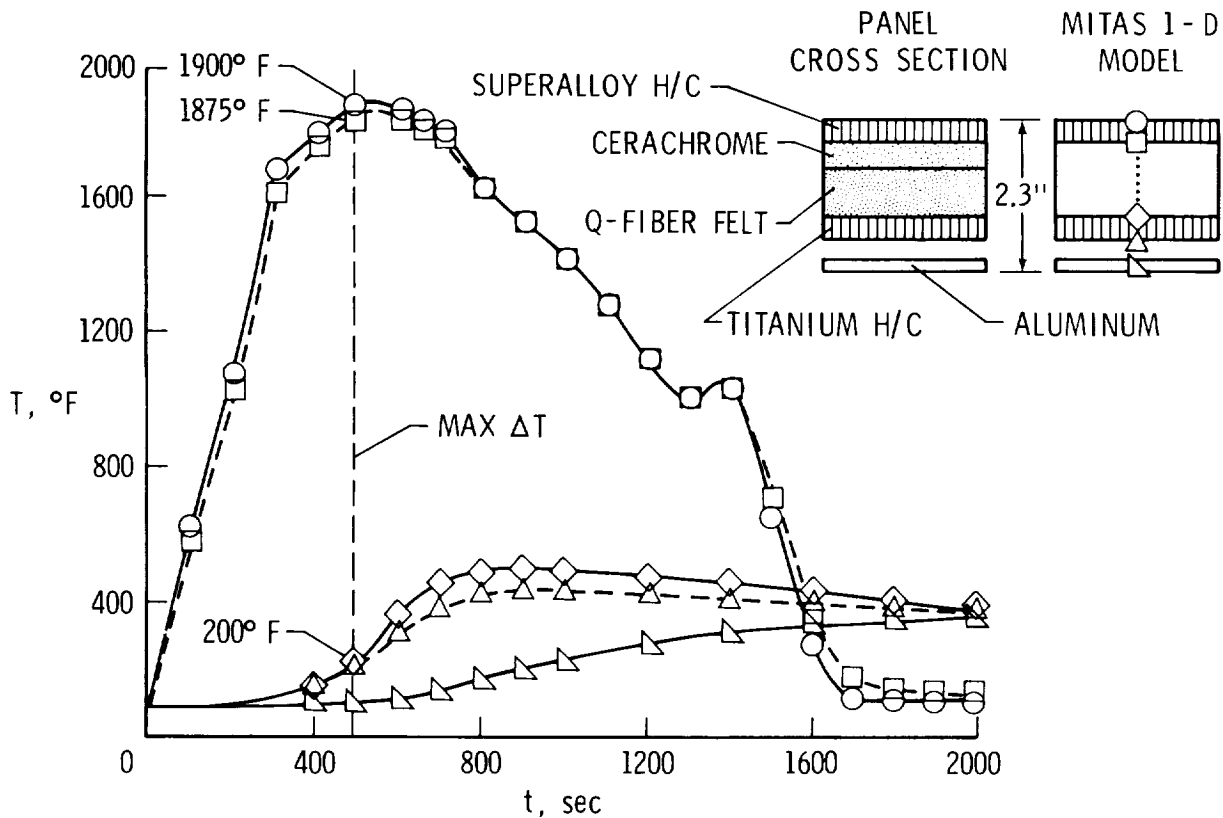


Figure 23

COMPRESSIVE STRESS IN INCONEL 617 HONEYCOMB INNER FACE SHEET

Thermal stresses for the curved panel were calculated using a linear elastic analysis (See fig. 22) with the temperatures described in figure 23 as the applied load. The highest compressive inplane stresses, indicated by the heavy line in the sketch shown in figure 24, were along the edge of the inner face sheet adjacent to the side closure. These stresses reached a maximum at the center of the side closure. The stresses are normalized by the yield stress for Inconel 617 at 1875° F determined for 0.005-inch-thick material which has experienced the braze cycle (ref. 3). The maximum stress calculated for a 12-inch-long panel is 2.3 times greater than the yield stress. Reducing the length of the panel by half while maintaining the 9.42-inch width lowered the maximum stress to a value slightly less than the yield stress. (Reducing the width of the panel by half while maintaining the 12-inch length only lowered the maximum stress to 1.7 times yield.)

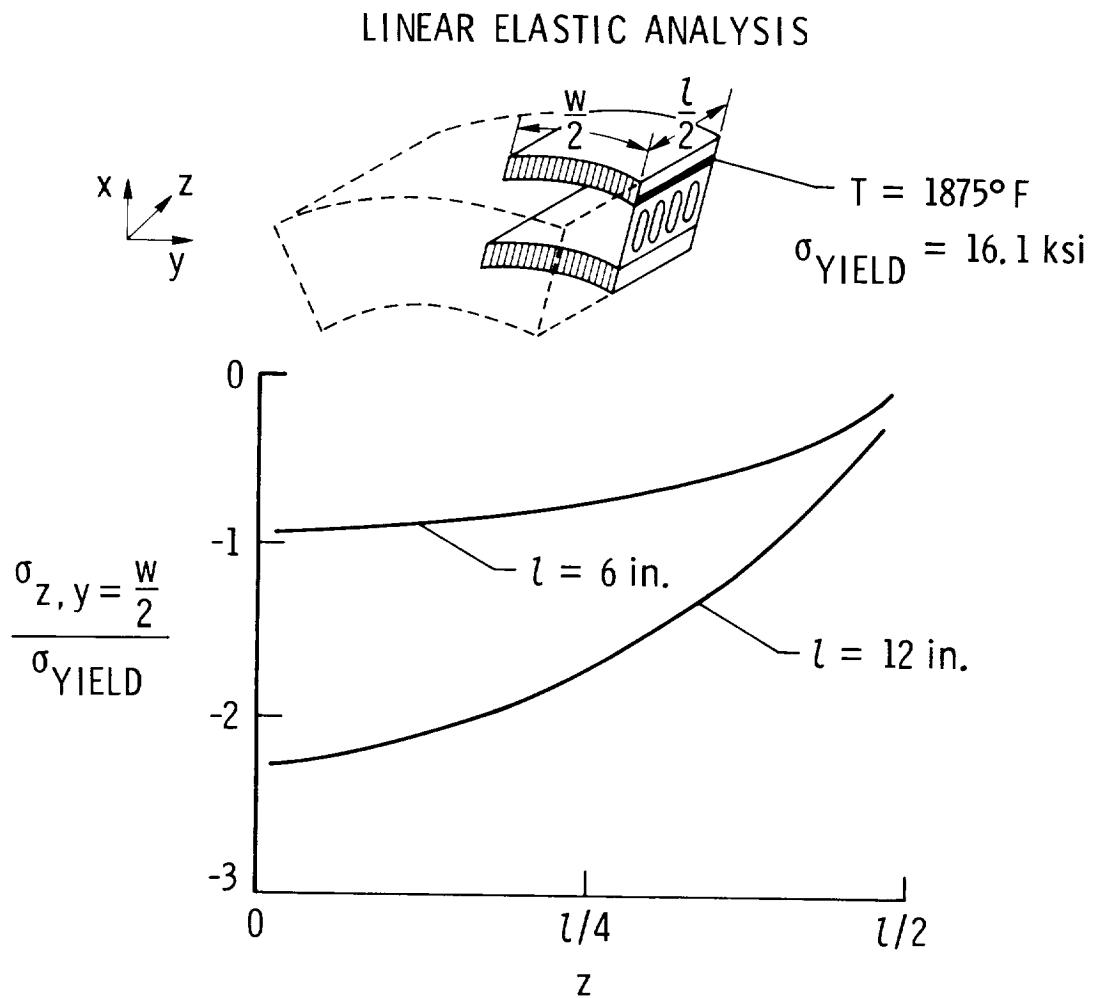


Figure 24

SHEAR STRESS IN INCONEL 617 HONEYCOMB INNER FACESHEET

Inplane shear stresses computed for the same location that was described in figure 24 are shown in figure 25. Shear stresses for the 12-inch-long, 9.42-inch-wide panel have maximum values of about 1.5 times yield stress, while stresses for a 6-inch-long panel were reduced to a value slightly less than yield. Therefore, both compressive stresses (fig. 24) and shear stresses were found to be more sensitive to a change in length than to a change in width. Thus, one way to control thermal stresses in curved TPS panels is to adjust the length of the panels.

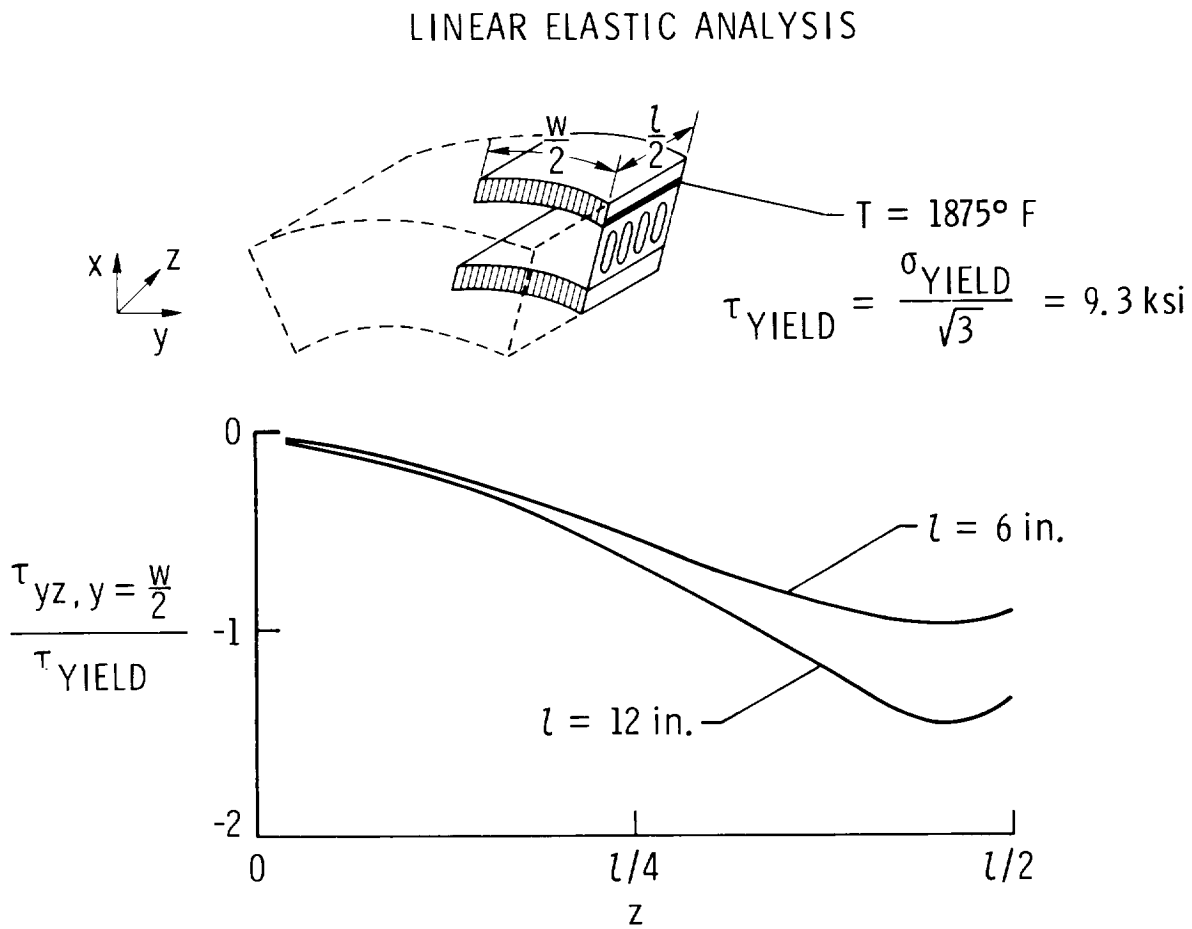


Figure 25

EFFECT OF NONLINEAR MATERIAL PROPERTIES ON THERMAL STRAIN

Even though the linear elastic analysis of a 12-inch-long panel indicated a maximum stress 2.3 times greater than yield stress, the strain associated with that stress (0.00282 in./in.) is less than the yield strain. Since thermal stress is induced by an applied strain (as opposed to an applied force), the strain calculated from a nonlinear analysis would be expected to also be about 0.00282 in./in.). As illustrated in figure 26, the stress and strain would be slightly less than yield conditions. Even if a full strain range of 0.00282 in./in. is assumed, the fatigue life calculated from the equation on the right in the figure (method of universal slopes with a 10 percent rule, ref. 14) is 1800 cycles. This life is adequate for space transportation vehicles that experience only one thermal cycle per mission.

Thus, two methods exist to control thermal stress in curved TPS panels. First, the size can be reduced as discussed previously, and second, plastic deformation can be allowed to occur at least on the first cycle, after which the remaining cycle life may be adequate.

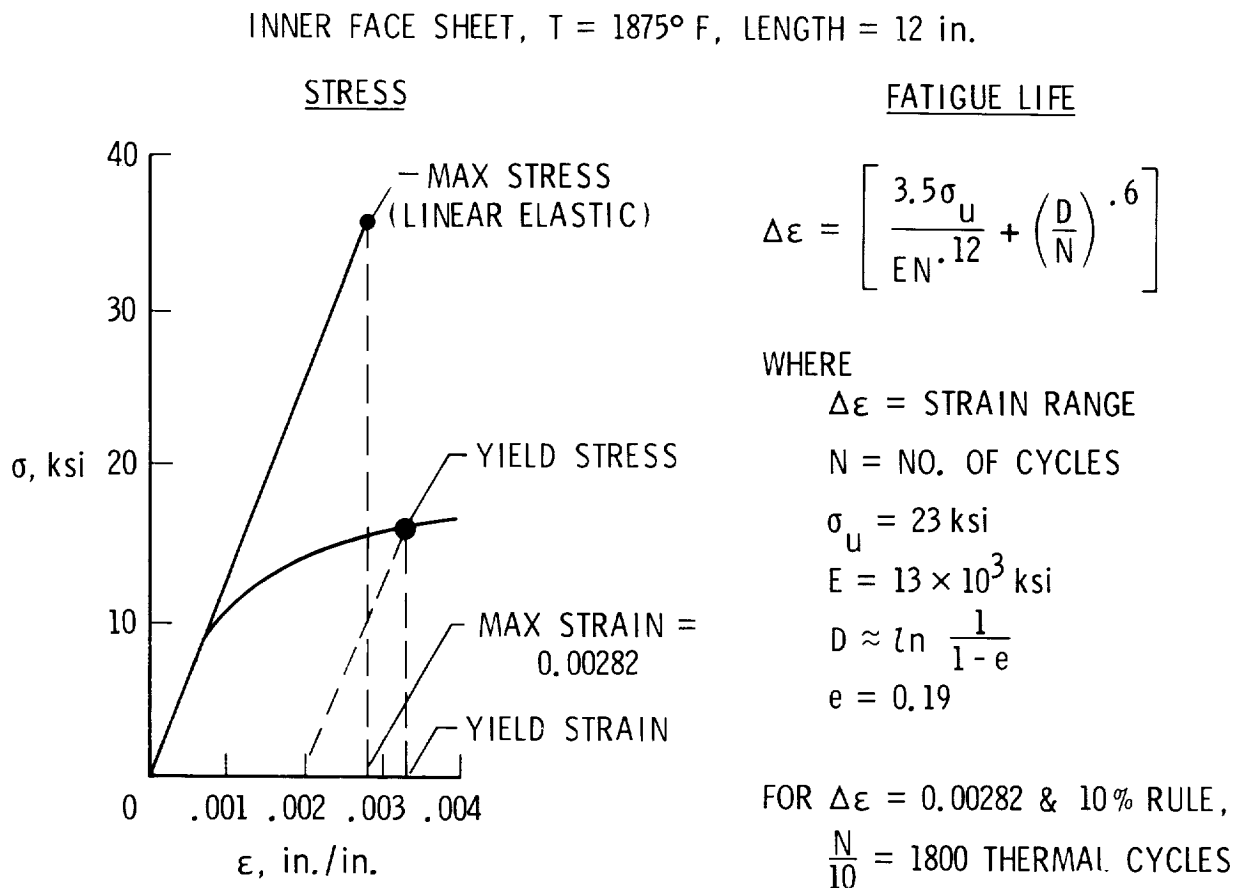


Figure 26

CURVED SUPERALLOY HONEYCOMB TPS PANELS

Even though much of the surface of Shuttle-type vehicles is flat or nearly flat, some locations, such as the chine areas, are necessarily curved. The fabrication of curved TPS panels often presents complexities not encountered in fabricating flat panels. A curved titanium multiwall panel was fabricated to demonstrate that the multiwall concept will lend itself to curved panels. A single curved superalloy honeycomb panel (fig. 27) has been fabricated, instrumented with thermocouples and strain gages, and exposed to radiant heat to determine thermal stresses. Reliable measured thermal strains have not been obtained for this panel because the very thin material (0.005-in.-thick face sheets and 0.003-in.-thick beaded side closures) deforms in local bending under very low load. Consequently, evaluation of the structural behavior of the curved panel in these tests may be limited to deflection measurements and post-test inspection.

The design of curved panels must include not only factors contributing to thermal stress but must also consider the effects of large surface pressure gradients that are normally less important in the design of flat TPS. An array of curved superalloy panels has been fabricated for aerothermal tests to evaluate their performance in a high-surface-pressure-gradient environment. The curved 20-panel array shown in figure 27 was installed into the cavity of the Curved Surface Test Apparatus (CSTA), so that the surface of the array was flush with the surface of the CSTA. The array was instrumented with thermocouples and pressure sensors and tested in the LaRC 8' High Temperature Tunnel to determine if heating would occur in the gaps between panels. Metal tabs, one of which is identified on the single panel in the figure, were located at the corner intersections of the panels to block flow in the gaps. All of the panels were attached with through-panel fasteners.

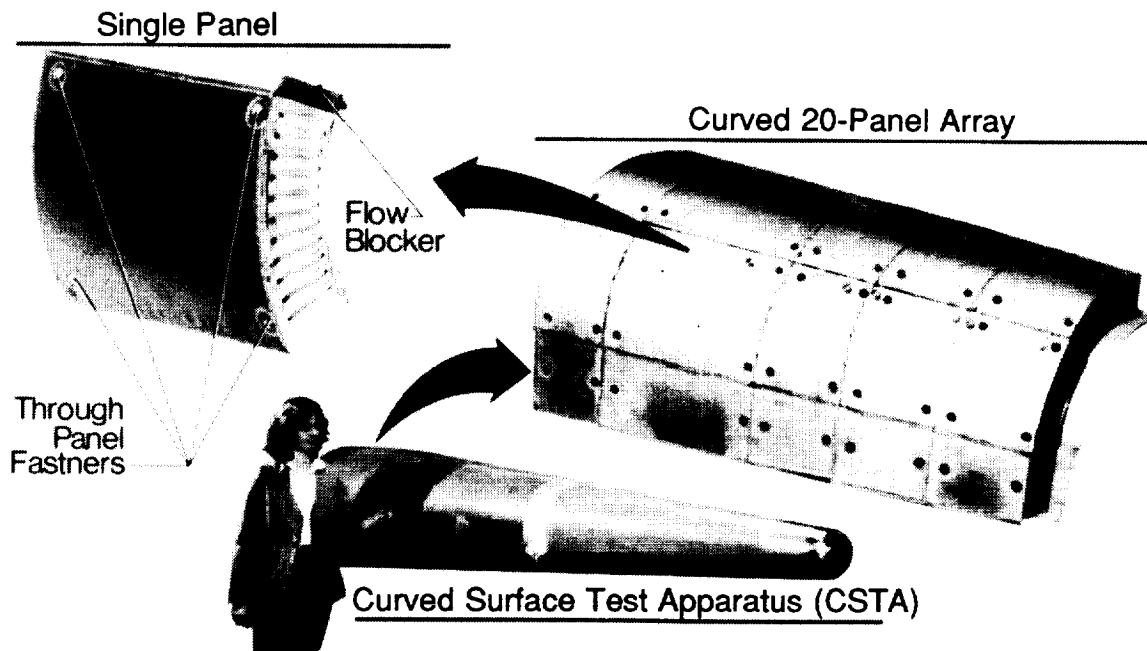


Figure 27

AEROTHERMAL TEST OF CURVED SUPERALLOY HONEYCOMB PREPACKAGED TPS

After the windward panels of the curved array were preheated with quartz lamps to a surface temperature of 2000° F, the array was exposed for 34 seconds to the most severe conditions that are within the normal operating range of the 8' High Temperature Tunnel. The tunnel dynamic pressure was approximately 1400 psf, and the pressure gradient along the curved surface of the array was approximately 2 psi per foot. The view on the left of figure 28 shows the array when it first reached the center of the hypersonic stream. Although the surface of the panels had cooled during the time the quartz lamps were turned off and the model was being inserted, the fastener plugs, which have high thermal mass compared to the panel face sheets, are still glowing. The view on the right of the figure shows the array after exposure to the flow for 34 seconds. The maximum surface temperature on the windward panels was approximately 1800° F. Post-test examination of the array revealed that panels near the aft seal of the cavity into which the panels were installed were damaged and that the seal had failed. Failure of the cavity seal allowed the hot gas at the surface of the panels to flow directly through the gaps between panels and through the seal to the base of the model. Consequently, no definitive conclusions can be made from these test results regarding gap heating.

The damaged panels in the array have been repaired, and the aft seal of the cavity, which was a sliding seal, has been replaced with a more positive, bellows-type seal. The array is currently available to be tested in the 8' High Temperature Tunnel.

Surface Pressure Gradient = 2 psi/ft

Dynamic Pressure = 1400 psf

MACH No. = 7

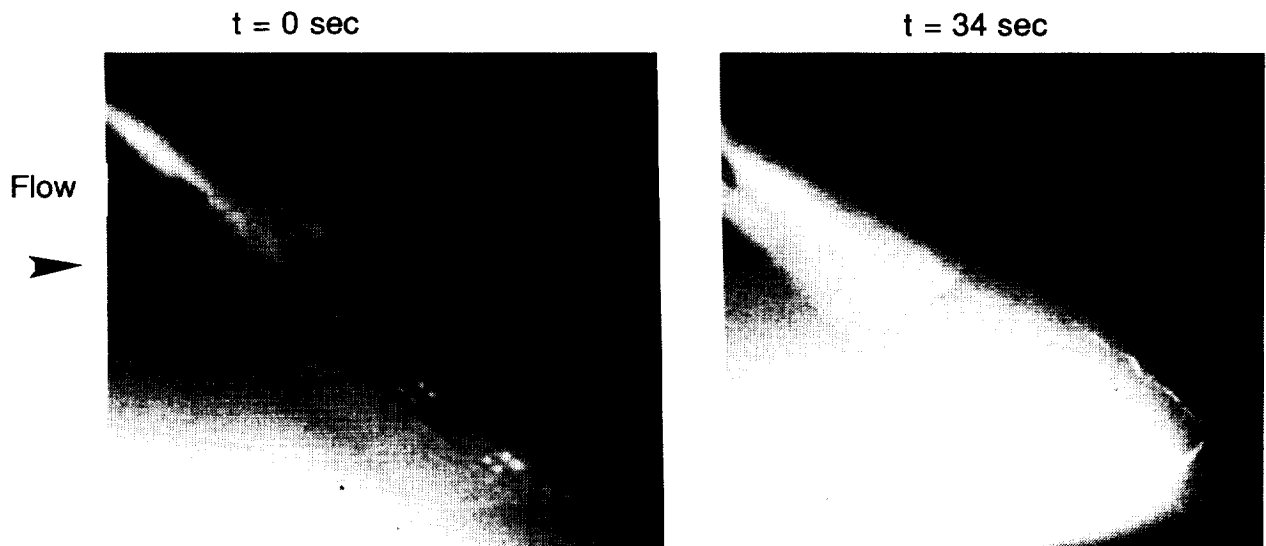


Figure 28

ORIGINAL PAGE
BLACK AND WHITE PHOTOGRAPH

ACC MULTIPOST TPS TEST ARTICLE

The same 1 ft. by 2 ft. ACC test model that was subjected to the thermal vacuum tests (fig. 7) was also subjected to aerothermal tests. The model, shown in figure 29, was instrumented with thermocouples through the thickness directly beneath the center portion where four panel corners intersect.

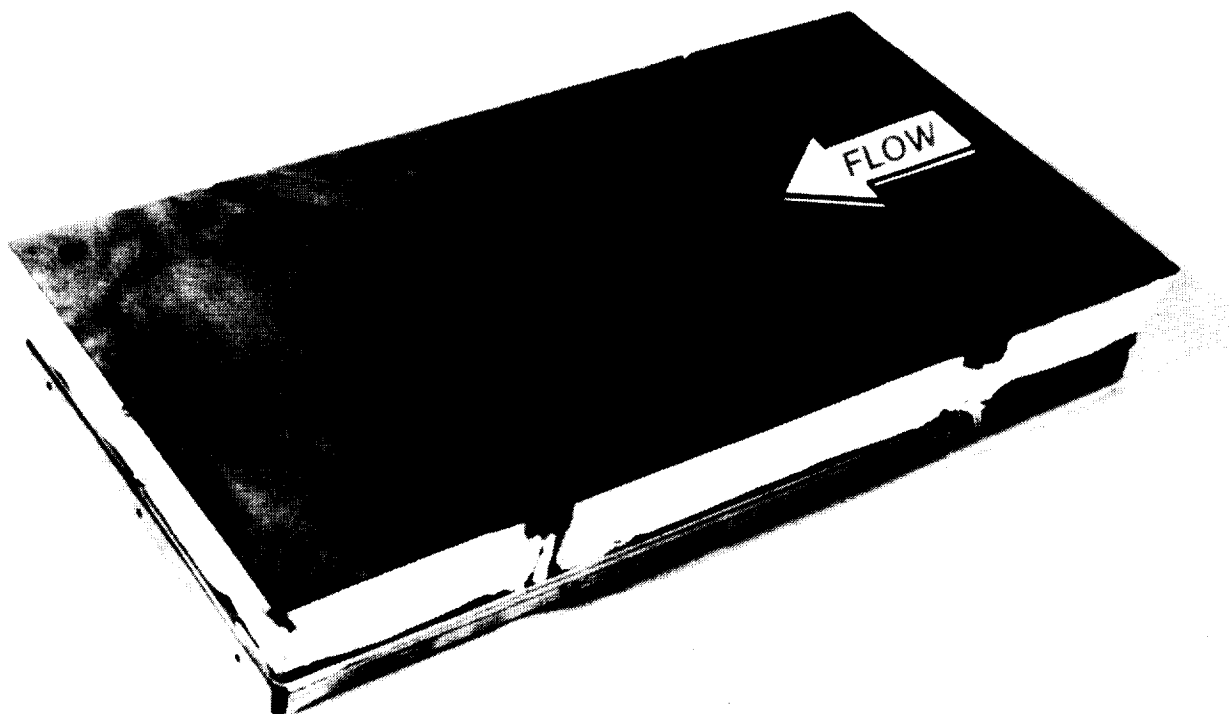


Figure 29

ORIGINAL PAGE
BLACK AND WHITE PHOTOGRAPH

ACC MULTIPOST TPS IN ARC-TUNNEL

The ACC test model is shown in figure 30 installed in the LaRC 20-MW Aerothermal Arc Tunnel. The model was mounted in a water-cooled holder at 15° angle of attack to the air stream with a 6-inch transition section between the nozzle and the model. Conditions were selected which gave a 2300° F surface temperature on the front of the model. Figure 6 (e) shows the model in the test stream. Only the light being radiated from the model was used to expose the film.



Figure 30

EFFECT OF AEROTHERMAL EXPOSURE ON GAP TEMPERATURE ACC MULTIPOST

A comparison of temperatures obtained during the arc-tunnel tests with those obtained during a thermal/vacuum test is shown in figure 31. The temperatures shown were measured at the center of the model where pieces of 4 separate panels intersect. Thermocouples placed at locations 1, 2, and 3 of the lower right-hand sketch measured the temperature at the ACC skin, at 1/3 of the depth of the model, and at the bottom of the model, respectively. The tunnel condition resulted in a surface temperature (location 1) nearly 100° F less than that obtained during the thermal/vacuum test. However, the temperature measured at location 2 during the arc-tunnel test was not less than that obtained during the thermal vacuum test, indicating that slight heating due to flow occurred in the gap region where one panel overlaps another. The lower temperature measured near the aluminum plate (location 3) during the tunnel test was encountered at other locations and probably reflects a larger heat-sink effect caused by a water-cooled holder which was not used in the thermal/vacuum tests. These results suggest modifications to the concept to reduce the local heating at the ACC panel intersections that include not only staggering the insulation packages so that they do not coincide with the panel intersections but also eliminating the vertical flanges that conduct heat into the insulation.

The ACC panel was not damaged by either the thermal/vacuum or arc-tunnel tests. The only change in appearance occurred during the arc-tunnel tests when erosion of copper electrodes caused an orange-colored copper deposit on part of the panel surface (fig. 30).

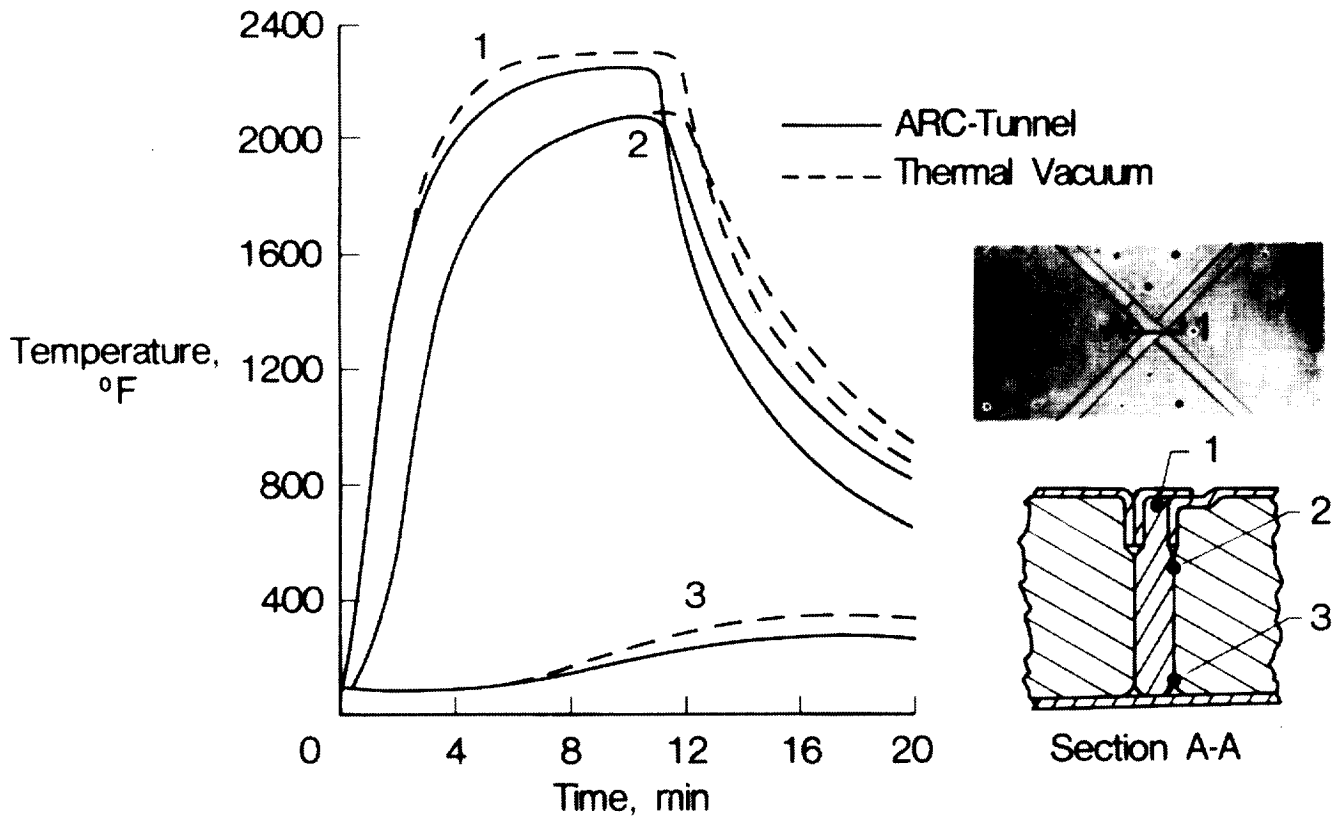


Figure 31

SUMMARY

The results from a variety of verification tests, including thermal, aerothermal, vibration, acoustic, lightning strike, and environmental exposure, indicate that the three TPS concepts (titanium multiwall, superalloy honeycomb prepackaged, and ACC multipost) are viable over a temperature range from 700° F to a temperature greater than 2300° F. However, the application of these concepts to specific vehicles will require additional verification tests dedicated to specific mission requirements.

- **Results from verification tests indicate TPS concepts are weight competitive and are adequate for generic entry environments**
 - **Thermal**
 - **Aerothermal**
 - **Vibration**
 - **Acoustic**
 - **Lightning strike**
 - **Environmental exposure**

- **Application to specific vehicles will require additional verification tests dedicated to specific mission requirements**

Figure 32

REFERENCES

1. Bohon, Herman L.; Shideler, John L.; and Rummmler, Donald R.: Radiative Metallic Thermal Protection Systems: A Status Report. *Journal of Spacecraft and Rockets*, Vol. 14, No. 10, pp. 626-631, October 1977.
2. Blair, W.; Meany, J.E.; and Rosenthal, H.A.: Re-Design and Fabrication of Titanium Multiwall Thermal Protection System (TPS) Test Panels. NASA CR-172247, 1984.
3. Blair, W.; Meany, J.E.; and Rosenthal, H.A.: Fabrication of Prepackaged Superalloy Honeycomb Thermal Protection System (TPS) Panels. NASA CR-3755, 1985.
4. While, D.M.: ACC Cover Panel Feasibility Study. In *Development of Advanced Carbon-Carbon (ACC) Composites*, Vol. II. NASA CR-165842-2, July 1982.
5. Matza, E.C.; and While, D.M.: Advanced Carbon-Carbon (ACC) Test Article Design and Fabrication. Vought Corp. Report 221RPTA018, May 1983.
6. Pittman, Claud M.; and Brinkley, Kay L.: One-Dimensional Numerical Analysis of the Transient Thermal Response of Multilayer Insulation Systems. NASA TMX 3370, April 1976.
7. Anon.: Lightning Test Waveforms and Techniques for Aerospace Vehicles and Hardware. Report of SAE Committee AE4L, June 20, 1978.
8. Avery, D.E.; Shideler, J.L.; and Stuckey, R.N.: Thermal and Aerothermal Performance of a Titanium Multiwall Thermal Protection System. NASA TP 1961, December 1981.
9. Pittman, C.M.; Brown, R.D.; and Shideler, J.L.: Evaluation of a Non-Catalytic Coating for Metallic TPS. NASA TM 85745, January 1984.
10. Olsen, G.C.; and Smith, R.E.: Analysis of Aerothermal Loads on Spherical Dome Protuberances. AIAA Paper 83-1557, June 1983.
11. Greaves, J.C.; and Linnett, J.W.: "Recombination of Atoms at Surfaces", Part 5: Oxygen Atoms at Oxide Surfaces. *Transactions of the Faraday Society*, Volume 55, 1959, p. 1346.
12. Boley, B.A.; and Weiner, J.H.: *Theory of Thermal Stress*. John Wiley and Sons, New York, 1960.
13. Anon.: SPAR Structural Analysis System Reference Manual, Volume 1. NASA CR-158970-1, December 1978.
14. Manson, S.S.: A Simple Procedure for Estimating High-Temperature Low-Cycle Fatigue. *Experimental Mechanics*, August 1968.

RECENT ADVANCES IN CARBON-CARBON SUBSTRATE TECHNOLOGY AT
NASA LANGLEY RESEARCH CENTER

Philip O. Ransone,
NASA Langley Research Center
Hampton, Virginia

Y. Robert Yamaki
Lockheed Engineering and Sciences Company
Hampton, Virginia

Howard G. Maahs
NASA Langley Research Center
Hampton, Virginia

INTRODUCTION

Figure 1 shows a comparison of specific strengths of candidate high-temperature materials as a function of temperature. From this figure, it is apparent why there is an interest in carbon-carbon composites for applications as strong, light-weight TPS, or as hot structure, for applications above 2500°F. The lower bound of the the carbon-carbon band is representative of the tensile strength of cross-ply Advanced Carbon-Carbon (ACC). The upper bound represents capabilities of various experimental carbon-carbon composites. Thin carbon-carbon composites, such as would be used as TPS panels or hot aero-structure, are usually constructed of layups of 2-D fabrics of carbon-fiber yarns (tows). Although the in-plane strengths of these composites can be very attractive, a major problem area is low interlaminar strength. The low interlaminar strength is the result of a relatively weak carbon matrix and poor interaction between the fibers and matrix. The purpose of the present paper is to discuss strategies being employed to improve the interlaminar strengths of the materials at the upper bound of the carbon-carbon band, and to present some recent encouraging results. The emphasis of these strategies is to improve interlaminar shear and tensile strengths while maintaining, or even improving, the inplane properties.

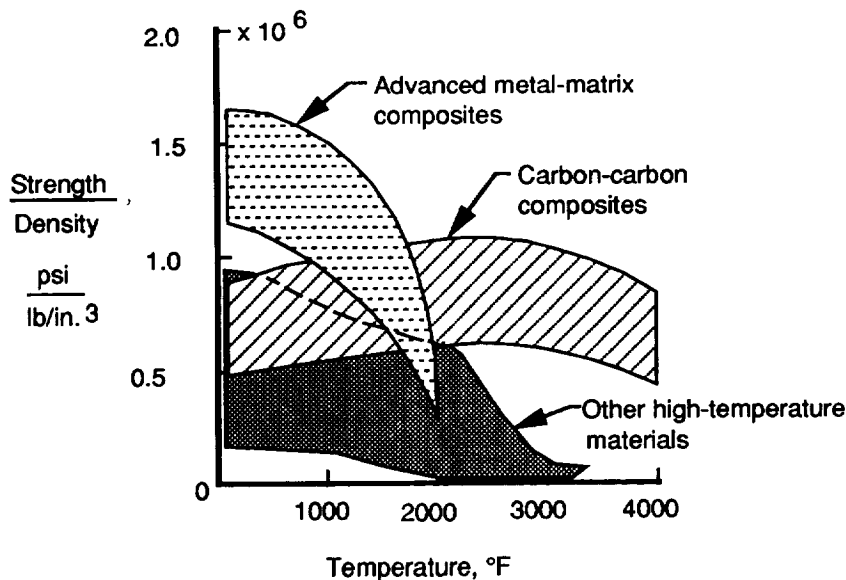


Figure 1. Specific strength versus temperature for candidate high-temperature materials

BASELINE ACC MECHANICAL PROPERTIES AND GOALS FOR IMPROVEMENT

In the 1978 to 1982 timeframe, NASA Langley sponsored the development of Advanced Carbon-Carbon (ACC) by LTV Corporation, with a major goal of obtaining a 25 percent increase in strength over that of Reinforced Carbon-Carbon (RCC), the material used on the wing-leading-edges and nose-cap of the Space Shuttle (ref. 1). Significant improvements in in-plane mechanical properties were realized with ACC, but its interlaminar strengths were actually lower than those of RCC. Even today, however, ACC largely remains the baseline to which new experimental materials are compared, and it is thusly used in this presentation. From 1982 to the present, investigators have endeavored to improve the interlaminar strengths of 2-D carbon-carbon composites over those of ACC, but improvements have not come without giving up some in-plane strength and/or stiffness (refs. 2,3). Conversely, attempts to improve in-plane properties over those of ACC have, at best, resulted in no improvement in interlaminar strengths and have usually resulted in a loss (ref. 3). Clearly, it is desirable to improve both the interlaminar and in-plane properties simultaneously. Figure 2 shows the mechanical properties of the baseline ACC-4 (the numeral 4 suffixed to ACC implies 4 densification steps after initial carbonization). The potential for improvements in 2-D carbon-carbon properties, which are believed by the authors to be achievable, are also indicated. The reference ACC property data are for 7- and 9-ply ACC-4 cross-ply panels fabricated by LTV Corporation as contract deliverables for reference 1.

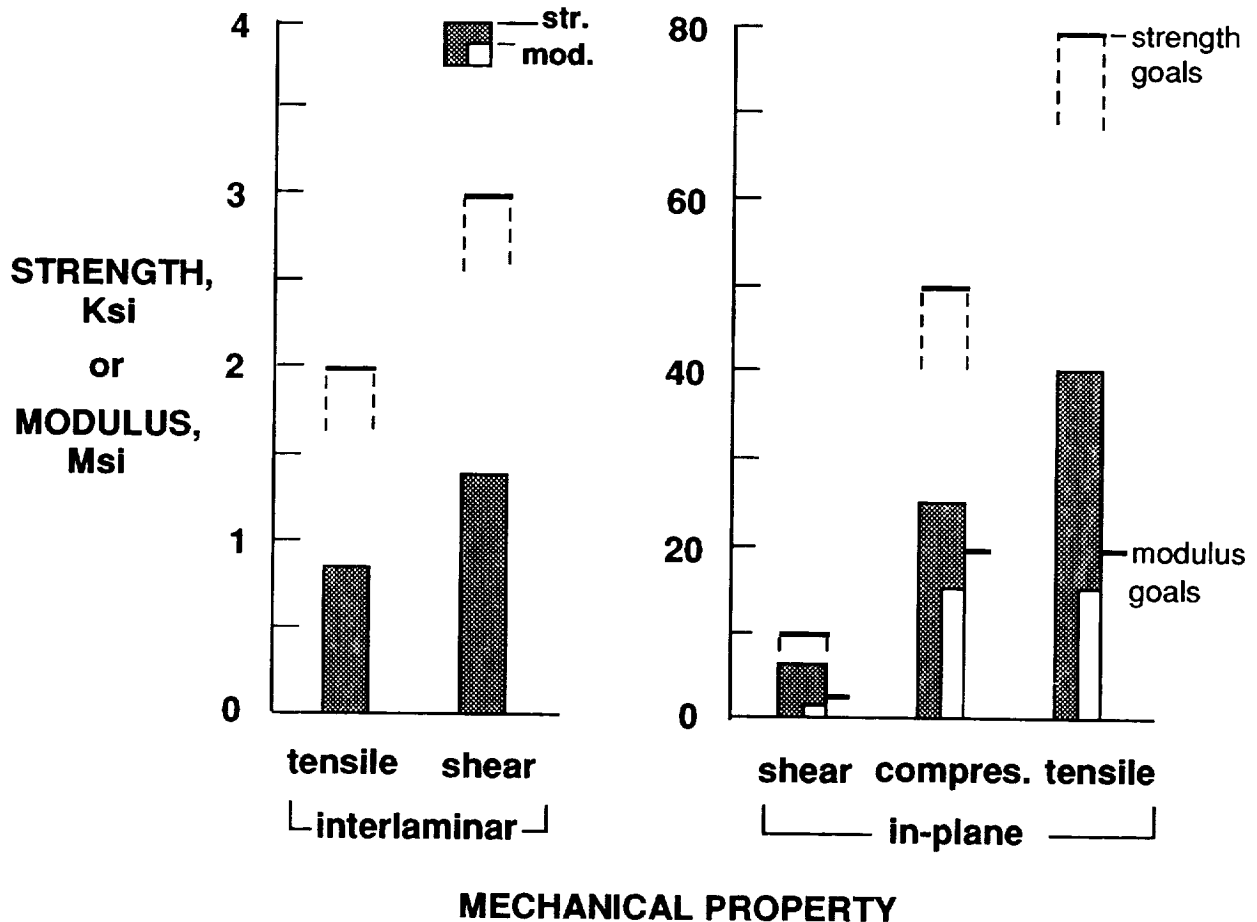


Figure 2. Baseline ACC mechanical properties and potential for improvement in 2-D carbon-carbon.

FACTORS CONTROLLING INTERLAMINAR STRENGTH IN 2-D CARBON-CARBON SUBSTRATES

The interlaminar strength of a 2-D reinforced carbon-carbon depends on many factors as listed in figure 3. The first factor, mechanical interaction of plies, has been the basis for many approaches to improving interlaminar strength in 2-D substrates. These approaches have generally involved the use of reinforcing fabrics having "rough" surfaces for the purpose of increasing fabric surface-area (for increased ply-to-ply contact) or for promoting nesting of tows or entanglement of fibers between adjacent plies. Examples of the use of such approaches can be found in references 2 and 3. The problem with these approaches, however, is that they are counterproductive to improving or even maintaining the in-plane strengths because tow strength is sacrificed. Factor 2, constituent properties, has been an area of investigation and reference 4 is an example of published results related to this area. Factor 3, fiber/matrix interaction, can have a significant influence on in-plane properties as well as interlaminar properties. Although the interlaminar strength can be significantly increased with increased surface chemical activity of the fiber, the in-plane tensile strength can be greatly diminished at appreciably lower levels of surface activity than required for maximum interlaminar strength. This research area is addressed in references 5-7. The inherent propensity for fiber-surface chemical activity may be dependent, to a large degree, on the fiber's surface microstructure (types of fiber microstructure and their effects on carbon-carbon composites are treated in ref. 8). The fiber's actual surface activity is dependent on the proprietary surface treatments given to the fiber and the post-surface-treatment thermal history of the fiber. The shape of the fiber and degree of crenulation of the surface may also affect mechanical interactions between the fibers and matrix. A discussion of the interaction of all these factors and their effects on mechanical properties of 2-D carbon-carbon can be found in reference 9.

- **MECHANICAL INTERACTION OF PLYS**
 - **DEGREE OF PLY-TO-PLY CONTACT**
 - **NESTING OF SURFACE RELIEF IN ADJACENT PLYS**
 - **ENTANGLEMENT OF FIBERS FROM ADJACENT PLYS**

- **CONSTITUENT PROPERTIES**
 - **MATRIX STRENGTH**
 - **FIBER VOLUME FRACTION**

- **FIBER / MATRIX INTERACTION**
 - **CHEMICAL**
 - **MECHANICAL**

Figure 3. Factors controlling interlaminar strength in 2-D carbon-carbon substrates.

STRATEGY FOR DEVELOPMENT OF HIGHER STRENGTH, THIN CARBON-CARBON SUBSTRATES

The NASA Langley strategy addresses the many factors listed in figure 4. The 8 harness-satin weave construction, which is used in the baseline ACC, is retained to minimize the frequency of fiber crimping. High frequencies of crimping are not conducive to good in-plane strength. Only continuous-filament tows are considered for the highest possible translation of fiber strength to the composite. A different approach to increasing mechanical contact between plies is being used in lieu of some approaches involving high-relief or "fuzzy" fabrics (refs. 2,3). It is reasoned that reductions in fabric thickness and tow size will increase the surface-to-volume ratio of the tows so that fiber-to-fiber contact across plies is increased. Also, the reduced fabric thickness reduces the crimp angle of the tows and should be beneficial to in-plane properties. Furthermore, the reduction of fabric thickness and/or tow size reduces the repeating unit dimensions in the composite, which should result in a redistribution and refinement of shrinkage damage that occurs during initial carbonization of the polymer matrix. This refinement and redistribution is expected to be beneficial to interlaminar strength. Combining these potential benefits with the selection of a fiber having the best mechanical properties, surface chemistry, and cross-section shape, and embedment of the optimum volume fraction of these fibers in the best-performing matrix should go a long way toward maximizing both the interlaminar and in-plane mechanical properties of the the 2-D composite. Through-the-thickness reinforcement is also being explored for applications where interlaminar strength requirements may exceed the potential of 2-D composite.

- **HARNNESS-SATIN WEAVES (AS OPPOSED TO PLAIN WEAVES)**
- **CONTINUOUS FILAMENT TOWS (AS OPPOSED TO STAPLE TOWS)**
- **REDUCED TOW SIZE / FABRIC THICKNESS**
- **FIBER TYPE**
- **FIBER SURFACE CHEMISTRY**
- **FIBER CROSS-SECTION SHAPE**
- **MATRIX**
 - **TYPE OF INITIAL MATRIX**
 - **TYPE OF DENSIFICATION MATRIX**
 - **VOLUME FRACTION**
- **THROUGH-THE-THICKNESS REINFORCEMENTS**
 - **WOVEN 3-D**
 - **STITCHED 2-D**

Figure 4. Strategy for development of higher strength, thin carbon-carbon substrates.

BENEFITS OF FINE-TOW, THIN FABRIC AND CVI DENSIFICATION ON MECHANICAL PROPERTIES OF 2-D CARBON-CARBON SUBSTRATE

A 2-D substrate was fabricated using a fine-tow, thin fabric constructed of T-300 fibers, the same fiber as used in ACC. The initial processing of the test material was similar to that used in fabrication of ACC, but densification was accomplished by CVI. The resulting composite was found to have 40 to 60 percent higher interlaminar strengths than for the ACC to which it is compared in figure 5. In-plane shear strength was improved by about 30 percent. The compressive and tensile strengths were improved by about 60 percent. Moduli are slightly lower than for ACC because the volume fraction of fibers in the fine-tow material was somewhat lower than that in ACC. The target volume fraction, although not as high as in ACC, was not achieved in this first attempt at making the fine-tow composite. It is anticipated that a fine-tow composite of the optimum volume fraction for CVI densification would have higher moduli without adversely affecting the strengths. It can also be seen from figure 5 that significant progress has been made toward achieving the program goals for strength improvement.

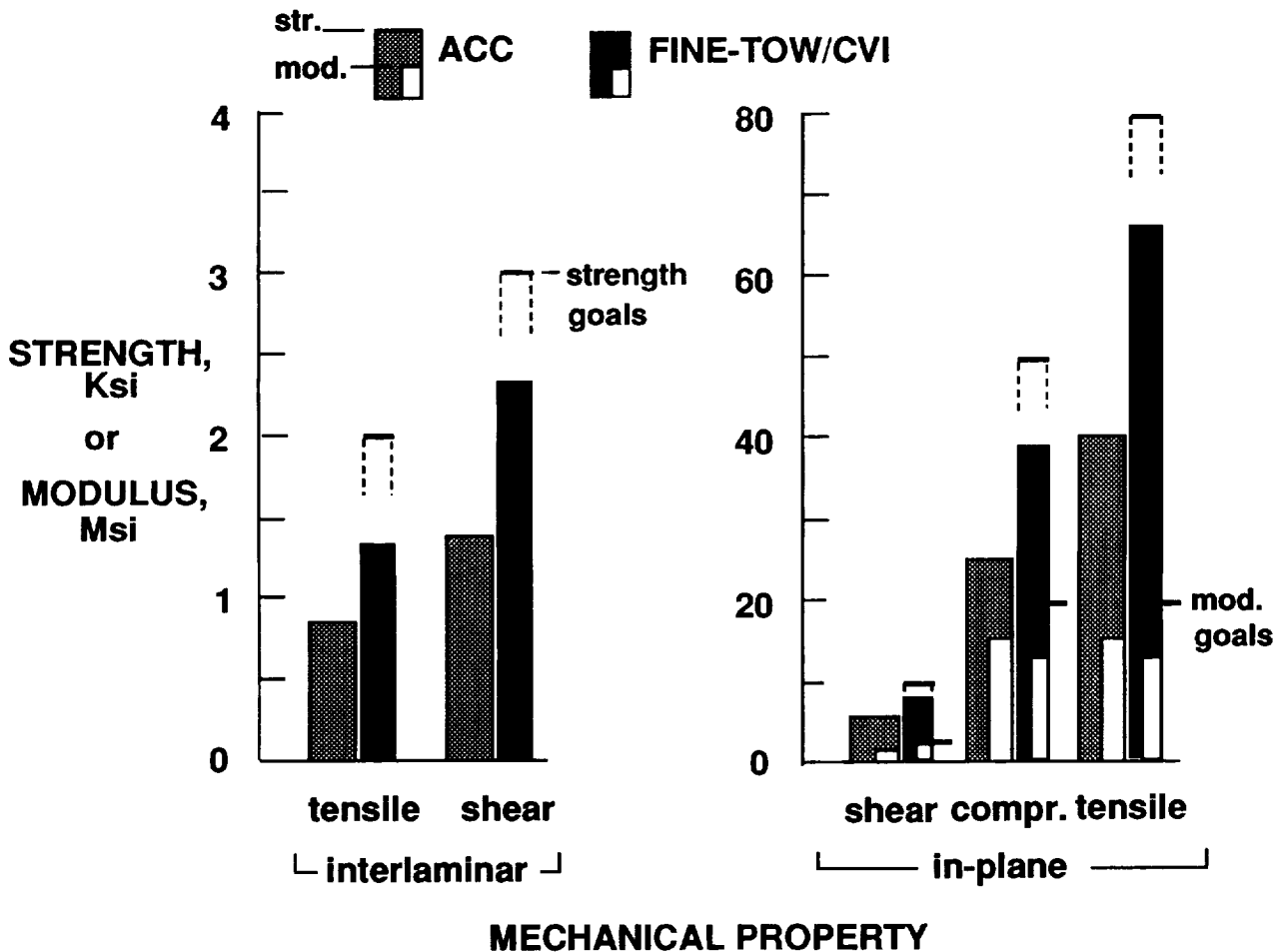


Figure 5. Benefits of fine-tow, thin fabric and CVI densification on mechanical properties of 2-D carbon-carbon substrate.

INFLUENCE OF FIBER SURFACE TREATMENT AND SIZING ON THE MECHANICAL PROPERTIES OF CARBON-CARBON COMPOSITES

The improvements in strength shown in figure 5 were obtained using T-300 fiber which had been heat-stabilized to a temperature above the expected use temperature of the carbon-carbon (C-C) composite. This temperature is high enough to remove the manufacturer's surface treatment (which is applied to the fiber to increase chemical bonding of the fiber and matrix in resin matrix composites). The influence of fiber surface treatment on fiber-matrix bonding in carbon-carbon composites has been investigated, and the results presented in the next several figures indicate the potential for this approach and also suggest limitations.

Since fiber surface treatment and fiber sizing can influence the nature of the interaction between the fibers and matrix, they can exert an important influence on the mechanical properties of the material. Investigations have been carried out to determine the importance and potential utility of these factors in determining the mechanical properties of phenolic-based C-C composites.

Fiber surface treatment studies have been conducted for a high strength (Hercules AS-4) and a high modulus (Hercules HM) fiber. The general relationships between the degree of fiber surface treatment and the resultant C-C mechanical properties have been consistent (refs. 5-7). Unidirectional composites have been used for experimental purposes, and the results obtained with Hercules HM fibers are typical. Figure 6 shows the interlaminar shear strengths obtained from C-C composites incorporating unsized HM fibers subjected by the manufacturer to different levels of surface treatment, here quantified by fiber surface oxygen concentration. It can be seen that the interlaminar shear strength can be controlled over a wide range, and the overall trend observed for all fibers investigated to date is for interlaminar tensile strength as well as interlaminar shear strength to increase with the degree of fiber surface treatment.

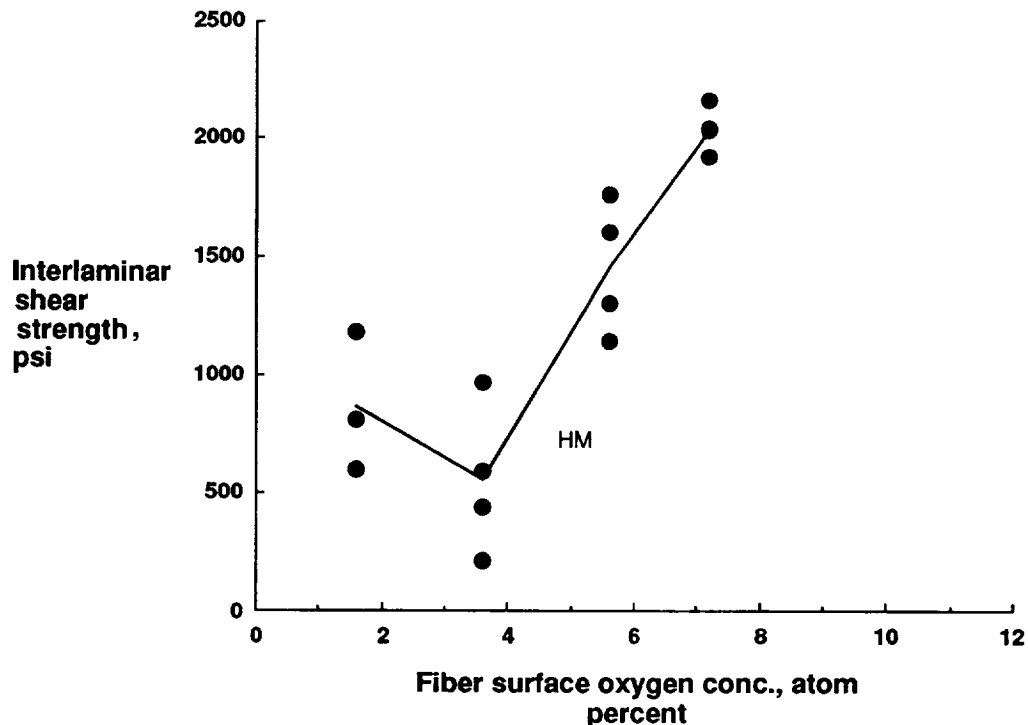


Figure 6. Relationship between interlaminar shear strength and fiber surface oxygen concentration for surface-treated Hercules HM fibers.

INFLUENCE OF FIBER SURFACE TREATMENT AND SIZING ON THE MECHANICAL PROPERTIES OF CARBON-CARBON COMPOSITES (CONT'D)

Different fiber surface treatment levels can produce differences in fiber-matrix interaction which are readily visible under magnification. Shown in figure 7 are scanning electron micrographs of polished sections of C-C composites incorporating HM fibers treated to 0, 50, and 150 percent of the commercial standard level. The corresponding fiber surface oxygen concentrations are 1.6, 3.6, and 7.2 atom percent, respectively. At the 0 percent treatment level, the undensified composite (top row) has numerous fiber-matrix gaps caused by matrix shrinkage during the initial pyrolysis. Note that as the fiber surface treatment level increases, the undensified composites exhibit relatively fewer gaps and also less distinct interfaces between the fibers and matrix. This difference is evident for both undensified and densified composites.

Top row: undensified
Bottom row: densified

Fiber surface treatment level:

0 Percent

**50
Percent**

**150
Percent**

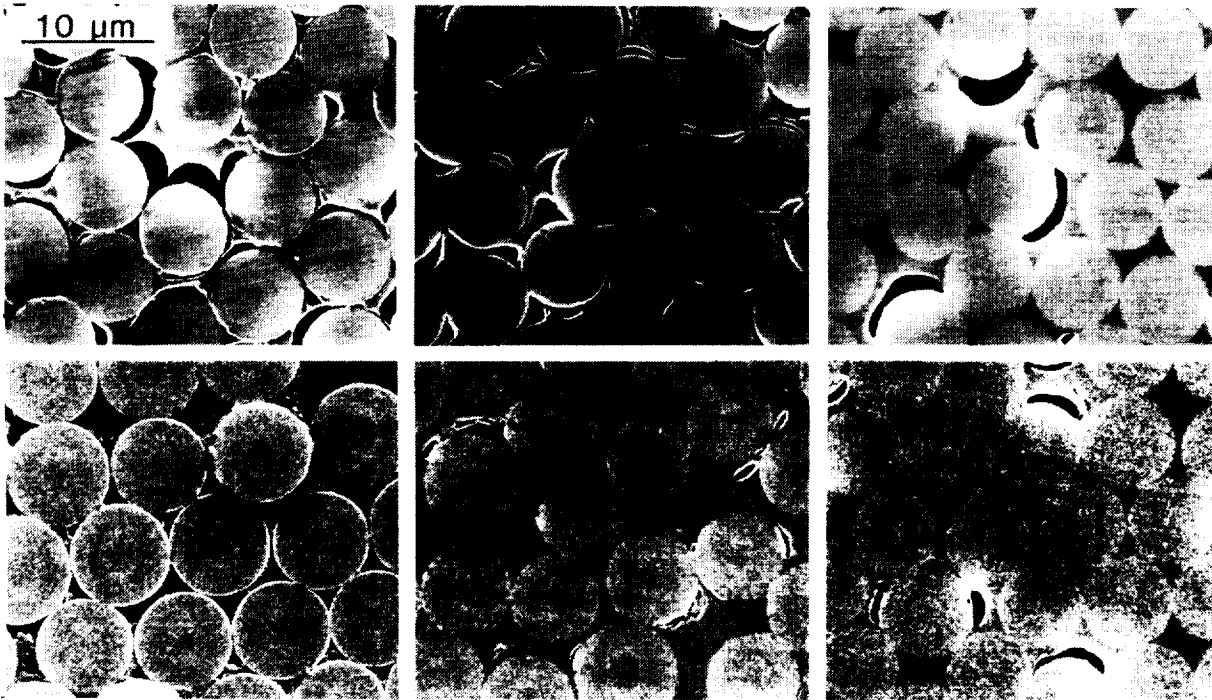


Figure 7. Fiber-matrix interactions in unidirectional composites with HM fibers treated to 0, 50, and 150 percent of standard treatment (fiber surface oxygen concentrations of 1.6, 3.6, and 7.2 atom percent, respectively).

INFLUENCE OF FIBER SURFACE TREATMENT AND SIZING ON THE MECHANICAL PROPERTIES OF CARBON-CARBON COMPOSITES (CONT'D)

Although increased C-C interlaminar strengths are desirable, the effect of increased fiber-matrix interaction on axial mechanical properties dictates that the degree of fiber surface treatment be chosen with some care. Figure 8 shows the axial tensile and compressive strengths for the unidirectional HM-fiber composites. For low to moderate fiber surface oxygen concentrations, composite tensile strength is little affected, but for high concentrations, a rapid decrease in strength occurs. On the other hand, compressive strength continually increases as the degree of fiber surface treatment is increased. Elastic modulus, in either tension or compression, is relatively unaffected by the degree of fiber surface treatment.

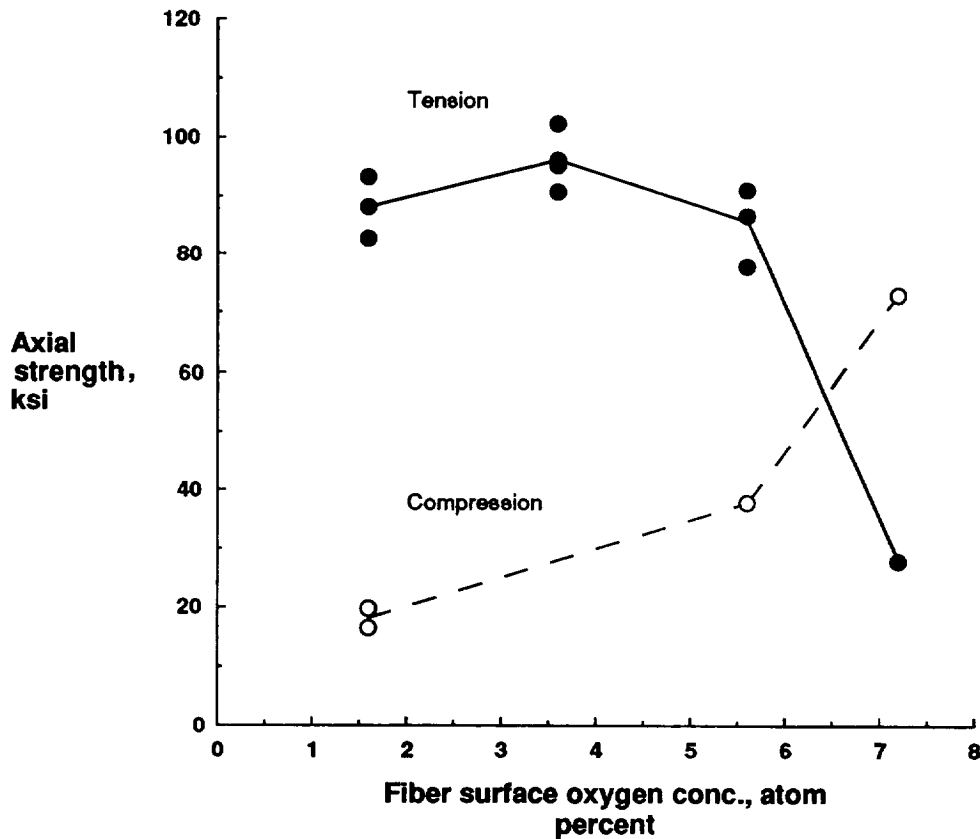
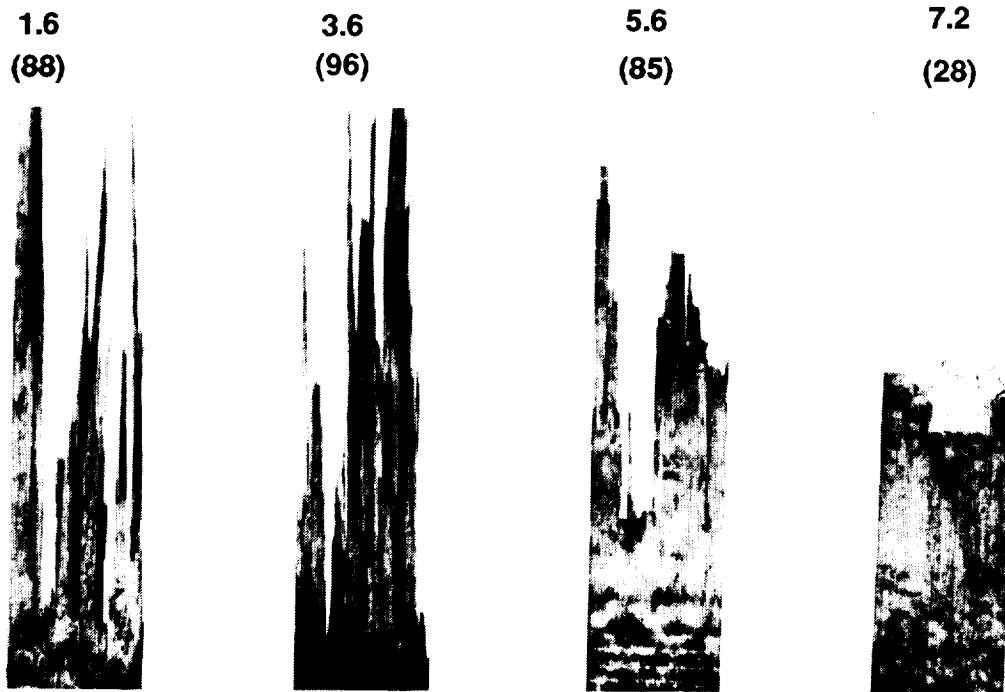


Figure 8. Relationship between axial tensile strength, compressive strength, and fiber surface oxygen concentration for surface treated Hercules HM fibers.

INFLUENCE OF FIBER SURFACE TREATMENT AND SIZING ON THE MECHANICAL PROPERTIES OF CARBON-CARBON COMPOSITES (CONT'D)

The influence of fiber surface treatment on the mechanical behavior of C-C composites is also apparent upon examining the tensile failure modes, as shown in figure 9. Note that as the fiber surface oxygen concentration increases, the decrease in tensile strength is accompanied by a change in failure mode from a fibrous one (with extensive fiber pull-out) to a brittle one (with little or no pull-out). Simultaneously, however, the interlaminar shear strength and compressive strength of the composite is increasing. This leads to the conclusion that, while a wide range of properties is possible by varying fiber surface treatment level, there is no one treatment level at which all mechanical properties are maximized, and some intermediate treatment levels are indicated when a balanced complement of properties is desired.

Fiber surface oxygen concentration, percent:
(Mean tensile strength, ksi)



Specimen width: 0.5 in.

Figure 9. Tensile failure modes of unidirectional C-C composites with surface treated Hercules HM fibers.

INFLUENCE OF FIBER SURFACE TREATMENT AND SIZING ON THE MECHANICAL PROPERTIES OF CARBON-CARBON COMPOSITES (CONT'D)

The most common form of reinforcement in structural C-C composites is woven fabric. In order to weave carbon fiber tow, some type of fiber sizing is generally required for handleability and durability, and this sizing, like fiber surface treatment, can influence fiber-matrix interaction. However, sizings for carbon fibers have been developed primarily for organic matrices, and these sizings are often intended for epoxy resins. Such resins have low char yields—on the order of ten percent, as opposed to phenolic resins with yields on the order of 60 percent.

Therefore, a study was conducted to determine whether it would be advantageous to employ a high-char sizing for the fabrication of C-C composites. Again, Hercules HM fiber was employed for the fabrication of unidirectional specimens, and four variants of this fiber were compared. The variants comprised combinations of surface-treated (HMS) and untreated (HMU) fibers with either phenolic resin (Ph) sizing or a Hercules epoxy-compatible (G) sizing. Figure 10 illustrates that, on a given fiber, the G sizing resulted in a higher interlaminar shear strength, and therefore greater fiber-matrix interaction, than the phenolic sizing; however, the presence or absence of fiber surface treatment (HMS vs. HMU) was a more influential factor in determining the interlaminar shear strength of the composites. The HMU-Ph composite possessed such a low level of fiber-matrix interaction that the composite delaminated during processing and was unusable for testing.

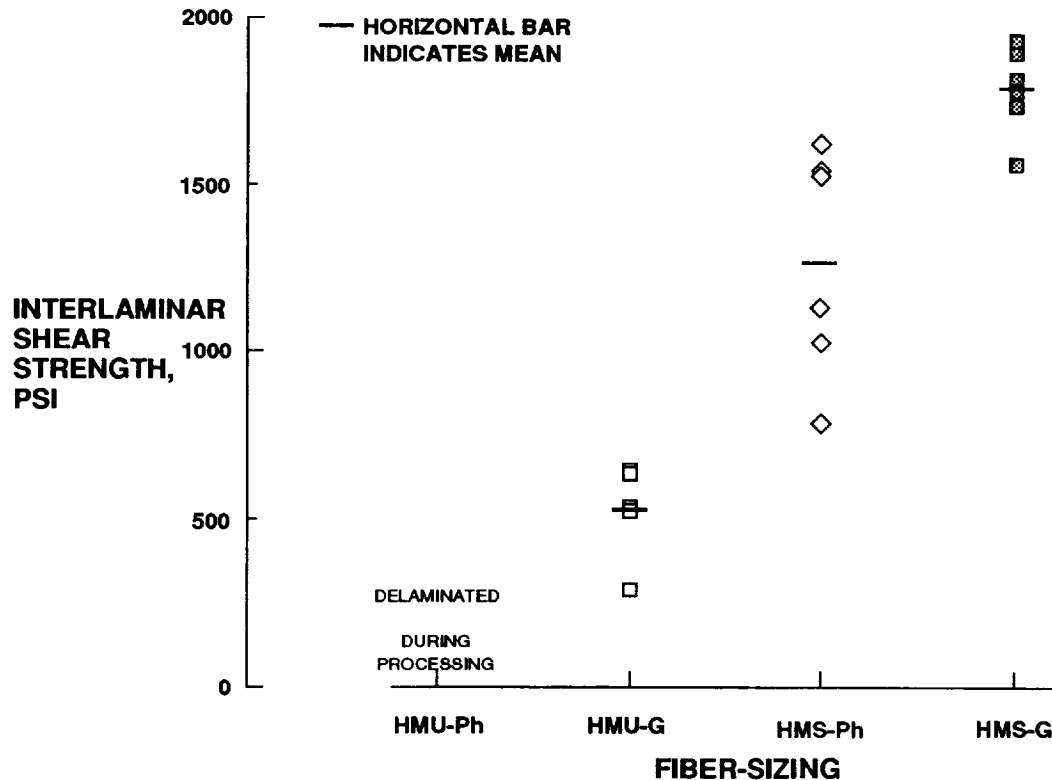


Figure 10. Interlaminar shear strengths for HMU-Ph, HMU-G, HMS-Ph, and HMS-G composites.

INFLUENCE OF FIBER SURFACE TREATMENT AND SIZING ON THE MECHANICAL PROPERTIES OF CARBON-CARBON COMPOSITES (CONT'D)

Figure 11 shows the compressive strengths for the same composites as in figure 10. It can be seen that the relative ranking of compressive strengths is the same as that for the interlaminar shear strength. This is not unexpected since, as mentioned previously, a higher degree of fiber-matrix interaction results in greater resistance not only to interlaminar fracture, but also to compressive fracture. While fiber surface treatment was found to be a more powerful influence on mechanical properties, another important conclusion of the investigation of sizing effects is that because the epoxy-compatible "G" sizing was not detrimental to performance, it is not considered necessary to employ specialty sizings for fabricating phenolic-based, fabric-reinforced C-C composites. However, this is not to say that the choice of sizing is inconsequential. Since the specific nature of sizing materials is generally held proprietary by each fiber manufacturer, there is no assurance that other sizings will perform similarly to the Hercules "G" sizing.

For fabrics woven from surface-treated fibers, the influences of both fiber surface treatment and sizing on mechanical properties need to be taken into account. Any attempt to "de-size" surface-treated, woven fabric will probably not be totally complete, and may well affect the underlying fiber surface treatment also.

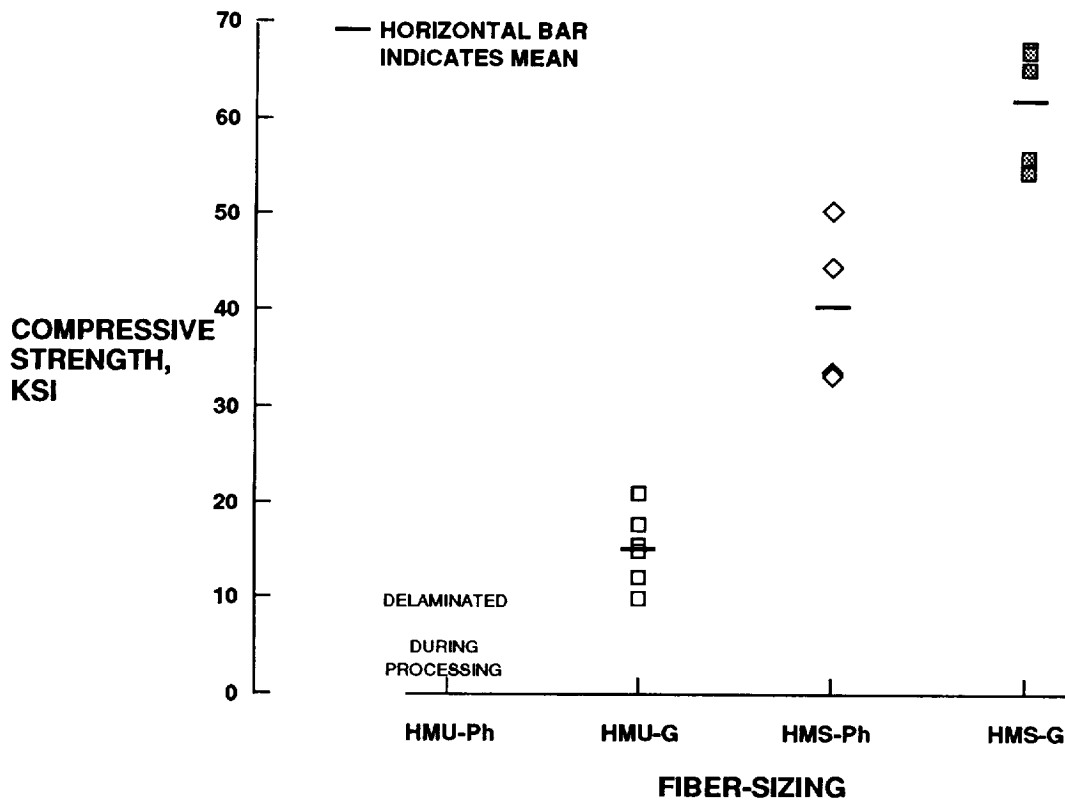


Figure 11. Compressive strengths for HMU-Ph, HMU-G, HMS-Ph, and HMS-G composites.

THROUGH-THE-THICKNESS REINFORCEMENT CONCEPTS FOR THIN CARBON-CARBON SUBSTRATES

The program goals shown in figure 2 for improving mechanical properties are believed to be attainable for 2-D reinforced substrates. For a particular application, the need may well arise for interlaminar strengths not attainable by 2-D substrates. Utilization of through-the-thickness (Z-direction) reinforcement is an approach to be considered in this situation. For such an approach, NASA Langley has evaluated thin woven 3-D orthogonal preforms, as in the example shown in figure 12a, and stitched layups of 2-D fabric, as in the example shown in figure 12b. Using these approaches, interlaminar strengths have been achieved which exceed the program goals. Unfortunately, these reinforcement constructions give rise to inherently lower volume fractions of fibers in the in-plane directions and in-plane stiffness suffers.

Although these types of reinforcements have the disadvantages of lower stiffness as well as poor drapability (preforms are relatively rigid), their use affords potential advantages. For example, the 3-D orthogonal construction could be used to produce preforms for integrally stiffened panels, or the stitching technique could be used to selectively reinforce 2-D panels near stiffeners and flanges where particularly high interlaminar strengths are required.

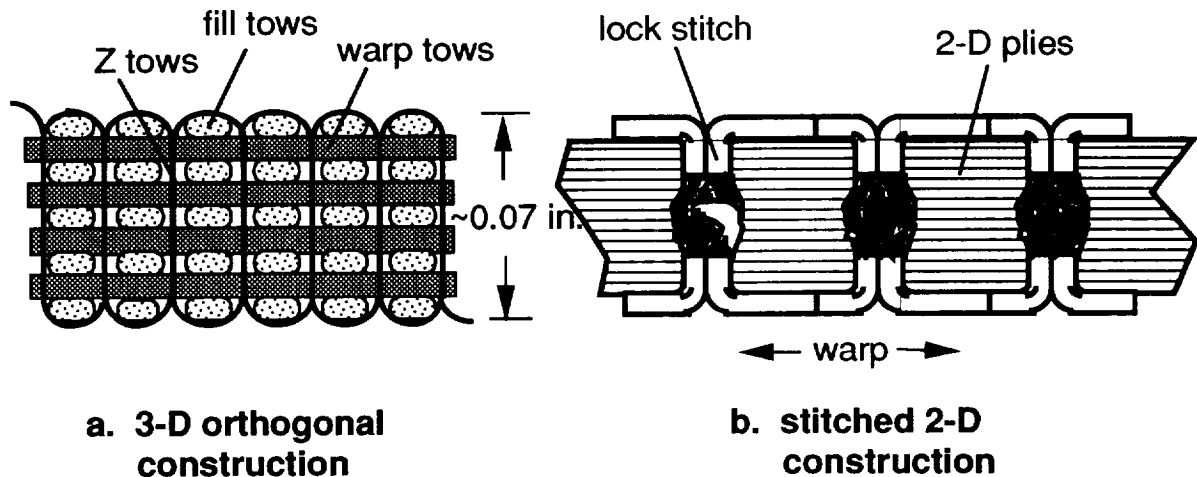


Figure 12. Through-the-thickness reinforcement concepts for thin carbon-carbon substrates.

STRENGTH BENEFITS OF A CVI-DENSIFIED 3-D ORTHOGONAL CARBON-CARBON COMPOSITE

Figure 13 compares the mechanical properties of a CVI-densified, 3-D orthogonal-reinforced carbon-carbon composite to those of the baseline ACC. The interlaminar tensile strength is well over twice that of the ACC and, in addition, exceeds the 2-D strength goal by some indeterminable amount (the 3-D strength exceeds the test capability, as indicated by the arrow at the top of the bar). The interlaminar shear strength exceeds the 2-D strength goal by as much as 50 percent and exceeds ACC strength by over 200 percent. The 3-D substrate has considerably more in-plane tensile and compressive strength than the ACC, but its tensile and compressive moduli are lower. The moduli are lower because of the much lower volume fraction of fiber in the 3-D composite (~43% compared to ~60% for ACC). The strengths remain high because the warp and fill tows are straight in the orthogonal construction; only the z-tows are weavers. Encouragingly, the in-plane shear strength and modulus of the 3-D composite remain comparable to ACC properties, in spite of the low volume fraction of fibers.

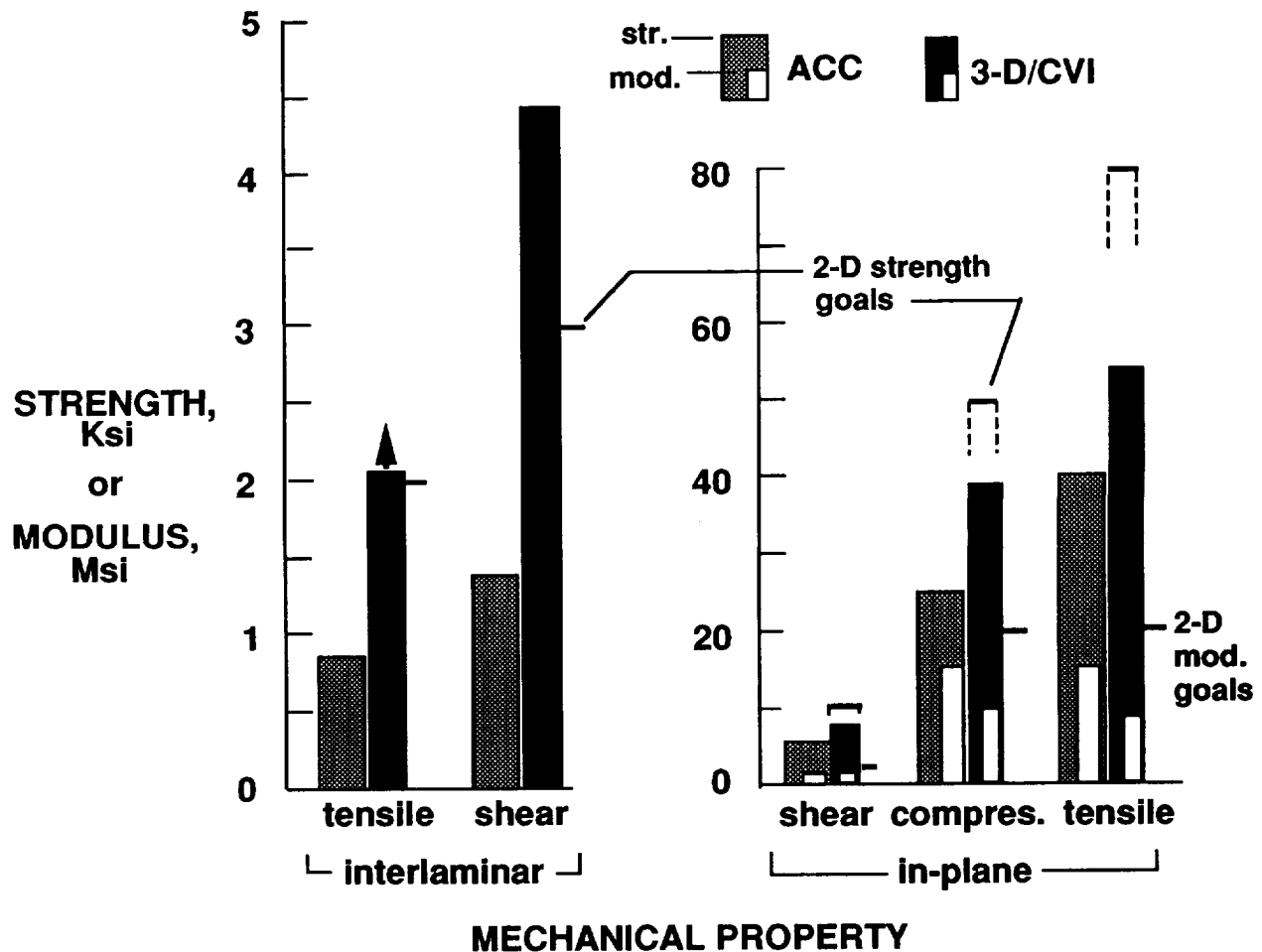


Figure 13. Strength benefits of a CVI-densified 3-D orthogonal carbon-carbon composite.

STITCHING AS INTERLAMINAR REINFORCEMENT IN THIN CARBON-CARBON COMPOSITES

Stitching of fabric lay-ups was investigated as a means of providing interlaminar reinforcement in C-C composites (ref. 10). Nine-ply lay-ups of dry Thornel T-300 fabric were reinforced by stitching with either two-strand or three-strand Torayca T-900 carbon thread in various stitch patterns with six to twelve stitches per inch in the x-direction and six to twelve stitch rows per in. in the y-direction. The resulting preforms, with interlaminar reinforcement densities ranging from 60,000 to 360,000 fibers per square inch, were processed into C-C composites using phenolic resin as the densifying agent. Mechanical testing indicated that stitching could provide markedly improved interlaminar properties in comparison with unstitched reinforcement; however, axial compressive strength was degraded.

In figure 14, unstitched, stitched, and three-dimensionally woven reinforcements are compared on the basis of interlaminar shear strength obtained from double-notch specimen tests. At a reinforcement density of approximately 300,000 fibers per square inch, it can be seen that the two-strand stitching furnishes a shear strength 50 percent higher than unstitched material, and that it is also more effective than the three-strand stitching at equivalent reinforcement densities. In comparison with the three-dimensionally woven Celion material, the two-strand stitching is able to achieve an approximately equivalent strength at a lower reinforcement density. Meaningful interlaminar tensile strength data could not be obtained for the stitched materials due to the inability of the existing test method to effectively transfer load to the reinforcing stitches; however, the interlaminar tensile strength for the stitched material is likely much higher than that for the unstitched material.

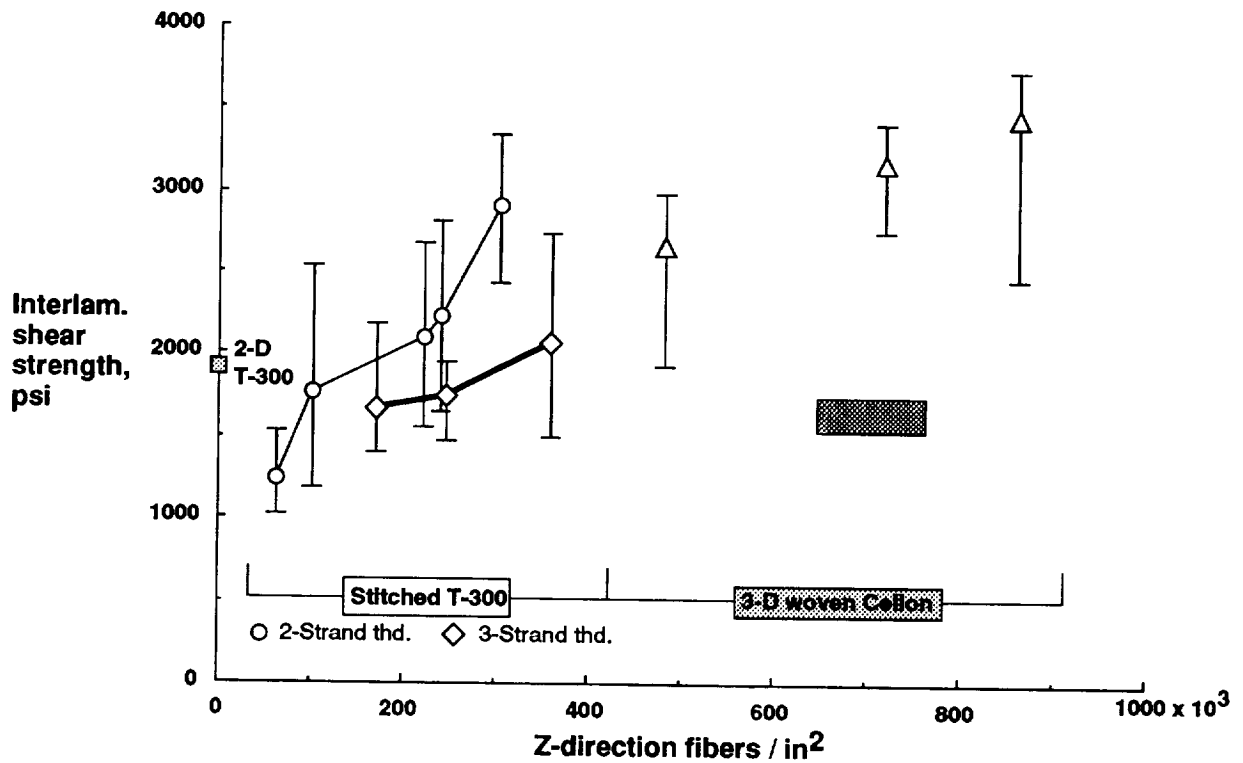


Figure 14. Comparison of interlaminar shear strengths for C-C composites reinforced with unstitched T-300 fabric, stitched T-300 fabric, and 3-D woven Celion fabric.

STITCHING AS INTERLAMINAR REINFORCEMENT IN THIN CARBON-CARBON COMPOSITES (CONT'D)

While stitching did markedly improve the interlaminar properties of fabric-reinforced C-C, it did produce degradation in the axial compressive strength of the material. Axial strengths are compared for unstitched, stitched, and three-dimensionally woven materials in figure 15. It can be seen that the stitched T-300 and 3-D woven Celion materials furnished approximately 60 to 65 percent of the compressive strength of the unstitched T-300 reinforcement. Tensile strength, however, suffered little or no degradation as a result of the stitching, and the stitched materials possessed approximately the same tensile strength as the three-dimensionally woven materials.

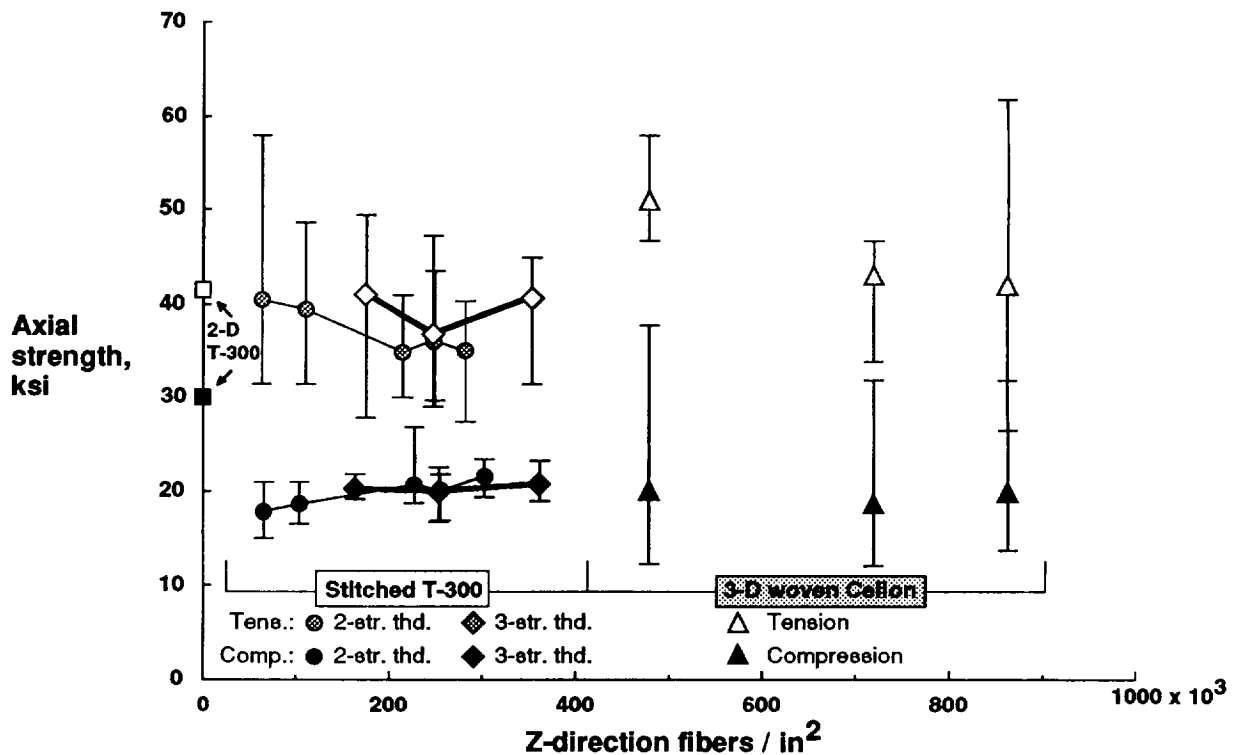


Figure 15. Comparison of tensile and compressive strengths for C-C composites reinforced with unstitched T-300 fabric, stitched T-300 fabric, and 3-D woven Celion fabric.

STITCHING AS INTERLAMINAR REINFORCEMENT IN THIN CARBON-CARBON COMPOSITES (CONT'D)

The axial moduli resulting from the unstitched, stitched, and three-dimensionally woven reinforcements are shown in figure 16. Not surprisingly, the data show that stiffness in either tension or compression tends to decrease as the proportion of z-direction reinforcement increases and the proportion of in-plane reinforcement correspondingly decreases.

In summary, it can be stated that stitching can produce marked improvements in the interlaminar properties of two-dimensional, fabric-reinforced C-C composites, accompanied by some degradation in compressive strength and both tensile and compressive moduli. Stitching is a reinforcement technique which lends itself to those particular applications driven by a need for high interlaminar properties; however, refinements such as optimized stitch patterns and thread weights could yield an improved balance of interlaminar and axial mechanical properties. In addition, stitching is a technique which affords considerable flexibility during fabrication since it can be applied to selected areas of structural components.

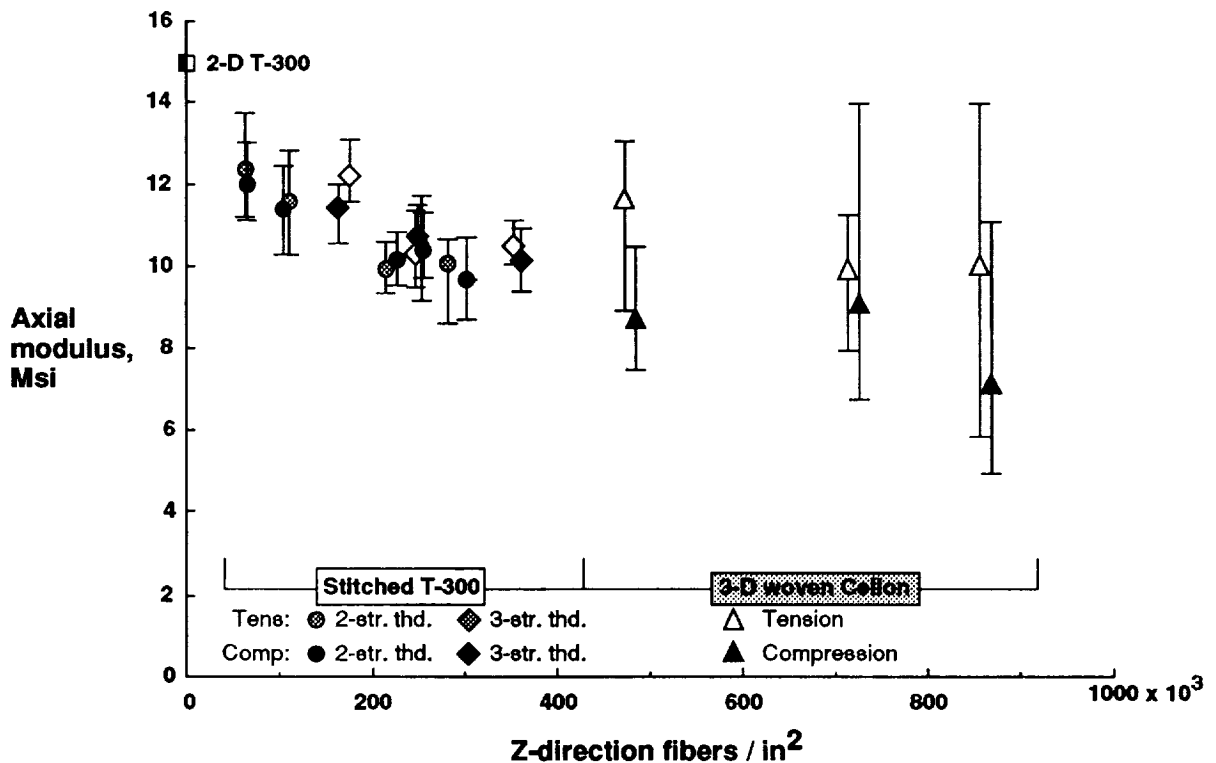


Figure 16. Comparison of tensile and compressive moduli for C-C composites reinforced with 2-D T-300 fabric, stitched T-300 fabric, and 3-D woven Celion fabric.

SUMMARY AND CONCLUSIONS

Thus far it has been demonstrated in this program that interlaminar strength of 2-D carbon-carbon can be significantly increased without having to give up in-plane strength. In fact, the use of the thin, fine-tow fabric improves in-plane strengths as well as interlaminar strengths. The improvements demonstrated thus far, for 2-D composites, have been achieved using reinforcements on which the fiber surface chemistry has mostly been removed as an unavoidable byproduct of fiber stabilization by heat-treatments. The use of newer high-strength, high-modulus fibers, which do not require heat stabilization, presents an opportunity to further improve interlaminar properties through optimization of fiber surface chemistry. Much higher percentages of improvement in interlaminar strengths are achieved by using 3-D orthogonal reinforcement; however, the use of through-the-thickness reinforcement, whether in the form of the 3-D orthogonal construction or the stitched 2-D construction, necessitates a tradeoff in stiffness (and in-plane compressive strength, depending on the type of densification matrix used). When the 2-D reinforcement is used in conjunction with CVI densification, interlaminar strengths are improved by 40 to 60 percent over baseline. At the same time, the in-plane tensile and compressive strengths are improved by 60 percent or better. When the 3-D orthogonal reinforcement is used in conjunction with CVI densification, interlaminar strengths are improved by 100 to 200 percent. The in-plane strengths are better than those of baseline ACC, including compressive strength. It is anticipated that similar results would be obtained if the 2-D stitched reinforcement were used in conjunction with CVI densification.

- **FINE TOW / THIN FABRIC COMBINATION SIMULTANEOUSLY IMPROVES IN-PLANE AND INTERLAMINAR STRENGTHS IN 2-D COMPOSITES**
- **OPTIMIZING FIBER SURFACE TREATMENT / SIZING AFFORDS HIGH POTENTIAL FOR IMPROVING INTERLAMINAR STRENGTHS**
- **THROUGH-THE-THICKNESS REINFORCEMENT NECESSITATES PROPERTY TRADE-OFFS**
- **SIGNIFICANT INCREASES ACHIEVED IN INTERLAMINAR STRENGTHS RELATIVE TO BASELINE:**

	<u>TENSILE</u>	<u>SHEAR</u>
2-D	40%	60%
3-D	100%	200%

Figure 17. Summary and conclusions

REFERENCES

1. Scott, R. O.; Shuford, D. M.; Webster, C. N.; and Payne, C.W.: Development of Advanced Carbon-Carbon (ACC) Composites, Vol. I- Materials Development. NASA Contractor Report 165842-1, July, 1982.
2. Tan, Stephen S.: 2-D Strengthening Mechanisms Program-Phase I, AFWAL-TR-88-4132, August, 1988.
3. Stover, E. R.; Price, R. J.; and Shih, W. T.: Effects of Fiber, Fabric and Matrix Process on Mechanical Properties of Some Advanced 2-D Carbon-Carbon Composites. Metal Matrix, Carbon, and Ceramic Matrix Composites, NASA CP-3097-Part 2, 1990, pp. 345-358.
4. Walker, M. S.; and Lee, S. C.: Material and Process Effects on the Interlaminar Strength of Structural Carbon-Carbon Materials. Metal Matrix, Carbon, and Ceramic Matrix Composites 1987, NASA CP-2482, 1987, pp. 327-342.
5. Maahs, Howard G.; Yamaki, Y. Robert: Effect of Fiber Surface Treatment Level on Interlaminar Strengths of Carbon-Carbon Composites. NASA TM 4033, June, 1988.
6. Yamaki, Y. Robert; and Maahs, Howard G.: Influence of Fiber Surface Treatment on the Mechanical Properties of Carbon-Carbon Composites. Metal Matrix, Carbon, and Ceramic Matrix Composites-part 1, NASA CP-3054, 1989, pp. 367-386.
7. Yamaki, Y. R.; and Maahs, H. G.: Influence of Fiber Sizing on the Mechanical Properties of Carbon-Carbon Composites. NASA TM-4346, 1992.
8. Phillips, W. M.; Brown, D. K.; Jacoy, P. J.; Landel, R. F.; Porter, C.; and Schmitigal, W. P.: Carbon-Carbon Composites Technology: Phase I, Final Report. PL-TR--91-3061, Sept. 1991.
9. Ransone, Philip O.; Maahs, Howard G.; and Spivack, Bruce D.: Influence of Matrix Type and Reinforcement Size and Type on Mechanical Properties of 2-D Carbon-Carbon Composites. Metal Matrix, Carbon and Ceramic Matrix Composites, NASA CP 3097-Part 2, 1990, pp. 395-418.
10. Yamaki, Y. Robert; Ransone, Philip O.; and Maahs, Howard G.: Investigation of Stitching As a Method of Interlaminar Reinforcement in Thin Carbon-Carbon Composites. Presented at the 16th Annual Conference on Composites, Materials, and Structures, Cocoa Beach Florida, January 13-16, 1992.

CURRENT RESEARCH IN OXIDATION-RESISTANT CARBON-CARBON COMPOSITES AT NASA LANGLEY

C. W. Ohlhorst, W. L. Vaughn, and D. M. Barrett
NASA Langley Research Center
Hampton, Virginia

OUTLINE

The significant potential of carbon-carbon composites for high-temperature structural applications is well established (refs. 1-3). For hypersonic vehicle applications, desirable properties include low density, high specific strength and stiffness, low coefficients of thermal expansion, and retention of mechanical properties above 3000°F. A significant problem associated with carbon materials, however, is that they oxidize rapidly in air at temperatures above about 800°F, and therefore, must be protected from oxidation. Successful development of effective methods of oxidation protection is key to the eventual utilization of carbon-carbon composites on hypersonic vehicles such as NASP.

In this presentation, the basic elements of an oxidation-protection system are described. Results from oxidation-performance evaluations of state-of-the art ACC-4 type material in simulated airframe vehicle environments (temperature, pressure, time) conducted at NASA Langley are also presented.

NASA Langley has an active research effort to improve the oxidation resistance of carbon-carbon materials for airframe structural and vehicle thermal protection applications. Conversion coating and sealant development research will be highlighted in this presentation.

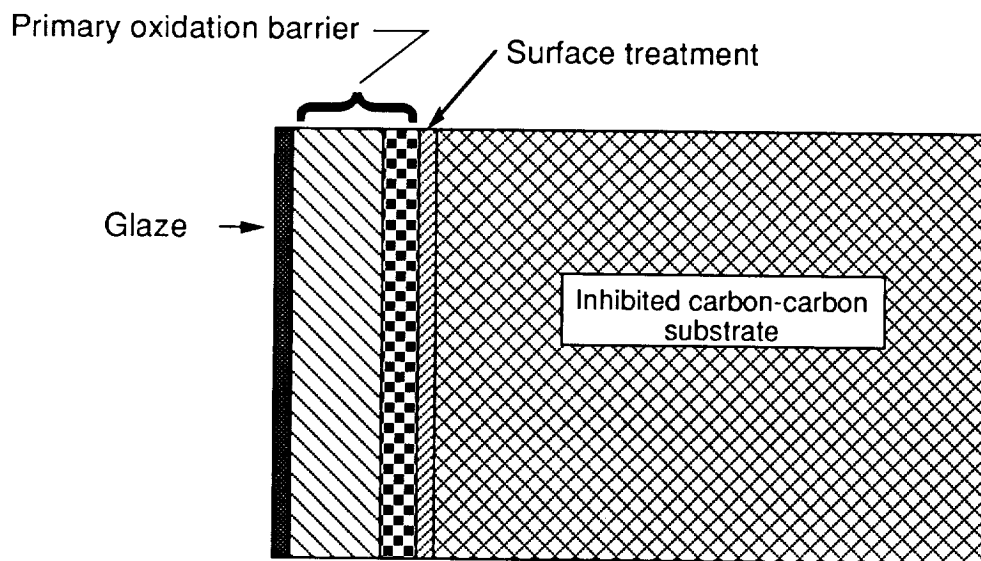
- Background
 - Oxidation-protection system concepts
 - Oxidation performance data
- Oxidation-protection system development at NASA Langley
 - Conversion coating
 - Sealant Development
- Conclusions

OXIDATION-PROTECTION SYSTEM CONCEPTS

This figure depicts some of the basic elements of oxidation-protection system (OPS) concepts that are currently being investigated for protecting carbon-carbon composites in cyclic, high-temperature, oxidizing environments. Many of these concepts are described in references 3-9 and elsewhere. Some concepts include oxidation inhibitors in the substrate to slow oxidation in the event that oxygen penetrates the coating through flaws and coating cracks.

Some OPS concepts include treatment of the substrate surface before depositing the first layer of coating. These treatments can be chemical or mechanical in nature or a combination of both. The primary purpose of these treatments is to improve the adhesion between the coating and the substrate.

Most of the coatings (labeled as primary oxidation barrier in figure) currently under development are applied in multiple layers and are based on boron carbide, silicon carbide and silicon nitride chemistries. Some OPS concepts include a glaze over the outer coating layers in order to seal cracks that develop during cooling from the high processing and use temperatures.



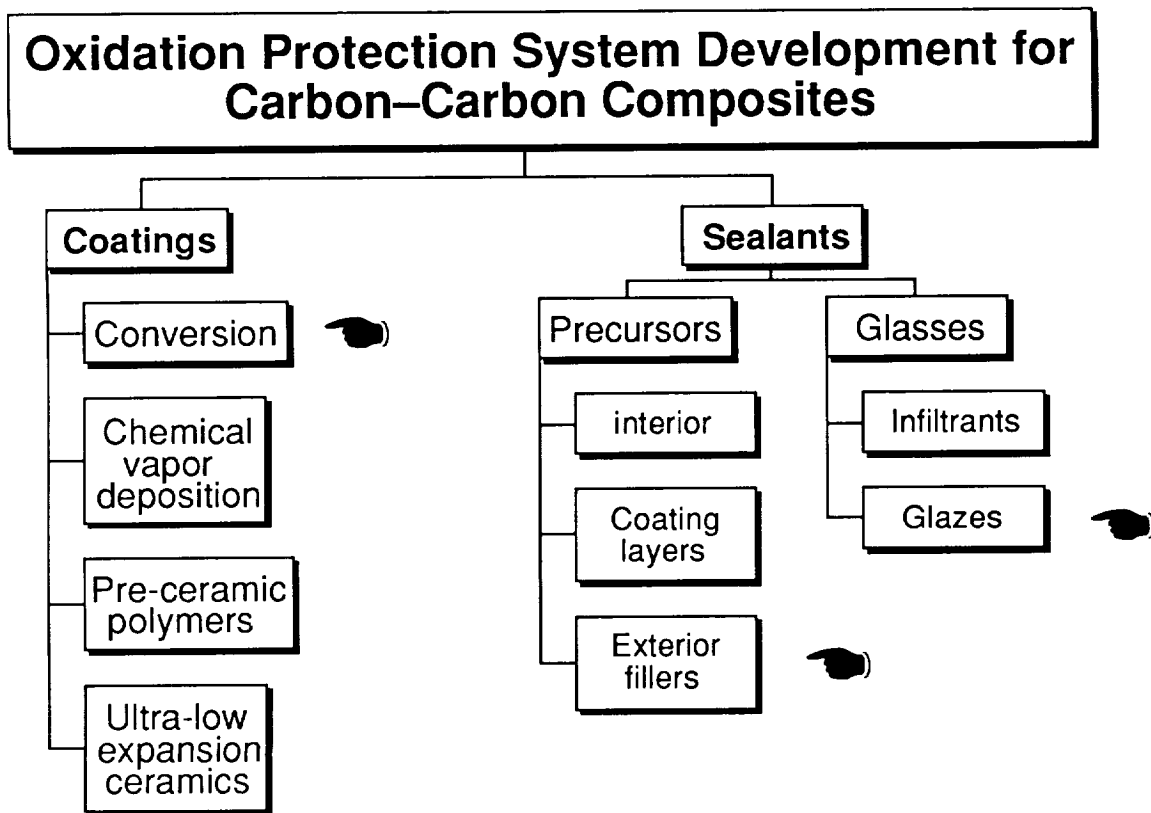
OXIDATION PROTECTION SYSTEM DEVELOPMENT FOR CARBON-CARBON COMPOSITES

This figure shows the breadth of research in the oxidation protection of carbon-carbon composites (C-C) being investigated at NASA Langley. The research can be split into the two broad categories of coatings and sealants.

The coating work investigates the application of refractory oxidation-resistant ceramics to the C-C. The coatings serve to reduce the diffusion of oxygen to the substrate. SiC is the most commonly used coating; Langley is investigating two methods to apply SiC: Pack conversion coatings, where the surface layer of carbon is converted to SiC at high temperatures; and chemical vapor deposition (CVD), where SiC is deposited from the gas phase onto the C-C at high temperatures. Pre-ceramic polymers are a method of applying a SiC or Si₃N₄ coating via the pyrolyzation of these polymers at high temperatures. The ultra-low expansion ceramics are a class of ceramics based on the sodium-zirconium-phosphate (NZP) family. The NZP ceramics may have low oxygen permeabilities as well as thermal expansion coefficients near those of C-C which may result in nearly crack free coatings.

The cracks in the current coating systems, due primarily to thermal expansion differences between C-C and the coatings, necessitates the use of sealants. The sealant material can be provided in two ways, as a precursor, or as an oxide glass. The precursors are materials such as B₄C that, when exposed to air, oxidize to B₂O₃ and form a sealing glass. The precursors can be added to the interior as inhibitors, in the coating as a sealant layer or as a filler in a exterior glaze. The glasses are oxides that can flow and seal the C-C and coatings at intermediate and high temperatures. Generally they are applied as an infiltrant into the substrate or are applied to the surface as a glaze, either with or without fillers.

In this paper we will be addressing some of the in-house research on conversion coatings, glazes, and precursor additions as exterior fillers in a glaze.

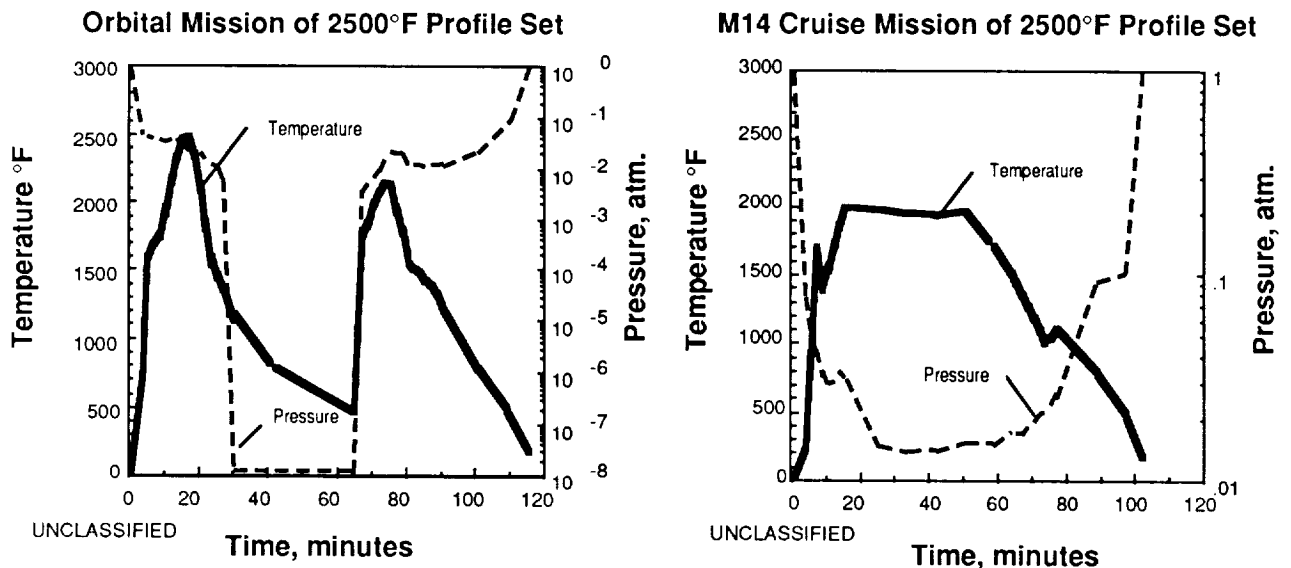


REPRESENTATIVE MISSION SIMULATION PROFILES

Fuselage <3' from Nose

In order to get meaningful oxidation performance data, materials must be tested in conditions that simulate the temperature and pressure environment which would be seen in actual flight. To define such conditions, a model of the National Aero-Space Plane (NASP) government baseline vehicle was "flown" in the simulator at NASA Ames-Dryden. From these simulated flights, temperature and pressure profiles were generated for four locations on the vehicle. These locations span the range of temperature conditions where carbon-carbon might be used. For each vehicle location, a profile set was generated which consisted of both an orbital mission and a cruise mission. Peak temperatures on the ascent leg of the orbital mission range from a high of 2800°F to a low of 1700°F. Each profile is designated by this peak ascent temperature. Simulating the ground environment is also important since it is established that moisture can significantly degrade oxidation protection coating performance (references 3, 5, 10, 11). Humidity conditions of 50% RH at 80°F were chosen after considering typical humidity conditions at NASA Ames-Dryden where the NASP X-30 vehicle will be based. The testing sequence used was cruise-humidity-orbit-humidity-cruise-humidity, etc.

This figure shows the temperature and pressure profiles for a point on the fuselage less than 3 feet from the nose. The maximum temperature for the ascent portion of the orbital mission is 2500°F. The maximum temperature during the entry leg is close to 2200°F. Temperatures peak at 2000°F with an extended period at 1950 °F for Mach 14 cruise mission. Pressures are generally less than 0.1 atm. during the hottest portions of both orbital and cruise missions.

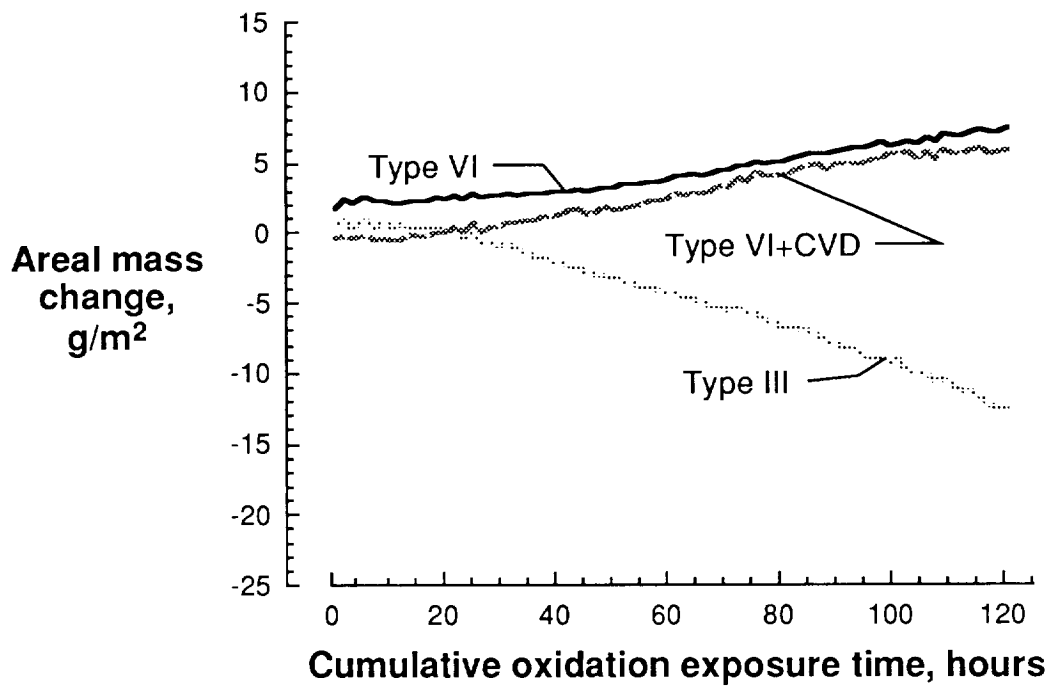


OXIDATION RESULTS FOR LTV CONVERSION COATED CARBON-CARBON COMPOSITES

1700°F Profile Set

This figure shows the areal mass change for one test coupon of each of three oxidation-protection system (OPS) concepts. The test coupons were supplied by LTV, and the substrate was LTV's ACC-4 in all cases. The type III coated system is a non-boronated SiC pack-conversion coating. The type VI coating is a boronated SiC pack-conversion coating system and the type VI + CVD is the type VI with an overlayer of CVD SiC. Two pack conversions are performed to produce the Type VI coating and this second pack conversion makes the Type VI coating more dense than the Type III coating. Data are shown for the 1700°F profile set.

The coupons were tested out to 120 hours. The Type III coating coupon loss weight gradually while the Type VI and Type VI + CVD coating coupons gained weight gradually. Clearly, the denser, boronated, Type VI-based coating systems are superior to the Type III coating system in these 1700°F profile set conditions.



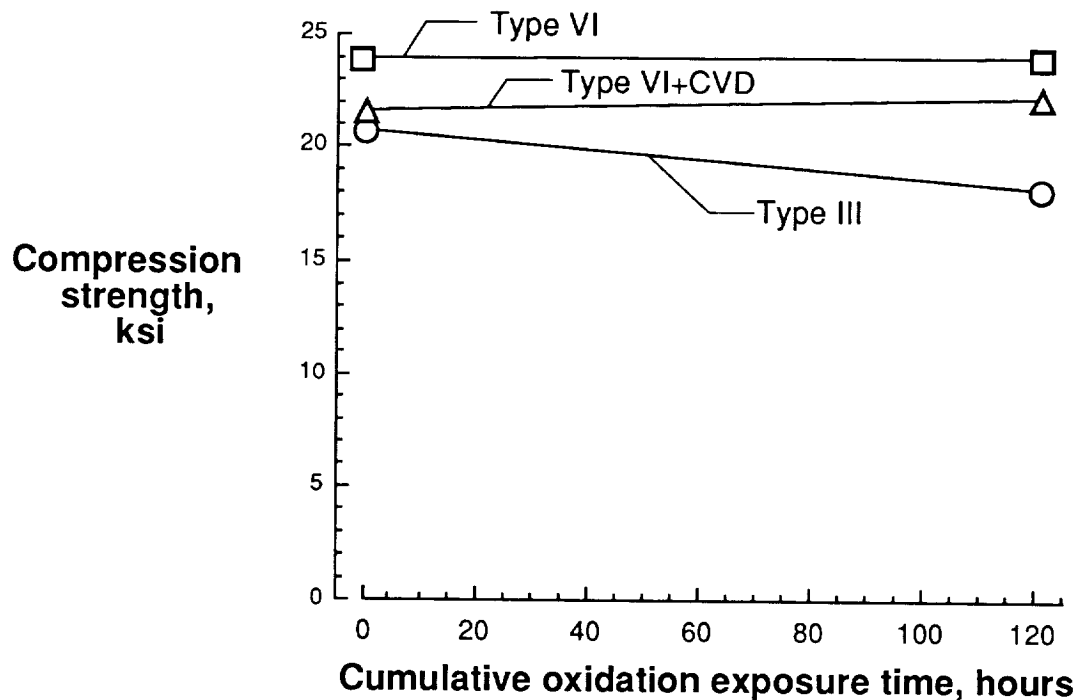
COMPRESSION STRENGTH RESULTS FOR LTV CONVERSION COATED CARBON-CARBON COMPOSITES

1700°F Profile Set

To be a viable candidate for use as airframe structure, materials must not only have good oxidation performance but also must retain their as-received mechanical property values. As an indicator of residual in-plane mechanical properties, compression tests are conducted on oxidatively exposed specimens to generate residual compressive strength and modulus values.

This figure shows the compressive strength for the three LTV conversion-coated carbon-carbon composite materials whose oxidation performance data were shown in the previous figure. Strength of as-received materials are plotted at zero time. Strengths are based on total specimen (engineering) thickness, including coating. Specimen thicknesses were in the order of 0.1 inches.

The Type III coating specimen lost compression strength whereas the Type VI and Type VI+CVD specimens showed no loss in compression strength over the full 120 hours of exposure time. Thus, not only do the Type VI-based materials lose no mass with cumulative exposure, they retain their mechanical properties.

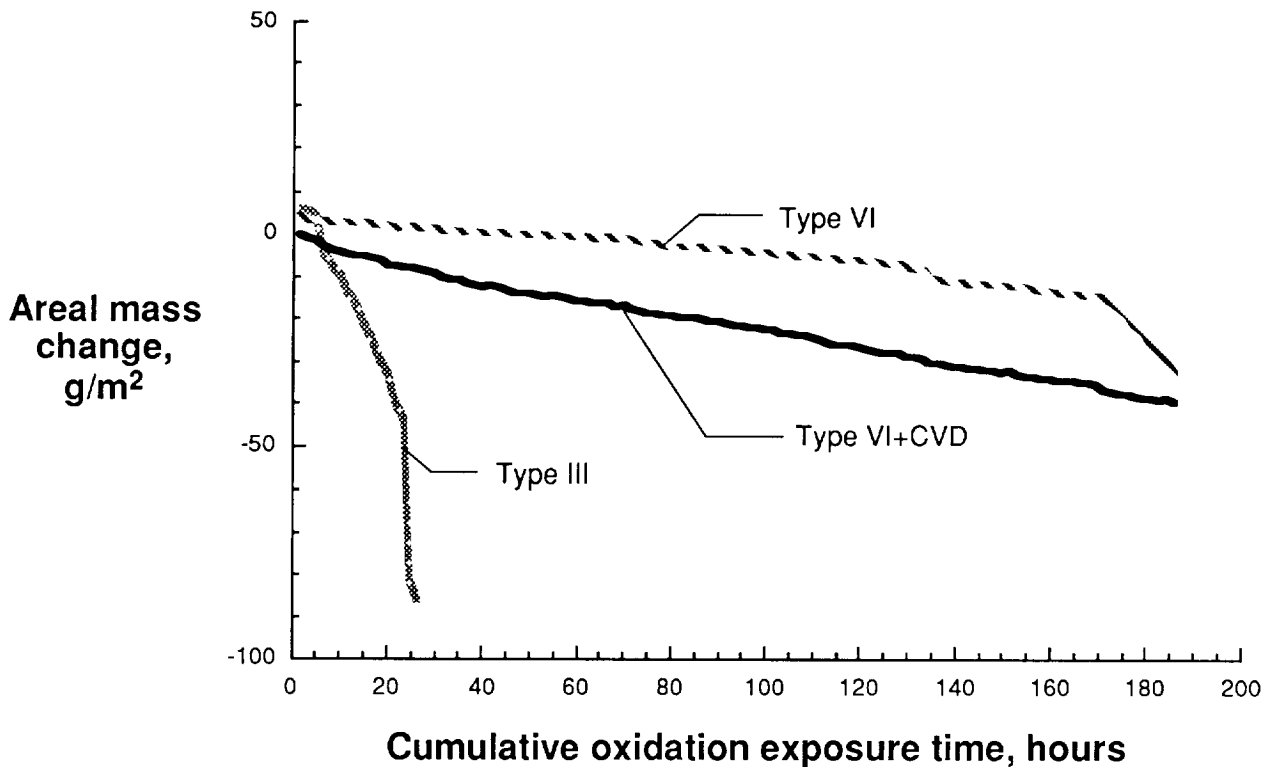


OXIDATION TEST RESULTS FOR LTV CONVERSION COATED CARBON-CARBON COMPOSITES

2500°F Profile Set

One test coupon of each of the three LTV OPS concepts was exposed to the 2500°F profile set conditions to determine the oxidation performance at higher temperatures. This figure shows the areal mass change for the coupons tested.

The Type III coupon lost mass rapidly and testing was discontinued after 25 hours. The Type VI and Type VI+CVD coupons lost weight gradually and tests were ended after 190 hours of testing. All three materials performed poorer at these higher temperatures than they had in the 1700°F profile set but again the Type VI-based coating systems were superior to the Type III coating system.

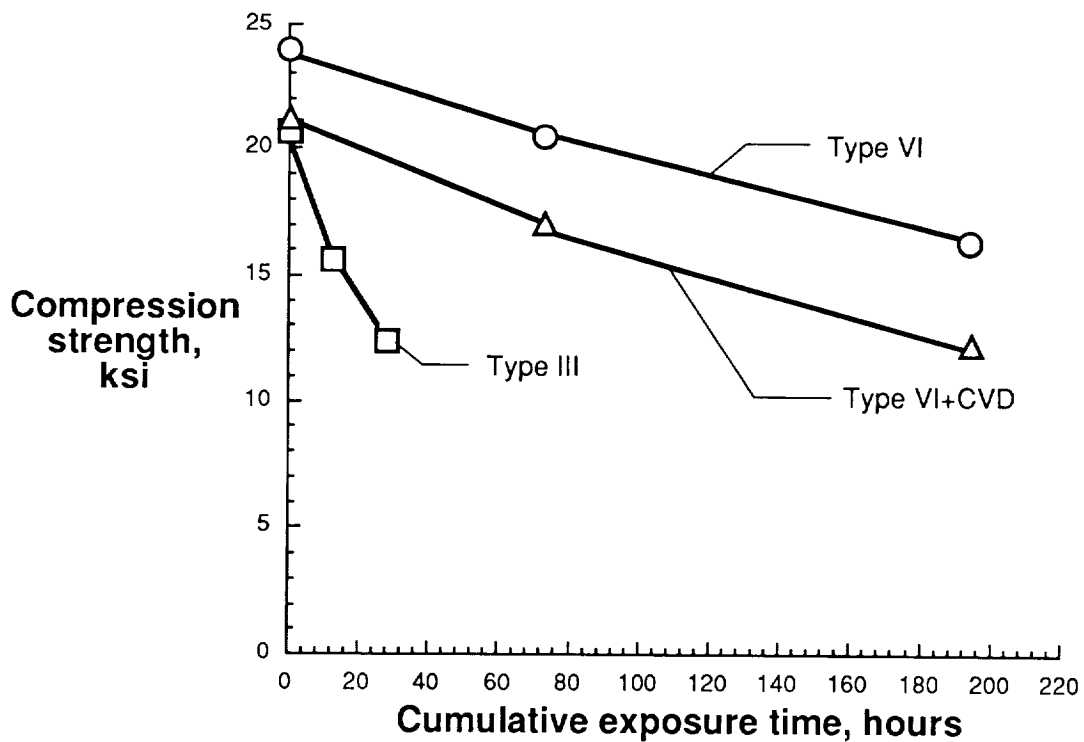


COMPRESSION STRENGTH RESULTS FOR LTV CONVERSION COATED CARBON-CARBON COMPOSITES

2500°F Profile Set

This figure shows the compressive strength for the three LTV conversion-coated carbon-carbon composite materials whose oxidation performance data were shown on the previous figure. Values for specimens run in the 2500°F profile set are plotted. Strength data are based on total specimen (engineering) thickness. Specimen thicknesses were in the order of 0.1 inches.

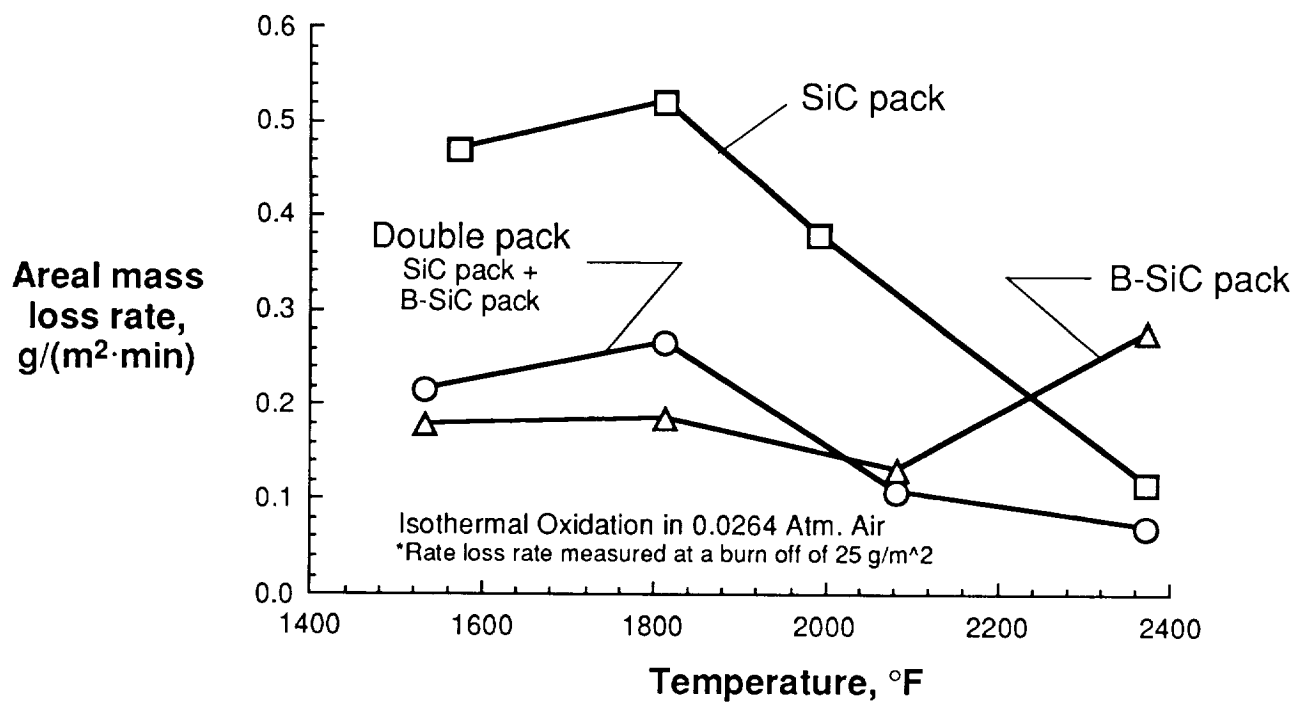
For all three systems, the strength decreased with cumulative exposure time. The Type III specimens lost strength much more rapidly than the other two coating systems indicating that this coating system does not protect the substrate as well as the other two systems. The trends of the Type VI and Type VI+CVD systems are similar. It is not clear why the Type VI+CVD specimens have lower strengths. The performance of all three material systems was poorer in this higher temperature environment than it was in the previously discussed 1700°F profile set environment.



EFFECT OF CONVERSION COATING TYPE ON THE MASS LOSS RATES FOR CARBON-CARBON COMPOSITES

NASA Langley is conducting in-house research to establish the influence of conversion coating type on the oxidation performance of carbon-carbon composites. Several varieties of pack conversion coatings have been applied to ACC-4 type substrate to determine their effect on oxidation performance. Shown below are the isothermal oxidation results for three coatings systems: one is a pure SiC conversion coating, one is a SiC conversion coating that incorporates boron and one is a combination coating which consists of a pure SiC conversion coating followed by a second, boronated SiC conversion coating. The tests were run in air at reduced pressure (0.0264 atm).

It is clear from the chart below that the presence of boron in the coating reduces the oxidation rate of the C-C. The decrease in rates with increasing temperature for all the samples is due to the closure of cracks in the coatings. The B-SiC coating was somewhat thinner (3-5 mils coating thickness) than the other two coatings (5-8 mils coating thickness), and this may account for its poorer performance above 2000°F.



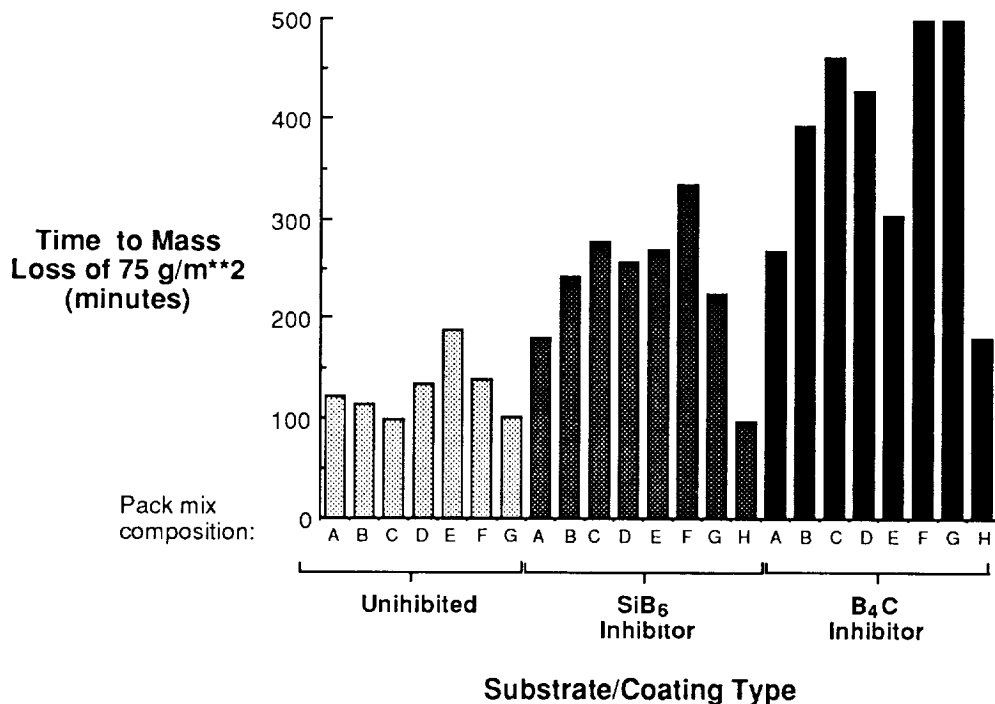
EFFECTS OF CONVERSION COATING AND INHIBITOR CHEMISTRY ON OXIDATION PERFORMANCE

1200°F , Cyclic, 1 atm

In-house research is also being conducted to establish the influence of conversion coating chemistry and substrate inhibitor chemistry on the oxidation performance of carbon-carbon. Experimentation has been involved with eight different combinations of alumina, boron, silicon, and silicon carbide particulates to produce boron doped, silicon carbide-based conversion coatings on carbon-carbon composite substrates.

Each of these eight different particulate combinations (A through H in the figure below) were used to produce coatings on uninhibited (ACC-4 type) and inhibited carbon-carbon composites. Two different inhibited carbon-carbon composite substrates were evaluated during this research investigation. One inhibited substrate contained silicon hexaboride and the other contained boron carbide.

The various coated composites were tested isothermally at 1200°F at 1 atm and periodically removed from the furnace for weighing. The figure shown below compares the time it takes to achieve a mass loss of 75g/m² for the different coating/substrate combinations produced. On the whole, inhibited substrates perform better than uninhibited, and the B₄C provides more protection than the SiB₆. It is clear also that there is a strong interaction between the nature of the pack mix composition and the nature of the inhibitor. The existence of such an interaction makes the task of optimizing OPS extremely difficult.

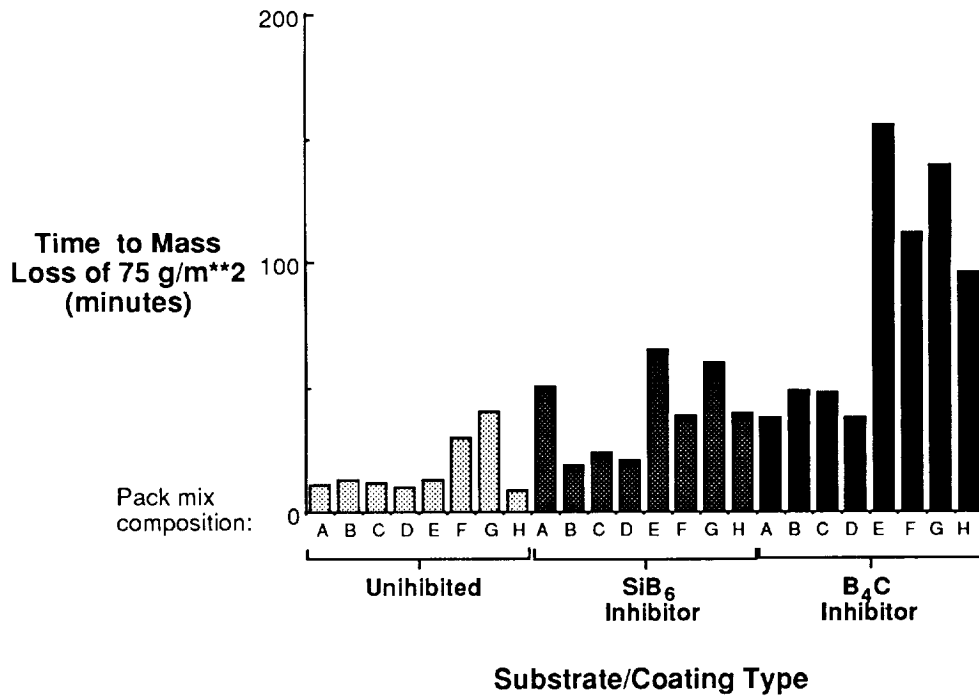


EFFECTS OF CONVERSION COATING AND INHIBITOR CHEMISTRY ON OXIDATION PERFORMANCE

1800°F, Cyclic, 1 atm

The figure shown below compares the time it takes to achieve a mass loss of 75g/m^2 for the different coating/substrate combinations discussed in the previous page when cyclically oxidized at 1800°F . The effect of different pack chemistry on performance is clearly evident again. For the B_4C -inhibited substrate, the E, F, G, and H compositions which have much longer lifetimes, have twice as much boron as the other four compositions.

A comparison of the figure below with the previous figure shows that relative ranking of oxidation performance depends not only on the pack chemistry and substrate chemistry but also on the exposure temperature. This result implies that oxidation protection systems need to be tailored for their service environment.

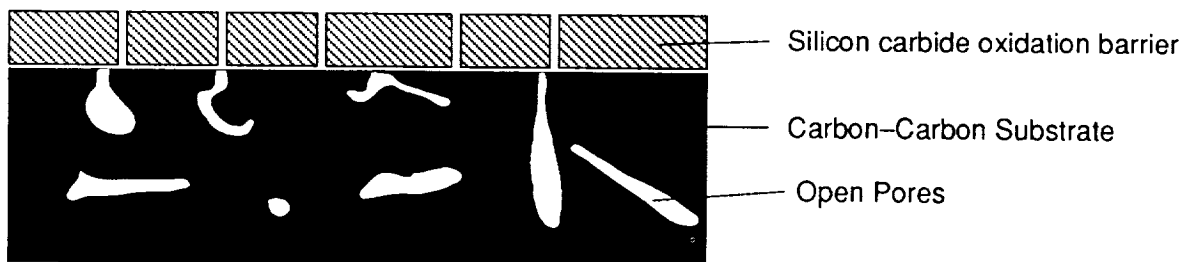
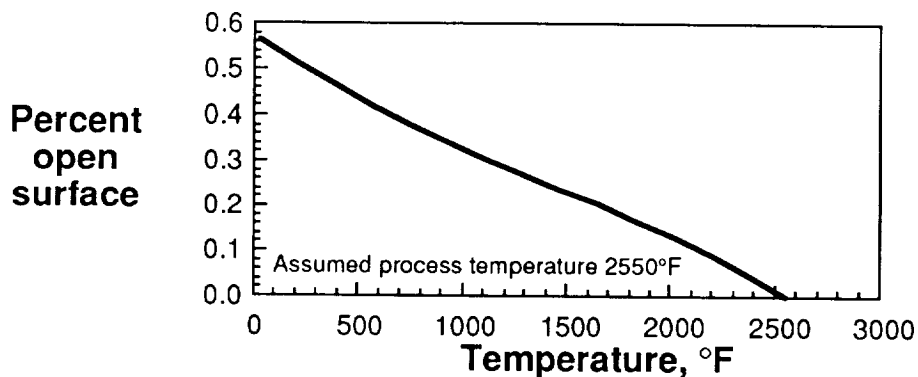


SURFACE CRACK OPENING DUE TO DIFFERENTIAL THERMAL EXPANSION BETWEEN CARBON-CARBON AND SILICON CARBIDE

Carbon-carbon composites have very low in-plane thermal expansions, averaging about 0.5 ppm/°F from room temperature to 2500°F. The typical materials used to coat C-C such as SiC or Si₃N₄ have expansions around 2 to 3 ppm/°F. This expansion difference leads to severe coating and substrate stresses. Typically, the coating will crack into small blocks that adhere to the C-C substrate. If the coatings are too thick they will usually fail the C-C in shear and disbond. The top figure below shows the calculated amount of open surface area (in the coating cracks) on a composite due to the differential expansion. The calculation is for a pure SiC deposited at 2550°F. This temperature is taken as the stress-free condition.

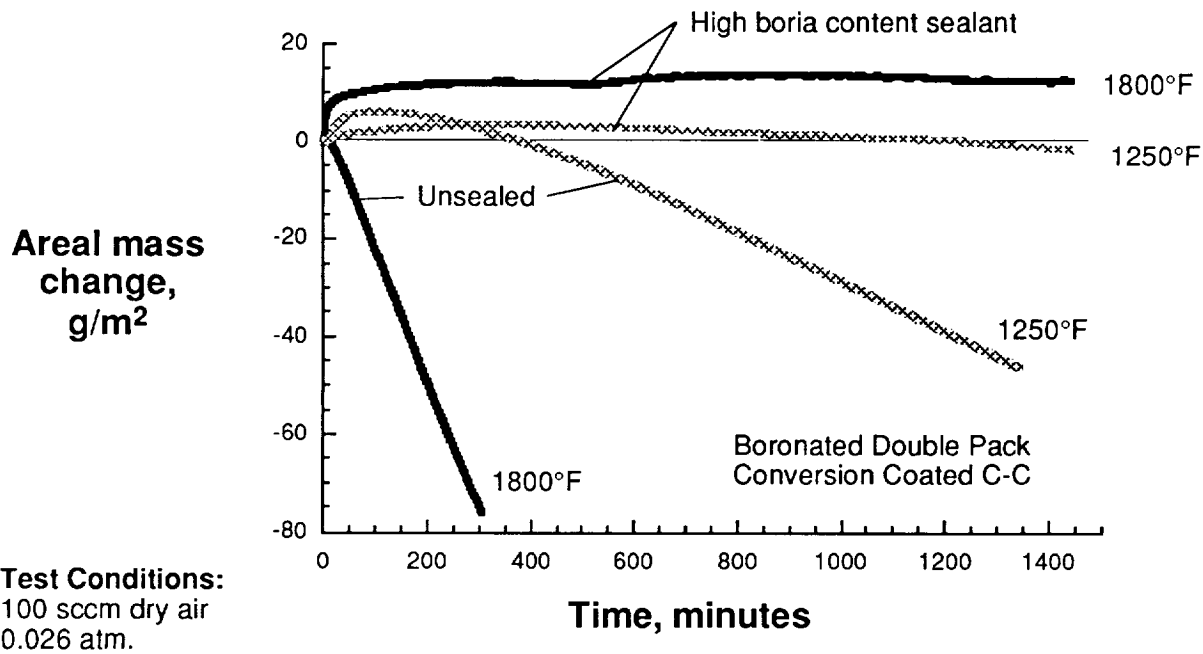
The surface cracks and substrate porosity lead to rapid diffusion of oxygen and reaction byproducts through the composite. At low temperatures the oxidation is controlled by the kinetics of the carbon oxidation reaction. As the temperature increases, the rates are controlled by the diffusion of oxygen and by-products through the coating cracks. Above the stress-free temperature for the coating, the oxidation is regulated solely by diffusion through the solid refractory layers and is virtually zero for low porosity coatings.

Sealants are required for the intermediate temperatures when the cracks have not yet closed and the temperatures are high enough for rapid oxidation. Appropriate sealants are glasses that are fluid at the intermediate temperatures, wet the carbon and the silicon carbide surfaces, and fill the cracks and pores. Although the diffusion of oxygen through these glass sealants generally is much higher than through pure silica glass, these sealants effectively prevent free access to the carbon surface through the coating cracks.



SEALANTS SIGNIFICANTLY IMPROVE OXIDATION RESISTANCE

The effectiveness of sealants is shown below. Plotted is the areal mass change versus time for a sealed and non-sealed boronated double pack conversion coated carbon-carbon composites tested isothermally at 1250° and 1800°F. The tests were run in air at reduced pressure (0.026 atm). The sealed coupons have been sealed with a high boria content glass. The improved oxidation performance of the sealed coupons over the non-sealed coupons is clearly evident. The sealed coupons show very little mass change after an initial mass gain, while the non-sealed samples show significant mass loss. The oxidation rates of the non-sealed coupons increase with temperature for the two temperatures shown.

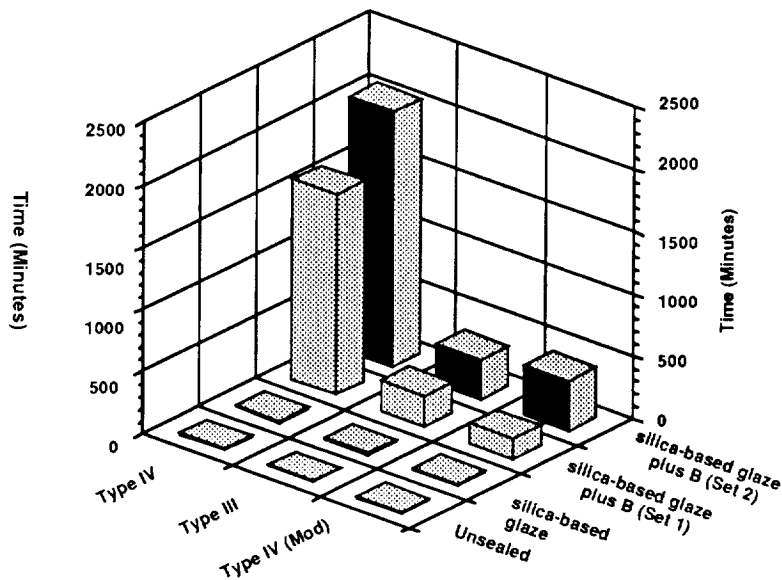


ADDITION OF PARTICULATES IMPROVES OXIDATION PERFORMANCE

Externally applied sealant glazes have demonstrated capabilities to extend oxidative lifetimes of coated carbon-carbon composites (reference 12). Research is being conducted at NASA Langley to determine whether additions of boron particulate fillers to the sealant glaze will further improve oxidation performance. The plot in the lower left-hand-side of this page depicts oxidation results for various coating-glaze combinations. The designations 'Type III', 'Type IV', and 'Type IV (Mod)' refer to NASA-produced conversion coatings similar in nature to those produced by LTV. Glaze parameters are (1) no glaze, (2) a silica-based glaze without fillers, and (3) a silica-based glaze with fifty percent boron particulate additions. The vertical axis is the elapsed time (in minutes) for a specimen to achieve a 75 g/m^2 weight loss. Two independently processed sets of fifty percent boron particulate loaded specimens were oxidized to verify test results. Oxidation testing involved oxidizing the specimens for fixed time intervals at 1800°F at 1 atm, removing the specimens from the furnace for weighing, and continuing this sequence of oxidizing and weighing until the specimens lost a total of 75 g/m^2 .

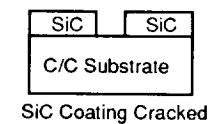
Of the nine combinations evaluated, the best combination is the Type IV conversion coating with a silica-based glaze plus fifty percent boron particulate addition. A very strong synergistic interaction between coating type and the nature of the glaze is clearly evident. Typically, sol-gel precursor chemicals are applied to the outside of previously coated carbon-carbon composite substrates. During firing, these sol-gel precursors polymerize and undergo condensation reactions which cause shrinkage and cracking in the formed silica. Additions of boron particulates to the glaze reduce this shrinkage and refine the cracking. The boron is also readily available to form bororia. Both the crack refinement and additional bororia reduce mass transport of oxidants to the substrate.

**1800F Lifetime Comparison Plot
(to achieve 75 g/m^2 mass loss)**

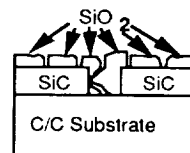


Mechanisms

CONVERSION, UNSEALED

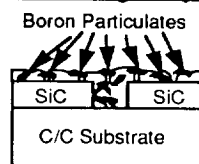


Silica-based glaze



Silica restricts oxygen access

Silica-based glaze plus B



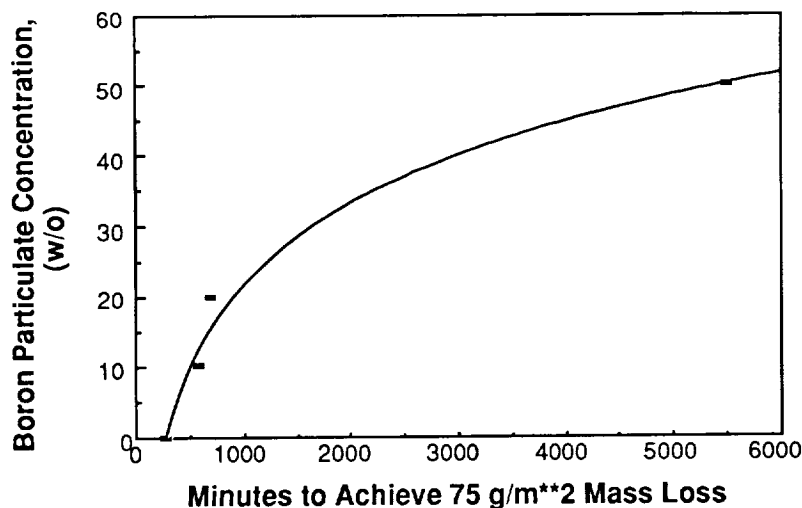
Benefits of boron particulates

EFFECTS OF BORON PARTICULATE CONCENTRATION IN SILICA-BASED GLAZES 1200°F, Cyclic, 1 atm

Because of the finding that particulate boron additions in silica-based glazes can significantly improve oxidation resistance, it is of interest to establish the most effective concentration levels for these particulates.

The study involved the addition of 0, 10, 20, and 50 weight percent of boron particulates to a silica-based sol gel solution which has been B-staged. B-staging involves a pretreatment of the silica-based sol gel solution which initiates cross-linking in the polymer. This initial cross-linking reduces shrinkage during the firing stage. The firing stage completes the condensation reaction and forms silica. After addition of the boron particulates to the B-staged silica-based sol gel, the precoated carbon-carbon composite substrates were dipped into a well-mixed solution and allowed to dry. This dipping/drying process was repeated three times. These specimens were fired in air according to an established schedule.

Next, the specimens were oxidatively tested. Plotted in the figure below are results for specimens tested isothermally at 1200°F at 1 atm. The specimens were periodically removed from the furnace for weighing. Oxidation resistance increases with an increase in concentration of boron. Since improved oxidation protection results from increases in boron particulate concentration, one may conclude that greater amounts of boria were formed in-situ during oxidation (due to the increased availability of boron) and hence the pools of boria formed in the cracks. These thicker layers of boria reduced the ingress of oxidants to the substrate.

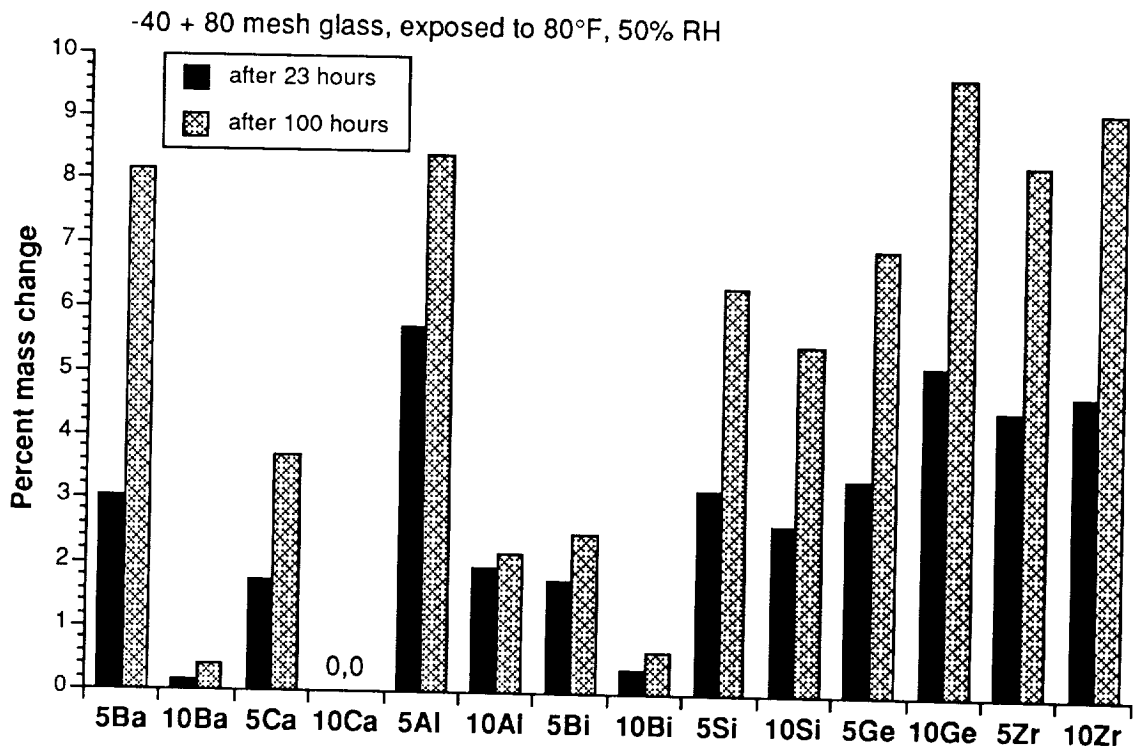


WATER ABSORPTION TESTS RESULTS FOR MODIFIED HIGH BORIA CONTENT GLASSES

A major drawback to the use of high boria content glasses as sealants on carbon-carbon composites is the poor moisture resistance of some compositions. If the boria glass hydrolyzes it can cause two problems: first, there is a volume increase of about 25 percent which can cause mechanical damage to the composite, and, secondly, the inevitable decomposition of the hydrated boria during service can cause rapid gas evolution which can lead to failure of the composite.

As part of a screening study to identify boria glasses having good moisture resistance, the moisture pick up rates for a series of glasses modified by various additives and ground to -40 +80 mesh were measured. The glass samples were exposed to an 80°F, 50-percent RH environment for 23 hours and 100 hours. The samples were removed and the mass changes recorded about every four hours. Shown below are the mass change results for selected glass compositions.

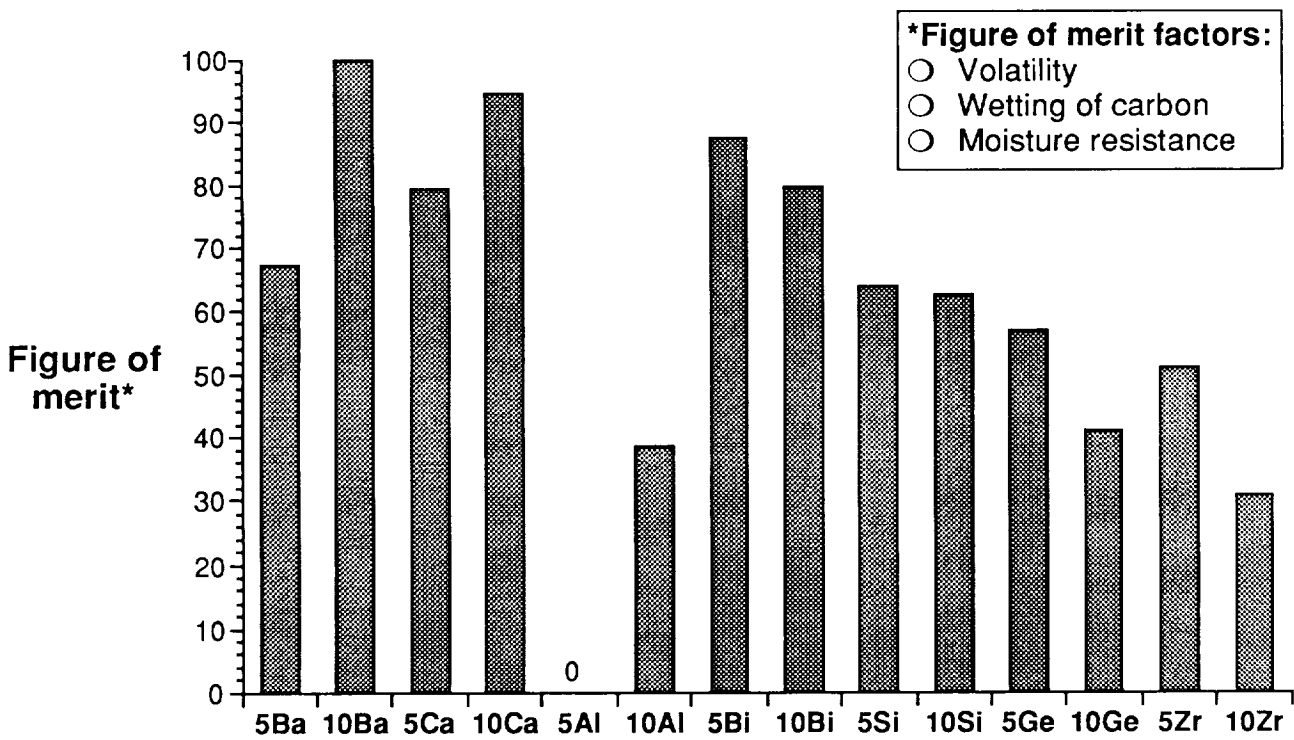
All the glasses showed parabolic kinetic behavior with at least one half the mass gain occurring in the first 25 hours. Three glasses are noteworthy: the 10 percent baria, the 10 percent calcia and the 10 percent bismuth oxide glasses, all showing less than 0.5 percent mass gain. Several of the glasses showed mass gains of as much as 10 percent, which is considered to be quite high in view of the relatively mild test conditions.



RELATIVE RANKINGS OF MOISTURE RESISTANT MODIFIED HIGH BORIA CONTENT GLASSES

The study to screen moisture resistant boria glasses also considered several properties besides moisture pickup. These include contact angles with carbon and SiC at 2200° and 2550°F, and vaporization at 2200° and 2550°F. The results of the individual tests were normalized and summed to acquire a figure of merit value. The chart below shows the figures of merit for selected glasses from the study. The best possible score was 100 and the worst 0.

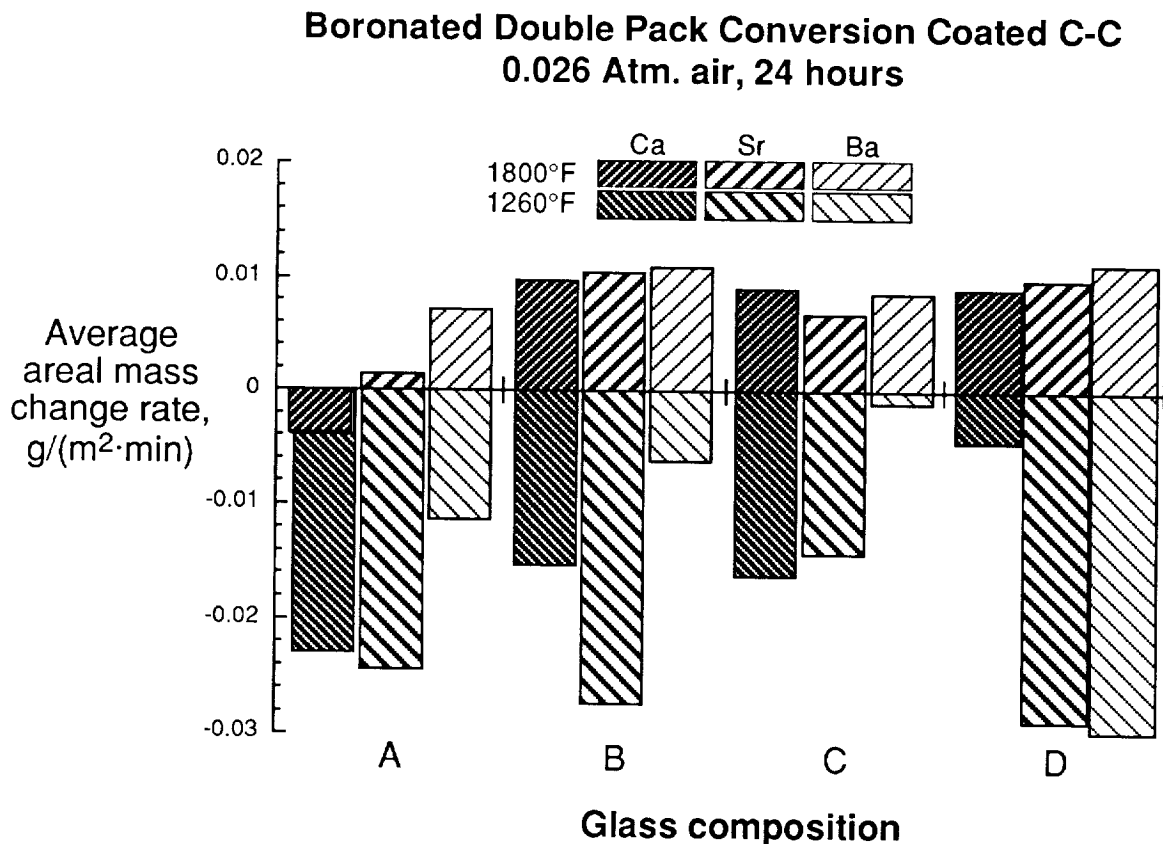
The 10 percent baria had the best overall properties followed by the 10 percent calcia glass. The 5 percent alumina glass had the overall worst performance. The bismuth oxides glasses had good moisture resistance and very small wetting angles, however they also had very high mass losses at high temperatures (2100°F) which would limit their possible use in sealants.



OXIDATION SCREENING OF MOISTURE RESISTANT BORATE GLASSES

As a result of the screening study discussed in the previous chart, a series of twelve glasses identified as having good potential for oxidation protection were applied to C-C coupons coated with a boronated double pack conversion coating. The sealant glasses were variations of baria-calcia- and strontia-lithia-borates. The sealed coupons were isothermally oxidized in a thermogravimetric analysis measuring apparatus at 0.026 atm of air with a flow rate of 100 sccm for 24 hours.

Two temperatures have been investigated to date, 1800° and 1260°F. These temperatures were chosen to represent two conditions of particular concern for oxidation-resistant carbon-carbon composites. 1800°F is a temperature near the maximum oxidation rate for unsealed pack conversion coated C-C and a temperature where sealants should perform well. 1260°C is a temperature at which it is expected that the sealants will not perform as well and where the oxidation rates typically have been found to be near a maximum for materials which have had a sealant applied. At 1800°F all the sealants performed well; only the 5-percent calcia "A" composition lost mass after 24 hours. Although all the coupons loss mass at 1260°F, some, such as the 5-percent boria "C" composition lost mass very slowly. At the measured loss rate, this composition would last many hundreds of hours before reaching the mass loss limit of 75 g/m². Currently the 5-percent baria "C" composition glass gives the lowest overall oxidation rate.



CONCLUSIONS

Successful development of effective methods of oxidation-protection is key to the eventual utilization of carbon-carbon composites on hypersonic vehicles. State-of-the-art boronated pack conversion coatings perform better in hypersonic vehicle airframe service environments than non-boronated pack coatings, although some loss in compressive strength is still seen after high temperature exposure.

Under use conditions of relatively low humidity, higher boron concentrations can improve oxidation protection. For higher humidity conditions, additions of small quantities of alkaline earth elements are showing promise as one means of increasing the moisture resistance of boria glasses without sacrificing their oxidation protection abilities.

To develop an effective oxidation protection system, a total material system approach is required because of the strong synergistic interactions that occur among the various constituents of the overall oxidation protection system.

- State-of-the-art boronated pack conversion coatings perform better than non-boronated
- Strong synergistic interaction exists among coating/inhibitor/sealant chemistries
- Additions of small quantities of alkaline earth elements increase moisture resistance of boria glasses without sacrificing their oxidation protection

REFERENCES

1. Stein, Bland A.; and Maahs, Howard G.: Carbon-Carbon Composites for Aero-Space Plane. First National Aero-Space Plane Technology Symposium, Langley Research Center, Hampton, VA, May 20-22, 1986, Vol. VIII-Materials, NASA CP-1008, 1986, pp. 243-279.
2. Stein, Bland A.; Maahs, Howard G. and Brewer, William D.: Airframe Materials for Hypersonic Vehicles. Metal-Matrix, Carbon, and Ceramic-Matrix Composites--1987, John D. Buckley, ed., NASA CP-2482, 1987, pp. 1-23.
3. Maahs, Howard G.; Ohlhorst, C. W.; Barrett, D. M.; Ransone, P. O.; and Sawyer, J. W.: Response of Carbon-Carbon Composites to Challenging Environments. Materials Research Society 1988 Spring Meeting, Reno, NV, Apr. 5-9, 1988, Symposium Proceedings Vol. 125, 1988, pp. 15-30.
4. Gray, Paul E.; and Sheehan, James E.: Oxidation Protected Carbon-Carbon Composite Development. GA Technologies Report GA-A18446, Apr. 1986.
5. Sheehan, J.E.: Ceramic Coating For Carbon Materials. GA Technologies Report GA-A18807, Apr. 1987.
6. Sheehan, J.E.; Kaae, J.L.; and Schiroky, G.H.: High-Temperature Coating For Carbon-Carbon Composites. GA Technologies Report GA-A18786, Apr. 1987.
7. Buckley, John D., editor: Metal-Matrix, Carbon, and Ceramic-Matrix Composites--1987, NASA CP-2482, 1987.
8. Maahs, Howard G., editor: Oxidation-Resistant Carbon-Carbon Composites For Hypersonic Vehicle Applications, NASA CP-2501, 1988.
9. Bush, I.; Schmidt, D.; and Tomashot, R., editors: Proceeding of the Air Force Workshop on Oxidation Protected Carbon-Carbon Composites (Below 3000°F). AFWAL-TR-88-4071, Mar. 1988.
10. Price, R.J.; Gray, P.E.; Engle, G.B.; and Sheehan, J.E.: Advanced Oxidation-Inhibited Matrix Systems For Structural Carbon-Carbon Composites. AFWAL-TR-87-4042, June 1987.
11. Singerman, S.A.; and Warburton, R.E.: Environmental Effects on Coated Inhibited Carbon/Carbon Composites. In Oxidation-Resistant Carbon-Carbon Composites for Hypersonic Vehicle Applications, Howard G. Maahs, ed., NASA CP-2501, 1988, pp. 67-74.
12. Barrett, David M.; Vaughn, Wallace L.; Maahs Howard G.; Ohlhorst, Craig W.; and Martin, Roderick H.: Performance Evaluations of Oxidation-Resistant Carbon-Carbon Composites in Simulated Hypersonic Vehicle Environments. Symposium on High Temperature Composites, Proceedings of the American Society for Composites, Dayton, OH, June 13-15, 1989, Lancaster PA, Technomic Publishing Co. pp. 282-297.

**THERMAL CONTROL/OXIDATION RESISTANT COATINGS
FOR TITANIUM-BASED ALLOYS**

Ronald K. Clark and Terryl A. Wallace
NASA Langley Research Center
Hampton, VA

George R. Cunningham
Lockheed Missiles and Space Company
Palo Alto, CA

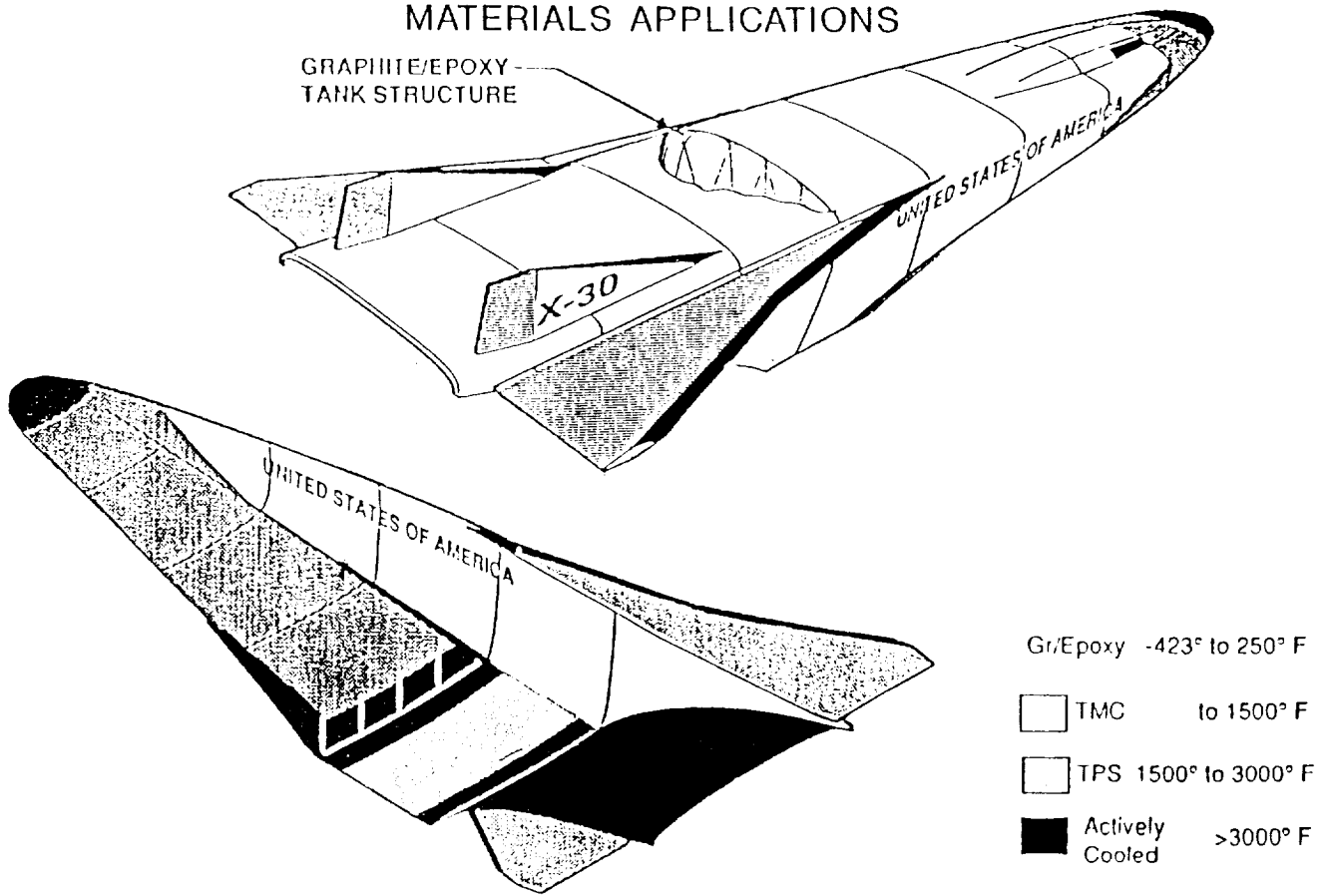
Karl E. Wiedemann
Analytical Services and Materials, Inc.
Hampton, VA

INTRODUCTION

Titanium-based alloys are candidate materials for hot structures and heat shields in hypersonic vehicles because of their low weight and high strength at elevated temperature. The figure shows a schematic diagram of the NASP vehicle configuration with regions for use of various materials systems mapped. Titanium-matrix composite (TMC) material, projected for use at temperatures to 1500°F, is shown over a significant portion of the vehicle. However, the range of conditions where they can be used is limited by their susceptibility to oxidation and loss of mechanical properties at high temperature. Protective coatings that shield these materials from oxidation will enable their use at higher temperatures. Further, coatings that provide a high emittance and low catalytic efficiency surface can significantly extend the applicability of these materials by reducing the net heating to the vehicle surfaces in hypersonic flight environments that contain dissociated species. The low catalytic efficiency reduces heat input from recombination of dissociated species in the environment and the high emittance results in greater heat flux rejection by radiation at the surface.

NASP VEHICLE CONFIGURATION

MATERIALS APPLICATIONS



THERMAL CONTROL/OXIDATION RESISTANT COATINGS FOR TITANIUM-BASED ALLOYS

Extensive research and development efforts have been expended toward development of thermal control and environmental protection coatings for NASP and generic hypersonic vehicle applications. The objective of the coatings development activities summarized here was to develop light-weight coatings for protecting advanced titanium alloys from oxidation in hypersonic vehicle applications. A number of new coating concepts have been evaluated. Coated samples were exposed to static oxidation tests at temperatures to 1000°C using a thermogravimetric apparatus. Samples were also exposed to simulated hypersonic flight conditions for up to 10 hr to determine their thermal and chemical stability and catalytic efficiency. The emittance of samples was determined before and after exposure to simulated hypersonic flight conditions.

Objective:

- Develop light-weight coatings for protecting advanced titanium alloys from oxidation in hypersonic applications
 - Thermal control thru high emittance and low catalysis
 - Oxidation protection thru oxygen barriers

Approach:

- Explore innovative new coating concepts/chemistries
- Conduct static/dynamic oxidation tests
- Determine heat transfer and oxidation characteristics

ENVIRONMENTAL RESISTANT COATINGS FOR TITANIUM-BASED ALLOYS

Environmental coatings provide protection of the substrate alloy by way of an oxygen barrier layer that retards oxidation and by the high emittance and low catalysis surface properties which lower the operating temperature for a given environment. In addition to these factors, successful coatings must be thermally and chemically stable and must be thin to minimize weight.

A variety of approaches to providing environmental coatings for hypersonic vehicle applications have been considered. Some approaches, such as pigmented paints, slurry coatings, and conversion coatings, have been abandoned because of thickness or weight considerations. Physical vapor deposition has limited potential for producing good coatings because of the difficulty in forming thin defect-free coatings. Two approaches that have good potential for forming micrometer-thick protective coatings are based on chemical vapor deposition (CVD) and sol-gel processes. Both of these methods are utilized for coatings development at NASA Langley Research Center (LaRC). CVD is being utilized in coatings development by Lockheed Missiles and Space Company under contract to NASA LaRC and sol-gel processes are being utilized for coatings research and development in the laboratory at LaRC.

Performance Requirements:

- Oxidation Protection
- Thermal/Chemical Stability
- Minimum Weight
- Low Catalytic Efficiency
- High Emittance

Approaches Considered:

- Pigmented Paints - Too Thick
- Slurry Coatings - Too Thick
- Reactive Coatings - Too Thick, Consume Substrate
- Physical Vapor Deposition - Difficult to Form Thin, Defect-Free Coating
- Chemical Vapor Deposition - Good Potential
- Sol-Gel - Good Potential

MATERIAL PROPERTIES THAT AFFECT STEADY STATE TEMPERATURE

The equilibrium temperature of a vehicle subjected to aerothermal heating is governed by the net rate of heat transfer to the vehicle, which is the difference between the heat input and the heat out. Heat input consists of two components: a convection heating term (q_{conv}) and a chemical recombination heating term ($q_{catalytic}$). The chemical recombination heating results when dissociated gas species (oxygen and nitrogen) present in the flow-field boundary layer recombine at the vehicle surface to form diatomic molecules. Heat is rejected (q_{out}) by the vehicle through radiative heat transfer. Thus the two material properties that have direct effect on the steady state temperature of a vehicle subject to aerothermal heating are catalytic efficiency of the surface and the hemispherical emittance of the surface: a low catalytic efficiency reduces the vehicle heating due to chemical recombination and a high emittance increases the heat rejection at the vehicle surface.

$$q_{net} = q_{conv} + q_{catalytic} - q_{out}$$

$$q_{catalytic} \propto \gamma \cdot h_R$$

$$q_{out} \propto \sigma \cdot \epsilon \cdot T^4$$

WHERE

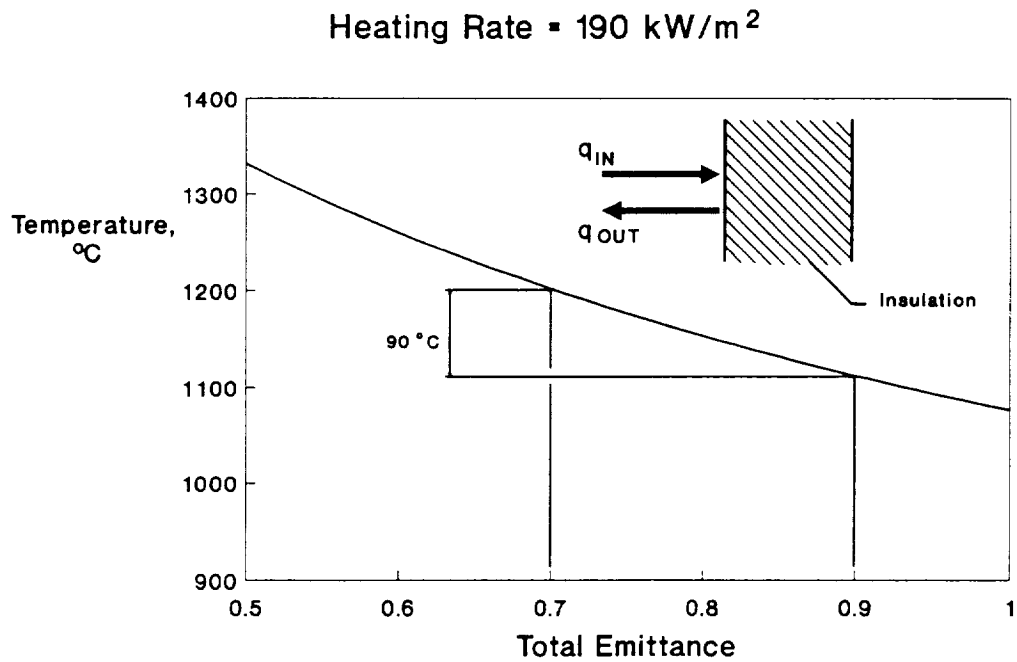
γ CATALYTIC EFFICIENCY

h_R HEAT OF RECOMBINATION

ϵ HEMISPHERICAL EMITTANCE

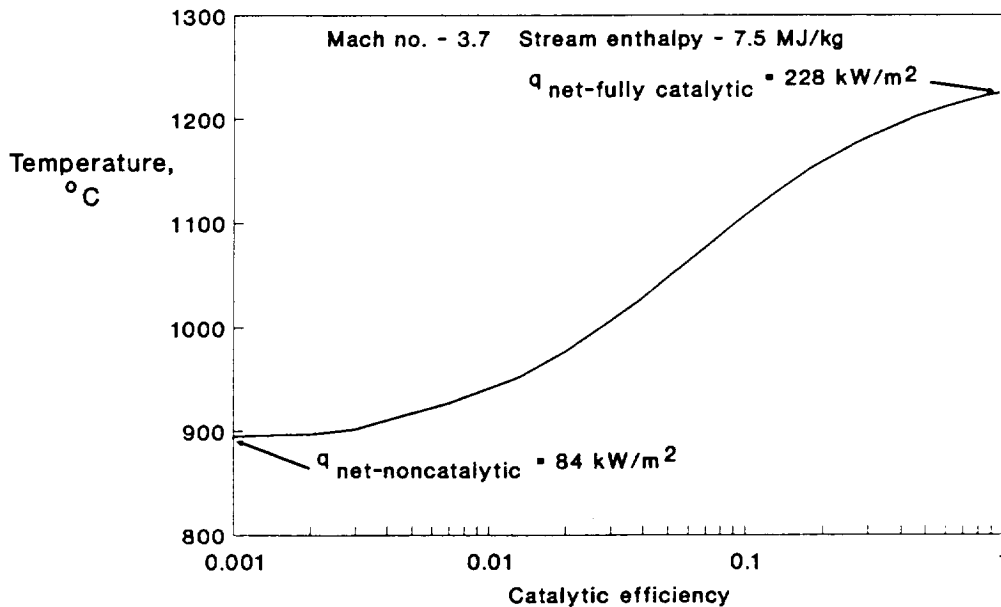
EFFECT OF EMITTANCE ON TEMPERATURE

The effect of emittance on surface temperature is demonstrated by the variation in equilibrium temperature with surface emittance for an insulated surface subjected to a constant heating rate. The figure shows a decrease of 90°C in temperature as the emittance increases from 0.7 to 0.9.



EFFECT OF CATALYTIC EFFICIENCY ON TEMPERATURE
TOTAL EMITTANCE - 0.8

The figure shows the variation in equilibrium temperature with catalytic efficiency for an insulated surface of 0.8 emittance exposed to a mild aerothermal environment (Mach no. 3.7 and 7.5 MJ/kg stream enthalpy). At very low catalytic efficiency levels the aerothermal heating is almost all due to convection heat transfer. At high catalytic efficiency levels, the total heating is more than double the convection heat transfer value. The figure shows that, for the very mild condition of this example, the impact of catalytic heating is to increase the equilibrium temperature by several hundred degrees.

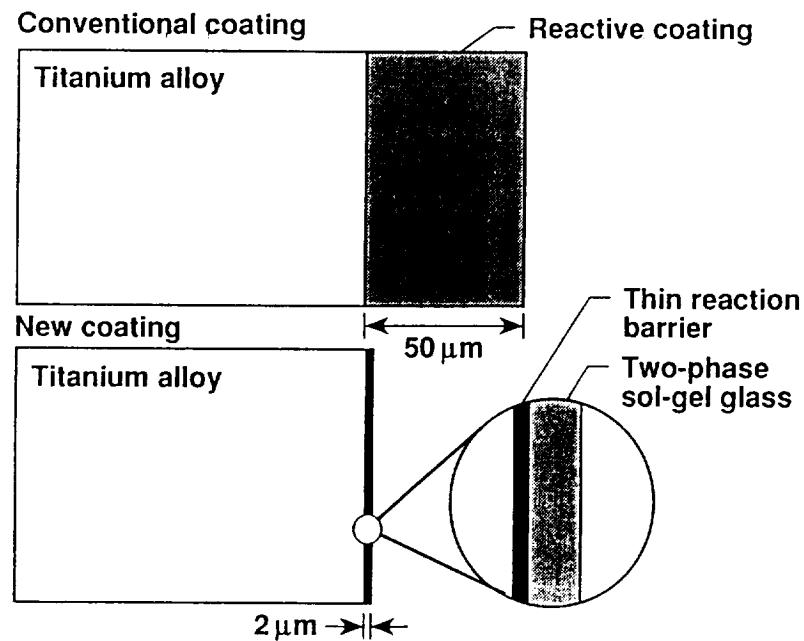


CONVENTIONAL REACTIVE COATING VERSUS THIN MULTI-LAYER GLASS COATING

Conventional coatings that provide good oxidation protection to metallic materials in high temperature oxidizing environments are commercially available. Conventional coatings on titanium-based alloys are typically formed by applying a slurry mixture to the surface and curing them in a furnace at high temperature. During the cure cycle the coating compound reacts with the alloy to form an intermetallic layer, which may be 25 to 50 μm in thickness. Concerns with use of this type coating include: reactive coatings consume substrate material as the coatings are formed, thick coatings represent a substantial weight penalty, and a very low ductility intermetallic layer at the surface may reduce the fracture toughness of the alloy.

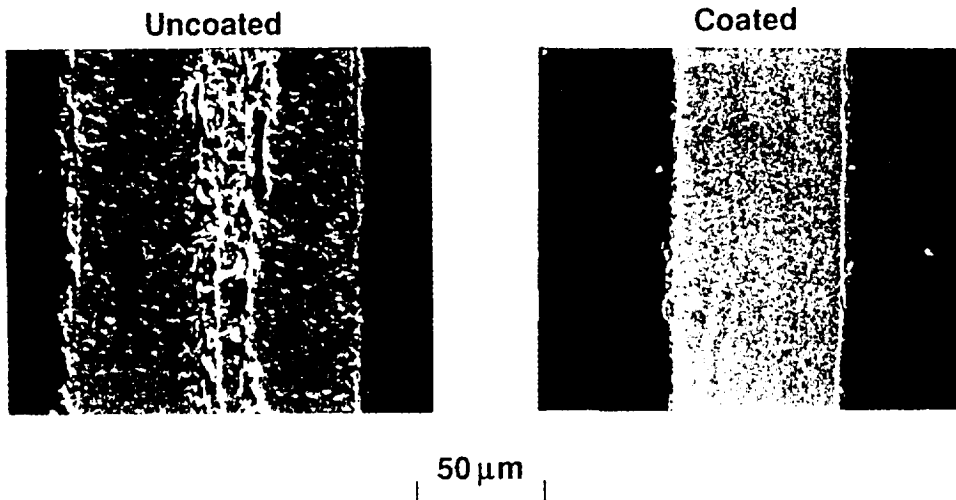
Development of new coatings was undertaken to overcome the limitations of conventional coatings. The focus of the coating research at LaRC was on achieving stable, thin, oxidation and/or thermal control coatings. Materials such as SiO_2 and Al_2O_3 , which have a low oxygen diffusivity, tend to react with titanium at high temperatures so the coating design includes multiple layers: a thin reaction barrier layer separating the alloy from a self-healing diffusion barrier layer. One form of diffusion barrier layer is shown in the figure: a two-phase glass wherein one phase becomes molten at high temperature and provides healing of any defects that form in the coating.

LaRC advances: Thin protective coatings from two-phase sol-gel glasses



CROSS-SECTIONAL MICROGRAPH OF CP TITANIUM
Static oxidation, 1 hr at 982°C

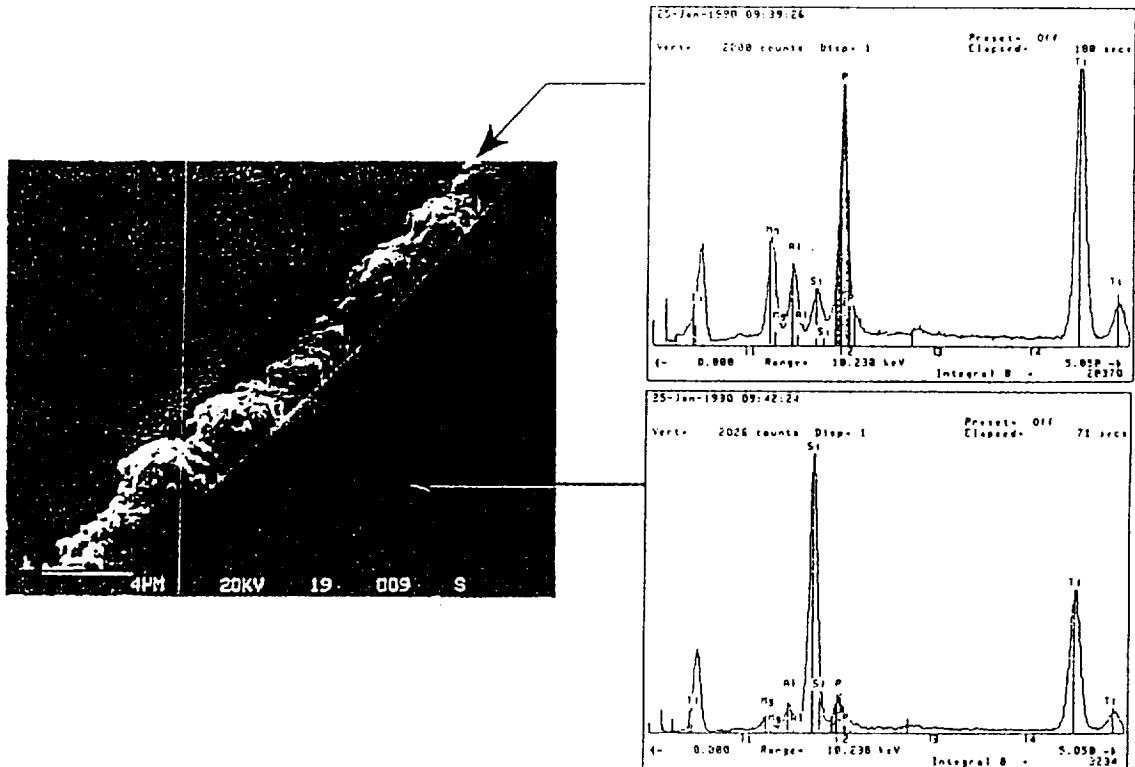
Many of the developmental activities related to sol-gel coatings technology were carried out using commercial purity titanium, which is highly reactive with oxygen at elevated temperature, so that coating imperfections and defects are easily observed. The figure shows cross-sectional micrographs of coated and uncoated titanium samples after static oxidation for 1 hr at 982°C. The uncoated sample was fully oxidized during that exposure, but the sample coated with a reaction barrier plus a two-phase glass shows no evidence of oxidation.



(Original figure unavailable)

**MICROGRAPH OF SURFACE OF COATED TITANIUM:
LOW MELT P-RICH PHASE FILLS CRACKS IN COATING
Oxidized 1 hr at 982°C**

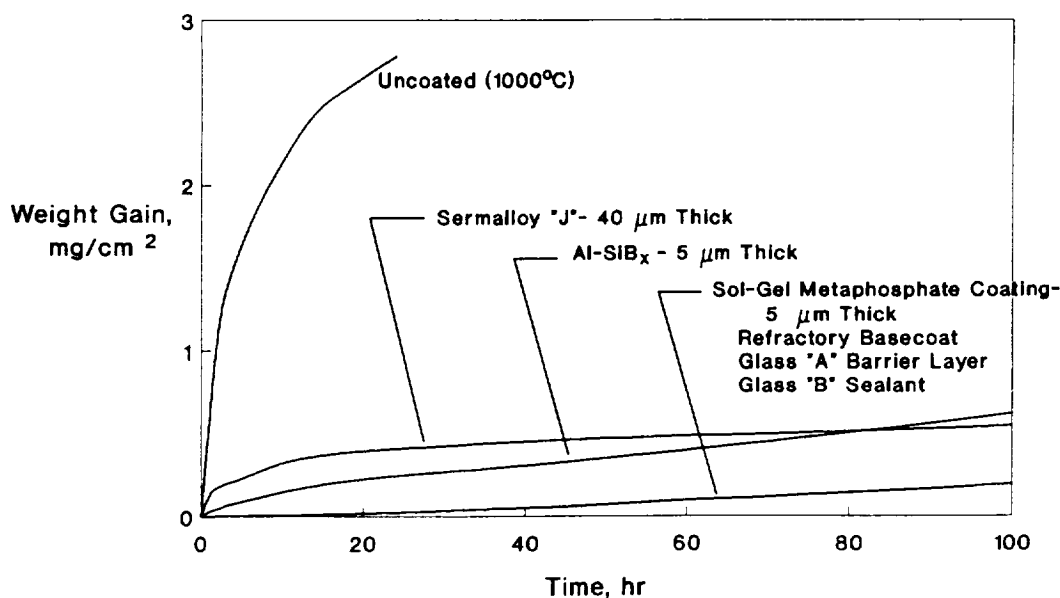
The figure contains a micrograph of the surface of a coated titanium sample that has been oxidized for 1 hr at 982°C. The surface is traversed by a 2- μm wide crack. Elemental analysis of the surface region of the crack showed the region to be phosphorus-rich, while the region distant from the crack is primarily silicon. These results provide graphic evidence of how the two-phase glass coating performs: microcracks that form in the glass coating are sealed by the lower melting phosphorus-rich glass phase which flows into the cracks to fill them. The two-phase glass coating is, therefore, self-healing.



(Original figure unavailable)

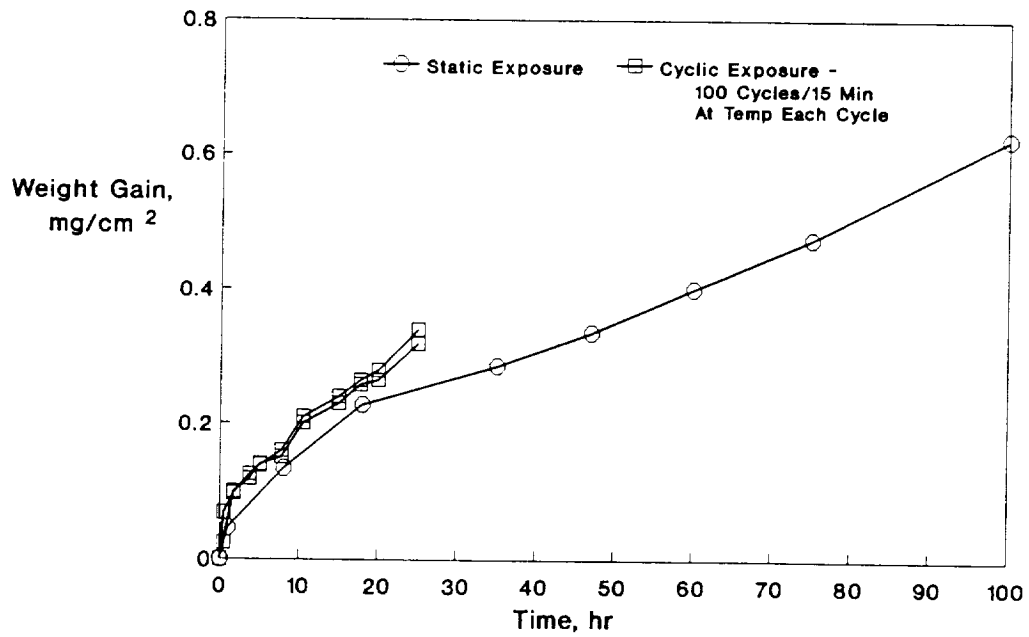
OXIDATION PROTECTIVE COATINGS STATIC OXIDATION OF Ti-14Al-21Nb AT 982°C

One assessment of the performance of oxidation protective coatings is obtained from static oxidation tests using a thermogravimetric apparatus that measures the weight change of a sample with time of exposure to oxidizing conditions. The figure shows weight gain for 982°C-100 hr static oxidation tests of Ti-14Al-21Nb samples with no coating and coated with Sermalloy "J", Al-SiB_x, and a multi-layer sol-gel coating. The Sermalloy "J" coating is a commercially available diffusion-type coating that measures about 40 μm in thickness. Because it performs very well as an oxidation protection coating it is included here as a reference for evaluating other coatings. The Al-SiB_x coating is a proprietary coating of Lockheed Missiles and Space Company. It is about 5 μm thick and is applied by physical vapor deposition (PVD) and chemical vapor deposition (CVD). Two 2 μm-thick layers of SiB_x (applied by CVD) are separated by a 1 μm-thick layer of aluminum (applied by PVD). The deposit is then cured in air at 982°C to form an "alumino-borosilicate-like" glass. The multi-layer sol-gel coating is about 5 μm thick and consists of a 0.5 μm thick refractory base-coat plus a two-layer-glass oxygen protection barrier layer. A 4 μm thick glass "A" serves as an oxygen diffusion barrier and a 0.5 μm thick glass "B", designed to be molten at the exposure temperature, functions to seal cracks and other defects in the diffusion barrier layer. For the conditions investigated here, all the coatings investigated provided some oxidation protection to the substrate. The multi-layer sol-gel coating provides the best oxidation protection for Ti-14Al-21Nb alloy and the Al-SiB_x and Sermalloy "J" coatings provide about equal protection.



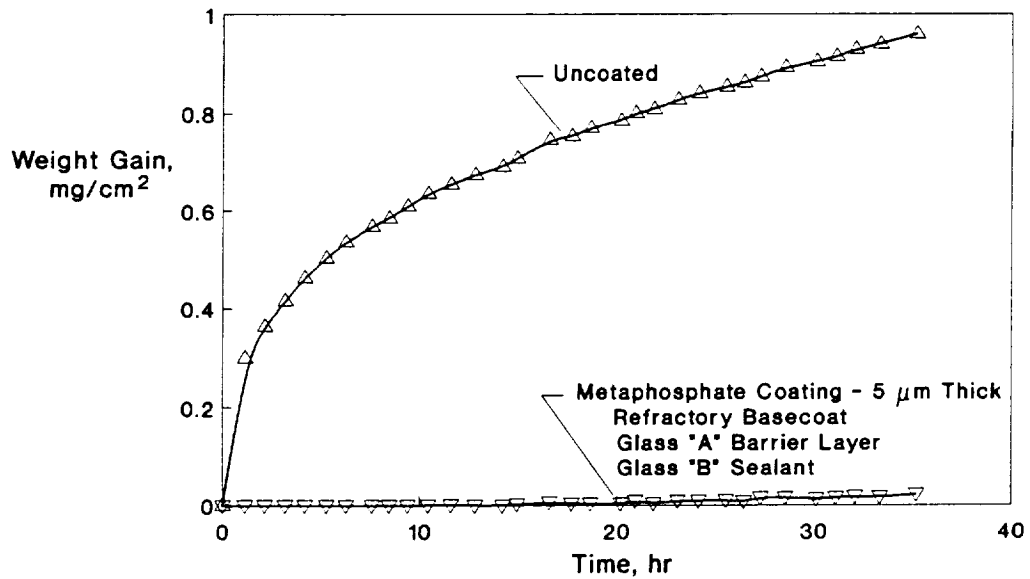
**Al-SiB_x COATING: STATIC VERSUS CYCLIC OXIDATION
Ti-14Al-21Nb IN AIR AT 982°C**

The Al-SiB_x coating has been evaluated under cyclic oxidation conditions. The figure shows cyclic oxidation weight gain data for 100 cycles with 15 min at temperature for each cycle. The total weight gain after 100 cycles was about 15% greater than for static oxidation exposure for the same cumulative times.



CYCLIC OXIDATION: SOL-GEL COATING ON BETA-21S ALLOY
Each Cycle Nominal 1 hr at 800°C

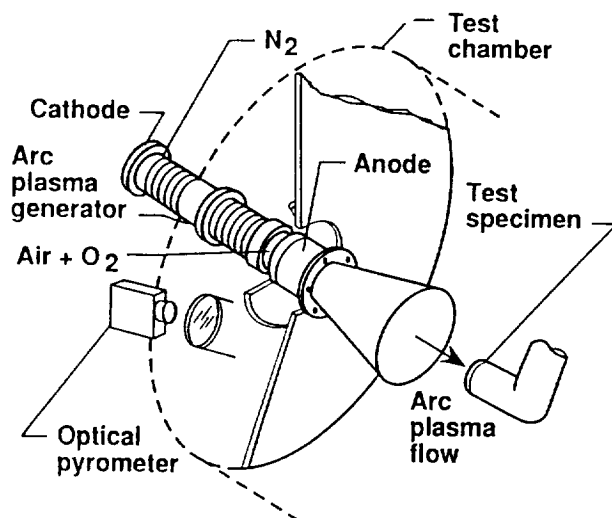
The figure shows weight gain data for 800°C cyclic oxidation tests of uncoated Beta-21S titanium alloy and the alloy with a 5 μm thick multi-layer metaphosphate coating. The data show that oxidation weight gain for the alloy with the coating was about 2% of the level for the uncoated alloy.



SCHEMATIC DIAGRAM OF LaRC HYMETS FACILITY

Thermal control/environmental coatings were tested under simulated hypersonic flight conditions at surface temperatures from 800 to 982°C in the NASA Langley Research Center Hypersonic Materials Environmental Test System (HYMETS). The HYMETS is a 100-kW constrictor-arc heated wind tunnel (Ref. 1). The test facility consists of the arc heater, a test chamber with three model insertion stings, and continuous-duty air pumps. Test samples, measuring 2.5 cm in diameter, were mounted on stagnation model adapters attached to the insertion stings. Another sting contained a water-cooled heating rate and pressure probe that measured the cold-wall heating rate and the surface pressure. The test gas was a mixture of air plus nitrogen and oxygen in ratios equivalent to air. High purity nitrogen was introduced at the cathode, and air and high purity oxygen were introduced in the plenum upstream of the supersonic nozzle. The temperature of the samples during exposure was monitored by a thermocouple attached to the back surface of the sample. The power input to the arc heater and the gas flow rate in the facility were controlled to maintain the desired sample temperature during tests.

The range of HYMETS test conditions that can be achieved are shown in the figure. These test conditions do not provide for full simulation of hypersonic flight conditions; however, the heating rate (the most critical test parameter) is representative of the levels encountered by a significant portion of a vehicle in hypersonic flight. Chemical equilibrium calculations for the operating conditions used in the present study indicate that oxygen in the test stream was almost fully dissociated (> 95%) and the nitrogen was only slightly dissociated (< 5%) (Ref. 2).

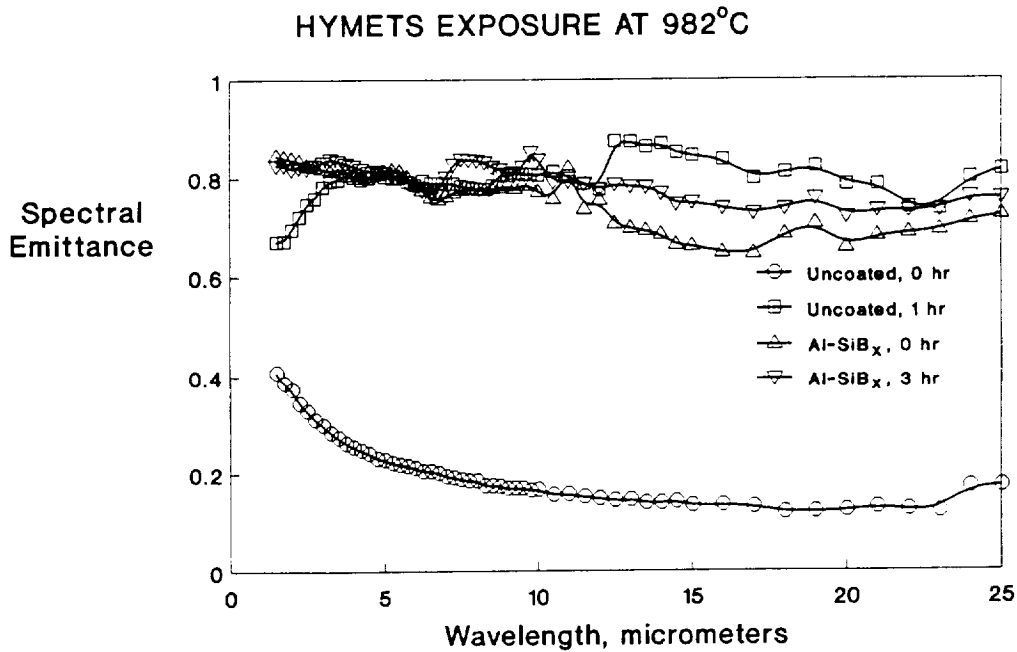


Range of test conditions

Specimen	2.5 cm diam., stagnation
Spec. Temp, °C	800 - 1500
Surface pressure, Pa	400 - 800
Free stream enthalpy, MJ/kg	4 - 11
Free stream Mach no.	3.5 - 4.0
Cold wall heating rate, kW/m ²	80 - 450

SPECTRAL EMITTANCE OF Ti₃Al-Nb ALLOY

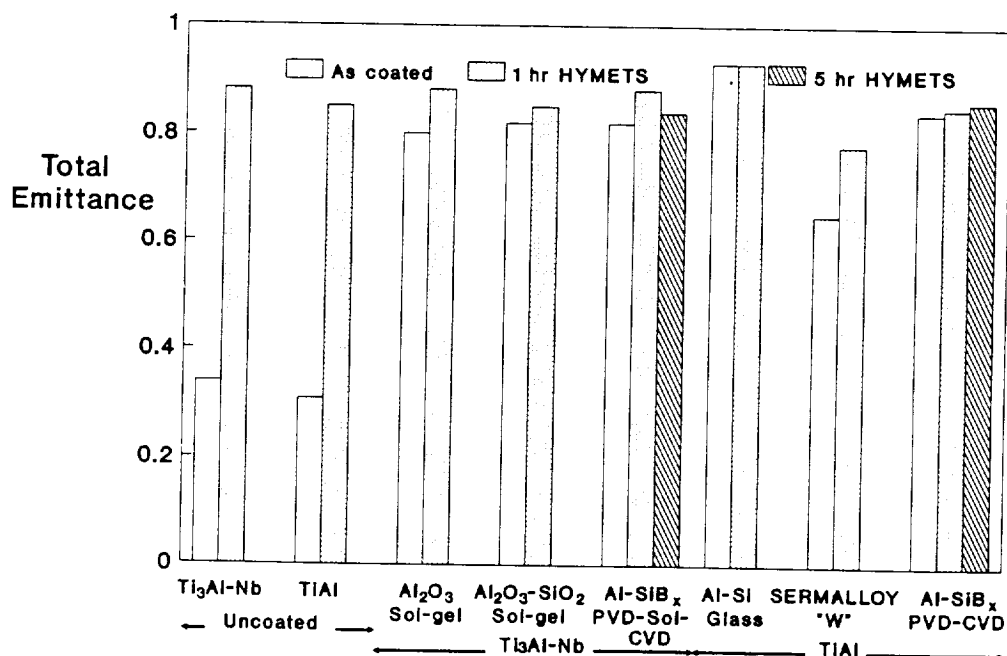
Room-temperature spectral near-normal reflectance measurements were made over the wavelength range of 1.5 to 25 μm using a Gier Dunkle Model HCDR 3 heated-cavity reflectometer (Ref. 3). Emittance was calculated from reflectance using the following relationships: absorptance equals unity minus reflectance, and (from Kirchhoff's law) emittance equals absorptance. The figure shows spectral emittance data for coated and uncoated Ti-14Al-21Nb alloy before and after testing in the HYMETS facility. The coating is a proprietary Al-SiB_x coating developed by Lockheed Missiles and Space Company. The emittance of the coated sample was uniformly high before and after testing. The low emittance of the uncoated sample before testing is typical of the emittance of bare metal surfaces. After testing, the uncoated sample exhibited a substantially higher emittance compared to the data before testing. The increase in emittance with testing of the uncoated sample was due to the heavy oxide layer that formed at the surface during testing.



**TITANIUM-ALUMINIDE ALLOYS AND COATINGS
TOTAL EMITTANCE AT 982°C**

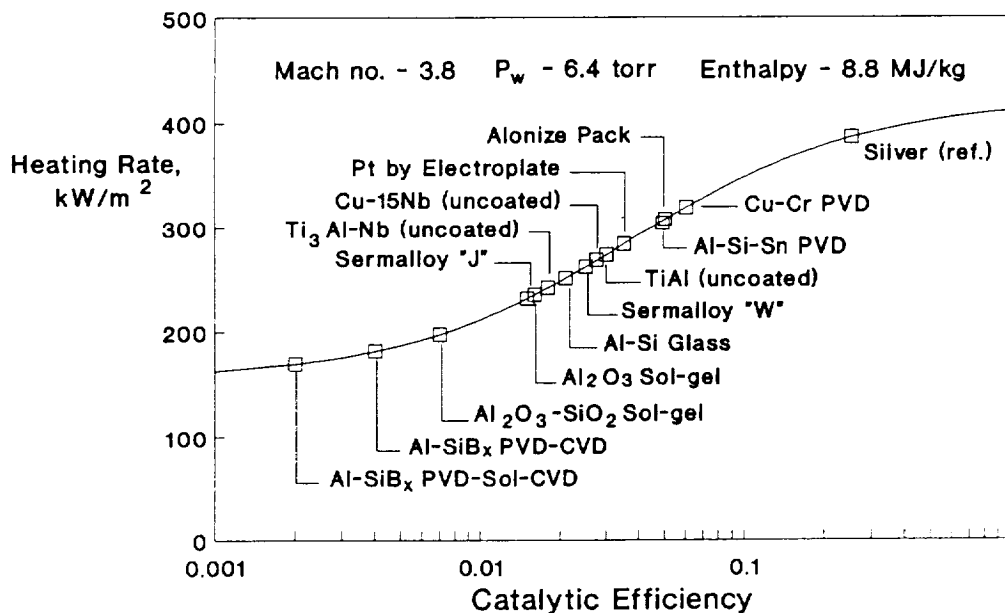
The total normal emittance at 982°C was obtained by numerically integrating the spectral emittance data over wavelength, where the spectral data was weighted by the Planck blackbody energy distribution function at 982°C (Ref. 4). The figure shows a comparison of total normal emittance of uncoated Ti₃Al-Nb and TiAl alloys and six coatings of current interest. Data are shown for two sol-gel coatings (Al₂O₃ and Al₂O₃-SiO₂), a glass slurry coating (Al-Si), a commercially available reactive coating (Sermalloy "W"), and two Al-SiB_x coatings (one produced by a three-step PVD-Sol-CVD process and one by a two-step PVD-CVD process).

The total emittance of the uncoated alloys after HYMETS testing was significantly higher than before testing. The Sermalloy "W" coated TiAl sample had a lower emittance than did the remaining coatings: in fact the Sermalloy "W" coating did not meet the performance requirement goal of 0.8 for emittance of thermal control coatings for hypersonic applications. Emittance data for other candidate thermal control coatings were reported in Ref. 5.



VARIATION IN COLD-WALL HEATING WITH CATALYTIC EFFICIENCY

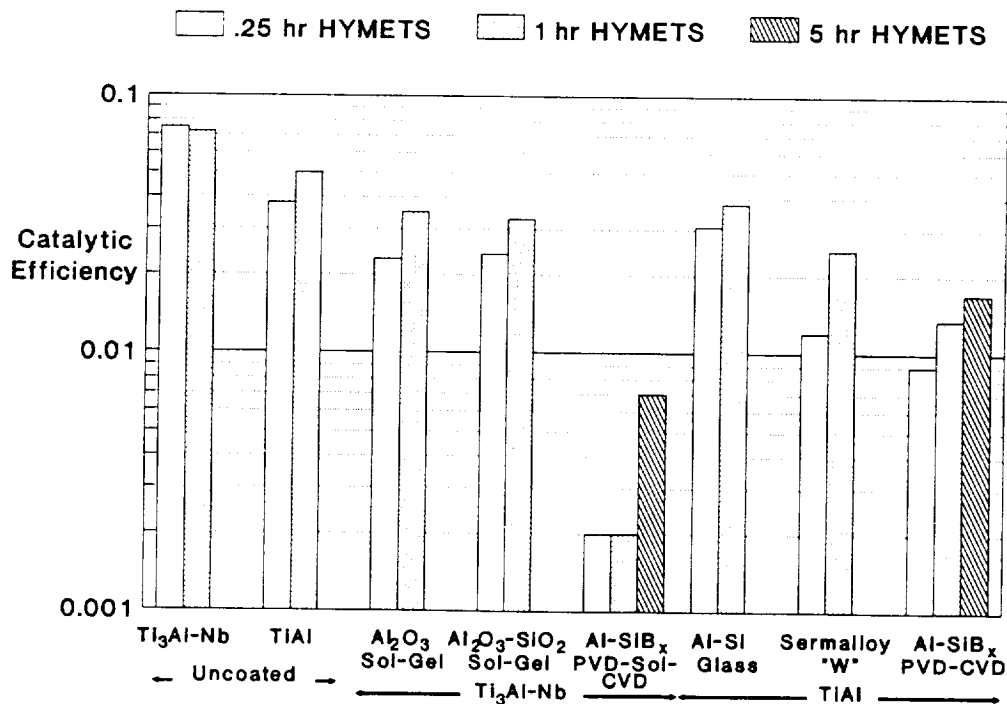
The figure shows the variation in cold-wall heat transfer with catalytic efficiency for a sample exposed to a Mach 3.8 flow with a total enthalpy of 8.8 MJ/kg and a wall pressure of 6.4 torr. For non-catalytic surfaces (very low catalytic efficiencies) the heating is almost totally due to convective heat transfer. The data show that, for this test condition, the catalytic heating (heating due to recombination of dissociated oxygen and nitrogen at the surface) to a fully catalytic surface is greater than the convective heating. As a point of reference, for a hypersonic vehicle operating at a surface temperature of 1175°C, a change in the heating rate from 200 kW/m² to 300 kW/m² could increase the equilibrium surface temperature by about 165°C. This figure also presents representative data for a number of coatings and for uncoated Ti₃Al-Nb, TiAl, and Cu-Nb alloys. Silver, which has a catalytic efficiency of 0.25 (Ref. 6), was used as a reference. The catalytic efficiencies of uncoated samples and some metallic coatings were somewhat lower than the catalytic efficiency of silver. The Al-SiB_x coatings and the Al₂O₃-SiO₂ coating had much lower catalytic efficiencies than the remaining coatings and the uncoated samples. Catalytic efficiency data for other coatings were reported in Ref. 5.



**TITANIUM-ALUMINIDE ALLOYS AND COATINGS
CATALYTIC EFFICIENCY AT 982°C**

The catalytic efficiencies of samples under steady-state heating conditions were determined using the aerothermal heating to the sample (calculated as the sum of energy radiated from the sample and energy conducted to the sample holder) with the HYMETS operating conditions and Goulard's solution to the stagnation laminar flow heating equation (Ref. 7 and 8). For hot structures at hypersonic flight conditions, these data are more important than the room temperature catalytic efficiencies shown in the previous figure.

This figure shows a comparison of catalytic efficiencies at 982°C for uncoated Ti₃Al-Nb and TiAl alloys and for six coatings. The catalytic efficiency of each of the coatings was somewhat lower than the catalytic efficiencies of the uncoated alloy samples. The lowest catalytic efficiencies were exhibited by the Al-SiB_x coatings: one formed by a three step PVD-sol-CVD process and one formed by a two step PVD-CVD process. Catalytic efficiency data for other coatings were reported in Ref. 5.



CONCLUDING REMARKS

NASA Langley Research Center has devoted extensive research and development effort to thermal control and oxidation-resistant coatings for titanium-based alloys. More than 40 different alloy-coatings systems have been evaluated for potential use as environmental/thermal control applications on hypersonic vehicles. A number of the coatings evaluated have a high emittance and a low catalytic efficiency compared to the uncoated alloys. The most attractive thermal control coating examined to date is an Al-SiB_x coating: its emittance is high and its catalytic efficiency is the lowest measured to date; with a thickness of 5 μm, it compares favorably with commercially available oxidation protection coatings that are up to 50 μm in thickness; and it is applied by processes that can be scaled-up to coat large structures.

NASA LaRC has made significant progress in development of oxidation protection coatings based on sol-gel processes. The oxidation protection by a 5 μm-thick multi-layer coating prepared by sol-gel processes is superior to any other coating evaluated to date.

REFERENCES

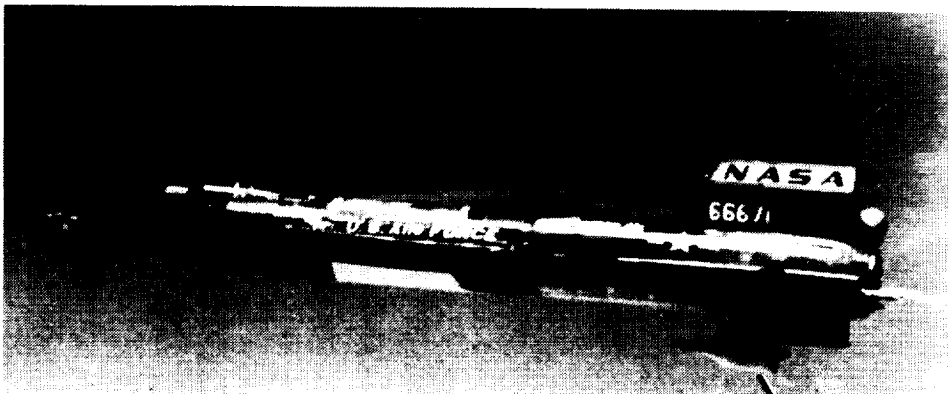
1. Schaefer, J. W.; Tong, H.; Clark, K. J.; Suchsland, K. E.; and Neuner, G. J.: Analytic and Experimental Evaluation of Flowing Air Test Conditions for Selected Metallics in a Shuttle TPS Application. NASA CR-2531, 1975.
2. Clark, R. K.; Cunnington, G. R.; and Robinson, J. C.: Vapor Vapor-Deposited Emittance-Catalysis Coatings for Superalloys in Heat-Shield Applications. J. Thermophysics and Heat Transfer, vol. 1, no. 1, Jan. 1987, pp. 28-34.
3. Dunkle, R. V.; Edwards, D. K.; Gier, J. T.; Nelson, K. E.; and Roddick, R. D.: Heated Cavity Reflectometer for Angular Reflectance Measurements. Masi, J. F.; and Tsai, D. H., eds: Progress in International Research on Thermodynamic and Transport Properties, Academic Press, New York, 1962.
4. Touloukian, Y. S.; and Dewitt, D. P., eds.: Thermal Radiative Properties--Nonmetallic Solids. IFI/Plenum, 1972.
5. Clark, R. K.; Wallace, T. A.; Mullaly, J. R.; and Wiedemann, K. E.: Oxidation/Thermal Control Coatings for Titanium-Aluminide Intermetallic Alloys. NASA TM-4152, 1990.
6. Linnett, J. W.; and Marsden, D. G. H.: The Kinetics of the Recombination of Oxygen Atoms at a Glass Surface. Proc. of the Royal Society, series A, vol. 234, March 1956, pp. 489-504.
7. Goulard, R.: On Catalytic Recombination Rates In Hypersonic Stagnation Heat Transfer. J. Jet Propulsion, vol. 28, 1958, pp. 737-745.
8. Wiedemann, K. E.; Clark, R. K.; and Sankaran, S. N.: Emittance, Catalysis, and Dynamic Oxidation of Ti-14Al-21Nb. NASA TP-2955, 1989.

ACTIVE COOLING FROM THE SIXTIES TO NASP

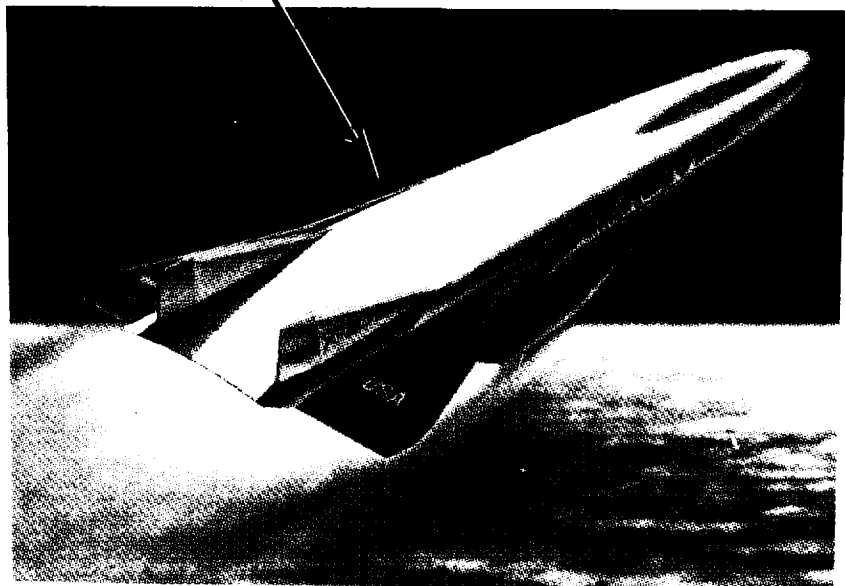
H. Neale Kelly and Max L. Blosser

INTRODUCTION

Vehicles, such as the X-15 or National Aero-Space Plane shown in figure 1, traveling at hypersonic speeds through the earth's atmosphere experience aerodynamic heating. The heating can be severe enough that a thermal protection system is required to limit the temperature of the vehicle structure. Although several categories of thermal protection systems are mentioned briefly, the majority of the present paper describes convectively cooled structures for large areas. Convective cooling is a method of limiting structural temperatures by circulating a coolant through the vehicle structure. Efforts to develop convectively cooled structures during the past 30 years — from early engine structures, which were intended to be tested on the X-15, to structural panels fabricated and tested under the National Aero-Space Plane (NASP) program — are described. Many of the lessons learned from these research efforts are presented.



X15/Hypersonic Research Engine



National Aero-space Plane

Figure 1

THERMAL PROTECTION SYSTEM CONCEPTS

Hypersonic vehicles encountering severe enough aerodynamic heating require a thermal protection system (TPS) to limit structural temperatures to acceptable levels. The type of TPS required depends largely on the magnitude and duration of the surface heating. Because the heating varies over the surface of a vehicle, several different types of TPS may be used on the same vehicle. Some of the TPS concepts which have been considered are indicated schematically in figure 2. The concepts are divided into three broad categories: passive, semi-passive and active. As defined in figure 2, passive concepts have no working fluid to remove heat — the heat is either radiated from the surface or absorbed in the structure. Semi-passive concepts have a working fluid which removes heat from the point of application, but require no external systems to provide or circulate the coolant during flight. Active concepts have an external system which provides coolant during the flight to continually remove heat from the structure or prevent heat from reaching the structure.

The simplest, lightest weight TPS concept which will accommodate the design surface heating is generally selected. The concepts, shown schematically in figure 2, are arranged in approximate order of increasing heat load capability. The passive systems are the simplest, but have the lowest heat load capability. The heat sink concept absorbs almost all the incident heat and stores it in the structure. Additional thermal mass may be added to increase the heat storage capability, but the concept is limited to short heat pulses. A hot structure design allows the structural temperature to rise until the heat being radiated from the surface is equal to the incident heating. This concept is not limited by the duration of the heat pulse, but is limited by the acceptable surface temperature for proposed materials. Currently, carbon-carbon material, which has the highest operating temperature of the materials being considered for hot structures is limited by its oxidation resistant coating to a maximum temperature of about 3000°F (this surface temperature corresponds to a radiation equilibrium heat flux of 55 Btu/ft²-sec for a surface emittance of 0.8). Insulation systems have features of both heat sink and hot structure. The surface becomes hot and radiates away most of the incident heating. Insulation prevents all but a fraction of the incident heating from reaching the underlying structure. The structure acts as a heat sink to store the heat that reaches it. Although both the magnitude and duration of the heating are limited for insulated systems, lower temperature structural materials can be used.

Two semi-passive concepts are illustrated in figure 2. Heat pipes are attractive for areas where there is a localized area of high heating with an adjacent area of low heating (below radiation equilibrium temperature for the heat pipe material). Heat is absorbed into the heat pipe at the highly heated area. The absorbed heat vaporizes a working fluid. The resulting vapor flows to a cooler region where it condenses and the heat is rejected. The condensed working fluid is returned to the highly heated region by capillary action. Ablators undergo a chemical reaction which generates gases that block much of the aerodynamic heating to the vehicle surface. However, the ablator is consumed in the process, thus requiring refurbishment and limiting the duration of its operation.

Three active cooling concepts are shown in figure 2. Both transpiration and film cooling operate on a principle similar to that of ablation — coolant ejected from the surface blocks most of the aerodynamic heating from reaching the structure. These two concepts use an external pumping system to bring the coolant from a remote reservoir and eject it from the surface. Transpiration cooling involves ejecting the coolant through a porous surface, whereas film cooling involves ejecting the coolant essentially parallel to the flow from discrete slots. The mass penalties associated with the expendable coolant usually

limit these concepts to small, highly heated regions. Convective cooling is accomplished by circulating coolant through passages in the structure to remove the absorbed heat due to aerodynamic heating. Almost all of the incident heating is transferred through the outer skin into the coolant. If the heat is transferred to the fuel before it is burned, the system is called a regenerative cooling system. Development of convectively cooled structures is the subject of the present paper and the following figures illustrate some of the fundamental issues which must be addressed to design such structures.

THERMAL PROTECTION SYSTEM CONCEPTS

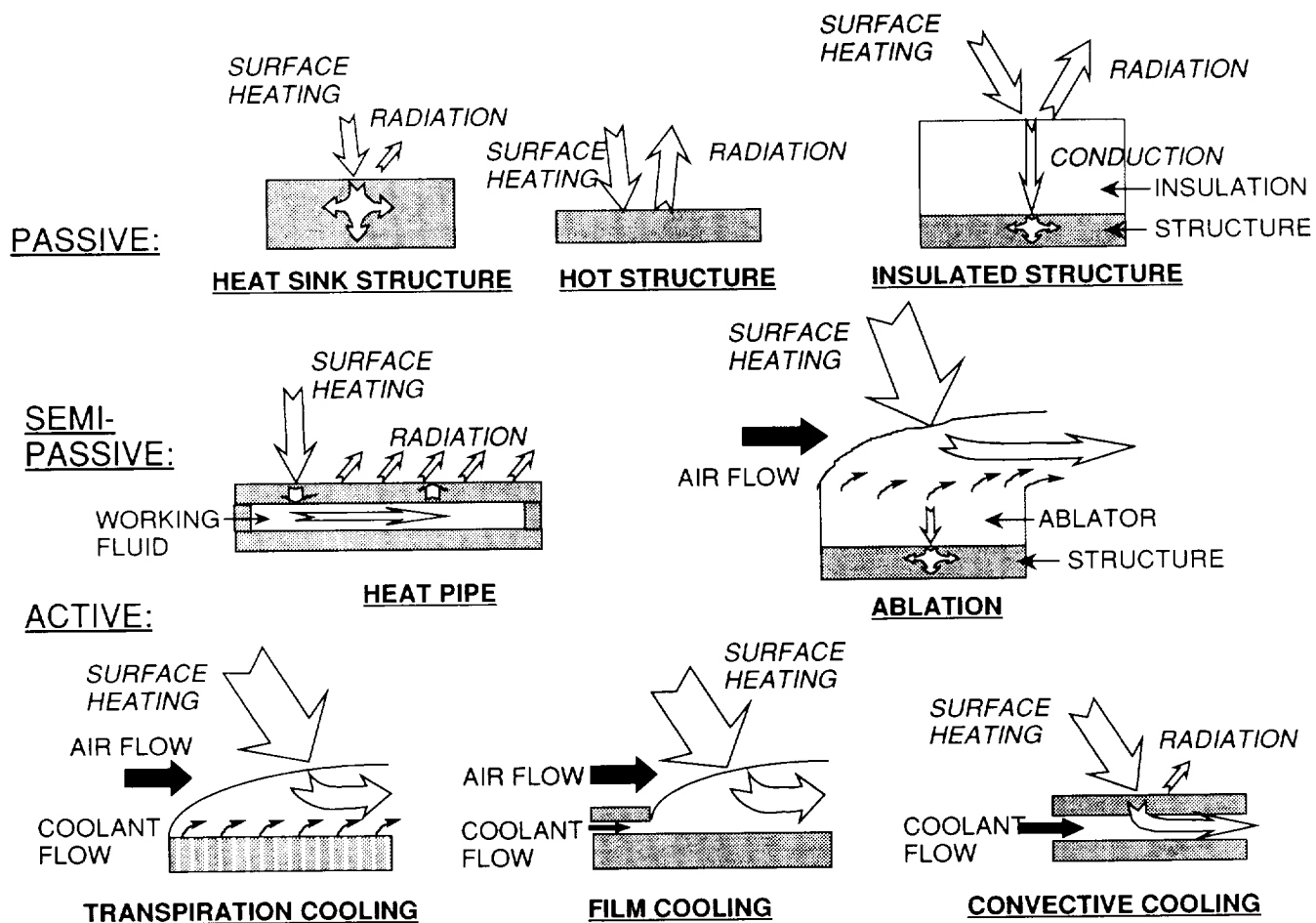


Figure 2

CONVECTIVELY COOLED STRUCTURE

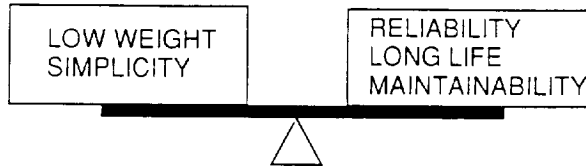
Design of convectively cooled structures requires balancing sometimes conflicting objectives. As for all aerospace structures, low weight is one of the most critical design objectives. Simplicity, reliability, long life and maintainability are also important.

Some of the fundamental design issues are illustrated in figure 3. The local thermal response of a convectively cooled structure is illustrated on the left of the figure. Most of the incident heat flux is conducted through the outer skin and transferred into the coolant, which carries it to another location on the vehicle. Because, for most actively cooled structures, the coolant keeps the surface temperature well below the radiation equilibrium temperature, the amount of heat radiated from the surface is usually considered negligible compared to the amount incident heat absorbed at the surface. The primary local thermal behavior is one dimensional and can be represented by the simple equations on figure 3. Assuming that all of the heat is conducted through the skin and is transferred into the coolant from the back surface of the skin, the temperatures can be calculated using the one-dimensional conduction and convection equations. In these equations the symbols are defined as follows: q is the heat flux; k is the thermal conductivity of the outer skin; t is the thickness of the outer skin; h is the convective heat transfer coefficient between the skin and the coolant; T_o is the temperature of the outer surface of the skin; T_i is the temperature of the inner surface of the skin; T_c is the temperature of the coolant; T_s is the temperature of the underlying structure; σ is the thermal stress in the outer skin; E is the modulus of elasticity of the skin material; and α is the coefficient of thermal expansion of the skin material. The two one-dimensional equations can be combined to produce an expression for the outer skin temperature, which is the maximum temperature of the cooled panel in this one-dimensional model. The temperature variation through the thickness of the outer skin can lead to significant thermal stresses, as illustrated on the right side of figure 3. If the outer skin were free to expand it would deform to a shape similar to that shown in the figure. However, the outer skin is usually attached to a much stiffer substructure which constrains its deformation. The outer skin can expand only as much as the substructure to which it is attached. The resulting thermal stress can be approximated by the one-dimensional equation shown in figure 3. Notice that the maximum stress depends on the difference between the outer skin temperature and the substructure temperature. If the substructure temperature is assumed to be the same as the coolant temperature, the equation for the outer skin temperature can be combined with the equation for thermal stress as shown on figure 3. From the resulting equation it can be seen that the standard practice of increasing the thickness to reduce mechanical stress would have the opposite effect for this thermal stress — the stress would increase! Therefore it is not always possible to design the skin considering only linear elastic behavior. These high local thermal stresses may lead to designs limited by more complicated material behavior such as creep and low cycle fatigue.

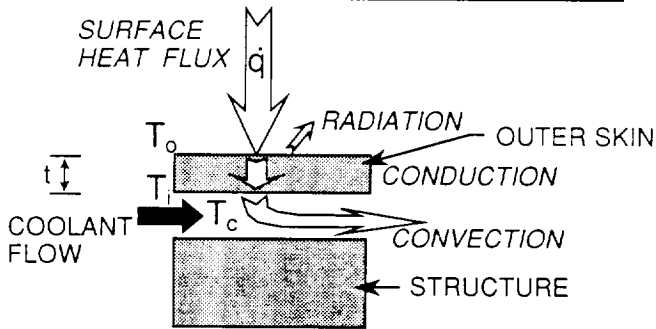
Local thermal stresses must be accommodated before a convectively cooled panel design can be successful. However, the cooled panel is only part of a cooling system and there are many other important considerations. Some of the other components of a cooling system are illustrated in the next figure.

CONVECTIVELY COOLED STRUCTURE

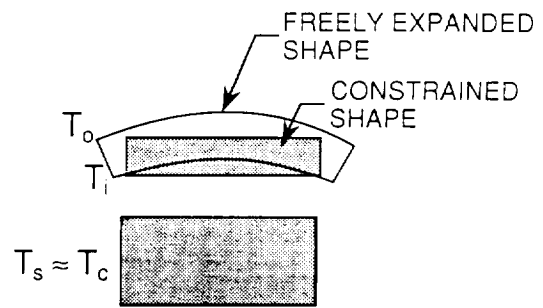
OBJECTIVES:



LOCAL THERMAL RESPONSE



LOCAL STRUCTURAL RESPONSE



1-D Conduction 1-D Convection

$$\dot{q} = \frac{k}{t}(T_o - T_i) \quad \dot{q} = h(T_i - T_c)$$

$$T_o = \dot{q} \left(\frac{t}{k} + \frac{1}{h} \right) + T_c$$

1-D Thermal Stress

$$\sigma_{\max} = E \alpha (T_o - T_s)$$

$$\sigma_{\max} = E \alpha \dot{q} \left(\frac{t}{k} + \frac{1}{h} \right)$$

Figure 3

CONVECTIVE COOLING SYSTEMS

Two different convective cooling systems are shown in figure 4: direct hydrogen cooling and indirect cooling. In the direct cooling system the hydrogen fuel flows directly through the cooled panel enroute to the engine to be burned. In the indirect system a secondary coolant, which may be a more easily pumped liquid instead of hydrogen, circulates through the cooled panel and then through a heat exchanger which transfers the heat to the hydrogen fuel. For both systems the heat transferred to the fuel has a beneficial effect on the combustion process. Because the heat is used rather than simply rejected overboard, this type of cooling is sometimes called regenerative cooling. Both systems circulate the coolant through many small passages in a cooled panel. An inlet manifold is required to feed coolant into the multiple passages and an outlet manifold is needed to remove coolant from the passages. Plumbing and a pump are necessary to route the coolant to and from the cooled panel. For the indirect cooling system an additional pump, a heat exchanger, and perhaps a secondary coolant reservoir may also be required. All of these items add complexity and weight, but are essential if an actively cooled structure is required to accommodate the aerodynamic or combustion heat loads. Also, some systems are designed with redundant coolant circuits in an attempt to increase reliability. However, this redundancy results in an increase in weight and complexity.

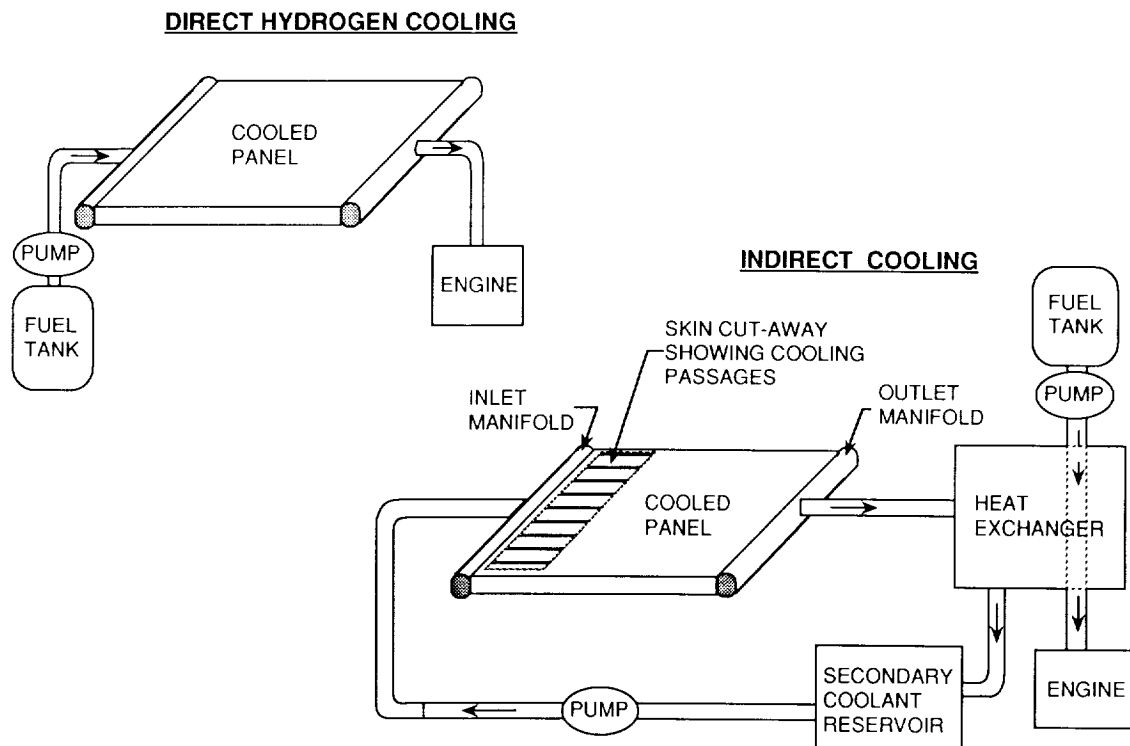


Figure 4

TIME LINE FOR DEVELOPMENT OF CONVECTIVELY COOLED STRUCTURES

A time line for the development of convectively cooled structures is shown in figure 5. During the late 1950's and 1960's there was considerable interest, both in NASA and the Air Force, in hypersonic vehicles. This interest included extensive system studies and, in some cases, the development and testing of convectively cooled structures. Unfortunately, the Air Force interest in hypersonics waned in the mid to late 1960's.

There has been continuous interest in both the Air Force and NASA in cooled structures for rockets. However, these are relatively short lived structures compared with the structure required for engines and airframes of hypersonic cruise type vehicles. Most of the cooled structures research for hypersonic cruise vehicles during the 1970's and early 1980's was at the Langley Research Center — although there was continuing interest in hypersonic cruise missiles at the Johns Hopkins Applied Physics Laboratory. Research on hypersonics reached a low ebb during the late 1970's and early 1980's. Subsequently, the advent of the National Aero-Space Plane (NASP) has led to a resurgence of interest in hypersonics.

The sections that follow provide a somewhat cursory review of the development of actively cooled structures (primarily at the Langley Research Center) and a summary of lessons learned over the past thirty years. Some of the early work was reported at the 1967 Hypersonics Conference (ref. 1). Much of the engine and airframe work, with the exception of the Hypersonic Research Engine (HRE) effort was reviewed at a 1978 symposium (ref. 2). The HRE work is reported in references 3 and 4. All of the previous work was summarized in papers by Wieting, Shore, McWithey, and Kelly at the First National Aero-Space Plane Symposium (ref. 5). The NASP actively cooled structures effort was reviewed by Kelly et al in papers presented at the Tenth National Aero-Space Plane Symposium (ref. 6) and a Society for Experimental Mechanics Testing Conference (ref. 7).

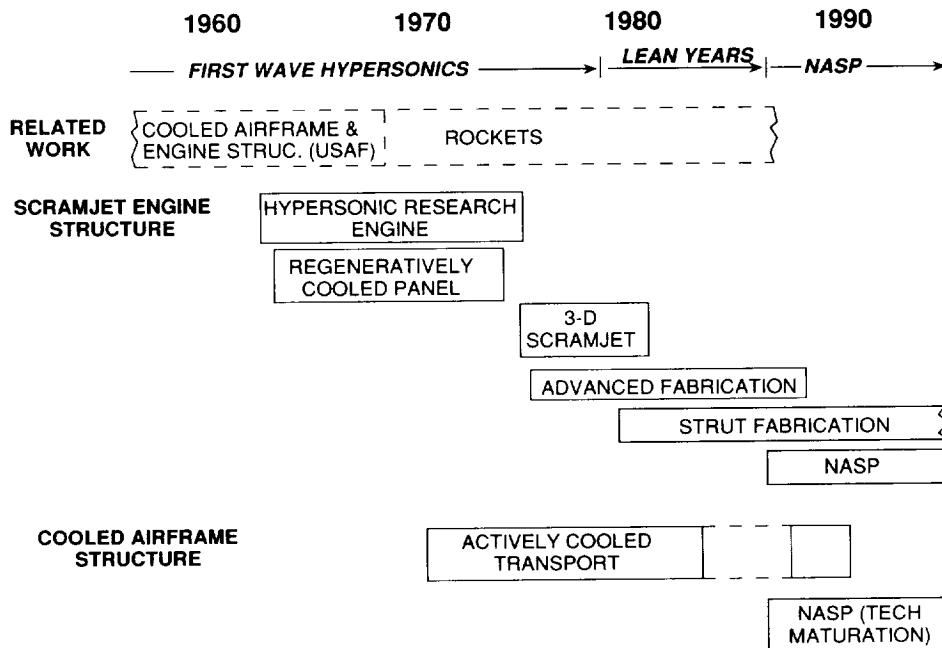
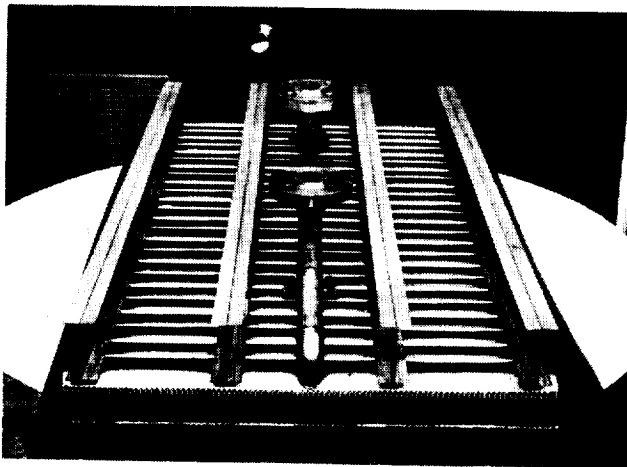


Figure 5

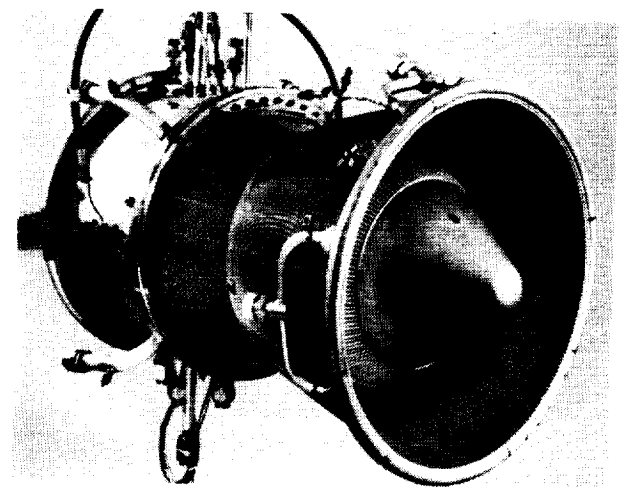
AIR FORCE ACTIVELY COOLED STRUCTURE

The level of sophistication reached by the early Air Force sponsored actively cooled structure development is illustrated by figure 6. An actively-cooled structural panel fabricated by Bell Aerosystems and a cooled engine test rig, fabricated by the Marquart Company as part of the Air Force hypersonic ramjet propulsion project are shown. The design and fabrication of a two by four foot, flat, hydrogen-cooled panel made of a superalloy, Haynes L-605, is documented in reference 8. An extensive reference list of some of the early Air Force cooling studies is also contained in reference 8. Unfortunately, because of waning interest in hypersonics, the Haynes L-605 panel, which developed leaks during proof pressure tests, was never tested.

As part of the Air Force's hypersonic ramjet propulsion program, a 20-inch-diameter by 30-inch-long regeneratively cooled combustion chamber and nozzle was fabricated and tested in a direct connect duct mode. (Air at temperatures, pressures, and flow rates representative of conditions exiting the inlet is supplied by the test facility through a duct connected to the combustor.) This test rig featured a brazed contoured Hastelloy X, D-shaped, cooling tube bundle wall with a Rene' 41 structural overwrap (ref. 9). The combustion chamber and nozzle specimen was exposed to conditions representative of Mach 4 to 6 operation and accumulated a total testing time of approximately one half hour, but was never exposed to the maximum design conditions — Mach 8 with the coolant flow rate equal to the fuel flow rate.



Hydrogen Cooled Panel of
L-605 Alloy



Hypersonic Ramjet Development Engine
2 Jul 68

Figure 6

REGENERATIVELY COOLED ENGINE STRUCTURES

Activity concerned with regeneratively cooled, air-breathing propulsion structures at NASA Langley Research Center is depicted in figure 7. In the 1960's Langley sponsored two comprehensive studies of hydrogen-cooled engine structures: one was a series of generic studies including thermal and structural design, fabrication, and experimental evaluation of regeneratively cooled panels (refs. 10-15); and the other involved the design, fabrication and testing of a complete Hypersonic Research Engine (HRE). The HRE project culminated in the testing of a boiler-plate, operating Aerothermodynamic Integration Model (AIM) in the Hypersonic Test Facility at NASA Lewis Research Center (refs. 3 and 16) and a complete flightweight, hydrogen-cooled Structural Assembly Model (SAM) in the Langley 8-Foot High Temperature Tunnel (refs. 3, 4, and 17). The AIM tests demonstrated the internal performance of the engine at Mach numbers of 5, 6, and 7 and the feasibility of ramjet to scramjet transition. The SAM tests confirmed the viability of the cooled structure; however, the coolant requirements for the HRE exceeded the heat capacity of the available hydrogen fuel and the thermal fatigue life was far shorter than desired (HRE had an anticipated fatigue life of only 135 operational cycles). Both the problems stemmed, in part, from the annular design and high compression ratio of the engine which resulted in large areas being exposed to an intense heating environment. A basic goal in the continuing research program was to develop an engine concept which required only a fraction of the total fuel heat sink for engine cooling and had a reasonable fatigue life.

Findings of the HRE project and additional propulsion studies led to the development of the Langley three-dimensional, airframe integrated scramjet which features a fixed geometry, modular concept (ref. 18). In-house and industry thermal-structural design studies described in references 19 through 22 produced viable design concepts for the integrated scramjet with cooling requirements that permit engine operation to Mach numbers of 9-10 without additional hydrogen for engine cooling. However, these studies reemphasized the need for advances in fabrication and materials technology to obtain reasonable structural life. Advanced fabrication development studies to improve thermal fatigue life (ref. 23) were successful and a fuel injection strut is currently being built for tests at NASA Langley. Ultimately tests of a hydrogen-cooled duct/strut model or one or more complete engine modules are planned for the 8-Foot High Temperature Tunnel which is being modified to accommodate operating engines.

(Figure 7 is shown on the next page.)

LANGLEY ACTIVITIES ON REGENERATIVELY COOLED AIR-BREATHING PROPULSION STRUCTURE

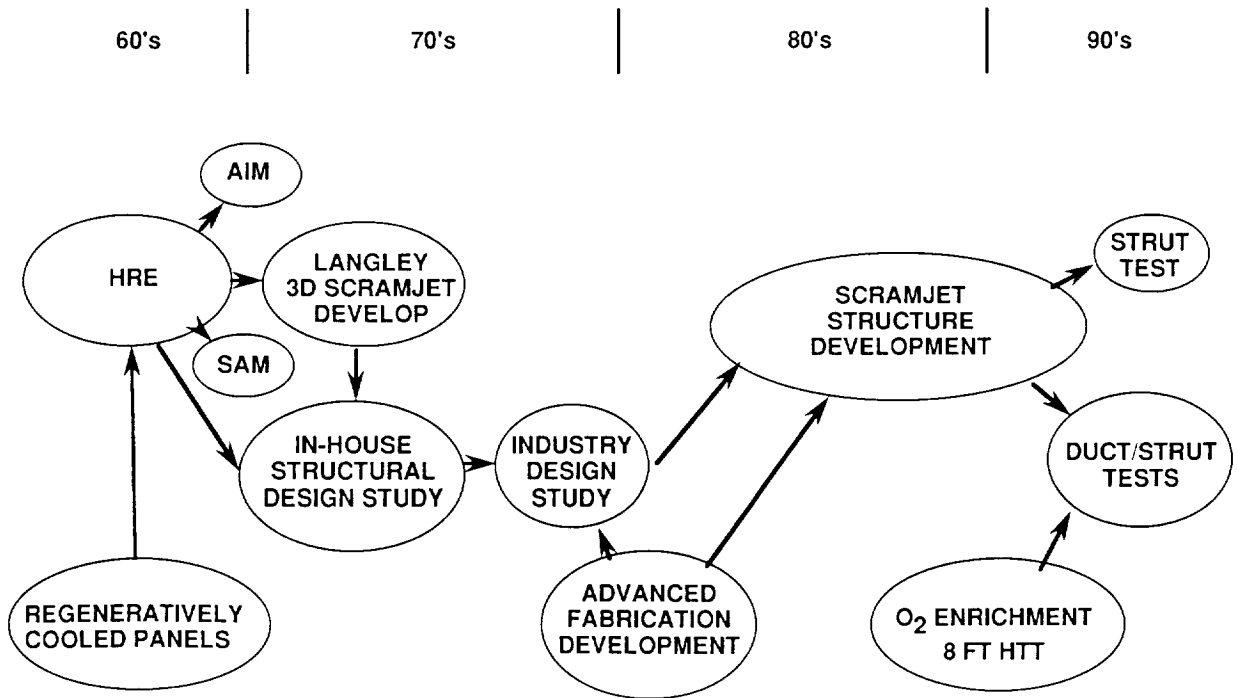


Figure 7

HYDROGEN-COOLED PROPULSION STRUCTURES

Both the regeneratively cooled panel and the HRE hydrogen-cooled structure were based on plate-fin heat exchanger technology (see figure 8) to form the cooled surfaces adjacent to the hot engine gases. These surfaces were fabricated by brazing pre-formed plain or offset fin material between cover sheets to form coolant passages. Design procedures in references 10 and 11 generally resulted in heat exchangers with very small coolant passages, as indicated by the photograph. An appreciation of the passage size can be gained by comparing the passages with the paper clip shown in figure 8. Because of the close spacing of the fins, foil-gage materials can be used to contain coolant pressures in excess of 1000 psi with surface temperatures of 2000°R. The offset fins promote heat transfer to the coolant and reduce the temperature difference between the heat exchanger surfaces, thereby reducing through-the-thickness thermal stresses.

TYPICAL HYDROGEN HEAT EXCHANGER

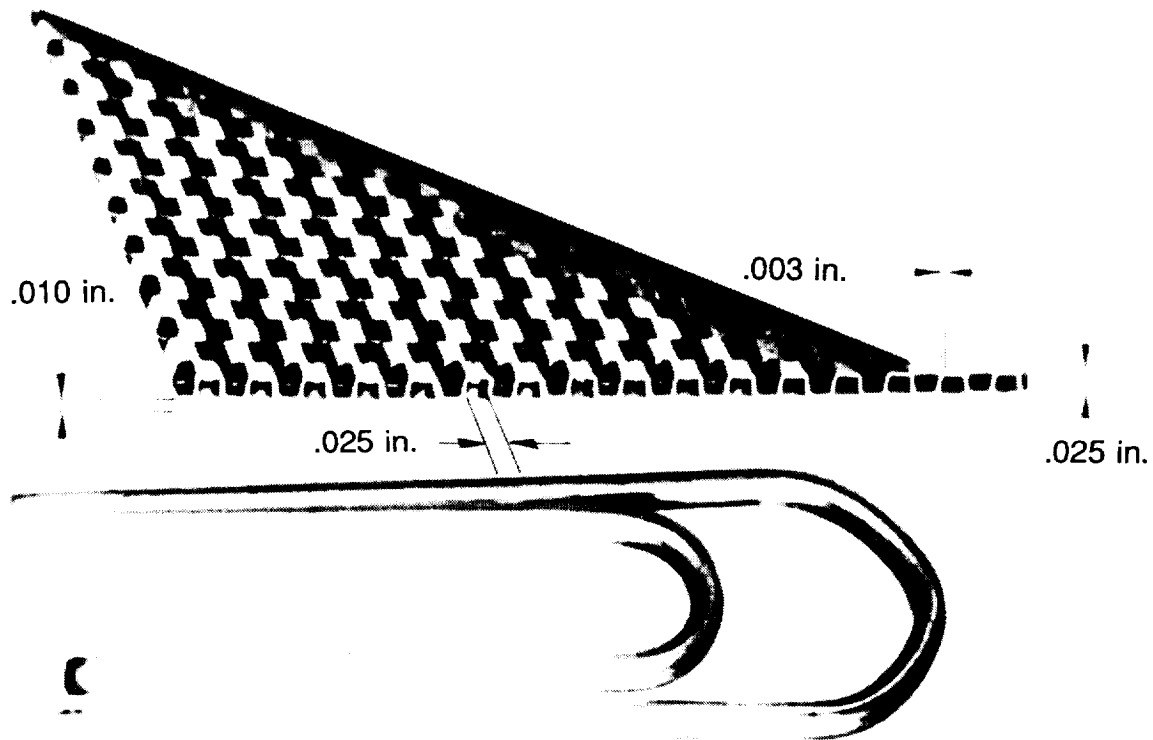


Figure 8

COOLED STRUCTURE CONCEPTS

Thermal and structural design studies presented in references 10 and 11 for heat fluxes from 10 to 500 Btu/ft²-sec and external pressure loadings from 7 to 250 psi (representative of engine structures) resulted in the three preferred concepts shown in figure 9. The terms "integral", "bonded", and "non-integral" were used in the reference studies and in figure 9 to distinguish the three concepts. For the "integral" concept, channels formed by the structure are used as coolant passages. For the "bonded" concept, a hot surface heat exchanger is metallurgically attached (brazed in the reference studies) directly to the primary structural panel. For the "non-integral" configuration, a primary heat exchanger, which absorbs the majority of the incident heat, is attached to the primary structure with mechanical slip joints or attachments that flex to accommodate differences in thermal growth. A secondary heat exchanger protects the primary structure from low-level heat leaks. The "non-integral" configuration tends to minimize thermal stress, reduces interactions between thermal and mechanical loads, and permits the use of low temperature (i.e., lightweight) materials for the primary structure. The reference studies indicate that the "integral" configuration was the preferred concept at low heat fluxes and low pressures. However, the structural passages are relatively inefficient heat exchangers and for moderate to high heat fluxes and moderate pressures, the "bonded" concept is superior. At high pressures and all heat flux levels the benefits of the "non-integral" concept outweigh the complexities and it becomes the preferred choice. (Note that in some subsequent sections of the present paper, the term "integral" is applied interchangeably to both "integral" and "bonded" concepts since both must sustain the combined mechanically and thermal induced loads.)

The studies indicate that thermal stresses are a primary concern in the design of regeneratively cooled panels. In-plane thermal stresses were minimized by careful manifold design to prevent uneven distributions of flow through the panels and thus the large thermal stresses associated with nonlinear in-plane temperature gradients are avoided. Unavoidable thermal stresses, resulting from temperature variations through the thickness of the panel, were found to be minimized through the use of small coolant passages and high flow velocities which increase heat transfer and reduce temperature gradients. However, the small coolant passages and high flow velocities also result in high coolant pressure losses through the panels. For the range of coolant flow rates and pressure losses considered, the resulting through-the-thickness temperature differences made thermal fatigue a problem. Pressure containment was found to be a minor problem, and, in general, minimum-gage materials were adequate for the internal pressures considered (300 to 1000 psi).

Material selection was found to be very important in the design of regeneratively cooled panels. For the heat exchanger portion of the concepts, elevated-temperature ductility of the material was found to be a determining factor for thermal fatigue life. Uncoated nickel-base superalloys appeared to be the best candidates for hydrogen-cooled panels. Waspalloy was chosen for the integral design. Hastelloy X and Inconel 625 were best choices for the heat exchanger portion of the other two concepts. (Although limited data indicated that Inconel 625 provided slightly improved performance, Hastelloy X, which is well characterized, was used in the design studies.) A subsequent advanced fabrication study (ref. 23) found Inconel 617 and Nickel 201 to offer significant improvements in thermal fatigue life. Inconel 718 was limited for use as the primary structure only.

COOLED STRUCTURE CONCEPTS

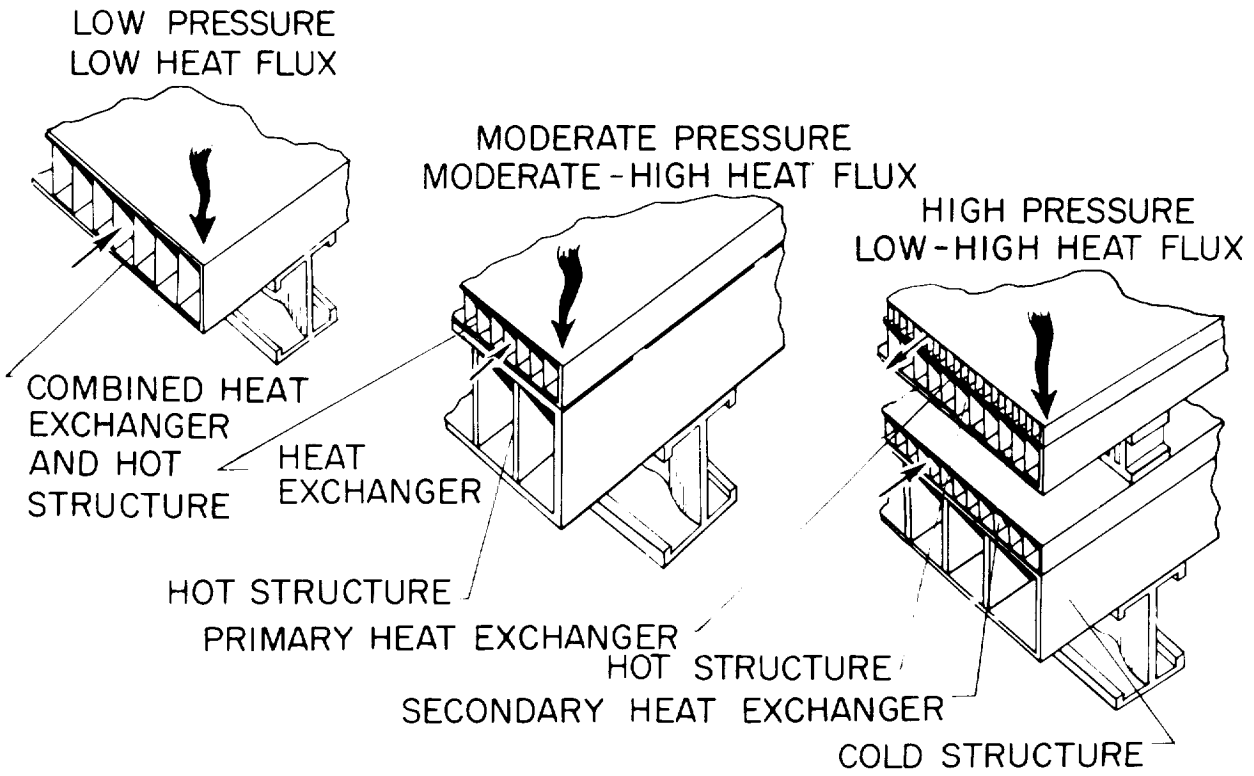


Figure 9

HYDROGEN-COOLED STRUCTURE WEIGHTS

Unit weights from the design studies of references 10 and 11 are shown for the three concepts (see figure 10) as a function of applied heat flux and external pressure loading. The weights are based on a 2- by 2-foot panel and a hydrogen outlet temperature of 1600°R. The weights include the heat exchanger, structural panels and beams, and allowances for manifolds, plumbing, and seals. Since distribution system weights and pumping penalties for the hydrogen coolant would be similar for the three concepts, these weights were ignored in the selection process. Unit weights were found to be a strong function of external pressure and a weak function of heat flux level. Shaded areas on figure 10 represent the minimum weight concept for specified pressures and heat flux. At low pressures the integral concept has the lowest weight; for higher pressures, heat transfer considerations limit the cooling fin height or depth of the panel so that the concept becomes heavier to accommodate the bending loads associated with higher pressures. At moderate pressures the bonded concept avoids the fin height problem but at the higher heat fluxes, the weight of the hot primary structure becomes excessive. For combined high heat flux and high pressure, the weight penalty for hot primary structure is greater than the weight for the additional components of the non-integral design so that the non-integral concept becomes the least-weight design.

In general, concept selection involves trades among panel weight, coolant flow rate, panel life and other factors unique to a specific mission. References 10 and 11 give detailed design information to assist in the concept selection process.

Following the thermal structural design studies, extensive fabrication and structural evaluation studies (refs. 12 and 13) were conducted for the integral and bonded heat-exchanger/hot-primary-structure concepts. Inconel 625, Hastelloy X, and Waspalloy parent metals and the Palniro family of gold-palladium-nickel braze alloys were used as materials in the studies. Tests included sheet alloy tensile tests, metallographic joint evaluations and burst, creep rupture, and cyclic flexural tests at operational temperatures. Additional information on the test and test results are given in the next figure.

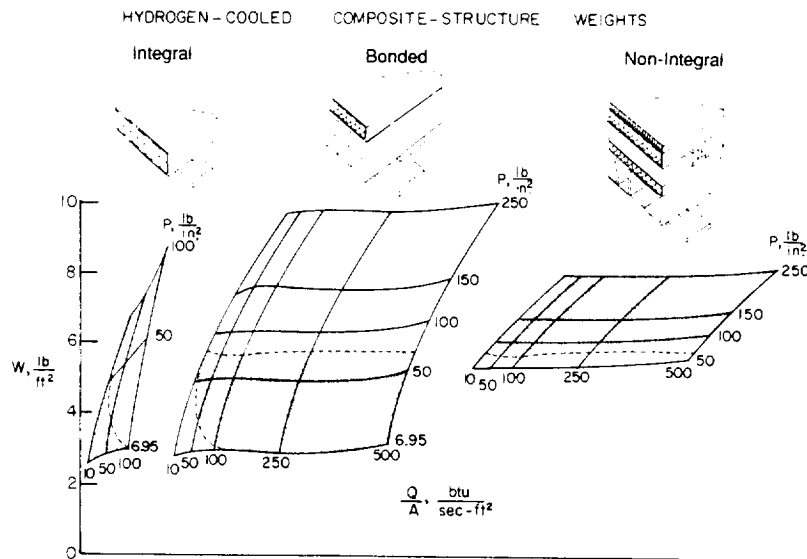


Figure 10

STRENGTH AND FATIGUE TEST RESULTS

Small 2- by 3-inch specimens were used to determine short-term burst and creep rupture properties for the plate-fin sandwich heat exchanger structures. For both types of tests the specimens were maintained at design operating temperatures in an electric furnace and pressurized with an inert gas. For the short-term burst tests, pressure was increased continuously at 20 psi/sec until failure occurred. For the rupture test, pressure was maintained at fixed levels and the specimens were allowed to creep until failure occurred. For the low-cycle fatigue test, 2- by 6-inch specimens were maintained at a test temperature of 1600°F by an electric furnace which enclosed the test apparatus as shown in figure 11. Strains were imposed mechanically by the oscillating ram and circular mandrels. Implicit in this testing method is the assumption that failure life depends on the maximum cycle temperature and cyclic strain level independent of whether the strain is mechanically or thermally induced.

Results from the tests are shown as ratios of mechanical properties of the plate-fin assemblies to the parent metal properties. The tests showed that about 85 percent of the parent metal strength was achieved in the burst tests but only 50 percent of the creep rupture strength (a 50 percent reduction in strength corresponds to a 98 percent reduction in life) and only 7 percent of the fatigue life of the parent metal could be achieved by the fabricated specimens. Many factors were found to influence the strength and fatigue life of the fabricated specimens: time at braze temperature, fin geometry, braze fillet shape, fin shape, face plate thickness, and material ductility. Creep rupture performance could be improved by increasing material gages; however, improvements in fatigue life (obtained in the integrated-scamjet development program and discussed subsequently) resulted from a redesign of the heat exchanger and the use of new fabrication techniques and better materials.

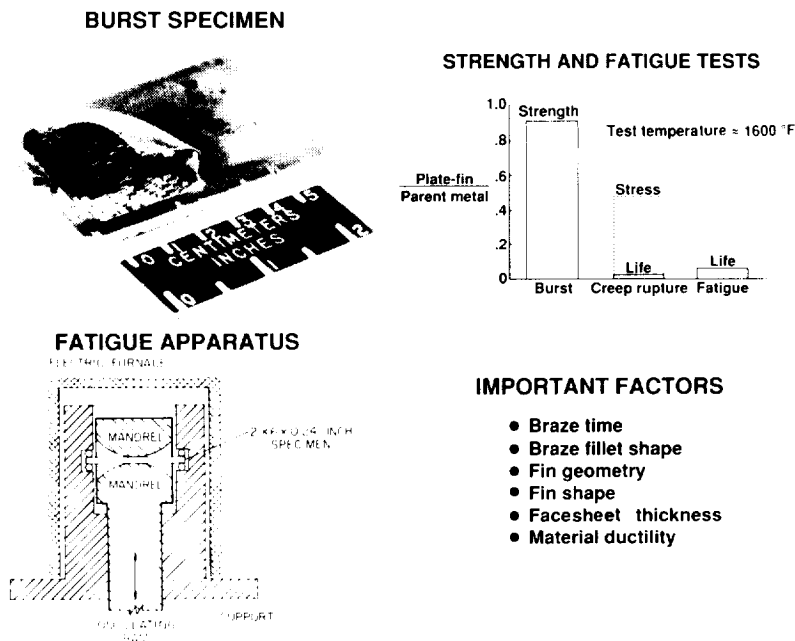


Figure 11

14- BY 20-INCH COOLED PANEL

As a culmination of the hydrogen-cooled panel studies, structural and thermal performance tests (ref. 15) were conducted on the 14- by 20-inch brazed plate-fin panel shown in figure 12. The panel consisted of an Inconel 625 heat exchanger brazed to an Inconel 718 structural panel which was supported by Inconel 718 I-beams (not shown). Clips spanning the backside of the structural panel were used to attach the panel to the I-beam supports. Inlet and outlet manifolds for distribution of the hydrogen coolant were integral parts of the structural panel. The panel was designed to sustain a 100 psi uniform surface pressure and a heat flux of 100 Btu/ft²-sec. The panel was tested in an inert gas atmosphere and a graphite heater was used to radiantly heat the cooled surface. Test conditions resulted in a maximum heat flux of 103 Btu/ft²-sec and a maximum temperature of 1470°F were imposed during the tests. A maximum uniform surface pressure of 115 psi was also applied at a temperature of 520°F. Panel heat transfer performance was generally lower than expected, apparently because of flow and heater non-uniformities. The average overall heat transfer coefficient was 63 percent of the value predicted for uniform hydrogen flow and uniform heating of the panel.

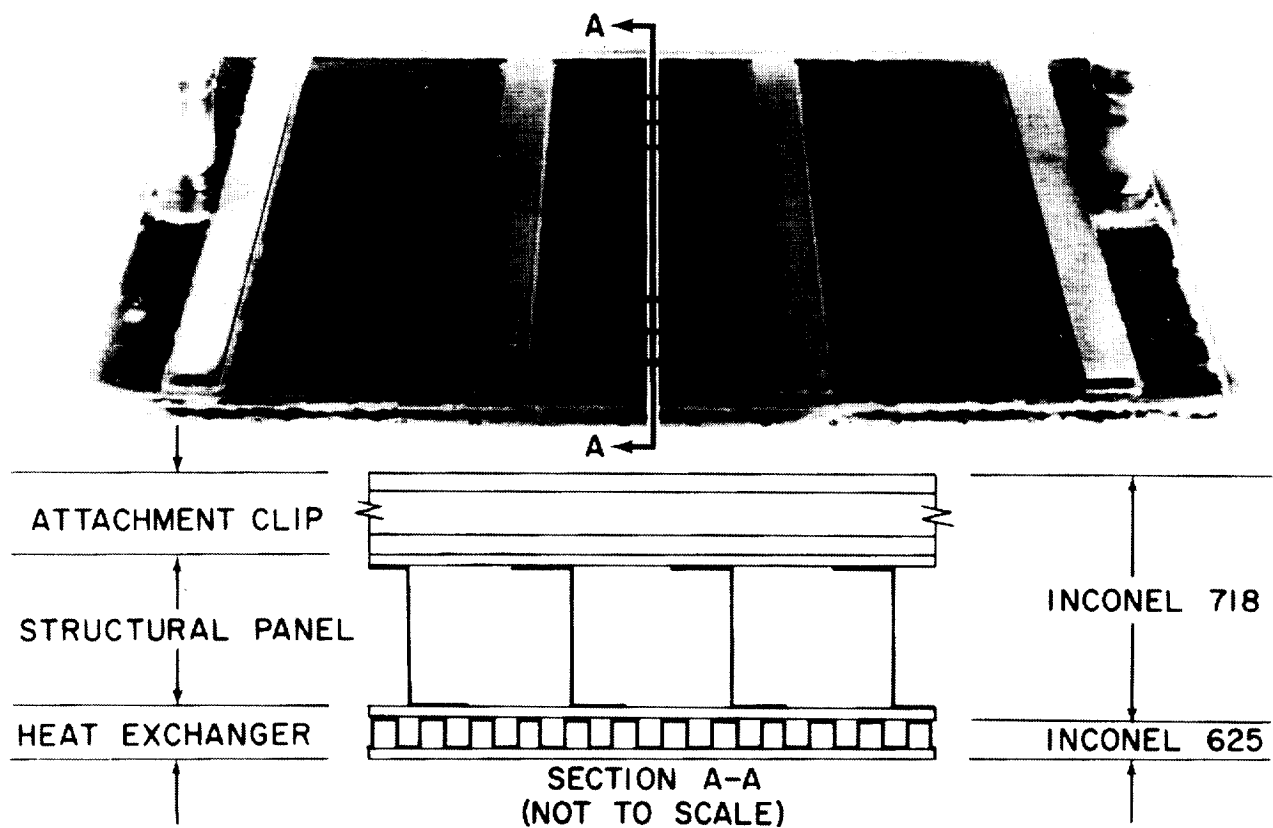


Figure 12

HYPERSONIC RESEARCH ENGINE

The Hypersonic Research Engine (HRE) was originally intended to be flight tested on the X-15 vehicle (ref. 3). The engine was designed to operate at Mach numbers from 3 to 8 at dynamic pressures up to 2000 psf. At Mach numbers above 6, it was to operate in the supersonic combustion mode. Below Mach 6 the combustion mode was not specified. HRE was to have a minimum life of 10 hours and 100 operational cycles, and to have a maximum weight of 800 pounds for compatibility with the X-15.

Subsequently, because of the demise of the X-15 project the HRE project was restructured and culminated in the testing of the boiler-plate Aerothermodynamic Integration Model (AIM) in the Hypersonic Test Facility at the Plum Brook Station of the NASA Lewis Research Center, and the flightweight, hydrogen-cooled Structural Assembly Model (SAM) in the NASA Langley Research Center 8-Foot High Temperature Tunnel. The former testing is documented in reference 16 and the latter in references 4 and 17.

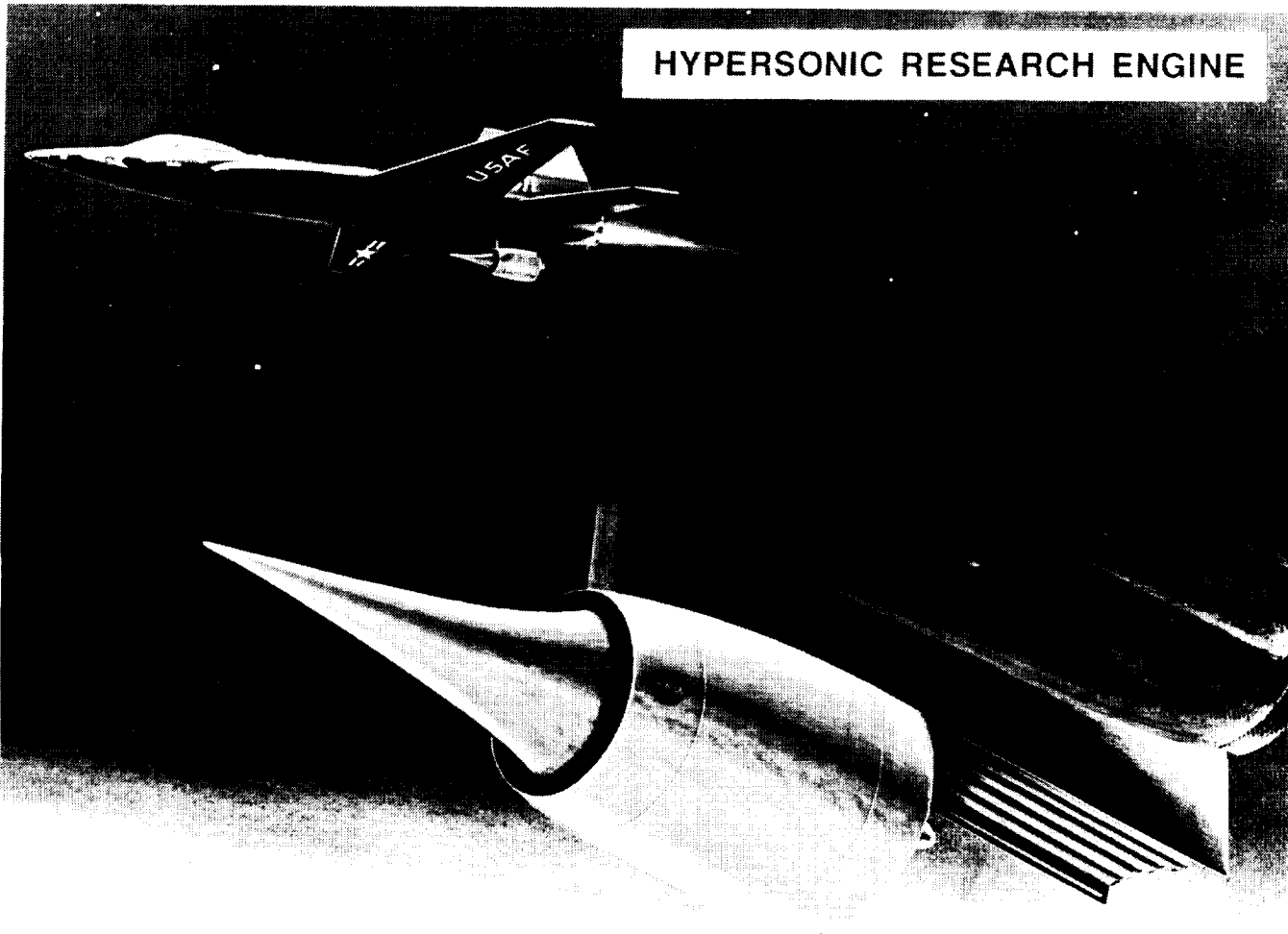


Figure 13

HRE INNER SHELL ASSEMBLY

Technology from the regeneratively cooled panel studies was incorporated in the design and fabrication of a full-scale Structural Assembly Model of the HRE engine for tests in a hypersonic flow stream. Approximately \$8 million was expended in development of hydrogen-cooled structures for the engine. Details of this development may be found in reference 24. The structure was designed for Mach 8 flight conditions and consisted of plate-fin sandwich shells with simple and compound curvatures. Use of the plate-fin sandwich construction and off-set fins resulted in a cooled structure that tolerated some blockage of flow area, permitted installation of inserts for various purposes, facilitated incorporation of manifolds into the structure, and resulted in smooth aerodynamic surfaces. The structural shells were fabricated as shown in figure 14, by laying up and brazing an assembly consisting of a precision formed Hastelloy X inner skin a layer of brazing foil, a layer of preformed Hastelloy X offset fin material, a second layer of brazing foil, and a precision formed outer skin of Hastelloy X. The final, precise shape of the inner and outer shells was obtained using successive applications of the "Electroshape" forming technique to form the outer skin, a spacer of appropriate thickness to simulate the fins and brazing material, and the inner skin in a single precision female mold. Precision forming was essential to obtain the close fit-up required for brazing. Manifolds, etc. were added during subsequent brazing operations. The Palniri family of gold-palladium-nickel brazing alloys were used because they were compatible with Hastelloy X, available in foil form and suitable for multiple brazing operations (the brazing temperature could be varied by changing the exact composition of the alloy). Five major components were mechanically joined and manifolded together to form the complete hydrogen-cooled Structural Assembly Model.

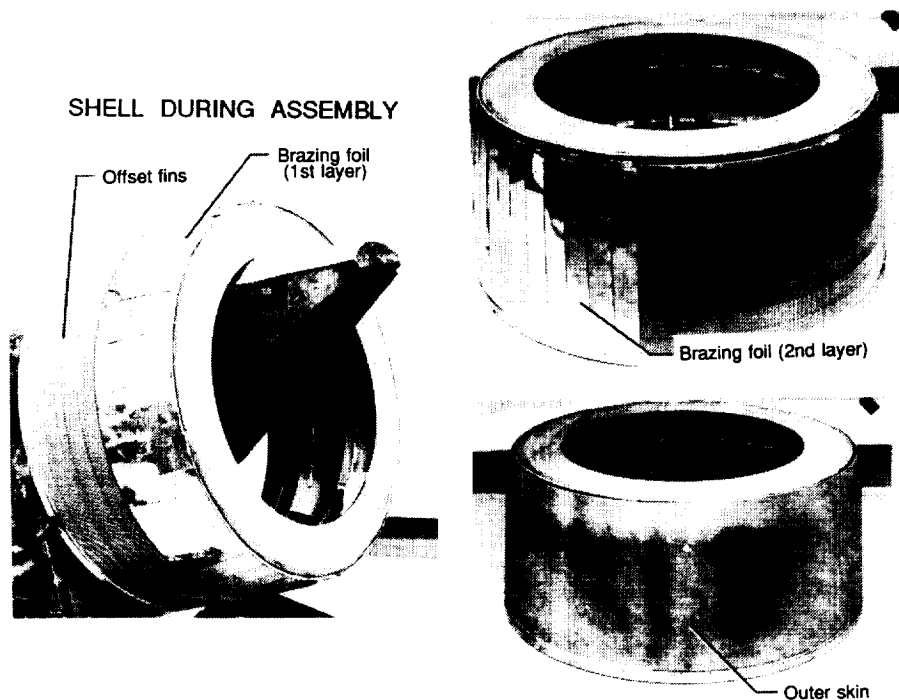


Figure 14

STRUCTURAL ASSEMBLY MODEL

Figure 15 shows the structural assembly model in the test position in the 8-Foot High Temperature Tunnel. To the right of the photograph is the 8-ft-diameter nozzle exit from which the facility derives its name. Flow in the open test section is from right to left.

The Structural Assembly Model (SAM) model was tested in the nominal Mach 7 stream of the Langley 8-Foot High Temperature Tunnel (under non-combustion conditions) for a total of 55 times to accumulate 30 minutes of exposure time which met or exceeded temperatures and temperature differences for the Mach 8 design conditions (ref. 17). Hydrogen coolant flow rates were adjusted and the transient effects of injecting a cold model into the hot test stream were used to improve the simulation of the conditions that would exist in an operating engine. Because there was no combustion in the engine during the tests, the temperature gradients resulting from steady-state wind tunnel conditions were less severe than the predicted operational gradients. However, the transient gradients resulting from introducing the unheated model into the hot airstream in the tunnel approximated the predicted steady-state operating thermal gradients. In addition, reduced coolant flow rates were used to compensate for the reduced heat fluxes in the non-operating SAM model so that the temperatures would reach the levels expected in an operating engine. Serviceability of the flight-weight plate-fin cooled structure was clearly demonstrated although the model was not tested to the full 100-cycle design life. The coolant system maintained acceptable temperature levels and tolerated large heating nonuniformities and inadvertent foreign object damage. Some minor hydrogen leakage was observed, but it was apparently inconsequential.

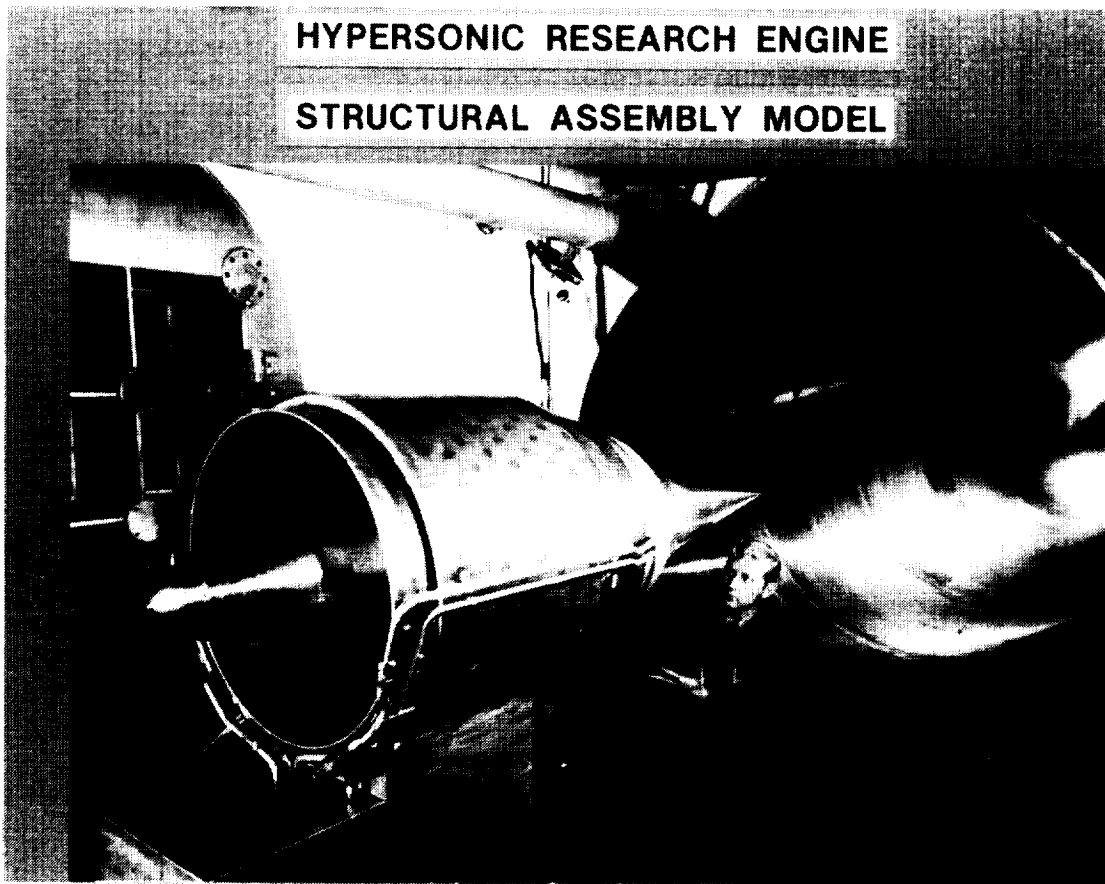


Figure 15

AIRFRAME INTEGRATED SCRAMJET

As indicated previously, the Langley Airframe Integrated Scramjet (see figure 16) was developed to overcome some of the shortcomings identified during the HRE studies: namely the limited fatigue life and the excessive coolant requirements. The modular engine uses the undersurface of the aircraft forebody to compress the flow entering the inlet and the undersurface of the afterbody to serve as an extension of the nozzle. The engine features swept compression surfaces, a cut-away cowl to permit operation over a wide range of Mach numbers, and three fuel injection struts with multiple fuel injection planes to promote and control fuel mixing and combustion. Structural advantages for this concept include, fixed geometry, minimal wetted surface area, and reduced heating rates. More detailed discussions of the conceptual design and performance may be found in reference 18.

The engine was designed to operate over a Mach number range from 4 to 10 at dynamic pressures ranging from 500 to 1500 psf. The highest heat load was encountered at Mach 10 with a dynamic pressure of 1500 psf; the most critical case for coolant/fuel matching occurred at Mach 10 with a dynamic pressure of 500 psf; and the most critical case for structural loading occurred at about Mach 5 during an engine unstart at the higher dynamic pressure (1500 psf). Design life for the LaRC scramjet was a minimum of 100 hours and 1000 thermal cycles — an order of magnitude greater than the HRE.

The salient structural design features of the Langley three-dimensional scramjet described in the figures and text to follow were derived from the Langley in-house and industry design studies. Additional details of the analysis methods, and the fuel injection strut design and fabrication are described in papers by Wieting and McWithey in reference 5. More complete descriptions of the design studies are given in references 19 through 22.

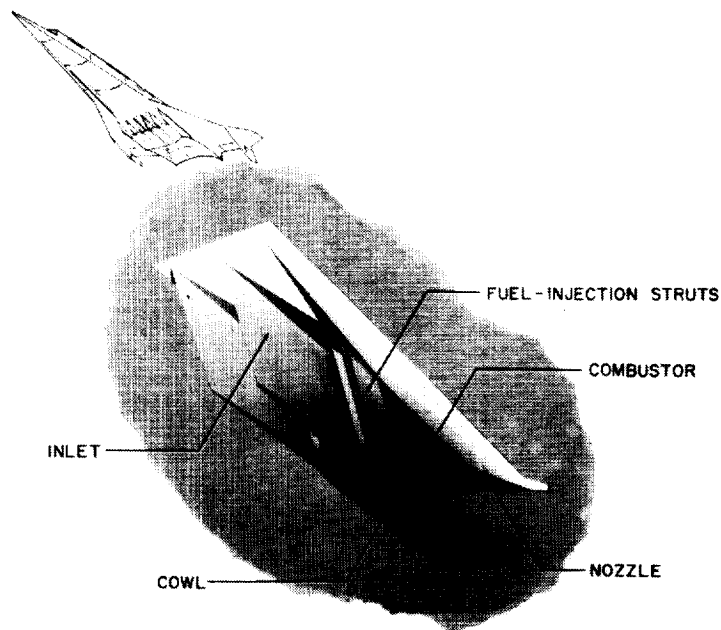


Figure 16

COOLED SCRAMJET STRUCTURE

The hydrogen-cooled scramjet structure concept which evolved from the design studies consists of a full depth brazed superalloy honeycomb structure with a brazed cooling jacket adjacent to the hot gases (see figure 17). The cooling jacket differed from that of the HRE in that fins which formed the coolant passages were photo-etched into the skin. This concept was selected primarily to increase the fatigue life (as will be discussed subsequently under advanced fabrication development); however, it also offers considerable design flexibility to meet localized requirements such as plain fins for relatively low heat flux (acrage) areas of the engine, and offset or pin fins for high heat flux areas such as the strut. The strut and cowl featured impingement cooling of the especially high heat flux stagnation regions. The structural channels of the strut are also used to form integral manifolds for coolant and fuel distribution. Additional innovative design features of the strut are described in the paper by McWithey in reference 5.

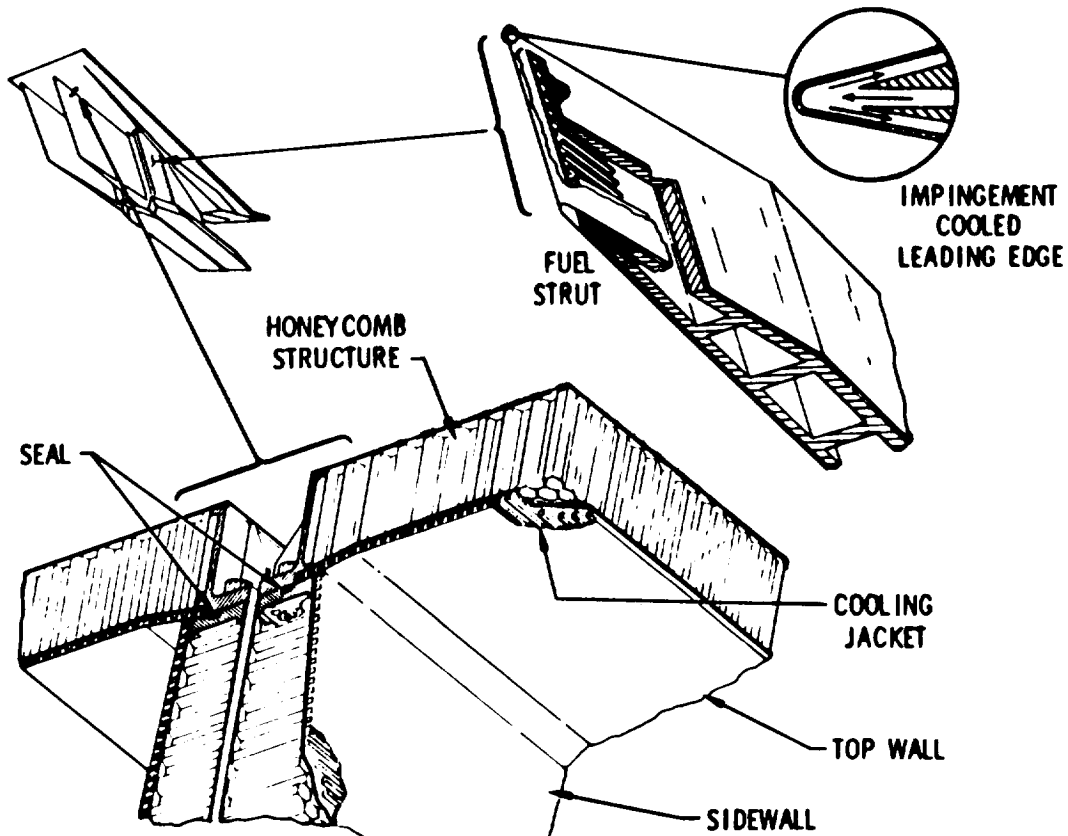


Figure 17

STUDIES OF LaRC SCRAMJET MODULE

In summary, the LaRC scramjet thermal/structural design studies which are described in detail in references 19 through 22 have shown that the basic design requirements for the scramjet can be met (see figure 18). The resulting configuration should have adequate cooling (with a coolant-to-fuel ratio ≤ 1) up to a Mach number of approximately 9-10, an expected life of at least 100 times that of the HRE, with a mass/unit-capture-area of approximately 2/3 that of HRE. (Note that the HRE was designed to a fixed weight limit and the structure was not fully optimized. However, for an annular engine the presence of the large inner body tends to negate the inherent advantages of a circular cross section for pressure containment.) The fuel injector strut, which is discussed in more detail in the paper by McWithey in reference 5, presented by far the most difficult design problem. Results of the advanced fabrication development studies, presented in the next figure, indicate that the selected cooling jacket design should meet and exceed the design life.

Thermal/Structures Studies Reveal

- 100 times life of HRE
- 2/3 mass/unit capture area of HRE
- 1/3 coolant/fuel requirement of HRE
(coolant required/fuel ≤ 1.0)
- Fuel injector strut most difficult design problem

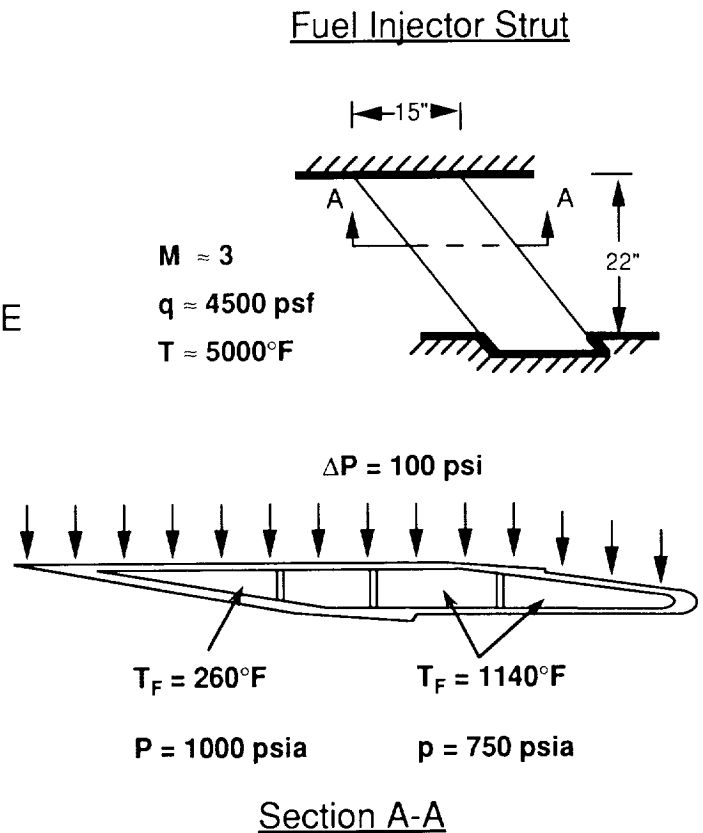


Figure 18

ADVANCED FABRICATION TECHNIQUES

Earlier studies of both the HRE and regeneratively cooled panels, indicated that, although hydrogen-cooled structures were viable, their anticipated fatigue life was extremely limited. Therefore, the advanced fabrication technique studies were undertaken with the goal of extending the usable life of cooled engine structure from the 100 cycle design life for the HRE to 1000 hours and 10,000 cycles of hot operation (cross-hatched region of figure 19) which represents an improvement of two orders of magnitude over the HRE. Predictions of the fatigue life as a function of the temperature difference between the hot aerodynamic skin and the back surface are shown in figure 19. Life goals appear attainable through a number of factors such as engine design, fabrication methods and material selection. Improvements attributable to these factors are graphically illustrated in figure 19. The bottom curve indicates anticipated life of the Hastelloy X coolant jacket of the HRE. The solid symbol at the right denotes the HRE design point and the open symbols indicate experimental data. A fundamental change in engine design to decrease the heat flux intensity and thus the temperature difference, as indicated by the horizontal arrow, is the first factor to increase the life of the airframe-integrated scramjet. An additional increase, as indicated by the vertical arrow, is obtained through an advanced fabrication technique. In this technique, the fin coolant passages are photo-chemically etched into the aerodynamic skin which eliminates the strain concentration caused by local thickening of the skin by the fin and eliminates the hot skin-to-fin braze joint configuration. However, the braze joint to the cooler primary structure is retained. The photo-chemical etching process can be used for a wide variety of plate-fin configurations. Two candidate configurations fabricated by this process are shown in figure 19. Finally, another increment in life is attained through the selection of a material with high thermal conductivity which decreases the temperature difference, and with high ductility which increases the fatigue life directly. Nickel 201 and Inconel 617 specimens were fabricated and tested and the results for Nickel 201 as indicated by the upper curve met the goal of 10,000 cycles for a design heat flux of 500 Btu/ft²-sec. Details of advanced fabrication studies, which included burst and creep-rupture evaluations in addition to fatigue evaluations, are presented in reference 23.

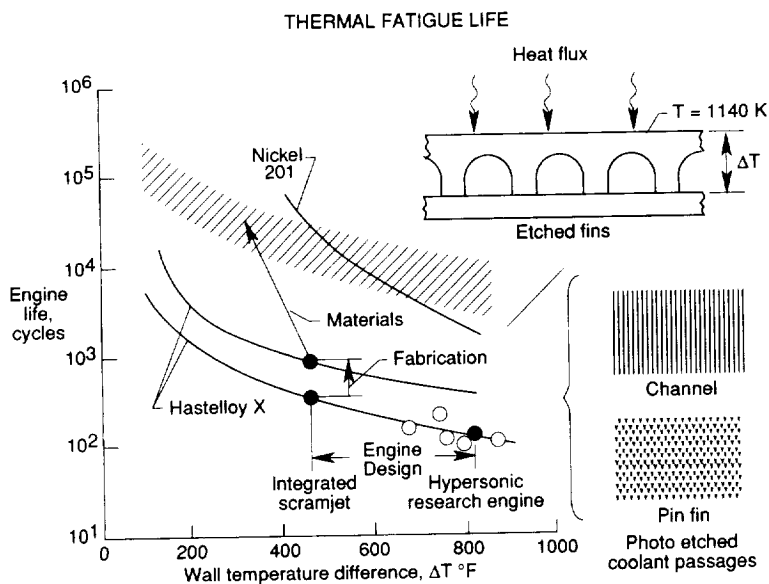


Figure 19

SCRAMJET ENGINE FUEL INJECTION STRUT

Efforts have been underway for several years to fabricate a fuel injection strut for the Langley Airframe Integrated Scramjet. The strut which is swept back 48 degrees has a 11.8-inch streamwise chord and is 28.8-inches long. The strut consists of an Inconel 718 structural body enclosed by Nickel 201 pin-fin cooling jackets.

The complexity of the strut is indicated by the cutaway mock-up on the left of figure 20. Structural cavities created by webs in the strut body form manifolds that direct hydrogen to and from the cooling jackets and manifolds that supply parallel and perpendicular fuel injectors.

Actual fabricated hardware parts are shown on the right of figure 20. The strut fabrication involves three brazing operations: (1) assembly of the strut body, (2) assembly of etched and cover sheets of the cooling jacket, and (3) final assembly of the formed cooling jackets and body. The forward jacket is shown in the formed condition and the aft jacket is shown prior to brazing to show the etched cooling passages. After forming, the cooling jackets will be hot sized to enhance fit-up between the jackets and the strut body prior to final braze.

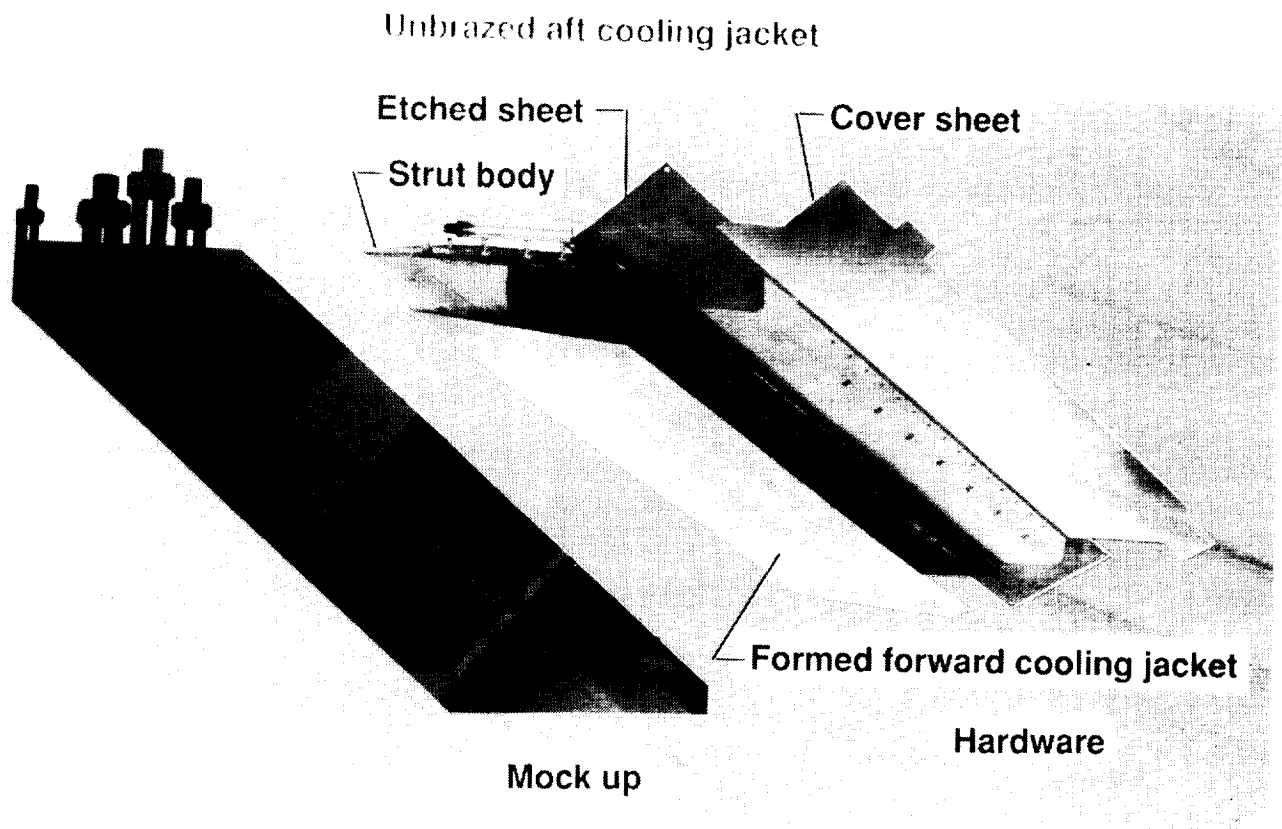


Figure 20

ACTIVELY COOLED AIRFRAME STRUCTURES

Extensive efforts have also been expended on development of secondary cooling circuit structural concepts for airframe structures (see figure 21). Systems studies indicated initial feasibility of the convective cooling approach and defined initial concepts. A series of design and fabrication studies were then conducted to further develop specific concepts. These studies included thermal-structural design, small specimen fatigue tests, fabrication development, and static and wind tunnel thermal-structural verification tests.

Although early studies for actively cooled airframe structures recognized problems in matching the instantaneous aerodynamic heat load with the heat sink capacity of the hydrogen fuel flowing to the engines and proposed partial heat shielding to reduce the absorbed heat load, both system studies (refs. 25-30) and hardware studies (refs. 31 and 32) concentrated on bare cooled structures with high-level cooling. Later studies (refs. 33-35) yielded a better understanding of the significance of heat sink matching and the mass penalties associated with high-level cooling. Selected general results from the actively cooled airframe structures studies are discussed next.

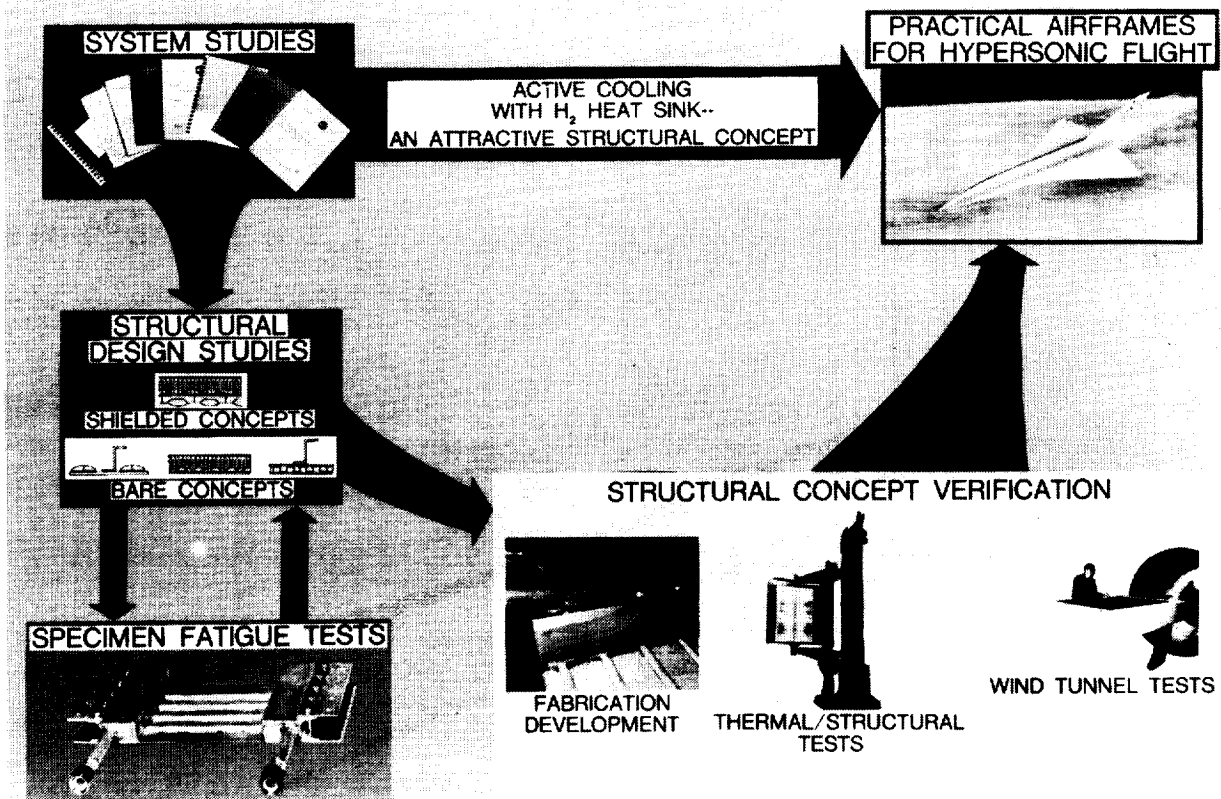


Figure 21

CONVECTIVELY COOLED CONCEPT SELECTION

Systems and hardware studies conducted in the mid 1970's yielded a coherent and consistent definition of the most attractive convectively cooled structural approach that combined both passive and active thermal protection. Recommended application regions for airframe concepts that combine passive and convective cooling are indicated in figure 22. Although the boundaries shown are specific to the constraints of the early studies, the trends are believed to have general applicability. At lower incident heat fluxes, an overcoated cooled structure is the favored concept. The overcoat, a moderate-temperature elastomeric material applied to the outer surface of the structure, is an outgrowth of the fail-safe abort studies described in reference 36. At higher heat fluxes the overcoat is replaced by high temperature insulation and heat shields. This approach represents a marriage of convective active cooling with the radiative heat shield technology developed for entry vehicles. Only at the highest heat flux levels where heat shields reach excessive temperatures would bare convectively cooled structures be used. Addition of a hot surface thermal protection to a bare convectively cooled structure reduces total mass, provides improved heat-load/heat-sink compatibility, increases safety and reliability, improves tolerance to off-design conditions, and eases fabrication difficulties.

APPLICATION REGIONS FOR CONVECTIVE/RADIATIVE COOLED AIRFRAME STRUCTURES

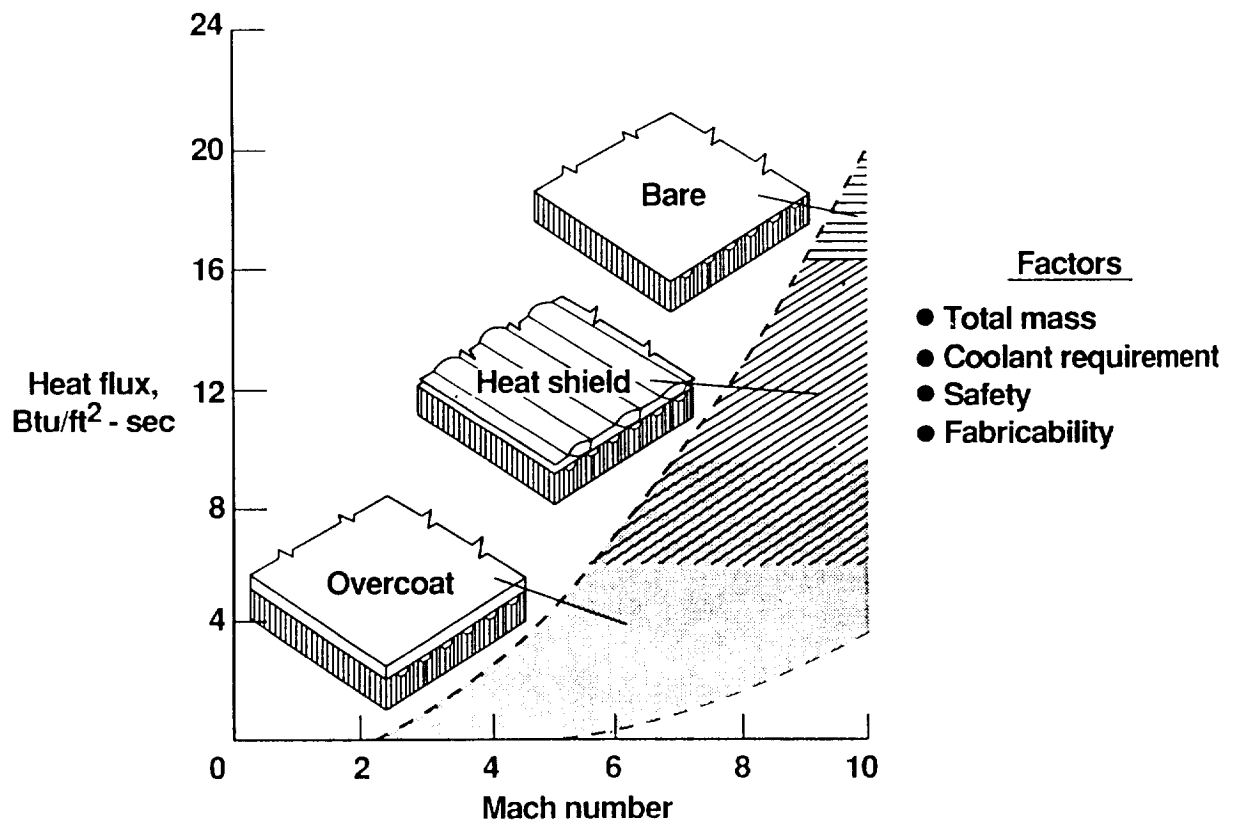


Figure 22

ACTIVELY COOLED PANEL PROGRAM - ALUMINUM CONCEPTS

To complement the system studies, a series of design and fabrication studies was undertaken to provide both bare and heat-shielded structural specimens for thermal-structural testing by NASA. Three bare concepts and one shielded concept were included in the studies. The full-scale 20-ft-long by 2-ft-wide panels were designed to meet Mach 6 to 8 transport requirements, to have 10,000 hours of life, and to survive 20,000 fully reversed limit load cycles. Each panel was designed to accommodate a heat flux of 12 Btu/ft²-sec, a uniform lateral load of 1 psi, and a uniaxial limit load of ± 1200 lb/in. The test panels were 4-ft-long segments of the full-scale panel.

The Bell Aerospace bare concept is a skin-stringer structure with dual (redundant) counterflow cooling passages, and uses glycol/water as a coolant (see lower right portion of figure 23). Coolant passages are quarter ellipse tubes with adjacent wire crack arresters adhesively bonded between a flat 0.032-inch-thick outer skin and a formed 0.020-inch-thick inner skin. The tubes contain the coolant pressure and eliminate peel stresses between the bonded skins. Both sets of cooling passages operate to maintain design temperatures during normal flight; should one of the redundant systems fail, either in the panel or distribution system, the panel has a life expectancy of 1/2 hour at normal operating conditions. The unit mass (includes panel, coolant inventory, pumping penalty, and coolant distribution system) for this concept is 4.25 lbm/ft².

The McDonnell Aircraft bare concept (not shown) has a single pass non-redundant cooling system (D-tubes) embedded in a honeycomb sandwich, which is designed to contain internal-coolant leaks. The coolant tubes are brazed to a manifold with double chambers to get full coolant flow along the transverse edge. The tube-manifold assembly is then soldered to the outer skin which forms one of the facesheets of the adhesively bonded honeycomb sandwich. Methanol/water is used as the coolant. The unit mass for this concept is 4.84 lbm/ft². Difficulties with the soldering process eventually led to abandonment of fabrication of the bare honeycomb sandwich concept. The heat shielded concept (shown in figure 23) is very similar to the bare honeycomb panel in that it uses small D-tubes and adhesively bonded honeycomb sandwich structure plus a layer of high temperature insulation and metallic heat shields. Since the insulation and corrugation stiffened Rene'41 heat shields operate at 1450°F, most of the incident heat is radiated away and the heat absorbed by the cooled panel is reduced by a factor of 10. As a result, the mass of the secondary cooling system is greatly reduced and the shielded concept has a unit mass of 4.52 lbm/ft² or 7 percent less than the corresponding bare concept. The much lower heat flux to the cooled panel permits use of adhesives to bond the cooling tubes to the outer face sheet rather than the soldering process needed for the bare panel.

The LaRC-Rockwell International concept (lower left of figure 23) uses a stringer-stiffened, brazed plate-fin sandwich (similar to hydrogen-cooled panels previously described for the HRE) with a rectangular-fin core for the main coolant passages. An auxiliary coolant passage outboard of the edge fasteners plus a thickened conduction plate provide longitudinal edge cooling. Stringers are adhesively bonded to the inner skin between frames. Glycol/water is used as the coolant. The unit mass for this concept is 4.46 lbm/ft².

References 20, 31, 32, 35, 37 and 38 discuss the design and fabrication of these actively cooled panels in more detail. Figure 23 is shown on next page.

ACTIVELY COOLED TEST PANELS

2- by 4-foot

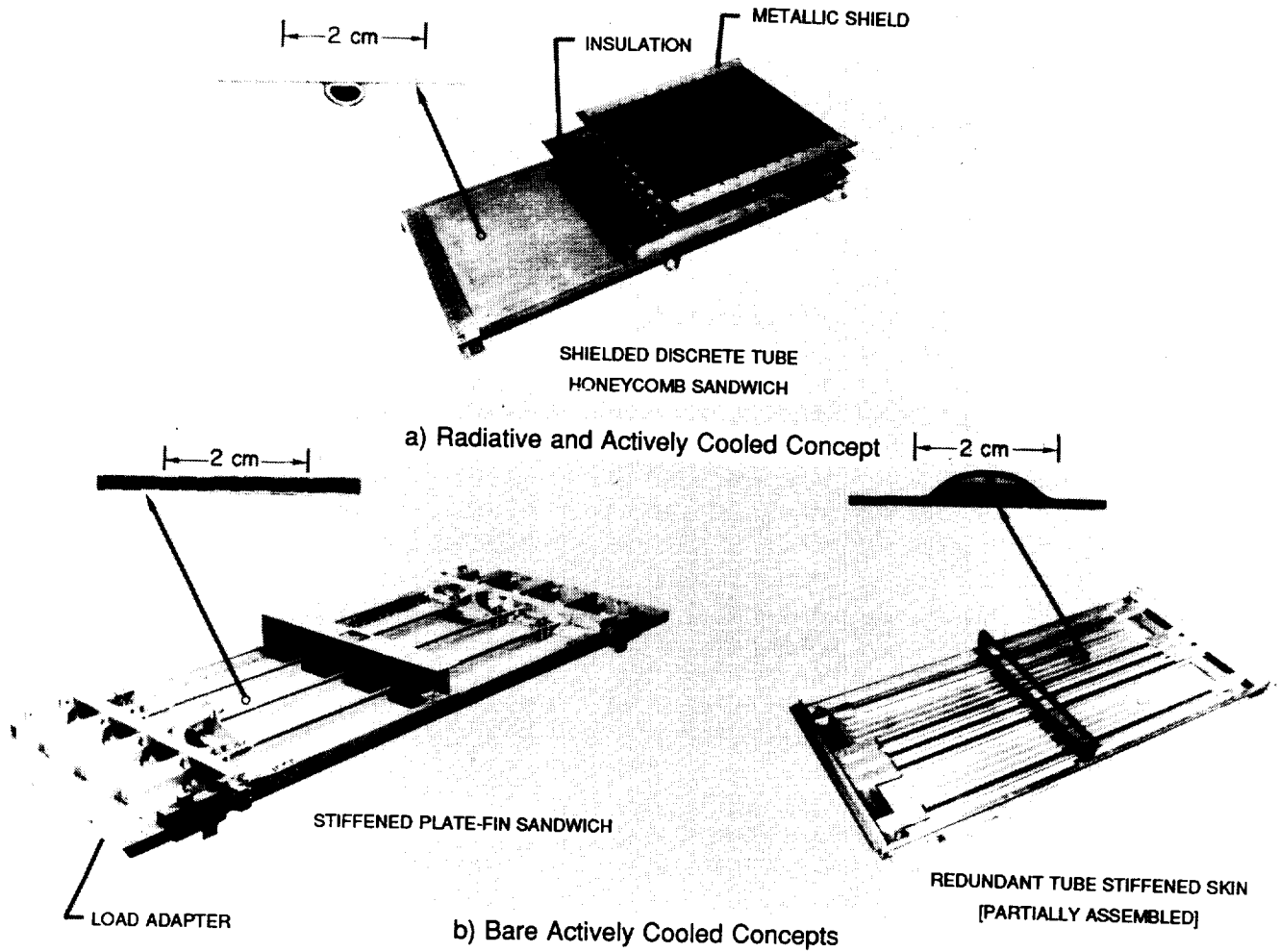


Figure 23

ACTIVELY COOLED HONEYCOMB SANDWICH AMBIENT TEMPERATURE FATIGUE TESTS

As part of the hardware design and fabrication studies, small specimens were fabricated and tested to determine fatigue life characteristics for each concept. Two of the bare honeycomb sandwich fatigue specimens are shown in figure 24. The upper specimen was used to check cooling-tube/facesheet characteristics and the lower specimen was used to check the assembled panel characteristics. Results from the fatigue tests indicated that: the fatigue life of 20,000 cycles was exceeded, the cooling tubes acted as crack arrestors for cracks induced in the facesheets, cracks in the facesheets which propagated past the coolant tubes did not penetrate into them, and leakage from cracks induced in the tubes was contained by the honeycomb sandwich. Finally, the tests also showed that there was a need to redesign the transverse joints to avoid excessive joint motion. Similar results were found for the transverse joints in the discrete tube concept and the plate fin concept, indicating that the need to cool the joints further complicates the difficult task of joint design.

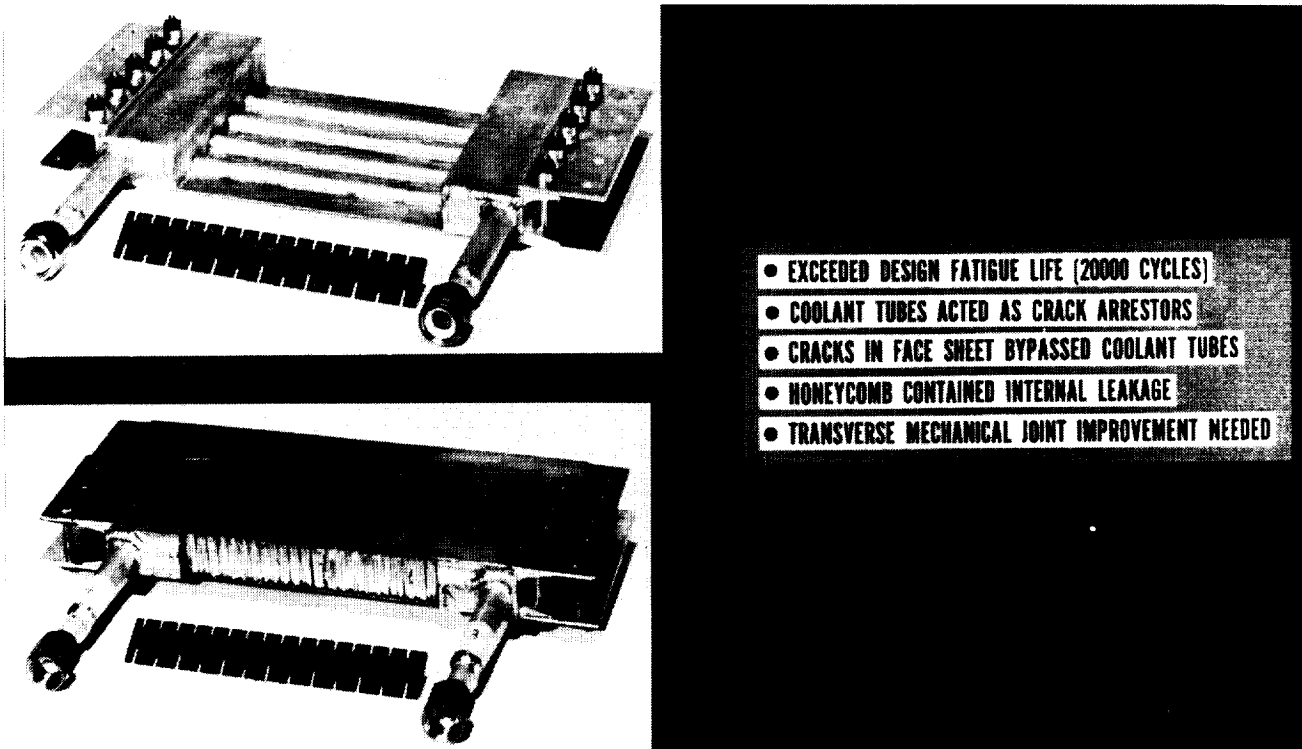


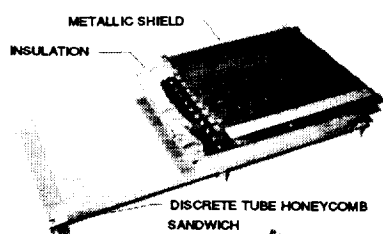
Figure 24

ORIGINAL PAGE
BLACK AND WHITE PHOTOGRAPH

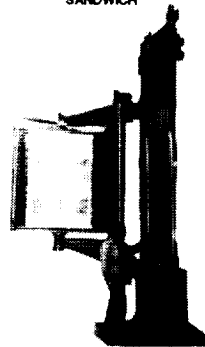
RADIANTLY AND ACTIVELY COOLED PANEL TEST RESULTS

As described in references 39 and 40 and shown in figure 25, the flight-weight heat-shielded convectively cooled panel was subjected to thermal-structural tests in the Active Cooling Test Stand (ACTS) shown at the bottom left of figure 25. The test represented design flight conditions for a Mach 6.7 transport and off-design conditions simulating flight maneuvers and cooling system failures. A total of 32 tests exposed the panel to 65 thermal cycles and multiple cycles of mechanical loading. The panel successfully withstood 55 hours of radiant heating at 12 Btu/ft²-sec, and 5000 cycles of uniaxial in-plane limit loading of ± 1200 lb/in. at operational temperatures. Additionally, the panel withstood off-design heating conditions for a simulated 2g maneuver from cruise conditions and simulated failures of the water/glycol cooling system without excessive temperatures on the structural panel. Wind tunnel tests in the Langley 8-Foot High Temperature Tunnel exposed the panel to 15 aerothermal cycles for a total of 137 seconds in a Mach 6.7 test stream. The panel responded as predicted and survived the extensive aerothermal and structural testing without significant damage to the structural panel, coolant leaks, or hot-gas ingress to the structural panel. However, the foil coverings on the insulation packages sustained damage sufficient to destroy their function of preventing water ingress to the layer of high-temperature insulation.

As an ancillary part of the investigation, a separate model of the heat shield was subjected to extensive thermal cycling (ref. 41). The 10.8-inch-wide by 23.9-inch-long model incorporated a mid-panel joint which was representative of the slip joint used in the full-scale design as were the other details of the heat shield. The heat shields survived exposure to 20,040 simulated flights (thermal cycles) and remained intact. However, a one percent shrinkage in the heat shield caused cracks and excessive wear to occur around the elongated fastener holes. Tensile tests of specimens machined from the heat shield showed an 80 percent loss in ductility and a 20 percent increase in yield strength compared to Rene'41 in the aged condition.



- 55 HOURS AT DESIGN HEATING CONDITIONS
- 65 THERMAL CYCLES
- 5000 LOAD CYCLES AT TEMPERATURE
- THERMAL AND STRUCTURAL PERFORMANCE WITHIN 10-PERCENT OF PREDICTED PERFORMANCE
- 132 SECONDS [TOTAL] IN M = 7 AEROTHERMAL ENVIRONMENT
- WITHSTOOD SIMULATED ABORT [COOLANT LOSS] HEATING TRAJECTORY
- NO EVIDENCE OF HOT GAS INGRESS OR STRUCTURAL FAILURE OR COOLANT LEAKS



THERMAL/STRUCTURAL TESTS



WIND TUNNEL TESTS

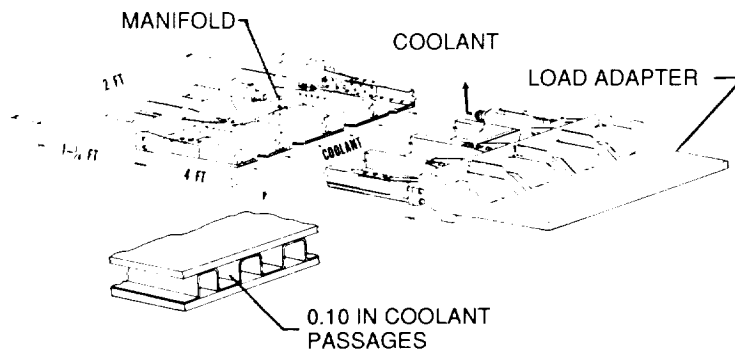
Figure 25

THERMAL-STRUCTURAL TESTS OF COOLED ALUMINUM PLATE/FIN PANEL

The LaRC-Rockwell glycol/water cooled aluminum structural panel (see figure 26) was tested under combined thermal and structural loading in the Active Cooling Test Stand shown in figure 25. More than 100 load cycles were applied at room temperature, and over 5000 load cycles were applied with the panel subjected to the design heat flux. The panel was subjected to 16 thermal cycles and more than 10 hours at elevated temperature. The maximum measured temperature was 231°F, and the maximum average heat flux was 11.8 Btu/ft²-sec. The coolant inlet temperature was varied from 48°F to 120°F in an attempt to simulate four-foot sections of the full scale 20-foot-long panel. The panel survived all of the testing with no evidence of structural damage. Visual and x-ray inspections indicated no cracking, and there were no significant changes in strain distribution during testing. Additional details of the investigation may be found in reference 42.

Several lessons were learned from this testing which will be even more important for testing of actively cooled structures at higher heat fluxes. (1) Sensors on the heated surface of an actively cooled structure encounter significant through-the-thickness temperature gradients, which must be factored into the data reduction. (2) Even for this high thermal conductivity aluminum panel, significant transient strains associated with thermal stress were observed during start up and shut down of the heaters. For lower conductivity materials subjected to higher heat fluxes, particular attention must be given to the thermal transients to avoid unrepresentative thermal stresses. (3) Because of entrance and transition effects in the coolant flow, thermal measurements from foreshortened coolant passages may not be representative of longer panels.

PANEL CONFIGURATION



TEST SUMMARY

HOT MECHANICAL LOAD CYCLES	5005
THERMAL CYCLES	16
TIME AT ELEVATED TEMPERATURE	10 HR 9 MIN
MAXIMUM MEASURED PANEL TEMPERATURE	231°F
MAXIMUM HEAT FLUX	11.8 BTU/(FT ² -SEC)
COOLANT INLET TEMPERATURE RANGE	48 TO 120°F

Figure 26

ACTIVE COOLING APPLICATIONS FOR NASP

The remainder of the present paper presents information taken from a review (ref. 6) of actively cooled structures development under the National Aero-Space Plane (NASP) project. Most of this work was performed under Work Breakdown Structure (WBS) elements 4.4.03 and 4.4.04 of the NASP Technology Maturation Program (TMP). Some additional information from the NASP Materials Consortium and the mainline engine program are also included. Details of the airframe studies (WBS elements 4.4.03 and 4.4.04) are presented in references 43 and 44.

Typical regions on NASP where active-cooling is required and the corresponding ascent conditions are indicated in figure 27. Fortunately for NASP, the most severe conditions occur during ascent when the cryogenic hydrogen fuel, which is an excellent coolant, is available as a heat sink. In many cases the more benign re-entry conditions dictate the maximum temperature requirements of the structure because the cryogenic fuel is not available as a coolant. The information presented in the present paper is limited to the acreage area applications (inlet ramp, nozzle, and engine interior), and is confined to convective cooling. Results of studies to develop cooled concepts for stagnation regions are described in references 45 and 46. Cooled airframe structures differ from engine structures in that, in addition to generally lower heat fluxes, the airframe structural loads are characteristically inplane loads. However, loads for engine structures arise primarily from the need to contain hot engine gases. Both engine and airframe structure must sustain thermal and coolant pressure loads.

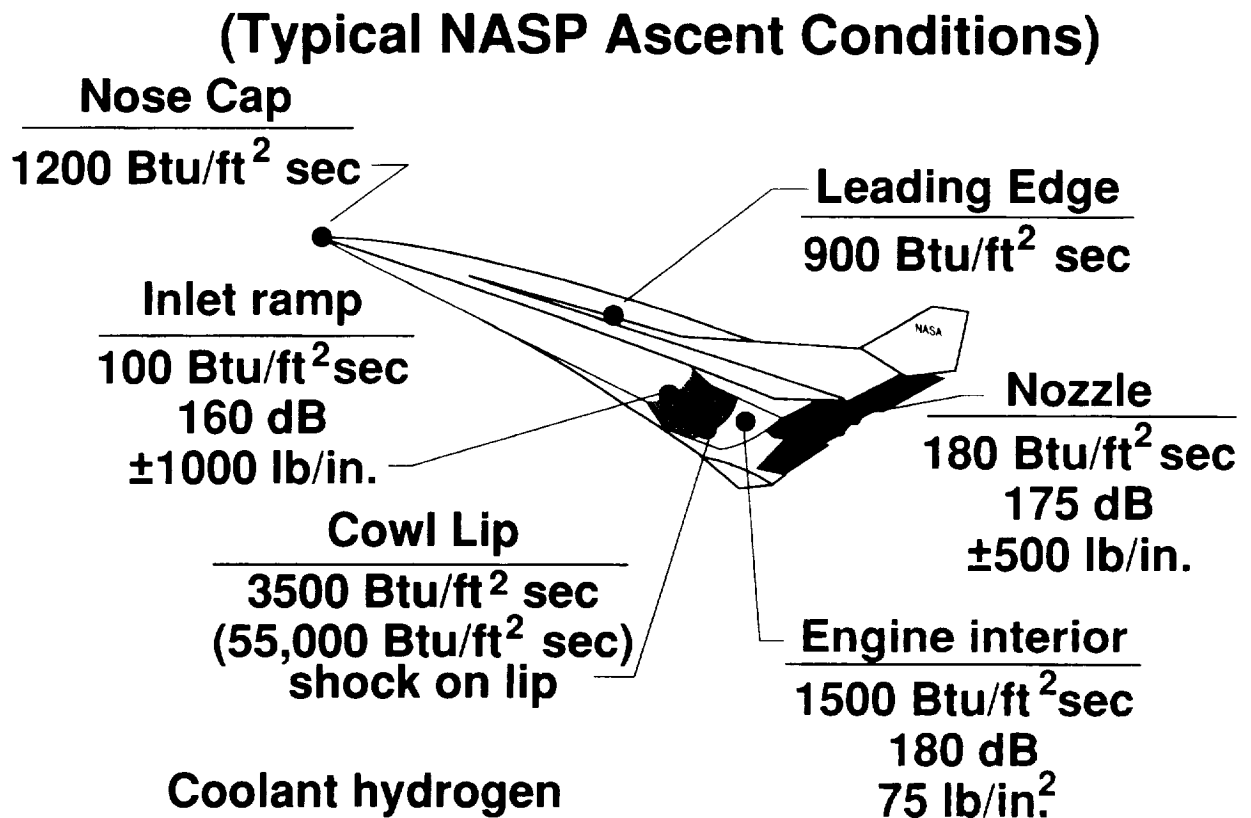


Figure 27

ACTIVELY COOLED PANELS MADE UNDER NASP TMP OPTION 3

The McDonnell Douglas Corporation NASP TMP Option 3 program (WBS 4.4.04) was conducted over a period of 5 years. Initial analytical studies included conceptual design and trade studies for inlet ramp, external nozzle, and control surface applications. Subsequent fabrication development efforts were limited to integral heat exchanger/structural concepts for the inlet ramp and non-integral heat exchanger/structural concepts for the nozzle. Several actively cooled panels were fabricated, two test facilities were constructed, checked-out and used to test the actively cooled panels. Details of the McDonnell Douglas work can be found in their TMP Option 3 Final report (ref. 44). Subcomponent (6 in. by 6 in.) and component (2 ft by 2 ft) panels fabricated at MDC's direction are shown in figure 28. The panels used a variety of materials (titanium metal matrix composite, beryllium, and copper/graphite), attachment concepts (integral and non-integral), and heat exchange configurations (D-groove and skin/tube). The subcomponent panels, which were part of the fabrication development, were tested at Wright Laboratories with gaseous nitrogen as a coolant. Subsequently the copper/graphite and beryllium platelet subcomponent panels and the full size component panels were tested in the hydrogen facility at WYLE Laboratories, Norco, California.

Details of the fabrication development and testing efforts are presented in references 47, 48 and 49.

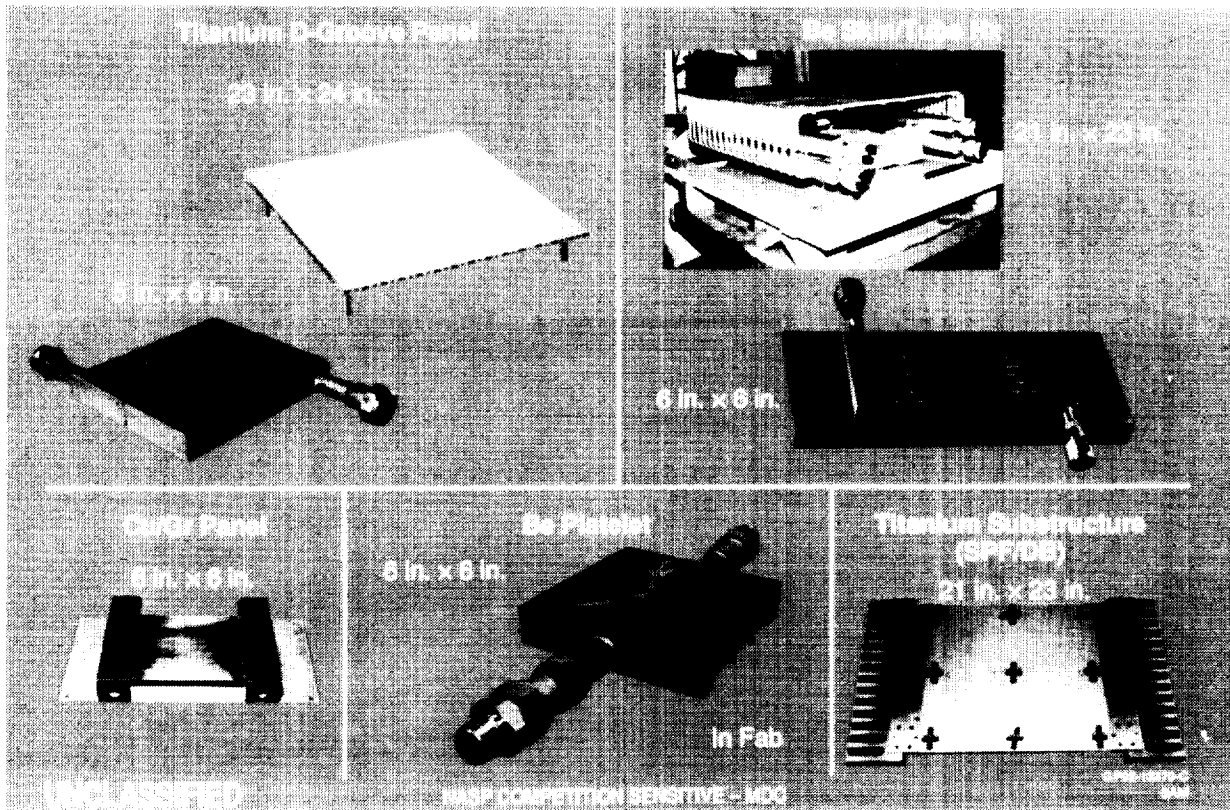


Figure 28

AFWAL SUBCOMPONENT PANEL TEST FACILITY

The Wright Laboratories (formerly AFWAL) active cooled thermal test facility provided the capability for testing of the subcomponent panels using room temperature N_2 as a coolant. The facility shown in figure 29 also incorporates a nitrogen tube trailer which is used to fill two 600 ft³ spheres. These spheres can be pressurized to approximately 4000 psi, which provides a reservoir for testing panels at pressures up to 2000 psi at flow rates on the order of 1 to 2 lb/sec. A graphite heater array provides heating rates up to 350 Btu/ft²-sec to the subcomponent panels. The test enclosure is also purged with nitrogen to protect the graphite heaters from oxidation. Additional details of the facility may be found in references 44 and 50.

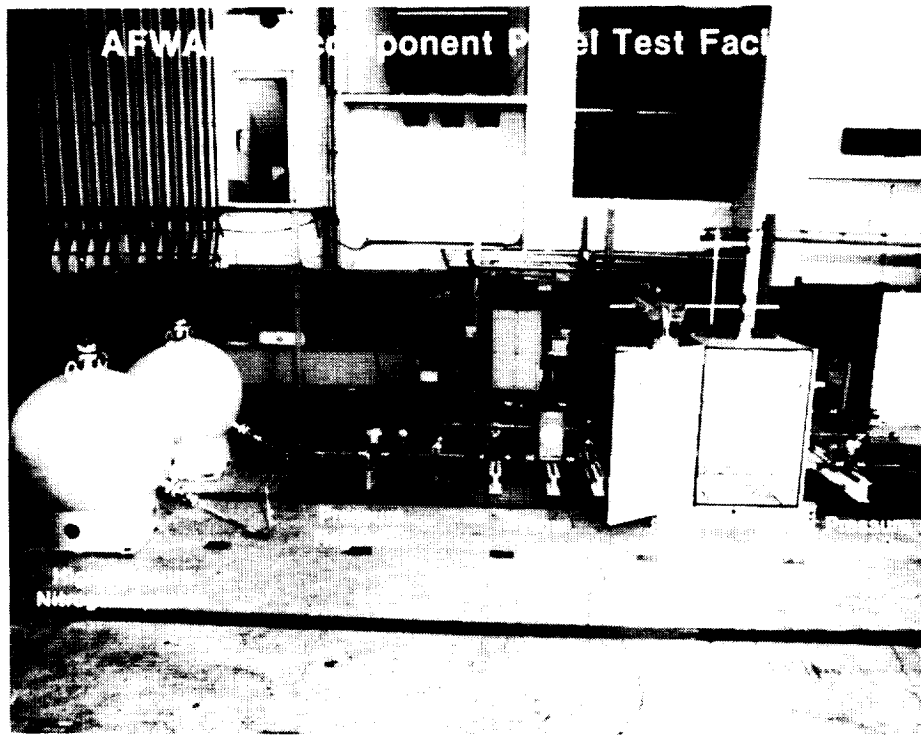


Figure 29

ORIGINAL PAGE
BLACK AND WHITE PHOTOGRAPH

WYLE LABORATORIES H₂ ACTIVE COOLING TEST FACILITY

A thermal/structural facility for testing actively cooled panels (see figure 30) was established at the WYLE, Norco test site. This facility, which can accommodate panels up to 2-ft by 4-ft, uses nitrogen or supercritical hydrogen as coolants. Hydrogen can be provided at temperatures between -360°F and +40°F, flow rates up to 2.3 lb/sec, and pressures up to 2000 psi. Heating capability extends up to approximate 280 Btu/ft²-sec. Additionally, the facility is capable of providing mechanical loads (either tension or compression) of up to 48,000 lbs. The test chamber is continuously purged with N₂ to protect and extend the life of the graphite heaters. Additional details of the facility are presented in references 44, 49 and 51.

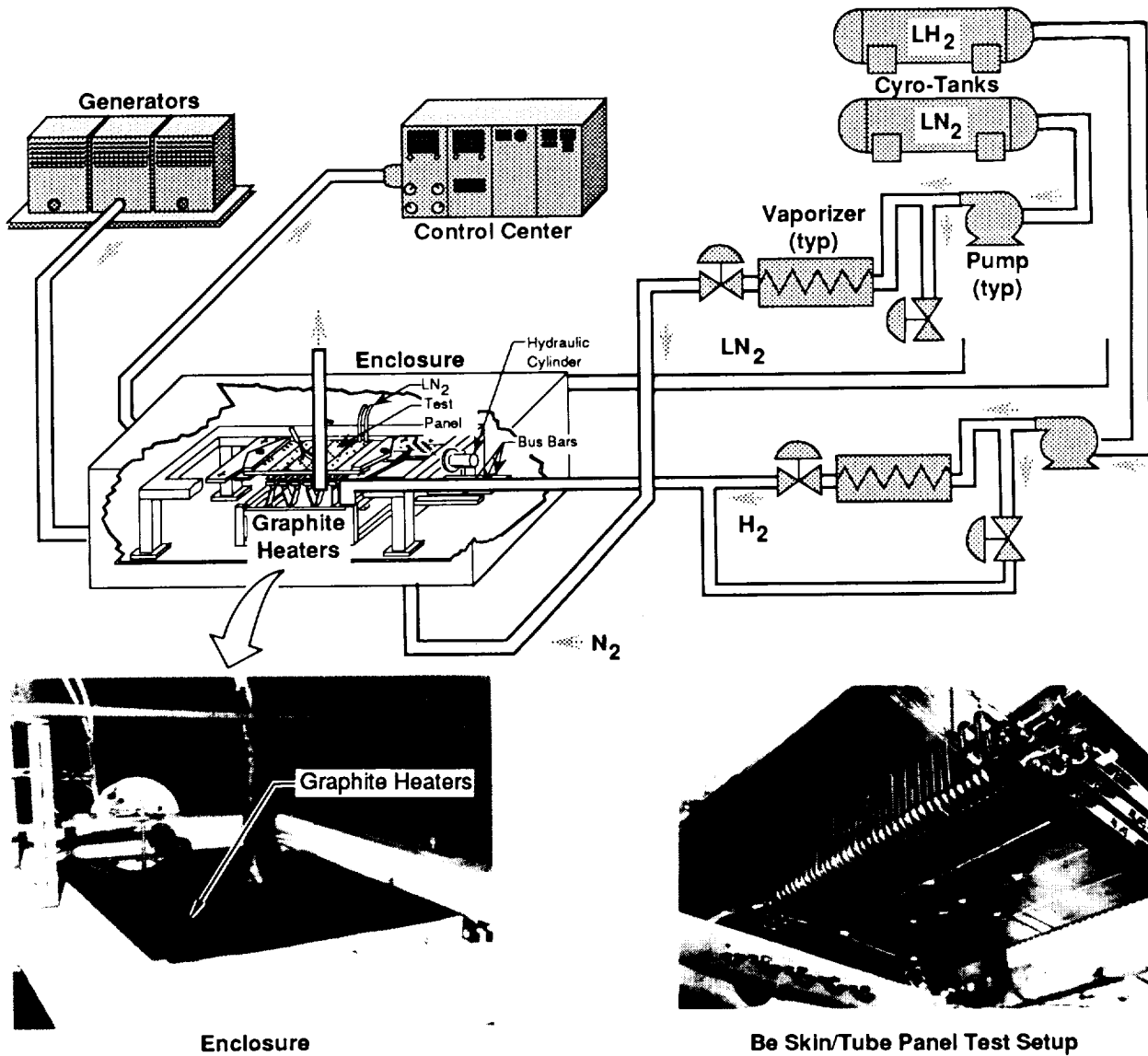


Figure 30

TITANIUM D-GROOVE PANEL

The titanium D-Groove panel (see figure 31) which was designed for an inlet ramp for NASP is representative of an integral heat exchanger/structural design in that the heat exchanger and substructure are metallurgically bonded to form a single entity. The panel was designed by McDonnell Douglas Corporation and fabricated by Rohr Industries. The materials of construction for this panel were the best high temperature titanium alloys currently available.

The panel materials are given below:

outer face sheet	•	SiC/Ti*
etched sheet	•	Ti-14Al-21Nb
honeycomb	•	Ti-15v-3Cr-3Sn-3Al
manifold/edge	•	Ti-6Al-2Sn-4Zr-2Mo
inner face sheet	•	SiC/Ti*

The design chosen extends the coolant passage as close to the edges as possible by folding the flow back on itself as it exits the manifold and enters the D-shaped coolant passages. This is done to prevent overheating of the panel-to-panel joint region. The manifolds also form the load path through which in-plane mechanical loads are transmitted from panel to panel.

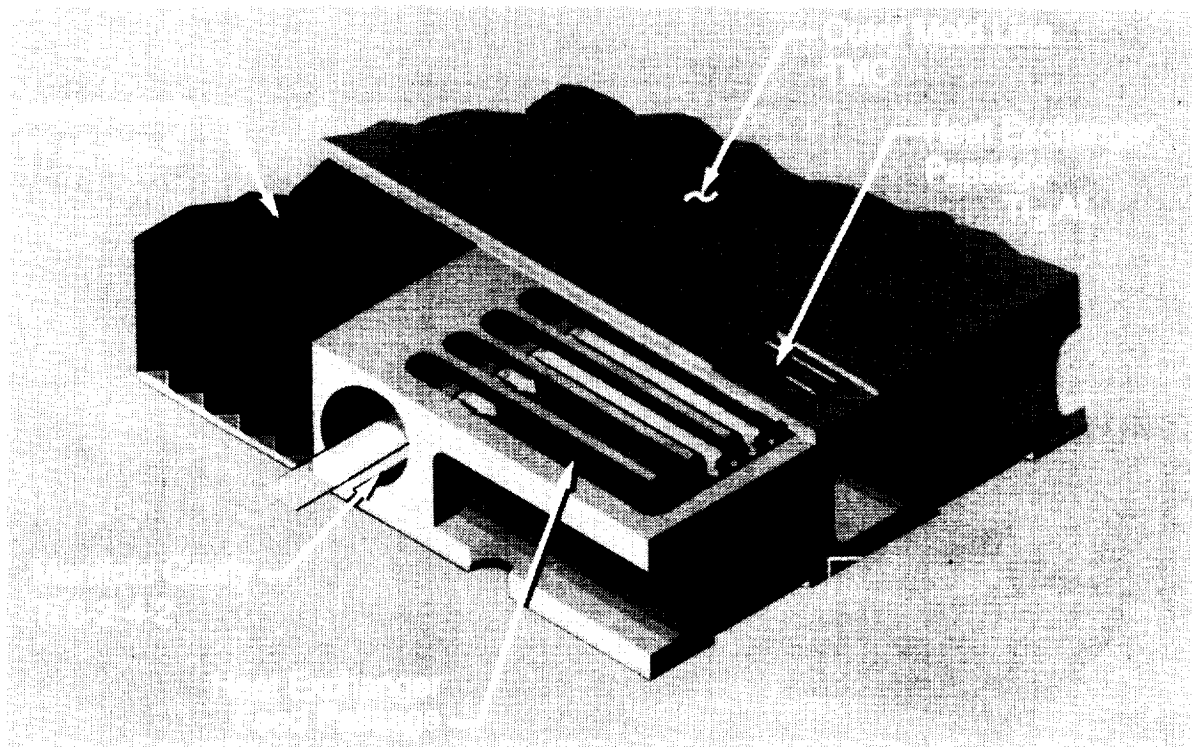


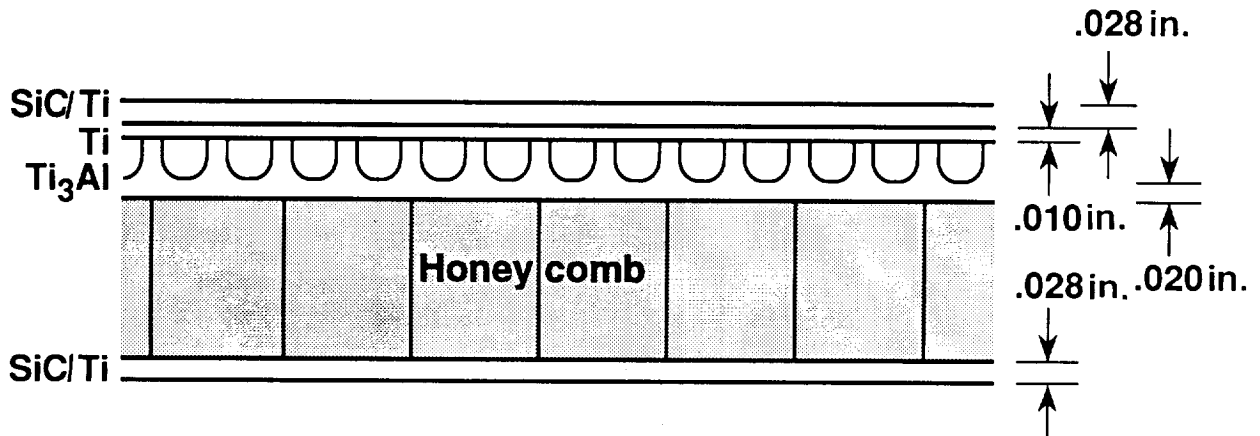
Figure 31

* The outer and inner facesheets are titanium matrix composites (TMC) comprised of 0.0056 in. diameter silicon carbide fibers (SCS-6) in a Ti-15V-3Cr-3Sn-3Al matrix.

TITANIUM D-GROOVE PANEL FAILURE

The 2-ft by 2-ft Titanium D-groove panel which had been hydrostatically tested previously to 3000 psi failed without warning at a pressure of approximately 1/10 that value as the panel was being pre-cooled with nitrogen prior to testing. Design and test conditions for the titanium D-groove at failure are summarized in figure 32. Exact conditions at failure are unknown since the data acquisition system had been deactivated, after the panel had been at approximately the indicated conditions for about one hour while malfunctioning test equipment was being repaired.

SiC Ti - Ti₃ Al GROOVED PANEL



- Design: 100 Btu/ft²sec, 1000 lb/in., 2000 psi LH₂ coolant
- Failed: Prior to test, during panel precooling with N₂
- Conditions: 0 Btu/ft²sec, 0 lb/in., 340 psi N₂ @ 20-40°F
- Residual stress 55 ksi; critical crack length 0.040 in.

Figure 32

HEAT EXCHANGER SKIN FRACTURE

The nature of the damage to the failed Titanium D-groove panel is shown in figure 33 (note that the photograph in the lower left corner of figure 33 shows load adaptors and carrying frame that are not part of the panel). While the exact cause of failure was not ascertained, it is believed that poor fracture toughness (as evidenced by the small critical crack length), residual stresses (because of the mismatch in thermal expansion characteristics of the cover and grooved sheets), and one or more flaws in the titanium aluminide grooved sheet were involved. The failure mechanism postulated from the post-test analysis suggests the following scenario: 1) a failure, quite possibly an overload or crack growth failure in the grooved titanium aluminide sheet, opened the honeycomb cavity to high pressure nitrogen; 2) since the honeycomb was not perforated, the honeycomb cells failed progressively at the braze joint with the top and bottom face sheets; 3) after a large enough area of the honeycomb had been disbonded from the skin, the internal pressure became large enough to rupture the skin (refs. 44 and 49).

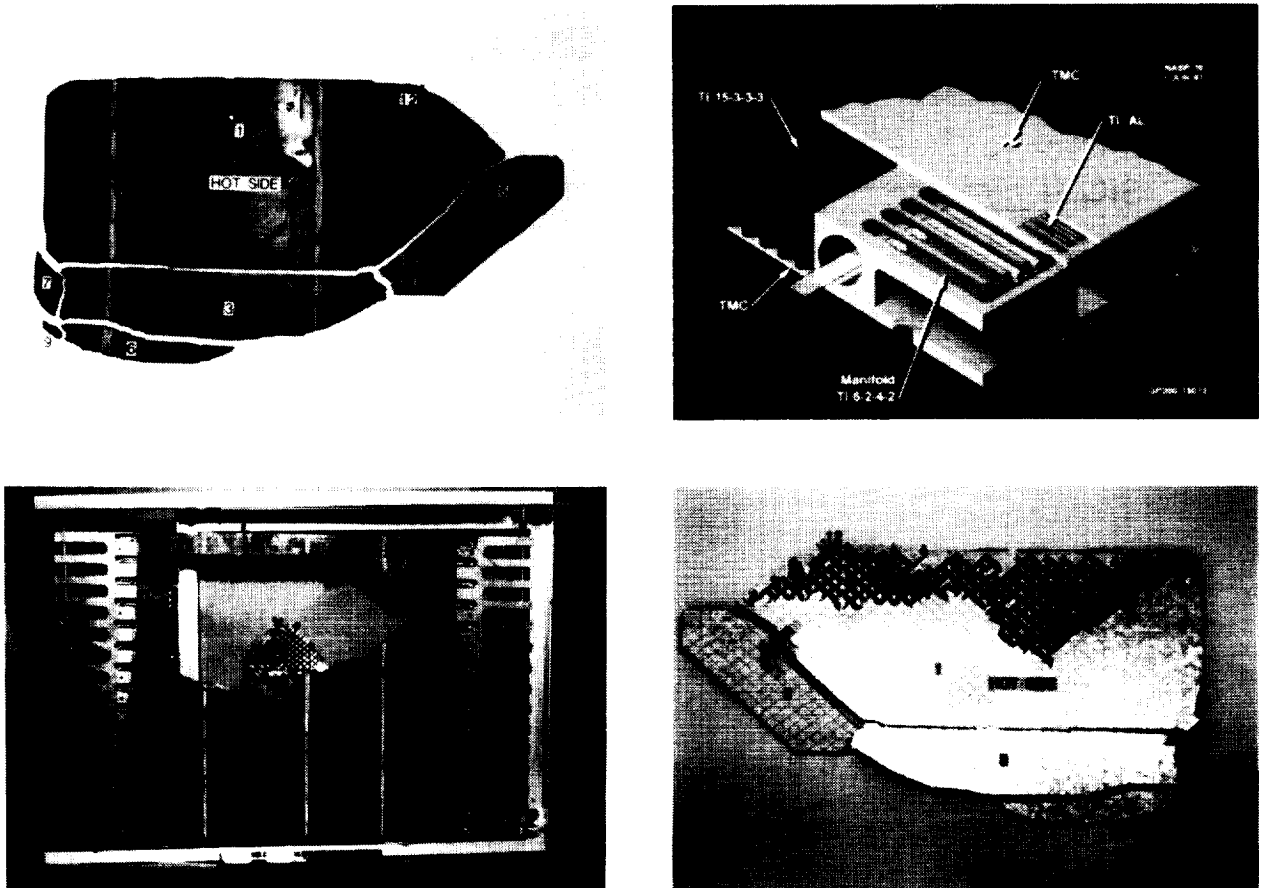


Figure 33

BERYLLIUM SKIN/TUBE PANEL

Figure 34 illustrates the conceptual design of an actively cooled panel for an exterior nozzle application as viewed from the back side. This concept employs a non-integral beryllium skin/tube heat exchanger mounted onto a four sheet titanium superplastically formed/diffusion-bonded (SPF/DB) sandwich structure by means of nine slide mechanisms which allow for differential thermal expansion between the heat exchanger and the titanium sub-structure. This panel concept which was chosen to demonstrate the efficient utilization of high-thermal-conductivity materials, features counter flowing coolant in adjacent coolant passages. Manifolds supplying coolant to the heat exchanger, which were not a flight-weight design, were of stainless steel. The design was developed by McDonnell Douglas Corporation and fabricated by Electrofusion Corporation.

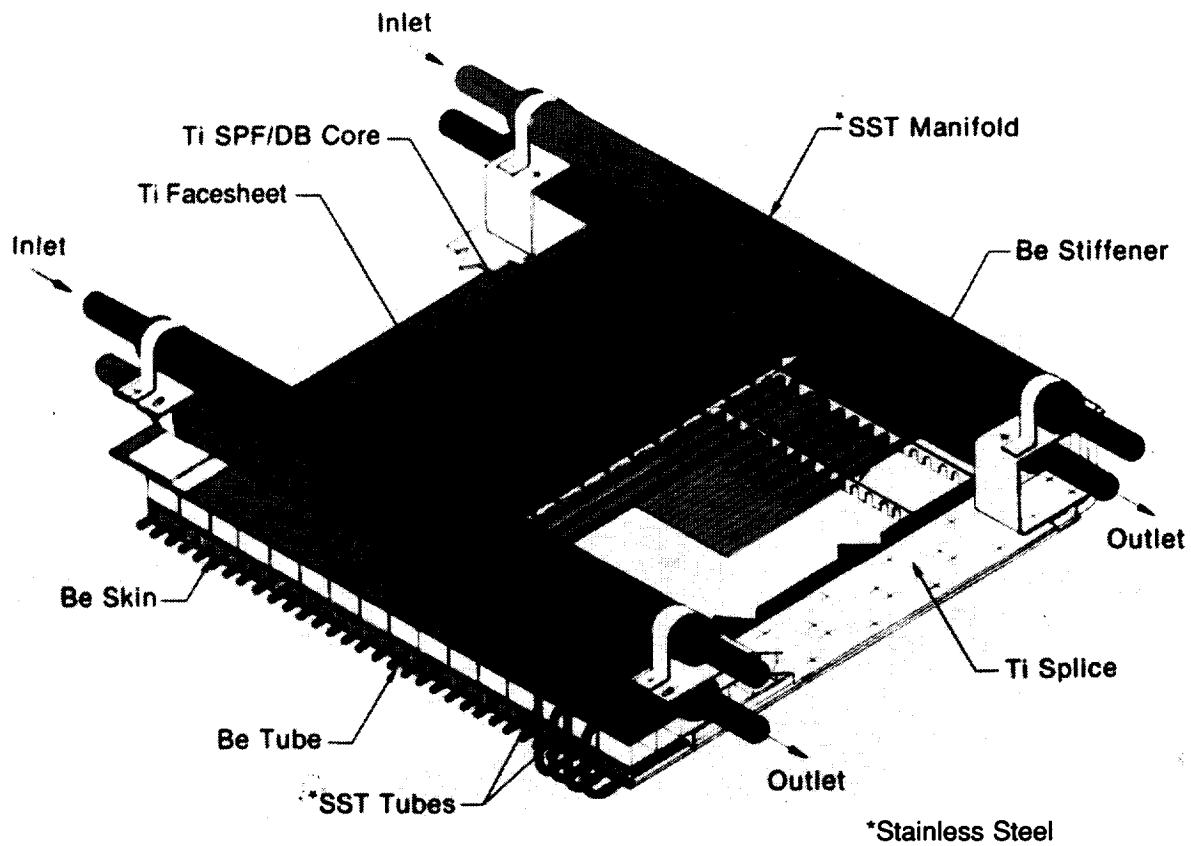


Figure 34

BERYLLIUM SKIN/TUBE PANEL MOUNTED IN WYLE TEST FACILITY

Figure 35 shows the heated surface of the beryllium skin/tube panel mounted in the WYLE load frame prior to testing. Part of the load fitting is visible at the left end of the panel. Also visible at both ends are copper heat exchangers which were used to maintain the load fittings at or near the same temperature as the titanium substructure. For actual testing a graphite heater array was mounted beneath the panel and the panel and heater were enclosed within a ceramic box to limit heat loss.

During initial testing the panel was exposed to eight heating periods of various intensity totaling 2.4 hours and reached a maximum heat flux of approximately 70 Btu/ft²-sec using hydrogen (at temperatures down to -90°F) as the coolant. Instrumentation difficulties occurred and all hot surface sensors were destroyed. The remaining thermal measurements agreed well with predictions; however, the strain measurements were less reliable. For more details, see references 44 and 49.

HEATED SIDE

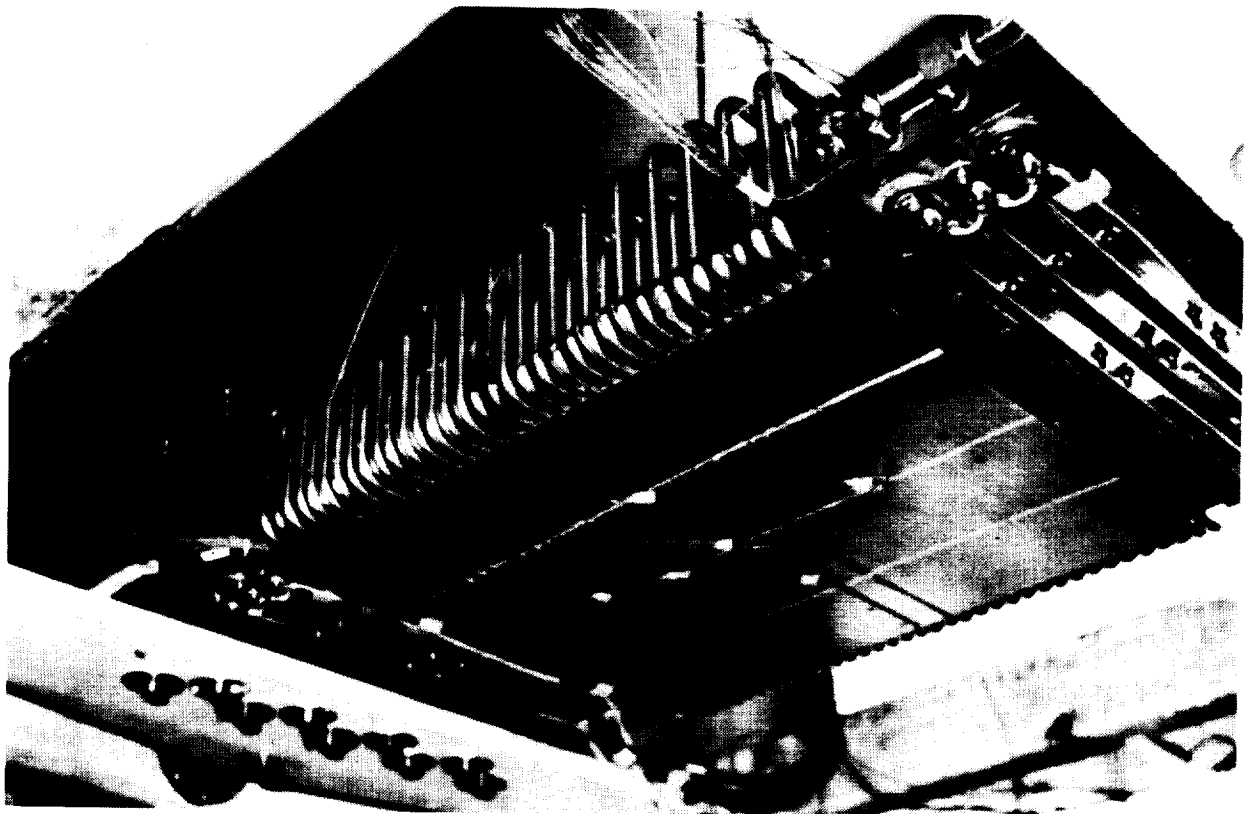


Figure 35

ORIGINAL FACE
BLACK AND WHITE PHOTOGRAPH

BERYLLIUM SKIN/TUBE PANEL SHATTERED DURING FAILURE

After the successful tests at 70 Btu/ft²-sec, the skin/tube panel failed catastrophically under essentially no load as the coolant inlet temperature was being lowered from -90°F to -150°F. The panel at the time of failure was at a temperature of approximately -126°F, contained cryogenic hydrogen at a pressure of 1600-1800 psi, and was exposed to a heating rate less than 1 Btu/ft²-sec. The panel had previously been hydrostatically tested to 3000 psi at ambient temperature. As indicated by figure 36 the beryllium heat exchanger surface was completely blown away, exposing the titanium structural subpanel which was undamaged. The entire beryllium panel actually shattered into thumbnail-size pieces.

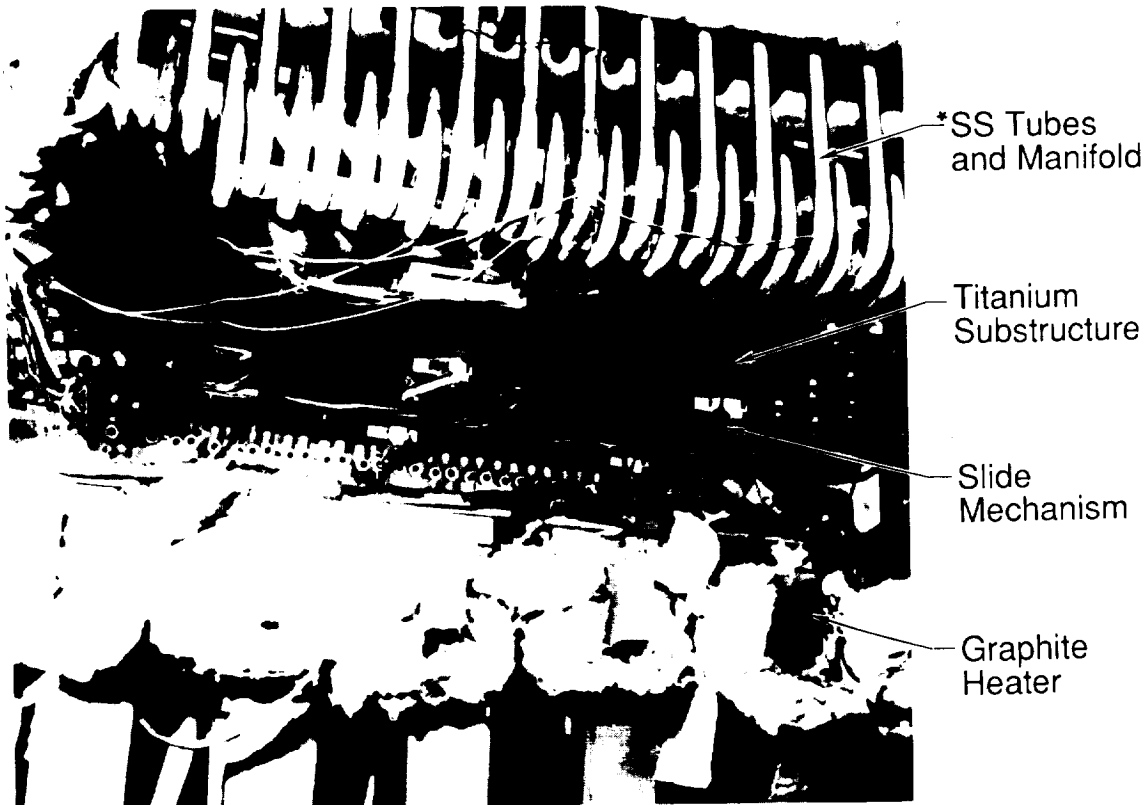


Figure 36

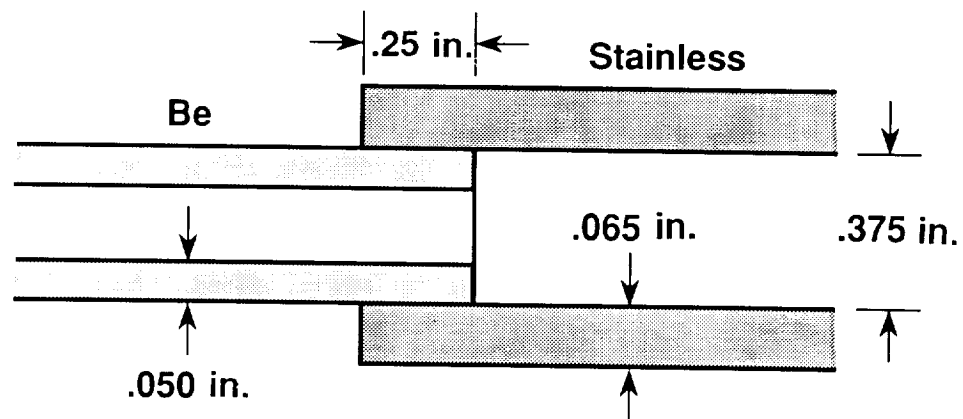
*Stainless Steel

ORIGINAL PAGE
BLACK AND WHITE PHOTOGRAPH

BERYLLIUM TUBE-SKIN PANEL

Design and test conditions at failure are summarized in figure 37. Large compressive circumferential stresses are induced in the beryllium tube by the stainless steel tube as the temperature of the joint decreases from the braze consolidation temperature of approximately 1000°F to the failure temperature of -126°F. This compression of the beryllium tube by the surrounding stainless steel tube also induces large axial bending stresses in the beryllium tube at the joint. These large axial tensile stresses, resulting from bending, exceed the strength capabilities of the beryllium at the failure temperature.

An extensive failure analysis concluded that a mismatch in thermal expansion characteristics of a dissimilar metal (beryllium-stainless steel) brazed tube joints in the coolant manifolds was the most probable cause of failure. As stated in reference 52, "Localized high stresses, resulting from brazing (together) materials having different coefficients of thermal expansion, initiated a brittle fracture of one or more beryllium tubes . . . (which) led to a rapid progressive break-up of the panel." (Note that the beryllium-stainless steel tube joint was an artifact of the test configuration and was not subjected to thermal stress analysis before testing.)



- Design: 160 Btu/ft²sec, 500 lb/in., 2000 psi LH₂ coolant
- Failed: As coolant temp being lowered from -90° to -150°F after a successful 70 Btu/ft²sec test
- Thermal stress: Be/347 stainless steel tube joint
 - Circumferential (under/joint) -61 ksi
 - Meridional bending (edge of joint) +58 ksi

Figure 37

BERYLLIUM PLATELET COMPONENTS

A subcomponent beryllium panel was fabricated as part of the NASP TMP Option 3 actively cooled panel activity. The design was developed by Aerojet TechSystems and McDonnell Douglas Corporation and the panel was fabricated by the Electrofusion Corporation. The panel construction details are shown in figure 38. A series of 55 D-shaped grooves were chemically milled into a .07-inch-thick beryllium plate. An orifice was electric discharge machined (EDM'd) into the end of each channel. A .030-inch-thick close-out sheet was brazed to the chemically milled plate. A variable area manifold was then brazed to each end of the heat exchanger panel, along with a beryllium egg-crate structure. Manifold inlet and outlet tubes (not shown in the photograph) were brazed to the manifold. Originally these tubes had a beryllium-stainless steel braze joint similar to the beryllium skin/tube manifold joints. Subsequently the stainless steel tubes were replaced with Inconel 718 tubes to avoid the coefficient of thermal expansion mismatch problem experienced with the beryllium skin/tube panel.

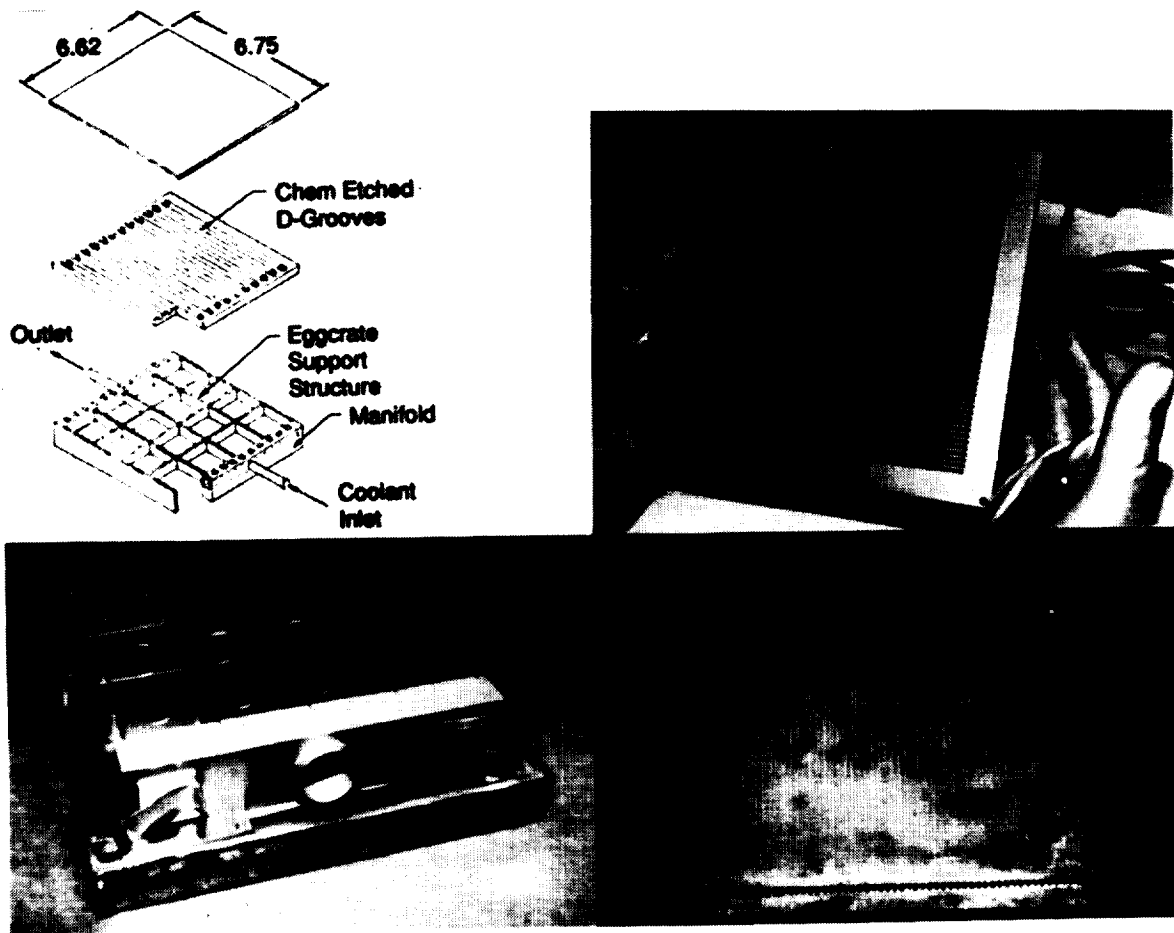


Figure 38

BERYLLIUM PLATELET PANEL TEST SUMMARY

The table in figure 39 summarizes the beryllium platelet panel tests at both Wright Laboratories and Wyle Laboratories. The panel as originally fabricated was tested at Wright Laboratories with gaseous nitrogen as the coolant. This panel had beryllium/stainless steel tube joints similar to those which failed in the beryllium tube-skin panel tests described previously. However, minimum temperatures encountered were approximately 40°F, which is well above the temperature at which the beryllium skin-tube panel failed. (Note that lower temperatures produce higher thermal stresses in the beryllium-stainless steel tube joint.) The panel was tested at various heating rates up to the maximum attainable with the graphite heater (280 Btu/ft²-sec) and exposed to 34 thermal cycles with heat fluxes of 200 or greater with no evidence of damage. Before testing with hydrogen coolant at significantly lower temperatures, the panel was modified to eliminate the beryllium-to-stainless-steel tube joint, as described previously. The modified panel was tested at WYLE laboratories with supercritical H₂ as the panel coolant at inlet temperatures as low as -200°F and heat fluxes as high as 280 Btu/ft²-sec. Subsequently the panel was exposed to an additional 98 thermal cycles at heat fluxes up to 200 Btu/ft²-sec with no evidence of damage. Post-test thermal analysis has produced very close agreement with measured test data. Further details are given in reference 44.

WRDC FACILITY TESTS

Heat Flux (Btu/ft ² - sec)	Flow Rate (lb/sec)	Coolant	Inlet Temperature (°F)	Inlet Pressure (psi)
50	1.5	N ₂	30	2000
100	1.5	N ₂	30	2000
150	2.5	N ₂	30	2000
200	2.3	N ₂	30	2000
250	2.3	N ₂	30	2000
280	2.3	N ₂	30	2000
200	0.8	N ₂	30	2000
200 30 Thermal Cycles	1.4	N ₂	30	2000

WYLE LABORATORIES TESTS

0-280 ↓ ↓ ↓ ↓	0.1-0.2	H ₂	40	2000
	0.1-0.2	H ₂	-70	2000
	0.1-0.2	H ₂	-140	2000
	0.1-0.2	H ₂	-200	2000
0-200 98 Thermal Cycles	0.1-0.2	H ₂	-70	2000

Figure 39

COPPER/GRAPHITE SUBCOMPONENT PANEL

A cross-section of the Cu/Gr panel fabricated by Sparta Incorporated under the McDonnell Douglas Corporation (MDC) Option-3 contract is illustrated in figure 40, together with the final assembled hardware. The Cu/Gr panel is made from two mated symmetric, grooved half panels. Each half panel uses a symmetric ply layup consisting of an outer copper foil layer, two plies of Cu/Gr (90° fiber orientation) and three plies of Cu/Gr with fibers in the 0° orientation. The cross-ply design increases the panel strength in the two orthogonal directions. Fifty-six nickel tubes, embedded within the two half sheets, serve to limit the diffusion of hydrogen into the Cu/Gr composite. The 6-inch square panel was part of the fabrication development and is equipped with non-flight type manifolds. Details of the design and fabrication are presented in reference 53.

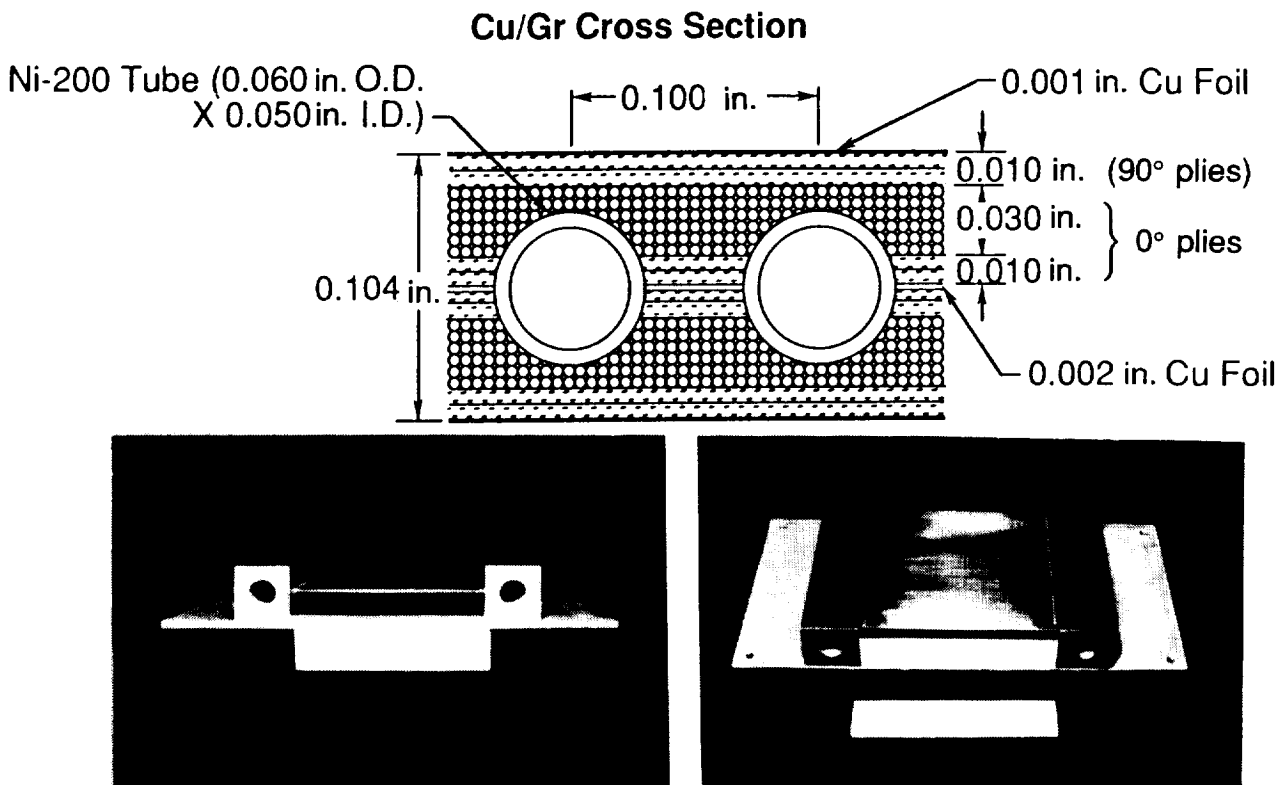


Figure 40

Cu/Gr SUBCOMPONENT PANEL TEST SUMMARY

The table shown in figure 41 summarizes the Cu/Gr panel tests at Wright Laboratories. Handling of the Cu/Gr panel prior to the tests resulted in several cracks in the bare nickel tubes immediately adjacent to the manifolds. As a consequence, the inlet N₂ pressure was limited to 1500 psi to minimize the impact of tube leakage. The panel successfully survived 50 thermal cycles at a heat flux of 200 Btu/ft²-sec and a maximum heat flux of 350 Btu/ft²-sec. However, as in all other tests, hot surface instrumentation failed at a heat flux of 98 Btu/ft²-sec or less. Trends indicated by the temperatures measured by back side thermocouples were similar to those predicted analytically; although the measured temperatures were consistently higher.

Subsequent to the tests at Wright Laboratories, copper was electroplated over the exposed tubes in an attempt to repair the leaks. These repairs were partially successful. Attempts to test the Cu/Gr panel with hydrogen at the Wyle test site were aborted because of the highly non-uniform thermal response of the panel. Post-test examination revealed that seven of the tubes at the far end of the inlet manifold were either totally or partially blocked by debris. These results emphasize the need for cleanliness when small coolant passages are involved. Additional information is presented in reference 44.

Heat Flux (Btu/ft ² - sec.)	Flow Rate (lb/sec)	Coolant	Inlet Temperature (°F)	Inlet Pressure (psi)
50	0.5-1.3	N ₂	30	1500
98	0.5	N ₂	30	1500
150	1.0	N ₂	30	1500
200	1.0	N ₂	30	1500
250	1.0	N ₂	30	1500
300	1.0	N ₂	30	1500
350	1.5	N ₂	30	1500
200 50 Thermal Cycles	0.4-1.0	N ₂	30	1500

Figure 41

Cu/Gr ACTIVELY COOLED PANEL

After some initial generic studies, the Rockwell actively cooled primary structure program (NASP TMP WBS 4.4.03) was focused on concepts suitable for the engine structure. An advanced copper graphite (Cu/Gr) design concept, similar to that developed under WBS 4.4.04, was selected for the diffuser and film cooling was selected for the combustor.

The heat exchanger for the diffuser panel (see figure 42) is integrally bonded to the support structure. The heat exchanger is made of cross-plyed Cu/Gr material with embedded Ni 200 coolant passages. The tubes are 0.005-in. thick and have an outer diameter of 0.060 in. The heat exchanger and honeycomb thicknesses are 0.104 in. and 1.0 in., respectively. The graphite fiber is P-130X, which has a thermal conductivity three times that of copper at room temperature.

The design loadings are heat flux = 800 Btu/ft²-sec, coolant pressure = 2000 psi, and aerodynamic pressure = 10 psi. Supporting analyses have been performed using the design conditions. These analyses show low thermal gradients in the heat exchanger and acceptable stresses in the Cu/Gr material. Classical lamination theory, three-dimensional, two-dimensional, and metal-matrix composite codes, were used in the analyses.

Three small heat exchanger fabrication articles were fabricated with each measuring 2 in. by 6 in. One of these articles was cut into 1 inch square pieces for thermal cycling tests. These tests were performed from cryogenic (-250°F) to elevated (800°, 1000°, and 2000°F) temperatures for 1, 5, and 50 cycles. It was concluded that the material and design were capable of a 1000°F operating temperature, although more testing is necessary.

Two 12 in. by 12 in. Cu/Gr actively cooled panels have been fabricated by SPARTA Incorporated (reference 53). Thermal testing will be performed in the Rocketdyne Materials Structural Thermal Validator (MSTV-1) shown in figure 43. Characterization tests will determine the effect of coolant pressure, flow rate, and heat flux variations. Thermal cycling will be performed by varying an applied heat flux between 200 and 800 Btu/ft²-sec to demonstrate cyclic life. Acoustic testing will be performed in a plane wave facility at the Rockwell North American facility to a maximum level of 168 db. To determine panel response at the higher engine environment, the panel can be characterized by vibration testing. These results can be superimposed onto the acoustic test results. Fatigue testing of heat-exchanger/honeycomb articles will be performed to determine the acoustic fatigue behavior of the design. Additional details of the Rockwell studies may be found in reference 43.

(Figure 42 is shown on the next page.)

Gr/Cu Actively Cooled Panel

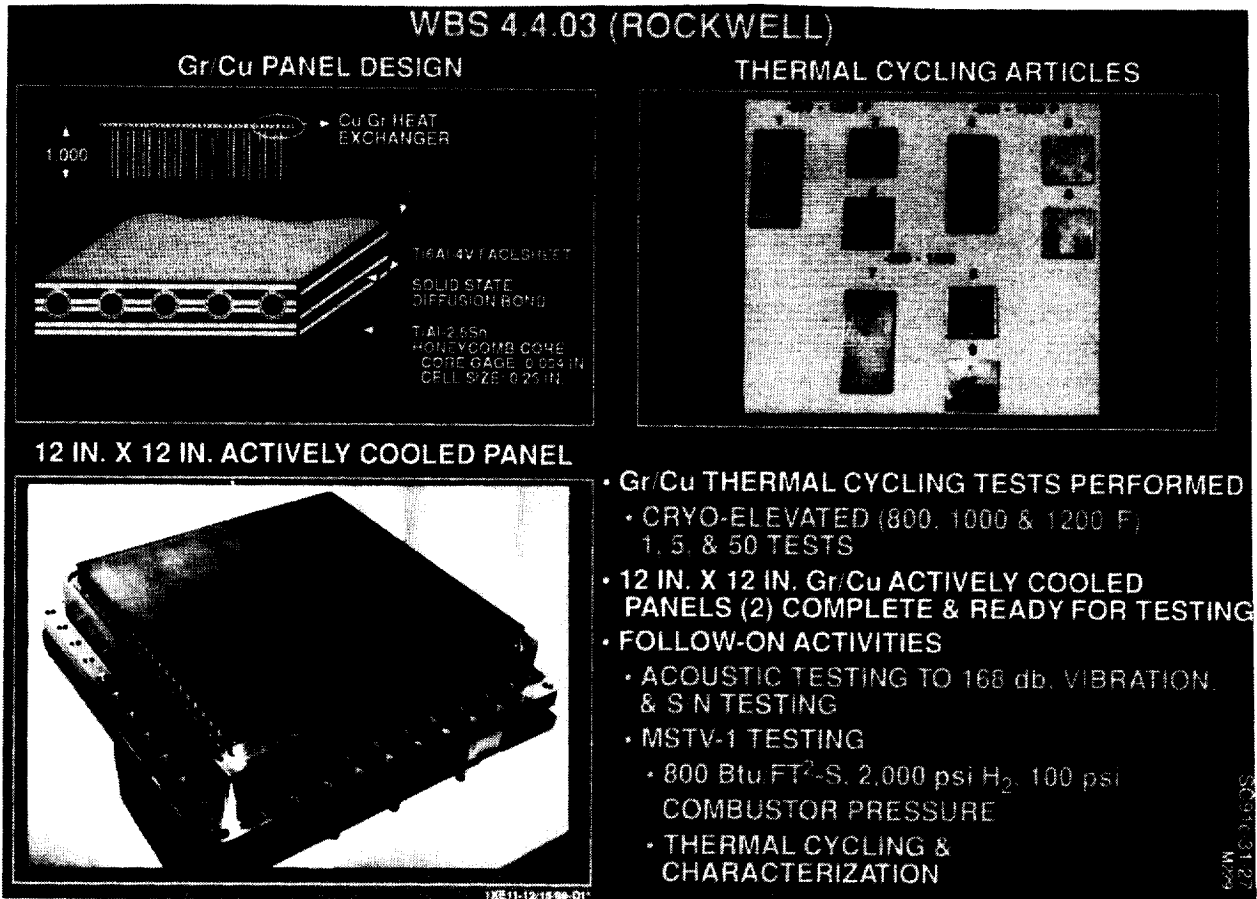


Figure 42

MATERIALS STRUCTURAL THERMAL VALIDATOR (MSTV-1) TEST RIG

The MSTV-1 test rig is a rectangular two dimensional hot gas generator, which burns liquid oxygen and gaseous hydrogen. The products of combustion, which will reach temperatures up to 6000°R, will be used to test actively cooled panels, attachments, seals and substructures. Fabrication of the MSTV-1 is complete and the test rig is currently being calibrated. The MSTV-1, shown in figure 43, is designed to supply a surface heat flux of 350 to 1400 Btu/ft²-sec with a chamber pressure of 65 to 350 psi, to a 12 in. by 12 in. actively cooled panel. The rig can operate from 30 to 50 seconds at maximum heat flux. Hydrogen coolant can be supplied to the panel test rig at a maximum rate of 2 lb/sec and an inlet pressure of 2670 psi at room temperature. An additional supply of 200°R hydrogen is also available. Real time calorimetry during the test of an actively cooled panel can also be provided. Tests of NARloy Z and Incoloy 909 cooled panels, attachments, seals and substructures are planned as part of the NASP program.

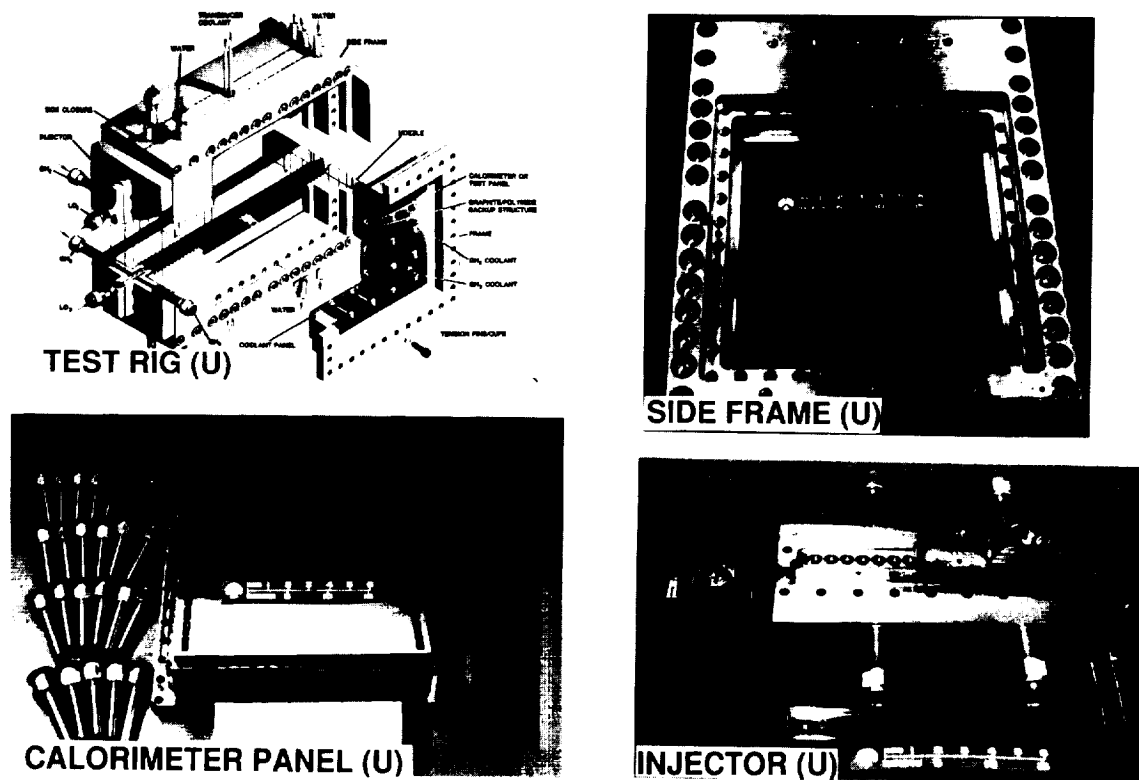


Figure 43

ORIGINAL PAGE
BLACK AND WHITE PHOTOGRAPH

MICROCHANNEL FABRICATION STUDIES

Very small grooves (microchannels) have been proposed as a means of reducing the weight of actively cooled panels and fabrication studies are underway. Microchannel grooves have been cut into Haynes 188, NARloy Z, and Incoloy 903 material using three fabrication processes; electric discharge machining (EDM), Electro-Chemical (ECM) etching and photoetching. Photographs of the channels are shown in figure 44. The microchannels are nominally .020-in.-wide by .010-in.-deep rectangles with a .003-in. radius on .038-in. centers for the EDM process, .023-in.-wide by .010-in.-deep ellipses on .034-in. centers for the ECM process and .020-in.-wide by .010-in.-deep semi-circles on .030-in. centers for the photoetching process.

EDM channels were cut into Haynes 188 by a subcontractor with a proprietary electrode and ECM channels were cut into Haynes 188 by a subcontractor using a proprietary etchant. Photoetching of Haynes 188 was unsuccessful. NARloy Z material could not be practically removed using the EDM process due to excessive tool wear, while ECM and photoetching processes exhibited varying degrees of success. A nitric acid solution was used as the etchant solution for the ECM process and a proprietary solution of ferric chloride and HCL was used as the etchant for the photoetching process. Using the photoetching process for NARloy Z resulted in the most repeatable channels and lands.

Channels were machined into Incoloy 903 using the EDM and the photoetching process. On the initial trial of the photoetch process a sludge formed in the Incoloy 903 channel prohibiting any further etching of the material. During the mechanical cleaning to remove the sludge, the photoresistant masking was inadvertently removed. The solution to keeping the masking attached to the surface of the Incoloy 903 was to slightly roughen the surface with a grit blast to provide adequate adhesion for the masking. Channels were then successfully cut into Incoloy 903 using a proprietary solution of ferric chloride and HCl. ECM of the Incoloy 903 panels is in progress. Details of the microchannel development are presented in reference 54.

(Figure 44 is shown on the next page.)

MICROCHANNEL FABRICATION DEVELOPMENT

FAB METHOD MATERIAL	EDM	ELECTROCHEM ETCH	PHOTOETCH
HAYNES 188			• UNABLE TO ETCH
NARloy Z	• TOOL WEAR UNACCEPTABLE		
INCOLOY 903		• IN PROGRESS	

Figure 44

ORIGINAL PAGE
BLACK AND WHITE PHOTOGRAPH

INCOLOY 909 DEMONSTRATOR PANEL

Early in the NASP Program an integral Incoloy 909 titanium actively cooled panel design was developed by Pratt and Whitney and Rohr Industries and the 20-inch-square demonstrator panel, shown in figure 45, was fabricated by Rohr Industries. The panel was designed to accommodate a heat flux of 320 Btu/ft²-sec, a hot gas surface pressure of 195 psi, a hydrogen coolant pressure of 1300 psi, and an acoustic load of 185 db with a maximum surface temperature of 1050° F. The panel features an Incoloy 909 heat exchanger and manifolds, sandwich panels on both the hot and cold sides of the assembly consisting of titanium 6-2-4-2 face sheets with 3-25 honeycomb core, and a titanium 6-2-4-2 egg crate type center structure.

There have been extensive correlations between results of dynamic structural analysis of the panel by Rohr Industries and tests of the panel by Pratt and Whitney. These correlations have included comparisons between results of finite element normal modes analysis and holographically measured mode shapes, and comparisons of predicted acoustic response with results of progressive wave tube tests at room temperature. The analysis considered sound sources and response mode shapes to 2500 hz, and accounted for partial structure exposure to the acoustic field, discrete frequency damping effects, and cross-modal coupled response. Despite the lack of rigorous structural damping data, there was good agreement between predicted and measured results.

An 8.9- by 9.0-inch, Incoloy 909 heat exchanger subcomponent panel was subjected to 15 thermal cycles at heating rate of 200 Btu/ft²-sec or greater (with a maximum flux of 260 Btu/ft²-sec) in the Wyle test facility with no evidence of panel damage.

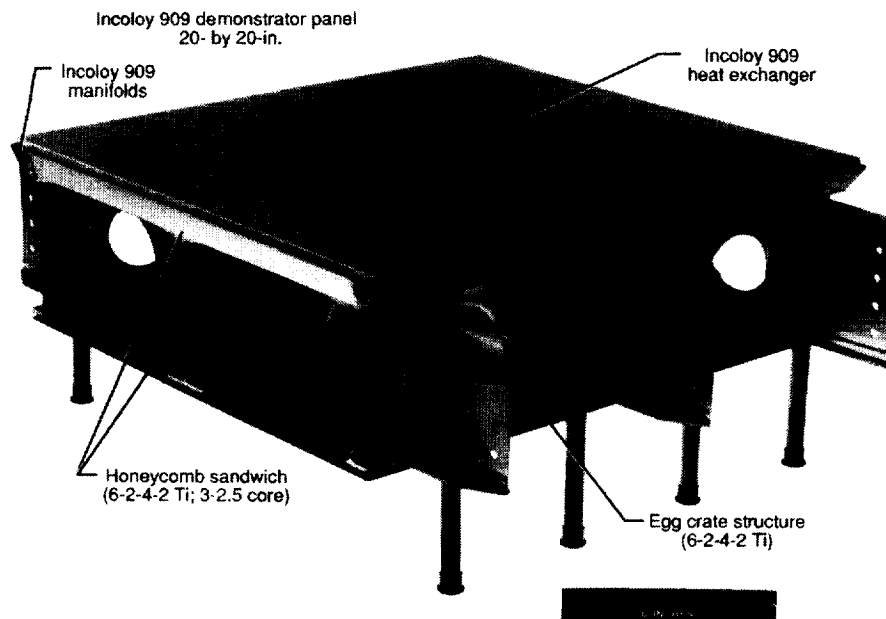


Figure 45

DEVELOPMENT OF C-SiC/REFRACTORY-METAL-TUBE HEAT EXCHANGERS

Considerable effort has gone into the development of a refractory-composite, skin-tube heat exchanger for a very high temperature, non-integral actively cooled structure. The primary incentive for this effort is to develop a cooled structure which can accommodate the very high heat fluxes encountered during ascent but does not require cooling during the more moderate (but still severe) heating during descent when the fuel/coolant is not available.

Based on initial material screening, design and optimization studies, and fabrication development efforts, carbon-silicon carbide was selected for the skin and Mo-50Re was selected for the tubes. The superior oxidation resistance of the silicon carbide matrix and compatibility of the coefficients of thermal expansion (CTE) of the tube and skin materials (relative to the other materials considered) were the primary factors leading to the material selections.

As indicated in figure 46 the continuing development of C-SiC/refractory-metal-tube heat exchangers has been a series of systematic studies involving both analytical and experimental efforts. The results, to date, have provided a detailed characterization of two-dimensional and three-dimensional C-SiC and refractory tubing materials, and have shown that through highly orthotropic tailoring, the mismatch of thermal expansion characteristic between the composite material and tubes can be minimized. The studies have established a data base for the materials, developed and demonstrated suitable fabrication techniques, and identified test techniques for validating the performance of the heat exchanger. Future plans include the fabrication and testing of a larger (8 in. by 12 in.) heat exchanger subcomponent. For additional details see references 54 and 55.

(Figure 46 is shown on the next page.)

DEVELOPMENT of C-SiC/REFRACTORY METAL-TUBE HEAT EXCHANGERS

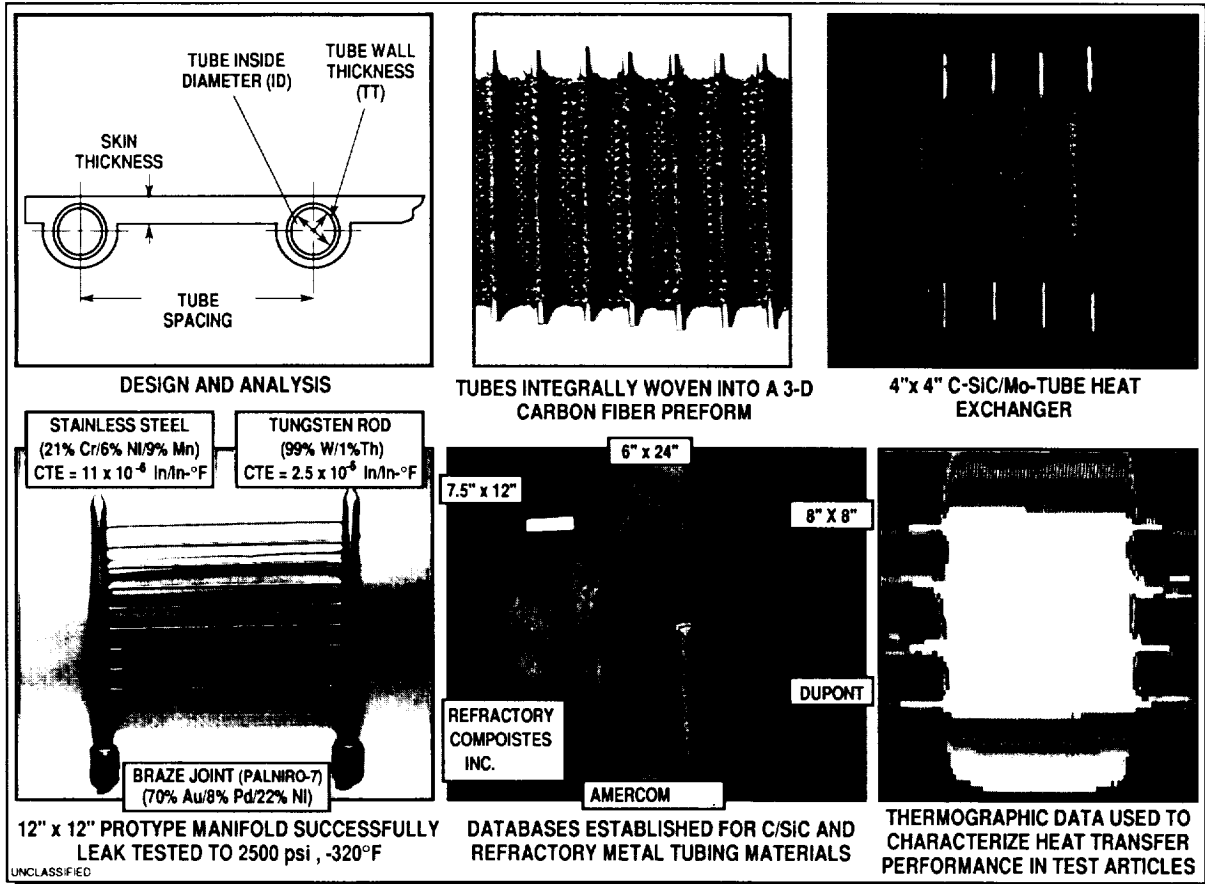


Figure 46

LESSONS LEARNED

A variety of important lessons (summarized in figure 47) have been learned from the actively cooled panels studies. In general, it can be said that the wide range of operational temperatures and the extremely hostile environment in which the panels are expected to operate tend to amplify the criticality of each element and add new dimensions to the design and development process. Seemingly minor details are important. For example, the use of non-perforated instead of perforated honeycomb core is believed to have been a factor in the catastrophic failure of the SiC/Ti panel. Similarly, a mismatch in thermal expansion characteristics was responsible for the Be skin/tube panel failure. Some of these critical details can be identified and resolved early by using small preliminary test specimens such as the joint fatigue specimens for the airframe structure panels. Material properties, which are sometimes considered secondary, (such as conductivity, thermal expansion, ductility, fracture toughness, etc.) assume primary importance because of the impact of heat transfer and the wide range of temperatures encountered. While not emphasized in the body of the paper, fabrication difficulties were encountered in the manufacture of each of the panels described in the paper. In contrast to uncooled structures which may function satisfactorily with less than perfect joints, the need for leak tight, unblocked coolant passages for cooled structures demands perfection in the fabrication process. Cleanliness is critical both in the fabrication process where foreign material or oxidation may produced substandard joints, and in operation where foreign material may block small coolant passages with potentially disastrous results. Current instrumentation techniques are inadequate for the hostile environment to which the hot surfaces of actively cooled panels are exposed. These hot surfaces often absorb large heat fluxes which may induce significant temperature gradients through-the-thickness of any instrumentation on that surface. Special techniques, perhaps optical, must be devised for hot surface strain and temperature measurements. Taken collectively the studies emphasize the need for testing through the entire anticipated operating range to uncover the "hidden flaws" which may occur in design or manufacturing.

Many critical concerns remain unresolved. Although the NASP studies did not progress to the point where fatigue life could be adequately investigated, it is known that thermal fatigue is a critical concern for actively cooled structures because of the large thermal stresses induced by the thermal gradients between the hot surface and the backside of the heat exchanger at the heat fluxes of concern. The present investigations also dramatically illustrate the importance of fracture toughness and thermal stress at low temperatures. Again, although not specifically addressed in the present paper but covered elsewhere during the tenth NASP Symposium, hydrogen and oxygen compatibility is a continuing concern. Finally, despite the advances in test facilities for actively cooled structures that have occurred under the auspices of the NASP Technology Maturation Program and the ongoing facility design and development activity, there is a pressing need to get higher heat flux facilities representative of engine environment checked-out and operational.

(Figure 47 is shown on the next page.)

LESSONS LEARNED

- **DETAILS ARE IMPORTANT**
- **SECONDARY MATERIAL PROPERTIES ARE SIGNIFICANT
(CONDUCTIVITY, THERMAL EXPANSION, DUCTILITY,
FRACTURE TOUGHNESS)**
- **FABRICATION IS DIFFICULT**
- **CLEANLINESS IS CRITICAL**
- **INSTRUMENTATION IS INADEQUATE**
- **TESTING IS ESSENTIAL**
- **CRITICAL CONCERNS ARE
FATIGUE LIFE
FRACTURE TOUGHNESS
HYDROGEN AND OXYGEN COMPATIBILITY
FACILITIES**

Figure 47

REFERENCES

1. Anon.: Conference on Hypersonic Aircraft Technology. NASA SP-148, Proceedings of a Conference held at Ames Research Center, Moffett Field, CA May 16-18, 1967.
2. Anon.: Recent Advances in Structures for Hypersonic Flight. NASA CP 2065, Proceedings of a Symposium held at Langley Research Center, Hampton, VA, September 6-8, 1978.
3. Staff of Langley Research Center and AiResearch Manufacturing Co., The Garret Corp.: Hypersonic Research Engine Project Technology Status 1971. NASA TMX-2572, September 1972.
4. Wieting, Allan R.: Aerodynamic and Thermal Analysis of Results of Tests of a Hydrogen-Cooled Scramjet Engine, (HRE-SAM) at Mach 6.3. NASA TMX-2767, May 1973.
5. Anon.: First National Aero-Space Plane Technology Conference, NASP CP 1006, Vol. VI, May 1986.
6. Kelly, H. N.; Mezines, S. A.; Purmort, W. P.; Henson, M. C.; Warburton, R. E.; and Phelps, J. D.: Actively-Cooled Panels. Presented at the Tenth National Aero-Space Plane Technology Symposium, Paper Number 154, April 23-26, 1991.
7. Kelly, H. Neale; and Sikora, Timothy P.: Actively Cooled Panel Testing Perils, Problems, and Pitfalls. Presented at the SEM Structural Testing Technology at High Temperatures Conference, Dayton, OH, November 4-6, 1991.
8. Anthony, Frank M.; and Huff, Roland D.: Analytical Evaluation of Actively Cooled Modified Monocoque Structural Sandwich Concepts. Technical Report AFFDL-TR-65-124, July 1965.
9. Atkins, T. G.: Hypersonic Ramjet Heat Transfer and Cooling Program. Volume I: Results of Regenerative Cooling Experiments. Technical Report AFAPL-TR-66-84, Vol. I, August 1966.
10. Flieder, W. G.; Richard, C. E.; Buchmann, O. A.; and Walters, F. M.: An Analytical Study of Hydrogen Cooled Panels for Application to Hypersonic Aircraft. NASA CR-1650, April 1971.
11. Walters, F. M. and Buchman, O. A.: Heat Transfer and Fluid Flow Analysis of Hydrogen-Cooled Panels and Manifold Systems. NASA CR-66925, July 1970.
12. Demogenes, C.; Jones, O.; Richard, C. E.; Duncan, J. D.; and Flieder, W. G.: Fabrication and Structural Evaluation for Regeneratively Cooled Panels. NASA CR-1651, March 1971.

13. Richard, C. E.; Duncan, J. D.; Demogenes, C.; and Flieder, W. G.: Low-Cycle Fatigue Evaluation for Regeneratively Cooled Panels. NASA CR-1884, October 1971.
14. Richard, C. E.; and Walters, E. M.: Comparison of Hydrogen and Methane as Coolants in Regeneratively Cooled Panels. NASA CR 1652, March 1971.
15. Richard, C. E.; Duncan, J. D.; Gellersen, E. W.; and Demogenes, C.: Thermal and Structural Tests of a Hydrogen Cooled Panel. NASA CR 2105, August 1972.
16. Jilly, L. F., Editor: Hypersonic Research Engine Project - Phase II Aerothermodynamic Integration Model Development. NASA CR-132654, May 1975.
17. Jilly, L. F., Editor: Hypersonic Research Engine Project - Phase II Structures Assembly Model (SAM) Test Report. NASA CR-111993, September 1971.
18. Henry, John R. and Anderson, Griffin Y.: Design Considerations for the Airframe - Integrated Scramjet. Presented at the First International Symposium on Air Breathing Engines, Marseille, France, June 19-23, 1972. (Also published as NASA TMX-2895, December 1973.)
19. Wieting, Allan R. and Guy, Robert W.: Preliminary Thermal Structural Design and Analysis of an Airframe-Integrated Hydrogen-Cooled Scramjet. AIAA Paper 75-137, Pasadena, CA, 1975. (Also published as Journal of Aircraft, Vol. 13, March 1976, pp. 192-197.)
20. Kelly, H. Neale; Wieting, Allan R.; Shore, Charles P.; and Nowak, Robert J.: Recent Advances in Convectively Cooled Engine and Airframe Structures for Hypersonic Flight. Presented at the Eleventh Congress of the International Council of the Aeronautical Sciences (ICAS), Lisbon, Portugal, Sept. 1978. (Also published as NASA CP-2065, September 1978.)
21. Buchman, O. A.: Thermal-Structural Design Study of an Airframe-Integrated Scramjet - Summary Report. NASA CR-3141, October 1979.
22. Killackey, J. J.; Katinszky, E. A.; Tepper, S.; Vuigner, A. A.; Wright, C. C.; and Stockwell, G. G.: Thermal-Structural Design Study of an Airframe-Integrated Scramjet - Final Report. NASA CR-159039, May 1980.
23. Buchman, O. A.; Arefin, V. V.; Warren, H. A.; Vuigner, A. A.; and Pohlman, M. J.: Advanced Techniques for Hydrogen-Cooled Engine Structures. NASA CR-3949, September 1985.
24. Jilly, L. F., Editor: Hypersonic Research Engine Project - Phase II Structures and Cooling Development. Final Technical Data Report NASA CR-112087, May 1972.
25. McConarty, W. A. and Anthony, F. M.: Design and Evaluation of Active Cooling Systems for Mach 6 Cruise Vehicle Wings. NASA CR-1916, 1971.

26. Helenbrook, R. G.; McConarty, W. A.; and Anthony, F. M.: Evaluation of Active Cooling Systems for a Mach 6 Hypersonic Transport Airframe. NASA CR-1917, 1971.
27. Helenbrook, R. G.; and Anthony, F. M.: Design of a Convective Cooling System for a Mach 6 Hypersonic Transport Airframe. NASA CR-1918, 1971.
28. Anthony, F. M.; Dukes, W. H.; and Helenbrook, R. G.: Internal Convective Cooling Systems for Hypersonic Aircraft. NASA CR-2480, 1974.
29. Brewer, G. D.; and Morris, R. E.: Study of Active Cooling for Supersonic Transports. NASA CR-132573, 1975.
30. Pirrello, C. J.; Baker, A. H.; and Stone, J. E.: A Fuselage/Tank Structure Study for Actively Cooled Hypersonic Cruise Vehicles - Summary. NASA CR-2551, 1976.
31. Nowak, Robert J.; and Kelly, H. Neale: Actively Cooled Airframe Structures for High-Speed Flight. Presented at the AIAA/ASME/SAE 17th Structures, Structural Dynamics and Materials Conference, King of Prussia, PA, May 5-7, 1975. (Also Journal of Aircraft, Vol. 14, No. 3, March 1977, pp. 244-250.)
32. Koch, L. C.; and Pagel, L. L. : High Heat Flux Actively Cooled Honeycomb Sandwich Structural Panel for a Hypersonic Aircraft. NASA CR-2959, 1978.
33. Pirrello, C. J.; and Herring, R. L.: Study of a Fail-Safe Abort System for an Actively Cooled Hypersonic Aircraft - Volume I, Technical Summary. NASA CR-2562, January 1976.
34. Herring, R. L.; and Stone, J. E.: Thermal Design for Areas of Interference Heating on Actively Cooled Hypersonic Aircraft. NASA CR-2828, December 1976.
35. Ellis, D. A.; Pagel, L. L.; and Schaeffer, D. M.: Design and Fabrication of a Radiative Actively Cooled Honeycomb Sandwich Structural Panel for a Hypersonic Aircraft. NASA CR-2957, March 1978.
36. Jones, R. A.; Braswell, D. O.; and Richie, C. B.: Fail-Safe System for Actively Cooled Supersonic and Hypersonic Aircraft. NASA TMX-3125, 1975.
37. Anthony, F. M.: Design and Fabrication of a Skin Stringer Discrete Tube Actively Cooled Structural Panel. NASA CP-2065, September 1978.
38. Smith, L. M.; and Beuyukian, C. S.: Actively Cooled Plate Fin Sandwich Structural Panels for Hypersonic Aircraft. NASA CR-3159, August 1979.
39. Shore, Charles P. and Weinstein, Irving: Aerothermal Performance of a Radiatively and Actively Cooled Panel at Mach 6.6. NASA TP-1595, December 1979.
40. Shore, Charles P.; Nowak, Robert J.; and Kelly, H. Neale: Flightweight Radiantly and Actively Cooled Panel - Thermal and Structural Performance. NASA TP-2074, October 1982.

41. Webb, Granville; Clark, Ronald K.; and Sharpe, Ellsworth L.: Thermal Fatigue Tests of a Radiative Heat Shield Panel for a Hypersonic Transport. NASA TM-87583, September 1985.
42. Blosser, Max L.; Nowak, Robert J.; and Rothgeb, Timothy M.: Thermal-Structural Tests of a Water/Glycol Cooled Aluminum Panel. Workshop on Correlation of Hot Structures Test Data with Analysis, November 1988, NASA CP 3065, Vol. I, pp. 158-178.
43. Purmort, Paul: NASP Technical Option 3 - Actively Cooled Primary Structures - Final Report. Rockwell International report NA-90-101 prepared under contract F33657-86-C-2127, May 1991.
44. Mezines, Sam: Generic Option No. 3 - Actively Cooled Metallic Primary Structure. NASP CR-1123, October 1991. Final Report Addendum. MDC Q0962, October, 1991.
45. Clay, Chris: Nose Cap Technology Developments. Paper No. 159, Tenth National Aero-Space Plane Technology Symposium, Monterey, CA, April 23-26, 1991.
46. Camarda, Charles J.: Results of Generic Studies of Leading Edges. Paper No. 155, Tenth National Aero-Space Plane Technology Symposium, Monterey, CA, April 23-26, 1991.
47. Bolser, David; Sullivan, Steve: Experiences in Fabricating Actively Cooled Structures. Fifth National Aero-Space Plane Technology Symposium, October 1988, NASP CP-5033, Vol. VI, pp. 267-296.
48. Popp, Robert; and Mezines, Sam: Recent Developments in Testing Actively Cooled Structures: Part 2 - Test Results. Fifth National Aero-Space Plane Technology Symposium, October 1988, NASP CP-5033, Vol. VI, pp. 321-350.
49. Mezines, S. A.: Actively Cooled Panel Test Results. Seventh National Aero-Space Plane Technology Symposium, October 1989, NASP CP 7045, Vol. VI, pp. 209-240.
50. Brammer, Donald; Capshaw, Norman; and Sikora, Timothy: Recent Developments in Testing Actively Cooled Structures: Part I - Testing. Fifth National Aero-Space Plane Technology Symposium, October 1988, NASP CP-5033, Vol. VI, pp. 297-320.
51. Smith, Drexel L.: Actively Cooled Hydrogen Test Facility, Paper No. 134, Tenth National Aero-Space Plane Technology Symposium, Monterey, CA, April 23-26, 1991.
52. Haller, Gerald R.; and Mezines, S. A.: Failure Analysis of Beryllium Skin/Tube Actively-Cooled Panel. Eighth National Aero-Space Plane Technology Symposium, March 1990, NASP CP 8051, pp. 149-170.

53. Vrable, Daniel L.; and Beavers, Fred L.: Design and Fabrication of Actively Cooled Gr/Cu Structures. Seventh National Aero-Space Plane Technology Symposium, October 1989, NASP CP-7045, Vol. VI, pp. 183-208.
54. Phelps, John D.; Kelly George J.; and Gersley, Jim G.: Microchannel Heat Exchanger Design for Hypersonic Engine Actively Cooled Flowpath Structure. Ninth National Aero-Space Plane Technology Symposium, November 1990, NASP CP-9057, Vol. VI, pp. 123-147.
55. Henson, M. C.; Adams, R. D.; Ahmad, A.; Fetter, S. D.; Kennedy, S. E.; Saathoff, W. M.; and Serinken, D. H.: Development of Refractory Composite Actively Cooled Panels for the NASP Airframe. Ninth National Aero-Space Plane Technology Symposium, November 1990, NASP CP 9057, Vol. VI, pp. 149-174.

ADVANCED TWO-PHASE HEAT TRANSFER SYSTEMS

Theodore D. Swanson
NASA Goddard Space Flight Center
Greenbelt, Maryland

Future large spacecraft, such as the EOS platforms, will require a significantly more capable thermal control system than is possible with current "passive" technology. Temperatures must be controlled much more tightly over a larger surface area. Numerous heat load sources will often be located inside the body of the spacecraft without a good view to space. Power levels and flux densities may be higher than can be accommodated with traditional technology. Integration and ground testing will almost certainly be much more difficult with such larger, more complex spacecraft. For these and similar reasons the Goddard Space Flight Center (GSFC) has been developing a new, more capable thermal control technology called capillary pumped loops (CPLs). CPLs represent an evolutionary improvement over heat pipes; they can transport much greater quantities of heat over much longer distances and can serve numerous heat load sources. In addition, CPLs can be fabricated into large cold plates that can be held to tight thermal gradients. Development of this technology began in the early 1980's and is now reaching maturity. CLPs have recently been baselined for the EOS-AM platform (1997 launch) and the COMET spacecraft (1992 launch). This presentation describes this new technology and its applications. Most of the viewgraphs are self descriptive. For those that are less clear additional comments are provided.

OBJECTIVES

- SUMMARIZE HISTORY OF TWO-PHASE TECHNOLOGY DEVELOPMENT AT GSFC
- DETAIL STATUS OF CURRENT TWO-PHASE THERMAL CONTROL TECHNOLOGY
- BRIEFLY DESCRIBE GSFC TEST AND DEVELOPMENT PROGRAM WHICH WILL MATURE THE TECHNOLOGY

TWO-PHASE THERMAL TECHNOLOGY

WHAT IS A CPL?

A CAPILLARY PUMP LOOP (CPL) IS A TWO-PHASE THERMAL CONTROL SYSTEM WHICH USES CAPILLARY FORCES TO

- TRANSFER HIGH HEAT LOADS OVER LONG DISTANCES
- OPERATE WITH SMALL TEMPERATURE DIFFERENTIALS BETWEEN HEAT SOURCES AND HEAT SINKS
- PROVIDE TIGHT TEMPERATURE CONTROL FOR HEAT SOURCES

A CPL SYSTEM CONSISTS OF

- EVAPORATOR ZONES
- A VAPOR TRANSPORT LINE
- CONDENSER (RADIATOR) ZONES
- A LIQUID TRANSPORT LINE
- A TWO PHASE ACCUMULATOR/RESERVOIR

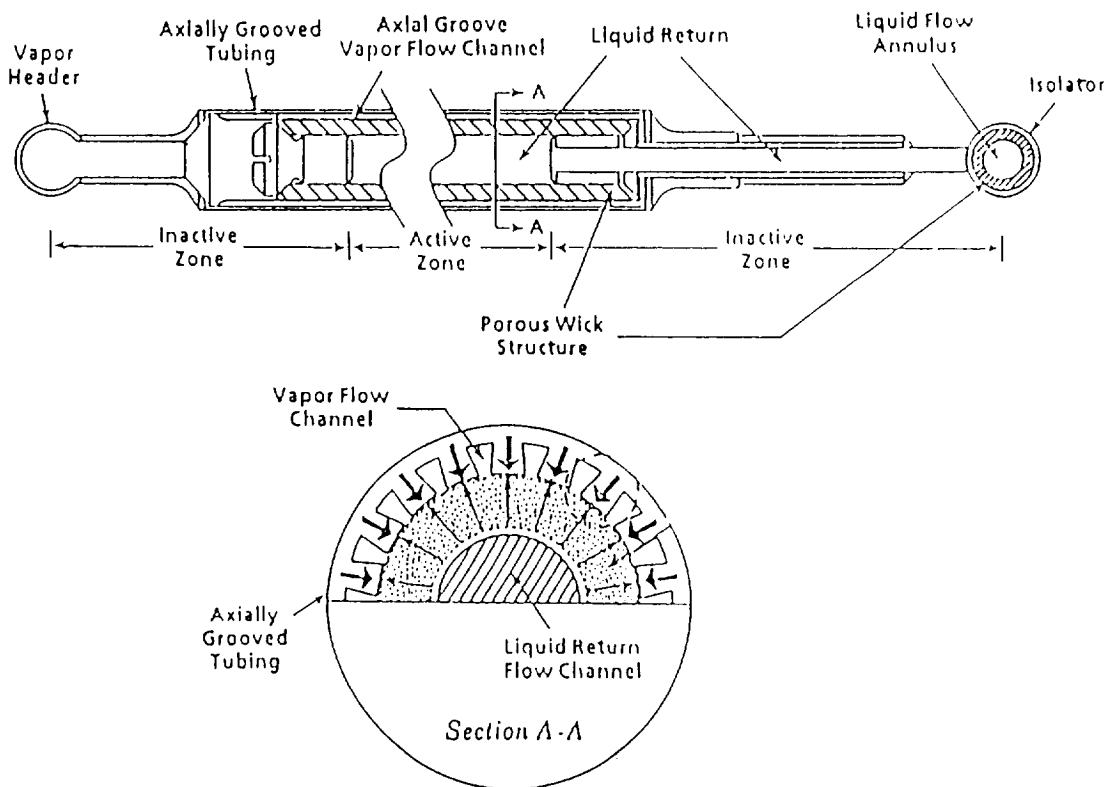
HOW DOES A CAPILLARY PUMP WORK?

- A POROUS WICK MATERIAL IS USED TO MAINTAIN THE WORKING FLUID AT THE HEAT TRANSFER SURFACE
- AS THE WORKING FLUID EVAPORATES, SURFACE TENSION FORCES CREATE A PRESSURE HEAD IN THE WICK, WHICH IN TURN DRIVES THE WORKING FLUID AROUND THE SYSTEM

$$\text{PRESSURE HEAD} = \frac{2 \times \text{SURFACE TENSION}}{\text{EFFECTIVE RADIUS}}$$

- EVAPORATION OF THE WORKING FLUID COOLS WHATEVER IS ATTACHED TO THE CAPILLARY PUMP

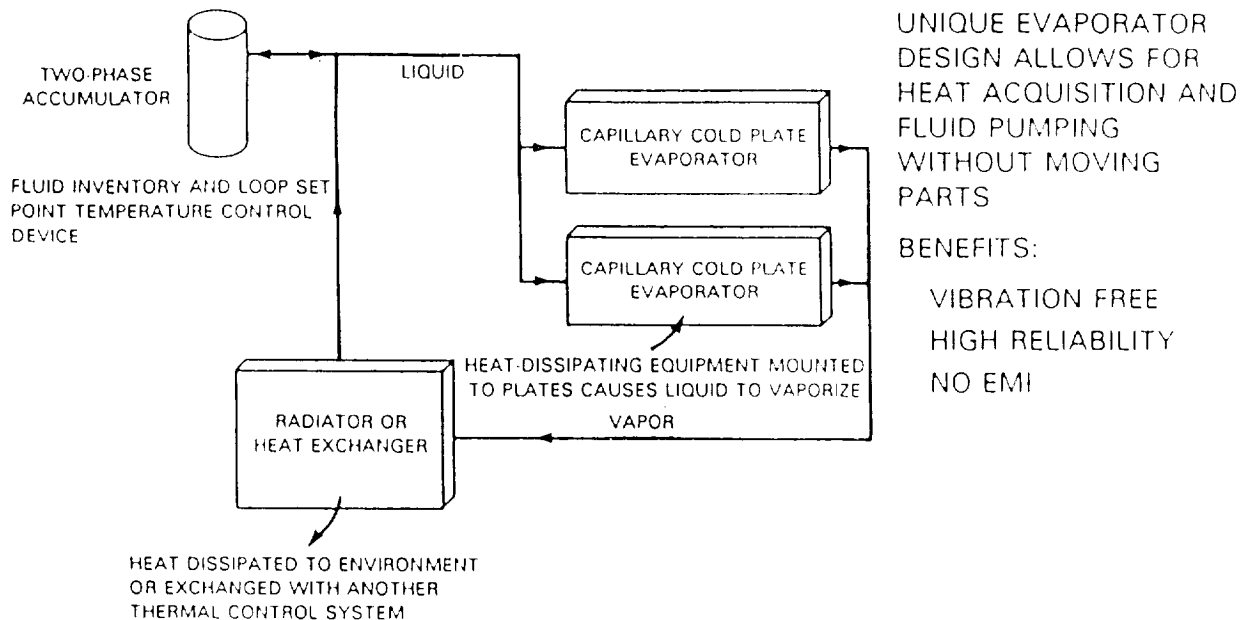
CAPILLARY PUMP



HOW DOES A CPL SYSTEM WORK?

- HEAT DISSIPATING COMPONENTS ARE ATTACHED TO COLD PLATES WHICH CONTAIN A NUMBER OF CAPILLARY PUMPS
- COMPONENTS ARE KEPT COOL THROUGH EVAPORATION OF THE WORKING FLUID
- THE VAPOR GENERATED IN THE COLD PLATES IS TRANSPORTED TO A HEAT EXCHANGER OR RADIATOR, WHERE IT IS CONDENSED. IN THIS WAY, THE HEAT IS DISSIPATED TO ANOTHER SYSTEM OR TO SPACE
- THE CONDENSED FLUID IS RETURNED TO THE COLD PLATES BY THE CAPILLARY PUMPING IN THE COLD PLATES AND THE CYCLE CONTINUES
- A TWO-PHASE RESERVOIR IS USED TO CONTROL THE TEMPERATURE AT WHICH EVAPORATION TAKES PLACE (AND THUS THE TEMPERATURE OF THE COMPONENTS BEING COOLED)

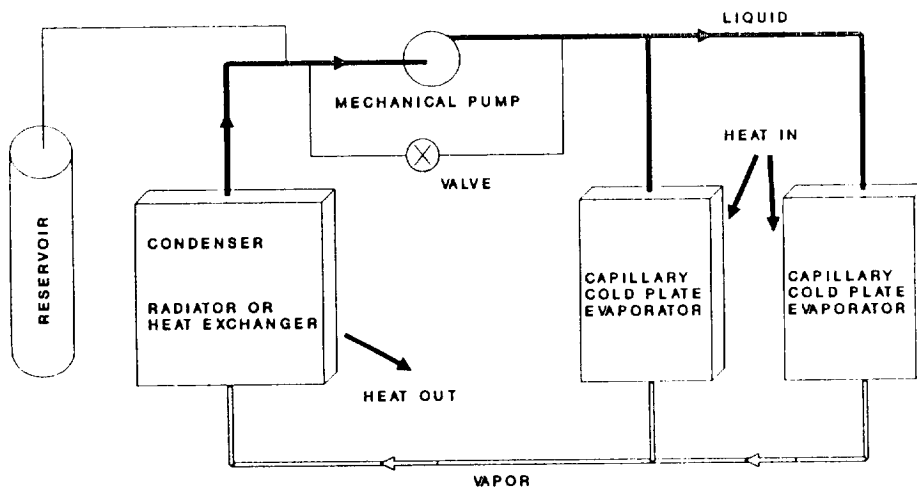
CAPILLARY PUMPED SYSTEMS



WHAT IS A HYBRID CPL?

- A HYBRID CPL CONTAINS A MECHANICAL PUMP IN SERIES WITH THE CAPILLARY COLD PLATES
- THE MECHANICAL PUMP CAN BE USED TO:
 - ALLOW GROUND TESTING IN MOST ORIENTATIONS
 - ALLOW THE USE OF HIGHER PRESSURE DROP COMPONENTS IN THE SYSTEM
 - INCREASE THE HEAT TRANSFER CAPACITY OF A CAPILLARY SYSTEM
 - ASSIST IN START-UP AND REPRIMING OF A CAPILLARY SYSTEM

CAPILLARY/MECHANICALLY PUMPED (HYBRID) LOOP



- CAN OPERATE AS A PURE CAPILLARY PUMP LOOP (CPL), A MECHANICAL-PUMP-ASSISTED CPL, OR AS A MECHANICALLY PUMPED SYSTEM
- INCREASED HEAT TRANSPORT CAPACITY ABOVE THAT FOR A CPL
- MAINTAINS BENEFITS OF PARENT SYSTEM IN EACH OPERATING RANGE
- ALLOWS ONE-G TESTING OF CPL SYSTEMS WITH HIGH TILTS

CAPILLARY PUMP LOOP HISTORY

<u>DATE</u>	<u>EVENT/SYSTEM</u>
LATE 1960'S	- CONCEPT DEVELOPED BY STENGER FOR WATER (LeRC)
LATE 1970'S	- REDISCOVERED BY BIENERT - SMALL SCALE CONCEPT DEMONSTRATION DEVELOPED
1982	- CPL-1: 10 METER TRANSPORT LENGTH USING AMMONIA; 7 kW CAPACITY
1985	- CPL/GAS FLIGHT EXPERIMENT
1986	- CPL/HITCHHIKER FLIGHT EXP.
1986	- CPL-2: SIMILAR IN SIZE TO CPL-1; TESTED AT JSC
1987	- HIGH POWER SPACECRAFT THERMAL MANAGEMENT SYSTEM: 25-52 kW, 10 METER LENGTH
1990	- INSTRUMENT THERMAL TEST BED (100W - 10 kW+)
1993	- CAPL FLIGHT EXPERIMENT

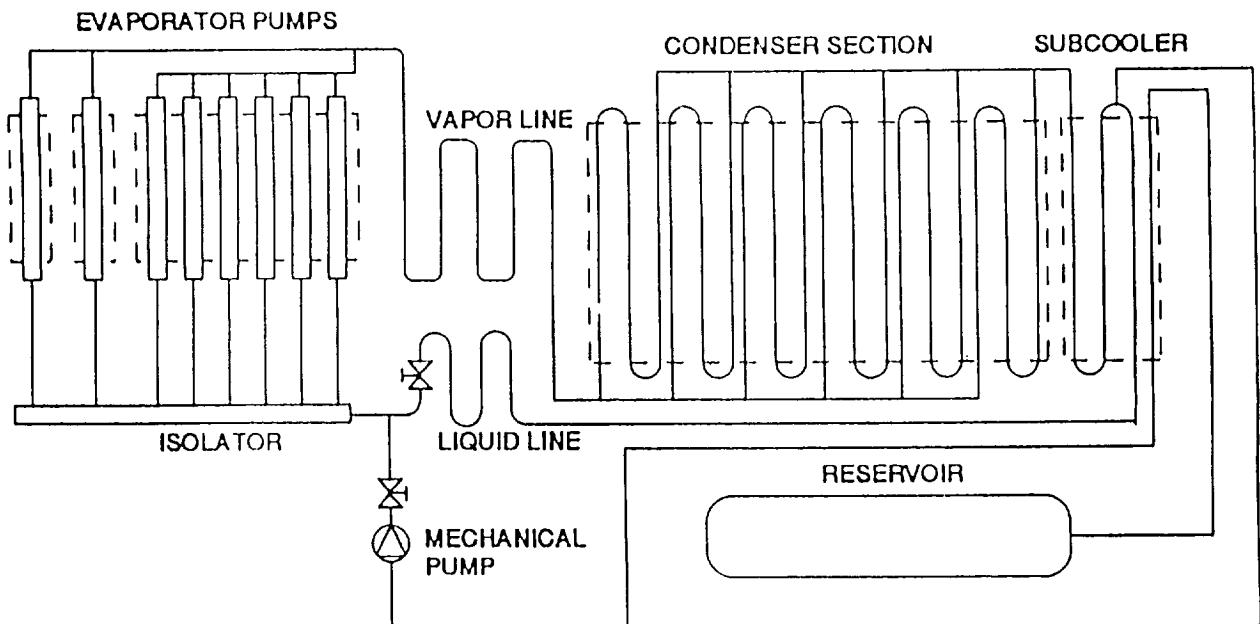
CAPILLARY PUMP LOOP KNOWN SYSTEMS

- GODDARD -
CPL-1
CPL-2
INSTRUMENT THERMAL TEST BED
FLIGHT EXPERIMENTS
- AIR FORCE
- BOEING
- DYNATHERM CORPORATION
- OAO CORPORATION
- GENERAL ELECTRIC
- MARTIN MARIETTA
- TRW
- ESA - DORNIER SYSTEMS
- UK - BRITISH AEROSPACE
- JAPAN
- USSR

GSFC GROUND TESTING

CPL 1 TEST RESULTS 1986 - 1989

The CPL I was the first, large scale, operational, ammonia based, two-phase capillary pumped loop. It was initially fabricated in 1984 and was used for a wide variety of testing through 1989. During this time a number of modifications were made, including the addition of a mechanical pump. Use of the mechanical pump creates a "hybrid" mode of operation in which the mechanical pump supplements the capillary pumping of the wicks. This has certain advantages, as are discussed in the following viewgraphs.



CPL-1

CHARACTERISTICS OF CPL-1 (CAPILLARY MODE)

- IT WORKED!
- HEAT TRANSPORT LIMIT ABOUT 6.4 KW
- DRYOUT USUAL FAILURE MODE AT 25 C
- DEPRIME USUAL FAILURE MODE AT 45 C
- STARTED-UP RELIABLY IN EARLY LIFE;
MORE DIFFICULT AFTER 5 YEARS
- TEMPERATURE OSCILLATIONS RARE

CPL-2 EVAPORATOR PUMP TESTS

The CPL II represented the second generation design of a capillary pumped loop. Functionally and physically it was very similar to the CPL I. It had the same power capacity (approximately 7 kW), number of evaporator pumps (8), reservoir design (open tank held vertically) and transport length (10 meters). However, the CPL II was less of a brassboard and more of a prototype. It was hard plumbed and made vacuum compatible. In addition, certain design details were changed in the hopes of improving performance.

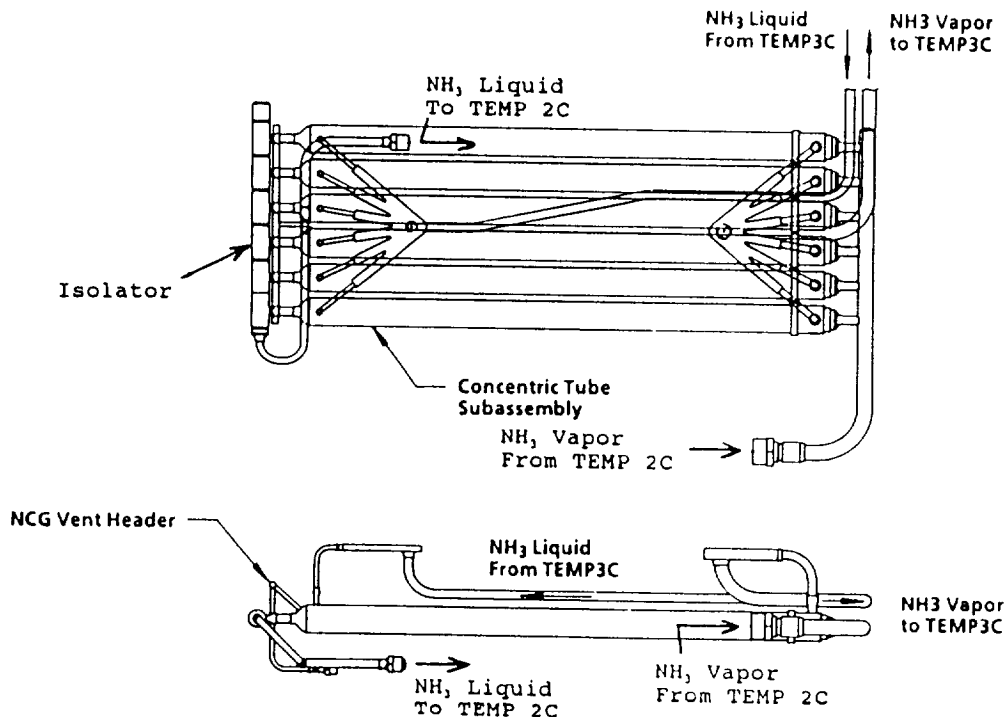
CHARACTERISTICS OF CPL-11 (CAPILLARY MODE)

- HEAT TRANSPORT LIMIT ABOUT 8.0 KW
- DEPRIMES USUAL FAILURE MODE
- NO DRYOUT EVER SEEN
- TEMPERATURE OSCILLATIONS OCCUR AT LOW POWERS IN SOME PUMPS
- OSCILLATIONS OCCASIONALLY LEAD TO DEPRIMES

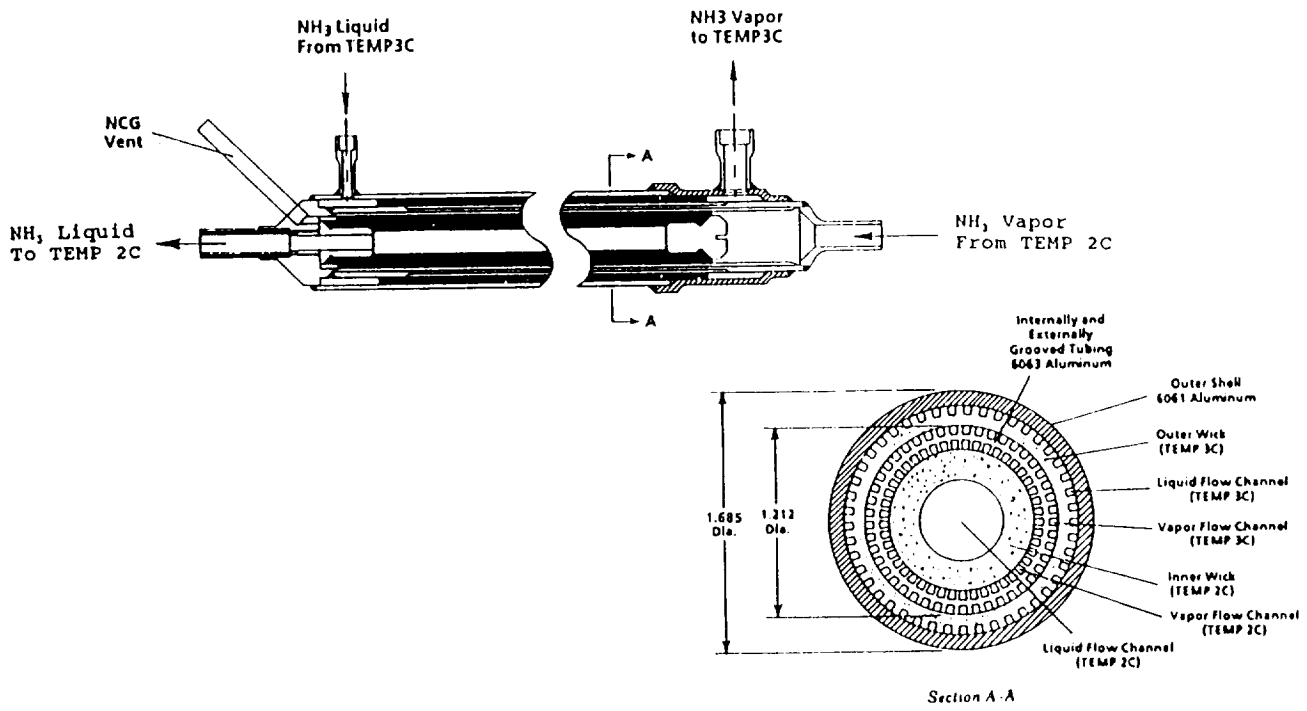
BI-DIRECTIONAL HEAT EXCHANGER

- DESIGNED TO COUPLE TWO TWO-PHASE HEAT TRANSFER SYSTEMS
- ACTS AS A CONDENSER IN ONE LOOP AND AN EVAPORATOR IN THE SECOND LOOP
- CAN BE OPERATED IN "REVERSE" - CONDENSING IN THE NORMALLY EVAPORATING LOOP AND VICE VERSA
- CONTAINS CAPILLARY WICK MATERIAL TO ALLOW REVERSE OPERATION AND FOR FLOW REGULATION AND DISTRIBUTION
- TRANSFERS 4 KW WITH A LOOP TO LOOP SATURATION TEMPERATURE DIFFERENCE OF LESS THAN 2 C
- COMPATIBLE WITH BOTH CPL AND HYBRID (MECHANICALLY PUMPED) TWO-PHASE HEAT TRANSFER SYSTEMS

TWO-PHASE/TWO-PHASE HEAT EXCHANGER

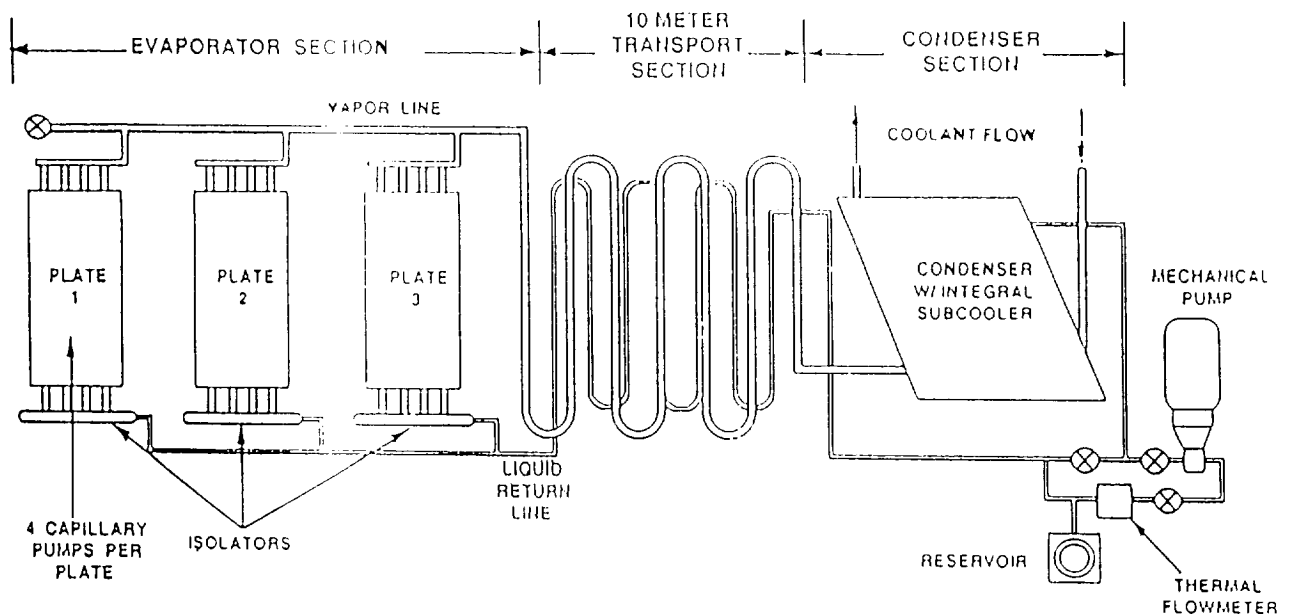


HEAT EXCHANGER SUBASSEMBLY



HIGH POWER THERMAL MANAGEMENT SYSTEM (HPSTM)

The High Power Thermal Management System (HPSTM) was functionally similar to the CPL II and III, but was larger. The three cold plates were each 2 ft. by 1 ft. (as opposed to the 1 ft. by 1 ft. plates of the CPL I and II) and had four pumps per plate. It also had a 10 meter transport length, an optional mechanical pump for "hybrid" mode operation, and an unwicked reservoir. It was designed for high power, and was able to achieve approximately 25 kW in a capillary mode, and over 50 kW in a hybrid mode. This loop has consistently performed exceptionally well for both startup and continuous operations.



EXPERIMENTAL APPARATUS FOR THE HIGH-POWER HYBRID CPL

HIGH POWER THERMAL MANAGEMENT SYSTEM

CAPILLARY MODE RESULTS

- STARTUP
12 DIFFERENT POWER PROFILES
NOT A SINGLE STARTUP FAILURE IN TWO YEARS OF TESTING
- LOW SYSTEM POWER LIMIT - 120 WATTS (10 WATTS PER
EVAPORATOR
- TRANSPORT LIMIT - 25 KILOWATTS
- LONG TERM STEADY STATE POWER - 20 KILOWATTS
(NO HIGHER POWER TESTED)
- SYSTEM OPERATED INTERMITTENTLY FOR ALMOST THREE
YEARS
- NO EVIDENCE OF NON CONDENSIBLE GAS

INSTRUMENT THERMAL TEST BED

The Instrument Thermal Test Bed (ITTB) represents a more modular, generic loop design. The ITTB is basically a skeletal loop which includes the transport plumbing, basic condenser, basic reservoir, a number of valves for quick system reconfiguration, complete instrumentation, cooling lines and control electronics. It is designed to permit both system and component level testing. The system can be quickly arranged for either capillary or "hybrid" mode of operation. Transport lengths can also readily be adjusted. In addition a test component such as a cold plate, reservoir or condenser can be easily "plugged in" to standardized ports and testing commenced within a matter of a few days, rather than the usual weeks. The ITTB is the largest known modular, two-phase test bed in the world. The facility has been operational for over a year and has already been used for a large variety of both system and component level testing.

LARGE SCALE TWO PHASE THERMAL TEST BED

- ▶ MODULAR DESIGN FOR EASY RECONFIGURATION
- ▶ COMPONENT AND SYSTEM LEVEL TESTING
- ▶ TECHNOLOGY DEVELOPMENT AND FLIGHT HARDWARE QUALIFICATION

INSTRUMENT THERMAL TEST BED (ITTB)

CONFIGURATION

INITIAL OPERATIONS IN NOVEMBER 1990

- CONSTRUCTED TO REFLECT SPACE STATION BASELINE
 - ▶ THERMAL CAPACITY 25 kW (CONDENSER LIMIT)
 - ▶ SYSTEM VOLUME 7.75 GALLONS + 6.25 GALLON SYSTEM RESERVOIR
 - ▶ VARIABLE TRANSPORT LENGTH UP TO 50 METERS

RECONFIGURED IN NOVEMBER 1991

- REFLECT EOS BASELINE DESIGN
 - ▶ TRANSPORT LENGTH REDUCED TO 12 METERS
 - ▶ REPLACED CONDENSER W HP/HX - 1600 W LIMIT
 - ▶ SYSTEM VOLUME 1.5 GALLONS + RESERVOIR

INSTRUMENT THERMAL TEST BED

OPERATION RESULTS

ORIGINAL CONFIGURATION

- PROTOTYPE CAPILLARY COLD PLATE (PCCP) EVAPORATORS
 - ▶ DEMONSTRATED OPERATION RANGE: 600 W TO 4000 W
 - ▶ LONG TERM OPERATION VERIFIED ABOVE 1800 W
- HPSTM EVAPORATORS
 - ▶ DEMONSTRATED OPERATION RANGE: 400 W TO 3200 W
 - ▶ LONG TERM OPERATION VERIFIED ABOVE 800 W
- CAPL COLD PLATES
 - ▶ DEMONSTRATED OPERATION RANGE: 600 W TO 1600 W
 - ▶ LONG - TERM OPERATION VERIFIED ABOVE 800 W

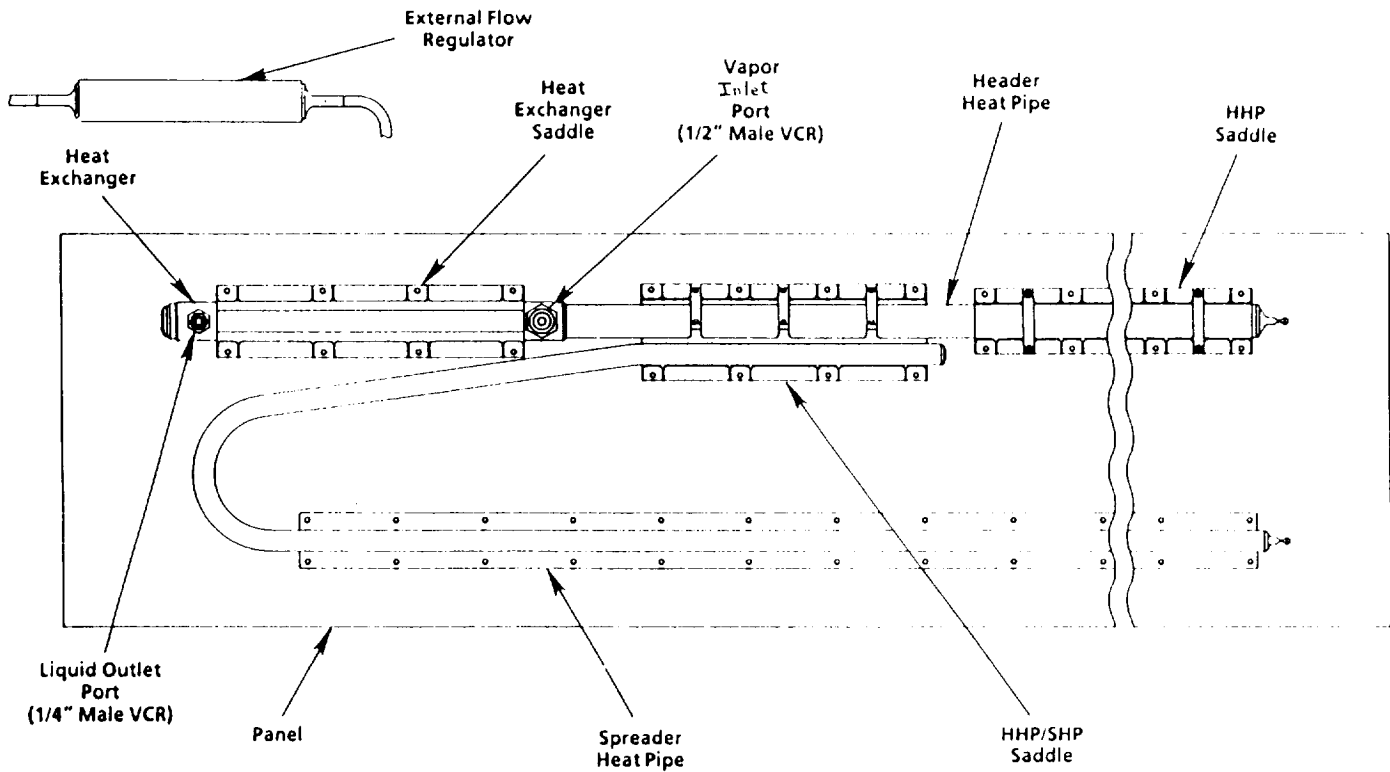
MODIFIED CONFIGURATION

- HPSTM RESULTS
 - ▶ LOW POWER LIMIT DETERMINED TO BE 100 W
 - ▶ LONG TERM OPERATION DEMONSTRATED AT 100 W
- CAPL COLD PLATE RESULTS
 - ▶ LOW POWER LIMIT DETERMINED TO BE 600 W
 - ▶ LONG TERM OPERATION DEMONSTRATED AT 600 W

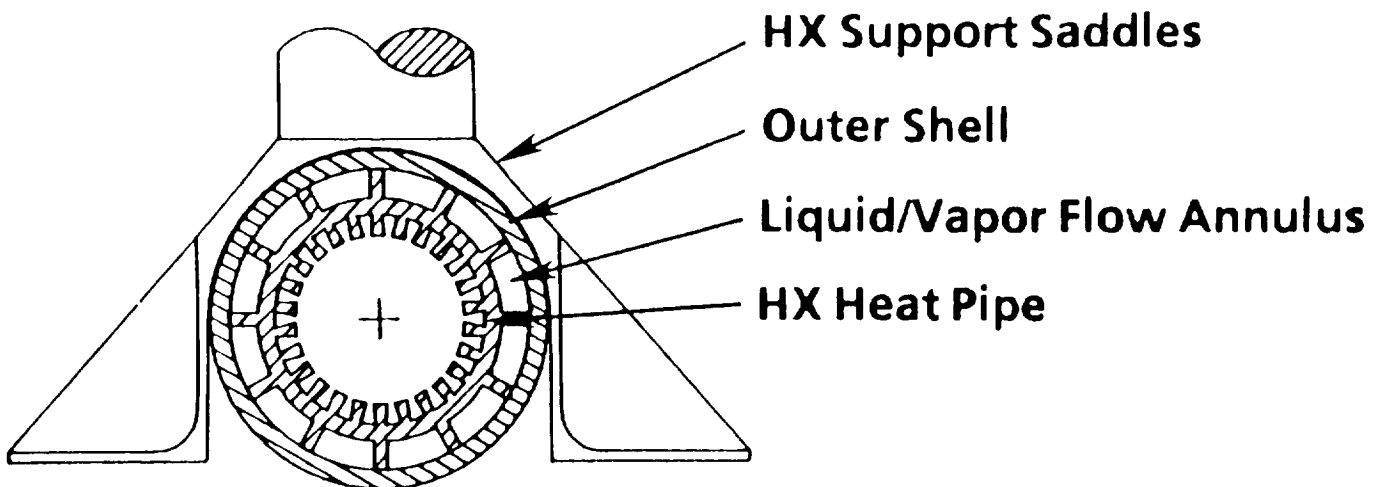
HEAT PIPE HEAT EXCHANGER TESTING

- TWO INDEPENDENT CAPL PROTOTYPE DESIGNS
 - ▶ AXIALLY GROOVED POROUS WICK HEAT EXCHANGER W/
HEADER AND SPREADER HEAT PIPE
 - ▶ HELICAL FIN HEAT EXCHANGER W/HEADER AND
SPREADER HEAT PIPE AS WELL AS STAND ALONE
POROUS WICK FLOW REGULATOR AND VAPOR BARRIER
- TEST PROGRAM CONDUCTED TO DETERMINE FLIGHT DESIGN
 - ▶ HEAT EXCHANGER MUST TRANSFER 350 W @ 5 C OR
LESS TEMPERATURE DIFFERENTIAL
 - ▶ HEADER HEAT PIPE TO DEMONSTRATE 432 W-M @ 35 C
 - ▶ SPREADER HEAT PIPE TO DEMONSTRATE 178 W-M @ 35 C
 - ▶ FLOW REGULATIONS AND NGC PROVISIONS
- EACH HP/HX WAS INSTALLED AS ITTB CONDENSER FOR TESTING

HPHX DESIGN



HPHX CROSS SECTION



INSTRUMENT THERMAL TEST BED

HEAT PIPE HEAT EXCHANGER RESULTS

- HEAT PIPE HEAT EXCHANGER TEST RESULTS
 - ▶ HELICAL FIN DESIGN SELECTED
 - ▶ AXIALLY GROOVED POROUS WICK DESIGN FAILED TO DEMONSTRATE HEAT TRANSFER REQUIREMENTS AND DISPLAYED HIGHER THAN EXPECTED PRESSURE DROPS
- HELICAL FIN PROTOTYPE CURRENTLY SERVES AS ITTB CONDENSER EVENTUALLY WILL BE INSTALLED IN MATERIALS LIFE TEST CPL

FUTURE PLANS

- RESERVOIR TESTING
 - ▶ TEST CAPL PROTOTYPE RESERVOIR IN ITTB TO DETERMINE PERFORMANCE IN EXPERIMENT SCALE LOOP
- EVAPORATORS
 - ▶ TEST INDIVIDUAL 1/2 INCH EVAPORATOR PUMPS
 - ▶ TEST COLD PLATE CONSTRUCTED OF 1/2 INCH PUMPS
- CAPL SYSTEM LEVEL TESTING
 - ▶ CONFIGURE ITTB WITH CAPL PROTOTYPE COLD PLATE, CONDENSER, MECHANICAL PUMP, AND RESERVOIR TO SIMULATE FULL SCALE CAPL SYSTEM

GSFC FLIGHT EXPERIMENTS

WHY FLY EXPERIMENTS ?

- FLUID AND THERMAL PHYSICAL PHENOMENA ARE KNOWN TO BE DIFFERENT IN MICRO-GRAVITY;
 - PRESSURE DROPS
 - HEAT TRANSFER COEFFICIENTS
 - MIXING EFFICIENCIES
- FLUID MANAGEMENT MUCH MORE DIFFICULT IN MICRO-GRAVITY.
- EXISTING ANALYTICAL MODELS WEAK AND UNVERIFIED.
- FLIGHT DATA THUS NEEDED TO OPTIMIZE DESIGN AND REDUCE RISK.
 - BENEFITS INCLUDE LOWER WEIGHT, LOWER EQUIPMENT COST, AND GREATER RELIABILITY.

GSFC THERMAL FLIGHT EXPERIMENTS

<u>EXPERIMENT</u>	<u>TYPE</u>	<u>POWER(KW)</u>	<u>STATUS</u>
CPL-GAS	CAPILLARY	0.2	FLOWN (1985)
CPL-HH/G	CAPILLARY	0.6	FLOWN (1986)
TEMP 2A3	MECHANICAL	0.9	MANIFESTED (7/92)
CAPL	CAPILLARY	1.2	MANIFESTED (10/93)

NOTE: THE CPL-GAS AND CPL-HH/G REPRESENT THE ONLY FLIGHT TESTS TO DATE OF ANY TWO-PHASE THERMAL CONTROL TECHNOLOGY. ALSO, THE TEMP 2A3 WILL BE THE FIRST TEST OF A MECHANICALLY PUMPED TWO-PHASE SYSTEM.

THERMAL ENERGY
MANAGEMENT PROCESSES

TEMP 2A-3

FLIGHT EXPERIMENT

TEMP 2A-3 FLIGHT EXPERIMENT OBJECTIVES

FIRST DEMONSTRATION OF A MECHANICALLY PUMPED TWO-PHASE AMMONIA THERMAL CONTROL SYSTEM IN MICRO-GRAVITY

EVALUATE MICRO-GRAVITY FLUID MANAGEMENT TECHNIQUES UTILIZING A PROPULSION TYPE RESERVOIR DESIGN

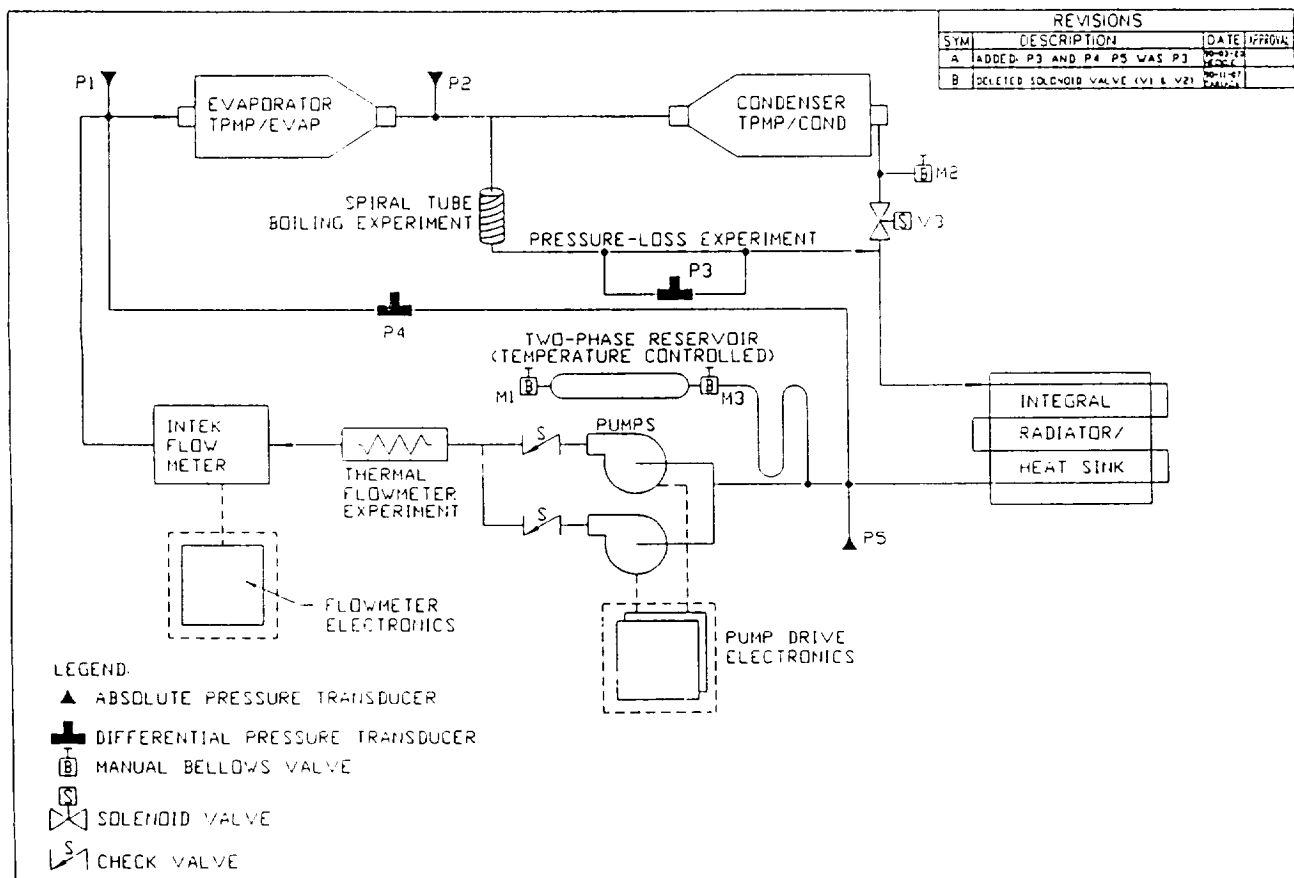
MEASURE PRESSURE LOSSES IN A TWO-PHASE FLOW LINE

MEASURE HEAT TRANSFER COEFFICIENTS IN A TWO-PHASE BOILER EXPERIMENT

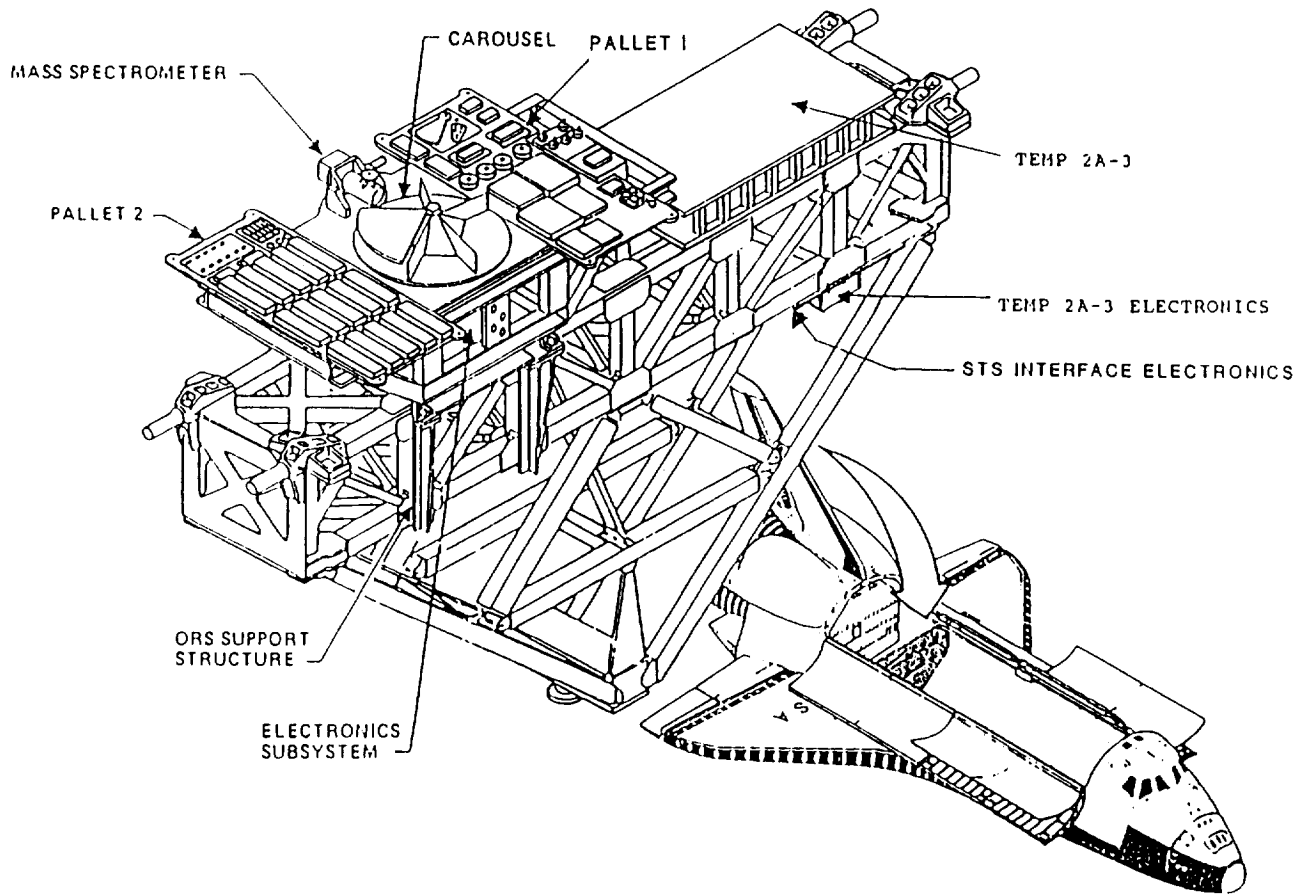
EVALUATE A DIRECT CONDENSATION RADIATOR

MEASURE ATOMIC OXYGEN EFFECTS ON JSC ANODIZED RADIATOR

NO RELEVANT MICRO-GRAVITY DATA IS AVAILABLE TODAY



EOIM-III/TEMP 2A-3 EXPERIMENT



CAPILLARY PUMPED LOOP

(CAPL)

FLIGHT EXPERIMENT

CAPL FLIGHT EXPERIMENT OBJECTIVES

TO DEMONSTRATE THE OPERATION OF A FULL SCALE CAPILLARY PUMPED HEAT TRANSFER SYSTEM IN MICROGRAVITY

DEMONSTRATE FLUID MANAGEMENT TECHNIQUES
NEW RESERVOIR DESIGN
CAPILLARY STARTER PUMP

VERIFY OPERATION OF HEAT PIPE HEAT EXCHANGER/RADIATOR

STUDY PRESSURE LOSSES IN CAPILLARY SYSTEMS

DEVELOP AND VERIFY ANALYTICAL MODELS

CAPILLARY COLD PLATES

PROVIDE CONSTANT TEMPERATURE HEAT SINK
PARALLEL PLATES DEMONSTRATE HEAT SHARING
NEW MINI-PUMP DESIGN (1/2 INCH DIA)

TWO-PHASE RESERVOIR

PROVIDES SATURATION TEMPERATURE CONTROL
AUTOMATICALLY ADJUSTS FLUID INVENTORY
UTILIZES CAPILLARY WICKS FOR FLUID MANAGEMENT

HEAT PIPE HEAT EXCHANGERS

PROVIDES HEAT REJECTION FOR CAPL
"SHIELDS" LOOP FROM METEORITE HITS
INCLUDES NON-CONDENSIBLE GAS TRAP

LIQUID AND VAPOR TRANSPORT LINES

DEMONSTRATES HEAT TRANSPORT OVER 8 METERS
PROVIDE MICRO-G DATA ON PRESSURE LOSSES
STAINLESS STEEL TUBING (1/4 AND 1/2 INCH DIA)

SYSTEM COMPONENTS

THERMISTORS - MICRO-G HEAT TRANSFER COEFFICIENTS
PRESSURE TRANSDUCERS - ABSOLUTE AND DIFFERENTIAL
FLOWMETER - NON-INTRUSIVE THERMAL DESIGN
MECHANICAL PUMP - PROVIDES BACKUP

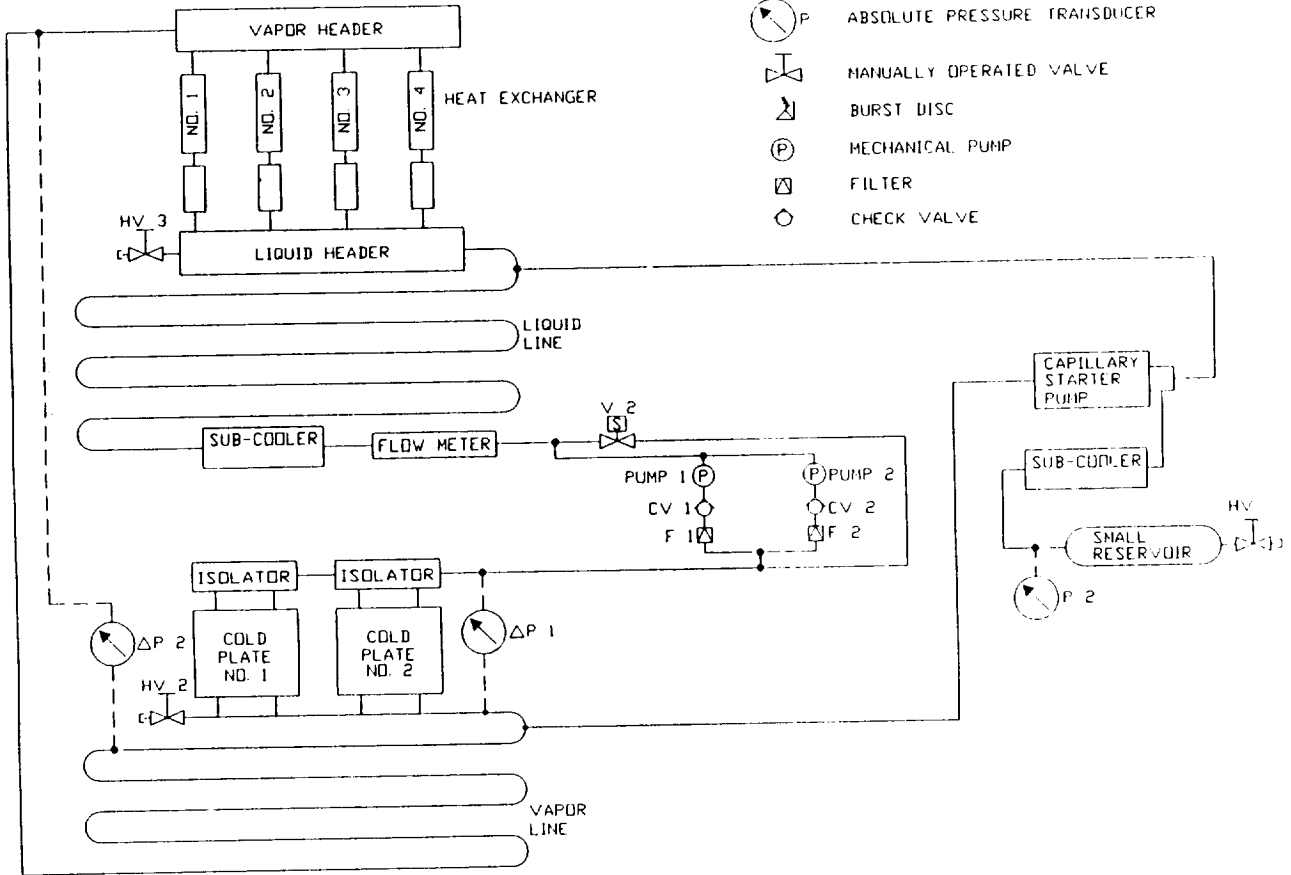
ANALYTICAL MODELLING

DEVELOP TWO-PHASE FLUID ANALYSIS CAPABILITY
MICRO-GRAVITY VERIFICATION OF FLUID MODELS

CAPL WILL PROVIDE THE EXPERTISE NEEDED FOR EOS

LEGEND

-  SOLENOID VALVE
-  ΔP DIFFERENTIAL PRESSURE TRANSDUCER
-  P ABSOLUTE PRESSURE TRANSDUCER
-  MANUALLY OPERATED VALVE
-  BURST DISC
-  P MECHANICAL PUMP
-  F FILTER
-  O CHECK VALVE



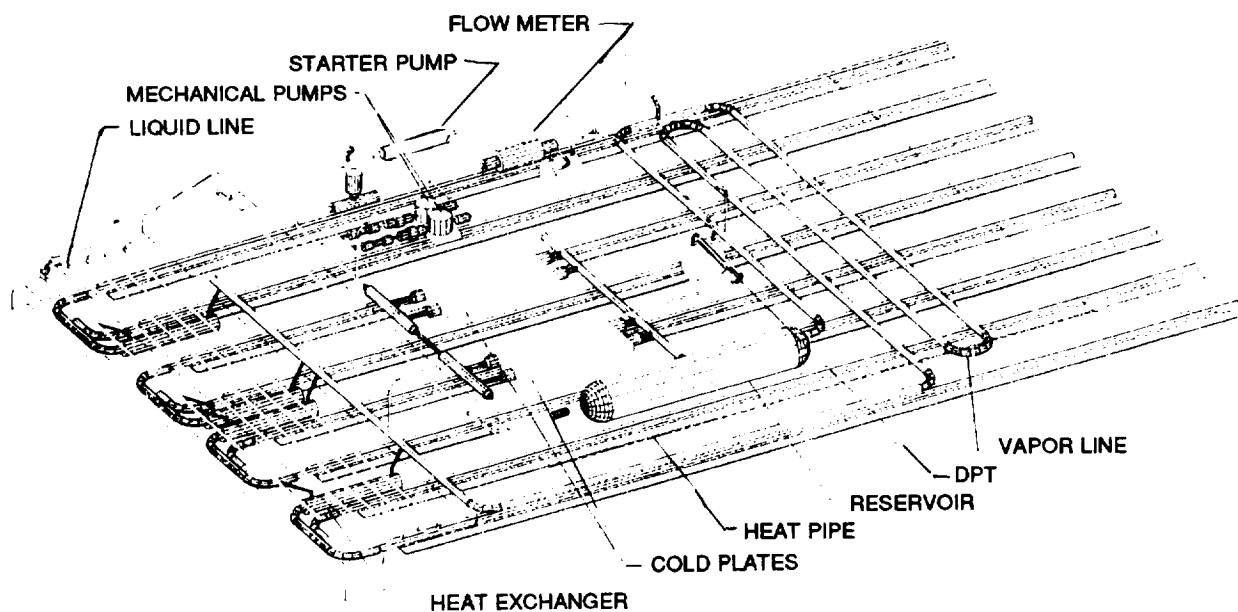
CAPL SCHEMATIC

CAPL CHARACTERISTICS

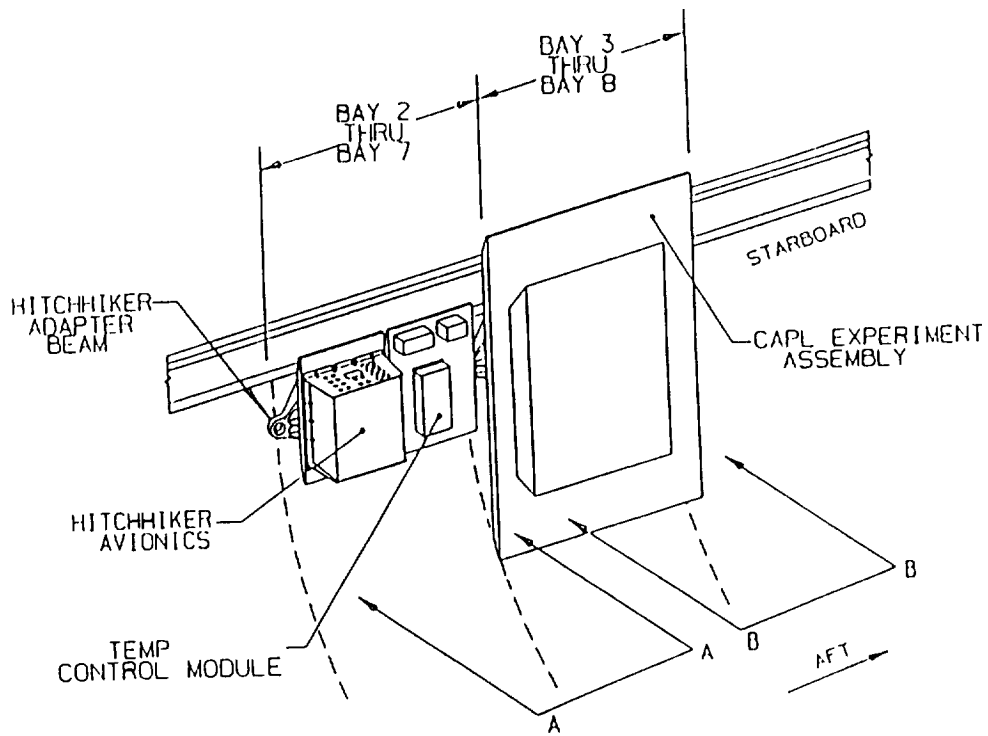
REVISED EOS BASELINE

<u>LATEST EOS</u>	<u>ORIGINAL CAPL</u>	<u>REVISED CAPL</u>
30 TO 300 WATTS	400 TO 1200 WATTS	50 TO 1200 WATTS
3 TO 8 METER LINES	15 METERS	8 METERS
FULLY FLOODED	PARTIAL/FULLY FLOOD	FULLY FLOODED
1/4" DIA VAPOR 1/8" DIA LIQUID	3/4" DIA VAPOR 3/8" DIA LIQUID	1/2" DIA VAPOR 1/4" DIA LIQUID
2 POUND CHARGE	8 POUND CHARGE	4 POUND CHARGE
1/2" DIA PUMPS	1" DIA PUMPS	1/2" DIA PUMPS
HPHX RADIATOR	HPHX RADIATOR	HPHX RADIATOR

ENHANCED CAPL COMPONENT LAYOUT



CAPL Hitchhiker-G Flight Configuration



JL 177/92-2

CRYOHP FLIGHT EXPERIMENT

CRYOHP OVERVIEW

- **Justification**
 - NASA -- EOS Platforms and Other Instrument Payloads
- **Comparison to Alternatives**
 - Heat Pipes Offer Redundancy and Design Flexibility Versus Direct Integration of Sensor/Cooler
- **Need for Space Flight**
 - No Micro Gravity Data for Cryogenic Heat Pipes
 - I-G Data Not Reliable, 100% Above Theory
 - Start-Up From Super Critical State Could be Significantly Different in Micro Gravity

Cryogenic Heat Pipes

Current NASA cryogenic heat pipe requirements:

- Up to one meter length
- Operation at 60-80 K
- Transport capacity of up to approximately 5 watts
- High-lift wick design to enhance ground testability

Current state-of-the-art cryogenic heat pipes:

- Axially grooved wick - poor lift capability
- Oxygen working fluid - safety considerations
- Should meet heat transport requirements; needs to be demonstrated

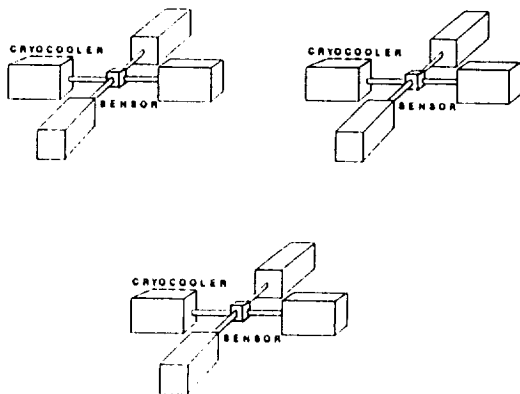
C.4

CRYOGENIC HEAT PIPE APPLICATION

This diagram depicts the concept of how cryogenic heat pipes may provide a benefit to cooling a sensor or set of sensors (or optics, electronics, etc.). By providing a buffer between the cryogenic cooler and the sensor to be cooled, it reduces the effect of the mechanical cooler's vibration and EMI. In addition, if a number of sensors need to be cooled on the same spacecraft cryogenic heat pipes could be used to provide a link to a central bank of cryocoolers. This concept would significantly reduce the number of cryocoolers needed, and hence their weight and cost.

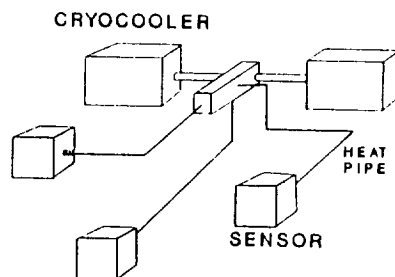
— OAET —

INDIVIDUALLY COOLED SENSORS



THREE SENSORS,
12 CRYOCOOLERS

CENTRAL BANK OF CRYOCOOLERS

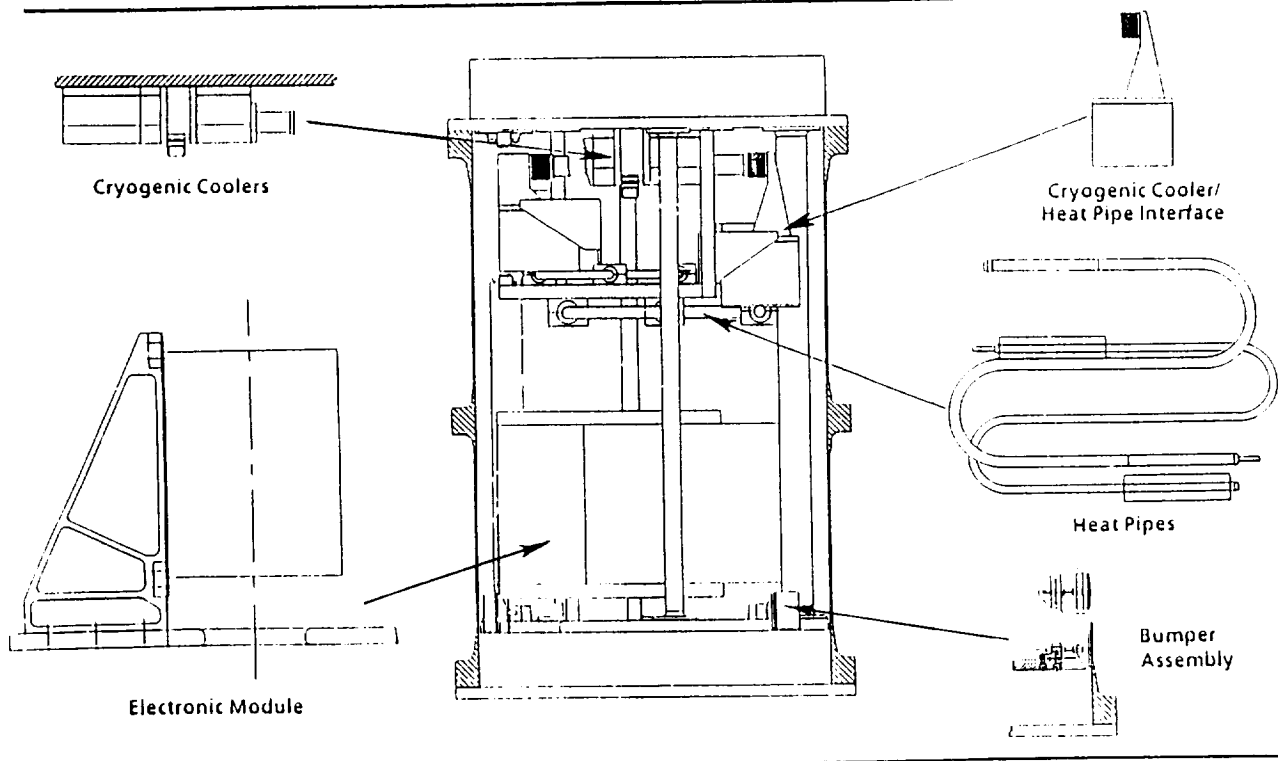


THREE SENSORS,
2 TO 6 CRYOCOOLERS

EXPERIMENT OBJECTIVES

- Primary - Cryogenic Heat Pipe
 - Oxygen Performance 70 - 110K
 - Correlation of Models
 - * Ground Testing
 - * Theory
 - 0-g Priming
 - Demonstrate 200 Watt-Inch Thermal Transport of Better
- Secondary
 - Cryogenic Test Bed
 - * Cryogenic Refrigerators
 - * Gain Flight Experience
 - Cooler Induced Vibration/Heat Pipe Transport

CRYOHP SUBSYSTEM IMPLEMENTATION



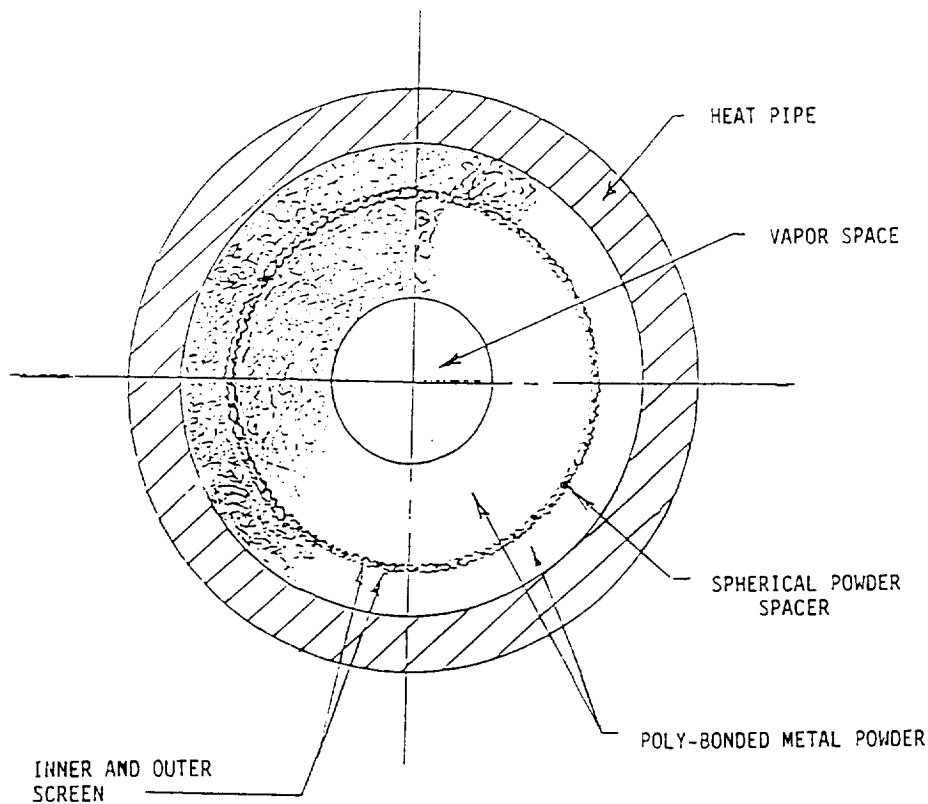
Sintered Powder Artery-Free Wick Cryogenic Heat Pipe Experiment (SPAC)

Specifications

- Total power capability of 4-5 watts at 70-80 K
- Overall thermal conductance of 1.0 W/°C
- One meter length, 15 mm OD, U-shaped heat pipe body
- Sintered powder metal wick material - no arteries or grooves
 - 5-15 times improvement in lift capability
 - 10-100 times better evaporative heat transfer coefficient than axial groove wick
- Nitrogen working fluid - decreased safety concern

Configuration

- Self-contained Hitchhiker payload in a modified GAS canister
- Projected launch date - September 1993



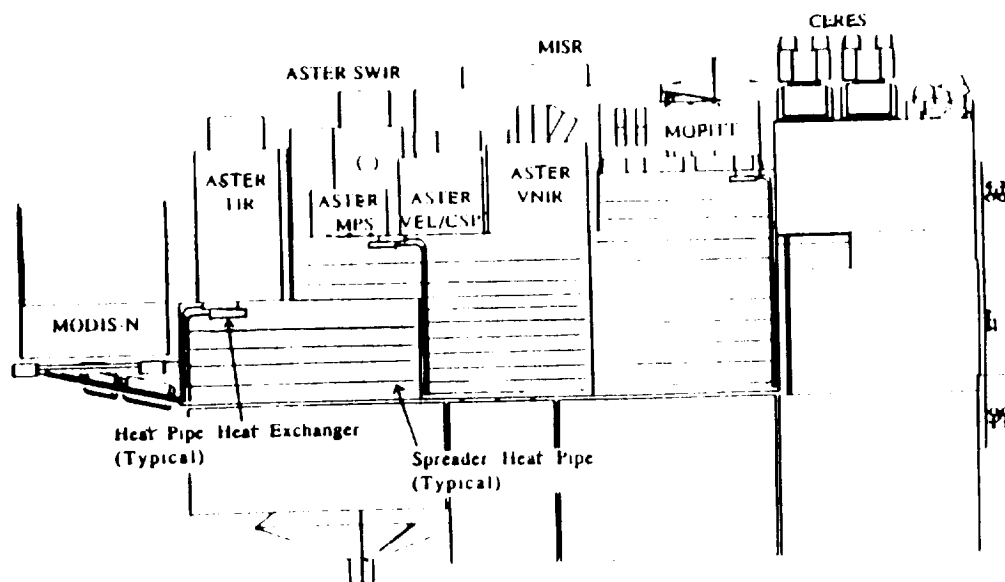
SPAC Heat Pipe Wick Cross Section

EOS-AM PLATFORM

EOS-AM SET THERMAL ACCOMMODATION

- * CENTRAL CPL THERMAL BUS BASELINED FOR ORIGINAL, LARGE EOS PLATFORM
- * EOS SCALED DOWN TO TWO SMALLER PLATFORMS, AN "AM" AND A "PM" SET.
 - SUITABILITY OF CPL THERMAL CONTROL SYSTEM REEVALUATED AGAINST HEAT PIPES
 - MINI-CPL CONCEPT ADOPTED AS NEW BASELINE
- * EOS-AM WILL HAVE THREE MINI-CPL LOOPS
 - TWO FOR THE ASTER INSTRUMENT (300 W AND 140 W)
 - ONE FOR THE MOPITT INSTRUMENT (270 W)

CPL MINI-LOOP - INSTRUMENT RADIATOR HEAT PIPE NETWORKS



ANALYTICAL TOOLS

GSFC ANALYTICAL TOOLS

SINDA/FLUINT

SOPHISTICATED, STATE-OF-THE ART NODAL MODEL; BASED ON FIRST PRINCIPLES; VERSATILE BUT COMPLEX; TRANSIENT CAPABILITY

SINFAC

MODULAR, EQUATION-OF-STATE APPROACH; QUASI STEADY STATE; MODERATE COMPLEXITY

CPL MODELER

USER FRIENDLY, SIMPLIFIED MODEL; STEADY STATE CAPABILITIES ONLY; CAPILLARY SYSTEMS ONLY

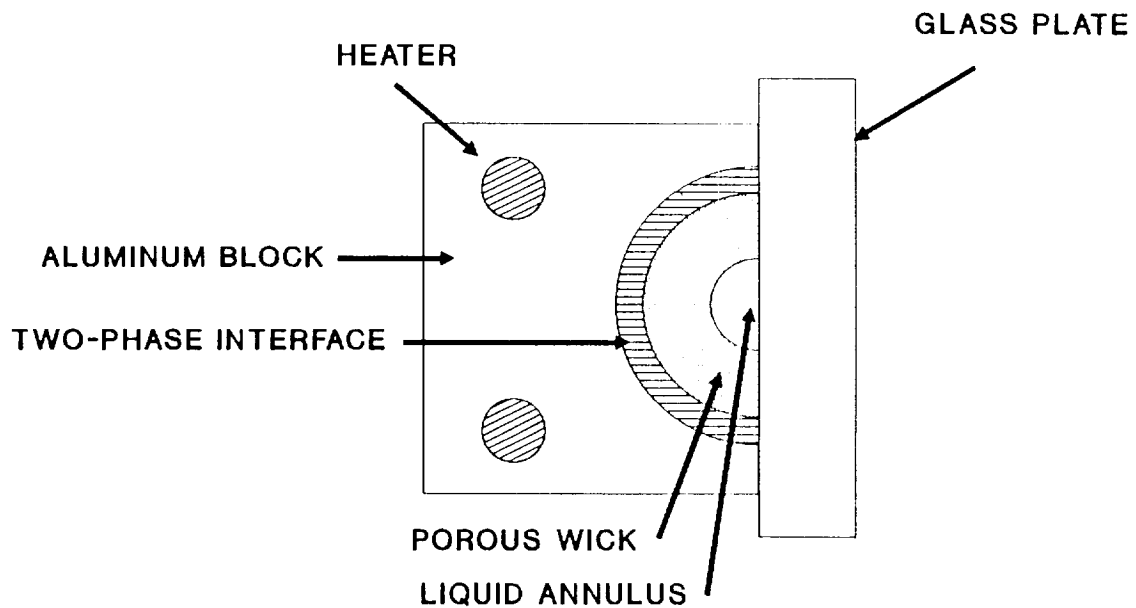
ADDITIONAL THERMAL TECHNOLOGY DEVELOPMENT

OTHER THERMAL RESEARCH EFFORTS

- CAPILLARY EVAPORATOR USING CERAMIC WICK
- TRANSPARENT CAPILLARY EVAPORATOR TO ALLOW FLOW VISUALIZATION STUDIES
- COMPONENTS FOR USE WITH AMMONIA, ESPECIALLY MECHANICAL PUMPS
- HEAT PUMPS

TRANSPARENT CAPILLARY EVAPORATOR

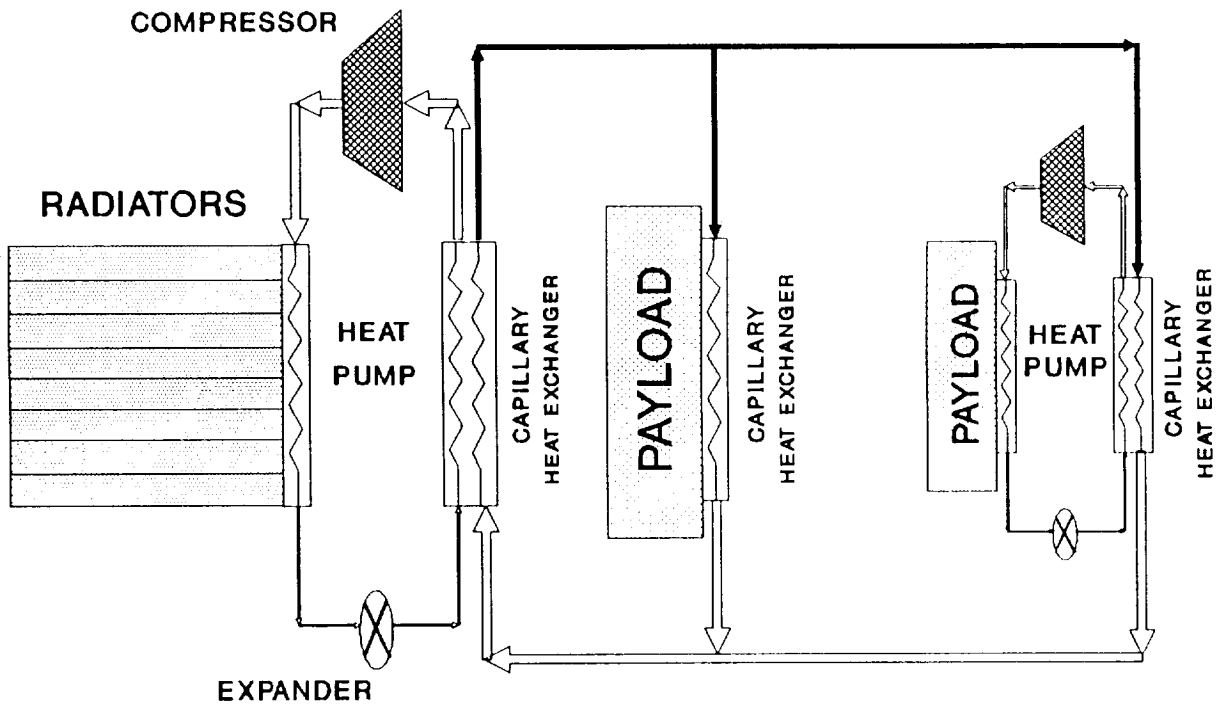
Capillary based evaporators have now been studied for almost a decade. Their performance at a component level is fairly well understood, but the internal workings of these devices is largely unknown. This is due to the difficulty of obtaining internal temperature measurements and in locating the liquid/vapor interface. The objective of this effort is to fabricate a see-through evaporator which will permit such measurements. While special construction techniques will be needed to fabricate such a device, it will essentially represent a conventional capillary evaporator sectioned longitudinally.



HEAT PUMP TWO-PHASE BUS CONCEPT

-INCREASE REJECTION TEMPERATURE/COOL PAYLOAD-

Recent analytical studies have indicated that for thermal control applications in a hot thermal sink, existing technology is inadequate. A prime example is a Lunar Base, where during the lunar day a conventional radiator would have to look at either the sun or the hot lunar surface. The effective sink temperature under these circumstances is about 35 °C, which is above normal room temperature. Hence, conventional heat rejection is impossible. A heat pump could be used to increase the heat rejection temperature in order to permit direct rejection. In addition, there are other reasons for developing space qualified heat pumps; energy management and conservation, refrigeration below central bus temperatures, and improved utilization of resources.



SMALL BUSINESS INNOVATIVE RESEARCH

RESEARCH PROGRAM TO PROVIDE SEED MONEY TO SMALL
BUSINESSES TO DEVELOP INNOVATIVE TECHNOLOGY
FOR THE SPACE PROGRAM AND COMMERCIAL APPLICATIONS

SBIR 1991 PHASE I STUDIES

- COMPACT HEAT EXCHANGERS FOR AMMONIA REFRIGERANT
 - ▶ DEVELOP COMPACT LOW MASS HEAT EXCHANGERS FOR USE WITH AMMONIA REFRIGERATION SYSTEMS IN LOW AND MICRO GRAVITY ENVIRONMENTS
 - ▶ PHASE A GOALS: DESIGN ALGORITHM, PROTOTYPE DESIGN OF SPECIFIC EQUIPMENT
- UTILIZATION OF LOW TO MEDIUM TEMPERATURE WASTE HEAT
 - ▶ CONVERT LOW TO MEDIUM TEMPERATURE WASTE HEAT TO ELECTRICAL POWER BY USE OF PYROELECTRICS
 - ▶ PHASE A GOALS: MEASURE USEFUL LIFETIME OF PYROELECTRIC CONVERSION MATERIAL, DETERMINE MATERIAL PROPERTIES DURING THERMAL AND ELECTRICAL CYCLING ELECTRICAL CYCLING PERIODS

SBIR PHASE II STUDIES

MODULAR CHEMICAL/MECHANICAL HEAT PUMP

- ▶ CONSTRUCT LOW LIFT/LONG LIFE, CHEMICAL/MECHANICAL HEAT PUMP TO DEMONSTRATE 20% + INCREASE IN COP OVER COMPARIBLE MECHANICAL DESIGN
- ▶ PHASE A IDENTIFIED POSSIBLE FLUID WORKING PAIRS AND 20% + COMPUTER BASED COP IMPROVEMENT OVER OTHER AVAILABLE VAPOR COMPRESSION SYSTEMS

SUMMARY

- **CPL'S DO WORK**
- **GOOD GROUND HERITAGE**
- **LIMITED FLIGHT DATA**
- **GOOD PEER REVIEW**

FUTURE

- **CONTINUED TESTING AND MODELING**
- **COMET**
- **CAPL FLIGHT EXPERIMENT**
- **EOS SPACECRAFT**
- **MILITARY APPLICATIONS**

THERMOSTRUCTURAL APPLICATIONS OF HEAT PIPES FOR COOLING LEADING EDGES OF HIGH-SPEED AEROSPACE VEHICLES

Charles J. Camarda
NASA Langley Research Center
Hampton, VA

David E. Glass
Analytical Services and Materials
Hampton, VA

INTRODUCTION

Stagnation regions, such as wing and engine leading edges and nose caps, are critical design areas of hypersonic aerospace vehicles because of the hostile thermal environment they experience during flight. The high local heating and aerodynamic forces cause very high temperatures, severe thermal gradients, and high stresses. In addition, as a hypersonic vehicle travels through the earth's atmosphere, the stagnation regions are subjected to a potentially severe oxidation and erosion environment. A further concern is that thermal-structural distortions may be large enough to interact with the fluid flow and cause coupling between the fluid, thermal and structural responses.

Design considerations for hypersonic aerospace vehicles can become extremely complex as the disciplines involved in the analysis and design of the vehicle become coupled. An air-breathing, single-stage-to-orbit vehicle, such as the National Aero-Space Plane (NASP), is subjected to severe aerothermal and acoustic loading; and yet many diverse, and often conflicting, design requirements must be satisfied. Mass is of critical importance to any hypersonic vehicle, in particular if the vehicle travels to orbit. The selection of the structural concepts, materials, and, if necessary, method of cooling (passive, ablative, active, and "semi-active" or heat-pipe cooling) strongly influence vehicle mass. The structural concepts and materials selected must satisfy structural, thermal, material and manufacturing requirements. Additional performance requirements such as reusability, reliability, and redundancy often complicate lightweight solutions to the design problem.

Analytical studies of the early 1970's (refs. 1 to 5) indicate that a solution to the thermal-structural problems associated with stagnation regions of hypersonic aerospace vehicles might be alleviated by the use of heat pipes to cool these regions. Radiant heat and wind tunnel tests of a heat-pipe-cooled wing leading edge designed for a shuttle-type vehicle (refs. 6 to 8) verified the feasibility of heat-pipe cooling for leading edges. Subsequent work (refs. 9 to 12) improved the design and made it lighter and advanced the analytical capability to predict transient and steady-state heat-pipe performance. Recent work on a novel refractory-composite/refractory-metal heat-pipe-cooled leading edge concept for the NASP combines advanced high-temperature materials, coatings, and fabrication techniques with an innovative thermal-structural design. Preliminary design studies (refs. 13-14) indicate that the new leading edge concept can reduce the mass by over 50 percent from an actively cooled design, can completely eliminate the need for active cooling, and can potentially provide failsafe and redundancy features. The present paper reviews the state-of-the-art of heat pipes for cooling wing leading edges of hypersonic vehicles from early application for space-shuttle-type space transportation systems to the present, single-stage-to-orbit NASP.

BRIEF HISTORY OF HIGH-TEMPERATURE HEAT-PIPE APPLICATIONS AS APPLIED TO LEADING-EDGE COOLING

In the early 1970's, several feasibility studies were performed to assess the application of heat pipes for cooling leading edges and nose caps of hypersonic vehicles (refs. 1-5). NASA Langley Research Center, through a contractual study (ref. 1), analytically verified the viability of heat pipes for cooling stagnation regions of hypersonic vehicles. In 1972, McDonnell Douglas Astronautics Co. (MDAC) compared four space shuttle wing leading edge concepts (ref. 2): a passive carbon-carbon concept, a passive coated-columbium concept, an ablative concept, and a liquid-metal/superalloy heat-pipe-cooled concept. The heat-pipe-cooled concept was determined to be a feasible and durable design concept, but was slightly heavier than the other candidate concepts. In 1973 MDAC fabricated a half-scale shuttle-type heat-pipe-cooled leading edge to verify feasibility of the concept (ref. 4). This model was tested by a series of radiant heat and aerothermal tests at NASA Langley Research Center from 1977 to 1978 (refs. 6-8) to verify heat pipe transient, startup, and steady-state performance. In 1979 MDAC received a follow-on contract to optimize a heat-pipe-cooled wing leading edge for a single-stage-to-orbit vehicle. Results of the follow-on study (ref. 9) indicated that the mass of a shuttle-type heat-pipe-cooled leading edge could be reduced by over 40 percent by use of a more efficient structural design. In 1986 MDAC received a contract to fabricate and build a sodium/superalloy heat-pipe-cooled leading edge component for an advanced shuttle-type vehicle (refs. 10 and 11). This advanced shuttle-type heat pipe was six-feet long and was tested at MDAC by radiant heating (ref. 11) and at Los Alamos National Laboratories by induction heating. NASA has also funded a grant with Georgia Institute of Technology which resulted in the development of a finite element solution for liquid-metal heat-pipe startup from the frozen state (ref. 12).

Recently, NASA Langley has been investigating the use of an advanced heat-pipe-cooled wing leading edge design which is based on high-temperature refractory-composite materials such as carbon-carbon for the structure, refractory-metals such as tungsten or molybdenum for the heat-pipe container, and lithium for the working fluid. The new concept described above is referred to as a refractory-composite/heat-pipe-cooled wing leading edge and is proposed for the wing leading edge of the National Aero-Space Plane (refs. 13 and 14).

The following discussions will summarize significant results of the above mentioned experiments and studies.

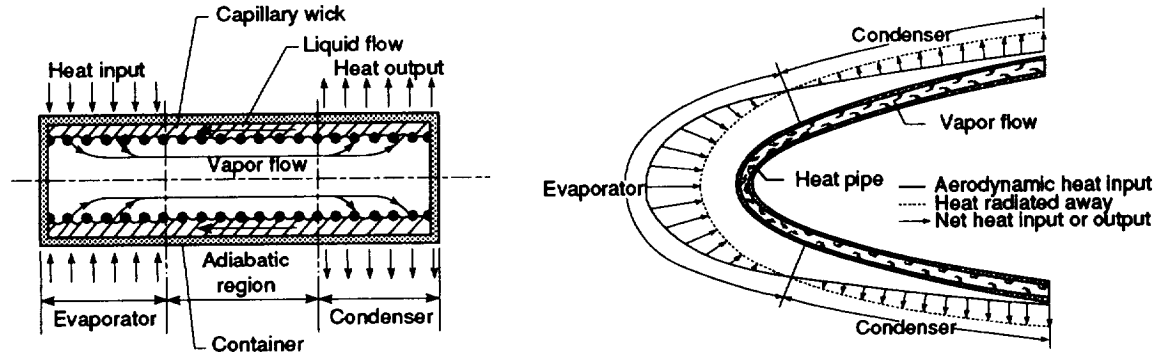
Early 1970's	Feasibility studies
1973	Half-scale shuttle-type heat-pipe-cooled wing leading edge (MDAC)
1975-1978	Radiant heat and aerothermal test at LaRC
1979	Follow-on study by MDAC to minimize mass
1985-1988	Finite element solution of startup from the frozen state (Ga. Tech.)
1986	Fabrication of Na/superalloy heat-pipe for wing of advanced STS (MDAC)
1989	Induction heating test of MDAC heat pipe at LANL
1991-present	NASP Government Work Package to design, fabricate, and test refractory-composite/heat-pipe-cooled wing leading edge (LaRC)

Figure 1. - Brief history of high-temperature heat-pipe applications as applied to leading-edge cooling.

PRINCIPLE OF OPERATION OF A HEAT PIPE AS APPLIED TO LEADING EDGE COOLING

A schematic diagram of the general principle of operation of a heat pipe and how it is applied to leading edge cooling is shown in figure 2. A heat pipe is a self-contained, two-phase heat transfer device which is composed of a container, a wick, and a working fluid. Heat input locally to one section of the heat pipe, the evaporator region, is conducted through the container and into the wick/working-fluid matrix, where it is absorbed by the evaporation of the working fluid. The heated vapor flows to a slightly cooler section of the heat pipe where the working fluid condenses and gives up its stored heat. The heat is then conducted through the wick/working-fluid matrix and container and is rejected. The location of the heat pipe where heat is rejected is called the condenser region. The cycle is completed with the return flow of liquid condensate back to the heated region (evaporator) by the capillary pumping action of the wick. During normal operation, heat pipes operate as devices of very high effective thermal conductance and maintain a nearly uniform temperature over the entire heat-pipe length.

Applied to the wing leading edge stagnation heating problem of high-speed aerospace vehicles, heat pipes transport the high net heat input near the stagnation region to cooler aft surfaces, raising the temperature there above the radiation equilibrium temperature and thus rejecting the heat by radiation. The location and extent of the evaporator and condenser regions, which are by definition areas in which there is a net inflow or outflow of heat, respectively, is dependent upon the magnitude and distribution of heating and will vary to satisfy an overall energy balance.



a) Schematic of heat pipe operation b) Heat pipe cooling applied to leading edge.

Figure 2. - Principle of operation of a heat pipe as applied to leading edge cooling.

HEAT-PIPE HEAT TRANSPORT LIMITS

A given heat pipe can operate over a range of temperatures; however, at each temperature there is a maximum axial heat transport capacity and radial heat flux above which normal heat pipe operation is disrupted. Four such operational limits are shown schematically in figure 3. These limits are the sonic, entrainment, wicking, and boiling limits. The sonic limit usually occurs at low vapor temperatures when the velocity of the vapor can become sonic and the axial heat transport in the heat pipe is limited by a choked-flow condition. During startup of a heat pipe from the frozen state, when the working fluid is solid, the axial heat transfer in the heat pipe is usually limited by sonic flow. Although the sonic limit alone typically does not cause a failure of the heat pipe, it causes the operating temperature of the heat pipe to rise which may cause other limiting conditions to be encountered. The entrainment limit occurs when the drag force of the vapor on the liquid condensate returning to the evaporator is sufficient to overcome the surface tension forces of the liquid within the wick and entrain liquid droplets in the vapor flow. The entrainment of liquid intended to flow to the evaporator region could lead to dryout of the wick in the evaporator region and result in over heating and excessive local temperatures there. The wicking limit is reached when the surface-tension pumping capability of the wick is just sufficient to provide the liquid mass flow rate needed to balance the applied heating rate. Liquid and vapor frictional losses tend to decrease the flow rate of liquid condensate to the evaporator region. Inertial forces caused by vehicle acceleration and gravity can tend to reduce or increase the flow of liquid condensate to the evaporator region. If the wicking limit is exceeded, dryout will occur in the evaporator and result in overheating.

Vaporization of the working fluid normally occurs in the evaporator region of the heat pipe at the liquid-vapor interface. At high radial heat input levels, however, the superheated liquid can reach a critical value at which boiling can occur near the heat pipe wall. The boiling limit is reached when the heating rate is high enough to cause the formation of a continuous vapor film at the heat pipe wall which inhibits the radial flow of heat into the working fluid. The boiling limit is usually not a limiting condition for liquid-metal heat pipes because of the high thermal conductivity of the liquid-metal working fluid and the large amount of superheat needed to initiate boiling.

The boiling limit is a limit on the radial heat flux density, whereas the sonic, entrainment and wicking limits are limits on the axial heat flux density. Further detailed explanations of heat-pipe theory and operating limit calculations can be found in references 15 and 16.

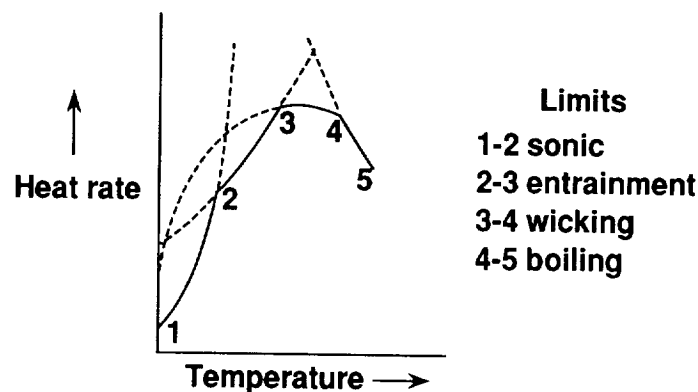


Figure 3. - Heat transport limits.

SHUTTLE-TYPE HEAT-PIPE-COOLED WING LEADING EDGE TEST MODEL

A one-half scale heat-pipe-cooled wing leading edge test model fabricated by MDAC for a shuttle-type vehicle and trajectory is shown in figure 4. The test model is six-inches in span, has a chord length of 22 in., and is 13-in. high at its base. It consists of 12 sodium-charged heat pipes which are brazed to each other and to the inner surface of a thin (0.02-in.-thick) Hastelloy-X skin. The heat pipes are Hastelloy-X circular cylinders which have an outer diameter of 0.5 in., a wall thickness of 0.05 in., and a wick thickness of 0.035 in. The wick consists of seven alternate layers of 100- and 200-mesh stainless-steel screen and is a concentric annulus design. The heat pipes are sized so that one heat pipe could become inoperative without compromising structural integrity, thus providing a fail-safe capability. The skin is coated externally with a high-emissivity ceramic paint to facilitate heat rejection by radiation.

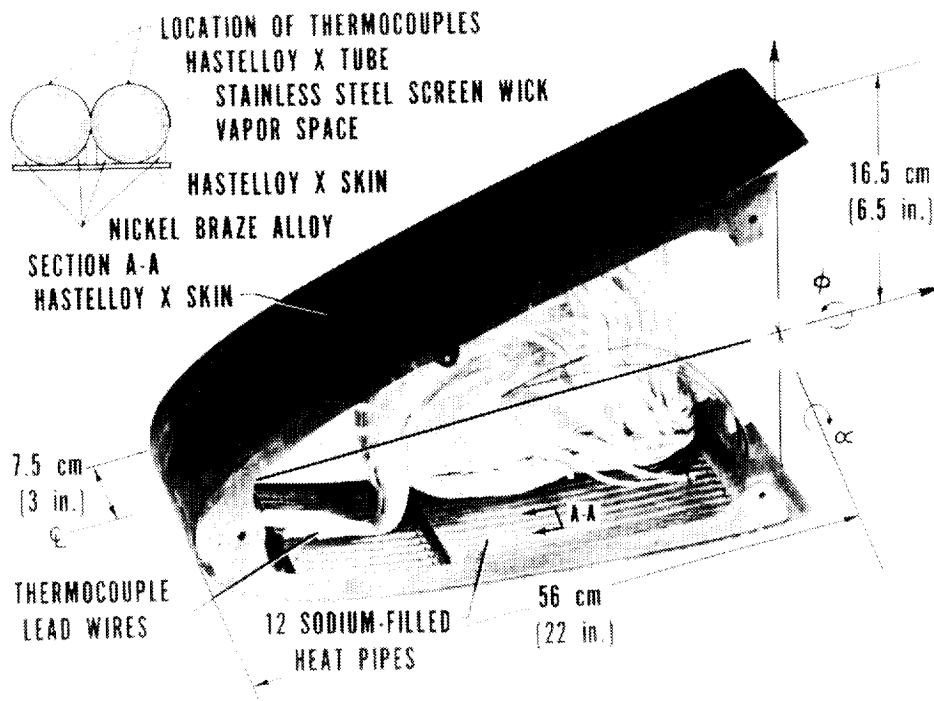


Figure 4. - Shuttle-type heat-pipe-cooled wing leading edge test model.

SHUTTLE-TYPE HEAT-PIPE-COOLED WING LEADING EDGE DURING A RADIANT HEAT TEST

Performance of the shuttle-type heat-pipe-cooled wing leading edge was studied by a series of radiant heat and aerothermal tests. The purpose of the radiant heat tests was to investigate heat-pipe startup from the frozen state (working fluid initially frozen or solid), and transient and steady-state thermal performance of the leading edge test model. For the radiant heat tests (fig. 5), angle of attack, α , was simulated by orienting the model at the angle α with respect to the horizontal to obtain the desired gravity effect and by positioning three radiant heaters about the model to provide a heating distribution representative of the aerodynamic heating distribution at that angle. Three water-cooled calorimeter gages were used, one in each of three separate feedback control loops, to regulate output of each lamp bank separately. Power to the lamp banks was varied to simulate a shuttle reentry heating trajectory. The test model was subjected to a total of seven radiant heat tests with cold-wall heating rates ranging from 21.1 to 34.8 Btu/ft²-s, angles of attack ranging from 0 to 20 degrees, and maximum surface temperatures ranging from 1130 °F to 1380 °F. Details of the radiant heating tests can be found in reference 6.

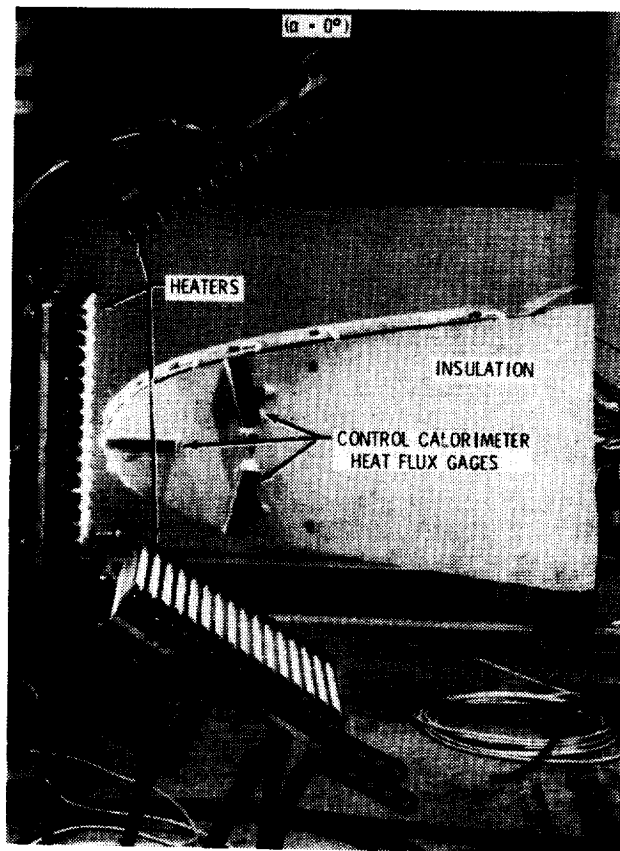


Figure 5. - Shuttle-type heat-pipe-cooled wing leading edge during a radiant heat test.

WIND TUNNEL CONFIGURATION OF HEAT-PIPE-COOLED WING LEADING EDGE

After completion of the radiant heat tests, the heat-pipe-cooled leading edge was fitted with spanwise extensions and aerodynamic fences (fig. 6) for aerothermal testing in the Langley 8-Foot High Temperature Tunnel. The purpose of the extensions and fences was to produce a two-dimensional flow field over the test model and to allow measurement of flow conditions over the leading edge. The purpose of the aerothermal tests was to investigate performance of the model subject to realistic aerothermal loads. To avoid unrealistically severe heat pulses and to insure proper startup of the heat pipe, the model was preheated prior to insertion into the test stream. A simple heater array was used to preheat the model; no attempt was made to simulate an aerodynamic heating distribution during preheating. The model withstood 27 supplemental radiant heat cycles lasting 30 minutes each during which the maximum surface temperatures ranged from 1100 °F to 1480 °F. Cold-wall stagnation heating rates ranged from 21.1 to 34.8 Btu/ft²-s for the radiant preheating cycles and hot-wall stagnation heating rates ranged from 21.5 to 37.2 Btu/ft²-s for the aerothermal tests. The maximum cold-wall heating rate of the aerothermal tests was 56.9 Btu/ft²-s and maximum heat-pipe operating temperatures ranged from 1090 °F to 1520 °F. The model was subjected to a total of eight aerothermal tests with angle of attack variations of 0-, 10-, and 20-degrees; and roll variations of 0- and 90-degrees. The 90-degree roll condition was included to investigate the effect of gravity on heat-pipe performance.

The heat pipes operated isothermally for these test conditions with maximum operating temperatures ranging from 1250 to 1520 °F. Near steady-state temperatures obtained during the aerothermal tests were in good agreement with analytical results. The pressure and heat-flux distributions were also in good agreement with design distributions.

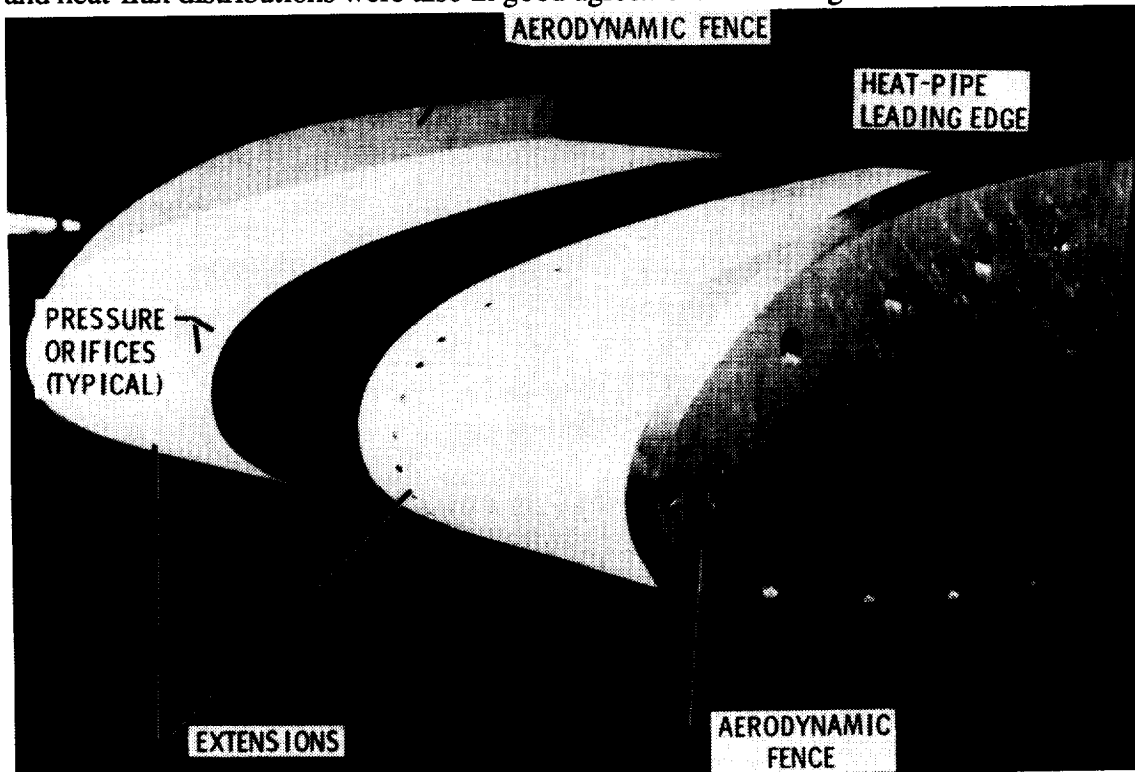


Figure 6. - Wind tunnel configuration of heat-pipe-cooled wing leading edge.

SIMPLIFIED MODEL OF TRANSIENT HEAT-PIPE STARTUP FROM THE FROZEN STATE

A schematic diagram of the simplified analysis model used to predict the heat-pipe startup, transient, and steady-state response is shown in figure 7. The simplified analysis assumes the momentum and energy equations are uncoupled and solves for heat pipe temperatures directly from an energy balance. The analysis method used is similar to that of reference 17 and assumes the initial temperature of the heat pipes is below the melting point of the working fluid and, consequently, the working fluid is in the frozen or solid state and the vapor pressure is low. Thus, free molecular flow conditions exist throughout the heat pipe and axial heat transfer is very low. As heat is applied, the temperature and vapor pressure of the most highly heated region increases until continuum flow conditions are established and the heat pipe begins to operate locally in that region. Additional heating causes the temperature of the continuum region to increase and the continuum front to extend into adjacent free molecular flow regions.

An aerodynamic heating distribution was approximated by six constant heat input regions as shown in figure 8. Continuum flow initiates in the region of highest heat input and is assumed to occur when the molecular mean free path of the sodium vapor is equal to or less than 0.01 times the diameter of the vapor space. During startup, axial heat transport, \dot{Q}_a , is assumed to occur from continuum flow regions at the sonic heat transport limit and all heat is assumed to be rejected by radiation, \dot{Q}_r . An effective volumetric heat capacity per unit heat-pipe length, C , was calculated as a function of temperature and was used in simple energy balances to determine continuum and free molecular region temperatures and to determine continuum region growth.

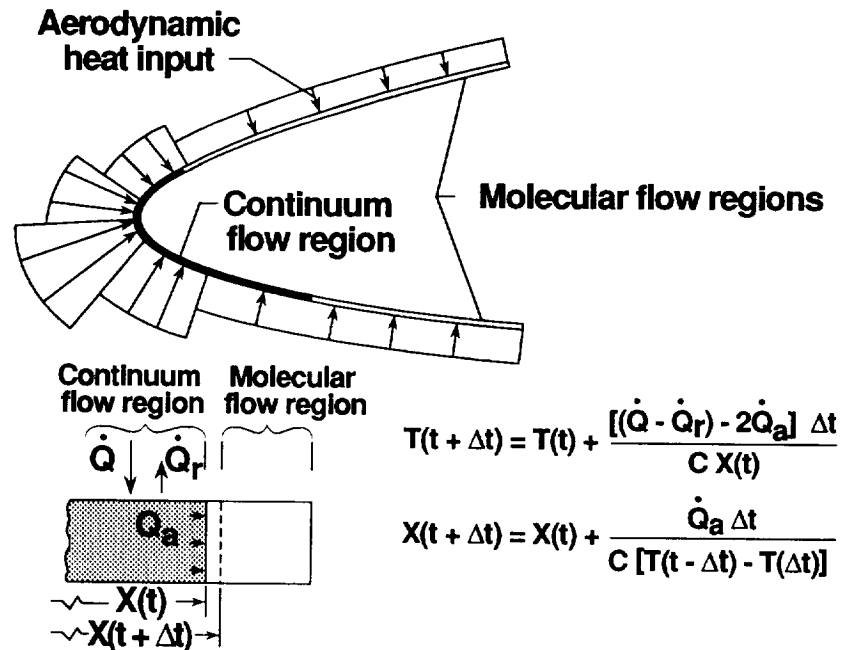


Figure 7. - Simplified model of transient heat-pipe startup from the frozen state.

RESULTS OF REENTRY SIMULATION TEST USING RADIANT HEATERS

Results of a radiant heating test which simulates a shuttle-type reentry heating trajectory are shown in figure 8. Experimental and analytical temperature histories at three locations along the upper surface of the leading edge agree except for times greater than 800 seconds at which point calculated temperatures are approximately 150 °F greater than experimental values. The lower than expected experimental temperatures are believed to be caused by heat lost by free convection during the experiment which was not accounted for in the analysis. The sharp rise in temperature at the onset of heating occurs because axial heat transport is low since free molecular flow conditions prevail in the vapor space. Hence, temperatures in the aft region ($l/l_T = 0.88$), for instance, rise slowly. When the continuum vapor front propagates to the aft region (at approximately time $t = 600$ seconds), the temperature there rises very rapidly to the continuum flow region temperature as shown in figure 8. No startup problems were encountered and the heat pipes became fully operational at $t = 700$ seconds and a temperature of about 1200 °F.

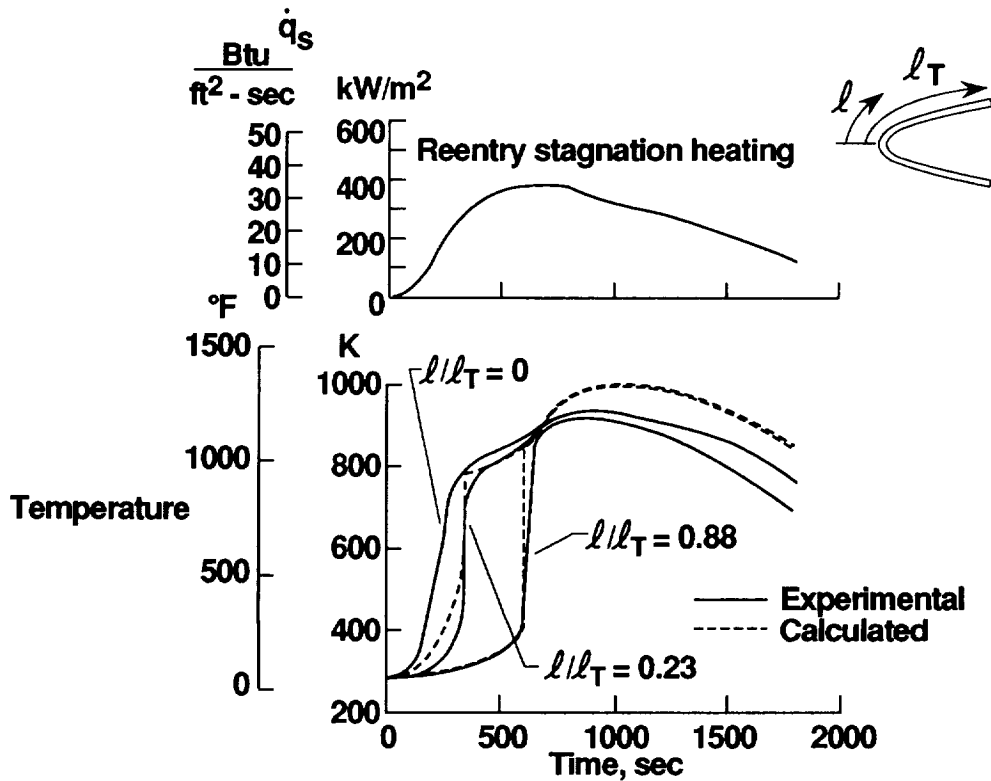


Figure 8. - Results of reentry simulation test using radiant heaters.

TEMPERATURE DISTRIBUTIONS DURING TRANSIENT HEAT-PIPE STARTUP

Temperature distributions along the lower and upper surfaces of the leading edge during three different phases of heat-pipe startup (unstarted, starting, and fully operational) are shown in figure 9 for a zero-degree angle-of-attack test ($\alpha = 0^\circ$). In the unstarted state, the working fluid is frozen and, hence, the temperature distribution is similar to that of an uncooled leading edge (i.e., high local temperatures near the locally heated nose region and a rapid drop in temperatures away from the nose region). Once continuum flow occurs, the heat pipe is partially started and there exists a local continuum flow region where temperatures are nearly uniform. Located next to the continuum flow region are two free molecular flow regions where axial heat transfer is low and large axial temperature gradients exist. Once the continuum flow region propagates to the extreme ends of the heat pipes, the heat pipes are assumed to be fully operational and nearly isothermal as shown in figure 9.

Although startup and transient heat pipe operation has been predicted with reasonable accuracy using simplified mathematical models, more work is necessary to predict accurately the transient heat-pipe operating limits. Slight variations in heat-pipe temperature and pressure can produce large variations in predicted operating limits and, hence, improved analytical methods are necessary. Finite element and finite difference methods can be used to solve the coupled momentum and energy equations and incorporate working fluid phase change, compressible fluid flow, and three-dimensional heat transfer.

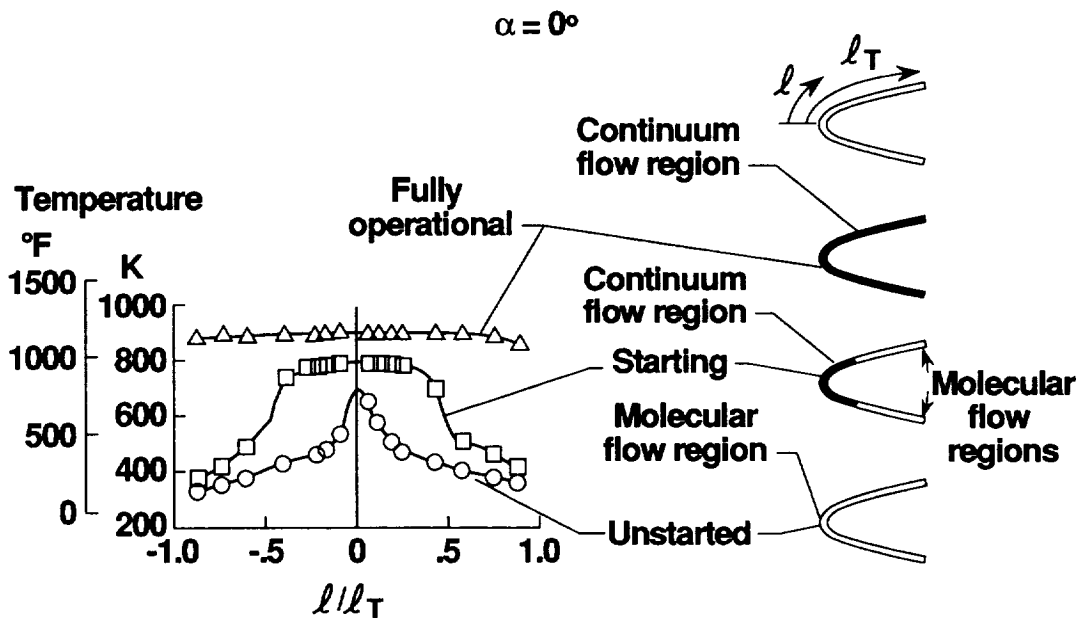


Figure 9. - Temperature distributions during transient heat-pipe startup.

THERMAL BUCKLING OF HEAT-PIPE-COOLED WING LEADING EDGE

Results of the aerothermal tests dramatically demonstrate the durability of the heat pipe leading edge. The initial configuration of the radiant heaters for the preheating of the model caused a wicking limit to occur prior to the first aerothermal test. The encounter with the wicking limit caused a wick dryout condition to occur locally in the upper aft region of the leading edge due to the location of the heaters. During this dryout condition, local temperatures exceeded 1900 °F. The high local temperatures, coupled with the constraint imposed by the side extensions in the lateral directions, caused local buckling of the aerodynamic skin in regions between the cylindrical heat pipes as shown in figure 10. However, the structural integrity of the test model was not severely compromised as demonstrated by the successful completion of the remaining six aerothermal tests.

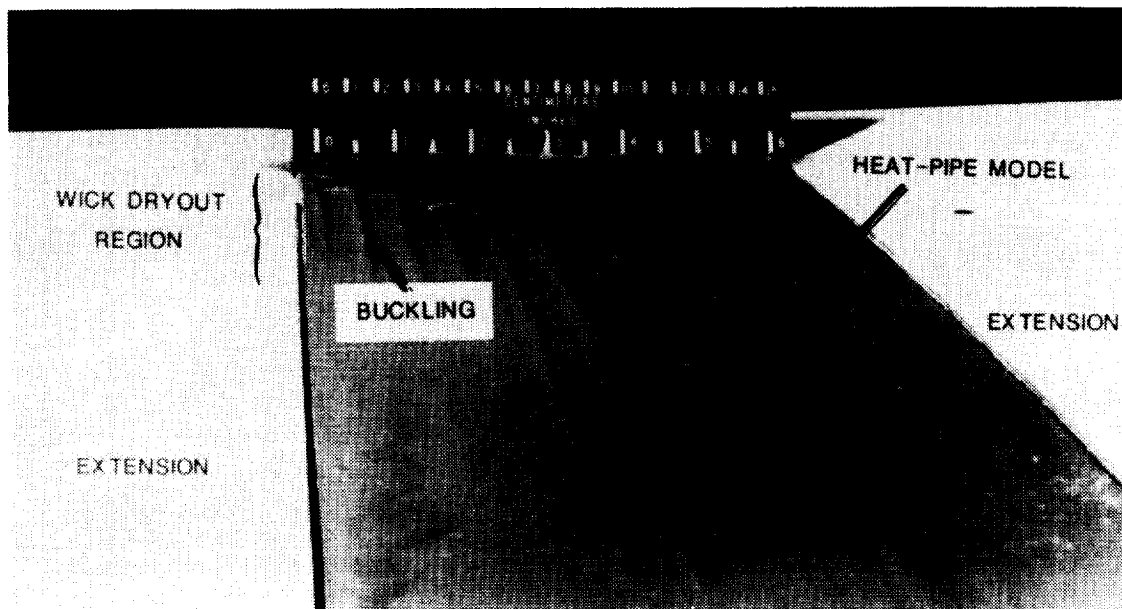


Figure 10. - Thermal buckling of heat-pipe-cooled wing leading edge.

EROSION DAMAGE OF HEAT-PIPE-COOLED WING LEADING EDGE

Debris in the test stream of the Eight-Foot High Temperature Tunnel (tests were performed prior to tunnel modification which reduced the debris threat) caused some erosion damage to the model as shown in figure 11. After two aerothermal tests, the nose region of the heat-pipe leading edge model was pitted and the zirconium coating on the stainless-steel water-cooled extensions was severely eroded. The thin Hastelloy-X skin (0.02-in. thick) suffered minor damage but no particle penetration. However, the high emissivity ceramic paint eroded near the nose and exposed the metal surface to oxidation by the airstream.

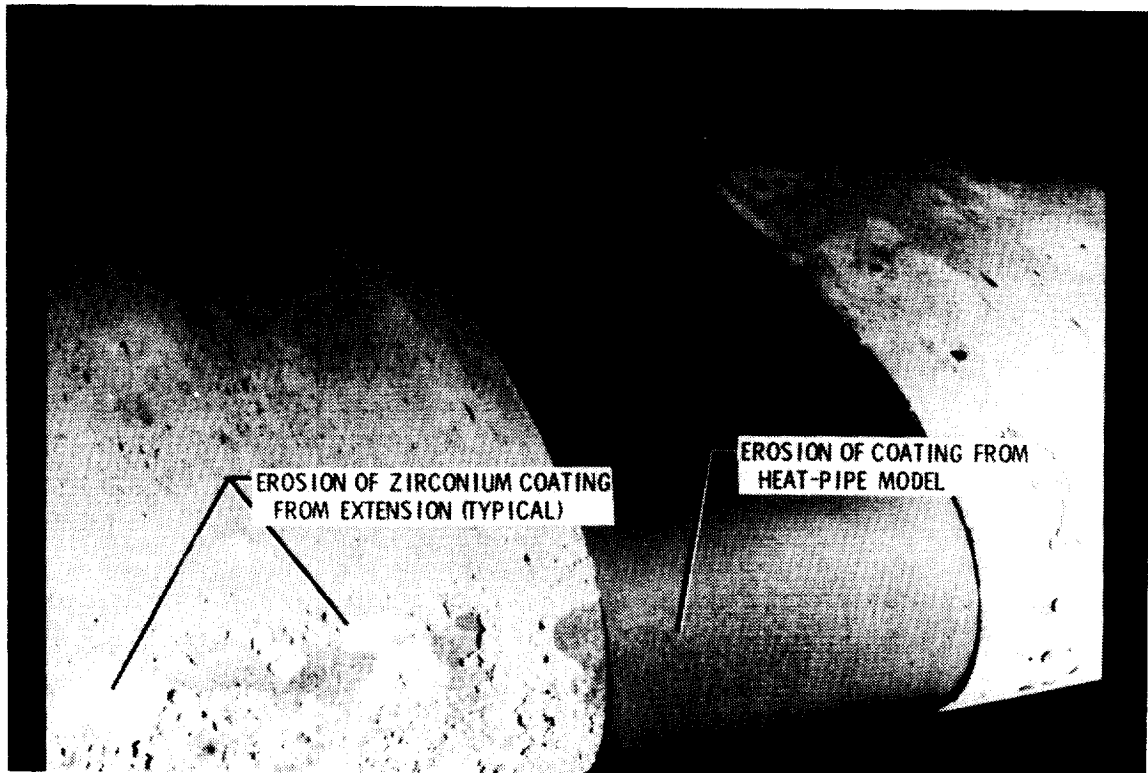


Figure 11. - Erosion damage of heat-pipe-cooled wing leading edge.

DEVELOPMENT OF NUMERICAL METHOD FOR PREDICTING TRANSIENT HEAT-PIPE OPERATION FROM THE FROZEN STATE USING FINITE ELEMENT ANALYSIS

A finite element analysis code has been developed which solves the coupled thermal-fluid heat pipe problem and is capable of accurately predicting heat-pipe temperatures and temperature gradients as well as liquid and vapor pressures and velocities. Numerical results for startup of a liquid-metal heat pipe subject to a typical aerodynamic heat input and representative of a radiant-heat test of a shuttle-type heat-pipe-cooled leading edge are shown in figure 12, and the results compare well with experimental results (refs. 6-8).

Since a typical aerodynamic heating distribution was approximated for both the experimental and numerical cases, the heat input at the stagnation region was much greater than in the aft regions. As expected, the temperatures began to rise in the stagnation region sooner than in the aft regions, resulting in a large temperature gradient in the heat pipe during start-up. For about the first 450 seconds, the heat pipe is not operational as the vapor density is still quite small. After 550 seconds, the vapor flow has transitioned from free molecular flow to continuum flow, and an isothermal region can be observed in the stagnation region, while most of the rest of the heat pipe is still at the initial temperature. The region of continuum flow continues to increase and becomes isothermal near a time of 1200 seconds. However, the temperature of the heat pipe continues to increase until a steady-state value is reached at a later time.

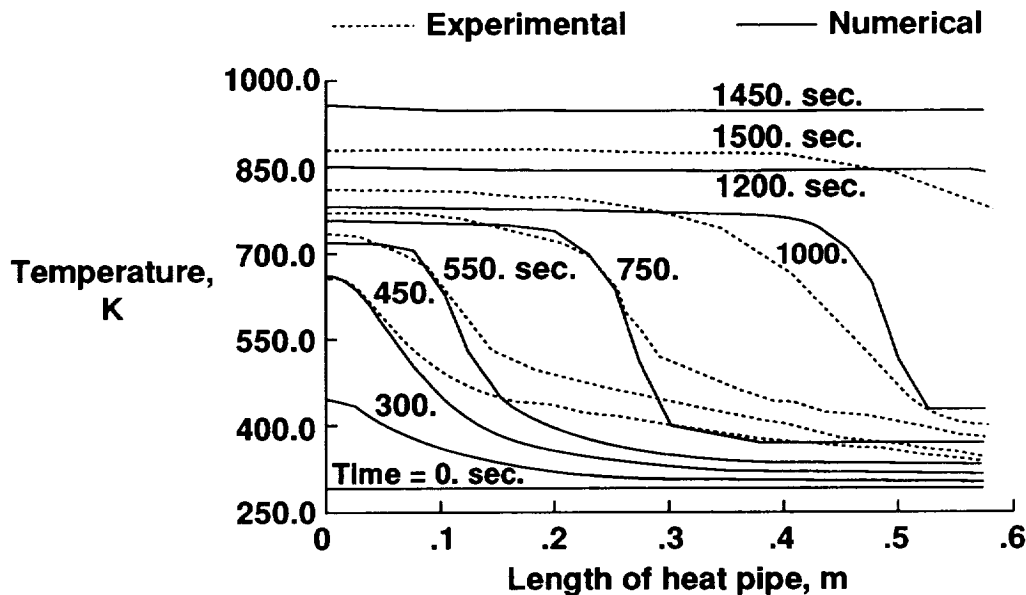
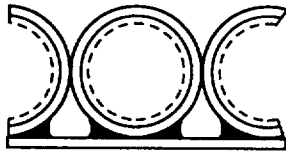


Figure 12. - Comparison of numerical and experimental temperature distributions in a heat-pipe-cooled leading edge during startup from the frozen state.

IMPROVED HEAT-PIPE DESIGN

A follow-on study contract was awarded to MDAC (NASA Contract NAS1-15554) to investigate thermostructural applications of heat pipes (ref. 9). A heat-pipe-cooled leading edge was designed for a single-stage-to-orbit vehicle and optimized with respect to mass to make it competitive with carbon-carbon and refractory-metal versions of the leading edge. The improved design, shown in figure 13, uses a Hastelloy-X D-tube corrugated section which is seam welded to a thin Hastelloy-X facesheet. The new configuration eliminates the need for the braze fillets of the cylindrical tube design (used to enhance heat conduction into the heat pipe) and reduces mass by approximately 44 percent compared to a design which uses circular cylindrical tubes brazed to a thin facesheet.



**3.4 lb/ft² - Not competitive
with carbon-carbon**



**1.9 lb/ft² - Competitive with
carbon-carbon**

Figure 13. - Improved heat pipe design.

HEAT-PIPE-COOLED WING LEADING EDGE DESIGN FOR AN ADVANCED SPACE TRANSPORTATION SYSTEM

A sodium/Hastelloy-X heat pipe was designed for use in the leading edge of an advanced space transportation system (refs. 10-11) and a single full-scale heat pipe was fabricated for testing. A schematic diagram of the heat pipe for the wing of an advanced shuttle-type vehicle is shown in figure 14. The heat pipe was designed to be oriented normal to the leading edge. Aft of the heat pipe, more conventional hot structure designs, for example, carbon-carbon, were assumed on the lower surface. The heat pipe is intended to reduce maximum wing leading edge temperatures during re-entry from 3500 °F to 1800 °F. The total length of the heat pipe necessary to radiate enough heat to reduce maximum temperatures to 1800 °F was determined from an energy balance over the entire heat pipe. A large angle of attack during re-entry would result in higher heat loads on the lower surface, thus providing a considerable heat sink on the upper surface. The heat pipe length on the lower surface was sized such that the radiation equilibrium temperature of the region beyond the end of the heat pipe was less than 2800 °F. This sizing operation resulted in a total heat pipe length of 69 in., with 3 in. of that on the lower surface.

The Hastelloy-X heat-pipe container had a rectangular cross section and a stainless steel wick which was diffusion bonded to the inner surface of the container. A 0.030-in.-thick "U-shaped" channel and a 0.060-in.-thick flat strip with a 0.030-in. step milled in its edges made up the heat pipe components. In the evaporator region, two layers of 50-mesh stainless-steel screen were placed between two layers of 200-mesh screen on the heated surface, while two layers of 200-mesh screen were used on the side walls. No screen was placed on the back wall in the evaporator region. In the condenser region, eight layers of 50-mesh screen were placed between two layers of 200-mesh screen on the heated surface, and two layers of 200-mesh screen were used on the other three walls. The purpose of the composite wick (50-mesh screen between 200-mesh screen) was to achieve the high capillary pressure provided by the 200-mesh screen and the high permeability of the 50-mesh screen.

The heat pipe was instrumented with internal pressure transducers and external thermocouples. Graphite heaters were used to heat the heat pipe during the tests. A burn-through of the heat pipe container occurred in the stagnation region during the second test. Post test X-rays indicated that the sodium working fluid had not been evenly distributed in the wick prior to testing. A second heat pipe was then assembled at Los Alamos National Laboratory (LANL) with spare parts which remained after fabrication of the first heat pipe. Tests were conducted to determine the basic performance limits of the heat pipe.

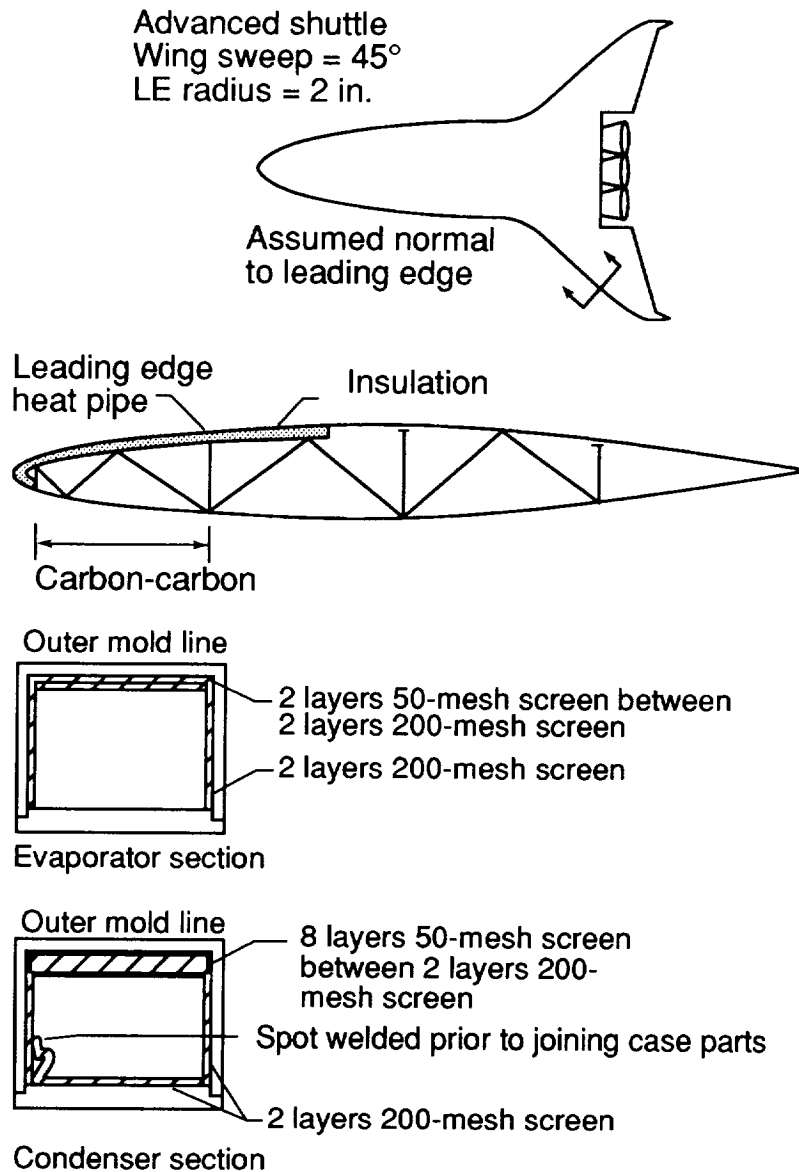


Figure 14. - Heat-pipe-cooled wing leading edge design for an advanced space transportation system.

SIX-FOOT-LONG HASTELLOY-X/SODIUM HEAT PIPE DURING INDUCTION HEATING TEST AT LOS ALAMOS NATIONAL LABORATORY

A radio frequency (RF) induction heating device was used for all of the testing of the Hastelloy-X/sodium heat pipe. To simulate the wing leading edge heating, a shaped RF induction concentrator was used. A mica sheet was attached to the heat pipe to insulate electrically the heat pipe from the RF concentrator. The specially designed heat source provided a stagnation zone heat input over the outside surface of the evaporator region of the heat pipe. The heat pipe was instrumented with eight thermocouples which were spot welded to the external surface. Thermocouples were attached to the middle of the evaporator and each end of the evaporator section, and five equally spaced thermocouples were located in the condenser section.

Several start-up tests of the heat pipe were conducted. It was found that the heat pipe was extremely sensitive to transients, both during and after start-up. A photograph of the heat pipe during steady state operation is shown in figure 15. It was observed that insulating three sides of the condenser assisted in both the start-up and steady-state operation of the heat pipe. The insulation reduced the axial thermal load on the heat pipe, and thus reduced the pumping requirements of the wick. Post test permeability analyses revealed that the composite wick, using a 200-mesh screen at the liquid vapor interface for high capillary pressures, did not provide the required pumping pressure. The inability to generate the required pumping pressures was probably due to a breach in the 200-mesh screen. With a tear in the 200-mesh screen, the maximum pumping pressures that could be generated resulted from the 50-mesh screen which was located next to the 200-mesh screen. Estimates of the capillary size which would cause a wicking limit to occur during the induction heating test are consistent with a 50-mesh screen and, thus tend to verify that a breach in the 200-mesh screen had occurred.

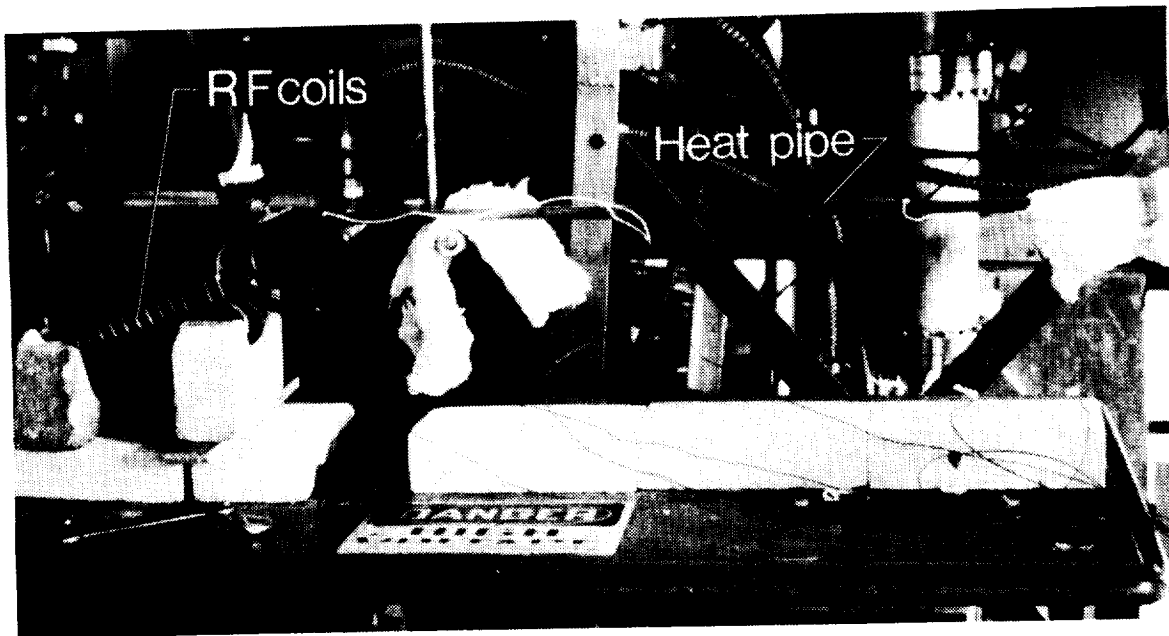


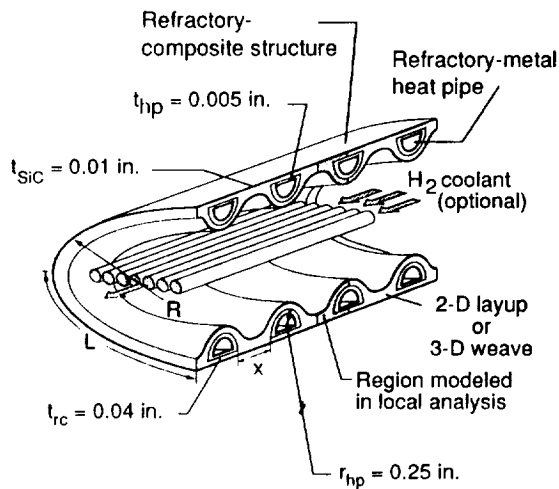
Figure 15. - Six-foot-long Hastelloy-X/sodium heat pipe during induction heating test at Los Alamos National Laboratory.

HEAT-PIPE-COOLED WING LEADING EDGE FOR THE NATIONAL AERO-SPACE PLANE

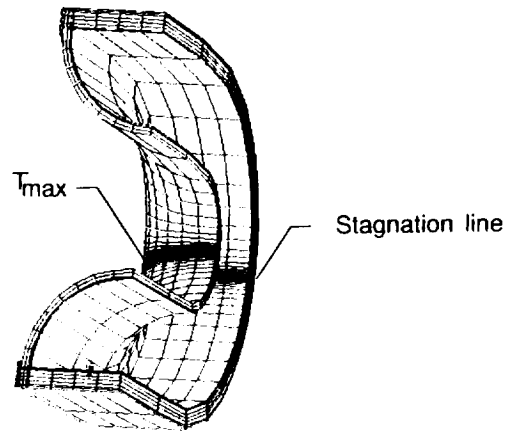
Heat pipes are being considered for use on the wing leading edge of the NASP. The concept being considered has refractory-metal heat pipes embedded in a refractory-composite structure. The refractory-composite structure is protected from oxidation by a thin layer of silicon carbide (SiC). If external radiative cooling to space is inadequate to reduce effectively the leading edge temperatures, additional radiative cooling to a heat exchanger, located inside the wing leading edge, may be used. Hydrogen fuel would be used for a coolant in the heat exchanger.

A schematic diagram of the heat-pipe-cooled wing leading edge for NASP is shown in figure 16. A region of both the upper and the lower surface of the leading edge is shaded to represent the region modeled in the finite element analysis. Since the maximum leading edge temperatures occur midway between heat pipes in the stagnation region, a simplified 1-D or 2-D analysis cannot adequately model the leading edge temperatures. Thus, a 3-D finite-element analysis was used for the thermal parametric study. Two different boundary conditions were considered for the interior of the leading edge: one for internal radiative cooling (cooled), and the other for a surface with no internal radiative cooling (uncooled). Thermal effects of both the 2-D layup and the 3-D woven refractory composite architectures were considered, and different refractory metals were considered for the heat pipe container. The heat pipe wall thickness, t_{hp} , remained constant at 0.005 in., the SiC coating thickness, t_{SiC} , remained constant at 0.010 in., the refractory-composite thickness, t_{rc} , remained constant at 0.040 in., and the semicircular heat-pipe cross-sectional radius, r_{hp} , remained constant at 0.25 in. The leading edge radius, heat-pipe length, and heat-pipe spacing were varied in the parametric analysis.

The Engineering Analysis Language (EAL) system (ref. 18) was used for the finite-element analysis. A parametric model was constructed using the Execution Control System language in EAL which enabled the physical dimensions of the leading edge, the refractory-composite and heat-pipe material properties, and the boundary conditions to be varied easily. The forward portion of the finite element model shown on the right hand side of figure 16 represents a leading edge with a 0.5-in. radius, and the lengths of the upper and lower surfaces have been reduced to 0.5 in. to allow all the elements to be included in the illustration. Elements are concentrated in the stagnation region where the temperature and heat flux gradients are the largest. Temperature dependent material properties are used throughout the analysis.



PARAMETERS USED IN FINITE ELEMENT MODEL



Temperature dependent properties

Thermal analysis:	4500 elements
Structural analysis:	14000 elements

FINITE ELEMENT MODEL

Figure 16. - Heat-pipe-cooled wing leading edge for the National Aero-Space Plane.

THERMAL FINITE ELEMENT ANALYSIS OF HEAT-PIPE-COOLED WING LEADING EDGE FOR NASP

The thermal finite element model and the parameters varied in the design study are shown in figure 17. The choice of refractory metals has been shown to have little effect on the maximum leading edge temperatures. In addition, the through-the-thickness thermal conductivity of 2-D advanced carbon-carbon (ACC) material is very low and has been shown to result in excessively high temperatures. As a result, a tungsten (W) heat pipe embedded in 3-D carbon/silicon-carbide (C/SiC) material is considered as a baseline for a series of parametric studies which follow. In each case, heat pipes are considered to extend from a given location on the bottom surface of the leading edge, around the stagnation region and for the same distance along the top surface of the leading edge. The heat pipe is assumed to have a "D-shaped" cross section, with an internal radius of 0.25 in. The parameters that have a significant effect on the maximum leading edge temperatures are the internal boundary condition (cooled or uncooled), the heat-pipe length, the distance between heat pipes, and the leading edge radius. The effect of the heat-pipe length, distance between heat pipes, and internal boundary condition on maximum leading edge temperatures are evaluated.

The maximum leading edge temperature is shown in figure 17 as a function of the heat pipe length ($12 \text{ in.} \leq L \leq 36 \text{ in.}$), the distance between heat pipes ($0.02 \text{ in.} \leq x \leq 0.20 \text{ in.}$) and the internal boundary condition (insulated and radiatively cooled (labeled uncooled and cooled, respectively, in the figure)). As expected, the maximum leading edge temperature increases with increasing distance between heat pipes. The maximum temperature decreases with increasing heat pipe length. This decrease in temperature results from an increase in the surface area that is at high temperature, and thus an increase in radiative heat losses. It is desirable to develop a passive design with no active hydrogen cooling. The heat-pipe-cooled leading edge concept enables a passive design for the assumed NASP heat flux distribution. Though the actively cooled designs result in temperatures below $3000 \text{ }^\circ\text{F}$ for even a 12-in.-long heat pipe with 0.20 in. between heat pipes, the active cooling provides a weight penalty such that longer heat pipes spaced closer together with no internal cooling is a more favorable design. As a result, an insulated design is chosen as the baseline. An uncooled leading edge with 30-in.-long heat pipes can maintain maximum temperatures below $2765 \text{ }^\circ\text{F}$. The heat pipe operating temperature for this case is $2197 \text{ }^\circ\text{F}$. Thus, the baseline design includes 30-in.-long heat pipes embedded in C/SiC, with heat pipes spaced 0.06 in. apart. Internal cooling is not used in the baseline design and the baseline design is represented by the large circular symbol in figure 17.

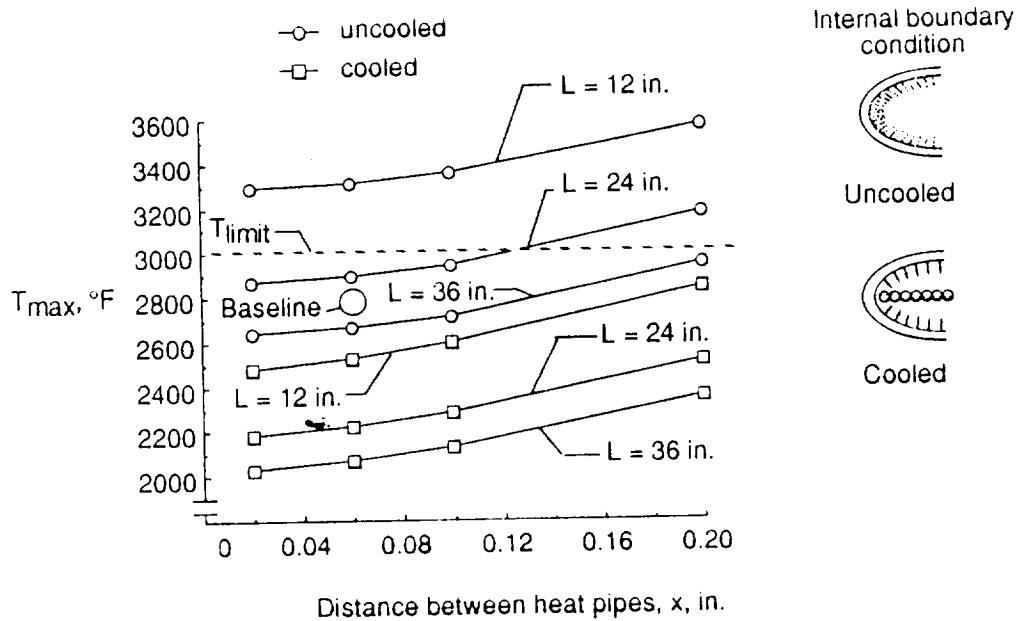


Figure 17. - Thermal finite element analysis of heat-pipe-cooled wing leading edge for NASP.

THERMAL/STRUCTURAL ANALYSIS OF HEAT-PIPE-COOLED WING LEADING EDGE FOR NASP

The finite element analysis used for the thermal parametric study was also used for the thermal-structural analysis. However, a much more refined mesh was used in the thermal-structural analysis than in the thermal analysis alone. The refractory-metal heat-pipe container material considered was molybdenum-47 wt.% rhenium (Mo-47Re) alloy. A 1-in. leading-edge radius was assumed. The thermal stresses in the chordwise direction for a Mo-47Re heat pipe embedded in a C/SiC leading edge are shown in figure 18. Chordwise normal stresses in the thin refractory-metal heat-pipe container material are compressive and quite high. The compressive stresses are higher than the proportional limit for the Mo-47Re at elevated temperature and stress relief by plastic deformation is expected. There are several reasons for the excessively large calculated stresses. The primary reason for the large stresses in the chordwise direction is that the finite element analysis is not able to account for slippage of the heat pipes in the composite structure. Slippage is expected because of the coefficient-of-thermal-expansion mismatch between the refractory-metal and the refractory-composite materials and the lack of sufficient bond strength between the materials. In addition, the analysis is linear and cannot adequately represent the nonlinear behavior of the materials.

Since the refractory-composite material is more brittle than the refractory-metal material and has very low through-the-thickness strength, it is believed that the principal mode of failure will be by cracking of the refractory-composite structure between adjacent heat pipes. This type of problem at elevated temperatures has been experienced previously with cracking of ceramic material with metallic inclusions. Researchers at Thermo Electron Corporation (refs. 19-20) alleviated thermal cracking in the SiC coating of a refractory-metal heat pipe by including a soft carbon middle layer which served as a means for strain isolation. In addition, researchers at General Dynamics were able to embed successfully refractory-metal tubes within C/SiC material (refs. 21-22) and develop an advanced actively cooled panel by tailoring the carbon-fiber preform to minimize the thermal expansion mismatch.

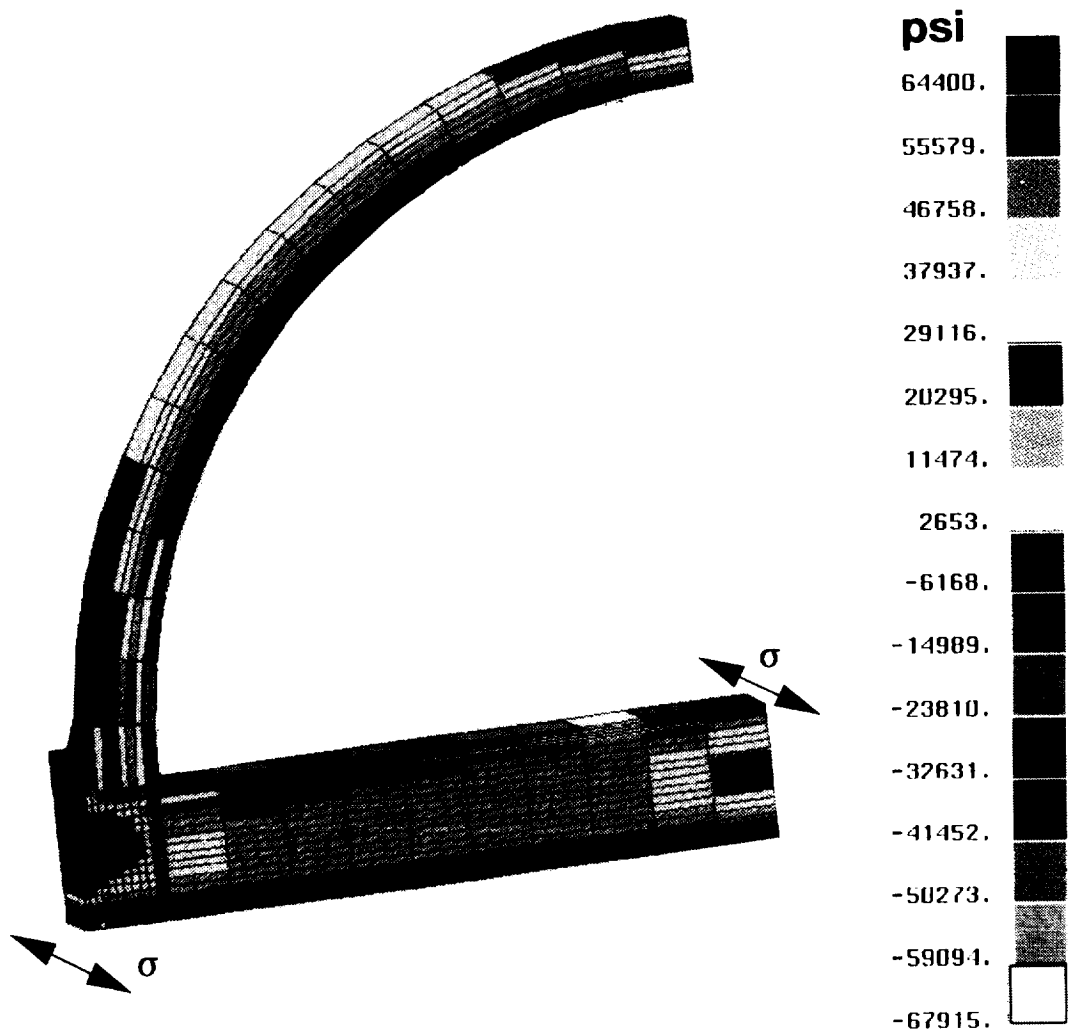


Figure 18. - Thermal/structural analysis of heat-pipe-cooled wing leading edge for NASP.

HEAT PIPE FABRICATION

The first step in the fabrication of the refractory-composite/heat-pipe-cooled leading edge for NASP is the fabrication of curved "D-shaped" refractory-metal tubes. "D-shaped" molybdenum tubes have been drawn by Tecomet Corporation. An attempt has been made to bend a 6-in.-long Mo "D-shaped" tube at Los Alamos National Laboratory (LANL). The tube was successfully bent at an elevated temperature. However, crimping of the tube occurred on the curved, inner portion of the tube, as shown in the top photograph of figure 19. Further attempts will be made to develop a procedure to bend the tubes and eliminate crimping of the inner surface. A screen wick will be used to pump the working fluid from the condenser to the evaporator. A photograph of the screen wick inserted in a Mo "D-shaped" tube is shown in the bottom photograph of figure 19. The wick is made up of three layers of 400-mesh Mo-41Re screen. A 0.1-in.-diameter artery can also be seen in the photograph. The purpose of the artery is to aid in the pumping of the working fluid with a minimum pressure loss.

Initially, "D-shaped" Mo tubes were drawn. However, due to ductility requirements at room temperature, Mo-Re is thought to be a more suitable material. Preliminary tests are underway to evaluate the ductility of different Mo-Re alloys. A Mo-11Re tube was successfully bent at room temperature, after which it was heated for four hours at 3000 °F. The tube then fractured when a subsequent attempt was made to bend it at room temperature. The tube was then bent at 392 °F. At this elevated temperature, the tube still fractured, but survived a bend of approximately 90° before fracture occurred. It is known that a higher rhenium content increases the ductility of molybdenum. Several alloys of molybdenum with higher percentages of rhenium content are now being considered for use as the heat-pipe container material.

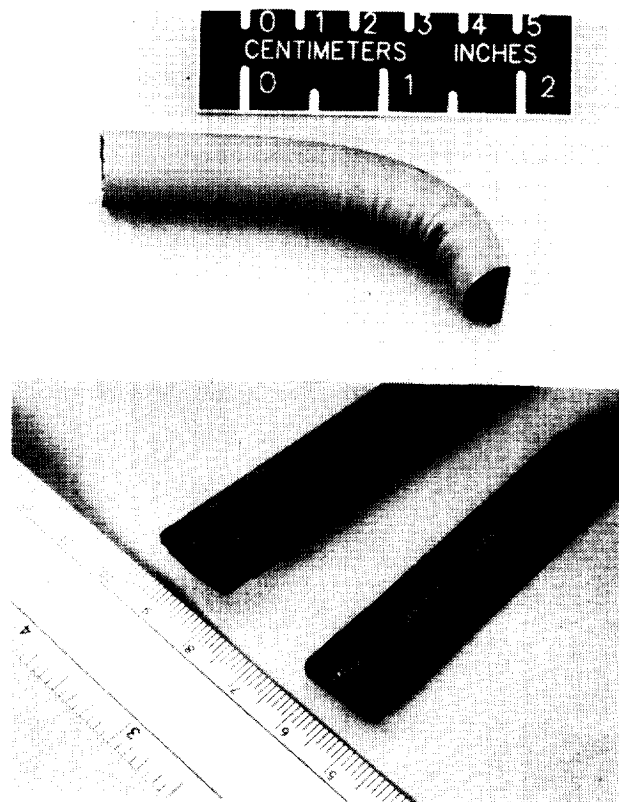


Figure 19. - Heat pipe fabrication.

EMBEDDING HEAT PIPES IN A REFRACTORY-COMPOSITE STRUCTURE

In the construction of the heat-pipe-cooled leading edge, several design considerations can be incorporated to reduce the thermal stresses and alleviate the potential problem of cracks in the C/SiC due to excessive through-the-thickness normal stresses. To reduce the heat pipe thermal stresses in the through-the-thickness and spanwise directions, a strain isolator can be placed between the heat pipe and the refractory-composite structure. If the strain isolator completely surrounds the heat pipe, it will add thermal resistance on the flat part of the heat pipe where heat is entering the heat pipe. In the stagnation region, this added thermal resistance cannot be tolerated because of the magnitude of heating there. However, if the strain isolator covers only the curved part of the heat pipe, as shown in figure 20, the heat pipe will be allowed to grow in the through-the-thickness, spanwise, and chordwise directions with minimal increase in maximum temperatures. For the uncooled designs, no heat is lost from the interior surface, so the thermal effect of the strain isolator should be negligible. In addition, the strain isolator will help reduce the stresses in the chordwise direction. As discussed previously, the heat pipe is expected to grow in the chordwise direction more than the refractory composite. A soft material can be placed at the ends of the heat pipes to allow for thermal expansion in the chordwise direction. The addition of a soft carbon strain isolator is similar in purpose to Thermo Electron's use of a soft carbon strain isolator sandwiched between W and SiC, in the construction of a ceramic liquid-metal heat pipe (refs. 19-20).

Tests are planned to evaluate the effectiveness of three different woven carbon preforms with strain isolators for reducing and surviving the thermal stresses. One preform that is being considered is a flat panel with webs that will be folded over the "D-shaped" heat pipe and strain isolator. The second preform being considered uses woven "D-shaped" channels through which the heat pipe and strain isolator will be inserted. The final preform being considered involves weaving the preform around a rectangular cross section consisting of the "D-shaped" heat pipe and a concave shaped strain isolator.

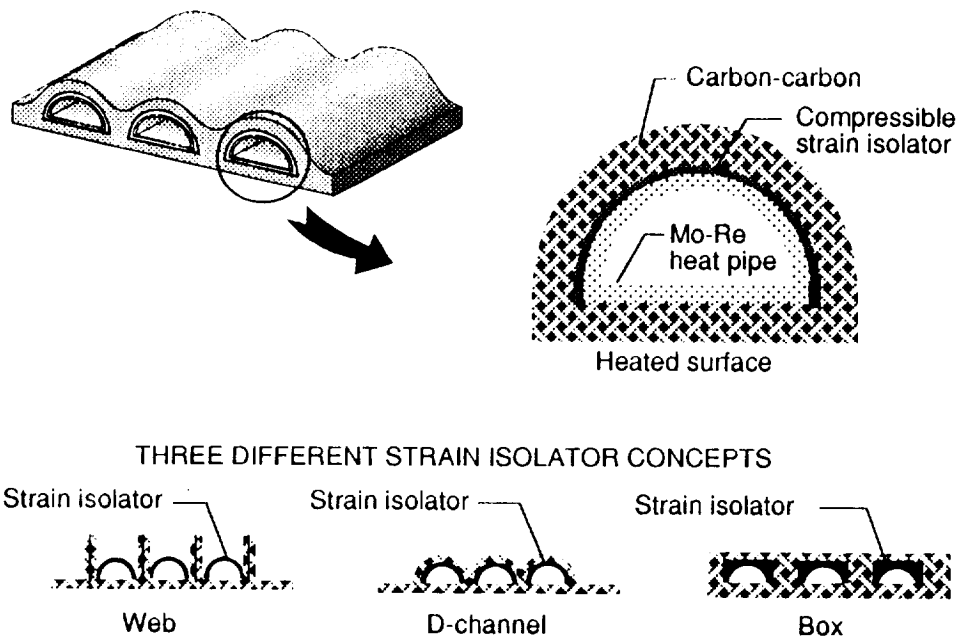


Figure 20. - Embedding heat pipes in a refractory-composite structure.

SUMMARY

Heat pipes have been considered for use on wing leading edge for over 20 years. Early concepts envisioned metal heat pipes cooling a metallic leading edge. Several superalloy/sodium heat pipes were fabricated and successfully tested for wing leading edge cooling. Results of radiant heat and aerothermal testing indicate the feasibility of using heat pipes to cool the stagnation region of shuttle-type space transportation systems. The test model withstood a total of seven radiant heating tests, eight aerothermal tests, and twenty-seven supplemental radiant heating tests. Cold-wall heating rates ranged from 21 to 57 Btu/ft²-s and maximum operating temperatures ranged from 1090 to 1520 °F. Follow-on studies investigated the application of heat pipes to cool the stagnation regions of single-stage-to-orbit and advanced shuttle vehicles. Results of those studies indicate that a "D-shaped" structural design can reduce the mass of the heat-pipe concept by over 44 percent compared to a circular heat-pipe geometry. Simple analytical models for heat-pipe startup from the frozen state (working fluid initially frozen) were adequate to approximate transient, startup, and steady-state heat-pipe performance. Improvement in analysis methods has resulted in the development of a finite-element analysis technique to predict heat-pipe startup from the frozen state. However, current requirements of light-weight design and reliability suggest that metallic heat pipes embedded in a refractory composite material should be used. This concept is the concept presently being evaluated for NASP.

A refractory-composite/heat-pipe-cooled wing leading edge is currently being considered for the National Aero-Space Plane (NASP). This concept uses high-temperature refractory-metal/lithium heat pipes embedded within a refractory-composite structure and is significantly lighter than an actively cooled wing leading edge because it eliminates the need for active cooling during ascent and descent. Since the NASP vehicle uses cryogenic hydrogen to cool structural components and then burns this fuel in the combustor, hydrogen necessary for descent cooling only, when the vehicle is unpowered, is considered to be a weight penalty. Details of the design of the refractory-composite/heat-pipe-cooled wing leading edge are currently being investigated. Issues such as thermal contact resistance and thermal stress are also being investigated.

REFERENCES

1. Silverstein, C. C.: A Feasibility Study of Heat-Pipe-Cooled Leading Edges for Hypersonic Cruise Aircraft. NASA CR 1857, 1971.
2. Niblock, G. A.; Reeder, J. C.; and Huneidi, F.: Four Space Shuttle Wing Leading Edge Concepts. *Journal of Spacecraft and Rockets*, Vol. 11, No. 5, May 1974, pp. 314-320.
3. Alario, J. P. and Prager, R. C.: Space Shuttle Orbiter Heat Pipe Application. NASA CR-128498, 1972.
4. Anon.: Study of Structural Active Cooling and Heat Sink Systems for Space Shuttle. NASA CR-123912, 1972.
5. Anon.: Design, Fabrication, Testing, and Delivery of Shuttle Heat Pipe Leading Edge Test Modules. NASA CR-124425, 1973.
6. Camarda, Charles J.: Analysis and Radiant Heating Tests of a Heat-Pipe-Cooled Leading Edge. NASA TN D-8468, August 1977.
7. Camarda, Charles J.: Aerothermal Tests of a Heat-Pipe-Cooled Leading Edge at Mach 7. NASA TP-1320, November 1978.
8. Camarda, Charles J.; and Masek, Robert V.: Design, Analysis and Tests of a Shuttle-Type Heat-Pipe-Cooled Leading Edge. *Journal of Spacecraft and Rockets*, Vol. 18, No. 1, January-February, 1981.
9. Peebles, M. E.; Reeder, J. C.; and Sontag, K. E.: Thermostructural Applications of Heat Pipes. NASA CR-159096, 1979.
10. Boman, B. L.; Citrin, E. C.; Garner, E. C.; and Stone, J. E.: Heat Pipes for Wing Leading Edges of Hypersonic Vehicles. NASA CR-181922, January 1990.
11. Boman, B.; and Elias, T.: Tests on a Sodium/Hastelloy X Wing Leading Edge Heat Pipe for Hypersonic Vehicles. Presented at the AIAA/ASME 5th Joint Thermophysics and Heat Transfer Conference, June 18-20, 1990, Seattle, WA. AIAA-90-1759.
12. Colwell, Gene T.; Jang, Jong H.; and Camarda, Charles J.: Modeling of Startup from the Frozen State. Paper presented at the Sixth International Heat Pipe Conference, Grenoble, France, May 25-29, 1987.
13. Glass, David E.; and Camarda, Charles J.: Results of Preliminary Design Studies of a Carbon-Carbon/Refractory-Metal Heat-Pipe Wing Leading Edge. NASP TM 1071, July 1989.
14. Glass, David E.; and Camarda, Charles J.: Preliminary Thermal/Structural Analysis of a Carbon-Carbon/Refractory-Metal Heat-Pipe-Cooled Wing Leading Edge. Paper Presented at the First Thermal Structures Conference, University of Virginia, Charlottesville, Virginia, November 13-15, 1990.
15. Dunn, P.; and Reay, D. A.: Heat Pipes. Pergamon Press, Oxford, 1982.

16. Chi, S. W.: Heat Pipe Theory and Practice. Hemisphere Publishing Corporation, Washington, D.C., 1976.
17. Cotter, T. P.: Heat Pipe Startup Dynamics. Heat Pipes, Volume XVI of AIAA Selected Reprint Series, edited by C. L. Tien, September 1973, pp. 42-45.
18. Whetstone, W. D.: EISI-EAL Engineering Analysis Language Reference Manual - EISI-EAL System Level 2091. Engineering Information Systems, Inc., July 1983.
19. Reagan, P.; Miskolczy, G.; and Huffman, F.: Development of a CVD Silicon-Carbide-Graphite-Tungsten Heat Pipe Structure. AIAA 16th Thermophysics Conference, Palo Alto, CA, June 23-25, 1981. AIAA-81-1160.
20. Reagan, Peter; Lieb, David; Miskolczy, Gabor; Goodale, Douglass; and Huffman, Fred: CVD Fabrication of Thermionic Converter and Heat Pipe, Ceramic Engineering and Science Proceedings, Vol. 4, July-August 1983, pp. 520-532.
21. Henson, M. C.; and Fetter, S. D.: Development of Refractory Materials for Actively Cooled Hypersonic Airframe Panels. Presented at the Tenth National Aero-Space Plane Technology Symposium, April 23-26, 1991. Paper No. 180.
22. Henson, M. C.; Adams, R. D.; Ahmad, A.; Fetter, S. D.; Kennedy, S. E.; Saathoff, W. M.; and Serinken, D. H.: Development of Refractory Composite Actively Cooled Panels for the NASP Airframe. Presented at the Ninth National Aero-Space Plane Technology Symposium, November 1-2, 1990. Paper No. 177.

ATTENDEES:

John Allred
NASA Langley
MS 443
Hampton, VA 23681

David M. Barrett
NASA Langley
MS 191
Hampton, VA 23681

Max L. Blosser
NASA Langley
MS 396
Hampton, VA 23681

Lynn Bowman
NASA Langley
MS 396
Hampton, VA 23681

Obie Bradley
NASA Langley
MS 434
Hampton, VA 23681

Greg Buck
NASA Langley
MS 408
Hampton, VA 23681

Dr. John Buckley
NASA Langley
MS 399
Hampton, VA 23681

Dr. Charles J. Camarda
NASA Langley
MS 396
Hampton, VA 23681

Dr. Ann Carlson
NASA Langley
MS 366
Hampton, VA 23681

John Chapman
NASA Langley
MS 234
Hampton, VA 23681

Dr. Sang H. Choi
NASA Langley
MS 493
Hampton, VA 23681

Craig Collier
NASA Langley
MS 350
Hampton, VA 23681

Dr. Ron Clark
NASA Langley
MS 194
Hampton, VA 23681

Don Curry
NASA Johnson
ES32
Houston, TX 77058

Kamran Daryabeigi
NASA Langley
MS 234
Hampton, VA 23681

John Deaton
NASA Langley
MS 213
Hampton, VA 23681

Dr. Rome Dunn
ME Dept.
NCA&T State University
Greensboro, NC 27411

Dr. Marco A. Egoavil
NASA Langley
MS 440
Hampton, VA 23681

Robin C. Elder
NASA Langley
MS 434
Hampton, VA 23681

R. E. Ellis
309 W. Brown Street
Souderton, PA 18164

Richard A. Foss
NASA Langley
MS 431
Hampton, VA 23681

Dr. David E. Glass
NASA Langley
MS 396
Hampton, VA 23681

Dr. Howard Goldstein
NASA Ames
MS 229-3
Moffett Field, CA 94035

Mark P. Gorton
NASA Langley
MS 396
Hampton, VA 23681

Dr. Roop Gupta
NASA Langley
MS 366
Hampton, VA 23681

Charles Hackett
NASA Langley
MS 408
Hampton, VA 23681

Tim Hackett
McDonnell Aircraft
P. O. Box 516
St. Louis, MO 61366-0516

Dr. Harris Hamilton
NASA Langley
MS 366
Hampton, VA 23681

Lin Hartung
NASA Langley
MS 366
Hampton, VA 23681

Jennifer Heeg
NASA Langley
MS 243
Hampton, VA 23681

Chip Holloway
NASA Langley
MS 433
Hampton, VA 23681

Thomas Horvath
NASA Langley
MS 408
Hampton, VA 23681

Bill James
NASA Langley
MS 189
Hampton, VA 23681

Stuart C. Jones
NASA Langley
MS 350
Hampton, VA 23681

H. Neale Kelly
NASA Langley
MS 396
Hampton, VA 23681

James Kervin
Technetics Corporation
1600 Industrial Drive
DeLand, FL 32724

William L. Kleb
NASA Langley
MS 366
Hampton, VA 23681

Dr. John J. Korte
NASA Langley
MS 156
Hampton, VA 23681

Dr. W. S. Lassiter
NASA Langley
MS 431
Hampton, VA 23681

Dr. Howard G. Maahs
NASA Langley
MS 188B
Hampton, VA 23681

Ian O. MacConochie
NASA Langley
MS 365
Hampton, VA 23681

Dr. John B. Malone
NASA Langley
MS 244
Hampton, VA 23681

Rob Marshall
NASA Langley
MS 490
Hampton, VA 23681

Robert R. McWithey
NASA Langley
MS 396
Hampton, VA 23681

Dr. R. C. Montgomery
NASA Langley
MS 161
Hampton, VA 23681

Dr. Robert T. Neece
NASA Langley
MS 490
Hampton, VA 23681

T. G. Nieh
Lockheed
3251 Hanover St.
Dalo Alto, CA 94304

Craig H. Ohlhorst
NASA Langley
MS 191
Hampton, VA 23681

F. R. Parker
NASA Langley
MS 231
Hampton, VA 23681

Dennis Petley
NASA Langley
MS 350
Hampton, VA 23681

Dr. Donald H. Phillips
NASA Langley
MS 231
Hampton, VA 23681

Anthony S. Pototzky
NASA Langley
MS 243
Hampton, VA 23681

Phil Ransone
NASA Langley
MS 191
Hampton, VA 23681

Dr. Dan Rasky
NASA Ames
MS 234-1
Moffett Field, CA 94035

Matt Rhode
NASA Langley
MS 408
Hampton, VA 23681

Dr. Donald Rummler
NASA Langley
MS 244
Hampton, VA 23681

Washito A. Sasamoto
NASA Langley
MS 288
Hampton, VA 23681

Dr. James W. Sawyer
NASA Langley
MS 396
Hampton, VA 23681

Stephen J. Scotti
NASA Langley
MS 396
Hampton, VA 23681

Jeff Seaton
NASA Langley
Hampton, VA 23681

John L. Shideler
NASA Langley
MS 396
Hampton, VA 23681

Shivakuhar
ME Dept.
NCA&T State University
Greensboro, NC 27411

Joseph G. Sikora
NASA Langley
MS 238
Hampton, VA 23681

Howard Stone
NASA Langley
MS 365
Hampton, VA 23681

Dr. Ted Swanson
NASA Goddard
Code 732-2
Greenbelt, MD 20771

Doyle P. Swofford
NASA Langley
MS 431
Hampton, VA 23681

Bob Tolokan
Technetics Corporation
1600 Industrial Drive
Deland, FL 32724

D. A. Throckmorton
NASA Langley
MS 366
Hampton, VA 23681

Dr. Wallace L. Vaughn
NASA Langley
MS 191
Hampton, VA 23681

Frank Vause
NASA Langley
MS 396
Hampton, VA 23681

Terryl Wallace
NASA Langley
MS 194
Hampton, VA 23681

Nate Watson
NASA Langley
Hampton, VA 23681

Dr. Christopher S. Welch
NASA Langley
MS 231
Hampton, VA 23681

R. E. Wright
NASA Langley
MS 234
Hampton, VA 23681

Kathryn Wurster
NASA Langley
MS 365
Hampton, VA 23681

Bob Yamaki
NASA Langley
MS 191
Hampton, VA 23681

REPORT DOCUMENTATION PAGE			Form Approved OMB No. 0704-0188	
Public reporting burden for this collection of information is estimated to average 1 hour per response, including the time for reviewing instructions, searching existing data sources, gathering and maintaining the data needed, and completing and reviewing the collection of information. Send comments regarding this burden estimate or any other aspect of this collection of information, including suggestions for reducing this burden, to Washington Headquarters Services, Directorate for Information Operations and Reports, 1215 Jefferson Davis Highway, Suite 1204, Arlington, VA 22202-4302, and to the Office of Management and Budget, Paperwork Reduction Project (0704-0188), Washington, DC 20503.				
1. AGENCY USE ONLY (Leave blank)	2. REPORT DATE October 1992	3. REPORT TYPE AND DATES COVERED Conference Publication		
4. TITLE AND SUBTITLE Current Technology for Thermal Protection Systems		5. FUNDING NUMBERS WU 506-43-31-04		
6. AUTHOR(S) Stephen J. Scotti, Compiler				
7. PERFORMING ORGANIZATION NAME(S) AND ADDRESS(ES) NASA Langley Research Center Hampton, VA 23681-0001		8. PERFORMING ORGANIZATION REPORT NUMBER L-17118		
9. SPONSORING/MONITORING AGENCY NAME(S) AND ADDRESS(ES) National Aeronautics and Space Administration Washington, DC 20546-0001		10. SPONSORING/MONITORING AGENCY REPORT NUMBER NASA CP-3157		
11. SUPPLEMENTARY NOTES				
12a. DISTRIBUTION/AVAILABILITY STATEMENT Unclassified-Unlimited Subject Category -18		12b. DISTRIBUTION CODE		
13. ABSTRACT (Maximum 200 words) Interest in thermal protection systems for high-speed vehicles is increasing because of the stringent requirements of such new projects as the Space Exploration Initiative, the National Aero-Space Plane, and the High-Speed Civil Transport, as well as the needs for improved capabilities in existing thermal protection systems in the Space Shuttle and in turbojet engines. This selection of 13 papers from NASA and industry summarizes the history and operational experience of thermal protection systems utilized in the national space program to date, and also covers recent development efforts in thermal insulation, refractory materials and coatings, actively cooled structures, and two-phase thermal control systems.				
14. SUBJECT TERMS Thermal protection systems; Thermal insulations; Heat pipes; High temperature materials and coatings; Active cooling			15. NUMBER OF PAGES 326	
			16. PRICE CODE A15	
17. SECURITY CLASSIFICATION OF REPORT Unclassified	18. SECURITY CLASSIFICATION OF THIS PAGE Unclassified	19. SECURITY CLASSIFICATION OF ABSTRACT Unclassified	20. LIMITATION OF ABSTRACT	

NSN 7540-01-280-5500

Standard Form 298 (Rev. 2-89)
Prescribed by ANSI Std. Z39-18
298-102

NASA Langley, 1992